Studies of the Martian Upper Atmosphere with the UCL Mars Thermosphere and Ionosphere General Circulation Model

William Peter Nicholson

Submitted for the degree of Doctor of Philosophy

Atmospheric Physics Laboratory

Department of Physics and Astronomy

University College London

October 2010

I, *William Peter Nicholson*, confirm that the work presented in this thesis is my own. Where information has been derived from other sources, I confirm that this has been indicated in the thesis.

Abstract

Simulations of the Martian upper atmosphere have been conducted with 'MarTIM', University College London's Martian thermosphere and ionosphere general circulation model (GCM). MarTIM, a finite difference model, solves the coupled non-linear Navier-Stokes equations of continuity and momentum as well as an energy equation with calculations conducted on a fixed co-rotating grid of variable size in the pressure coordinate system. From its lower boundary of 0.883 Pa (∼60 km) to its upper boundary of 9.9×10^{-8} Pa (∼200−350 km), it evaluates the main sources of solar forcing (EUV/UV and IR absorption) while self-consistently determining the composition of four of the major gas species, CO_2, N_2, CO and O. These four major gases are mutually diffused throughout the model in a typical run.

Development of MarTIM includes a consideration of the importance of neutral species diffusion and advection on the thermodynamics of the modelled Martian atmosphere. The influence on the modelled atmosphere of including additional neutral species is investigated. Next, a new infrared heating parameterization has been introduced from background research of detailed non-LTE modelling. This has allowed MarTIM to study thermospheric polar warming features as found in Mars Odyssey accelerometer data.

MarTIM's lower boundary is coupled to the Mars Climate Database (MCD v4.3) developed by the University of Oxford, the Open University and Laboratoire de Météorologie Dynamique. This database of GCM results provides MarTIM a physically self-consistent lower boundary derived from multiple runs of the aforementioned circulation models. Consequently the effects of dust storms, non-migrating tides and the influence of Martian topography are studied by prescription of MarTIM's lower boundary. MarTIM is also compared against density and temperature measurements derived from SPICAM stellar occultation profiles.

Lastly, a new ionospheric code has been developed through collaboration with Laboratoire de Planétologie de Grenoble. This has provided a more sophisticated ionosphere model that solves a one-dimensional kinetic Boltzmann transport equation for the suprathermal population of electrons present in the Martian ionosphere. MarTIM can now self-consistently describe an ionosphere produced by both primary (photoionisation) and secondary ionisation (suprathermal electron propagation). This new ionospheric model has been used to study the variation in secondary ionization efficiency (ratio of secondary to primary ion production) through a large range of seasonal and solar conditions.

Acknowledgements

My PhD simply would not have been completed had it not been for the kind and generous help of so many people. Too many to mention, but here are the most important!

- Atmospheric Physics Laboratory staff - in particular my primary supervisor Professor Alan D. Aylward and secondary supervisor Dr Anasuya Aruliah.
- Dr Chris Smith, formerly of the Atmospheric Physics Laboratory - for patiently and very helpfully answering my many, many questions as well as offering invaluable advice and support.
- Dr John Deacon, Astrophysics Computer Manager, UCL Physics and Astronomy, Astrophysics Group - many thanks for keeping my eMac in working order!
- Dr Jean Lilensten and Dr Guillaume Gronoff, Laboratoire de Planétologie de Grenoble and Dr Cyril Simon, Belgian Institute for Space Aeronomy - it was a pleasure working with you all! I am particularly proud to have published my first paper with you. Hopefully we can work together again one day soon!
- Dr Paul Withers, Center for Space Physics, Boston University - for kindly providing me the dataset of Mars Odyssey aerobraking measurements.
- Dr François Forget, Laboratoire de Météorologie Dynamique, Paris - for kindly providing me the dataset of Mars Express UV spectrometer density measurements.

And finally, many thanks to the two examiners, Professor Andrew J. Coates, Mullard Space Science Laboratory and Professor Peter L. Read, Oxford University, for taking the time to consider the work described in this thesis.

For Mum

Contents

List of Figures

List of Tables

Chapter 1

Introduction and Background Theory

1.1 Introduction to the Martian Environment

Mars, fourth planet from the Sun, ranking third in brightness as seen from Earth, continues to intrigue space scientists and astronomers around the globe. Its dramatic environment, dynamic and highly variable atmosphere has been the focus of no less than sixteen space agency missions since the Viking landers touched down in the mid-1970's. At the time of writing (early 2010) there are two unmanned exploration 'rovers' and one lander craft carrying out scientific experiments on the surface of Mars as well as three orbiters observing, taking measurements or otherwise studying its atmosphere. Furthermore with both European and American space agencies placing Mars exploration as major parts of their respective space science strategies, often with a manned mission as the ultimate goal, one can well imagine the exploration of Mars with such focus continuing through the next few decades.

In prehistoric times Mars intrigued humanity because of its blood-red colour, which was associated with warfare by the Babylonian, Greek and Roman civilisations. Indeed the planet is named Mars after the Roman god of war. With the advent of the telescope astronomers were able to observe and study Mars' many varied features. For example, from his observations of the Syrtis Major feature Christiaan Huygens concluded in 1659 that the rotation period of Mars was about 24 hours (Lang and Whitney, 1991). We now know the exact Martian day to be 24 hours, 37 minutes 22.6 seconds, remarkably similar to Earth. Further comparisons can be drawn between Earth and Mars with the rotational axes of both planets being tilted to almost the same degree (obliquity 23.45° and 25.19° respectively) such that both planets experience seasons (although Mars does take longer to complete an orbit of the Sun; 686 days to Earth's 365). Later observations established the presence of an atmosphere on Mars by virtue of (a) the northern and southern polar caps that wax and wane with the seasons as gaseous material is condensed from and sublimed to the atmosphere (James et al., 1992), (b) the formation of yellow dust clouds that

occasionally grow and coalesce to envelope the entire planet (Kahn et al., 1992) and (c) the repeated appearance of white clouds over the Martian surface (Lang and Whitney, 1991).

The fundamental attributes of the Martian atmosphere remained only vaguely known for many centuries until the dawn of space-age exploration. The Viking landers of the mid-1970's established the principal chemical components as they descended to the surface. Carbon dioxide, nitrogen and argon are the major species with trace amounts of molecular oxygen and carbon monoxide (Lang and Whitney (1991), see Table 1.1(a)). The Martian atmosphere is very thin with a surface pressure only $1/160^{th}$ that of the Earth's and since CO_2 is such an active coolant it is also a cold atmosphere with an average temperature at the Viking 1 lander site of $-63°$C. This combination makes Mars' atmosphere capable of holding only a very little water, it is in fact saturated with water vapour, always on the verge of snowing. As the surface temperature drops with the approach of winter carbon dioxide begins to condense onto the surface at high latitudes. Whether the CO_2 deposits are the result of direct vapor condensation at the ground (frost) or of atmospheric condensation and precipitation (snow) is still unknown (Giuranna et al., 2008) but certainly at the poles broad white polar caps of frozen carbon dioxide form, growing to occupy up to 30% of the winter hemisphere. Over the course of a year then, as the seasons pass, the average surface pressure varies some 20% as the northern and southern poles exchange and recycle one-fourth of the atmospheric carbon dioxide between their polar caps. This large scale atmospheric flow - the condensation flow - is one of several circulation features discussed during the course of this thesis.

Table 1.1: (a) Composition of the present day Martian lower atmosphere (<120 km) (Haberle, 2002) and (b) selected orbital, bulk and observational Mars parameters (`http://nssdc.gsfc.nasa.gov/planetary/factsheet/marsfact.html`).

(a) Lower atmosphere composition

Constituent	Abundance
CO_2	95.32%
N_2	2.7%
^{40}Ar	1.6%
O_2	0.13%
CO	0.07%
H_2O	0.03% (variable)
Ne	2.5 ppm
Kr	0.3 ppm
Xe	0.08 ppm
O_3	0.04-0.2 ppm (variable)
Dust	0 to $\gg$5 (visible optical depth)

(b) Selected Mars parameters

Parameter	Value
Semimajor axis (10^6 km)	227.92
Semimajor axis (AU)	1.52366
Orbital eccentricity	0.09341
Perihelion (10^6 km)	206.62
Aphelion (10^6 km)	249.23
Sidereal rotation period (hrs)	24.6229
Sidereal orbit period (days)	686.980
Obliquity to orbit (deg)	25.19
Mean surface pressure (mb)	6.36
Total mass of atmosphere (kg)	$\sim 2.5\times10^{16}$
Mean surface temperature (K)	$\sim$210

Since the time of the Viking missions the study of Mars' atmosphere has remained a challenge,

however in recent years spacecraft observations have been complemented by sophisticated computer modelling efforts that allow for better interpretation of spacecraft data. For example in the lower atmosphere modern day two and three dimensional models can rely upon detailed maps of the Martian surface topography, such as that retrieved by the Mars Orbiter Laser Altimeter (MOLA) onboard Mars Global Surveyor (Forget et al., 1995). Such data has proved invaluable in describing the surface hugging boundary layer and lowest altitude regions of an environment very much under the dynamic stresses and strains of perhaps the most dramatic topographic relief in the solar system. Even in the absence of the CO_2 condensation flow mentioned above, there would still be an appreciable hemispheric flux due to the extreme pole-to-pole gradient in topography and commensurate seasonal change in atmospheric scale height (Withers, 2003). A recent Mars general circulation model intercomparison (Wilson et al., 2006) highlighted the achievements of lower atmosphere models in describing the qualitative aspects of the zonal mean circulation (wind, temperature and mass transport streamfunction). The models showed excellent agreement with one another and against lower atmosphere data sets such as, for example, the radiative properties provided by the Thermal Emission Spectrometer onboard Mars Global Surveyor (Christensen et al., 1998). They were similarly capable of describing large scale wave phenomena associated with solar driven, dust enhanced oscillations and their effects on atmospheric variables over a range of optical depths and Mars orbital positions.

This PhD thesis however is concerned with the study of Mars' middle and upper atmosphere, a region where spacecraft data was often scarce (and in many respects still is) in its temporal and spatial coverage as missions aimed to place robotic landers on the planetary surface or were simply concerned with studying weather phenomena in the lower levels of the atmosphere. However underrated, an understanding of the tenuous upper atmosphere is paramount for the successful passage of lander type missions and for the understanding about Earth's atmosphere that can be garnered through comparison to Mars. Much information has been gained for example as spacecraft skim through the upper atmosphere on highly eccentric orbit-insertion trajectories as a means of braking into their final circular science orbits (e.g. Keating et al. (1998)). Data received from these 'aerobraking' procedures alongside modelling efforts have, for example, identified many wave phenomena propagating upwards all the way from the surface and usually with topographic dependent features superimposed on top (Forbes and Hagan, 2000). Such effects are not as prominant on Earth as they are on Mars thus making Mars an intriguing laboratory for study.

The principal methodology of this PhD is to use a general circulation model of the Martian middle and upper atmosphere to describe in detail some of the many varied processes that shape and define their thermodynamics. Furthermore we consider the extent to which the upper atmosphere region is coupled to the lower atmosphere, how this affects the middle atmosphere and to what degree other processes define the atmospheric structure. We compare the model results against suitable spacecraft data both to validate the computation but also to better understand the data itself. In particular we use recent CO_2 density and temperature measurements from the SPICAM instrument onboard the Mars

Express spacecraft (Forget et al., 2009) to consider the cold nightside middle atmosphere. Comparison will also be made against other models of the Martian upper atmosphere when and where appropriate with conclusions being drawn from the similarities and differences in the modelling results.

1.2 Basic Atmospheric Physics

Our study is concerned with the large-scale modelling of the physics, dynamics and energetics of the Martian middle and upper atmosphere. Our approach does not deal with describing the discrete molecular motion of every individual atom or molecule. Rather we regard the atmosphere as a continuous fluid medium, a *continuum* where the various physical quantities that characterize the state of the atmosphere can be described at any point by referring to an *air parcel*. An air parcel can be regarded as a sample volume element containing a large enough number of atoms and molecules for us to need only consider the totality of their motions and yet a volume that is very small as compared to the rest of the atmosphere (Holton, 2004). The concept of an air parcel allows us to describe phenomena occurring in any sample space or localized region on the understanding that it too is a continuum.

By choosing to describe the atmosphere in terms of a continuum we make the first of many necessary approximations as we develop the simulation. Ultimately we do wish to characterize the state of the modelled atmosphere at a range of locations, local times, seasons and solar conditions with unique values at each point in the model to learn more about how the various physical processes come together to create the observed Martian atmosphere. Thus in this introductory chapter we begin by describing the general physical concepts we rely on before moving on to develop more specific principles.

1.2.1 The Equation of State

We start by describing the basic behaviour of the gas in our air parcel. According to laboratory experiment all gases are found to follow approximately the same equation of state (relating the pressure, volume and temperature of any material) over a wide range of conditions (Wallace and Hobbs, 1977). To the level of detail required here we can assume that the thermodynamic state of atmospheric gases obey the ideal gas equation exactly. This relationship may be written:

$$PV = mRT \tag{1.1}$$

with P, V, m and T as the pressure, volume, mass and temperature of the gas and R as the gas constant for 1 kg of the particular gas in question (note $m/V = \rho$). Alternatively we may write:

$$P\alpha = RT \tag{1.2}$$

where α is the specific volume of 1 kg of gas i.e. the volume occupied by a unit mass ($\alpha = 1/\rho$).

However according to Avogadro's hypothesis gases containing the same number of molecules occupy the same volumes when considered at the same temperature and pressure (Wallace and Hobbs, 1977).

Thus the values of the gas constants, R, for those individual gases considered will be numerically the same and can be referred to with a single *universal* gas constant R^* (R^*=μR, where μ is the mean molecular weight of the gas in the atmosphere i.e. the volume weighted average of the molecular weights of the constituents). Hence we may also write the equation of state as:

$$P\alpha = (R^*/\mu)T \tag{1.3}$$

Thus we have the relationship used in our model to describe the state of both individual gases and mixtures of gases.

1.2.2 Hydrostatic Equilibrium

Perhaps the most fundamental simplification made in our approach to atmospheric modelling is that, to first approximation, the pressure and density structure of the neutral atmosphere is governed by the hydrostatic equation, with the atmosphere said to be in a state of hydrostatic equilibrium. That is to say, in the vertical direction the most important forces acting on our air parcel are the pressure gradient and gravity (Brasseur and Solomon, 1986) and that in the absence of atmospheric motions these two forces exactly balance (Holton, 2004). The situation is shown in Figure 1.1 where we consider the vertical forces on a column of air with unit cross-sectional area.

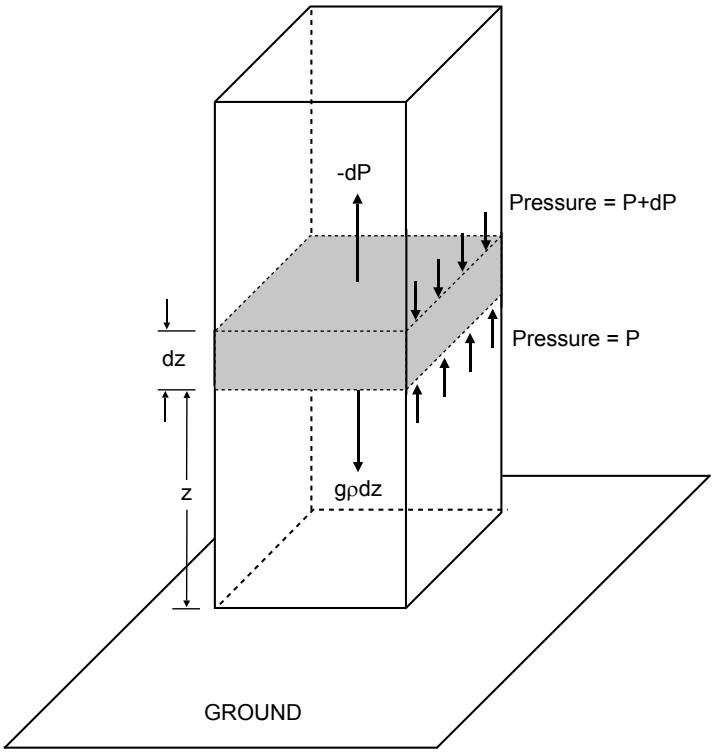

Figure 1.1: Diagram representing the balance of forces in a column of atmosphere from which hydrostatic equilibrium is defined (after Holton (2004)).

By equating the force of gravity on a slab at some altitude z to the vertical pressure gradient across that slab we can say:

$$-dP = g\rho\, dz \tag{1.4}$$

The negative sign ensuring pressure decreases with increasing height. So although the atmosphere is in motion at all times, say on the microscopic scale, we assume that at any point in the atmosphere on the larger macroscopic scale that there always exists a balance between gravitational and pressure forces and thus that overall there is no vertical acceleration.

Now if we state that the pressure at some arbitrary altitude z is $P(z)$ then integrate to the top of the atmosphere ($z = \infty$, $P(\infty) = 0$) we have:

$$-\int_{P(z)}^{P(\infty)} dP = \int_z^\infty g\rho\, dz$$
$$P(z) = \int_z^\infty g\rho\, dz$$

And hence the atmosphere is said to be in hydrostatic equilibrium if at any altitude level the pressure is equal to the weight of the air in the vertical column of unit cross-sectional area lying above that level (Wallace and Hobbs, 1977). Although in the thermosphere thermal heating may cause departures from hydrostatic equilibrium the time scales of vertical motion produced are long enough to assume quasi-hydrostatic equilibrium as an approximation of the real atmosphere (Smith, 2006). Similarly we don't consider any intense small-scale systems such as tornadoes that could create departures from equilibrium (Holton, 2004).

1.2.3 The Variation of Pressure and Density with Altitude

The variation of pressure and density with altitude has several important implications on the physical state of the atmosphere. If we rearrange the equation of state $P\alpha = (R^*/\mu)T$ (equation 1.3), replace α with $1/\rho$ and substitute into equation 1.4 to eliminate ρ we have:

$$P\alpha = (R^*/\mu)T$$
$$\text{becomes } \rho = \frac{P}{T}\frac{\mu}{R^*}$$
$$\text{so that } \frac{-dP}{P} = \frac{g\mu}{TR^*}dz \tag{1.5}$$

Then if we rearrange equation 1.5 and integrate between some arbitrary reference altitude $z'{=}z_0$ and altitude $z'{=}z$ we arrive at the following result for pressure as a function of z (Thomas and Stamnes, 1999):

$$P(z) = P(z_0)exp\left[-\int_{z_0}^{z} dz'/H(z')\right] \tag{1.6}$$

Furthermore, by rearrangement of the equation of state we can also arrive at the following forms of this relationship:

$$n(z) = n(z_0)\frac{T(z_0)}{T(z)}exp\left[-\int_{z_0}^{z} dz'/H(z')\right] \tag{1.7}$$

$$\rho(z) = \rho(z_0)\frac{T(z_0)}{T(z)}exp\left[-\int_{z_0}^{z} dz'/H(z')\right] \tag{1.8}$$

These relationships can be simplified if we assume that gravity, temperature and mean molecular weight are constant with height. Integrating the argument of the exponential in equation 1.6 we obtain (Thomas and Stamnes, 1999):

$$P(z) \approx P(z_0)exp\left(\frac{-(z-z_0)}{H}\right) \tag{1.9}$$

And similar expressions can be obtained for number and mass density ($n(z)$ and $\rho(z)$). In the above we introduce the pressure scale height $H(z)$=$R^*T(z)/g\mu$ (first introduced by S. Chapman and adopted in all aeronomic problems relating to the logarithmic gradient of pressure (Banks and Kockarts, 1973)). Note how if $(z-z_0)$ is set successively equal to $0, H, 2H, 3H, \ldots$, etc that $(P(z)/P(z_0))$ is equal to 1, $exp(-1)$, $exp(-2)$, $exp(-3)$, ..., and so on. Thus the pressure decreases by a factor e for each increase in the scale height H.

Since atmospheric pressure and density govern much of the local physics their exponential decrease with altitude suggested by equation 1.9 implies that vastly different physical behaviour of gases can be expected with a change in altitude of only a few scale heights (Smith, 2006). Principally, this is because the frequency of collisions between gas molecules varies inversely with the atmospheric pressure and density so that in atmospheric layers separated by only a few scale heights the mean free path between collisions will increase exponentially (Salby, 1996). As will be discussed in section 1.5 the collision frequency plays a determining role in whether internal molecular energy states are in a local or non-local thermodynamic equilibrium. This has important implications for the magnitude of solar forced infrared heating and CO_2 radiative cooling (López-Puertas and Taylor, 2001). Additionally, the mean free path between collisions also controls processes such as molecular diffusion. Thus the variation in the frequency of collisions will also influence properties such as air viscosity and thermal conductivity (Salby, 1996).

Finally, in the upper atmosphere, the variation in mixing of atmospheric species through collisions will significantly change whether a particular species dominates the distribution. Notice for example how the scale height is proportional to the gas constant for a unit mass of a gas that in turn is inversely proportional to the molecular weight of that gas. This suggests that the pressure and densities of heavier gases fall off more rapidly with altitude than do those of lighter gases. There are exceptions to these examples such as when other physical processes are involved (e.g. chemically short-lived species) but these will be introduced in later chapters as necessary.

1.2.4 The Adiabatic Lapse Rate and Atmospheric Stability

Now that the basic atmospheric environment has been introduced we discuss some of the ways in which our air parcel interacts with this environment. In broad terms the interaction can be described as either *diabatic* or *adiabatic*. The former refers to an exchange of heat (energy) between our air parcel and the atmosphere (thus a net heating or cooling) while the latter indicates the absence of such heat transfers (thus energy conserving). The distinction between these exchanges is often simply a question of time scales. Diabatic heat transfer, for example through diffusion or thermal conduction, can be quite slow compared to the other processes that influence our air parcel (Salby, 1996). Conversely processes involving some sort of motion, such as air parcel expansion or advection, often operate on time scales short enough that no heat transfer can take place. Consequently describing the interaction between our air parcel and the atmosphere through notions of adiabatic behaviour can be a good approximation for many applications.

The first law of thermodynamics gives $dq = c_P dT - \alpha dP$ (Wallace and Hobbs, 1977). Assuming the air parcel expands adiabatically so that dq, the net heating rate per unit mass, is zero then this law expresses the inverse relationship between pressure and temperature as the air parcel changes its physical state (pressure, volume or temperature change) through expansion cooling or compression heating associated with adiabatic processes. Substituting for dP from the hydrostatic equation 1.4, and noting how $\alpha = 1/\rho$ cancels out, we arrive at the *adiabatic lapse rate*:

$$\frac{dT}{dz} = \frac{-g}{c_P} = \Gamma_D \tag{1.10}$$

Where c_P is the heat capacity per unit mass at constant pressure and the subscript D indicates this is specifically the dry adiabatic lapse rate (the presence of some vapour would require a separate derivation). This relationship describes the change in temperature of our air parcel as it is displaced in a hydrostatically stratified environment when it does not communicate thermally with that environment i.e. when the interaction with its surroundings is purely mechanical (Salby, 1996). As our air parcel rises adiabatically through the atmosphere the pressure around it drops so it expands and its volume increases. Term αdP from the first law of thermodynamics shows that work is done by the gas on its surroundings so that the internal energy ($c_P dT$) decreases and thus temperature follows suit.

From here we can consider the stability of the atmosphere to such adiabatic displacement and its relationship to the vertical temperature gradient (the lapse rate). To do so we introduce a new state variable, the potential temperature θ, that is simply the temperature that our air parcel would have if it were expanded or compressed adiabatically about some standard pressure (Holton, 2004). Starting from the same form for the first law of thermodynamics as above and integrating to characterise a change in state from pressure P_0 and temperature θ to a state with pressure P and temperature T, we obtain Poisson's equation:

$$\theta = T\left(\frac{P_0}{P}\right)^{\frac{R}{c_P}} \tag{1.11}$$

For adiabatic motion the potential temperature is conserved as the air parcel moves through the atmosphere. So an air parcel descending to greater pressure experiences an increase in temperature due to the compression work performed on it. This temperature increase is proportional to the increase in pressure such that the parcel's potential temperature is conserved.

Finally then if the potential temperature is a function of height we can compare the adiabatic motion of the air parcel to the lapse rate of the background atmosphere (see equation 1.12) and consider what variation of temperature with altitude is stable i.e. the stability of the atmosphere to convective overturn.

$$\frac{T}{\theta}\frac{\partial\theta}{\partial z} = \Gamma_D - \Gamma \tag{1.12}$$

From equation 1.12 we see how if the lapse rate Γ is less than the adiabatic lapse rate Γ_D, so that the potential temperature θ increases with altitude, then the atmosphere is said to be statically stable or stably stratified (Holton, 2004). Thus if our air parcel is displaced downward adiabatically it will meet colder air and so be positively buoyant and return to its equilibrium level. Meanwhile if our air parcel is displaced upwards adiabatically it will meet warmer more rarefied air and be negatively buoyant and so fall back to its equilibrium level. Of course in the converse situation, where the lapse rate Γ is greater than the adiabatic lapse rate Γ_D, the potential temperature θ decreases with altitude. The rising parcel of air will find itself surrounded by cooler and denser air and continues to rise. Thus a strongly negative lapse rate is unstable.

Ultimately diabatic processes, such as heat transfer, will always prove to be important for the overall long-term maintenance of the general circulation despite our focus here on shorter time scale adiabatic effects (Salby, 1996). The most obvious reason for this is simply that the principal and abundant source of energy for heat transfers is of course the Sun through the absorption of solar flux either directly by the atmosphere at EUV/UV wavelengths or when re-radiated by the surface in the infrared. The Sun's powerful diurnal energy input will always drive the thermodynamic state of the atmosphere, on a long enough time scale.

1.2.5 The Gravitational Potential

It is important to be clear about what we mean by 'altitude' when developing and using an atmospheric model, especially one that focuses on a particularly dynamic and energetic region of the atmosphere. For example, it will be important to keep a clear account of whether energy is gained or lost as air parcels rise and fall through the atmosphere, something requiring at a fundamental level a strict description of position in the planet's gravitational field. There are many different zeroth altitude levels available for us to use (e.g. sea level, ground level, a particular pressure level, etc) and an appropriate choice of such a reference level for our coordinate system can significantly simplify the subsequent mathematics.

For such distinctions it is perhaps most appropriate, and certainly convenient, to introduce the geopotential Φ J kg^{-1} or m^2 s^{-2} for a unit mass (Wallace and Hobbs, 1977). This is defined as the work done against the planet's gravitational field in order to raise a mass of 1 kg from mean sea level to a height

z. Assuming the idealised situation of a homogeneous spherical planet we can assume gravity is always directed toward the centre of that planet. As such when modelling from within a frame rotating with the planet one can represent gravity in terms of the gradient of the geopotential $\nabla\Phi{=}{-}g$ i.e. everywhere perpendicular to geopotential surfaces. If we can choose horizontal surfaces in our model atmosphere to coincide with surfaces of constant geopotential then the force of gravity can be assumed to not have any horizontal component at all. This will prove quite a convenient approximation we will use later on.

If the force acting on 1 kg at height z above some reference level is numerically equal to g then the work done in raising it from z to $z + dz$ is gdz:

$$d\Phi = gdz \tag{1.13}$$

and so the geopotential $\Phi(z)$ at height z is given by:

$$\Phi(z) = \int_0^z gdz \tag{1.14}$$

The reference level $g(0)$ is typically defined to be mean sea level in the case of Earth. For Mars, researchers often use the gravitational equipotential surface whose average value at the equator is equal to the mean radius as determined by the MOLA instrument onboard Mars Orbiter ($3.396{\times}10^6$ m, see Forget et al. (2008)). The altitude is then the altitude to this reference ellipsoid and is termed the 'areocentric' altitude. As mentioned already and detailed further in Chapter 2 we simply assume a spherical planet shape. In any event when we refer to altitude or height we are referring to the geopotential height by defining $Z = \Phi(z)/g(0)$.

1.3 The Navier-Stokes Equations

Above, we introduced general statements describing the physical environment we wish to deal with and introduced a few of the assumptions one can make when it comes to modelling this environment. We described the pertinent *diagnostic* equations that express the interrelationships between dependent variables that are valid at any instant in time (Wallace and Hobbs, 1977). Now we can move on to discuss the more descriptive and complex characteristics of the dynamics and energetics of this environment, i.e. the *prognostic* equations that give us the time rates of change of the dependent variables, equations of global scale atmospheric flow and atmospheric physics.

The circulation of a planetary atmosphere can be described in its most fundamental form by three basic governing principles (Brasseur and Solomon, 1986): Newtons laws of motion, conservation of energy and conservation of mass. Furthermore in this and many other studies of atmospheric physics we continue to assume that the neutral atmosphere can be treated like a continuous fluid medium or a continuum. This means for example that we assume the mean free path between collisions is much shorter than the distance over which macroscopic quantities can significantly vary (Holton, 2004) and we can use well-established fluid dynamics formulations rather than dealing with discrete molecular motions. As noted above, we consider volume elements that contain a large enough number of molecules for us to need

only consider the totality of their motions but where the volume elements are very small in size when compared to the rest of the atmosphere. The set of equations introduced here are the Navier-Stokes equations, a set of nonlinear partial differential equations well known in fluid mechanics that fulfill the requirements as set out above.

1.3.1 The Momentum Equation

Newton's second law of motion describes the response of an air parcel to the sum of the external forces acting on the parcel. Both real and apparent external forces must be considered. Real forces are those that act on the center of mass of the air parcel with magnitudes proportional to its mass. The real forces we are interested in are the force of gravitation, the pressure gradient force and the frictional drag force exerted by neighbouring air parcels or the underlying surface. When considering the real forces only the equation of motion takes the form:

$$\frac{d\underline{v}}{dt} = \underline{g}^* - \frac{1}{\rho}\nabla P + \underline{F} \tag{1.15}$$

The force of gravitation, $\underline{g}^*$, the first term on the right hand side of equation 1.15, is the true gravitational acceleration, which for an idealised homogeneous spherical planet is directed toward the center of that planet. Next we have the pressure gradient force, $(1/\rho)\nabla P$, the second term on the right hand side of equation 1.15. This is the force directed in the opposite direction to ∇P i.e. towards lower pressures and as you can see it is proportional to the gradient of the pressure field. Although the gradient operator implies a three-dimensional field, later chapters discuss how the dominance of hydrostatic equilibrium allows us to separate horizontal from vertical motions so that their partial derivatives can be dealt with separately. For now then ∇P is to be considered a two-dimensional horizontal term at a constant altitude z and further discussion of its form is left to section 2.2.1 of Chapter 2.

The frictional drag force $\underline{F}$ is the final real force we must consider. It is proportional to the velocity of the air parcel and includes a consideration of internal friction within the air parcel (e.g. viscous interaction within the air parcel itself causing resistance to flow) as well as shearing stresses external to the air parcel (e.g. viscous interaction with the surface or other air parcels). Its full form is given in Koskinen (2008) and O'Neill and Chorlton (1989) while the form used in this work is given in Chapter 2, equation 2.13.

Next we deal with the apparent forces acting on the air parcel. These are the reaction forces we introduce to compensate for the acceleration of our frame of reference as we apply Newtons second law of motion to a coordinate system that co-rotates with the planet below. Although scalar quantities appear the same in inertial (subscript 'I') and noninertial (e.g. rotating, subscript 'R') reference frames (Salby, 1996) we do however need a relationship to modify vector quantities $\underline{A}(x, y, z, t)$ between these two frames. The situation is shown schematically in Figure 1.2 for a reference frame rotating with angular velocity $\underline{\Omega}$. The vector $\underline{A}$ remains constant with respect to this rotating frame while at the same time, from the point of view of the inertial frame, the vector will move (in interval dt) because of the rotation

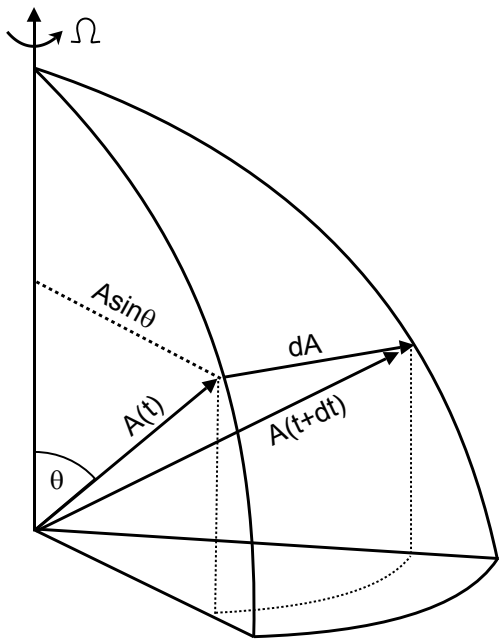

Figure 1.2: Schematic of vector $\underline{A}$ fixed in a rotating frame but changing in an inertial frame (after Salby (1996)).

by increment $d\underline{A}$, perpendicular to the plane of $\underline{A}$ and $\underline{\Omega}$. The magnitude of increment $d\underline{A}$ is:

$$|d\underline{A}| = A sin\theta \ . \ \Omega dt$$

Thus in the inertial frame vector $\underline{A}$ changes at a rate:

$$\left|\frac{d_I \underline{A}}{dt}\right| = A\Omega sin\theta \tag{1.16}$$

again, perpendicular to the plane of $\underline{A}$ and $\underline{\Omega}$. From equation 1.16 it follows that the vectorial increment is:

$$\left(\frac{d_I \underline{A}}{dt}\right) = \underline{\Omega} \times \underline{A} \tag{1.17}$$

Therefore the general time rate of change of vector $\underline{A}(x, y, z, t)$ in an inertial frame that has a rate of change $d_R\underline{A}/dt$ in a rotating frame is just the summation of the time rates of change in each frame:

$$\frac{d_I \underline{A}}{dt} = \frac{d_R \underline{A}}{dt} + \underline{\Omega} \times \underline{A} \tag{1.18}$$

Where Ω is the rotation rate of the planet and of the atmosphere, which once again we assume co-rotates with the planet below.

So for example if we apply this relationship to the position vector $\underline{r}$ for our air parcel we get:

$$\frac{d_I \underline{r}}{dt} = \frac{d_R \underline{r}}{dt} + \underline{\Omega} \times \underline{r}$$

$$\text{i.e. } \underline{v}_I = \underline{v}_R + \underline{\Omega} \times \underline{r} \tag{1.19}$$

which simply states that the absolute inertial velocity of an object in a rotating frame is equal to its velocity relative to the frame *plus* the velocity due to the rotation of the frame itself. If we now apply relationship 1.18 to $\underline{v}_I$ we get:

$$\frac{d_I \underline{v}_I}{dt} = \frac{d_R}{dt}(\underline{v}_R + \underline{\Omega} \times \underline{r}) + \underline{\Omega} \times (\underline{v}_R + \underline{\Omega} \times \underline{r})$$

and now substitute for $\underline{v}_I$ from equation 1.19:

$$\frac{d_I \underline{v}_I}{dt} = \frac{d_R \underline{v}_R}{dt} + 2\underline{\Omega} \times \underline{v}_R - \Omega^2 \underline{R} \tag{1.20}$$

where $\underline{R}$ is a vector perpendicular to the axis of rotation with magnitude equal to the distance to the axis of rotation. Equation 1.20 states that the acceleration following the motion in an inertial system equals the rate of change of relative velocity following the relative motion in the rotating frame *plus* the centripetal acceleration caused by the rotation of the coordinates. Hence a more appropriate form of Newton's Second law for our purposes, i.e. applied to a rotating coordinate system, is in fact:

$$\frac{d\underline{v}}{dt} = \underline{g} - \frac{1}{\rho}\nabla P + \underline{F} - 2\underline{\Omega} \times \underline{v} \tag{1.21}$$

with the subscript R dropped for clarity.

The terms in equation 1.21 deserve further explanation. The first term on the right hand side, $\underline{g}$ is the effective (or apparent) gravity. It can be related to the true gravitational attraction $\underline{g}^*$ in equation 1.15 by the relationship $\underline{g} = \underline{g}^* + \Omega^2 \underline{R}$. When observed from a fixed inertial frame a unit mass undergoes a uniform acceleration directed towards the axis of rotation i.e. the centripetal acceleration (Holton, 2004). However, with respect to the rotating frame the unit mass is at rest even though the true gravitational force $\underline{g}^*$ still acts toward the center of the planet. So to balance the forces on the mass and to apply Newton's second law within the rotating frame we include the additional apparent force, the centrifugal force $\Omega^2 \underline{R}$, that is equal and opposite to the centripetal acceleration. Hence effective gravity $\underline{g}$, per unit mass, is the vectorial sum of the true gravitational force $\underline{g}^*$ that draws all air parcels towards the center of mass of the planet *plus* the (usually much smaller) apparent centrifugal force $\Omega^2 \underline{R}$ that is the reaction force of the centripetal acceleration (Holton, 2004). Since a body co-rotating with the planet below has no way of separately sensing the true gravitational and centrifugal components of effective gravity force there is nothing to be gained by expressing the two as separate forces in the equations of motion. Hence the centrifugal force term $\Omega^2 \underline{R}$ does not appear explicitly in the equations of motion, rather it is included implicitly as a part of $\underline{g}$.

The second and third term on the right hand side of equation 1.21 remain unchanged from their counterparts in equation 1.15. The final term on the right hand side of equation 1.21 is the Coriolis force. This is in fact the only apparent force we need add to the statement of Newton's second law when dealing with an object moving in a rotating coordinate system. The Coriolis force arises as a consequence of an object conserving angular momentum as it moves in the rotating frame. Any displacement in latitude or altitude will change the distance R to the axis of rotation and thus the absolute angular velocity $\Omega + \frac{u}{R}$, where u is the eastward velocity of the object relative to the planet, must also change if absolute angular

momentum is to be conserved. Since Ω is a constant then the relative zonal velocity u must change and the object will behave as if a (artificial) zonally directed deflection force were acting. The effects of the Coriolis force are discussed in more detail in later chapters.

1.3.2 Conservation of Energy and the Energy Equation

A theoretical treatment of the atmosphere also requires a description of the fundamental thermal behaviour. The starting point here is conservation of energy as embodied in the First Law of Thermodynamics relating the total time rate of change of internal energy within our air parcel to the work done on it by various sources and the subsequent change in its temperature as it moves through the atmosphere (Holton, 2004).

The importance of such a treatment lies in the fact that under certain assumptions changes in temperature will be reflected in the expansion or contraction of our air parcel. Consider for example expressing the hydrostatic equation 1.4 in terms of the geopotential (equation 1.13) rather than the geometric height:

$$\begin{aligned} gdz = d\Phi &= -\left(\frac{RT}{P}\right)dP \\ &= -RTdlnP \end{aligned}$$

thus the variation of geopotential with respect to pressure depends only on temperature. Furthermore, integration in the vertical direction between two pressure surfaces (defining a pressure layer) yields an expression for the 'thickness' (subscript T) of this atmospheric layer (Holton, 2004):

$$\begin{aligned} Z_T = z_2 - z_1 &= \frac{R}{g_0}\int_{P(1)}^{P(2)} TdlnP \\ &= Hln\left(\frac{P}{P_0}\right) \end{aligned} \tag{1.22}$$

where we define a layer mean temperature as (Salby, 1996):

$$\begin{aligned} \langle T\rangle &= \frac{\int_{P(1)}^{P(2)} TdlnP}{\int_{P(1)}^{P(2)} dlnP} \\ &= \frac{\int_{P(1)}^{P(2)} TdlnP}{ln\left(\frac{P(2)}{P(1)}\right)} \end{aligned} \tag{1.23}$$

and a layer mean scale height $\langle H\rangle = R\langle T\rangle/g_0$. In this way we can show that the thickness of atmospheric layers when bounded by isobaric surfaces is proportional to the mean temperature of the layer in question (Holton, 2004). Hence any physical processes that change the temperature field ultimately change the distribution of the horizontal pressure gradient force ($F = (-1/\rho).\nabla P$ (at constant z)), which will feedback on all other atmospheric properties (Wallace and Hobbs, 1977).

Starting from the usual form of the First Law of Thermodynamics the derivation proceeds as follows:

$$dq = c_v dt + Pd\alpha \tag{1.24}$$

taking the derivative with respect to time:

$$\frac{dq}{dt} = c_v \frac{dT}{dt} + P\frac{d\alpha}{dt} \tag{1.25}$$

where $\dot{Q}$ ($\equiv \frac{dq}{dT}$) represents the net heating rate per unit mass per unit time due to some physical processes and dt is an infinitesimal time interval. Taking the total derivative of the equation of state (in the form $P\alpha$=RT) with respect to time so we can substitute for $P\frac{d\alpha}{dt}$ in the above and noting that $c_P = c_v + R$ gives:

$$\dot{Q} = c_P \frac{dT}{dt} - \alpha \frac{dP}{dt} \tag{1.26}$$

This is the basic equation describing the change in enthalpy per unit mass of atmosphere (Achilleos et al., 1998). Again, the $\dot{Q}$ term represents the diabatic processes involved in the net heating and cooling of the parcel e.g. solar EUV/UV heating or thermal conduction etc. Those included in MarTIM are discussed in Chapter 2. The two terms on the right hand side express the inverse relationship between pressure and temperature that describes the cooling due to expansion or heating due to compression associated with adiabatic processes in our (compressible fluid) air parcel. The first term on the right hand side corresponds to the change in enthalpy as energy is added to or removed from the parcel. The second term represents the rate of working by the parcel against the surrounding atmosphere as it expands and vice-versa as it contracts. It represents a conversion between thermal and mechanical energy (Holton, 2004).

1.3.3 The Continuity Equation

The last basic principle governing circulation of a planetary atmosphere is the conservation of mass - also known as the continuity equation. This states that the net rate of mass inflow must equal the rate of accumulation of mass within the sample volume. And if we deal with a unit volume (such as our air parcel for example) then the increase in mass within the volume is also the local density change. Hence:

$$\frac{\partial \rho}{\partial t} + \nabla.(\rho V) = 0 \tag{1.27}$$

The continuity equation relates the time rate of change of density and volume of an air parcel as it moves through the atmosphere. Put simply when an air parcel is deformed by a large-scale motion field in the absence of sources or sinks of mass its dimensions are changed so as to conserve its original volume. Local density change is caused entirely by divergence or convergence of local mass flux. Though the air parcel is compressible i.e. it may experience volume changes, they are usually gradual hydrostatic changes due to the expansion and compression that accompanies hydrostatic pressure changes. When the continuity equation is derived with pressure as a vertical coordinate these hydrostatic expansion and compression effects are implicitly taken into account without adding complexity to the relation (Wallace and Hobbs, 1977).

1.3.4 Reference Frames

Two types of reference frame are commonly used in fluid dynamics, the Eulerian frame and the Lagrangian frame (Holton, 2004). In the former case one would calculate physical quantities at points fixed relative to the (co-rotating) coordinate system. In the latter case one would perform the calculations at a grid point that was moving as it followed the flowing motion of the fluid. We choose to perform our calculations in the Eulerian frame for the convenience of being able to relate field variables such as temperature, pressure, geopotential height, etc to one another by sets of partial differential equations in space and time. The alternative in the Lagrangian frame would require us to follow the time evolution of each field variable as the coordinate system itself moved with the fluid flow.

With our choice of reference frame made it is necessary to derive a relationship between the total derivatives introduced above i.e. derivatives in the Lagrangian system that follow the motion of a particular air parcel, and the rate of change of field variables at a point on our fixed grid i.e. the local or partial derivatives in our Eulerian frame.

$$\frac{dA}{dt} = \frac{\partial A}{\partial t} + \underline{v}.\nabla A \tag{1.28}$$

This form of the time derivative essentially makes the statement that changes in field variables as we follow the motion of an air parcel are equal to the local rate of change at a particular point on our fixed grid plus the advective rate of change due to action of the fluid streamline passing over that grid point.

1.4 Structure of the Martian Atmosphere

With the basic concepts of atmospheric physics introduced above we now describe how these physical principles come together to create some of the phenomena observed in the present day Martian atmosphere. We also discuss some of the phenomena one would expect to see in the Martian atmosphere as indicated by computer simulation when direct observational data has been scarce or derived from other sources. And finally we highlight through comparison to the atmospheres of the other terrestrial planets how many of these observed and expected effects are specific to the Martian environment.

1.4.1 The Martian Atmosphere

All atmospheres, regardless of their diversity, can be defined as a series of atmospheric layers whose distinguishing physical characteristics are typically described with reference to their temperature variation. The layers are called *spheres* and we define each layer to be a region where the temperature variation with respect to altitude has a constant sign (Brasseur and Solomon, 1986). Moving upwards from the surface of Mars (and making reference to Figure 1.3) we pass through the *troposphere*, *mesosphere*, and *thermosphere* before passing through the *exosphere* from where high velocity neutral particles can escape the gravitational potential of the planet. Notice also the *ionosphere* region that starts at approximately 120 km and extends upwards essentially through the rest of the entire atmosphere, dropping in number

density (as the neutral densities do too) as one passes into the Martian near-space environment. Finally we also name the boundaries between two adjacent layers with the term *pause* (Brasseur and Solomon, 1986), referring to the upper boundary of the layer below.

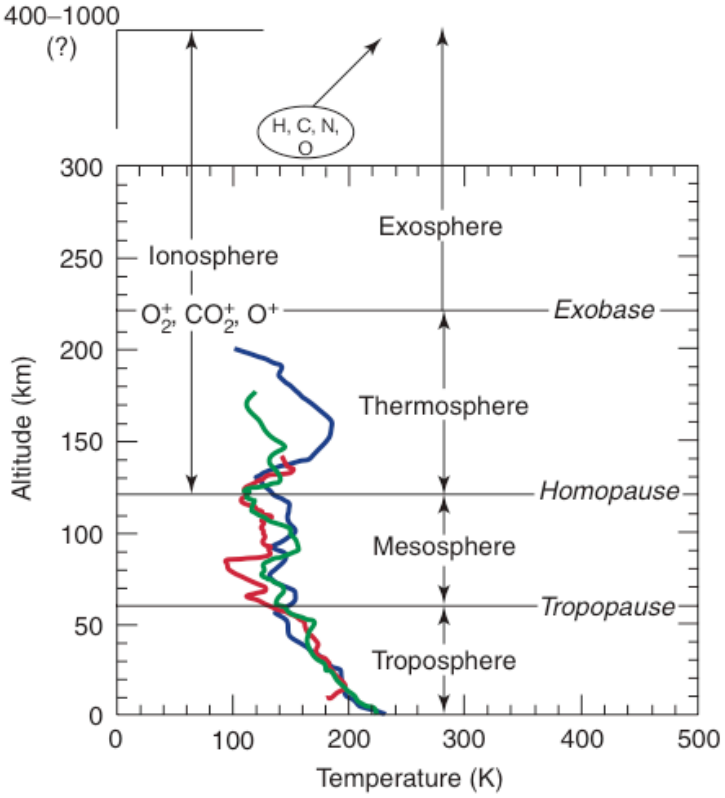

Figure 1.3: Temperature structure of the Martian atmosphere (from Haberle (2002)).

1.4.2 The Troposphere

The primary source of energy in the troposphere is convective heat transfer from the Martian surface (Izakov, 1976) as it re-radiates in infrared the absorbed high energy UV and visible solar radiation that will have passed almost unhindered through the atmosphere above. Also important is solar absorption directly in the lower atmosphere by suspended airborne dust whipped up by surface winds. Note the highly variable topographic relief (Figure 1.4) with its striking hemispheric dichotomy that, acting to manipulate the low altitude heating structure and horizontal wind flow, has a driving role in many of the phenomena encountered in this thesis. In this region turbulent motions dominate to efficiently mix species together preventing separation by molecular diffusion so that no single species dominates the composition (Banks and Kockarts, 1973). It is this mixing that acts to convect the heat radiated by the surface upwards in altitude. Indeed the Greek word 'tropos' literally means 'turning', which in the context of the turbulent troposphere could also reasonably be associated with instability. The flow of near-surface horizontal winds over some of the largest mountains and longest valleys in the solar system creates turbulence that evolves into atmospheric waves with a spectrum of wavelengths that propagate

and influence higher altitudes far above the surface, much like the situation at Earth (Müller-Wodarg, 1997).

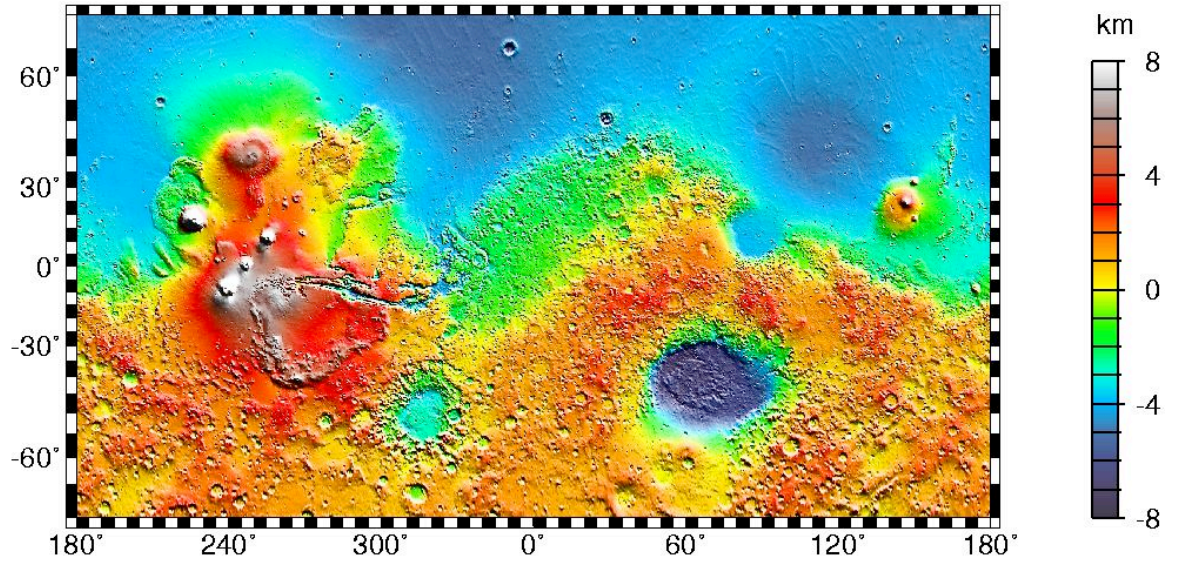

Figure 1.4: Global high resolution topographic shaded relief map of Mars from MOLA data (see `http://nssdc.gsfc.nasa.gov/planetary/image/mgs_mars_topo.jpg`). The colour scale represents height of topography above or below the mean Mars radius as determined by the MOLA instrument onboard Mars Orbiter (3.396×10^6 m, see Forget et al. (2008) or section 1.2.5 above).

However, unlike Earth, the troposphere is much deeper on Mars extending to approximately 60 km (versus ∼12 km for Earth) before the tropopause is reached (Withers, 2003). Additionally this tropopause boundary is less defined on Mars as it is on Earth, where the 'freezing out' of water vapour limits its vertical reach in a well defined manner and acts as a 'lid' on the lower atmosphere circulation (Barnes, 1990). In the case of Mars the suspended dust is not limited in the same way and so can be lifted to several tens of kilometres in altitude (Withers, 2003). This continued presence of dust at altitude in the Martian atmosphere, and the additional deep domain of heating it provides, produces a strong thermal forcing and a very robust zonal-mean circulation that extends from the lower atmosphere well into the middle atmosphere (Barnes, 1990). The presence of dust in the Martian atmosphere is in fact a feature we'll come back to often through the course of this thesis given the strong influence it has on the dynamics and energetics throughout the atmosphere. And not just localised to the region where, for example, a dust storm may be raging.

To quantify some of these statements, recall our discussion in section 1.2.4. There it was highlighted how the adiabatic lapse rate (equation 1.10) and the potential temperature (equation 1.11) determined the stability of the atmosphere to convective overturn as an air parcel was heated convectively by the ground, rose, expanded and cooled. Now if we consider that the Martian troposphere has an observed average lapse rate of ∼2.5 K km^{-1} (based upon Viking and Pathfinder lander entry measurements) we see how this is much less than the calculated dry adiabatic lapse rate ∼4.3 K km^{-1} (Haberle, 2002). Hence

the troposphere can be considered stable with the absorption of radiation by suspended dust particles providing the additional heating needed to maintain this stability (in comparison to Earth where the heating is provided by latent heat released with the condensation of water vapour).

1.4.3 The Mesosphere

The troposphere terminates at the tropopause, a level at which the temperature decrease with altitude generally ceases. In the region above, the mesosphere ('middle' sphere), temperatures become nearly constant with altitude although they do still exhibit oscillatory behaviour associated with vertically propagating gravity, planetary and tidal waves from the troposphere below (Zurek, 1992). These phenomena are highly variable responding in kind to variation in lower atmosphere dust content, the solar cycle and to Mars' position in orbit around the sun (Barth et al., 1992; Lewis and Barker, 2005). Their influence can be seen quite clearly in the temperature profiles of Figure 1.3 where the blue, green and red lines (for Viking 1, 2 and Pathfinder missions respectively) show highly detailed, turbulent structure that is surely the influence of a whole spectrum of waves with many different wavelengths (Haberle, 2002).

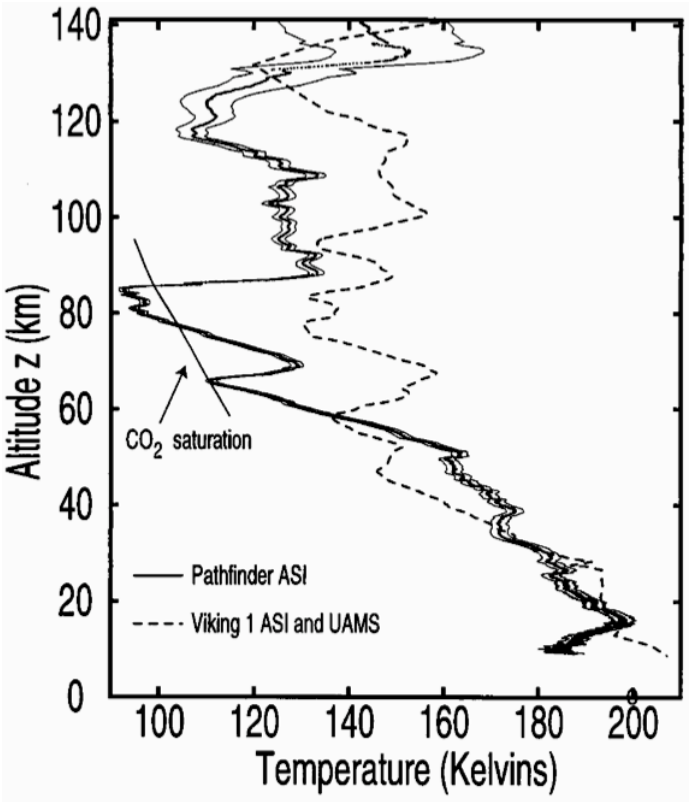

Figure 1.5: Atmospheric temperature profile from entry phase of Mars Pathfinder and Viking 1 (Magalhães et al., 1999).

The mesosphere is perhaps most notable for being the coldest region in the Martian atmosphere throughout the year, during both day and night times. This is a result of the combined effect of a reduction in the available direct solar heating, which mostly occurs in the thermosphere overhead,

alongside the dominant CO_2 15-μm infrared cooling mechanism. It is this cooling mechanism and in particular the vibration-translational interaction of atomic oxygen in the O(^{3}P) state with carbon dioxide that is extremely efficient at cooling the local atmosphere, despite the small abundance of O(^{3}P) (see for example López-Valverde and López-Puertas (1994a,b)). These effects act as an efficient thermostat for the column of atmosphere lying above, reducing the overall variation in middle and upper atmosphere temperatures as the solar cycle progresses. Modelling work by Bougher and Roble (1991) for example suggested a thermospheric variation of only ∼110 K for Mars versus ∼518 K for Earth because of the dominance of CO_2 and its cooling processes in the mesosphere anchors the temperature variation at Mars versus those at Earth.

The extent of this cold mesosphere can be seen in the early morning (0300-hrs) entry temperature profile from the Mars Pathfinder mission (Magalhães et al., 1999) as shown in Figure 1.5. In this figure we see how temperatures reach as low as 92.6 K at 85 km and so are at or below the CO_2 saturation curve between 85 and 77 km, with an average supersaturation of 4.8 K. The measurements were well outside any instrument uncertainties and thus give a clear indication of extremes to which the Martian middle atmosphere can extend.

1.4.4 The Thermosphere

At approximately 120 km we reach the thermosphere ('hot' sphere) where the rarefied atmospheric structure changes markedly. Temperatures increase swiftly with altitude as absorption of incident solar radiation in the far and extreme ultraviolet region becomes increasingly important, rapidly dominating other energy sources. In response to the temperature gradient that results from such heating the effectiveness of downwards vertical thermal conduction begins to develop, eventually to balance the solar heating input. Molecular diffusion thereby dissipates the heat toward the lower thermosphere and mesosphere where radiative cooling to space acts strongly as already described. Modelling work (Bougher et al., 1990, 1994) finds that the abundance of CO_2, even at these high altitudes, contributes significantly to Mars' thermosphere being cooler than Earth (aside from other contributing factors), where radiation to space by infrared active species in the thermosphere is relatively unimportant (Smith, 2006).

The solar influence on the Martian thermosphere is representative of another important difference in the comparison between Mars and Earth. Firstly Mars' greater distance from the Sun (aphelion, solar longitude 70^o, 1.639 AU; perihelion, solar longitude 250^o, 1.405 AU) means it receives about half as much annually averaged sunlight as Earth. Next its eccentric orbit (eccentricity 0.0934) means it experiences a much greater change in available insolation from summer solstice in the northern hemisphere (aphelion) to that in the south (perihelion), a variation 40% compared to Earth's 6% (Withers, 2003; Forbes, 2004). As a result peak thermospheric temperatures are seen (in three-dimensional modelling work) to vary by 20, 43 and 60 K between northern and southern solstices for SMIN (200 to 220 K), SMED (261 to 304 K) and SMAX (310 to 370 K) conditions respectively (Bougher et al., 1999b, 2000). Such modelled results can be compared against the selected Mars dayside upper atmosphere spacecraft measurements

of temperatures presented in Table 1.2 (based upon a similar table presented in Bougher et al. (2000)). The somewhat restricted range of seasonal and solar cycle temperatures, as noted already, is apparent both in the modelling work and the spacecraft data.

Table 1.2: Selected Mars dayside upper atmosphere spacecraft observations (after Bougher et al. (2000)).

Mission	$F_{10.7}$ Index	Ls	Sun-Mars (AU)	T_{exo} (K)
Mariner 4	77.0	139.0	1.553	212.0
Mariner 6 / 7	167.0-188.0	200.0	1.425	315.0-350.0
Mariner 9 (nominal)	103.0	306.0	1.440	325.0
Mariner 9 (extended)	100.0	38.0	1.630	268.0
Viking 1	69.0	96.0	1.647	186.0
Viking 2	76.0	117.0	1.612	145.0
MGS 1	93.0	256.0	1.382	220.0
MGS 2	127.0	48.5	1.653	230.0

Note: after Bougher et al. (2000), MGS 1 is Mars Global Surveyor phase 1 aerobraking, MGS 2 is Mars Global Surveyor phase 2 aerobraking. All results are for dayside upper atmosphere with solar zenith angle less than 90^o.

One final, remarkable difference between Earth and Mars is the presence in the Martian thermosphere of tidal wave propagation that can, for certain types of wave, be traced back to the lower atmosphere (as noted earlier). In fact many important components of thermospheric tidal disturbances can be linked to the Martian surface topography. Forbes et al. (2002), for example, discuses how the dynamical effects of Mars topography can extend throughout the atmospheric column right the way to the exobase (the upper boundary of the thermosphere). The direct excitation of tidal oscillations by solar insolation will occur on any rotating planetary atmosphere (Forbes, 2004). These oscillations (of various atmospheric fields) will be independent of longitude as long as the atmosphere (or surface) where absorption occurs is zonally symmetric. Thus their zonal phase speeds will be equal to the planetary rotation: they will appear to propagate westward at the same speed as the apparent motion sun from the point of view of an observer on the ground, they are "migrating" tides (Hagan et al., 2003).

However when radiative processes such as solar insolation interact with a zonally in-homogeneous atmospheric absorber concentration or with a surface whose properties (such as heat capacity or soil moisture) vary with location (Wilson and Hamilton, 1996) (such as due to Mars' dramatic topography), then the tidal disturbances produced will have periods and phase speeds that may be faster or slower than the apparent motion of the Sun. Indeed they may even propagate eastward or be standing waves (Hagan et al., 2003). These are known as "non-migrating" tides (Forbes, 2002) and again, what marks the Martian atmosphere out from Earth's, is the presence of such non-sun-synchronous oscillations of significant amplitude all the way up to the thermosphere. Thus while the vertical propagation of non-migrating tides also occurs in the terrestrial atmosphere those tides that result are more than an order

of magnitude weaker than the tides that follow (migrate with) the Sun (Wilson and Hamilton, 1996).

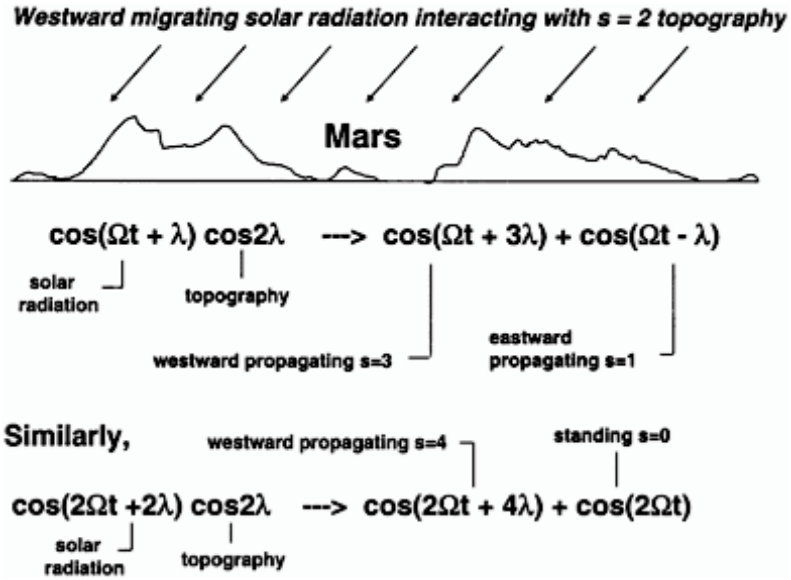

Figure 1.6: Illustration of solar radiation interacting with zonally in-homogeneous topography dominated by zonal wavenumber 2 giving rise to "non-migrating" tidal oscillations (from Forbes (2004)).

Figure 1.6, from Forbes (2004), highlights how if one assumes the surface modulation of solar insolation by topography is characterised by zonal wavenumber s=2 then the interaction with the 24-h period westward-migrating solar radiation will excite westward s=3 and eastward s=−1 propagating diurnal tides. Here, s, is the zonal wavenumber, whose magnitude represents the number of wave crests that occur along a latitude circle and whose sign indicates the zonal direction of propagation (Hagan et al., 2003). The eastward s=−1 oscillation, which is often referred to as the diurnal Kelvin wave (DKW), is of particular note given that it is in near-resonance in the Martian atmosphere (Forbes, 2004; Lewis and Barker, 2005). This means the vertical wavelength of this oscillation is typically comparable to the depth of the effective heating region through which it is excited (Zurek, 1988), constructive interference between the two enhancing its significance. Thus this oscillation in particular is expected to significantly affect the whole vertical atmospheric column (Forbes and Hagan, 2000; Forbes et al., 2001; Angelats i Coll et al., 2005). Also illustrated in Figure 1.6 is the 12-h period migrating component interacting with topography to generate westward propagating s=4 and standing s=0 semidiurnal tides.

Such non-migrating components have indeed been observed in accelerometer measurements from 110 to 170 km (Keating et al., 1998; Creasey et al., 2006b; Keating et al., 2007) as well as in Radio Science measurements with studies that use electron density data as a proxy to study the background neutral atmosphere (Bougher et al., 2001, 2004; Wang and Nielsen, 2004b; Cahoy et al., 2006; Hinson et al., 2008). Once again their magnitude on Mars can be significantly greater than the analogous oscillations at Earth given that, as Wang and Nielsen (2004b) explains, the surface pressure on Earth is ∼100 times larger than at Mars. Therefore any possible impression the terrestrial topography could have on the

atmosphere is easily damped by the atmosphere itself. Also, the Martian topography varies significantly in altitude (∼30 km) whereas the oceans on Earth tend to smooth over most of the terrestrial terrain.

1.4.5 The Exosphere

Finally we reach the last named region of the atmosphere, the *exosphere* ('outer' sphere). In the lower regions of the atmosphere molecules interact through collisions that restrict their motion to what essentially amounts to a so called "random walk". Indeed the principal reason we can apply the prognostic and diagnostic statements made in this chapter was because each gas molecule in our air parcel underwent enough collisions to establish a statistical equilibrium with every other molecule (Ratcliffe, 1972). A high frequency of collisions thereby formed the basis for our definition of the continuum. However, in the uppermost regions of the atmosphere above about 220 to 230 km (depending on solar activity (Haberle, 2002)), molecular collisions are so rare that a significant fraction of constituents pass out of the atmosphere undisturbed without sustaining a single collision. So, in the exosphere, the mean free path between collisions is so long that individual molecules follow ballistic trajectories that are determined by their molecular velocity at the exobase (usually in the high velocity tail of the Maxwellian distribution) and that occur mainly under the influence of gravity. The altitude at and above which the criteria that defines the exobase is met (the critical level) is therefore the level at which the mean free path exceeds the atmospheric scale height. While the heavier molecules that begin to escape are typically captured by the planet's gravitational potential and thus return to the atmosphere along parabolic trajectories a proportion of lighter molecules (albeit a very small proportion, currently) do indeed escape to space. Additionally, the temperature in the high upper atmosphere reaches a saturation value as the number density continues to decrease with altitude and solar radiation is no longer sufficiently absorbed to enhance the temperature gradient (Banks and Kockarts, 1973). Hence temperature becomes constant with altitude (Müller-Wodarg, 1997).

1.4.6 The Ionosphere

Extending upwards from approximately 90 km is the ionosphere, the region of the upper atmosphere where charged particles (electrons and ions) with appreciable thermal energy co-exist and interact with the neutral background atmosphere (Bauer, 1973). The principal production of ionospheric 'plasma' is from the absorption of a fraction of solar EUV and X-ray radiation (photoionisation) when photons with wavelengths shorter than the ionisation threshold of atmospheric constituents ionise (liberate) electrons (photoelectrons) from the atmospheric neutral species. Any excess energy of the photon is transformed into the kinetic energy of the ion-electron pair (Rishbeth and Garriott, 1969; Fox et al., 2008).

Another important ionospheric production process is inelastic collision between atmospheric constituents and precipitating energetic electrons (so called suprathermal electrons). In the case of Earth this is fundamental in producing the well known aurora at the geomagnetic poles (Lummerzheim and Lilensten, 1994b) with precipitating electron energies ranging from 5 eV to several keV. These electrons

are guided by the geomagnetic field and penetrate well into the atmosphere; an atmosphere of increasing neutral density where they lose energy through collisions with the ambient gas. The aurora results when the neutrals (and ions) are left in vibrationally and electronically excited states (Lummerzheim and Lilensten, 1994b). On Earth many auroral emission features are excited by secondary electrons i.e. electrons ejected by suprathermal (or primary electron) collision with the background atmosphere. These electrons contribute, for example, to the well known auroral green and red doublet lines of atomic oxygen at 5577 Å and 6300 Å (Rees et al., 1969). Ultimately the neutral background atmosphere absorbs the suprathermal electron energy (Stamnes and Rees, 1983b) providing an important source of ambient electron heating in the ionosphere.

Interactions in the Martian ionosphere take place in an environment fundamentally different to Earth's given the absence on Mars of any appreciable intrinsic magnetic field (Luhmann et al., 1992; Acuña et al., 1998). This means the topside atmosphere is directly exposed to the solar wind and interaction between the two, often to altitudes as low as 250 km (Lundin et al., 2006), results in an efficient transfer of the energy and momentum to both neutral and charged particles. Thus over time the neutral and ionic atmosphere will be eroded as ionospheric plasma is accelerated and transported away by convective electric field generated by the flow of the interplanetary magnetic field past Mars and parallel to the those field lines (Wang and Nielsen, 2002; Nagy et al., 2004) as they wrap around Mars.

What also makes the Martian ionic environment intriguing are the localised 'magnetic anomalies', crustal magnetic remnants left over from an era when Mars perhaps did have a global field (Acuña et al., 1998). This magnetic topography has a very complex structure and creates so-called 'mini-magnetospheres' that manipulate the solar wind interaction downwards into and horizontal convection across the Martian ionosphere (Breus et al., 2005). Thus while the Earth's ionosphere is contained within a prominent magnetic field, at Mars it is perhaps more appropriate to to define the upper boundary of the ionosphere as the ionopause; a region where the interaction between the solar wind and the ionospheric plasma represents a highly conductive boundary through which the interplanetary magnetic field gradually diffuses (Bauer, 1973) constricting vertical plasma motion.

In the main part of the ionosphere, in the region of the electron density peak, photochemistry controls the ion component densities with O_2^+ as the main ionospheric ion with a peak density of approximately 10^{11} m^{-3} at an altitude of 130 km (Blelly et al., 2005). Ionospheric measurements and modelling work confirm that the dayside ionosphere below ∼180 km is not subject to vertical or horizontal transport of ions such that photochemical equilibrium, how deep the solar EUV radiation penetrates into the neutral atmosphere and the neutral atmospheric structure itself control the main electron density peak (Zhang et al., 1990; Bougher et al., 2001). Such considerations place the typical primary ionospheric peak altitude at 125−135 km and electron density $\sim 10^{11}$ m^{-3} (Pätzold et al., 2005). A secondary peak is often observed (∼110 km and ∼50% electron density of primary (Pätzold et al., 2005)) due to high energy X-ray photons. This appears more like a shoulder to the main electron peak though sometimes does not appear at all (Fox and Yeager, 2006; Fox, 2004a; Fox et al., 1996). There are very few observations

of the ionosphere below 90−100 km although recently Pätzold et al. (2005) observed a sporadic third ionospheric layer at altitudes ranging from 65 to 110 km with average peak electron density 0.8×10^{10} m^{-3}. Its origin was attributed to charge exchange of magnesium and iron derived from ablation of meteorites entering the atmosphere (Pätzold et al., 2005). This was also predicted by, for example, Blelly et al. (2005) (1×10^{10} m^{-3} at ∼80 km). Blelly et al. (2005) also predicted an ionospheric layer due to cosmic rays at 35 km ($1-5\times10^{8}$ m^{-3}).

1.4.7 Turbulence and Diffusive Separation

Figure 1.3 highlights another way of defining atmospheric structure, based around the dominance of turbulent over diffusive mixing processes. In the lower regions of the atmosphere turbulent motions, typified by chaotic and frequent collisions, dominate to efficiently mix species together. This tends to prevent the separation of any one species by molecular diffusion so that no single species dominates the composition (Banks and Kockarts, 1973). Thus although you would expect there to be a scale height ($H=R^*T/g\mu$) for each atmospheric component (given the dependence on μ), and indeed an associated pressure distribution for each species, one finds in fact that composition in this region is constant with altitude. The lower atmosphere behaves as if it were composed of a single species whose molar mass is the average of all the gases present locally (Wayne, 1985). These swift collision dominated turbulent mixing processes, acting on small localised scales, do not discriminate against a particular molecular mass. Instead they redistribute species in opposition to the gravitational attraction that would otherwise try to separate them by diffusion over greater length scales. This region, the 'sphere' over which turbulence dominates, is known as the *homosphere*, as in 'same' sphere (see Figure 1.3) and we refer to the turbulent process as *eddy diffusion*.

The vertical extent of this chaotic region is determined by the relative distance between collisional events i.e. the mean free path. Thus at lower altitudes the mean free path is short because pressure and number density are so high. In turn turbulent motions (known as eddies) with high collision rates mean the rate of molecular separation is negligible (its time scale is so long) compared to the rate of turbulent mixing. Conversely at higher altitudes, where collisions are less frequent, the process of *molecular diffusion* can take a more dominant role as gravitational separation of the species based upon molecular mass acts before any mixing process randomises the distribution. This upper altitude region, where gravitational separation dominates by molecular diffusion processes, is known as the *heterosphere*, as in 'different' sphere. At these higher altitudes there is a gradual increase in the abundance of successively lighter constituents that one can appreciate by noticing the dependance of scale height H on the inverse of molecular mass (again $H=R^*T/g\mu$). Lighter species will have larger scale heights resulting in a smaller decrease in number density with altitude. Clearly there will also be a strong dependence on the temperature structure dictating that at low temperatures the transition to lighter species takes place at lower altitudes whereas a transition at high temperatures will occur at higher altitudes (Wallace and Hobbs, 1977). The boundary between the *homosphere* and the *heterosphere* is known as the *homopause*

and is usually quoted as the 1.26 nanobar pressure level at solar zenith angle 45° to 60°, which is modelled to vary by 15 km (115-130 km) from aphelion to perihelion (Bougher et al., 2000).

1.5 Modelling Carbon Dioxide Radiative Transfer

The dominance of CO_2 throughout the Martian atmosphere (95.32% abundance below ∼120 km (Haberle, 2002)) demands that a more complete consideration be made of its radiative effect on the energy balance. The high abundance results in more complex radiative behaviour for Mars than other planets where CO_2 is a lesser constituent (e.g. Earth abundance 0.036% (López-Puertas and Taylor, 2001)). If one wishes to conduct realistic simulations of the radiative energy balance involving or including Martian gaseous CO_2, where there is a large variation of optical depths throughout the atmosphere, then a larger range of transition band strengths would need to be considered including in particular those higher order lines and bands that are too weak to be important on Earth but which do contribute when the abundance is as high as it is on Mars. According to López-Puertas and Taylor (2001), for example, it is frequently necessary to cover more than five orders of magnitude in line strength while at the same time paying particular attention to the overlapping of CO_2 gas lines and bands. Unfortunately the complexity of the problem requires a highly intricate modelling strategy be adopted placing large demands on computer resources. The necessary parameterisations MarTIM uses to simplify the computation while still capturing the essence of CO_2 radiative effects is left for Chapter 2. For now, a brief introduction is given to the mathematics and physics of the problem we wish to parameterise.

1.5.1 Atmospheric Radiative Transfer

Whether it be solar EUV, UV or IR photon flux radiating downwards or IR flux radiating upwards from the surface (e.g. Earth shine) it is important to consider how the radiative energy passing through the atmosphere is manipulated as it interacts with the molecules of the atmosphere itself. The importance lies in taking account of how the various energy sources are absorbed or emitted by the atmospheric components, how incident radiation causes excitation and de-excitation of internal molecular energy levels and how this may ultimately lead to atmospheric heating or cooling. The theory of radiative transfer is the basic theory that performs this task. It allows us to discuss the interaction of radiation with matter and how the extinction of radiation (coefficient e_ν) by absorbing molecules i.e. reduction by both absorption and scattering, occurs alongside the emission properties of molecules (coefficient j_ν) i.e. spontaneous and stimulated emission, to change the amount of radiation L_ν (the radiance or specific intensity, $\mathrm{W.m^{-2}.sr^{-1}.Hz^{-1}}$) along a particular path length ds.

Under condition of thermodynamic equilibrium Kirchhoff's law states that the emission and absorption coefficients will be related by a general function that depends only on temperature (López-Puertas and Taylor, 2001). This is known as the source function, $J_\nu = \frac{j_\nu}{e_\nu}$, $\mathrm{W.m^{-2}.sr^{-1}.Hz^{-1}}$. If there are no other kinds of interaction then absorption and emission must combine to govern the change in radiance

that occurs and it is this relationship that the radiative transfer equation describes:

$$\frac{dL_\nu}{ds} = -e_\nu n[L_\nu - J_\nu] \tag{1.29}$$

The formal integral form of the radiative transfer equation states that the radiance $L_\nu(s, \underline{s})$ at a point P in the atmosphere in a particular direction $\underline{s}$ is a product of (1) the contribution of the radiance at some boundary point $L_\nu(s_0, \underline{s})$ (such as at the 'top' of the atmosphere) attenuated by (2) the absorbing atmosphere between that boundary and the point in question plus a consideration for (3) any emission of radiation from the atmosphere along the path to the point $k_\nu(s')n(s')J_\nu(s', \underline{s})$ (which will also be attenuated before reaching point P) (López-Puertas and Taylor, 2001). Thus:

$$L_\nu(s, \underline{s}) = L_\nu(s_0, \underline{s})exp[-\tau_\nu(s_0, s)] + \int_0^{\tau_\nu(s_0,s)} J_\nu(s', \underline{s})exp[-\tau_\nu(s', s)]d\tau_\nu \tag{1.30}$$

where if simple scattering is ignored then the extinction coefficient is the same as the absorption coefficient, thus $e_\nu = k_\nu$ (m^2) and where the optical thickness τ_ν is introduced to represent the extinction over path length ds.

It is important to remember that the energy balance of internal molecular levels and the efficiency of energy transfer between them and other molecules is not just determined by the exchange of photons. Collisional energy transfers are equally important in the determination of internal energy level population (López-Valverde et al., 1999). The efficiency of collisional processes will naturally introduce a relationship to altitude given the dependence of the collision frequency on density and thus on pressure. In the lower regions of the atmosphere collisional processes occur alongside radiative processes at a sufficient rate to constantly maintain an equilibrium between (1) external energy inputs, (2) energy exchanges between internal states and (3) energy outputs (by radiative processes etc). The internal population distribution of the molecules will be determined predominantly by collisions and their radiating properties can be defined by a single local kinetic temperature. This is known as a *local thermodynamic equilibrium.*

However at high altitude, where pressure and CO_2 number density has decreased significantly the mean free path between collisions will be much greater. Thus the rate of collisional processes will be far less than at lower altitudes. This has knock on effects for the efficiencies of transferring energy to, from and between internal molecular modes during collisions as molecular states are no longer able to rely on this collisional kinetic energy reservoir to supplement whatever energy changes are occurring due to radiative processes. The equilibrium will no longer be sustained by collisional processes and we will have a situation known as *non-local thermodynamic equilibrium* where the population distribution is dominated by radiative processes that may be entirely non-local to the region being studied. Parameterising these two equilibrium states and the transition between them is very important for an accurate description of the thermodynamic and radiative state of the Martian atmosphere.

1.5.2 Local Thermodynamic Equilibrium

In the case of local thermodynamic equilibrium we have the situation where an equilibrium exists for an air parcel (in terms of the inputs and outputs of energy) where a single temperature ($T_{ke}(z)$ at height

z) can be used to define almost its entire radiative and thermodynamic state. Thus much like a full thermodynamic equilibrium the source function J_ν is given by the well known Planck function at the local temperature:

$$B_\nu(T) = \frac{2h\nu^3}{c^2} \frac{1}{[exp(h\nu/kT) - 1]} \tag{1.31}$$

giving the distribution of photon energies in units (W m^{-2} Hz^{-1} sr^{-1}) in the particular direction $\underline{s}$. This local temperature will also describe the distribution of the molecular velocities with a Maxwellian, T_{ke}=$2E_{ke}/(3k)$, where k is the Boltzmann constant and E_{ke} is the mean kinetic energy of molecules. Finally the temperature would determine the form of Boltzmann's law that describes the internal population of excited states of the molecules (i.e. equation 1.32 showing a two level system example, where g_x represents the level degeneracies).

$$\frac{n_{upper}}{n_{lower}} = \frac{g_{upper}}{g_{lower}} exp\left(-\frac{h\nu}{kT_{ke}}\right) \tag{1.32}$$

Thus, as in the case of a full thermodynamic equilibrium, both the translational and internal energy of the air parcel can be described by well known functions of temperature so that the state of matter and of the radiation field are completely known (López-Valverde et al., 1999) and heating/cooling rates are more straightforward to obtain (e.g. see López-Valverde and López-Puertas (1994a,a); López-Valverde et al. (1998)).

The notion that this is a "local" equilibrium is an important point to bear in mind. A strictly observed thermodynamic equilibrium would require a closed and isolated system so that the distribution of internal energy could reach an equilibrium with the radiation field at a single unique temperature. Clearly a planetary atmosphere is not such a system, it is not in full thermodynamic equilibrium. Temperature gradients for example introduce flows of heat energy rather than temperature being the same everywhere. Additionally, the local radiation field (L_ν) may not necessarily be described by the Planck function at the local temperature ($B_\nu(T_K)$) (López-Valverde et al., 1999). However, as long as exchanges of translational kinetic energy by collisions is swift enough then a translational equilibrium can be maintained in that region of the atmosphere. As the kinetic energy is varied from region to region by non-local processes (e.g. solar forcing) the redistribution of this energy is quick enough (faster than the redistribution by internal forms at least) to prevent localised regions departing from a Maxwellian velocity distribution nor from a Boltzmann description of level population. And again, the localised radiating properties would still be described by a source function that is the Planck blackbody function, J_ν=$B_\nu(T_K)$, at the local temperature.

The excited internal states are said to be coupled to the local kinetic temperature by thermal collisions (López-Puertas and Taylor, 2001). Collisional processes supplement the energy gains and losses of the radiative field and you have an atmosphere where different regions can be described by different local kinetic temperatures. Neighbouring air parcels can be described as if they were in thermodynamic equilibrium at whatever kinetic temperature prevails locally while the atmosphere as a whole can still have a net gain or loss of radiative energy (because the radiation field may be quite different to the Planck

function at the local temperature) as long as, locally, collisions are sufficient to keep the molecular energy level populations in equilibrium with the reservoir of collisional energy. As long as the net gains or losses of radiant energy are small enough to maintain the source of collisional energy then the atmosphere, under local thermodynamic equilibrium, can still undergo heating and cooling.

1.5.3 Non-local Thermodynamic Equilibrium

The principal difference between a local and non-local thermodynamic equilibrium is that the energy level population distribution will no longer be described by a Boltzmann distribution. Regarding interactions and exchanges of translational energy through collisions one would expect the upper state population of a transition itself to be depleted in non-local with respect to local thermodynamic equilibrium. Typically this is because the frequency of collisions is insufficient to maintain a Boltzmann distribution and resupply the energy lost by spontaneous emission or whatever combination of processes lead to the energy loss (for example, photochemical). As noted above, this usually occurs at high altitudes where the mean free path between molecular collisions is large enough to significantly reduce the rate of translational energy transfer.

However, additionally, non-LTE situations can arise if the energy distribution and level populations are dominated by radiative processes, simply because these may very well not be local in nature. The radiative field could have an intensity, directional distribution and frequency spectrum that bares little relation to the Planck function at the local kinetic temperature (López-Puertas and Taylor, 2001). Such a non-local radiative field will likely push the energy level distributions further from that of a Boltzmann, either to be less populated than in LTE (as absorption of radiation and collisional excitation processes fail to significantly excite molecular levels) or to be more populated than in LTE (due to a strong radiative field from an upwelling flux of photons such as Earth shine).

In either of the above cases there will no longer an equilibrium between the energy input, exchange and output of the molecular energy states. Instead the energy level populations will be determined by a mixture of (less efficient / frequent) collisional interactions, the exchange of energy quanta and a non-local radiative field. Those populations will no longer be described by a Boltzmann and the energy balance and equations of heating / cooling rates will be more complex than in LTE (López-Valverde and López-Puertas, 1994a,a, 2001).

1.6 Structure and Aims of this Thesis

This PhD thesis is concerned with the study of Mars' middle and upper atmosphere, i.e. the mesosphere and thermosphere. Firstly, in Chapter 2, we develop and parameterise the mathematics and physics discussed above and place it into the context of our general circulation model, MarTIM. This includes discussing any additional mathematics, assumptions and approximations made. Then, in Chapter 3, general model improvements and updates to input datasets (versus previous model versions) are validated

by experiment. Next, in Chapter 4, we introduce a new IR heating parameterisation into the model, in the middle atmosphere, and show that this results in temperature and circulation enhancements throughout the model, which result in better comparison against Mars Odyssey accelerometer derived temperatures (Keating et al., 2003; Withers, 2006). In Chapter 5 we use the model to study the extent to which the upper atmosphere region is coupled to the lower atmosphere through the middle atmosphere. We consider which atmospheric fields are involved in this coupling, the amount by which they are manipulated and to what degree other processes define the atmospheric structure. Here we compare our model results to recent SPICAM number density and temperature measurements (Forget et al., 2009). Finally, in Chapter 6, we introduce a more sophisticated ionosphere model and study the variation in both primary and secondary electron production rate with season and solar cycle.

Chapter 2

MarTIM: Mars Thermosphere and Ionosphere Model

2.1 The Model: An Introduction

Studies have been conducted using a general circulation model named "MarTIM", which stands for "Mars Thermosphere and Ionosphere Model" that follows in a long tradition of atmospheric modelling at the Atmospheric Physics Laboratory (APL), University College London (UCL). In this chapter we briefly discuss the history of MarTIM's development and then give its present day description, before highlighting which studies have been completed for this PhD. The main aim of this chapter is given to deriving the mathematics and physics used by MarTIM to simulate the Martian atmosphere and to describing the various parameterisations and assumptions used in the simulations.

2.1.1 Model History

MarTIM is a forward Euler time-stepping model that solves the coupled non-linear Navier-Stokes equations of momentum as well as equations for energy and for mass continuity. Calculations are conducted on a co-rotating three-dimensional grid of variable size with horizontal grid points described by spherical polar coordinates and vertical grid points located at fixed pressure coordinates. MarTIM was first developed by former APL PhD student Tracy Moffat-Griffin (Moffat, 2005) as an amalgam of another APL model and various physics subroutines. The main energetic and dynamical core of MarTIM was converted from a Titan atmospheric global circulation model (Müller-Wodarg et al., 2000). Onto this was added a tidal module from the APL models CTIM (Müller-Wodarg, 1997) and CMAT2 (Harris, 2001) and finally the Mars Climate Database, which was first coupled to MarTIM as version 3.1 (Forget et al., 1995; Lewis et al., 1999; Forget et al., 1999). Moffat (2005) also included a simple photoionization and charge exchange scheme to calculate the Martian ionosphere, derived from Peters (2001). The initial photoionisation of neutral species and subsequent production/loss charge exchange chemistry embodied

by 23 chemical reactions (see Table 2.2) yielded a peak electron density of 2×10^5 cm^{-3} at 135 km for solar minimum conditions. Most of this work was summarised in the paper (Moffat-Griffin et al., 2007), where the thermal structure and dynamics for solar minimum conditions were studied.

2.1.2 Present Day Description

From its lower boundary of 0.883 Pa (∼60 km) to its upper boundary of 3.66×10^{-8} Pa (∼200-350 km depending on solar cycle and orbital conditions) MarTIM evaluates, for each time step, the main sources of solar forcing (EUV/UV and IR absorption) and the principal cooling rate from the CO_2 15-μm radiative band. MarTIM also calculates the resulting three-dimensional variation in neutral atmospheric temperature and wind velocities and self-consistently determines the neutral composition (number and mass densities, mass and volume mixing ratios, mean molecular weight) due to the mutual diffusion and advection of four of the main neutral gases, CO_2, N_2, CO and O. On this last point, note in this thesis MarTIM has been developed to include the diffusion and advection of any number of neutral species and so in Chapter 3 we investigate the effect that adding the three most prominent minor species (Ar, O_2 and NO) has on the thermodynamics of the modelled atmosphere.

As a first principles numerical model MarTIM must be provided with some form of input atmosphere from which to begin its numerical iterations. One can use either an externally sourced one-dimensional globally averaged input atmosphere or take an established steady state MarTIM result and read this back in as a three-dimensional input atmosphere. The former provides profiles of neutral temperature and number density with zero velocity winds being assumed throughout. Such an input can be obtained from other models or from available spacecraft data. Typically, however, we read in a previous MarTIM result. In doing so one can deliberately perturb the atmosphere from its steady state solution and study the variation that results. Lower boundary conditions, in the simplest case, are set with constant temperature and number density as well as zero velocity winds although other more physically self-consistent descriptions of the lower boundary can be used. Upper boundary conditions are defined with zero energy gradients to allow vertically propagating wave structures to dissipate rather than be reflected back downwards. A simple photoionization and chemistry scheme (which assumes photochemical equilibrium) is used to calculate the Martian ionosphere, as noted above. The effects of ion diffusion are not as yet included nor are any effects due to crustal sources of magnetic field.

Improvements to this basic model description include the coupling of MarTIM's lower boundary to the Mars Climate Database (MCD) version 4.3 developed at the Open University, at the Atmospheric, Oceanic and Planetary Physics group (AOPP), University of Oxford and at Laboratoire de Météorologie Dynamique (LMD), Paris (Forget et al., 2008; Millour et al., 2008; Millour and Forget, 2008; Angelats i Coll et al., 2005). The MCD v4.3 is derived from multiple runs of the aforementioned circulation models and is used to provide a physically self-consistent description of MarTIM's 0.883 Pa lower boundary. Not only does this allow the effects of lower atmosphere dust storms and gravity wave features to be included but the extension of MCD v4.3 to approximately 240 km allows us to compare directly the simulations

of MarTIM to equivalent results from the MCD. For this thesis the coupled MarTIM-MCD model was used to study the complex yet understudied Martian middle atmosphere (∼60-130 km) using the recently available density and temperature profiles from the Mars Express SPectroscopy for the Investigation of the Characteristics of the Atmosphere of Mars (MEX/SPICAM) stellar occultations (Forget et al., 2009). This work will be discussed in Chapter 5.

A recent collaboration with the Laboratoire de Planétologie de Grenoble (LPG) has provided a more sophisticated ionosphere model that solves a one-dimensional kinetic Boltzmann transport equation for the suprathermal population of electrons present in the Martian ionosphere. This kinetic model calculates the degradation in energy of suprathermal electrons as they propagate through the Martian atmosphere. It uses a fixed altitude grid between 80 and 500 km, independent of MarTIM's vertical pressure grid, and an energy grid between 0.1 and 280 eV. Interpolations between the two vertical grids are calculated as necessary. The principal source of suprathermal electrons for the kinetic code are the solar produced photoelectrons with a calculated dependence on solar zenith angle, solar activity and solar longitude. Alternative precipitating sources from available plasma observations (e.g. Acuña et al. (1998)) can also be used as an upper boundary condition if desired allowing, for example, the creation of the Martian night side aurora from the influx of auroral electrons to be studied (see Bertaux et al. (2005b)) or indeed the intricate night side ionospheric structure (Fillingim et al., 2007).

The 1D kinetic model has been coupled to MarTIM in such a way that a solution for the electron energy and altitude distribution is calculated at each of MarTIM's 2D latitude and longitude grid points, thereby creating a 3D solution for the ionosphere. An early version of the coupled model, which we refered to as *Trans*-TIM, was recently used to study the variation in the production efficiency of secondary electrons (that is, electrons produced by impact between primary/suprathermal electrons and the neutral components of the background atmosphere), see Nicholson et al. (2009). This work will be discussed further in Chapter 6.

2.2 Basic Model Structure and Design

2.2.1 Fundamental Assumptions and Approximations

The basic assumptions and approximations regarding the model design are:

1. The three-dimensional grid system is defined in the Eulerian frame using spherical polar coordinates and is fixed and co-rotating about an idealised homogeneous spherical planet.

    - Our use of the Eulerian frame as opposed to the Lagrangian frame was discussed in section 1.3.4 regarding the simplification to the governing mathematics this grid system provided. The Eulerian frame is convenient in that we are able to relate field variables such as temperature, pressure, geopotential height, etc to one another by sets of partial differential equations in space and time. The Lagrangian frame would require us to follow the fluid itself and therein

describe the more complex time evolution of each field variable as the coordinate system itself moved with the fluid flow.

2. Hydrostatic equilibrium (section 1.2.2, equation 1.4) can be assumed throughout the model.

   - Thus we assume that the various forms of energy input and output occur on time scales long enough to maintain hydrostatic equilibrium. Equivalently we assume there are no vertical motions of any significant magnitude other than those that can be treated as small perturbations from hydrostatic equilibrium. This state is often termed *quasi-hydrostatic equilibrium* (Smith, 2006).
   - Additionally this assumes that the collision frequency between molecules is sufficiently high that the thermodynamics of the gas in that region can be considered collectively using the diagnostic relationships discussed in Chapter 1 rather than on an individual molecule basis.

3. Pressure can be used as the vertical coordinate and the isobaric levels are only ever very slightly tilted with respect to the horizontal so that we can define a coordinate system that is approximately orthogonal.

   - In section 1.2.5 the gravitational potential was introduced and it was stated that, assuming the idealised situation of a homogeneous spherical planet, we could assume gravity is always directed toward the centre of the planet. Consequently gravity is everywhere perpendicular to surfaces of constant geopotential and has no horizontal component at all. Now, we make the further assumption that pressure levels are only ever very slightly tilted with respect to these surfaces of constant gravitational potential altitude. Thus we can effectively make a small angle approximation between these two surfaces and assume that they are indeed aligned and horizontal with the (x, y, P) system considered approximately orthogonal (Smith, 2006) and gravity constant horizontally.
   - This also allows us to derive a monotonic and very simple relationship between pressure and height that can be easily parameterised in the model. See section 2.2.2 below.
   - Finally we also assume gravity is constant in the vertical direction. This assumption can be made given that the vertical extent of the middle and upper atmosphere is only a small fraction of Mars' planetary radius thus gravity would not be expected to vary significantly.

4. We can separate out horizontal and vertical motions and deal with their partial derivatives separately.

   - We define the horizontal gradient evaluated on surfaces of constant geopotential height in Cartesian coordinates (Koskinen, 2008) with:

$$\nabla_z = \frac{\partial}{\partial x}\hat{\mathbf{e}}_x + \frac{\partial}{\partial y}\hat{\mathbf{e}}_y \tag{2.1}$$

- Likewise an equivalent del operator can be defined in spherical polar coordinates evaluated on isobaric surfaces (O'Neill and Chorlton, 1989) with:

$$\nabla_P = \frac{1}{r}\frac{\partial}{\partial\theta}\hat{\mathbf{e}}_\theta + \frac{1}{r\sin\theta}\frac{\partial}{\partial\phi}\hat{\mathbf{e}}_\phi \tag{2.2}$$

- From these two differential operators we can also describe the divergence of a vector and the Laplacian of a scalar and vector and these will be introduced later.

2.2.2 Pressure Coordinate System

From assumption 3 of section 2.2.1: in creating our global circulation model we use pressure as the vertical coordinate system. The basic idea is to replace the vertical coordinate of geopotential altitude (Z) with that of pressure (P). Thus partial differentials are evaluated with pressure as the independent variable to be held constant and altitude as the dependent variable.

The Simple Monotonic Pressure-Height Relationship

An advantage of such a conversion that allows convenient calculation of functions with respect to integer pressure levels can be derived immediately. From the discussion in section 1.2.3, Chapter 1 we derived equation 1.9 regarding the variation of pressure with altitude:

$$P(z) = P_0\ exp\left(\frac{-(z-z_0)}{H}\right)$$

from which we can generalise any reference to pressure levels by using integer values of a vertical grid point variable n:

$$Ln\left(\frac{P_n}{P_{n-1}}\right) = \frac{-(z_n - z_{n-1})}{H} = -\gamma$$

Here the vertical resolution is specified in terms of pressure scale heights with the dimensionless variable γ, which is typically set to 0.5 i.e. 2 pressure levels per scale height.

We specify the lower boundary pressure to be 0.883 Pa (n=1) and label (constant) pressure levels with integer values of n typically up to 9.9×10^{-8} Pa (n=33). From here it is straightforward to derive:

$$P_n = P_0\ exp[-\gamma(n-1)] \tag{2.3}$$

Thus we can see that quite a simple single valued monotonic relationship exists between the two variables n and $P(z)$ in each vertical column of the atmosphere.

Often a further conversion between pressure coordinates and the integer vertical grid point variable n is required and this can be achieved by applying the chain rule to equation 2.3:

$$\frac{\partial A}{\partial P} = \frac{\partial A}{\partial n}\frac{\partial n}{\partial P} = \frac{-1}{\gamma P}\frac{\partial A}{\partial n}$$

which is good for both scalar $A(x,y,z,t)$ and vector $\underline{A}(x,y,z,t)$ quantities.

Basic Conversions to Pressure Coordinates

The conversion to pressure coordinates for a scalar $A(x, y, z, t)$ into $A(x, y, P(x, y, t), t)$ in the horizontal plane can be shown (Smith, 2006) to be:

$$\nabla_z A = \nabla_P A + \rho \nabla_P \Phi . \frac{\partial A}{\partial P} \tag{2.4}$$

likewise for vector $\underline{A}(x, y, z, t)$ into $\underline{A}(x, y, P(x, y, z, t), t)$:

$$\nabla_z \underline{A} = \nabla_P \underline{A} + \rho \nabla_P \Phi . \frac{\partial \underline{A}}{\partial P} \tag{2.5}$$

This relationship also holds for partial derivatives in time.

In the vertical direction the relationship between the two coordinate systems for partial derivatives of both scalar $A(x, y, z, t)$ and vector $\underline{A}(x, y, z, t)$ quantities is given by the chain rule as:

$$\frac{\partial A}{\partial Z} = \frac{\partial A}{\partial P} \frac{\partial P}{\partial Z} = -\rho g \frac{\partial A}{\partial P} \tag{2.6}$$

using the equation of hydrostatic equilibrium (equation 1.4) to represent the change in pressure with altitude ($\frac{\partial P}{\partial Z}$).

Fundamental Conversions to Pressure Coordinates

With the basic scalar, vector and partial derivative conversions between altitude 'Z' and pressure 'P' frames introduced we can now recast some of the more fundamental relationships introduced in Chapter 1. Firstly for hydrostatic equilibrium (as discussed in section 1.2.2) we apply equation 2.6 to the geopotential term Φ to get a statement of hydrostatic equilibrium in the 'P' frame equivalent to equation 1.4 in the 'Z' frame:

$$\begin{aligned} \text{'Z' frame:} \quad & -dP = g\rho \, dz \text{ (from equation 1.4)} \\ \text{'P' frame:} \quad & \frac{\partial \Phi}{\partial P} = \frac{-1}{\rho} = -\alpha \end{aligned} \tag{2.7}$$

Another important example is the relationship between the pressure gradient in the 'Z' frame to the geopotential in the 'P' frame. From the introduction of the momentum equation in section 1.3.1 we have the pressure gradient force $\frac{1}{\rho}\nabla P$ in the 'Z' frame directed in the opposite direction to ∇P i.e. towards lower pressures. This was the second term in the momentum equation 1.21. Now we convert to the 'P' frame by applying equation 2.4 to the pressure P to get:

$$\nabla_z P = \rho \nabla_P \Phi \ (= g\rho \nabla_P z)$$

Hence:

$$\text{'Z' frame (from equation 1.21):} \ \frac{1}{\rho}\nabla_z P \rightarrow \nabla_P \Phi : \text{'P' frame} \tag{2.8}$$

Where the term in parenthesis ($g\rho\nabla_P z$) considers the implication of assumption 3, i.e. that pressure levels are only ever very slightly tilted with respect to horizontal surfaces of constant gravitational potential

altitude. We are saying the pressure gradient force is both (a) the gradient of the gravitational potential along our integer pressure surfaces and (b) the component of gravitational acceleration acting along pressure surfaces that are only ever slightly tilted (Smith, 2006).

Finally, being able to express Lagrangian total derivative in terms of the Eulerian local derivative, introduced in section 1.3.4 with equation 1.28 is an important tool given that we work in the Eulerian frame. The conversion to pressure coordinates requires equation 2.5 to be applied to the advection term $\underline{v}.\nabla_z$, giving:

$$\left.\frac{dA}{dt}\right|_P = \left.\frac{\partial A}{\partial t}\right|_P + \underline{v}.\nabla_P A + \underline{v}\frac{dP}{dt}\frac{\partial A}{\partial P} \tag{2.9}$$

2.2.3 Coordinate Reference Frame

The schematic representation of Figure 2.1 is used as our chosen coordinate reference frame, which from assumption 1 of section 2.2.1 is defined in the Eulerian frame using spherical polar coordinates. It is fixed and co-rotates with the idealised homogeneous spherical planet below.

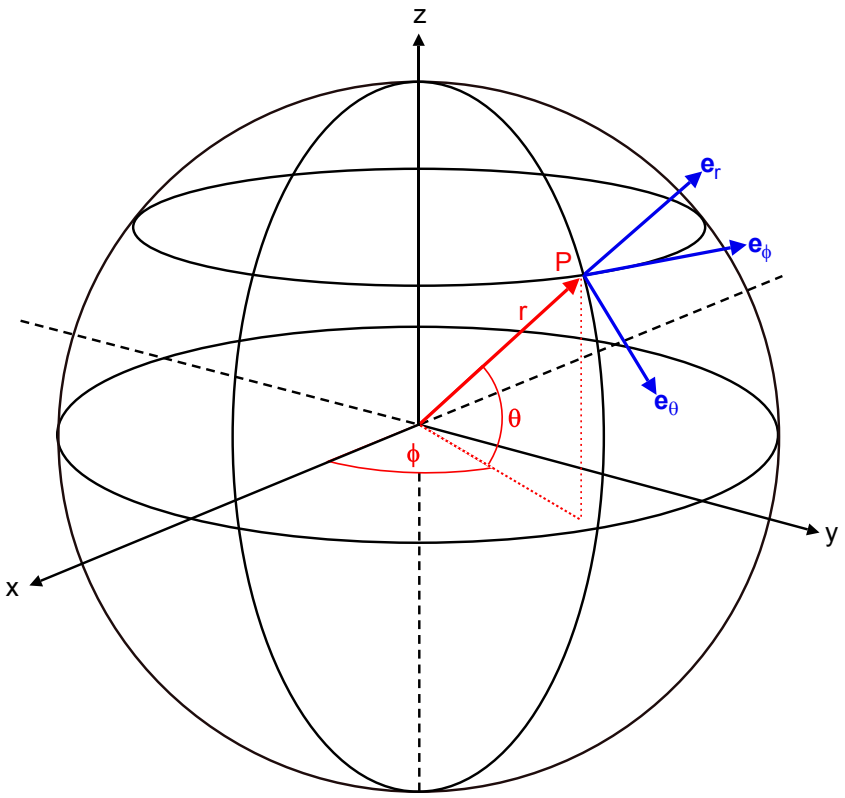

Figure 2.1: MarTIM's Eulerian coordinate reference frame.

- $\phi \rightarrow$ Longitude in the easterly direction. Positive winds (unit vector $\underline{e_\phi}$) flow eastwards.
- $\theta \rightarrow$ Latitude measured from the equator. Positive winds (unit vector $\underline{e_\theta}$) flow southwards.
- P or $n \rightarrow$ Integer pressure levels. Positive displacement (unit vector $\underline{e_r}$) is upwards.

From assumption 4 of section 2.2.1 we use the del operator defined in spherical polar coordinates by equation 2.2. Therefore the horizontal velocity vector $\underline{v}$, which is given by $\underline{v}=v_\theta \underline{e_\theta} + v_\phi \underline{e_\phi}$, is composed of the components:

$$v_\phi = r\cos\theta \frac{d\phi}{dt} \text{ (the zonal velocity component)} \tag{2.10}$$

$$v_\theta = r\frac{d\theta}{dt} \text{ (the meridional velocity component)} \tag{2.11}$$

and we deal with vertical velocity later on. Note also that the distance r to point P in Figure 2.1 is nearly always replaced by the mean planet radius (R_P=a).

2.3 The Primitive Equations

The basic governing equations introduced in Chapter 1, the Navier-Stokes equations, provide our starting point for numerical solutions to time evolution of large-scale atmospheric dynamics. They are known as the 'primitive equations' and are the basic form of Eulerian equations for fluid motion (Jacobson, 1999). The term 'primitive' makes reference to their being fundamental to the description of fluid motion. With the mathematical tools and modelling approximations introduced above we can now go ahead and express the Navier-Stokes set of equations from section 1.3 in the pressure coordinate system.

2.3.1 Momentum Equation

Taking equation 1.21 from Chapter 1, Newton's Second law applied to a rotating coordinate system, we need only convert the pressure gradient force term $\frac{1}{\rho}\nabla_z P$ into pressure coordinates. This was done just above and led to equation 2.8, which gave us $\nabla_P \Phi$. Thus for the horizontal momentum equation, where gravity is assumed to have no component, we have:

$$\frac{d\underline{v}}{dt} = -\nabla_P \Phi + \underline{F} - 2\underline{\Omega} \times \underline{v} \tag{2.12}$$

with $\underline{F}$ from Achilleos et al. (1998):

$$\underline{F} = \frac{(\mu_m + \mu_\tau)}{\rho}\nabla_P^2 \underline{v} + g^2 \frac{\partial}{\partial P}\left((\mu_m + \mu_\tau)\rho \frac{\partial \underline{v}}{\partial P}\right) \tag{2.13}$$

Finally, substitute the total derivative with the local derivative from equation 2.9 above to get the momentum equation in the Eulerian frame and in the pressure coordinate system:

$$\frac{\partial \underline{v}}{\partial t} = -(\underline{v}.\nabla)\underline{v} - \nabla_P \Phi + \underline{F} - 2\underline{\Omega} \times \underline{v} \tag{2.14}$$

with the Coriolis force:

$$2\underline{\Omega} \times \underline{v} = 2\Omega v_\phi \sin\theta \underline{\hat{\mathbf{e}}}_\theta - 2\Omega v_\theta \sin\theta \underline{\hat{\mathbf{e}}}_\phi \tag{2.15}$$

in the 2D, horizontal form we use across constant pressure level surfaces. We have not included $-2\Omega v_\phi \cos\theta \underline{\hat{\mathbf{e}}}_r$, the vertical component of the Coriolis force for a zonal displacement, because it is usually

much smaller than the gravitational force (Holton, 2004). Also, term $2\Omega v_r \cos\theta \underline{\hat{\mathbf{e}}}_\phi$, the zonal component of the Coriolis force for a vertical displacement, is not included because vertical motions are assumed to be negligible in hydrostatic equilibrium.

2.3.2 Energy Equation

For the energy equation we take equation 1.26 and express the total derivative $c_P \frac{dT}{dt}$ in terms of the Eulerian local derivative in pressure coordinates using equation 2.9, replacing scalar A with temperature T as necessary. First recall equation 1.26:

$$\dot{Q} = c_P \frac{dT}{dt} - \alpha \frac{dP}{dt}$$

and then proceed as described:

$$c_P \frac{dT}{dt} = c_P \frac{\partial T}{\partial t} + c_P \underline{v}.\nabla_P T + \omega c_P \frac{\partial T}{\partial P}$$
$$\frac{dh}{dt} = \left.\frac{\partial h}{\partial t}\right|_P + \underline{v}.\nabla_P h + \omega \frac{\partial h}{\partial P}$$

where $h{=}c_P T$ is the specific enthalpy per unit mass. Substituting this back into energy equation 1.26 gives:

$$\left.\frac{\partial h}{\partial t}\right|_P = -\underline{v}.\nabla_P h - \omega \frac{\partial h}{\partial P} + \frac{\omega}{\rho} + \dot{Q} \tag{2.16}$$

which is the energy equation for the specific enthalpy change ∂h per unit time per unit mass. Here, ω/ρ represents the work done by the vertical pressure gradient on the motion relative to the fixed pressure surfaces (ω, discussed in section 2.3.3 below). A positive value of ω corresponds to subsidence, leading to (adiabatic) heating while a negative value corresponds to upwelling, leading to (adiabatic) cooling (Smith, 2006).

Now we need an expression for the kinetic energy conservation. For this we take the scalar product of the horizontal momentum equation 2.14 with $\underline{v}$ (Achilleos et al., 1998). This gives:

$$\left.\frac{\partial \epsilon_{ke}}{\partial t}\right|_P = -\underline{v}.\nabla_P \epsilon_{ke} - \omega \frac{\partial \epsilon_{ke}}{\partial P} - \underline{v}.\nabla_P \Phi + \underline{v}.\underline{F} \tag{2.17}$$

where $\epsilon_{ke}{=}\frac{1}{2}\underline{v}.\underline{v}$ is the kinetic energy per unit time per unit mass. Finally it is a simple matter to add equations 2.16 and 2.17 together, noting that we introduce the sum $\epsilon = h + \epsilon_{ke}$ to represent the total internal energy. Thus:

$$\frac{\partial \epsilon}{\partial t} = -\underline{v}.\nabla_P(\epsilon + \Phi) - \omega \frac{\partial}{\partial P}(\epsilon + \Phi) + \underline{v}.\underline{F} + \dot{Q} \tag{2.18}$$

This form of the energy equation states that the local derivative, with respect to time, of total internal energy (as the sum of specific enthalpy and kinetic energy) is equal to the transport of total energy through the horizontal winds flowing along isobaric levels *plus* the change in total energy as air parcels expand or contract with any vertical (ω) motion relative to isobaric levels. We discuss the vertical motion (ω) in more detail shortly (see section 2.3.3 below).

Additionally we include dynamic forces ($\underline{v}.\underline{F}$), related to viscous stress ($\dot{Q}_\eta$) and the thermal conductivity ($\dot{Q}_\kappa$), both of which do work on the gas (equations 2.20 and 2.19 respectively) and a contingent for any external sources or sinks of energy ($\dot{Q}$). We split $\dot{Q}$ into three separate terms to take into account (1) the energy input due to solar EUV and UV photon flux ($\dot{Q}_{EUV,UV}$, discussed in section 2.5), (2) the energy input due to solar IR photon flux ($\dot{Q}_{IR}$, discussed in section 2.6) and (3) the energy output due to deactivation of excited levels predominantly involving neutral CO_2 and O ($\dot{Q}_{CO2}$, also discussed in section 2.6). Note that each of these $\dot{Q}$ terms represent energy inputs into the model and thus may contribute to heating ($\dot{Q}_\eta$, $\dot{Q}_{EUV,UV}$ and $\dot{Q}_{IR}$) or cooling ($\dot{Q}_\kappa$ and $\dot{Q}_{CO2}$).

The Transport of Heat Energy by Thermal Conduction

To include the dynamic forces acting on our air parcel we first consider the transport of energy by thermal conductivity. Ordinarily an expression for this behaviour would depend upon the adopted interaction potentials between the various neutral constituents i.e. quantum mechanical concerns. However, it would seem from the analysis of experimental data (Banks and Kockarts, 1973; Bauer, 1973) that a theoretical expression for thermal conductivity can be represented by:

$$\kappa_m = \lambda T^s$$
$$\text{and } \kappa_\tau = \rho c_p K_\tau$$

Where subscripts m and τ indicate molecular and turbulent components respectively. Also λ=1.5 and s=1.23 for CO_2 (Bauer, 1973) and K_τ is the eddy diffusion coefficient (see section 2.4).

To put these terms in context theory states that conductivity is the transport of thermal energy in any medium in which a temperature difference exists (Gombosi, 1994). Thus in the simplest of cases the rate of transport, i.e. the flux (molecular F_m and turbulent F_τ) is found to be directly proportional to the temperature gradient, its direction being opposite to the direction of the temperature gradient at that point. Hence:

$$F_m = -\kappa_m \frac{\partial T}{\partial z}$$
$$F_\tau = -\kappa_\tau \frac{\partial T}{\partial z}$$

Thus atmospheric constituents with higher temperatures will have a larger mean kinetic energy than those at lower temperature giving a net flow of energy from higher temperatures to lower temperatures, even if there is an isotropy to the molecular motion. This net flow is the essence of thermal conduction, acting to remove gradients in temperature and restore equilibrium to the energy distribution.

For coding purposes we parameterise the following divergence of the thermal conductive flux for MarTIM's thermal conductivity terms (Smith, 2006):

$$\dot{Q}_\kappa = \frac{\kappa}{\rho}\nabla_P^2 T + g^2 \frac{\partial}{\partial P}\left(\kappa\rho\frac{\partial T}{\partial P}\right) \tag{2.19}$$
$$\text{with } \kappa = \kappa_m + \kappa_\tau$$

Here the first term on the right hand side is the horizontal component and the second term the vertical component of thermal conductivity.

Redistribution and Dissipation of Kinetic Energy by Viscosity

With the transport of any air parcel it is necessary that viscosity, and its effects on the thermal and kinetic energy of the gas, be considered. Viscosity is inevitable as a consequence of internal friction within moving fluid elements (Gombosi, 1994). As noted earlier, the frictional drag force is proportional to the velocity of the air parcel. In addition, friction also exists between individual air parcel's because they move with different velocities. Such viscous interaction acts to dissipate kinetic energy and momentum between one region and the next. Although the momentum must always be conserved by such processes the kinetic energy need not be i.e. energy can be converted from one form to another. Thus typically an amount of kinetic energy will be converted to thermal energy so as to conserve momentum overall. Hence viscosity will both redistribute and dissipate kinetic energy into the form of heating (Smith, 2006).

Viscosity is actually found to be analogous to thermal conduction in its theoretical and semi-empirical formulation (Banks and Kockarts, 1973), i.e. viscosity also depends upon quantum mechanics, interaction potentials, etc. An appropriate expression is thus:

$$\eta_m = \mu T^{\beta}$$

$$\text{and } \eta_\tau = \text{Pr}\rho K_\tau$$

Again, subscripts m and τ indicate molecular and turbulent components respectively and K_τ is the eddy diffusion coefficient (see section 2.4). Term Pr is the turbulent Prandtl number, which is an empirical parameter that describes the relative magnitudes of heat and momentum fluxes due to eddies (Smith, 2006). Mars orbiter entry experiments, e.g. Rouzaud et al. (2004), suggest Pr=0.66. Coefficient μ equals 3.43×10^{-7} for N_2 and 3.90×10^{-7} for O and β equals 0.69 for both N_2 and O (Banks and Kockarts, 1973). For CO_2 we use the following theoretical expression from Banks and Kockarts (1973):

$$\mu_{\text{CO}_2} = (5/16d^2)(kmT/\pi)^{0.5}$$

where m is the molecular mass and d is the molecular diameter.

Next, while we understood thermal conduction to be a flux of thermal energy directly related to the removal of temperature gradients as a system returned to an equilibrium state (following some energy inbalance e.g. localised heat input), we can now relate viscosity to velocity gradients in exactly the same way. Viscosity acts to remove velocity differences (accelerations) and restore an equilibrium to the velocity field. Thus:

$$q_\eta = -\eta\frac{\partial u}{\partial z}$$

Where q_η is the shearing stress i.e. the force acting on neighbouring fluid elements moving with velocity u, by virtue of their viscosity. From Smith (2006) we have the total energy change due to viscosity in

pressure coordinates:

$$\dot{Q}_\eta = g^2 \frac{\partial}{\partial P}\left(\eta\rho\underline{v}.\frac{\partial \underline{v}}{\partial P}\right) \tag{2.20}$$

$$\text{with } \eta = \eta_m + \eta_\tau$$

Representing the redistribution and dissipation of kinetic energy by viscosity changing both the internal and kinetic energy of the gas.

2.3.3 Continuity Equation and the Vertical Wind

To finish our introduction of the model assumptions and mathematics we now define the vertical wind. By assuming the dominance of hydrostatic equilibrium we have largely removed the need to consider any vertical motion. As such we consider vertical winds to be small perturbations from hydrostatic equilibrium and solve the continuity equation 1.27 to ensure these smaller vertical motions are consistent with mass conservation.

Firstly we define the vertical pressure velocity ω as $\omega = \frac{dP}{dt}$. This is the Lagrangian derivative of pressure i.e. the vertical wind in the pressure frame relative to the pressure levels. The solution for ω comes from the continuity equation, expressed in terms of the pressure coordinate system, and links vertical winds relative to constant pressure levels to the horizontal winds flowing along them:

$$\frac{\partial \omega}{\partial P} = -\nabla_P.\underline{v} \tag{2.21}$$

Equation 2.21 is the principal reason and advantage of using pressure as the vertical coordinate: the divergence of horizontal winds on isobaric surfaces ensures mass continuity by requiring that for example the matter carried away by horizontal winds is supplied by vertical flows.

So then to link the vertical wind velocity in the pressure coordinate system ($\omega = \frac{dP}{dt}$) to the vertical wind in the geopotential height frame ($v_z = \frac{dz}{dt}$) we take the latter and express the total derivative in terms of the local derivative at a particular pressure level:

$$\begin{aligned} v_z = \frac{dz}{dt} &= \left.\frac{\partial z}{\partial t}\right|_P + \underline{v}.\nabla_P z + v_z\frac{\partial z}{\partial P} \\ &= \frac{1}{g}\left.\frac{\partial \Phi}{\partial t}\right|_P + \frac{1}{g}\underline{v}.\nabla_P\Phi - \frac{\omega}{\rho g} \end{aligned} \tag{2.22}$$

The first term represents the vertical motion of our constant pressure levels through a point fixed in space, the second term represents the horizontal winds that blow along the the pressure levels, which by virtue of our small angle approximation between levels of geopotential and pressure may include some vertical component and finally the third term represents winds that blow vertically relative to the fixed pressure levels.

2.4 Neutral Diffusion

The theory of neutral species diffusion deals with the physics of neutral species mixing in the gravitational field of a planet. Its role in manipulating the atmospheric composition lead to the distinction between the heterosphere and homosphere in Chapter 1 with respect to small scale turbulent motions (eddy diffusion) and larger scale diffusive motions (molecular diffusion). To account for neutral species diffusion in MarTIM we follow the procedure described by Chapman and Cowling (1970) and used by Müller-Wodarg et al. (2006). Thus we calculate the dynamical redistribution of individual species by explicitly calculating (1) the transport by molecular and eddy diffusion processes and (2) the advective and convective transport by winds. Expressions for transport by (1) are only conducted in the vertical direction since vertical gradients of variables associated with composition (mass mixing ratios etc) are far greater than complementary horizontal gradients (making horizontal diffusion negligible). However, expressions for transport by (2) are conducted in both vertical and horizontal directions, since clearly horizontal winds will be a major feature of any thermosphere and play an important role in the transport of atmospheric constituents.

Transport by Molecular Diffusion Processes

For the calculation of transport by molecular diffusion we first require statements describing the molecular diffusion velocities, w_i^D (for species i). From Müller-Wodarg et al. (2006) we have:

$$d_i = \frac{\partial Y_i}{\partial z} - \left(1 - \frac{m_i}{m} - \frac{H}{m}\frac{\partial m}{\partial z}\right)\frac{Y_i}{H} = -\sum_{j\neq i}\frac{mY_iY_j}{m_j\mathfrak{D}_{ij}}(w_i^D - w_j^D) \tag{2.23}$$

where Y_i=ρ_i/ρ and m_i are the mass fraction and molecular mass of the ith constituent, m is the mean molecular mass of the atmosphere and w_i^D is the vertical diffusion velocity (also of the ith constituent). Equation 2.23 for N species results in $N-1$ independent equations with $N-1$ unknowns (the molecular diffusion velocities w_i^D), which when rearranged into a matrix can be solved with Cramer's rule. For the N^{th} species we are required to assume that there is no net flow through an elementary surface due to molecular diffusion, thus:

$$\sum_{i=1}^{N} Y_i w_i^D = 0 \tag{2.24}$$

which means ultimately that the mass fraction of the N^{th} species can be integrated and expressed in terms of the other $N-1$ species as $Y_N = 1 - \sum_{i=1}^{N-1} Y_i$. Note we ignore self-diffusion $i = j$ and assume $ij = ji$.

The binary diffusion coefficient's $\mathfrak{D}_{ij}$ are taken from the study of Marrero and Mason (1972) who considered many different published experimental results for these coefficients and in particular their temperature dependence. These coefficients are simply the proportionality constants between the molecular flux $\underline{J_i}$ (molecules per square centimeter per second) and the composition gradient ∇x_i (mole fractions) of a species within a nonuniform mixture. They are the linkage between the bulk source of gas and

the mass flux away from this concentration as diffusion attempts to remove composition gradients from the region of study. The diffusion coefficients are positive constants, with units m^2s^{-1}, defined in a two-component mixture by the phenomenological equations:

$$\underline{J_1} = -n\mathfrak{D}_{12}\nabla x_1 + x_1\underline{J}$$
$$\underline{J_2} = -n\mathfrak{D}_{21}\nabla x_2 + x_2\underline{J}$$

The extrapolation to a multicomponent form is reported as being 'excessively' complex in the calculation of molecular flux. So instead Marrero and Mason (1972) quote that a simpler method can be used that relates the composition gradient of a species to differences in fluxes of gas pairs. In this way we actually describe multicomponent diffusion in terms of the diffusion coefficients for binary mixtures, hence the references above to species i and j.

For the temperature dependence in the experimental results of the diffusion coefficients $\mathfrak{D}_{ij}$ that were studied by Marrero and Mason (1972) they present the following semi-empirical equations:

$$ln(p\mathfrak{D}_{ij}) = lnA + slnT - ln\left(ln\left(\frac{\phi_0}{kT}\right)\right)^2 - S/T - S'/T^2 \tag{2.25}$$

which is valid for the data presented in table 12 of that study. For the data in table 13 we use:

$$ln(p\mathfrak{D}_{ij}) = lnA + slnT - S/T \tag{2.26}$$

and it is by using these two equations that we can calculate the diffusion coefficients for MarTIM's neutral species (and many others) using the large range of coefficients provided by Marrero and Mason (1972).

Transport by Eddy Diffusion Processes

For the calculation of transport by eddy diffusion we define the vertical eddy diffusion velocity ($w_i^{K_\tau}$) along with the eddy diffusion coefficient K_τ (units m^2s^{-1}) with:

$$w_i^{K_\tau} = -K_\tau \frac{\partial ln(Y_i)}{\partial z} \tag{2.27}$$

where K_τ is adopted from the work of Bougher et al. (1990) and is set to a maximum value of 1.5×10^3 m^2s^{-1} at and above the turbopause (whose pressure is defined as $P_{turbo} = 1.2\times10^{-4}$ Pa), while below being calculated at pressure P with:

$$K_\tau = 1500\left(\frac{P}{P_{turbo}}\right)^{-0.5} \tag{2.28}$$

Here, the eddy diffusion coefficient K_τ is used to parameterise all those turbulent processes occurring in the heterosphere where short mean free path 'random walks', i.e. turbulent eddies, dominate the mixing of atmospheric constituents. K_τ must capture the net effect of all those processes too small to be resolved by MarTIM's model grid and so is inherently approximate in its nature.

The magnitude of K_τ is usually set to be much lower in three-dimensional models ($\sim$1.0-2.0$\times10^3$ m^2s^{-1}, peaking near 125 km (Bougher et al., 1999b, 2000)) than it is in one-dimensional continuity-diffusion models ($\sim$5.0$\times10^3$ to 1.5$\times10^4$ m^2s^{-1}, at 125 km (Stewart and Hanson, 1982; Nier and McElroy, 1977)). This is because 1-D models are unable to resolve the atmospheric mixing that global-scale circulation produces within 3-D models. This therefore reduces the requirement for a large vertical eddy diffusion in 3-D models (Bougher et al., 2000) and generally limits the role eddy conduction plays in the modelled atmosphere (Bougher et al., 1999b, 2000).

And Finally, the Dynamical Redistribution of Neutral Gas Species

Finally to bring the transport by molecular and eddy diffusion processes alongside a description of the transport brought about by horizontal winds we apply the continuity equation 2.21 to the mass fraction Y_i of species i. Hence the continuity equation for the i^{th} constituent is given in spherical pressure coordinates as:

$$\frac{\partial Y_i}{\partial t} + u_\theta \frac{1}{a}\frac{\partial Y_i}{\partial \theta} + u_\phi \frac{1}{a\sin\theta}\frac{\partial Y_i}{\partial \phi} + w\frac{\partial Y_i}{\partial P} = \frac{g}{a^2}\frac{\partial}{\partial P}\left(a^2 \rho Y_i (w_i^D + w_i^{K_\tau})\right) + J_i \tag{2.29}$$

Here then we have the time development of each mass fraction (first term, left hand side) depending upon the advection of neutral species by horizontal winds (second and third terms, left hand side), vertical winds (fourth term, left hand side) and the (vertical only) molecular and eddy diffusion in altitude (terms on the right hand side). Chemical production and loss is described with the last term, J_i, but this is currently set to zero in MarTIM.

2.5 EUV and UV Heating

The solar EUV/UV flux is one of the most important energy inputs into the model energy balance equation, becoming dominant in its influence in the upper layers of MarTIM's thermosphere. The wavelength regions of the solar spectrum that are absorbed in the thermospheres of solar system planets are generally characterized by wavelengths less than 200 nm (Fox et al., 2008). MarTIM calculates the neutral mass heating rate (J s^{-1} kg^{-1}) as being proportional to the number of molecules per unit area that are absorbing radiation along the ray path through the atmosphere to the point in question (Müller-Wodarg, 1997). Thus we need to calculate the column depth of atmosphere along that ray path with Beer's law. This states that the absorption of radiation increases exponentially with the optical depth of the absorbing species. It is then a simple matter to calculate the intensity of solar photon flux at any point in the atmosphere as a product of the attenuation of the flux at the top of the atmosphere:

$$\begin{aligned} I(z,\lambda,\chi) &= I_\infty(\lambda) exp[-\tau(z,\lambda,\chi)] \\ \text{with } \tau(z,\lambda,\chi) &\equiv \sum_s n_s(z)\sigma_s^a(\lambda) ds_\lambda \end{aligned} \tag{2.30}$$

Here $\tau(z,\lambda,\chi)$ is the optical depth, which includes a consideration of the column density ($\int_z^\infty n_s(z) ds_\lambda$), along an incremental path length ds_λ in the direction of the solar flux with MarTIM providing the neutral

number density $n_s(z)$ for neutral species s as required. The path length ds_λ under the assumption of a plane horizontally stratified atmosphere is equal to $-dzsec\chi$, where χ is the solar zenith angle. Such an assumption is good for solar zenith angles less than about 75^o (Schunk and Nagy, 2000). For larger zenith angles the curvature of the atmosphere requires a complex function of χ known as the Chapman function $Ch(X_p, \chi_p)$ (Smith III and Smith, 1972) to solve for the χ dependence of path length. The wavelength dependent absorption cross sections $\sigma_s^a(\lambda)$ for neutral species s are obtained from a variety of sources and will be discussed in Chapter 3. Finally $I_\infty(\lambda)$ is the solar flux at the top of the atmosphere, the discussion of which has also been left to Chapter 3.

Finally we calculate the heating rate with:

$$\dot{Q}_{EUV,UV} = \frac{\epsilon_{fac}}{\rho} \sum_s n_s(z) \int_\lambda I(z, \lambda, \chi) \sigma_s^a(\lambda) d\lambda \tag{2.31}$$

where the division by ρ ensures this is a statement of heating rate per unit mass. Here the term ϵ_{fac} is an efficiency factor representing the fraction of absorbed solar flux energy that is converted into heat energy. Solar energy is transformed into heat by various different processes such as photodissociation, photoelectron-impact dissociation, exothermic neutral-neutral or neutral-ion reactions and dissociative recombination of ions with electrons (Fox et al., 2008). The efficiency factor ϵ_{fac} is therefore a simplification of the real atmosphere since in MarTIM these processes are neglected and ionisation and dissociation processes are treated with separate parameterisations. Therefore the efficiency factor allows us to still compute the heating rate from the dominant solar flux. Past work has established that the heating efficiencies on Mars range from 16 to 22% at altitudes above 100 km (Fox et al., 1996).

Figure 2.2 presents the results of the above discussion. The solid blue line represents the optical depth, $\tau(z, \lambda, \chi)$ from equation 2.30, against the top x-axis. Since the optical depth is derived from the column density, which for most atmospheric gases shows an exponential variation with altitude, a similar behaviour would be expected for τ (Banks and Kockarts, 1973). And because τ itself is the argument of an exponential (in equation 2.30) it follows that the strongest absorption of radiation occurs about the level of unit optical depth (Wallace and Hobbs, 1977) and that complete attenuation occurs extremely rapidly after that position. The dotted blue line marks the point of unit optical depth in Figure 2.2 and the solid red line, which represents the rate of incident flux absorption due solely to the contribution from CO_2 (i.e. the heating rate due solely to CO_2, equation 2.31 for s=CO_2 normalised against the bottom x-axis), shows that maximum absorption occurs in a similar vertical region. Finally the solid black line represents the attenuation of incident radiation due to this atmospheric absorption ($I(z, \lambda, \chi)$ from equation 2.30, also normalised against the bottom x-axis). This line indicates the cumulative depletion that the beam of radiation has experienced as a result of passage through the atmosphere above. We would expect the monochromatic radiation of the incident beam to be diminished by a factor e when and where the optical depth is unity, Figure 2.2 shows this to be the case.

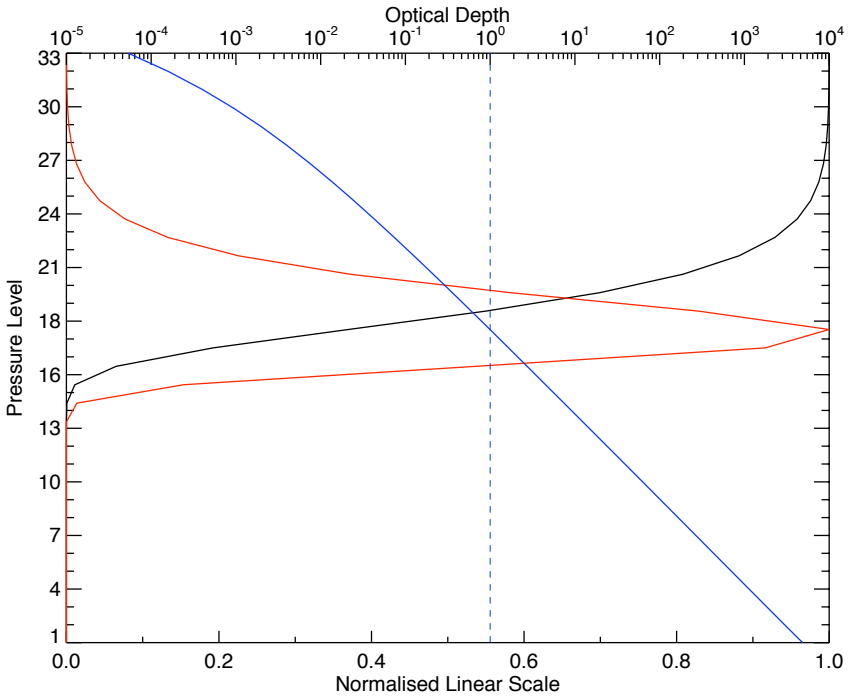

Figure 2.2: Vertical profile of solar EUV/UV absorption. Solid blue line represents optical depth ($\tau(z, \lambda, \chi)$) while short-dashed blue line marks out τ=1. Top x-axis in both cases. Red line represents rate of absorption (normalised) due solely to the contribution from CO_2 i.e. the heating rate due solely to CO_2 (bottom x-axis). Black line represents attenuation of incident radiation (normalised, bottom x-axis).

2.6 Modelling Carbon Dioxide Radiative Transfer

As was mentioned in Chapter 1, section 1.5, any global circulation model of the Martian atmosphere must include some consideration of the radiative behaviour of carbon dioxide given its dominant presence throughout the atmosphere. We noted how more complex radiative behaviour would be expected on Mars than occurs on other planets where CO_2 is a lesser constituent. The basic theory of radiative transfer was introduced as an appropriate starting point as it deals with the interaction of radiation (solar and surface IR) with matter. Then the importance of collisional processes and translational energy transfer was noted with respect to different regions of the atmosphere and the efficiencies of these processes. Now in Chapter 2 we discuss the necessary parameterisations MarTIM uses to simplify the computation of this behaviour while capturing the essence of CO_2 radiative effects.

2.6.1 The Carbon Dioxide Molecule

The major difficulty here is how the radiant energy interacts with the (typically complex) molecular structure of the atmospheric molecular species. For example, some of the absorbed radiant flux may not end up as heating of the air parcel but instead contribute to the excitation of some internal state (vibrational, rotational, etc) of the molecule. Thus our concern is with the structure of the atmospheric

constituents and the specific ways in which they could interact with the radiation field.

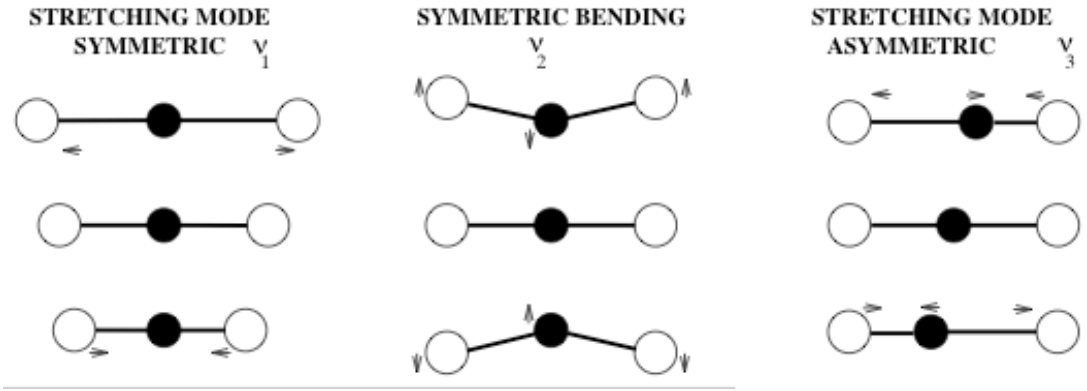

Figure 2.3: The fundamental vibrations of the CO_2 molecule (figure 1 of López-Valverde et al. (1999)).

In the Martian atmosphere the dominant species, CO_2, is a linear triatomic molecule. It can store internal energy as rotations and vibrations. It has three fundamental vibrational modes (López-Valverde et al., 1999) (within which there is a more finely resolved rotational structure) and thus any vibration of the molecule can be considered to be a linear combination of these (see Figure 2.3). The three modes are (1) the vibrational or symmetric stretching mode ν_1 (transition energy 1235 cm^{-1}, 15-μm band), which is mostly inactive as there is no change in dipole moment associated with the vibration, (2) the symmetric bending mode ν_2 (transition energy 667 cm^{-1}, 7.6-μm band), which is a perpendicular motion that is doubly degenerate since it can take place in either of two perpendicular directions and (3) the asymmetric mode ν_3 (transition energy 2349 cm^{-1}, 4.3-μm band), which is a parallel motion.

One can summarise the radiative interactions that exchange energy with CO_2 in terms of the following three fundamental processes: (1) spontaneous emission, (2) induced emissions and (3) absorption. Thus a CO_2 molecule absorbing a photon of the correct wavelength corresponding to a transition will cause an excitation of one or more vibrational or rotational states (López-Puertas and Taylor, 2001). The molecule may 'relax' to a lower energy state by emission of a photon although the total emitted energy may be greater or less than that of the photon absorbed. For example the absorption of 2.7-μm photons gives rise to excitation of the $(\nu_1 + \nu_3)$ vibrational combination state with the CO_2 subsequently emitting only the ν_3 photon at 4.3-μm (López-Valverde and López-Puertas, 1994a,b). The energy associated with electronic transitions usually means the absorption/emission of visible or UV photons, while vibrational transitions involve near to middle infrared photons and finally rotational level transitions involve far infrared photons (López-Puertas and Taylor, 2001).

Collisional processes also play an important role in the energy balance of an ensemble of molecules. Collisions can transfer energy quanta between colliding molecules, the vibration-vibration transfer between the $\nu_2 = 2$ and $\nu_2 = 0$ states for example deactivates the former and produces two molecules in the $(0, 1^1, 0)$ state. Also of great importance are collisions between unstable species and the CO_2 molecule. For example atomic oxygen in the $O(^3P)$ state is extremely efficient at activating one or more of the

vibrational states of CO_2, despite the smaller abundance of O in the Martian atmosphere. Collisional processes that connect molecular vibrational levels can be categorised as:

1. Thermal, or vibrational-translation (V-T) processes:
    - Where the vibrational internal energy of the upper level is converted into or taken from the translational energy of the collision partner.
    - Lead the population states into LTE.
2. Non-Thermal, or vibrational-vibrational (V-V) processes:
    - Where the vibrational internal energy of the upper level is converted into or taken from a non-translational source of energy.
    - Drive population states out of LTE.

2.6.2 The Two-Level Modelling Approach

The processes of interest to us are those that alter the molecules' internal electronic states and the populations of vibrational and rotational energy levels and how this may result in an overall cooling or heating of an air parcel's molecular constituents. The heating rate h_ν is related to the divergence of radiative flux as the flux interacts with matter. This will give us the net rate at which the energy (per unit volume) of the radiation is increased or decreased by, respectively, emission and absorption by matter. Equivalently we can also express the heating rate in terms of the change in radiance by integrating equation 1.29 over all solid angles. Thus we have the statements:

$$\begin{aligned} h_\nu(P) &= -\nabla.\underline{F}_\nu \\ &= -\int_\omega \frac{dL_\nu(P,s)}{ds} d\omega \\ &= 4\pi e_\nu n[\overline{L}_\nu - \overline{J}_\nu] \end{aligned} \tag{2.32}$$

Thus, in order to model the radiative balance in the atmosphere researchers need firstly to work towards solutions to the radiative transfer equation (equation 1.30) to describe the change in radiance $L_\nu(s,\underline{s})$ at a point $P(s)$ in the atmosphere. This typically means searching for the absorption coefficient k_ν and the form of the source function $J_\nu(T)$. In the case of non-local thermodynamic equilibrium the situation is complex because the source function depends on the radiance at other points and directions. For the case of local thermodynamic equilibrium we are afforded a significant advantage in that the form of the source function is given by the well known Planck function (equation 2.33), which expresses the radiance as a function of temperature and frequency:

$$B_\nu(T) = \frac{2h\nu^3}{c^2} \frac{1}{[exp(h\nu/kT) - 1]} \tag{2.33}$$

Generally the source function for a particular interaction is expressed as a function of the number densities of the populations of the upper and lower vibrational energy levels of the transition of interest.

An obvious simplification to the real atmosphere would then be to assume that our molecule(s) of interest consist only of these two levels, a method often referred to as the "two-level approach". Then we solve a separate equation, known as the statistical equilibrium equation, which describes the populations of these levels as the balance between all microscopic processes that affect the populations. The statistical equilibrium equation (*SEE*) is more formally known as the principle of detailed balance, which is to say that one considers all those interactions between radiation and matter or collisions with matter that cause excitation or de-excitation amongst molecular energy levels. From this the population relationship of the two levels can be described. In a thermodynamic equilibrium situation the effects of transitions in both directions cancel out so that there is no net excitation or de-excitation of either level allowing the source function and the absorption coefficient to be derived (the former being found to be equal to the Planck function). On the other hand in the non thermodynamic equilibrium situation excitation and de-excitation processes alone will not balance and a more complex form of the source function and absorption coefficient needs to be found. For both cases one works towards a form of the source function (and absorption coefficient) suitable to be included in the radiative transfer equation prior to integration.

2.6.3 Modelling Difficulties and Complexity

The task of modelling CO_2 heating and cooling rates in the Martian atmosphere requires a self consistent picture of how both radiative transitions and collisional processes populate or deactivate the excited vibrational level(s) of interest. At least in LTE the source function, absorption coefficient and population distribution can be readily determined based upon a single kinetic temperature. However in non-LTE one must look at how the vibrational level populations and their transitions are affected by radiation processes (spontaneous and induced emission and photon absorption) and how this depends upon the number density of excited levels, as well as the exchange of photons between atmospheric layers (that may be one or two scale heights away) and between different energy levels (and for optically thick conditions there may be many).

As this all occurs alongside collisional processes (thermal and non-thermal) one must consider the many diverse ways solar energy could be thermalised, all the possible energy modes and transitions over all possible radiative and collisional processes, accurately determining the radiation field and all with the appropriate distribution functions. Finally, the whole process must include a consideration of how the various prominent isotopes respond. Again since all these processes are coupled to one another a simultaneous solution is required of both the radiative transfer and statistical equilibrium equations (López-Valverde et al., 1999) to describe respectively the local radiation field and population distribution. Upon completion the heating or cooling produced by the excitation or de-excitation will be an especially useful calculated output.

The number of equations to consider and the associated computational demands can be quite large if, as in the case of CO_2, the gas contains strong absorption bands and resonant energy levels with efficient energy transfer processes (meaning a very complete scheme of vibrational-to-vibrational (V-

V) collisional processes must be considered) (López-Valverde et al., 1999). As already mentioned, the almost pure CO_2 Martian atmosphere produces a large variation of optical depths making the transfer of radiation important for a large range of band strengths. This is particularly true for cooling rate calculations where one finds that no single approximation is appropriate at all altitudes for the many different molecular levels that need to be considered (López-Valverde and López-Puertas, 2001). Though simplifications such as the two level approach already discussed offer some assistance quite often a high computational cost can not be avoided. Other complications arise with regard the various rate coefficients for the collisional processes since many reaction rates are not completely known yet or are associated with large uncertainties due to a lack of dedicated laboratory experiments.

With all the above stated, simplifications are an absolute necessity to both the statistical equilibrium and radiative transfer equations, defining simple expressions that accurately approximate the source function and the population of molecular states. For the radiative transfer equation one common approach is to use the cool-to-space method in situations where the exchange of photons between layers can be neglected (López-Valverde and López-Puertas, 1994a). An example would be a non-LTE situation high in the atmosphere where it's optically thin such that radiative processes are important only as a loss mechanism i.e. collisional processes are more effective in exciting vibrational levels than the absorption of a weak radiative field radiating upwards from the lower atmosphere. The cool-to-space approximation therefore assumes that the net radiative losses are due only to photons emitted upward directly to space, it ignores absorption of radiation and induced emissions from layers above and below. As a consequence we are offered a simplified solution for the source function to aid computation. However such an approximation is not appropriate at all levels, in the mesosphere for example absorption of radiation from the warmer layers below is significant and should provide level excitation and heating yet the cool-to-space approximation ignores such absorption and as a result tends to overestimate the cooling in this region (and below). For the statistical equilibrium equation the two-level approach already discussed is a preferred method (see section 2.6.5). Once again this means dealing with level population calculations in terms of two levels; an excited state and a ground state, with V-T collisional excitation and relaxation of the excited state being the only processes considered i.e. no allowance is made for V-V exchanges, their being deemed a very minor importance for cooling rates for example.

2.6.4 The IR Heating Parameterisation

As is the case with solar EUV and UV radiation, the absorption of solar radiation by IR-active molecules in the Martian atmosphere produces heating of the CO_2 gas. The problem of parameterising this effect on Mars was the subject of the study by López-Valverde and López-Puertas (1994b) who proposed computing the heating rate in LTE directly from photoabsorption coefficients and the magnitude of the incident solar flux. This is advantageous since both parameters can be known to high accuracy and can be swiftly calculated. Furthermore there is a weaker dependence on the thermal structure and composition of the atmosphere than in the cooling calculation and this makes it more suitable to tabulations.

Unfortunately in a non-LTE situation only a small fraction of the incident solar radiation ends up as atmospheric heating, a large amount of the energy initially absorbed is re-emitted back to space by scattering and fluorescence processes. This is because at higher altitudes, where non-LTE conditions are prevalent, several CO_2 bands like the 15 μm band can efficiently radiate energy to space as the upper atmosphere becomes optically thin and emission to space becomes comparable to collisional processes. Also, the energy taken from the solar flux is momentarily stored as excitation energy of the CO_2 vibrational state closest in transition to the solar flux frequency before it can be released to the atmospheric molecules as kinetic energy (through V-T collisional processes). A large amount of energy can be stored in the ν_2 and ν_3 reservoirs for example. If these processes are not frequent enough (as is the situation in non-LTE) the energy may be re-emitted back to space at the same frequency or lost to other vibrational levels by efficient non-thermal V-V collisions (who may go on to radiate the energy to space anyway).

To be able to connect the LTE and non-LTE atmospheric regions by a single scheme once the LTE problem had been solved López-Valverde et al. (1998) simply proposed applying a single profile of non-LTE correcting factors to the LTE result. These factors would be defined solely against a pressure grid and (once interpolated onto MarTIM's pressure grid and multiplied through by the LTE result) would be able to calculate the heating rate while automatically accounting for whether LTE or non-LTE conditions prevail thus giving a better account of the fraction of absorbed energy that is eventually thermalised.

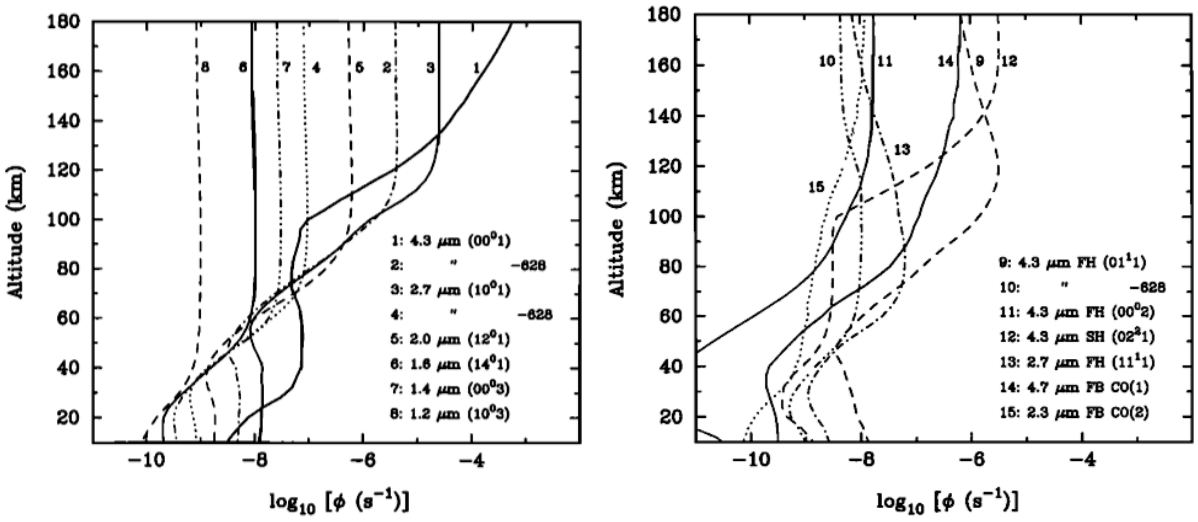

Figure 2.4: Photoabsorption coefficients (number of photons per CO_2 molecule in the ground state per second) for the main isotope 626 and two bands of the 628 isotope (López-Valverde and López-Puertas, 1994a,b).

For the solution to the LTE problem we turn to the work of López-Valverde and López-Puertas (1994a,b); López-Puertas and Taylor (2001) who gave the method for calculating the required photoabsorption coefficient rates for the most important CO_2 bands. These coefficients give the rate at which CO_2 molecules are excited (in a given molecular band) as being equal to the rate at which the solar flux is reduced as it radiates through the atmosphere. The calculation can also be described as the flux

divergence i.e. the number of photons taken per absorbing molecule per second. The required calculation is given by equation 2.34 and profiles of the photoabsorption coefficients calculated are shown in Figure 2.4 for sun overhead conditions, as published by López-Valverde and López-Puertas (1994a,b) as a result of their radiative transfer model of CO_2 and CO IR emissions in the Martian atmosphere. The CO_2 bands chosen for the solar absorption included in their model can be found in Table 2 of López-Valverde and López-Puertas (1994a). Thus we have:

$$\phi(z) = -\phi_\nu(\infty)\cos(\chi)\frac{1}{n_a(z)}\frac{dW}{dz} \tag{2.34}$$

Here $\phi_\nu(\infty)$ is the solar flux at the top of the atmosphere, χ is the solar zenith angle, W is the equivalent width of the band for the optical path ranging from the top of the atmosphere down to altitude z and $n_a(z)$ is the number density of absorbing molecules at z. The atmospheric curvature is taken into account by using the Chapman function as was the case for our EUV/UV heating calculation.

The solution for the equivalent widths (that is the width of a square-sided line that has the same integrated absorption as the line in question) of the bands considered requires a calculation of the flux transmission and I refer the reader to López-Valverde and López-Puertas (1994a), section 2 for further information. Note how the overall rate at which energy is gained from the solar flux can be calculated by integrating equation 2.35 over frequency ν:

$$h_\nu = \mu\phi_\nu(\infty)\frac{d[exp(-\tau_\nu(z,\infty)/\mu)]}{dz} \tag{2.35}$$

where $\phi_\nu(\infty)$ is the solar flux at the top of the atmosphere, μ is the cosine of the solar zenith angle and τ is the optical depth along the ray path taken by the solar flux photon.

Finally then, for MarTIM, Moffat (2005) took the photoabsorption coefficients presented in Figure 2.4 and constructed equation 2.36 to provide MarTIM a calculation for the heating rate produced by absorption of solar flux IR on Mars:

$$\dot{Q}_{IR}(z) = \frac{1}{\beta(z)}\left(k_{4.3\mu m}(z) + k_{2.7\mu m}(z).[n_{co_2}(z)] + k_{4.7\mu m}(z).[n_{co}(z)]\right) \tag{2.36}$$

As noted above, to be able to connect the LTE and non-LTE atmospheric regions by a single scheme once the LTE problem had been solved López-Valverde et al. (1998) proposed applying a single profile of non-LTE correcting factors ($\frac{1}{\beta(z)}$ in equation 2.36) defined solely against a pressure grid to the LTE result. With the factors interpolated onto MarTIM's pressure grid the heating rate calculated will automatically avoid the complications of the full calculation. It should be able to account for whether LTE or non-LTE conditions prevail and give a better calculation of the fraction of absorbed energy that is eventually thermalised. The required tabulation can be found in table one of López-Valverde et al. (1998) and are represented by the $\frac{1}{\beta(z)}$ term in equation 2.36. Note that one need not correct for the solar zenith angle on the tabulated LTE-to-non-LTE correction terms in the same way as required for the solar heating rate itself since the work of López-Valverde et al. (1998) showed that this was not an important effect, the variation in solar heating rate with solar zenith angle being the same regardless of whether LTE or non-LTE was followed.

If one defines heating to be the conversion of solar radiative energy into kinetic energy of atmospheric molecules then in non-LTE this would be much smaller because at least some proportion of the energy would go into populating the upper energy levels. So for example energy absorbed in the 2.7 μm and 4.3 μm regions would relax through the ν_2 bending levels either collisionally (important for the 4.3 μm) or radiatively (important for the 2.7 μm). In comparison, for the LTE case, the upper levels are already thermalised so the net absorption of energy will be less and instead this energy will be more efficiently converted into kinetic energy. The work of López-Valverde et al. (1998) highlighted how the switch between LTE and non-LTE occurred at about 100km as the collisional V-T deactivation became less efficient and an increasing fraction of the energy transferred to the bending levels is emitted back to space. At an altitude of 85 km the error in applying an LTE solution is already on the order of 20% (compared to if non-LTE effects were correctly considered) and increases rapidly above this altitude. Thus were it not for the non-LTE correction factors ($\frac{1}{\beta(z)}$ in equation 2.36) the heating in MarTIM would occur at a much faster LTE rate.

2.6.5 The IR Cooling Parameterisation

The kind of fast simple scheme implemented for the CO_2 infrared heating rate cannot, unfortunately, be applied to the thermal cooling rates, principally because these rates are strongly affected by the thermal structure of the background neutral atmosphere in ways that weren't a problem for the heating calculation. Nonetheless we need to include the effect on the radiative cooling rates that the non-LTE departure of excited energy levels from a Boltzmann distribution will have. You would expect cooling rates to be much greater than they actually are if molecular energy levels were in LTE at the high kinetic temperatures found in the thermosphere. Instead when spontaneous emission to space competes with V-T collisions then the number density of the emitting levels will be reduced significantly due to collisional relaxations. This is a notable effect in Martian emissions to space such as 4.3 and 2.7 μm and for the CO_2(0,1,0) state of the major 626 isotope above about 90km. Importantly, it depends non-linearly on the temperature structure both at the altitude level in question and, due to radiative transfer, the level a few scale heights away.

The method used in MarTIM was taken from an original study designed as a delivery for the "Martian Environment Models" project (ESA contract 11369/95/$nl/jgCCN2$) (López-Valverde and López-Puertas, 2001). It is a 1D parameterisation that computes the non-LTE heating rates (though usually cooling rates since they are always negative) from CO_2 emission at 15 μm in the Martian upper atmosphere. Note then that it is a simplified (parameterised) version of a more complete non-LTE model developed by López-Valverde and López-Puertas (1994a,b), thus the full model has been reduced to a more simple treatment of the radiative transfer and statistical equilibrium equations. For the latter they consider how the the complete model contained dozens of molecular vibrational levels, bands and processes while at the same time only a few of these actually significantly contributed to the thermal cooling at 15 μm. This allowed the "Martian Environment Models" project to make the two level model

approximation (Figure 2.5) where the contributing behaviour of only two excited levels, the 626 fundamental band and the isotopic fundamental band, were considered. The various processes and radiative transitions included for the two excited states were coupled to the ground states via V-T collisions and they also included a V-V exchange between the two states. The first level is a 626-(010) and the 626-Fundamental Band, while the second level can be viewed as an "equivalent state" comprising the weaker isotopic bands of the 636, 628, 627 isotopes and the 626 first hot bands and their vibrational-rotational bands.

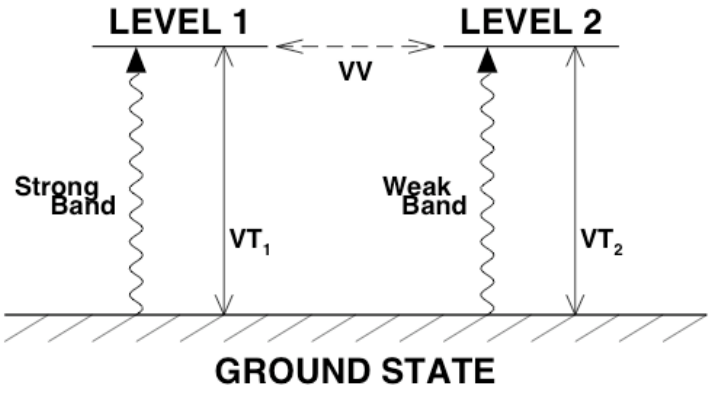

Figure 2.5: Schematic diagram of CO_2 levels and transitions in the simplified model.

Thus one can summarise the collisional productions and losses the model considers as being:

1. Collisional production of the strong band from all V-T processes in which it participates P_1.
2. Specific collisional loses of the strong band due to all V-T and V-V processes in which it participates l_1.
3. Collisional production of the weaker band from all V-T processes in which it participates P_2.
4. Specific collisional losses of the weaker band from all V-T and V-V processes l_2.
5. Specific collisional production of the strong band via V-V exchange from the (010) state of the other isotope p_{12}.
6. Specific collisional production of the weaker band via V-V exchange from the (010) state of the other isotope p_{21}.

Where the populations of the excited states n_1^* and n_2^* are obtained by solving analytically two coupled statistical equilibrium equations:

$$n_2^* = \frac{l_1 P_2 + \alpha_2 P_1 p_{21}}{l_1 l_2 - p_{12} p_{21}}$$
$$n_1^* = \frac{P_1}{l_1} + \alpha_1 \frac{n_2 p_{12}}{l_1} n_2^*$$

Terms α_1 and α_2 are combinations of molecular and universal constants supplied by the code and the rate coefficients for the collisional processes that the model deals with have been summarised in table 2.1.

Table 2.1: Carbon Dioxide radiative and collisional processes and their rate coefficients in the cooling parameterisation.

#	Type	Process	Rate Coefficient
1	V-T	$CO_2{}^i(0,1,0) + CO_2 \rightleftharpoons CO_2{}^i(0,0,0) + CO_2$	$4.2 \times 10^{-12}\ exp(-29.9A + 30.4B)$
2	V-T	$CO_2{}^i(0,1,0) + CO, N_2 \rightleftharpoons CO_2{}^i(0,0,0) + CO, N_2$	$2.1 \times 10^{-12}\ exp(-26.6A + 22.3B)$
3	V-T	$CO_2{}^i(0,1,0) + O(^3P) \rightleftharpoons CO_2{}^i(0,0,0) + O(^3P)$	3.0×10^{-12}
4	V-V	$CO_2{}^i(0,1,0) + CO_2 \rightleftharpoons CO_2{}^i(0,0,0) + CO_2(0,1^1,0)$	$2.49 \times 10^{-11}/2$

Note: Rate coefficients in the forward sense of the process in cm^3s^{-1}, T is temperature in Kelvin, $A = 10^2/T$, $B = 10^4/T$, i equals isotopes 626, 636, 628 and 627 respectively.

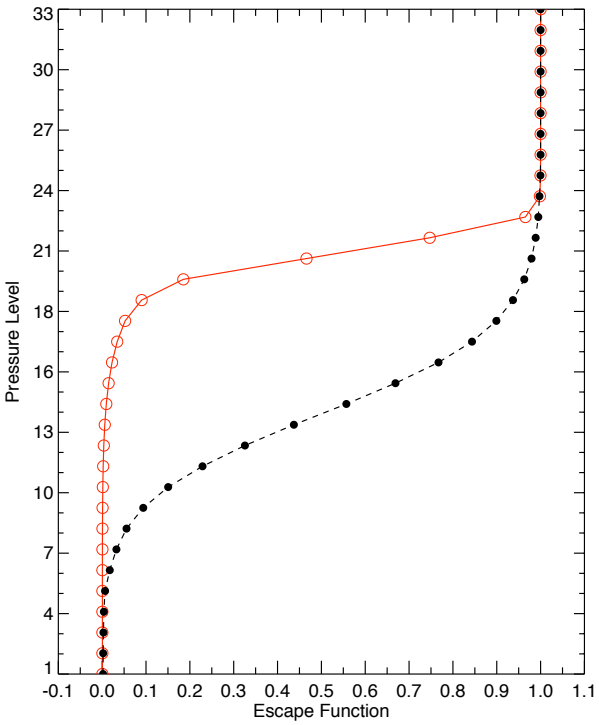

Figure 2.6: MarTIM CO_2 cooling parameterisation escape-to-space functions i.e the flux transmission to space, the probability of CO_2 emissions radiating directly to space. The red line represents the strong band of the two-level model and the black line represents the weak band.

For the radiative transfer equation a frequent simplification, as we mentioned in the "Modelling Difficulties and Complexity" section above, is the cool-to-space approximation. This ignores the contribution that radiation and matter interactions make to and from other atmospheric layers instead considering

only the exchange term with the upper boundary (i.e. to space). In the context of the "Martian Environment Models" parameterisation then the cool-to-space approach gives the cooling rate $q(z)$ of a given vibration-rotation band at a given altitude z as:

$$\begin{aligned} q(z) &= -\pi J(z) \frac{d\mathcal{T}(z,\infty)}{dz} \\ &= -hc\overline{\nu}\frac{\beta}{4} A\mathcal{T}(z,\infty) n^*(z) \end{aligned} \tag{2.37}$$

where $\mathcal{T}(z)$ is the flux transmission to space at altitude z integrated over the band (see Figure 2.6). This is also known as the escape function. Term $J(z)$ is the source function of the whole vibration-rotation band at height (z), A is the Einstein coefficient for spontaneous emission, $\beta = 1.8$ is a diffusivity factor for the angle integration and finally n^* is the population of the upper excited state. Although we stated earlier how the cool-to-space approximation could only be in optically thin conditions where radiative transfer between levels could be ignored, equation 2.37 does in fact also work in optically thick situations through the inclusion of the escape function $\mathcal{T}$ and the allowance of V-V exchanges between excited states. As part of the delivery of the "Martian Environment Models" project the average escape function profile for each band in the two level model used was tabulated and supplied with the parameterisation. This single profile is employed regardless of the background thermal structure in the calculation of the cool-to-space equation with only small disagreement versus the full solution.

So with the radiative transfer between levels accounted for using the radiative transfer equation and the population of excited states due to collisional processes solved with the statistical equilibrium equation we can finally calculate the cooling rate itself with equation 2.38:

$$\begin{aligned} \dot{Q}_{15\mu m}(z) &= \dot{Q}_{strong}(z) + \dot{Q}_{weak}(z) \\ &= -hc\frac{\beta}{4}\left[\overline{\nu}_1 A_1 \mathcal{T}_1(z,\infty) n_1^*(z) + \overline{\nu}_2 A_2 \mathcal{T}_2(z,\infty) n_2^*(z)\right] \end{aligned} \tag{2.38}$$

where as noted already the escape functions $\mathcal{T}$ are supplied with the routine as tabulated profiles and where MarTIM supplies the local values of temperature, pressure and volume mixing ratios of CO_2 and its major collisional partners (CO, N_2 and O).

2.7 Stationary State Ionosphere

Part of the work of Moffat (2005) included adding a basic ionosphere to MarTIM with photoionisation calculated self-consistently and a set of ionic reactions describing ionospheric chemistry. The scheme employed relied upon the assumption of photochemical equilibrium to solve simultaneously the 23 ionospheric differential reactions that were included (see Table 2.2). Thus this "Stationary State Hypothesis" (SSH) assumes that the rates of reaction are so quick that one can assume steady state solutions are reached almost immediately (or at least on time scales faster than MarTIM's neutral time step).

From an equation of continuity for the distribution of charged particles in the ionosphere we have:

$$\frac{\partial N}{\partial t} = q - L(N) - \nabla.(N\underline{v}) \tag{2.39}$$

then assuming diffusion processes can be ignored (last term, right hand side) and that chemical processes are pre-dominant (so that $\partial N/\partial t$=0) we have simply that $q = L(N)$ from which the number density of the product, in steady state can be easily solved. This method is most appropriate in describing the ionosphere around the altitude region of the peak electron density and is particularly useful in being able to work with multi-step reaction schemes while providing swift and accurate results.

Typically only neutral gas densities are available at the beginning of a run and so MarTIM must generate the initial ion densities from solar photoionisation. Only then can the production and loss ion chemistry adapt the ion densities to their steady state values. The expression used within MarTIM for the altitude and solar zenith angle dependent total ion production rate $P_s(z, \chi)$ for ion species s is:

$$P_s(z,\chi) = n_s(z) \int_\lambda I_\infty(\lambda) exp[-\tau(z,\lambda,\chi)] \sigma_s^i(\lambda) \left(\frac{\lambda}{hc}\right) d\lambda \tag{2.40}$$

Here, the multiplication by $\left(\frac{\lambda}{hc}\right)$ converts energy flux (erg/cm^2/s) into photon flux (photons/cm^2/s) so that $P_s(z, \chi)$ is expressed in units of number of ions created. For the electron number density (n_e) we simply assume charge neutrality throughout the model atmosphere so that $\sum_s n_s = n_e$.

2.8 Numerical Modelling Techniques

2.8.1 Initial Atmosphere

As was mentioned in section 2.1.2 MarTIM is a first principle numerical model and so must be provided with some form of input atmosphere from which to begin its numerical iterations. One can use either an externally sourced one-dimensional globally averaged input atmosphere or take an established steady state MarTIM result and read this back in as a three-dimensional input atmosphere. Since MarTIM's initial atmosphere for this PhD work has significant design differences to that of Moffat (2005) we leave further description of the initial atmosphere for Chapter 3.

2.8.2 Finite Difference Method

MarTIM solves the momentum equation 2.14 and energy equation 2.18 on a co-rotating grid of (typically) 37 evenly spaced latitude points and 72 longitude points (forming a 5° by 5° horizontal grid) and of 33 pressure levels spaced at 0.5 scale heights. All of these dimensions can be varied if necessary as long as consideration is given to the suitability and scope of the included parameterisations. Partial derivatives in space using this grid system are approximated using the finite difference method, which is based upon the Taylor series expansion about the particular grid point of the functions to be differentiated. The first and second derivatives with respect to a grid space variable are calculated with:

$$\frac{\partial f}{\partial x} \approx \frac{f_{i+1} - f_{i-1}}{2\delta x} \tag{2.41}$$

$$\frac{\partial^2 f}{\partial x^2} \approx \frac{f_{i+1} - 2f_i + f_{i-1}}{\delta x^2} \tag{2.42}$$

Table 2.2: MarTIM ionosphere reactions and their rate coefficients.

#	Reaction	Rate coefficient
1	$CO_2^+ + O \rightarrow CO + O_2^+$	1.6×10^{-10}
2	$CO_2^+ + O \rightarrow CO_2 + O^+$	1.0×10^{-10}
3	$O^+ + CO_2 \rightarrow O_2^+ + CO$	1.2×10^{-9}
4	$O_2^+ + e^- \rightarrow O + O$	$1.6 \times 10^{-7} \left(\frac{300}{T_e}\right)^{0.55}$
5	$CO_2^+ + e^- \rightarrow CO + O$	$1.4 \times 10^{-4} \left(\frac{1}{T_e}\right)$
6	$CO_2^+ + NO \rightarrow NO^+ + CO_2$	1.2×10^{-10}
7	$CO_2^+ + O_2 \rightarrow CO_2 + O_2^+$	5.0×10^{-11}
8	$N_2^+ + CO_2 \rightarrow N_2 + CO_2^+$	8.0×10^{-10}
9	$N_2^+ + O \rightarrow NO^+ + N$	1.4×10^{-10}
10	$N_2^+ + e^- \rightarrow N + N$	$3.5 \times 10^{-7} \left(\frac{300}{T_e}\right)^{0.5}$
11	$N_2^+ + CO \rightarrow N_2 + CO^+$	7.4×10^{-11}
12	$NO^+ + e^- \rightarrow N(^2d) + O$	$1.1 \times 10^{-7} \left(\frac{1000}{T_e}\right)^{1.2}$
13	$O_2^+ + NO \rightarrow NO^+ + O_2$	6.3×10^{-10}
14	$CO^+ + CO_2 \rightarrow CO_2^+ + CO$	1.1×10^{-9}
15	$N_2^+ + O_2 \rightarrow O_2^+ + N_2$	6.0×10^{-11}
16	$O_2^+ + N_2 \rightarrow NO^+ + NO$	1.0×10^{-16}
17	$O^+ + NO \rightarrow NO^+ + O$	8.0×10^{-13}
18	$N_2^+ + O \rightarrow O^+ + N_2$	9.8×10^{-12}
19	$N_2^+ + NO \rightarrow NO^+ + N_2$	4.1×10^{-10}
20	$CO^+ + O \rightarrow O^+ + CO$	1.4×10^{-10}
21	$CO^+ + O_2 \rightarrow O_2^+ + CO$	1.2×10^{-10}
22	$O^+ + N_2 \rightarrow NO^+ + N$	$1.2 \times 10^{-12} \left(\frac{300}{T_e}\right)^{0.41}$
23	$CO^+ + NO \rightarrow NO^+ + CO$	3.3×10^{-10}

Note: All rate coefficients have units $cm^3 s^{-1}$.

For the numerical integration with time we use forward time-stepping technique:

$$f(t + \delta t) \approx f(t) + \frac{\partial f}{\partial t} \delta t \tag{2.43}$$

2.8.3 Model Boundary Conditions

Upper Boundary

At the upper boundary we deliberately set the values of total energy (internal plus kinetic), neutral temperature, neutral mass mixing ratios and horizontal wind velocities to be the same as the level below,

thus the vertical gradients of these variables vanish between the two uppermost levels. This prevents there being an upward vertical mass flow out of the model nor downwards into the model. It also damps the reflection of any vertically propagating wave structures without disturbing their delineation in the rest of the model.

Lower Boundary

Typically the lower boundary is kept absolutely constant throughout the course of a simulation. This also means that it is kept constant even if an established steady state MarTIM result is read back in as a three-dimensional input atmosphere. The lower boundary will always retain the values set by the one-dimensional globally averaged input atmosphere that was originally read in. Hence the lower boundary will always have constant values in both time and horizontal space (across the pressure level) for variables of neutral temperature, number density. Also the wind velocities will be maintained at zero magnitude.

Solutions at the Poles

We define the polar regions to begin two latitude steps away from the actual (north or south) pole. This allows us to automatically avoid singularities in model differential equations while still resolving high latitude values. The temperatures, velocities, mass mixing ratios and mean molecular weight are all averaged at the longitude grid circle two latitude steps away from the pole and then this average copied onto the pole itself. Then the latitude one step away from the pole is simply interpolated from these two values.

2.8.4 Smoothing

Numerical models such as MarTIM that use finite difference methods to solve systems of differential equations are prone to computational instabilities. Problems can arise as the integrations proceed due to spurious nonlinear growth of roundoff or truncation errors. Additionally when wave structures associated with the inherent periodic nature of the solution, such as cycles based upon planetary rotation (period 24-hrs), are integrated alongside higher frequency components short wavelength oscillations can begin to appear that become unstable and "blow-up" (to infinity) after a certain number of time steps. In fact quite often the structures that appear cannot actually be resolved by the model, their frequency being shorter than the Nyquist frequency i.e. the so called "2-grid interval waves". Yet through the process known as 'aliasing' the model interprets these high frequency, short wavelength waves as actually being of longer wavelength. Hence they tend to add to the problem of spurious error growth.

As a result it is necessary to include filtering and/or smoothing operators that are calculated while the model numerical integrations proceed that remove the shortest resolvable components while leaving all others as close to their original amplitudes as possible (and without altering the phases of such components). Note of course that this situation often represents a difficult partnership between removing the highest frequency structures that are growing uncontrollably and erroneously as a simulation runs

while at the same time keeping those higher frequency structures that actually have a physically justified presence in the solution. In the horizontal direction we follow the procedure discussed by Shapiro (1970) who developed a strategy based upon expressing the model function Z in terms of a sum of Fourier components. For our purposes we use the smoothing element:

$$\overline{Z}_{ij}^{ij} = Z_{ij} + \frac{S}{4}\left(Z_{i-1,j} + Z_{i+1,j} + Z_{i,j-1} + Z_{i,j+1} - 4Z_{ij}\right) \tag{2.44}$$

where i and j are grid point indices and the element is used twice, once with $S = -1$ and again with $S = 1$.

In the vertical direction we apply a Savitzky-Golay smoothing filter (sometimes called a moving window average) taken directly from Press et al. (1992), section 14.8, p644. The premise of this scheme is that the function being smoothed f_i is replaced with a linear combination g_i of itself and some nearby neighbours:

$$g_i = \sum_{n=-n_L}^{n_R} = c_n f_{i+n} \tag{2.45}$$

with the Savitzky-Golay filter coefficients c_n=$-0.086, 0.343, 0.486, 0.343, -0.086$ and equation 2.45 taken from equation 14.8.1 of the aforementioned reference. Thus the scheme computes each g_i as the average of the data points from f_{i-n_L} to f_{i+n_R}, for some fixed $n_L = n_R$ (in our case $n_L = n_R = 2$). The filter coefficients are chosen so as to preserve higher moments of the original function i.e. to approximate the underlying function (within the moving window) not by a constant, since this would simply return the average, but rather by a polynomial of some higher order. The coefficients allow for a least-squares fit of the polynomial to all points within the moving window and then the point g_i is taken as the value of the polynomial at position i. Rather than computing these coefficients within MarTIM they are simply taken as a result of the study conducted in Press et al. (1992) and we refer the reader to this text for more details.

2.9 Closing Remarks

We finish the description of MarTIM by defining a few commonly used parameters. In reference to the seasons on Mars and to the heliocentric distance between the Sun and Mars we refer to the *areocentric longitude* or *Ls* of the Sun. We follow the definition used by the Mars Climate Database (Lewis et al., 1999) with Ls = 0° (1.56 AU) at the vernal equinox of the northern hemisphere, aphelion at Ls = 71° (1.67 AU) and perihelion at Ls = 251° (1.38 AU). The term *sol* will be used to denote a mean Martian solar day of 88,775 seconds. Each sol is subdivided into 24 true solar hours that we simply refer to as hours for short. In assigning numbers to Martian years we adopt the arbitrary calendar convention proposed by R. Todd Clancy (Clancy et al., Journal of Geophys. Res 105, p 9553, 2000) that Mars year 1 (MY1) began at Ls = 0° on 11^{th} April 1955. Finally, a year on Mars is 668.6 sols long.

In the following chapters MarTIM is used to study the Mars' middle and upper atmosphere, i.e. the

mesosphere and thermosphere. In Chapter 3, general model improvements and updates to input datasets (versus previous versions) are validated by experiment:

- An update to the solar XUV/EUV/UV flux model, used to provide the solar irradiances (term $I_\infty(\lambda)$ in equation 2.30) from which the atmospheric heating rate is calculated (equation 2.31), is introduced and discussed. The solar fluxes now come from the 'SOLAR2000 Research Grade v2.28' model (Tobiska et al., 2000; Tobiska, 2004b).

- The photoabsorption cross sections, also used in calculating the atmospheric heating rate in equation 2.31 (term $\sigma_s^a(\lambda)$), are updated. This allows us to include the variation in CO_2 cross section with temperature.

- Finally, we introduce a new neutral diffusion and advection subroutine which self-consistently determines the composition of an atmosphere composed of any number of neutral species. We use this to justify why including the mutual diffusion of the four neutral species CO_2, N_2, CO and O is an appropriate selection for capturing the bulk properties of the Martian atmosphere.

Next, in Chapter 4, we introduce a new IR heating parameterisation into the model, in the middle atmosphere:

- The new IR heating parameterisation (equations 4.1 and 4.2 and Figure 4.1) is shown to significantly enhance both temperature and circulation magnitudes and structures throughout the atmosphere and at all local times. Simulations in section 4.3 show that MarTIM compares better against Mars Odyssey accelerometer derived temperatures (Keating et al., 2003; Withers, 2006) with the new IR heating parameterisation than with the old.

- Finally, MarTIM temperatures are compared against 6 years worth of exospheric measurements from Mars Global Surveyor Precise Orbit Determination (POD) results over a large range of solar and seasonal conditions. MarTIM's enhanced circulation features (with the new IR parameterisation) alongside molecular thermal conduction are shown to act as a 'dynamical thermostat' to regulate the upper atmosphere temperatures when the solar $F_{10.7}$ flux increases.

In Chapter 5 we use MarTIM, with its new IR heating parameterisation, to study the extent to which the upper atmosphere region is coupled to the lower atmosphere through the middle atmosphere:

- MarTIM is coupled to the Mars Climate Database (Lewis and Read, 2003; Lewis and Barker, 2005; Lewis et al., 1999; Forget et al., 2008; Millour et al., 2008; Millour and Forget, 2008; Angelats i Coll et al., 2005) providing a more physically self-consistent description of the lower boundary at 0.883 Pa.

- We consider which atmospheric fields are involved in this coupling, the amount by which they are manipulated and to what degree other processes define the atmospheric structure. Here we compare

our model results to recent SPICAM number density and temperature measurements (Forget et al., 2009).

Finally, in Chapter 6, we introduce a more sophisticated ionosphere model and study the variation in both primary and secondary electron production rate with season and solar cycle:

- The ratio of secondary to primary electron and ion production, i.e. the efficiency, is studied using MarTIM's background neutral atmosphere. A parameterisation is developed that allows the variation in efficiency with solar cycle and solar longitude to be described with a simple function. This work was published in Nicholson et al. (2009)

Chapter 3

Improvements to the Standard MarTIM

3.1 Introduction

In this first chapter to detail numerical experiments undertaken with MarTIM we link the work of Moffat (2005) to the standard form of the code that will be used throughout the rest of this thesis. Before MarTIM is developed to study more complex phenomena we first complete some extra validation of the model's established solutions from Moffat (2005) and reconsider some of the approximations that were necessary in that work. We also update various input data sets where newer versions exist and we consider the benefits that these changes give to our standard MarTIM simulation. Appropriate evidence will be presented as necessary to justify the choices and changes made.

Finally we introduce a new neutral diffusion and advection subroutine which self-consistently determines the composition (number and mass densities, mass and volume mixing ratios, mean molecular weight) of an atmosphere composed of any number of neutral species. Thus, whereas the Moffat (2005) version of MarTIM could only model three neutral species, here we consider how self-consistently adding neutral species previously considered to be minor (by virtue of their low number density and mixing ratio) can alter the thermodynamics of the modelled atmosphere. The physical consistency of MarTIM's modelled diffusion and advection using this new subroutine is also considered by following a tracer neutral species and assessing the variation in composition that results as it moves through the modelled atmosphere. Lastly we justify why including the mutual diffusion of the four neutral species CO_2, N_2, CO and O is an appropriate selection for capturing the bulk properties of the Martian atmosphere.

3.2 Initial MarTIM Development

3.2.1 New Solar Flux Model

The solar XUV/EUV/UV flux model used to provide the solar irradiances from which the atmospheric heating rate is calculated (using equation 2.31) has been changed to the 'SOLAR2000 Research Grade v2.28' model (Tobiska et al., 2000; Tobiska, 2004b). This is a change to the solar flux irradiances used in Moffat (2005), which came from Torr and Torr (1985), and is advantageous because it allows MarTIM to benefit from the large body of research (solar measurements and modelling) conducted over recent years towards the better representation of spectral irradiances. For this latest version of SOLAR2000 the empirical solar irradiances are provided by Space Environment technologies (see `http://www.spacewx.com/`) while the algorithms used to assess this data come from various sources.

The research grade version 2.28 of SOLAR2000 supports three different algorithms for calculating the spectral irradiances and the user can request which particular algorithm they wish to use. Model sets "S2K+ASTM490", "S2K+VUV2002" and "VUV2002" are available. The first combines a reference solar spectrum and an empirical model of temporally resolved irradiances, the third is the model of Woods et al. (2000) which uses the daily F10.7 flux as a proxy to model FUV and UV irradiances as measured by the UARS spacecraft. Finally the "S2K+VUV2002" algorithm represents a combination of these two. Such functionality means we have more flexibility when comparing to other global circulation models. It also means that if a particular spectral region is better represented by a certain algorithm then we can compare the results from each to isolate the effect of enhancement in that spectral region (see for example Fox (2004a) regarding the Martian thermosphere and ionosphere response to enhanced solar soft X-ray fluxes). All modelling algorithms allow temporal variations in solar activity to be considered when no specific date is implied. However, past irradiances can also be returned for any specific day starting from the 1^{st} of January 1949, making use of empirical data where appropriate.

The SOLAR2000 model returns the solar flux energy in a variety of different spectral formats. It can be averaged into groups of wavelength bins each of different width (in terms of wavelength) depending on the region of the solar spectrum being considered and depending on how the data is to be used. There are groupings with 39, 867 and 1210 bins available as well as a 1 nm binned format. The 39 wavelength bins grouping has its first bin from 1.86 to 2.95 nm, its last at 100.1 to 105 nm and includes 14 individual solar emission lines (Cox, 2000). This grouping is commonly used by the aeronomy community (Tobiska, 2004a). The 867 and 1210 wavelength groupings allow a greater number of line and continua emissions in the EUV part of the spectrum to be finely represented. The 1210 wavelength grouping more finely represents the high energy X-ray region than the other groupings.

Here we have chosen to use the 1 nm binned data, rather than that used in Moffat (2005) where the 5 nm wavelength resolution grid of the Torr and Torr (1985) data was interpolated onto a 2.5 nm wavelength grid for use in MarTIM. Using the 1 nm binned data means MarTIM more accurately represents the prominent solar emission lines such as the Lyman-alpha line at 121.6 nm as well as including a detailed

delineation of the various spectral regions and the relationship between their intensity and variability. For example MarTIM can now be used to investigate the behaviour due to a high energy region of the solar spectrum, such as the XUV, that is much less intense than low energy regions, such as the UV or visible, but which shows greater variability over the solar cycle (see Figure 3.1 below).

Only the wavelength range from 0.5 to 300.5 nm was included as this took us well beyond the maximum wavelength at which any atmospheric species would respond to the solar flux (with respect to the new absorption cross sections used, see section 3.2.2 below). Then since SOLAR2000 is defined for a heliocentric distance of 1 AU we calculate the greater Mars-to-Sun orbital distance, accounting for eccentricity, and multiply the solar fluxes across the whole wavelength spectrum by the inverse square of that greater distance before passing them onto MarTIM. Finally, we use the 10.7-centimeter radio flux ($F_{10.7}$) as a reference measure of solar EUV/UV activity, as is the case with other global circulation modelling studies (see for example Bougher et al. (1999b); González-Galindo et al. (2005, 2009b)). This value is simply an output of SOLAR2000 whose numerical value has no computational role in the calculations but is used to put MarTIM's results in context with those other studies. We must search through SOLAR2000 output to find irradiances that are represented by whatever particular $F_{10.7}$ value we require.

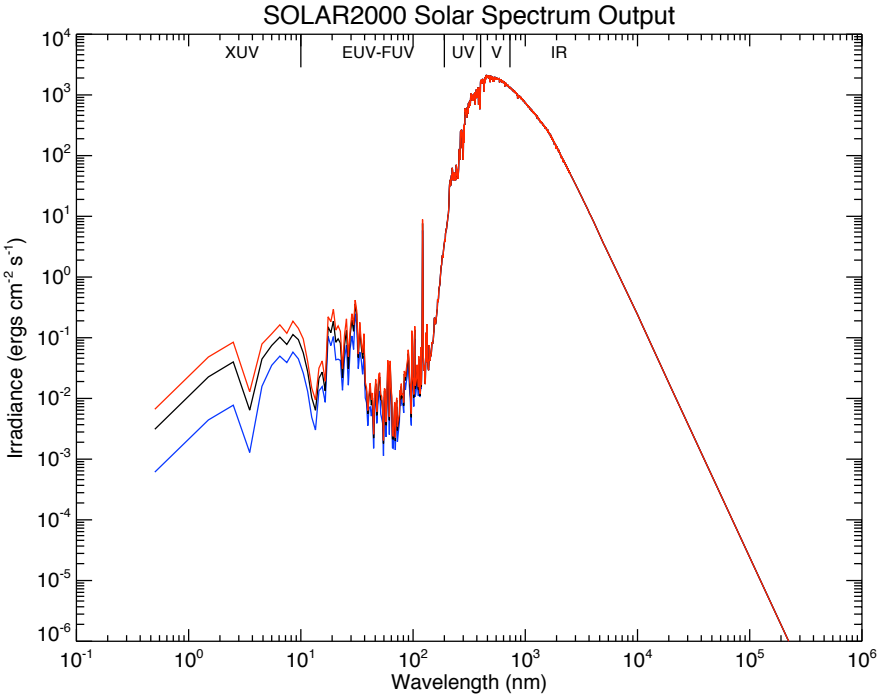

Figure 3.1: MarTIM's new SOLAR2000 solar irradiance input for *SMIN* (blue), *SMED* (black) and *SMAX* (red). Note that the full solar spectrum is shown here for completeness even though MarTIM only uses a wavelength grid from 0.5 to 300.5 nm.

The most common solar flux intensities used in this thesis have been categorized into low, medium and high solar activities, as is common with other global circulation modelling studies (Bougher et al.,

1999b; González-Galindo et al., 2005, 2009b). These are listed below and shown in Figure 3.1. Should the need arise for any other solar flux intensity to be used in a particular study this will be indicated in the text. In all cases 1 nm bins are used, with energy flux units ergs cm^{-2} s^{-1} and using the model algorithm S2K+ASTM490. The commonly used intensities are:

- Solar minimum flux, for which $F_{10.7}$ was 67.2, is referred to with the acronym *SMIN* (blue line).
- Solar medium flux, for which $F_{10.7}$ was 129.9, is referred to with the acronym *SMED* (black line).
- Solar maximum flux, for which $F_{10.7}$ was 204.3, is referred to with the acronym *SMAX* (red line).

Note how Figure 3.1 illustrates the greater variation in intensity over the solar cycle (blue line through to red line) in the higher energy regions of the solar spectrum than in the lower energy regions (as mentioned earlier). However, as Fox et al. (2008) points out, although most of the solar energy flux is in the visible and infrared regions of the solar spectrum the photoabsorption cross-sections for most of the major atmospheric species in these regions are in fact negligible. Thus to build a more complete picture of atmospheric heating using the new SOLAR2000 flux we required similarly highly resolved and up-to-date absorption cross sections.

3.2.2 New Neutral Photoabsorption Cross-Sections

With the improvements in MarTIM's solar flux model given by SOLAR2000 it was appropriate to find photoabsorption cross sections that could take advantage of the 1 nm binned resolution. It was also appropriate to find cross sections that used the latest techniques in cross-section measurement. For example the study of photoabsorption in the terrestrial atmosphere has provided a better understanding of absorption by molecular oxygen and the variation in its cross-section through approximately 5 orders of magnitude in the Schumann-Runge bands between 175 and 205 nm (Brasseur and Solomon, 2005). The work of Yoshino et al. (1992) gives almost 24,000 different wavelengths in the Schmann-Runge bands where the O_2 cross section has been measured. High resolution measurements were found for all of the seven neutral species represented in MarTIM. Even though this data is averaged for use in MarTIM it is reassuring to be able to rely on such detailed experimental results.

Perhaps more important for the study of Mars are the new carbon dioxide absorption cross sections that were obtained, not only because CO_2 is the major absorber of solar flux throughout the Martian atmosphere but also because its cross section shows an important variation with atmospheric temperature, which will affect MarTIM's results. The CO_2 absorption cross section variation with temperature was first discussed by DeMore and Patapoff (1972) near 180 nm from 200 to 300 K and then by Lewis and Carver (1983) from 120 to 197 nm at 200, 300 and 370 K. The latter study showed the temperature effect was generally small at short wavelengths, passing through a minimum near 140 nm before increasing steadily towards 190 nm. Indeed longward of 175 nm the absorption cross section began to show a significant temperature dependence whereby the cross sections at some wavelengths were measured to increase by a factor of about 20 as the temperature was increased from 200 to 370 K.

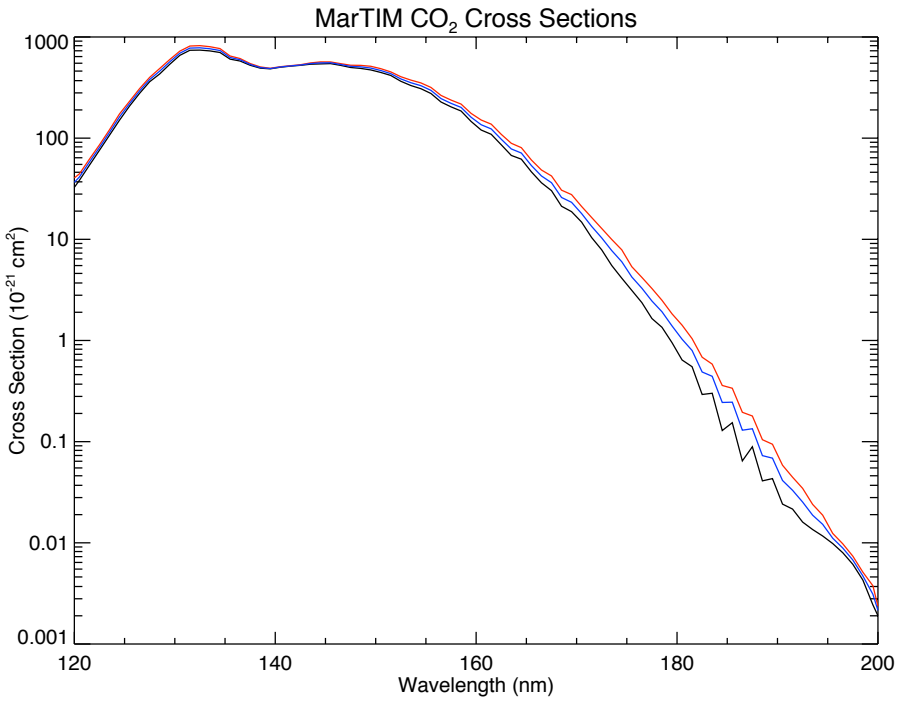

Figure 3.2: MarTIM's new CO_2 photoabsorption cross section versus wavelength at 195 K (black), 245 K (blue) and 295 K (red).

Other works, such as Anbar et al. (1993) and Yoshino et al. (1996), looked to parameterize the temperature dependence of CO_2 cross sections. Experimental studies from Yoshino et al. (1996) onwards characterised the temperature dependence by measuring relative and absolute cross-sections at 195 and 295 K. These temperatures were chosen because they bracketed the temperatures appropriate to the analyses of Martian VUV airglow features (Stark et al., 2006). In MarTIM we follow this lead and also parameterise the temperature dependence at and between 195 and 295 K using the function described by Anbar et al. (1993) for what is essentially a linear fit in the cross section between the two temperatures:

$$\sigma(T,\lambda) = \sigma(T_0,\lambda) + \frac{\sigma(T_1,\lambda) - \sigma(T_0,\lambda)}{T_1 - T_0}(T - T_0) \tag{3.1}$$

where T_0=195 K and T_1=295 K. Here we benefit from more recent experimental results in that Stark et al. (2006), Parkinson et al. (2003) and Yoshino et al. (1996) all include separate data sets at 195 and 295 K. Thus below 195 K and above 295 K we assume no temperature dependence in the cross-section and use the appropriate data set, while between these two temperatures we use equation 3.1. The overall result on the CO_2 photoabsorption cross sections once interpolated onto the 1 nm wavelength grid, as defined by SOLAR2000, is shown in Figure 3.2 between wavelengths 120 and 200 nm, the region where the temperature dependence becomes significant.

For each neutral species research was aimed at finding photo-absorption cross-sections for the calculation of solar flux absorption and its representation as a heat source in MarTIM's modelled atmosphere. Total, absolute, ionization and dissociation cross sections were sometimes discussed together in a single report but often separately in individual reports. The distinction between these various data sets relates

to the intricate range of different processes that could occur when an atmospheric atom or molecule interacts with a solar flux photon. Usually this begins with some sort of excitation after which there are various mechanisms for molecular fragmentation, energy transfer and energy quenching (Wayne, 1985) and most of these usually require very high resolution cross sections for their calculation (for example the exceptional resolution in the O_2 cross sections noted earlier).

For MarTIM's purposes the appropriate data were the 'total' or 'absolute' absorption cross sections as they encompassed, in a single cross-section measurement, all the various mechanisms that a species-solar flux interaction could initiate. This is because in MarTIM's heating rate calculation (equation 2.31) we simply assume that a flat fraction of the absorbed energy is converted to heat. It would be far too costly in terms of computation to include parameterisations for all possible solar flux-neutral species interaction mechanisms. Thus we ignore whether absorption leads to ionization or to photodissocation nor have concern for the fine structure that occurs in the wavelength regime between these regions (Fox et al., 2008). Consequently we chose 'total' or absolute' cross sections to calculate the required heating rate.

The main resource for obtaining the various cross sections was the NASA JPL Data Evaluation number 15 (Sander et al., 2006) and the associated web access from the spectral atlas of the Max-Planck Institute for Chemistry at `http://www.atmosphere.mpg.de/enid/2295`. Another prominent database used was that of the Harvard-Smithsonian Center for Astrophysics (CfA) at `http://www.cfa.harvard.edu/amp/tools.html`. Finally the results from several studies by The University of British Columbia (usually W. F. Chan and G. Cooper) using the electron energy loss technique had been made available by `ftp` at `chem.ubc.ca` in the directory `pub/cooper`. Appendix A lists the references for each data set but we do not discuss specific details of the absorption cross-section structures any further.

3.2.3 MarTIM Total Solar Heating Rate: A Brief Comparison

With the two updated database inputs of (a) the SOLAR2000 solar irradiances on a more resolved 1 nm wavelength grid and (b) the up-to-date photoabsorption cross sections that also take advantage of the 1 nm wavelength grid, we now briefly consider the effect these inputs have on MarTIM's solar EUV/UV heating rate and its vertical structure.

From equation 2.31 of Chapter 2 the thermospheric solar EUV/UV heating rate is calculated with:

$$\dot{Q}_{EUV,UV} = \frac{\epsilon_{fac}}{\rho} \sum_s n_s(z) \int_\lambda I(z,\lambda,\chi)\sigma_s^a(\lambda)d\lambda$$

$$\text{with } I(z,\lambda,\chi) = I_\infty(\lambda)exp[-\tau(z,\lambda,\chi)]$$

$$\text{and } \tau(z,\lambda,\chi) \equiv \sum_s n_s(z)\sigma_s^a(\lambda)ds_\lambda$$

The division by ρ ensures this gives the heating rate per unit mass and the efficiency factor ϵ_{fac} is used to represent the overall fraction of the absorbed energy assumed to be converted to heat i.e. broadly ignoring the intricate details of the various mechanisms that a solar flux-neutral species interaction could

initiate. Typically we set ϵ_{fac} equal to 22% (see section 2.5, Chapter 2).

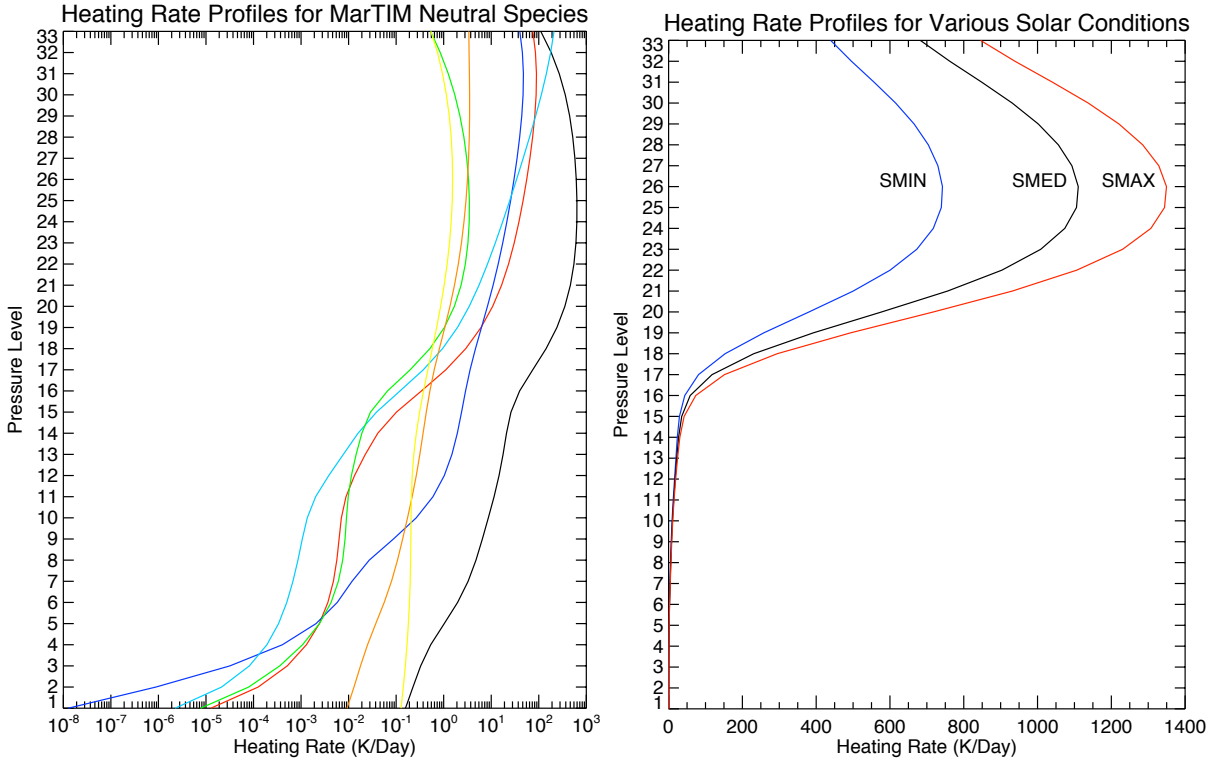

(a) (b)

Figure 3.3: (a) Comparison of different heating rate contributions from MarTIM's various neutral species for SMIN conditions. CO_2 (black line), N_2 (red line), CO (blue line), O (cyan line), O_2 (orange line), Ar (green line) and NO (yellow line). (b) Comparison of different heating rate contributions from previously defined solar conditions (see section 3.2.1 and Figure 3.1 above). Equinox conditions at the sub-solar point throughout.

The resulting heating rate in units of Kelvin per day (K/day) is shown in Figure 3.3(a) for SMIN, equinox conditions separated into the contributions from individual neutral species. Then in Figure 3.3(b) the total heating rates (sum over species, also in units K/day) are shown for the three most common solar flux intensities used in this thesis (as described in section 3.2.1 and Figure 3.1 above). Figure 3.3(a) shows that CO_2 provides the major EUV/UV heating source throughout almost the entire vertical extent of the atmosphere. It is only at the uppermost pressure level where O takes over as the dominant heating neutral. This reflects the dominance of CO_2 number density and the magnitude of its absorption cross section (since it is a triatomic molecule) over and above the other neutral species in MarTIM. This dominance is to such an extent that any variations in the absorption cross section with wavelength of any other neutral species is never enough to enhance their absorption rate. So even if absorption by CO_2 were weaker than that of another neutral species at no wavelength nor altitude is this sufficient to counter the dominant role CO_2 number density $n_{CO_2}(z)$ has on the heating calculation. Modelling theory from other GCM's (González-Galindo et al., 2005) also suggest that CO_2 is more

dominant in absorbing EUV/UV radiation and creating the heating rate.

The total heating rates (sum over neutral species) shown in Figure 3.3(b) for the three most common solar flux intensities used in this thesis are in qualitative agreement with the profiles obtained by Bougher et al. (1999b) and González-Galindo et al. (2005). Thus the higher the total irradiance (the area under the irradiance versus wavelength curves of Figure 3.1 above) then the higher the maximum total heating rate that results. However there are differences in the magnitudes of the peak EUV/UV heating rates between MarTIM and these other studies. MarTIM shows a rate of 1100 K/day versus 1300 and 900 K/day from Bougher et al. (1999b) and González-Galindo et al. (2005) respectively (for solar medium conditions). Such differences can be attributed to the background neutral atmosphere each model uses, for which there is limited data available to verify the mixing ratios. So for example the fact that the LMD and MTGCM models (González-Galindo et al. (2005) and Bougher et al. (1999b), respectively) include different photochemical schemes means their modelled thermospheric densities are likely to be different to one another (and in in turn MarTIM).

Finally, note that although the maximum total heating rate for SMED conditions isn't exactly halfway between the rates for SMIN and SMAX that this is most likely due to the $F_{10.7}$ cm radio flux not always being a reliable indicator of UV emissions (this waveband being the most important for atmospheric absorption) (Bauer, 1999; Rottman, 1999). Since the $F_{10.7}$ proxy is generated in layers of the solar atmosphere (upper chromosphere to lower corona) quite different and distinct from the source regions of UV radiation (lower chromosphere to the corona) it may will be that these areas are affected by quite different physical processes and thus the UV flux won't necessarily correlate well with the 10.7 cm flux (i.e. non-linearly, Rottman (1999)). But as long as we are careful and ensure we are comparing MarTIM results to other models that use the same value for the $F_{10.7}$ proxy then this should be acceptable.

3.2.4 Atomic Oxygen Content and the V-T$_{CO_2-O}$ Coefficient

A Correction to Moffat (2005)

The work of Moffat (2005) used a value of 1.1×10^{-13} cm^{3}s^{-1} for the CO_2-O relaxation rate coefficient. This plays a dominant role in the parameterisation of middle atmosphere cooling due to CO_2 emission at 15-μm. As was noted in Moffat (2005) 1.1×10^{-13} cm^{3}s^{-1} is lower than the value normally cited in other similar GCM studies (Bougher et al., 2000), review papers (Bougher et al., 1994; Huestis et al., 2008) and indeed in the research documents that accompanied the CO_2 15-μm cooling rate parameterisation (López-Valverde and López-Puertas, 1994a,b, 2001) where values of the order $1-3\times10^{-12}$ cm^{3}s^{-1} are usually quoted.

The difference in the value of this rate coefficient was justified in terms of the uncertainties in MarTIM's atomic oxygen number density for which there were (and still are) few direct measurements of to constrain MarTIM with. Following work with members of the Max-Planck Institute for Solar System Research, Germany it was suggested that MarTIM's high altitude O density was larger than typically accepted. This would have greatly enhanced the role that the CO_2-O relaxation rate coefficient would

play in the parameterisation of cooling due to CO_2 emission at 15-μm within MarTIM's simulated heat budget. As no other major thermospheric heat sources or increases to existing heat sources could be justified to balance the enhanced CO_2 15-μm cooling it was instead necessary to reduce the role this cooling played. This could be achieved either by using an alternative input atmosphere with a lower atomic oxygen content or by lowering the CO_2-O relaxation rate coefficient. Since an alternative input atmosphere was not available it was concluded that lowering the CO_2-O relaxation rate coefficient to 1.1×10^{-13} cm^3s^{-1} was a necessary substitute to achieve a satisfactory thermodynamic response from MarTIM.

The above changes allowed MarTIM in Moffat (2005) to simulate temperatures that compared well against modelled and measured values. Subsequently, however, the source of MarTIM's large atomic oxygen content was traced to a coding error in the setup of the initial atmosphere that biased the simulation and enhanced MarTIM's atomic oxygen number density throughout the atmosphere. The miscalculation that created the bias was traced to the calculation of volume mixing ratios, which proceeds as:

$$\chi_i = \frac{n_i}{\sum_{s=1}^{7} n_s} \text{ for } i = 1_{\mathrm{CO_2}}, 2_{N2}, 3_{CO}, 4_{Ar}, 5_{O2}, 6_{NO} \tag{3.2}$$

with the volume mixing ratio of the final species (7_{O}) being calculated by subtracting the first six from unity.

However, in Moffat (2005) the following calculation was used to obtain the O mixing ratio:

$$\chi_{7_{\mathrm{O}}} = 1 - \chi_{1_{\mathrm{CO_2}}} - \chi_{2_{\mathrm{N_2}}} \tag{3.3}$$

presumably because MarTIM could only calculate the mutual diffusion and advection of 3 species and CO_2, N_2 and O were chosen because of their major role in Mars' neutral composition. Not including the summation $\sum_{i=3}^{6} \chi_i$ on the right hand side of equation 3.3 created an enhancement to the atomic oxygen volume mixing ratio and in turn to the CO_2 15-μm cooling rate. Consequently, reducing the value of the CO_2-O relaxation rate coefficient will have counterbalanced the effect of the O volume mixing ratio bias. With a suitable correction we now have no problem using a value for the CO_2-O relaxation rate coefficient of 1.5×10^{-12} cm^3s^{-1}, much closer to those typically cited.

The Importance of CO_2 15-μm cooling and the V-$T_{\mathrm{CO_2-O}}$ Coefficient

Theoretical studies bear out the important role that O(^{3}P) collisions with CO_2 have on the CO_2 15-μm cooling rate in the energy budgets of the three terrestrial planets. This is especially true at Venus and Mars given that CO_2 is by far the major constituent and that oxygen compounds are a major product of its photodissociation. Despite the smaller abundance of atomic oxygen in the Martian atmosphere collisions between O in the O(^{3}P) state and CO_2 molecules are notable for being extremely efficient at exciting CO_2 (ν=2) vibrational states, resulting in enhanced 15-μm emissions and cooling in regions of non-local thermodynamic equilibrium such as the thermosphere (Bougher et al., 2000). The O to CO_2

ratio thereby reflects both the dissociation of the upper atmosphere but also the expected effectiveness of the CO_2 15-μm cooling mechanism. The CO_2 15-μm cooling results in quite a limited variation in temperatures over the 11-year solar cycle for both Venus and Mars ($\sim$76 K and $\sim$110 K respectively Bougher and Dickinson (1988)) and alongside other processes efficiently damps the exospheric temperature response (relative to Earth) due to solar EUV variability associated with the $\sim$27-day rotation of the sun (10% and 30-50% respectively Forbes et al. (2006, 2008)). Additionally, three-dimensional modelling work has shown how dependent the simulation of appropriate temperatures are on the correct recreation of the O to CO_2 ratio. For example a higher ratio was suggested by Keating et al. (1998) in order to explain the discrepancy between the temperature deduced from Mars Global Surveyor aerobraking data and the temperature calculated by modelling work of Bougher et al. (1997) (120 K versus 150 K at 130 km (Chaufray et al., 2009)).

The effectiveness of CO_2-O collisions on the CO_2 15-μm emission cooling mechanism depends upon the atomic oxygen and carbon dioxide abundances and also on the collisional energy transfer rate coefficient between CO_2 and O i.e. the relaxation rate (Bougher et al., 1994, 2000). For the former there is unfortunately a fair uncertainty in the upper atmospheric O abundance, which has never actually been directly measured but instead only inferred from 130.4 nm oxygen triplet UV airglow measurements (e.g. Stewart et al. (1992); Leblanc et al. (2006); Chaufray et al. (2009)) and ionospheric calculations (e.g. Fox and Dalgarno (1979)). For SMIN conditions an O to CO_2 mixing ratio of 1.25 % at 130 km was deduced from the Viking descent probe ion measurements (Hanson et al., 1977). The Mariner 6 and 7 airglow data suggested 2 to 3 % at 135 km for SMAX conditions (Stewart, 1972; Bougher et al., 1999b). Stewart et al. (1992) was able to reproduce the emission intensity profile of Mariner 9 UVS data, also at SMAX conditions, by using an O to CO_2 mixing ratio of 0.7 % at the 1.2 nbar pressure level while a ratio of 0.2 % provided the best fit of the latitude and local time variations when compared against the MTGCM model (Bougher et al., 1990). More recently UV airglow measurements by the SPICAM instrument onboard the Mars Express spacecraft for SMED conditions (Chaufray et al., 2009) found an atomic oxygen density of $1.2^{+1.2}_{-0.5}\times10^7$ cm^{-3} at the exobase. When extrapolated down to 135 km this gave an O/CO_2 mixing ratio of 0.6 to 1.2 %.

Modelling work (Bougher et al., 1999b, 2000; McDunn et al., 2010) has established how thermospheric winds transport O atoms from their dayside photo-production region to the nightside and polar latitudes. These works identified how the O to CO_2 ratio at the altitude of the mid-afternoon ionospheric peak ($\sim$130 km) is maintained by photochemically produced CO_2^+ being quickly converted to O_2^+ by reaction with O. Typical values were simulated to vary from 1 to 4 % at 130 km over a range of solar activities and heliocentric distances (Bougher et al., 2000; Fox, 2004a).

Regarding the collisional energy transfer rate coefficient between CO_2 and O, the measured quantity commonly quoted is the rate coefficient for O-CO_2 deactivation (relaxation), which is the reverse of excitation (Bougher et al., 1994). This coefficient remains to be properly constrained, despite almost two decades of debate, by laboratory measurements in the appropriate temperature range (200-400 K)

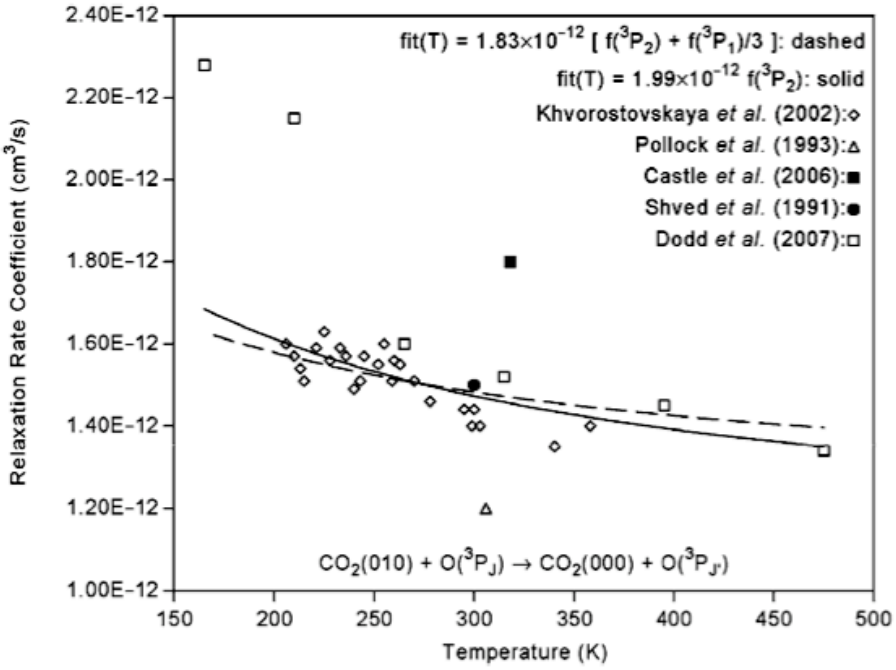

Figure 3.4: The estimated temperature dependence of the CO_2-O relaxation rate (Huestis et al., 2008).

as recent reviews have confirmed (for example Forbes et al. (2006); Huestis et al. (2008), see Figure 3.4). Nonetheless the review by Huestis et al. (2008) gave $\sim 1.5\times10^{-12}$ cm^3s^{-1} as the recommended room temperature value and it was noted that recent GCM simulations have used values up to $\sim 3.0\times10^{-12}$ cm^3s^{-1} (and higher) because of the different thermospheric temperatures experienced at the terrestrial planets. González-Galindo et al. (2009b) for example required a value of 3×10^{-12} cm^3s^{-1} to be able to reproduce the observed temperatures in the Martian upper atmosphere. This was referred to as a 'traditional value' given it's use in previous GCM simulations (Bougher et al., 1994, 1999b, 2000).

In conclusion, while neither the atomic oxygen content nor the O-CO_2 deactivation coefficient have been definitively constrained, both have been estimated to within a reasonable range. Thus we look to model the Martian atmosphere beginning from these most commonly cited values and discuss the effect this has on a MarTIM simulation. Removing the bias introduced in equation 3.3 allowed a value of 1.5×10^{-12} cm^3s^{-1} to be used for the O-CO_2 deactivation coefficient i.e. much closer to the coefficient value typically used in similar studies. It is from this point that we begin the new work for this PhD.

3.3 The Standard MarTIM Model Simulation

Given the above improvements and modifications we now define the standard way in which a MarTIM simulation can be conducted, which we refer to as a *base run*, and discuss the results this gives us.

3.3.1 The Initial Atmosphere

Since MarTIM is a first principles numerical model it must be provided with some form of input atmosphere from which to begin its numerical iterations. Having access to an input atmosphere that is physically consistent and preferably is sourced from observational data remains a challenge mainly because of the lack of available spacecraft data with sufficient spatial resolution to provide MarTIM a proper three-dimensional initial atmosphere, furthermore one that is appropriate for the particular seasonal and solar cycle conditions being studied. Instead, in the standard base run, we must begin with an externally sourced one-dimensional globally averaged input atmosphere that consists of neutral number density profiles (in m^{-3} for CO_2, N_2, O, CO, Ar, O_2 and NO) and a separately sourced parameterisation for a one-dimensional neutral temperature profile.

The neutral number density profiles are based upon the 1D model of Fox and Dalgarno (1979) that showed satisfactory fits to the Viking profiles from Nier and McElroy (1976). This input data set, shown in Figure 3.5(a), also contains the heights (km) and pressures (Pa) against which the number densities are defined. The neutral temperature parameterisation comes from Krasnopolsky (2002) and was designed to match Viking 1 density profiles (Nier and McElroy, 1976) for solar minimum conditions, the results of 3D models (Bougher et al., 1999b, 2000) used to analyse observational data from the Far Ultraviolet Spectroscopic Explorer (FUSE) satellite (Krasnopolsky and Feldman, 2001) for solar medium conditions and Mariner 6 and 7 measurements (Anderson and Hord, 1971) for solar maximum conditions. Figure 3.5(b) shows the initial temperature profiles we use for solar minimum, medium and maximum conditions and equation 3.4 reproduces the parameterisation from Krasnopolsky (2002):

$$T(z) = T_\infty - (T_\infty - T_{Meso}) exp\left(\frac{-(h(z) - h_{Meso})^2}{11.4 T_\infty}\right) \tag{3.4}$$

Here T_∞ is the exospheric temperature while T_{Meso} and h_{Meso} are the temperature and altitude of the mesopause. As in the case of Krasnopolsky (2002) the exospheric temperature T_∞ is set to 200 K for solar minimum conditions, to T_∞ = 270 K for solar medium conditions and to T_∞ = 350 K for solar maximum conditions. In all cases T_{Meso} is set and fixed to 125 K and h_{Meso} is set to 90 km.

Although both sets of input data had been designed or modelled to achieve satisfactory fits to spacecraft data this is usually only for the particular location and local time of the observations. But again, since MarTIM is a 3D GCM, once we interpolate these profiles onto MarTIM's vertical pressure grid they must be copied across all latitude and longitude arrays. Consequently the standard base run begins from a globally averaged (horizontally uniform) initial atmosphere that only has structure in the vertical direction and for which only one location can be verified as being appropriate to the actual Martian atmosphere. Furthermore in this initial atmosphere we also set all wind velocity magnitudes to zero because data on velocities remain as poorly constrained as temperature and composition data.

Since the above combination of settings is clearly unphysical we rely upon MarTIM to iterate toward a more physically consistent solution. In particular we ensure that the atmospheric gases at each MarTIM grid point obey the ideal gas equation exactly (P=nkT) so that even though a globally averaged input

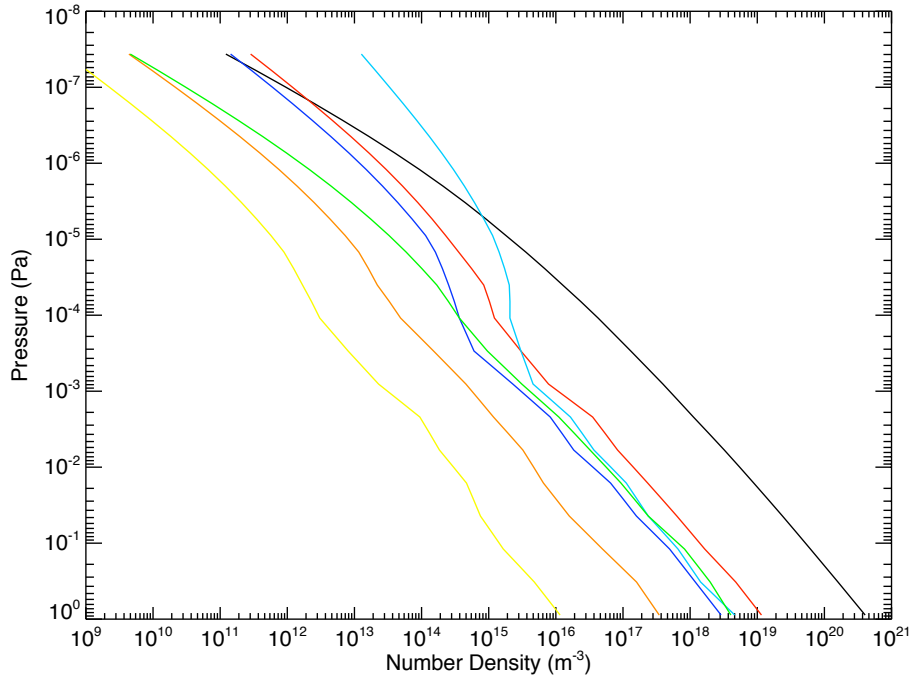

(a)

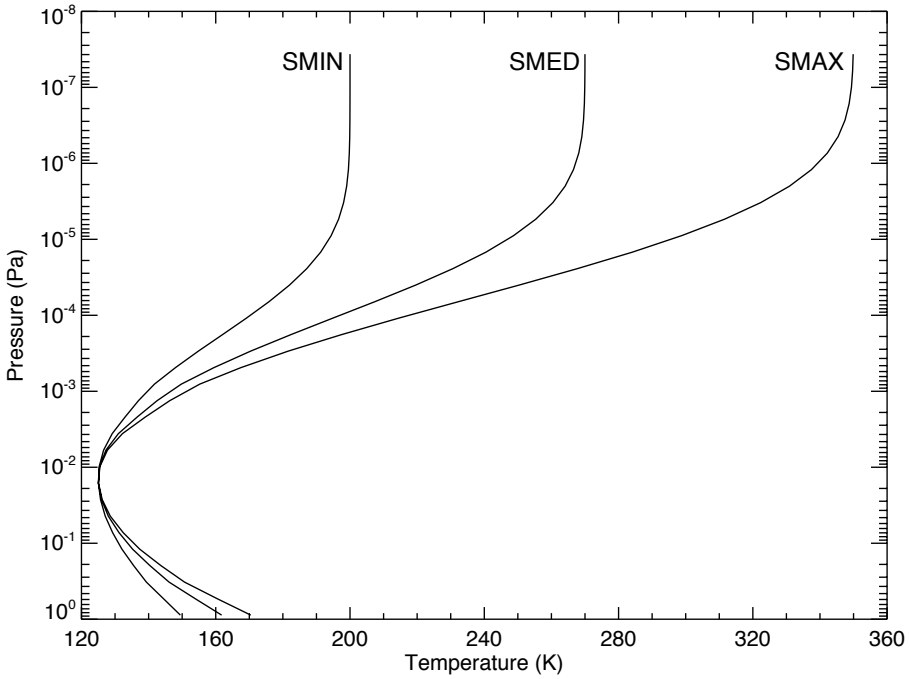

(b)

Figure 3.5: (a) MarTIM's initial (ideal gas) neutral number density profiles for CO_2 (black line), N_2 (red line), CO (blue line), O (cyan line), O_2 (orange line), Ar (green line) and NO (yellow line) and (b) MarTIM's initial temperature profiles for solar minimum, medium and maximum.

atmosphere is being used without any horizontal structure we know that there is a physically consistent link between MarTIM's vertical pressure coordinate, the composition and the temperature. Also, fol-

lowing the enhancements to the neutral diffusion and advection subroutine we decided to study whether including a different number of neutral species in the initial atmosphere affected the result, knowing that this new subroutine could self-consistently determine their composition. This work is discussed in section 3.4 below.

Generally we decide which neutral species to include in a particular study depending on whether theory suggests they play an important thermodynamic role or that their number density is significant in the Martian atmosphere. Then the chosen neutral number densities and the heights they are defined against are interpolated onto MarTIM's vertical pressure grid. These heights are also used to define the temperature profile using equation 3.4 so that finally the total number density can be calculated from the ideal gas equation. Since the heights against which the number densities are defined do not change from one species to the next, in turn neither will the temperature profile and thus neither will the total number density at each pressure level. Hence, regardless of how many neutral species are included in a particular study the total number density remains the same. This will mean that as more species are included in each new study the individual number densities of those species that were already present will be reduced by an equal amount determined by the new species added. However the mixing ratios of the species that were already present will remain the same with respect to one another.

Finally, given the initial atmosphere is unphysical, it is appropriate for us to put an emphasis on ensuring the physical consistency of MarTIM's result once it has iterated sufficiently forwards from the initial atmosphere. An appropriate stopping point for such a model run is when the solution is said to have reached *steady state* so that the same result (in terms of simulated temperature for example) is calculated at the same local time at the same location on consecutive days and iterating further would not change the result. This usually occurs from day 7 onwards. It is at this point that we can strictly compare MarTIM's results to other GCM simulations and available spacecraft and/or observational data. A typical MarTIM base run uses a 5° by 5° latitude by longitude grid, with 33 vertical pressure levels from 0.883 to 9.9×10^{-8} Pa at a resolution of 0.5 scale heights. The iteration time step is usually set to 10 seconds.

3.3.2 The MarTIM Base Run

We now discuss the results from a typical MarTIM simulation that was completed using the four neutral species CO_2, N_2, CO and O. Carbon dioxide was included because it is by far the most dominant species in the Martian atmosphere and as has been discussed it provides the major EUV heating source throughout the entire model. Atomic oxygen was included because of the important role it plays in the enhancement of the CO_2 15-μm cooling mechanism, which as will be shown dominates the middle atmosphere energy balance. Nitrogen and carbon monoxide were included as they are the next most dominant neutral species in terms of composition (number density, mixing ratios etc) and because their significant absorption of solar flux in the EUV region has been shown to play an important role in MarTIM's EUV heating rate. Various combinations of parameters for the CO_2-O relaxation rate coefficient,

the EUV heating efficiency and the eddy diffusion coefficient were investigated, constrained within the typical boundaries suggested by background research, in order to generate realistic thermospheric temperature magnitudes and global circulation structures. In this subsection we use 1.5×10^{-12} cm^3s^{-1} for the V-T_{CO_2-O} coefficient, 22% for the EUV heating efficiency and 1500 m^2s^{-1} for the eddy diffusion coefficient.

Energy Balance

The energy balance contrasts the major heating and cooling terms and gives us an indication of how the associated physics is manipulating the model atmosphere. A well modelled energy balance is therefore fundamental in obtaining and explaining physically consistent thermal and wind structures. Figure 3.6 shows the major thermospheric energy inputs (EUV/UV heating, near-IR heating) and outputs (thermal conduction and 15-μm radiative cooling). The results, for SMIN equinox conditions, have been globally averaged to remove any local time effects and to give us a perspective on MarTIM's heat balance as a whole.

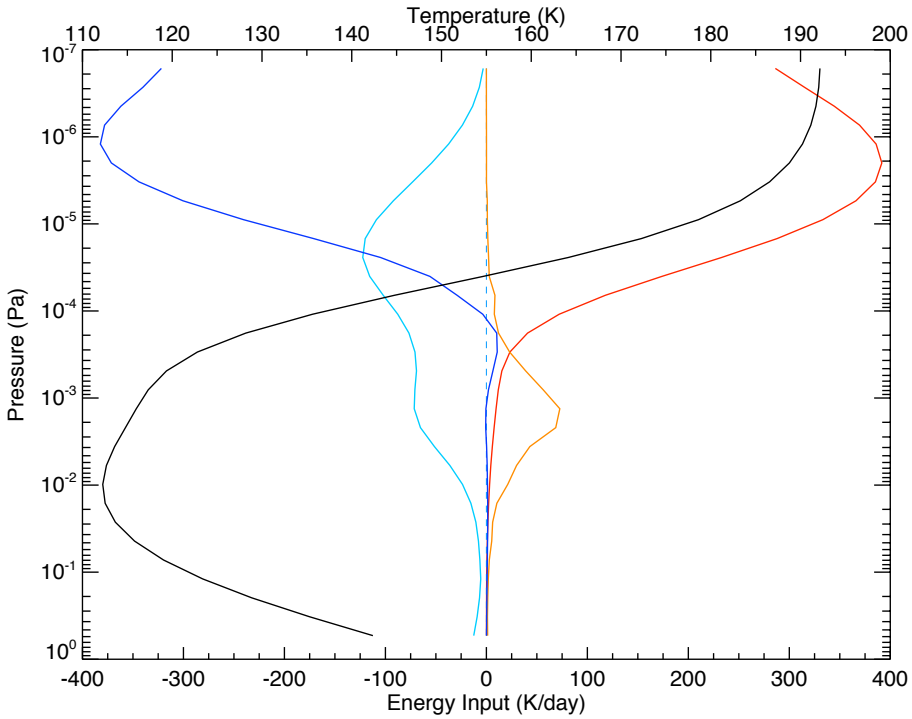

Figure 3.6: MarTIM base run steady state result: the major (globally averaged) energy inputs. Red line: EUV/UV heating; orange: near-IR radiative heating; cyan: 15-μm radiative cooling; blue: vertical thermal conduction; black: globally averaged temperatures. SMIN ($F_{10.7}$=67.2), Ls=180° (1.466 AU).

Figure 3.6 confirms that the thermosphere is dominated by intense heating from the absorption of short wavelength solar UV and EUV radiation ($\leq$170 nm) at relatively high altitudes (red line) and that this thermal energy is then conducted downward to the lower atmosphere (blue line), typically the mesosphere, where radiative cooling by infrared active molecules, CO_2, becomes most effective (cyan line)

(Müller-Wodarg et al., 2008). This middle atmosphere is also where IR radiative heating is a prominent heat source (orange line) since this region is in local thermodynamic equilibrium so that energy is efficiently absorbed by the IR active neutral species present (again, CO_2 dominates). Clearly MarTIM's IR heating parameterisation reflects this trend quite well. Finally, from the resulting temperature profile (black line), the mesosphere (pressure level ∼10, 9.81×10^{-3} Pa) and thermosphere (upper boundary pressure level ∼32, 1.64×10^{-7} Pa) effectively pin the thermal structure between their two extremes and the global average temperature increases rapidly with altitude between the two; a defining thermal signature for the thermospheres of all solar system planets (Achilleos et al., 1998).

In the high thermosphere MarTIM indicates that the maximum globally averaged rate of EUV/UV heating (∼392 K/day) occurs at pressure level 27 (1.99×10^{-6} Pa), which is at an average altitude of ∼163 km. Its structure was discussed in section 2.5; the maximum absorption of solar radiation occurs about the level of unit optical depth (Wallace and Hobbs, 1977) with this occurring about the level where cumulative depletion of the beam is a factor of e as a result of passage through the atmosphere above. This heating is mainly compensated for by molecular thermal conduction whose vertical distribution of cooling clearly mirrors that of EUV/UV heating. Its structure was introduced in section 2.3.2; the energy flux (rate of energy transport) is directly proportional to the temperature gradient (Gombosi, 1994). Hence as we move upwards through the thermosphere the solar heating input heats the atmosphere and the temperature increases. Then this growing temperature gradient is matched by a deepening thermal conduction cooling through equation 2.19.

Moving down through the middle atmosphere, infrared heating begins to dominate the average energy input between pressure level 9 and 17 (1.62×10^{-2} and 2.96×10^{-4} Pa). From Figure 3.6 the peak global average IR heating input (∼72.74 K/day) occurs at pressure level 14 (1.33×10^{-3} Pa), which is at an average altitude of ∼103 km. The localised nature of this heating structure was alluded to in section 2.6.4 where equation 2.35, involving the exponential of the optical depth, described how energy is gained from the solar flux as the flux itself is attenuated. Hence one might expect the solar IR radiation heating structure to be analogous to that of EUV/UV heating. However application of tabulated non-LTE correction factors reflects how in the upper atmosphere (where non-LTE dominates) much of the absorbed energy is re-emitted to space before having a chance to thermalise the neutral CO_2 present. Indeed the photoabsorption coefficients of Figure 2.4 start declining at around ∼100 km (as we come down in altitude) where the largest attenuation of the solar flux takes place (López-Puertas and Taylor, 2001). Above this altitude the CO_2 bands are sufficiently optically thin to allow emission to space. It is only in the middle atmosphere that this energy is more efficiently expressed as heating where the optical depth has sufficiently increased and LTE dominates so that collisional energy transfer allows the absorbed energy to be expressed as heat. The net effect is that there is little IR heating above ∼115 km.

Finally the CO_2 15-μm radiative cooling shows the most intricate structure given its complex non-linear dependence on temperature and the enhancement from O-CO_2 V-T processes. From Figure 2.6 in section 2.6.5 the flux transmission to space for both bands of the simplified CO_2 model are asymptotic

at high altitudes (reaching 1.0). Thus as we move upwards into the non-LTE optically thin regions of the atmosphere a greater fraction of the CO_2 15-μm radiative flux will simply escape directly to space and thus cool the atmosphere, without there being any reabsorption. This would suggest that the cooling rate should generally increase with altitude. Certainly the maximum rate of $\sim$−122.2 K/day at pressure level 22 (2.43×10^{-5} Pa, $\sim$133 km) and the structure of the cooling profile with altitude, bears this out. This increase in cooling with altitude will also be related to the increase in atomic oxygen content relative to carbon dioxide in the upper atmosphere that occurs due to gravitational fractionation by molecular diffusion. However, a second bulbous cooling region occurring at pressure level 14 (1.33×10^{-3} Pa, $\sim$103 km) with a global average magnitude of $\sim$−71.3 K/day seems to go against this trend. This region of cooling reflects the enhancement to CO_2 cooling rates that occurs as we move into this LTE region of the atmosphere over what might be expected had the non-LTE situation remained. Finally, the decrease in cooling that occurs in the uppermost and lowermost regions of the atmosphere can be linked to the net decrease in atomic oxygen number density in these regions.

Longitudinal Energy Balance Structure

Figures 3.7(a), 3.7(b) and 3.7(c) show equatorial plots of, respectively, (a) the EUV/UV heating rate, (b) the IR radiative balance (sum of IR heating and CO_2 15-μm cooling) and (c) the (log to base 10) O to CO_2 ratio. These have been included to give an indication of the structure, now in both longitude and altitude, of the dominant energy balance terms rather than just in the global average of Figure 3.6.

Notice how in Figure 3.7(a) the structure of the peak EUV/UV heating region (in particular from local time 1200-hrs to 1700-hrs) seems to trace out the curve of the O to CO_2 ratio structure from 1000-hrs to 2000-hrs in Figure 3.7(c). Thermospheric winds are known to preferentially transport O atoms from their dayside photo-production region to the nightside and polar latitudes (Bougher et al., 1999b, 2000; McDunn et al., 2010). Thus, as the relative amount of CO_2 increases on the dayside as you scan across at a constant pressure level the rate of EUV/UV heating increases too (CO_2 being the dominant heating component at these wavelengths, as discussed earlier). Conversely the peak CO_2 cooling mechanism structures are predominantly where the O to CO_2 ratio maximises i.e. where O is dominant. Thus at local time 1000-hrs and 2400-hrs at pressure level $\sim$20-22 (6.61×10^{-5}-2.43×10^{-5} Pa) we see the most IR radiative cooling in Figure 3.7(b) occurring in the same local time locations of peak O to CO_2 ratio in Figure 3.7(c) (for the same pressure level).

Overall, Figures 3.7(a), 3.7(b) and 3.7(c) show how the modelled atmosphere has reached an equilibrium between the important energy inputs and outputs that has a strong dependance on the relative amounts of atomic oxygen and carbon dioxide.

Temperature and Circulation Structures

The dynamics of the Martian atmosphere has a very important role within the energy balance alongside the localised processes discussed above. Temperature structures and expansion drive wind flow on a

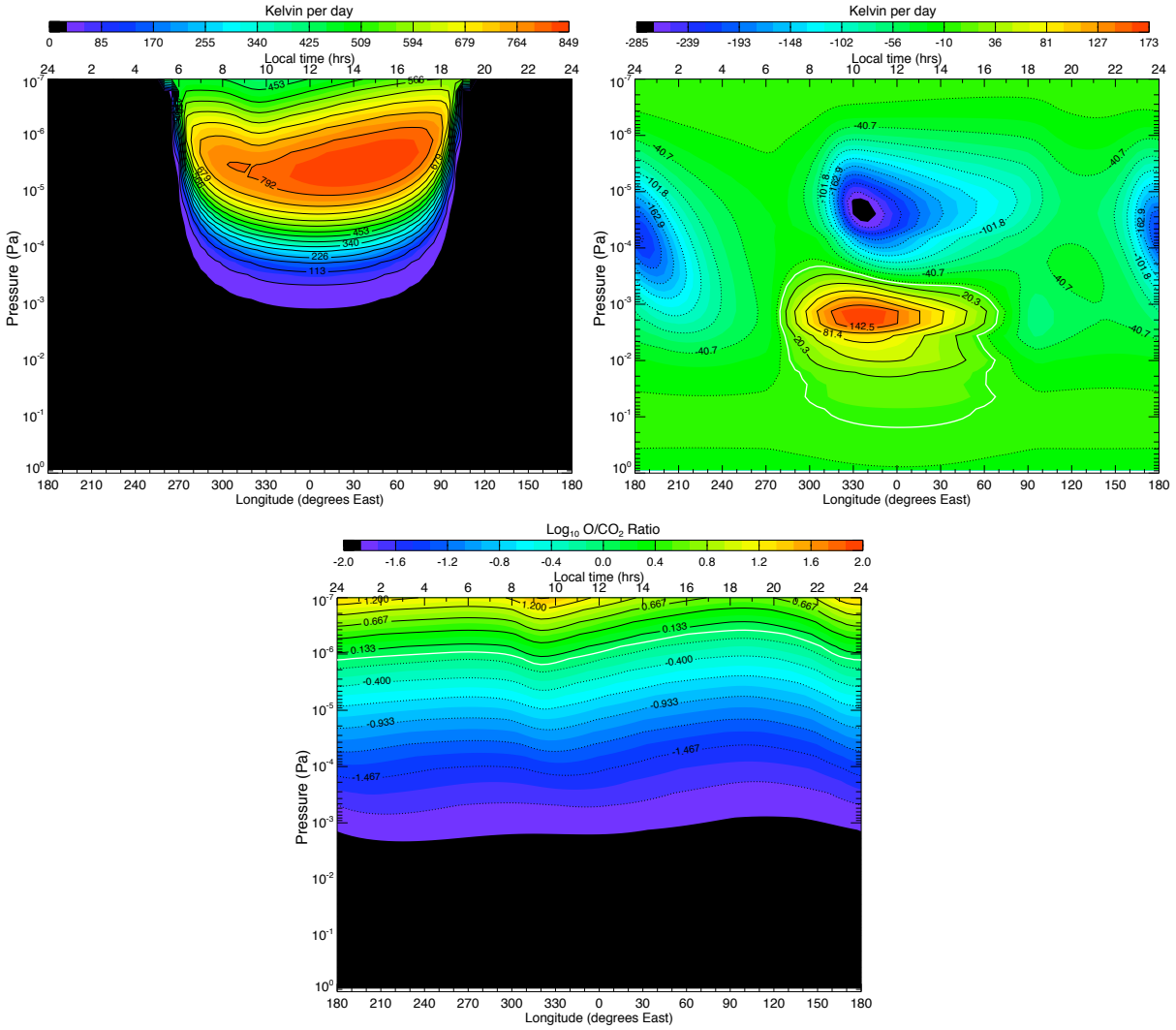

Figure 3.7: (Top left) MarTIM base run EUV/UV heating rate, (top right) IR radiative balance and (bottom) $\log_{10}$ of the O to CO_2 ratio. Equatorial profiles for SMIN ($F_{10.7}$ 67.2), Ls 180° (1.466 AU) conditions. Solid (dashed) contours indicate positive (negative) magnitudes. White contours indicates zero magnitudes.

global scale. However, the convergence and divergence of the wind field usually occurs on sufficiently short timescales to add or subtract heat via atmospheric adiabatic expansion and contraction. In this way energy can be exchanged in form from potential to kinetic then transported and redistributed on a three-dimensional global scale to influence the precise latitude-longitude distribution of the temperature and geopotential height structures, as previous studies have shown (Bougher et al., 1999b, 2000; González-Galindo et al., 2009b,a). In addition, modelling work by Bougher et al. (1999b) suggested that the role of global dynamics should play a progressively more important role as the solar cycle advances. Thus accurately recreating this equilibrium between dynamic and thermal structures is therefore important.

The individual figures in the left hand column of Figure 3.8 show the steady-state temperatures, vertical winds and adiabatic heating or cooling (term ω/ρ from equation 2.16) at pressure level 14

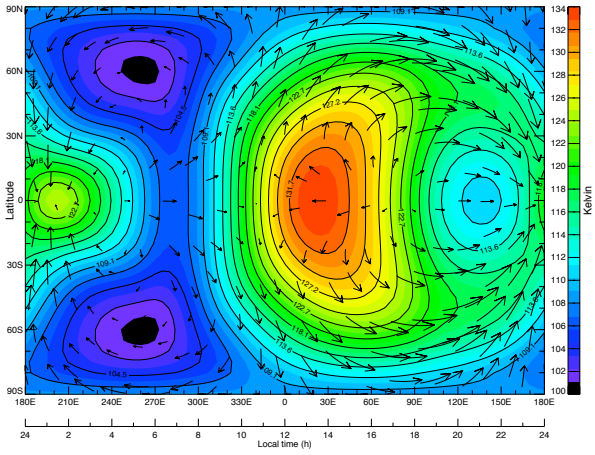

(a) Temperatures (K) (PL 14)

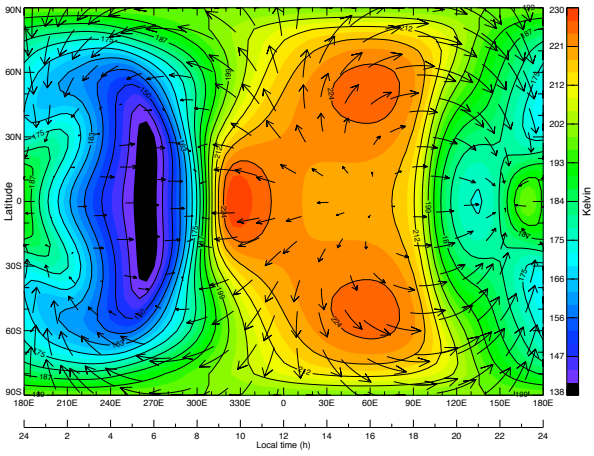

(b) Temperatures (K) (PL 30)

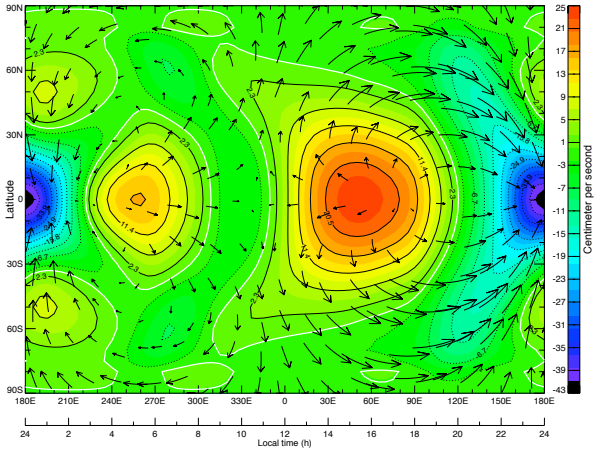

(c) Vertical velocity (cm/s) (PL 14)

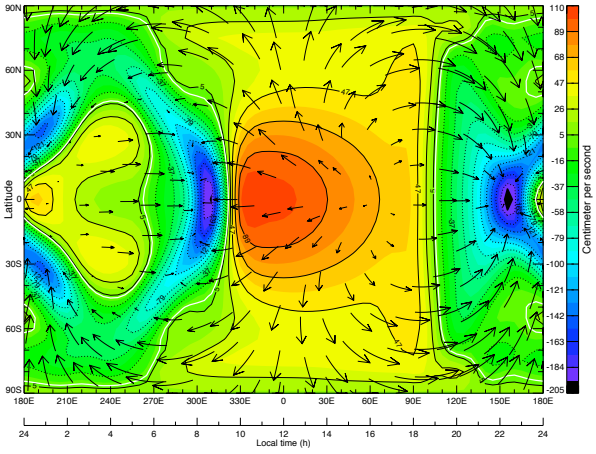

(d) Vertical velocity (cm/s) (PL 30)

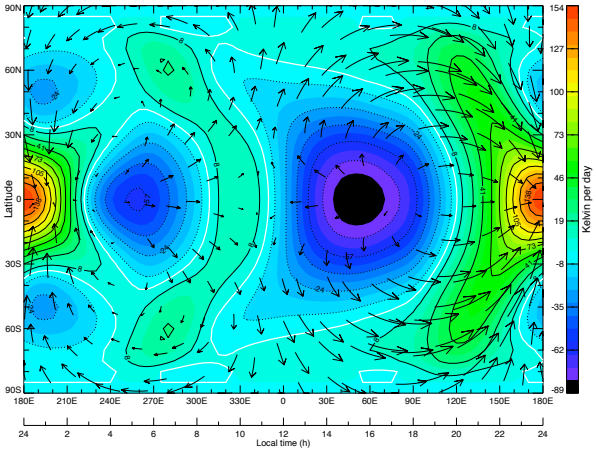

(e) Adiabatic heating term (ω/ρ, K/day) (PL 14)

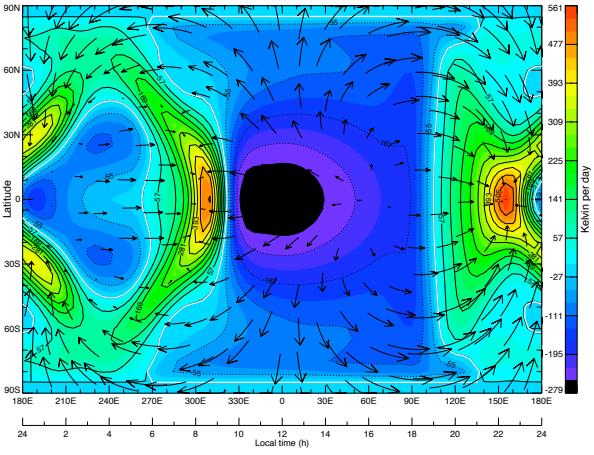

(f) Adiabatic heating term (ω/ρ, K/day) (PL 30)

Figure 3.8: MarTIM base run steady state result: day 15, PL 14 and 30 (1.33×10^{-3} Pa, ∼103 km and 4.45×10^{-7} Pa, ∼188 km respectively) for various output fields. Solid (dashed) contours indicate positive (negative) magnitudes. White contours indicates zero magnitudes.

(1.33×10^{-3} Pa), which is where the peak IR heating occurs. The figures in the right hand column of Figure 3.8 show the same output fields in the upper thermosphere pressure level 30 (4.45×10^{-7} Pa). Additionally, the arrows displayed on all plots show the horizontal wind flow along the resultant streamlines at these pressure levels. The dynamics of the simulation are dominated by the solar energy input into the middle and upper atmosphere and the manner by which the potential energy generated by this differential heating is converted into the kinetic energy of the wind field (Wallace and Hobbs, 1977). Then, from Bougher et al. (1999b), the combination of a symmetric solar heating plus Mars' rotation produces the asymmetric circulation patterns shown throughout Figure 3.8.

In the middle atmosphere the IR heating input generates a dominant thermal structure over the equator, due to the equinox conditions of this run, just after midday (Figure 3.8(a)). This drives a divergent flow upward (Figure 3.8(c)) and horizontally away from the dayside, which is then deflected eastwards in both hemispheres by the Coriolis force due to the presence of the planetary rotation. The effect is most prominent further away from the equator as indicated by the longer, thicker arrows over the evening terminator in both hemispheres at higher latitudes. Maximum wind speeds reach ∼56 m/s eastward at around 1800-hrs and 34 m/s westward at about 0600-hrs.

Differential advection of O and any enhancement it might give to CO_2 15-μm cooling is less important at pressure level 14 (1.33×10^{-3} Pa) since this is below the homopause (1.80×10^{-4} Pa) and so turbulent mixing still dominates (e.g. Figure 3.7(c) shows very little variation in O/CO_2 ratio across PL 14). However, wind flowing along constant pressure levels also drops in altitude, according to the hypsometric equation ($\delta z \approx -g^{-1}RT\delta lnP$, Holton (2004)), as it moves towards the cooler polar regions and the night side and the thickness of a given atmospheric column decreases. Thus, while the upward flow on the dayside (∼1500-hrs, Figure 3.8(c)) gives rise to strong adiabatic cooling, as indicated by Figure 3.8(e), the convergence (strong subsidence) of the wind field on the equator at 2400-hrs generates a localised adiabatic heating component there. Then in Figure 3.8(a) we see how this translates into the hot region at 0100-hrs i.e. slightly to the east of the adiabatic heating component location due to the thermal lag of the atmosphere. Finally this deep nightside heating creates a pressure gradient that drives winds back towards the dayside i.e. the upwelling at 0500-hrs in Figure 3.8(c).

The thermal and dynamic processes in the middle atmosphere have an influence on the upper atmosphere temperature and wind structures, such as those in Figure 3.8(b) at pressure level 30 (4.45×10^{-7} Pa). This can be most easily seen by the bifurcation of a single hot region on the dayside into two separate temperature peaks at ±60° latitude near 1600-hrs. The solar EUV heating component creates the overall hot dayside region but the column integrated IR heating upwards of pressure level 14 (1.33×10^{-3} Pa) and the commensurate adiabatic expansion generates a cooling about the equator throughout the afternoon leaving the localised temperature peaks observed in Figure 3.8(b) (González-Galindo et al., 2009b; Strobel, 2002).

Overall, however, the far greater magnitudes of the heating and cooling processes in the upper atmosphere in comparison to the middle atmosphere play a dominant role in the structures of temperature

and wind fields that result in the upper atmosphere. For example the convergence of westward and eastward equatorial flows at ∼0800-hrs and the subsequent subsidence generates a prominent hot region at 1000-hrs over the equator the magnitude of which rivals that of the two afternoon temperature peaks. Clearly, the fact that the adiabatic heating at the point of convergence (∼477 K/day) is more than double the maximum heating that occurs anywhere at pressure level 14 (1.33×10^{-3} Pa) means significant differences will result. The individual figures on the right hand side of Figure 3.8 show this to be the case. Also, the much greater day-to-night temperature contrast drives more powerful winds than those at pressure level 14 that now reach speeds up to 176 m/s eastwards and 164 m/s westwards (again, over the evening and morning terminators). It is this flow away from the dayside that preferentially transports O neutrals to the nightside, given their lighter mass, thereby introducing the relative increase in CO_2 on the dayside and decrease on the nightside (as was shown above in Figure 3.7(c)).

As stated by Bougher et al. (2000) the combination of Mars' wind field and the planetary rotation precludes an effective isolation of the day and nightside. The simulated localised nightside hot regions and dayside cool regions due to convergence or divergence (respectively) of horizontal flows at both pressure levels in Figure 3.8 shows this relationship in MarTIM.

3.4 The Impact of Neutral Diffusion and Advection on the Martian Thermosphere

The major development to the new version of MarTIM was to consider the effect that diffusion and advection have on the modelled atmosphere. Recall in the description above of the standard base run that the nominal version considers the mutual diffusion and advection of the four neutral species, CO_2, N_2, O and CO only. Meanwhile the other three available neutral species Ar, O_2 and NO were not included either because their number densities and mixing ratios were especially low (by their individual or combined presence in the model) or because their thermodynamic influence on the modelled atmosphere (e.g. response to solar EUV/UV flux) was thought to be negligible. Now we consider whether this is actually the case.

3.4.1 Influence of the New Diffusion and Advection Subroutine

First, the physical consistency of MarTIM's new diffusion and advection subroutine was assessed by following a tracer neutral species and considering the variation in composition that resulted as it moved through the modelled atmosphere. This tracer species was inserted into the initial globally averaged atmosphere at one location only. Each new study used a different location for injection and a different molecular mass for the injected species so that (1) the governing physics of specific atmospheric regions could be studied, (2) the vertical coupling of the model between these regions could be studied and (3) the role that species mass played could be considered. Table 3.1 details the various studies listing the pressure level at which the tracer species was injected as well as its molecular mass and number mixing

ratio at the point of injection. The tracer species was introduced at the subsolar point in all studies and equinox solar minimum conditions were used throughout.

Table 3.1: New diffusion and advection subroutine experiments.

#	Pressure Level	Pressure (Pa)	Molecular Mass (amu)	Initial Number Mixing Ratios[a] (CO_2, N_2, CO, O, M_{Tracer})
1	25	5.43×10^{-6} Pa	60	0.462, 0.073, 0.036, 0.428, 0.001
2	25	5.43×10^{-6} Pa	40	0.462, 0.073, 0.036, 0.428, 0.001
3	25	5.43×10^{-6} Pa	4	0.462, 0.073, 0.036, 0.428, 0.001
4	10	9.81×10^{-3} Pa	60	0.956, 0.025, 0.006, 0.012, 0.001
5	10	9.81×10^{-3} Pa	40	0.956, 0.025, 0.006, 0.012, 0.001
6	10	9.81×10^{-3} Pa	4	0.956, 0.025, 0.006, 0.012, 0.001

[a]Number mixing ratios at the grid point of injection only. Mixing ratio M_{Tracer} set to zero everywhere else.

The number mixing ratio for the tracer species in the initial atmosphere was set arbitrarily to 0.001 (0.1%). Then the mass and volume mixing ratio were calculated in the usual self-consistent manner for the four major species (CO_2, N_2, O, CO), as described earlier, except we also included the fifth tracer species. It is important to note that since the tracer species was injected at one grid point only, in the entire model, the number densities and mixing ratios of all the other species, on a global average, remained virtually unchanged from a standard base run. Even more-so as the simulation proceeded and the tracer species was diluted through the model. Also, because the tracer species was not assigned any photoabsorption cross sections, it could not add any direct solar heating to the background atmosphere. Therefore the tracer species had a totally negligible influence on the thermodynamic response of the modelled atmosphere; the atmosphere remained largely unchanged from the discussion in section 3.3.2 (this is shown in the next subsection). In this way we can study how the new diffusion and advection subroutine iterates the tracer species around the model without the model actually being influenced by its presence (i.e. in the absence of any feedback effects).

Checking the Background Atmosphere

To show that the background atmosphere was left unchanged by the addition of the tracer species we compare latitude by longitude temperature contour plots at the pressure levels where the species were introduced (PL 10 and 25, see Table 3.1). Figure 3.9 shows temperatures (with winds overlaid) at pressure levels 10 and 25 (top and bottom rows, respectively). The left hand column shows the basic MarTIM result already discussed earlier in section 3.3.2. The right hand column shows the results from the experiments of Table 3.1, top right represents experiment 4 (PL 10, 60 amu tracer added) while bottom right represents experiment 1 (PL 25, 60 amu tracer added). However, note that experiments 1, 2 and 3 returned precisely the same background atmosphere as one another as did experiments 4, 5 and

6. Thus the top right plot of Figure 3.9 can also represent experiment 5 and 6 and the bottom right plot can also represent experiment 2 and 3. For reference, Table 3.2 lists the specific temperature and wind maximum (minimum in parenthesis) magnitudes.

Table 3.2: Comparison of background atmosphere temperatures and wind speeds.

Experiment	Pressure Level[b]	Temperature[a] (K)	Zonal Winds[a] (m/s)	Meridional Winds[a] (m/s)
Basic MarTIM	25	221.0 (134.2)	163.1 (−147.2)	149.4 (−149.4)
Experiments 1, 2 and 3	25	220.0 (133.8)	162.6 (−146.6)	148.8 (−148.8)
Basic MarTIM	10	120.5 (103.4)	15.3 (−7.0)	14.6 (−14.6)
Experiments 4, 5 and 6	10	120.5 (103.4)	15.2 (−7.0)	14.6 (−14.6)

[a]Maximum (minimum).

[b]Pressure level 10 (9.81×10^{-3} Pa) is in the homosphere, pressure level 25 (5.43×10^{-6} Pa) is in the heterosphere. The homopause is at approximately pressure level 18 (1.80×10^{-4} Pa).

From Figure 3.9 and Table 3.2 it can be seen that the background atmosphere remains largely untouched by the addition of the tracer species in the various experiments of Table 3.1. The largest differences occur higher in the atmosphere where the solar energy input approaches its maximum (e.g. plots at PL 25). From Table 3.2 this can be seen to result in tracer species experiments using background atmosphere temperatures that are ∼99.5% the magnitude of those from section 3.3.2. The corresponding zonal wind speeds show a match of ∼99.6%, while the meridional wind speeds match by ∼99.5%. At pressure level 10 the match between the various background atmospheres is almost exact. Given that, in section 3.3.2 (with CO_2, N_2, CO and O), the background atmosphere reached equilibrium at about day 7 whereas in this section, (with the tracer species added), simulations are run through to day 200 (to allow the tracer species to be move throughout the atmosphere), we feel the majority of experimental time in this section is spent under essentially the same background atmosphere equilibrium conditions as section 3.3.2.

Horizontal Advection of Tracer Species across Pressure Level 25 (5.43×10^{-6} Pa)

Across horizontal constant pressure levels we only calculate the advection of neutral species by global wind circulation. Thus horizontal neutral diffusion is not considered. This is different to the vertical direction where both diffusion and advection are considered (see later). From Chapter 2, the continuity equation for the mass fraction Y_i of the i^{th} constituent is given by (Müller-Wodarg et al., 2006):

$$\frac{\partial Y_i}{\partial t} + u_\theta \frac{1}{a}\frac{\partial Y_i}{\partial \theta} + u_\phi \frac{1}{a sin\theta}\frac{\partial Y_i}{\partial \phi} + w\frac{\partial Y_i}{\partial P} = \frac{g}{a^2}\frac{\partial}{\partial P}\left(a^2 \rho Y_i (w_i^D + w_i^{K_\tau})\right) + J_i \tag{3.5}$$

Where, for the i^{th} constituent, $Y_i = \rho_i/\rho$ is the mass fraction, w_i^D is the vertical diffusion velocity and $w_i^{K_\tau}$ is the vertical eddy diffusion velocity. Here the horizontal advection is described by the second and

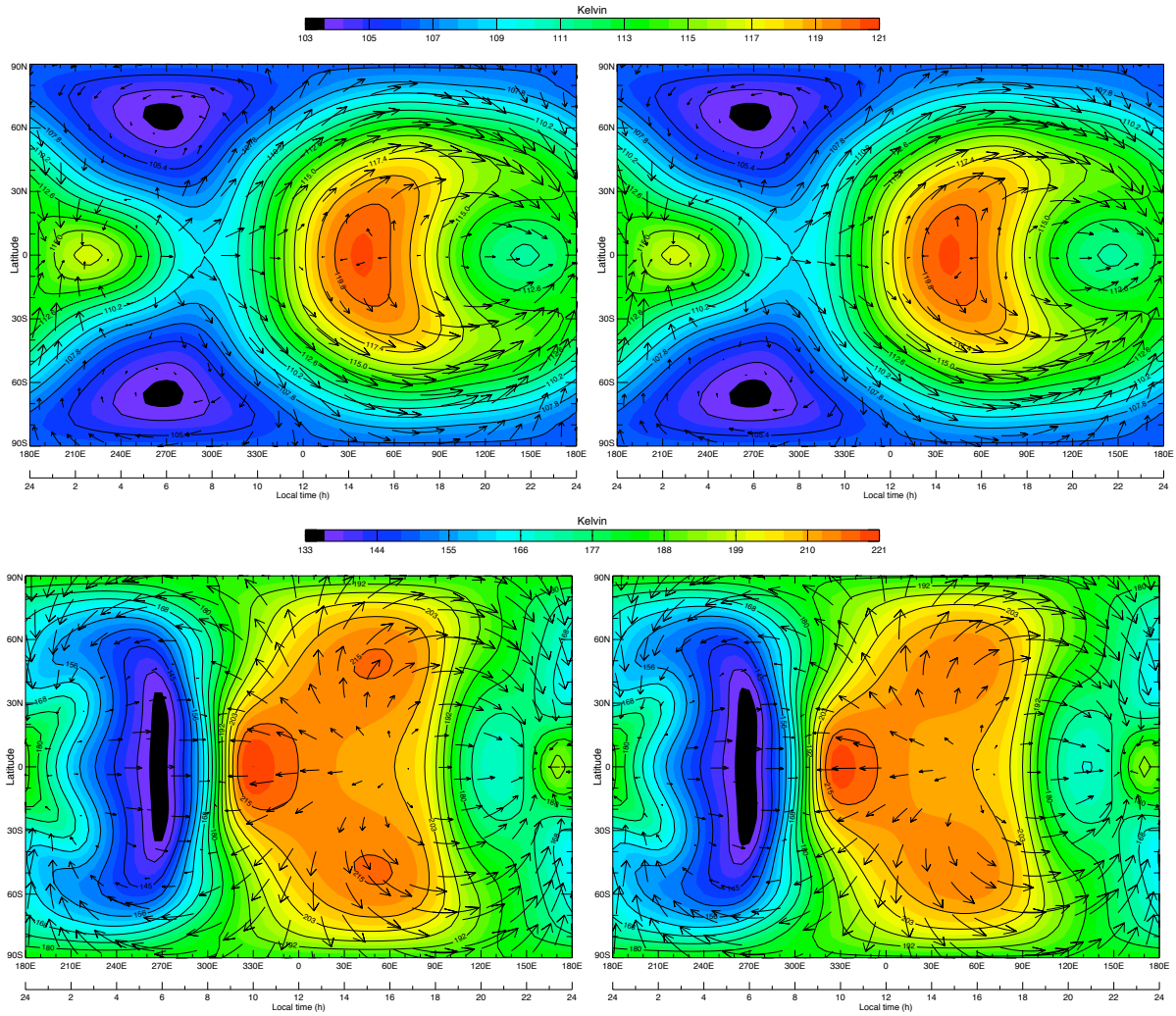

Figure 3.9: Comparison of latitude by longitude temperatures (with coordinated colour scales). Left column is the basic MarTIM result from section 3.3.2. Right column use the results from experiments of Table 3.1. Top row is PL 10 (9.81×10^{-3} Pa), thus top right represents experiment 4, 5 and 6 from Table 3.1. Bottom row is PL 25 (5.43×10^{-6} Pa), thus bottom right represents experiment 1, 2 and 3 from Table 3.1.

third terms on the left hand side, with the smaller vertical wind advection given by the fourth term on the left hand side. We solve for $\partial Y_i/\partial t$, for further reference see section 2.4, Chapter 2.

Horizontal diffusion was not included in the derivation of equation 3.5 simply because of its small magnitude in comparison to the magnitude of horizontal winds. The relative importance is very much biased towards wind-driven mixing rather than diffusion in the horizontal plane. From Marrero and Mason (1972), kinetic theory states that transport is entirely due to molecules in motion. For diffusion, on the microscopic scale, the concern is the immense number of molecules that move chaotically through the atmosphere. We expect collisions will dominate the overall rate of transport. For example, at standard temperature and pressure molecules have molecular speeds on the order 10^4 cm/s. However,

actual diffusion velocities are far slower (∼1 cm/s) because of the very short mean free path and thus the very great number of collisions (Marrero and Mason, 1972; Gombosi, 1994). In comparison for transport by horizontal winds on the larger macroscopic scale (indeed the global scale) a typical MarTIM result for SMIN, equinox conditions (1.466 AU) simulates wind speeds between a minimum of 0.06 m/s (−1.47 m/s) at pressure level 2, 5.36×10^{-1} Pa (not including the zero velocity lower boundary) and a maximum of 177.07 m/s (−164.98 m/s) at pressure level 33, 9.94×10^{-8} Pa. Consequently the bulk horizontal transport of neutral species on constant pressure levels will be dominated by advection rather than diffusion.

A good example of the two-dimensional advection of the tracer species in latitude and longitude is represented by Figures 3.10 and 3.11, which show the iteration of the 4 amu species from experiment 3 throughout pressure level 25 (where it was injected). Figure 3.10 shows successive days from day 1 to 5 as well as a snapshot of day 10. Then Figure 3.11 shows snapshots at various days from day 15 through to day 200. In these figures it is clear to see how the tracer species is advected by the global circulation. In addition, Figure 3.12 indicates the role that the pressure gradient ($\partial U/\partial\theta$) and Coriolis acceleration ($2\Omega v_\phi \sin\theta$) terms (meridional components only) as well as the geopotential height of pressure level 25 play in these iterations. Firstly the top left contour plot of Figure 3.10 (at the end of day 1) shows that the single point source of tracer species has expanded into a region symmetric about the equator. This region has also drifted eastwards as the expansion of the atmosphere at the subsolar point, shown in Figure 3.12(c), introduces a 'downhill' flow along the isobaric surface. This expansion was created by the prominent hot region at 1000-hrs generated by the convergence of horizontal winds and subsequent adiabatic heating, just as we saw earlier in Figure 3.8(b) regarding PL 30 (4.45×10^{-7} Pa). Note how the bifurcation of the temperature field, creating separate hot regions at ±60° latitude near 1600-hrs in Figure 3.12(d), is not as prominent as it was in Figure 3.8(b). This is simply because the solar EUV heating rate is still increasing with pressure level and plays a more dominant role at PL 30 than here at PL 25 (5.43×10^{-6} Pa). The reasons for its creation are the same though: column integrated IR heating upwards of pressure level 14 (1.33×10^{-3} Pa) causing adiabatic expansion and cooling about the equator throughout the afternoon.

From the end of day 1 and through to the end of day 2 (top left and top right contour plots, Figure 3.10) we see curvature structures beginning to form in the expansion of the tracer species i.e. higher latitudes have flowed further eastward. The number density structure seems to follow the curvature of the mid-to-late afternoon geopotential height contours of Figure 3.12(c) as well as the general direction of the circulation flow. Through days 3 to 5 the development of this eastward flow can be clearly seen in Figure 3.10. Figures 3.12(a) and 3.12(b) indicate how acceleration due to the pressure gradient as well as the Coriolis acceleration work to deflect the tracer species flow eastwards in both hemispheres on the dayside. In the northern hemisphere for example the pressure gradient drives flow towards the north pole for these equinox conditions (shades of blue at high latitudes on the dayside in Figure 3.12(a)) but the Coriolis force introduces an acceleration first eastwards then southwards due to the presence of the

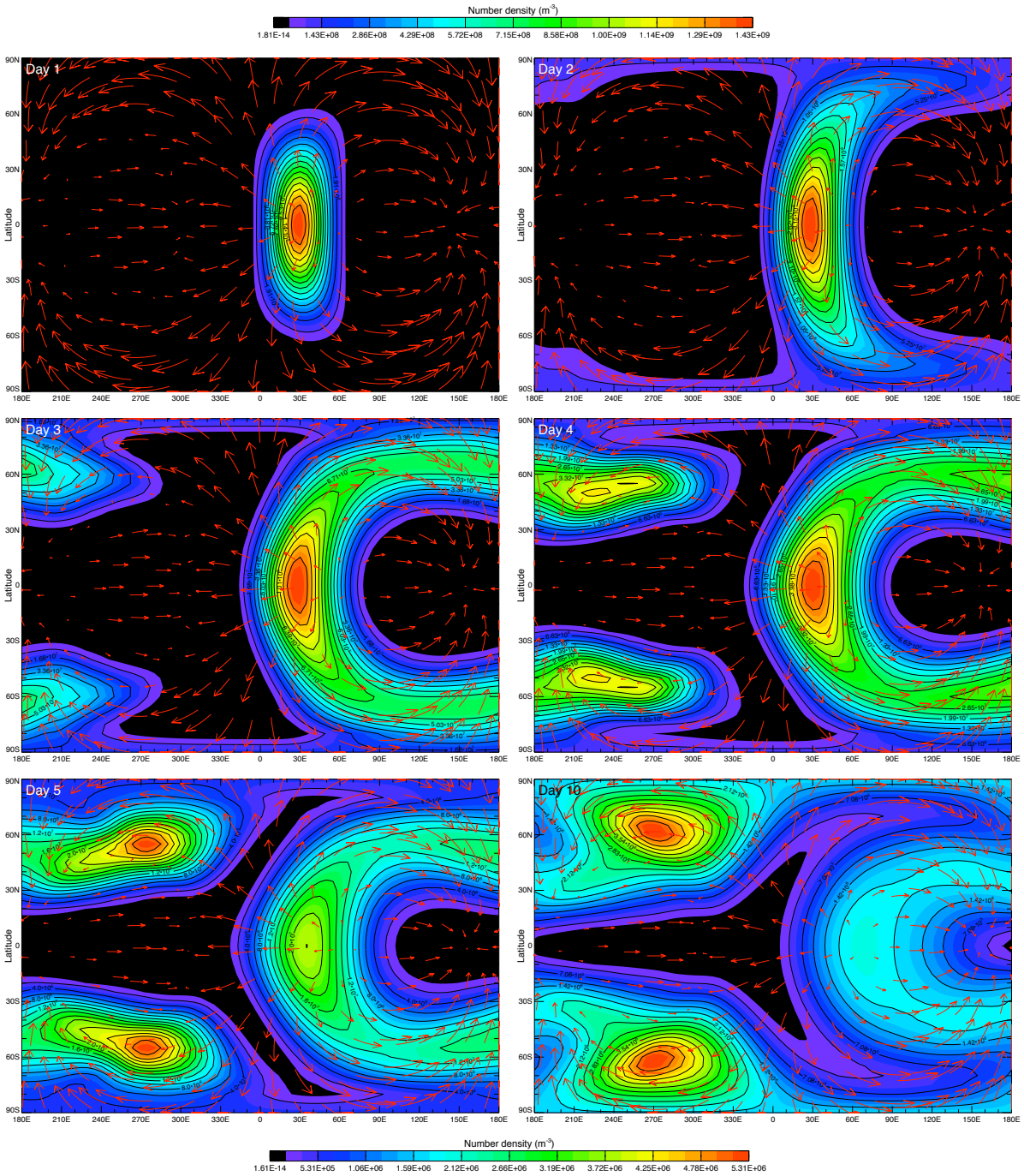

Figure 3.10: Tracer species number density fields at PL 25 (5.43×10^{-6} Pa), experiment 3, 4 amu, days 1 to 5 and day 10 (top to bottom, left to right). Top and bottom colour scales represent day 1 and day 10 respectively.

planetary rotation (shades of red at high latitudes on the dayside in Figure 3.12(b)). Finally, through the evening terminator, the winds converge at 2200-hrs and generate a hot region nearer 2300-hrs (Figure 3.12(d)) and expansion at 2400-hrs (Figure 3.12(c)). Therefore, at first, the tracer species seems to converge toward the equator at 2400-hrs but the pressure gradient there, produced by the expansion,

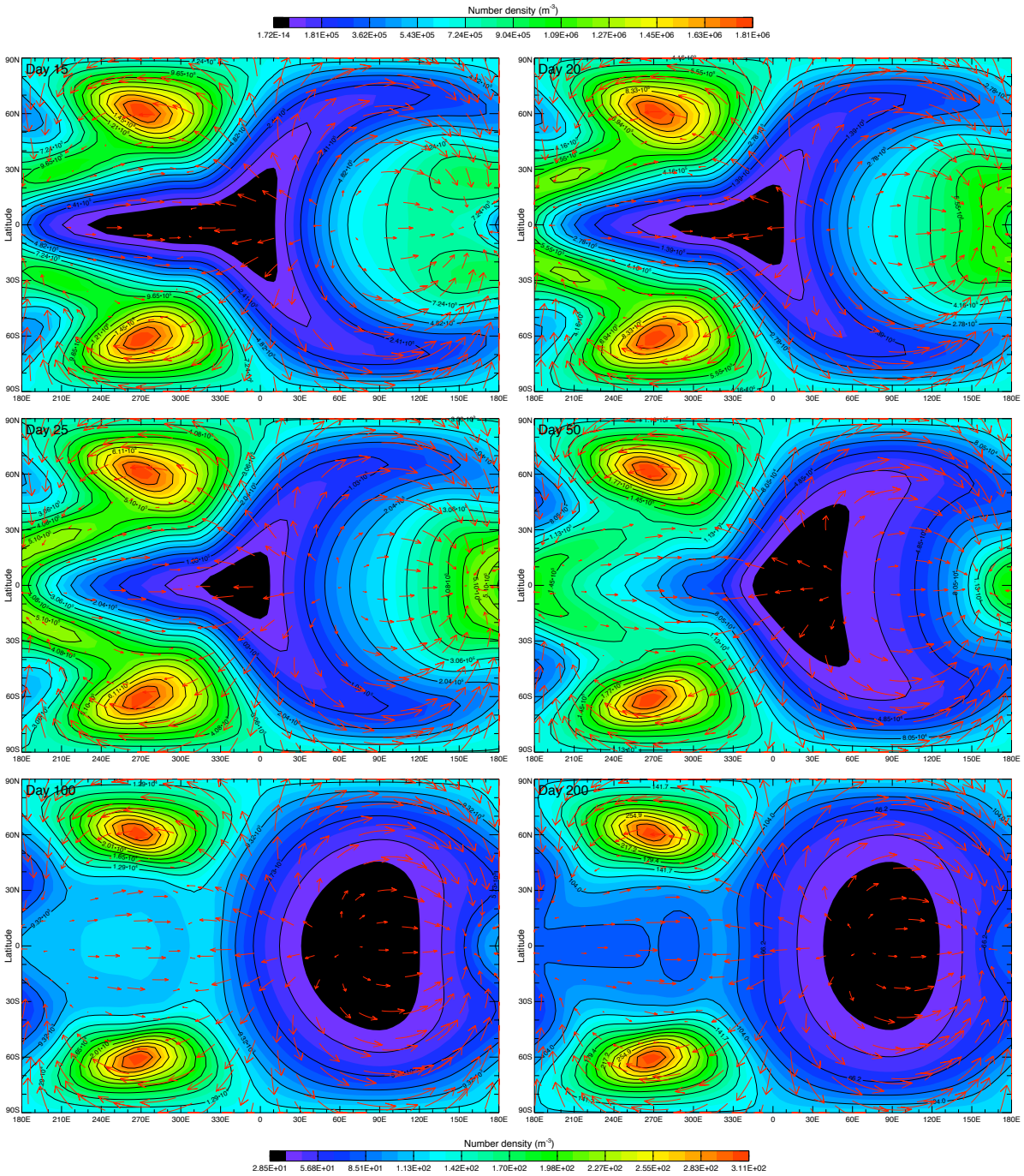

Figure 3.11: Tracer species number density fields at PL 25 (5.43×10^{-6} Pa), experiment 3, 4 amu, days 15, 20, 25, 50, 100 and 200 (top to bottom, left to right). Top and bottom colour scales represent day 15 and day 200 respectively.

prevents complete convergence (unlike the massless wind vectors), thus Figure 3.10 shows the tracer species flowing around the equatorial 2400-hrs region (e.g. day 5).

Next, by day 10 (bottom right contour plot of Figure 3.10), it is clear that the tracer species is beginning to converge to high latitude (approximately $\pm60°$ latitude) deep nightside regions in both

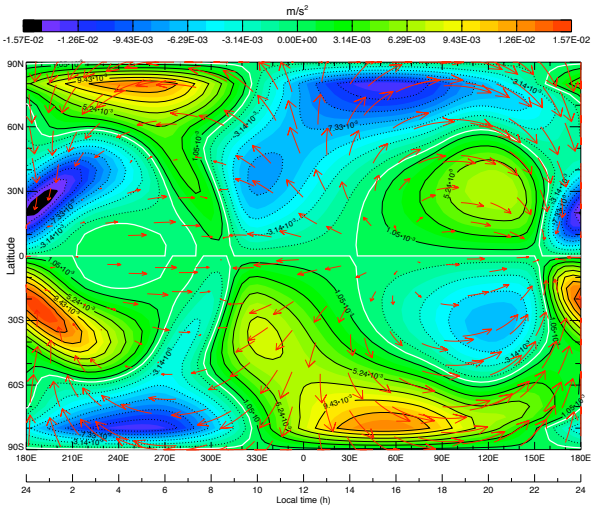

(a) Pressure gradient (m/s^2, $^+$ve is south), $\partial U/\partial\theta$, PL 25.

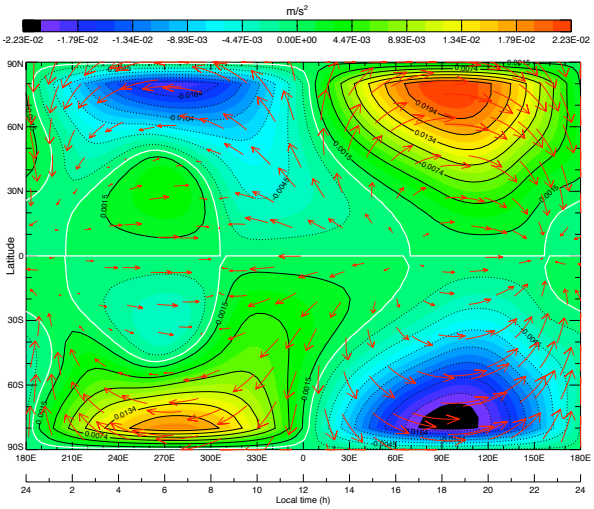

(b) Coriolis acceleration (m/s^2, $^+$ve is south), $2\Omega v_\phi \sin\theta$, PL 25.

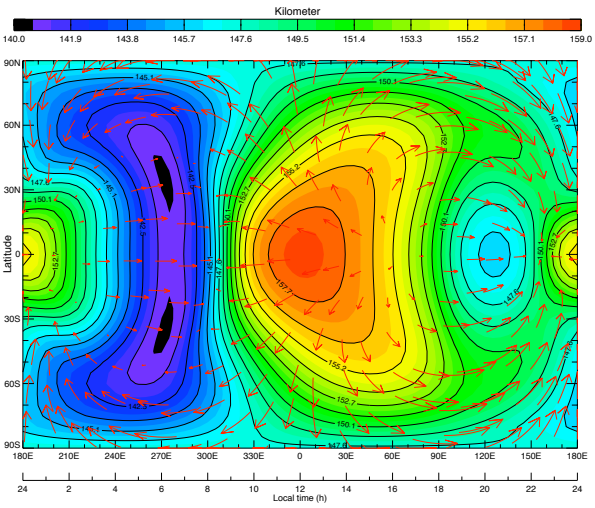

(c) Geopotential heights (km), PL 25.

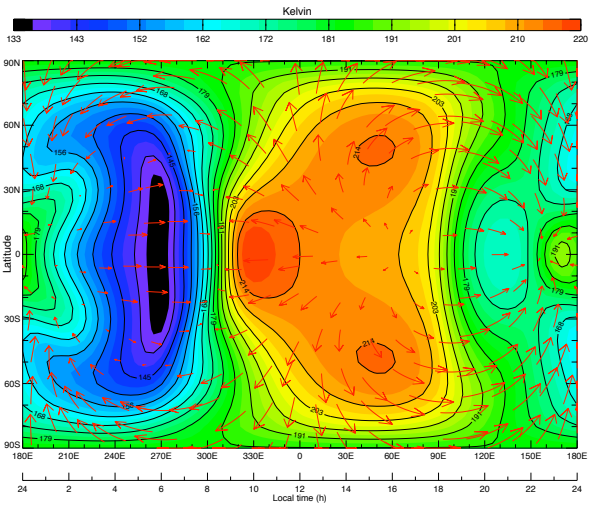

(d) Temperatures (K), PL 25.

Figure 3.12: Experiment 3, 4 amu, day 200 at PL 25 (5.43×10^{-6} Pa) for various output fields. Solid (dashed) contours indicate positive (negative) magnitudes. White contours indicates zero magnitudes.

hemispheres. Moreover, days 15 to 25 (top left and right and middle left contour plots of Figure 3.11) show how the flow from 180°E (2400-hrs) to 300°E (0800-hrs) is poleward from the equatorial regions to these convergence points (rather than equatorward as it had been in the afternoon). This links to that expansion at 2400-hrs described just above in Figure 3.12(c). The expansion leads to the pressure gradient acceleration shown in Figure 3.12(a) where shades of blue in the northern hemisphere from 2400-hrs to 0800-hrs are structured from the equator to ±60° latitude thereby driving the flow back towards the poles and away from the 2400-hrs expansion region. The tracer species flow shown in the contour plots of Figure 3.11 show this same structuring. This situation develops fully throughout the remaining period of the simulation so that by day 200 (bottom right contour plot of Figure 3.11) the majority of tracer species material has converged to these high latitude, nightside locations.

The transport of the tracer species in experiment 3 (4 amu) is very similar to that of atomic oxygen (16 amu) in the background atmosphere; both species preferentially transported by winds because of their relatively lighter mass versus the CO_2 dominant background atmosphere (McDunn et al., 2010). This can be seen from Figure 3.13 (top plot), which shows the steady state tracer species number mixing ratio from experiment 3 (Table 3.1) at PL 25. Then, the bottom plot of Figure 3.13 shows the steady state O number mixing ratio at PL 25 for both (left plot) the basic MarTIM simulation without any tracer species added (from section 3.3.2 earlier) and also (right plot) experiment 3 simulation (again,

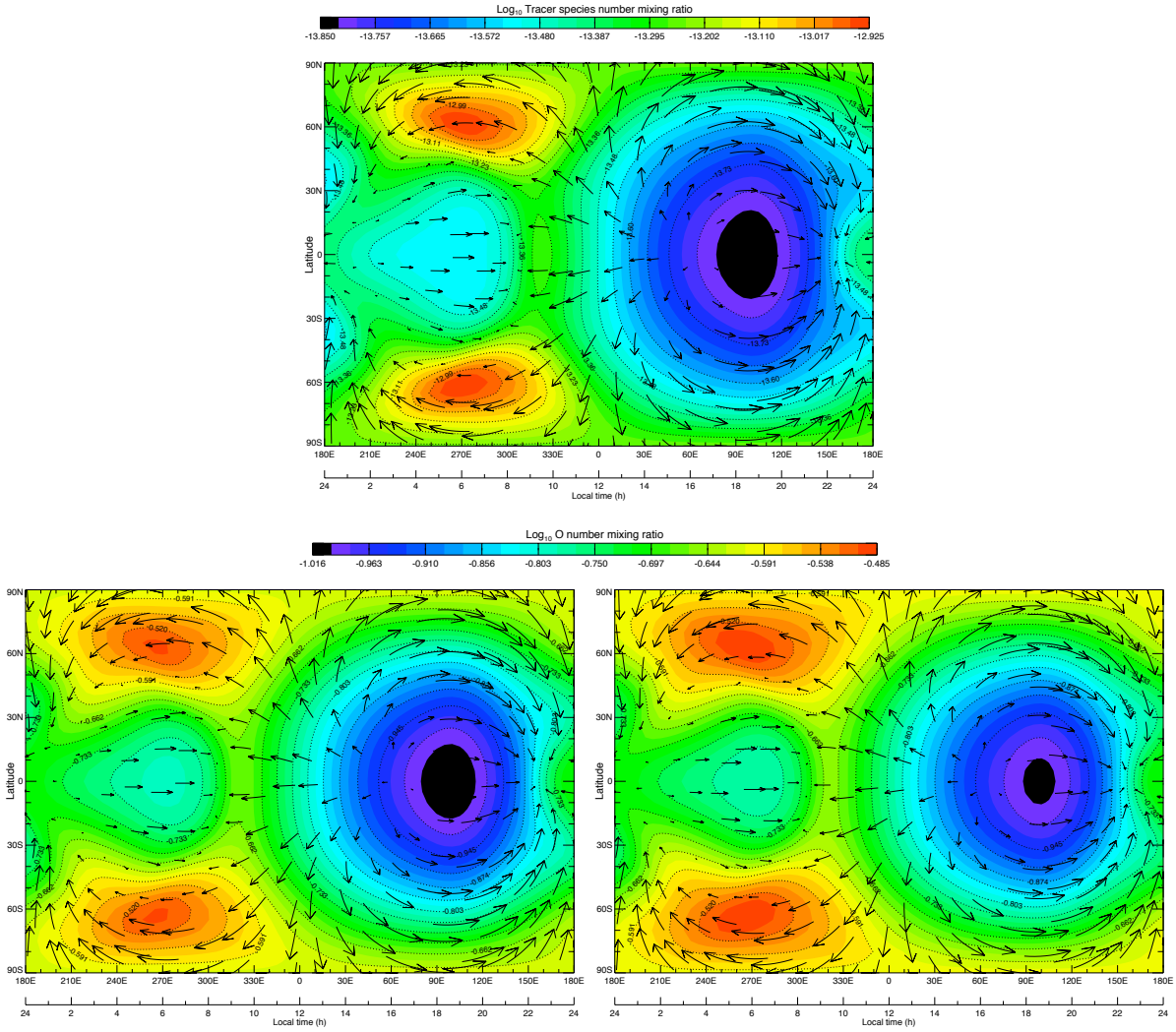

Figure 3.13: (Top) Tracer species number mixing ratio, PL 25 (5.43×10^{-6} Pa), experiment 3 (Table 3.1). (Bottom) Comparison of O mixing ratios at PL 25 (with coordinated colour scale shown), left column is the basic MarTIM result from section 3.3.2 earlier. Right column uses the results from experiment 3 of Table 3.1.

Table 3.1). Here we can see that both the tracer species and atomic oxygen have maximum number mixing ratios at high latitude, nightside locations. Meanwhile there is a large region centered over the equator (equinox conditions) on the dayside with very little presence from either of these two species.

From McDunn et al. (2010), thermospheric winds are known to transport O atoms from their dayside source region to the nightside and polar latitudes (Bougher et al., 1999b, 2000; Bertaux et al., 2005a), atomic oxygen being preferentially transported because of its lighter mass. Therefore the similarity in the steady state structure of atomic oxygen (16 amu) and the tracer species of experiment 3 (4 amu) shows the tracer species being transported in a manner we would expect.

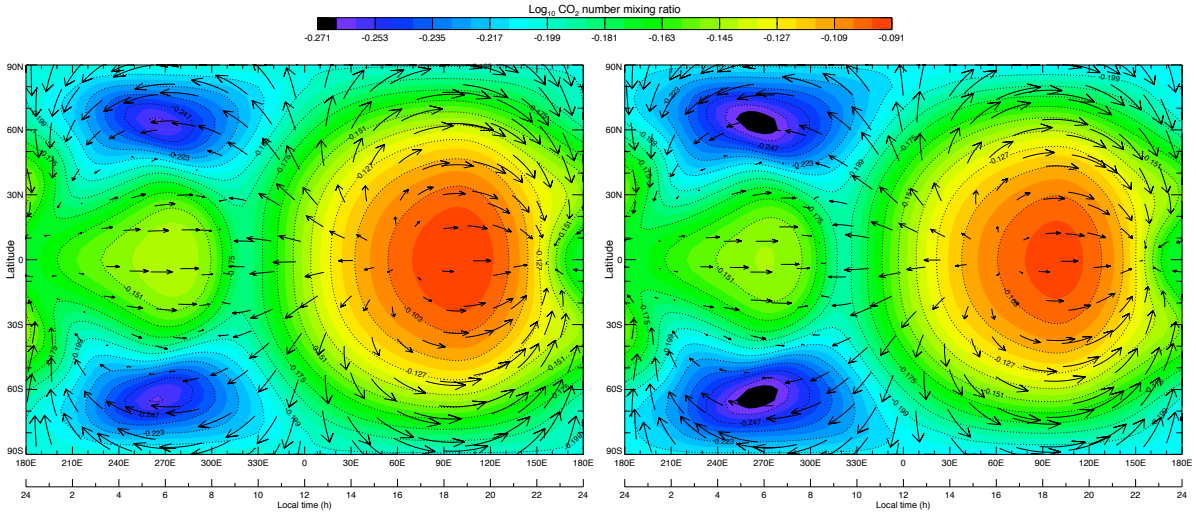

Figure 3.14: Comparison of CO_2 number mixing ratios at PL 25 (with coordinated colour scale shown), left column is the basic MarTIM result from section 3.3.2 earlier. Right column uses the results from experiment 3 of Table 3.1.

Regarding the heavier species, Figure 3.14 shows the steady state CO_2 number mixing ratio at PL 25 (5.43×10^{-6} Pa). As before the left plot shows the result for the basic MarTIM simulation without any tracer species added (section 3.3.2 earlier) while the right plot shows the result for experiment 3 (Table 3.1). Sure enough with the mixing ratio structure of CO_2 we essentially see the inverse of the situation for O and/or the tracer species. It has a maximum mixing ratio over the equator on the dayside with very little presence at high latitudes on the nightside. These points indicate that the background atmosphere both with (this section) and without (section 3.3.2) any tracer species added settle to the same equilibrium with lighter species advection from the dayside over to the nightside being favoured and resulting in heavier species remaining on the dayside in regions of large expansion and despite high wind magnitudes.

It is important to note the colour scales shown in Figures 3.10 and 3.11. These show that although over the course of the 200 day run the tracer species is being advected horizontally across the pressure level by circulation features (and so also influenced by the structure of the geopotential surface) there is also a change in the net amount of material on the pressure level itself. Thus there is a vertical diffusion and advection of material to other pressure levels at the same time as the horizontal advection. With respect to experiment 3 at pressure level 25; by the end of day 1 the number density (m^{-3}) has a maximum of $\sim1.43\times10^{9}$. This becomes $\sim5.31\times10^{6}$ by the end of day 10, then $\sim1.81\times10^{6}$ by the end of

day 15 and finally a maximum of $\sim 3.11 \times 10^2$ by the end of day 200.

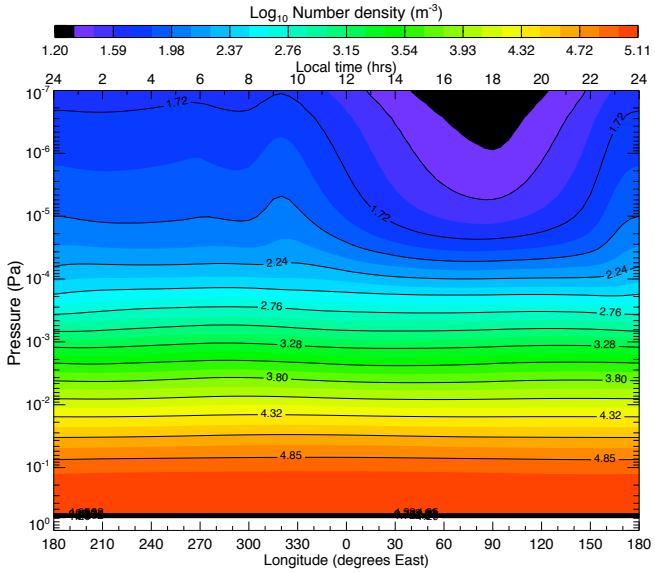

Figure 3.15: Tracer species number density fields ($\log_{10}$) at day 200 versus longitude (along the equator) for experiment 3 (4 amu).

The spread of material vertically is indicated by Figure 3.15 which shows a pressure level by longitudinal slice of tracer species number density along the equator for experiment 3 (4 amu) at day 200. The dearth of tracer species on the dayside at PL 25 (that we saw above in Figure 3.13) can be clearly seen as well as a buildup of material at 320°E about where eastward and westward winds converge (e.g. see red arrows overlaid on Figure 3.11, bottom right). Note how at lower pressure levels where solar energy input and thus winds magnitudes are less, e.g. below PL 18 (1.80×10^{-4} Pa), there is little variation in tracer species structure along the equator for any longitude. The slower wind magnitudes and reduced tracer species structure also relates to geopotential height gradients at these lower pressure levels that are far less than in the upper atmosphere. For example the geopotential height at PL 10 (not shown) ranges from a maximum of ∼91.2 km to a minimum of ∼89.7 km. Compare this ∼1.5 km range to the ∼19 km range at PL 25 (Figure 3.12(c)). The faster spread of material horizontally at upper pressure levels prior to the slower vertical diffusion and advection to the rest of the atmosphere therefore plays just as important a role in lower atmosphere mixing alongside the slower horizontal advection at those lower pressure levels. Vertical diffusion and advection is discussed further below.

The Influence of Molecular Mass on Advection and Diffusion

If we now compare the above description of experiment 3 (4 amu) to the results of experiment 1 (60 amu) and experiment 2 (40 amu), both of which were also introduced at pressure level 25, the effect of a heavier tracer species iterating in the same background environment can be studied. Figure 3.16 shows the number density iteration for days 10, 25, 50 and 200 for experiment 2 (40 amu). Then, Figure 3.17 shows exactly the same plots as Figure 3.16 but for experiment 1 (60 amu). Both of these figures are to

be compared with the equivalent contour plots from Figures 3.10 and 3.11 for experiment 3 (4 amu).

From both Figure 3.16 and 3.17 clearly heavier 40 amu and 60 amu molecular mass tracer species do not expand as far in latitude as did the lighter mass 4 amu species. The advection is now more generally zonal, eastwards maintained largely about the equator and downhill away from the expansion of the subsolar point on the dayside. Additionally it appears advection was a slower process for the 40 and 60 amu mass tracer species in that movement throughout PL 25, in both latitude and longitude, is far less than for the 4 amu species (consider the range over which expansion has occurred by day 10 for example). The advection of heavier tracer species appears to follow the minimum of geopotential height (Figure 3.12(c)) more closely than the lighter tracer species did i.e. the tracer species flow being directed toward lower altitudes by the pressure gradient to greater extent than being influenced by circulation structures. For example in the 40 amu case at day 200 (bottom right contour plot of Figure 3.16) most of the tracer species converges to the two geopotential height minimums at 260°E-270°E (∼0600-hrs), ±30° to ±40°. Tracer species number density structure also mimics the geopotential height minimum at

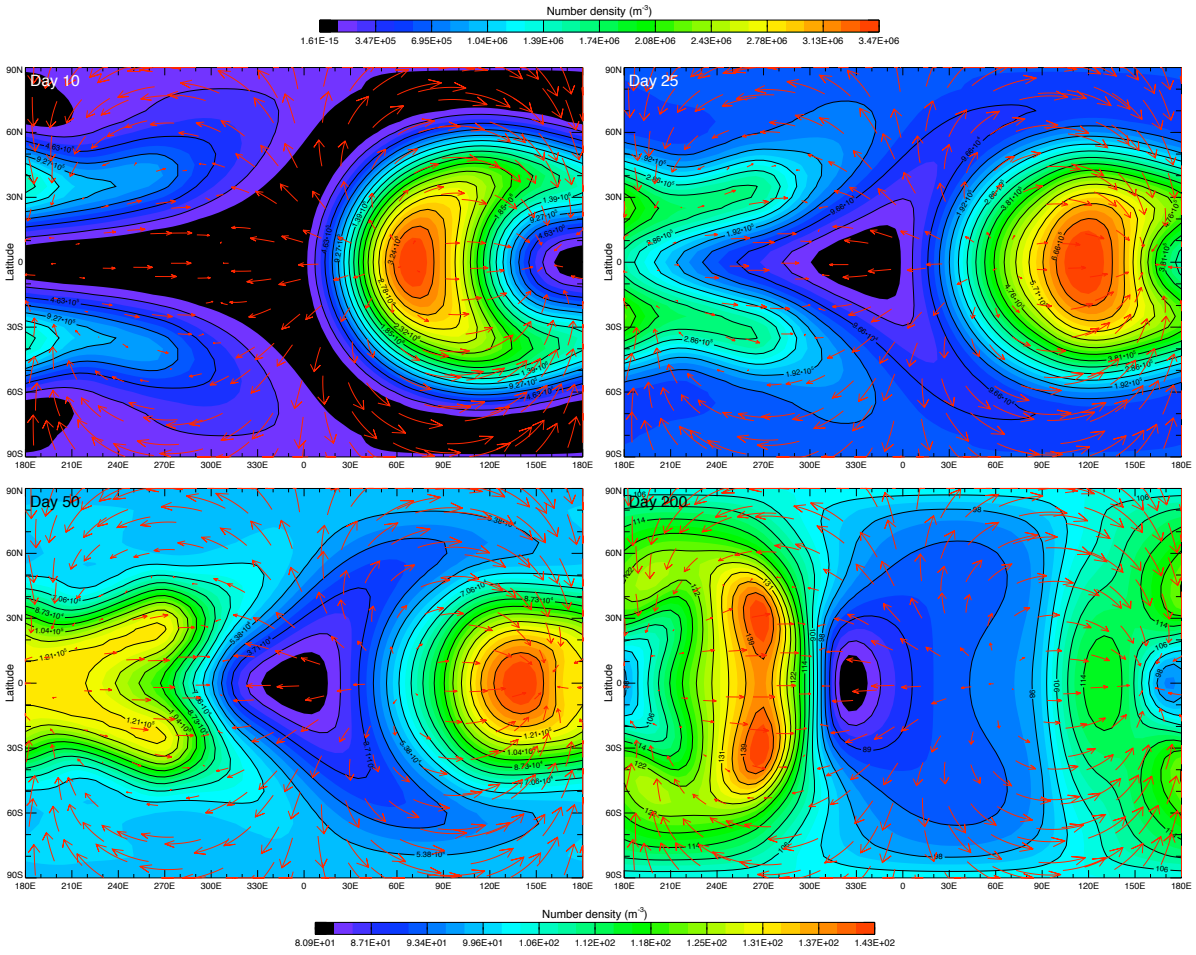

Figure 3.16: Tracer species number density fields at PL 25 (5.43×10^{-6} Pa), experiment 2, 40 amu, days 10, 25, 50 and 200 (top to bottom, left to right). Top and bottom colour scales represent day 10 and day 200 respectively.

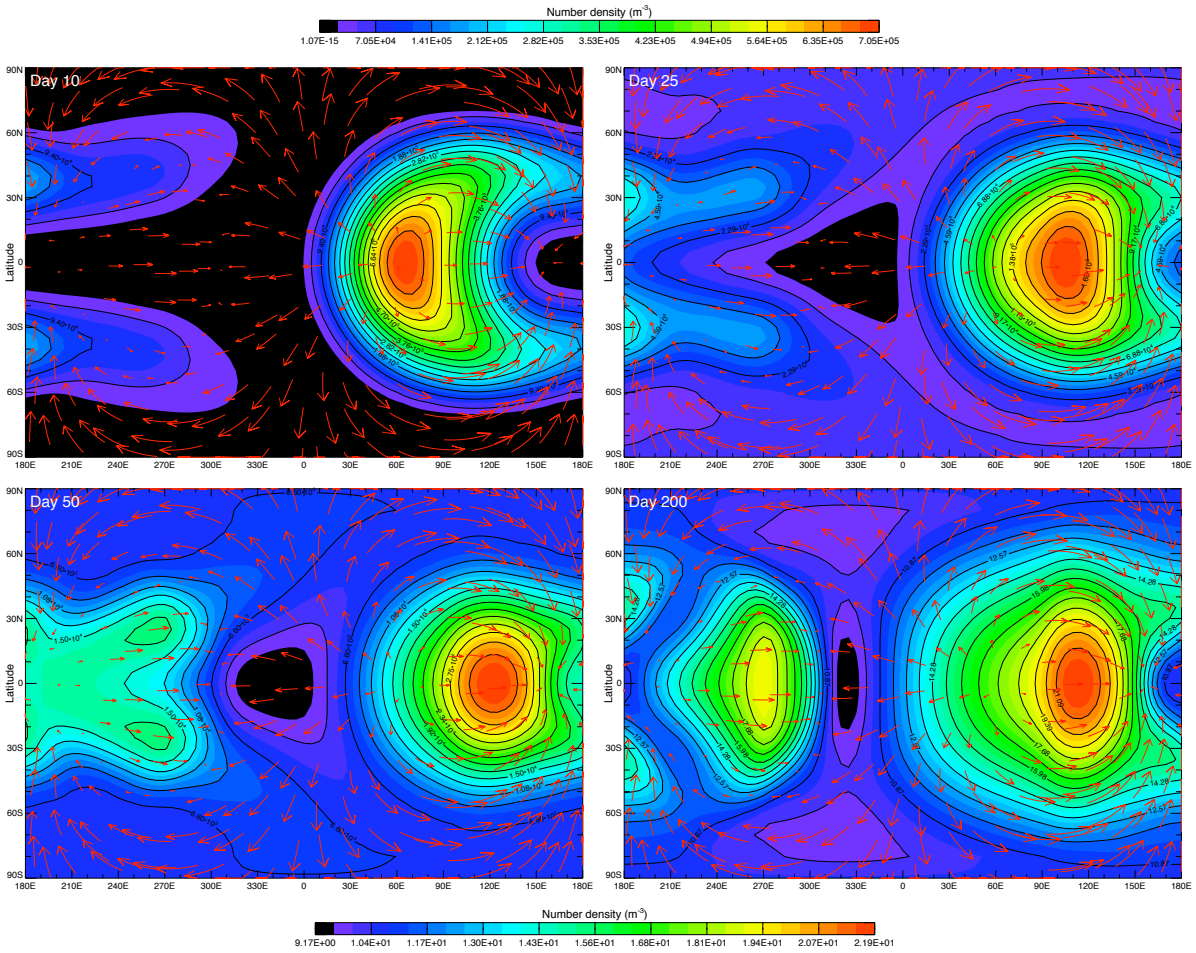

Figure 3.17: Tracer species number density fields at PL 25 (5.43×10^{-6} Pa), experiment 1, 60 amu, days 10, 25, 50 and 200 (top to bottom, left to right). Top and bottom colour scales represent day 10 and day 200 respectively.

120°E-130°E (2000-hrs) on the equator followed by a dearth of number density at 170°E to 180°E (2300-2400-hrs) occurring at the point of expansion at 180°E (2400-hrs) mentioned earlier due to the heating caused by the convergence of winds at 150°E (2200-hrs). There is also the number density presence at latitudes ±60° from 170°E to 300°E (2300-hrs to 0800-hrs), which also traces out the geopotential height minimum.

However, in the 60 amu case (experiment 1, Figure 3.17) and to lesser extent the 40 amu case (experiment 2, Figure 3.16), the colour scales show that the major mixing of heavier species occurs vertically between pressure levels rather than horizontally across pressure levels. For example the colour scale below Figure 3.17, representing day 200, shows that number density at PL 25 is at most $\sim2.2\times10^{1}$ m^{-3}. Compared to the $\sim10^{12}$ m^{-3} number density at PL 25 in the initial atmosphere this shows that the 60 amu tracer species has virtually disappeared from PL 25 by day 200. The vertical spread of the 60 and 40 amu tracer species by day 200 is shown in Figure 3.18. For comparison the result for CO_2 (44 amu) is also shown. Unlike the vertical spread of the 4 amu experiment 3 (see Figure 3.15) the heavier

species show a much reduced structure versus longitude, even at high altitude. So, whereas in Figure 3.15 there was a clear dearth in tracer species on the dayside in the upper atmosphere, in Figure 3.18 there seems to be only a slight build up of material throughout the dayside towards the evening terminator around 120°E, 2000-hrs (e.g. contours of number density cross upwards over constant pressure levels as you move from 320°E, 0900-hrs to 120°E, 2000-hrs). Then just after 2000-hrs there is a small drop in number density before a second increase toward 0900-hrs.

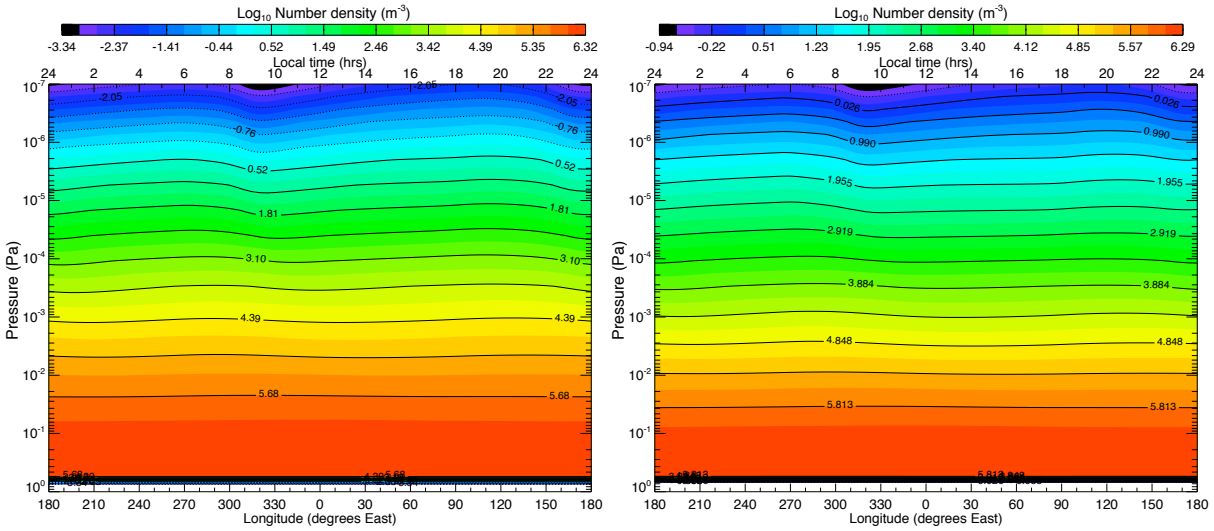

(a) Experiment 1, 60 amu, day 200.

(b) Experiment 2, 40 amu, day 200.

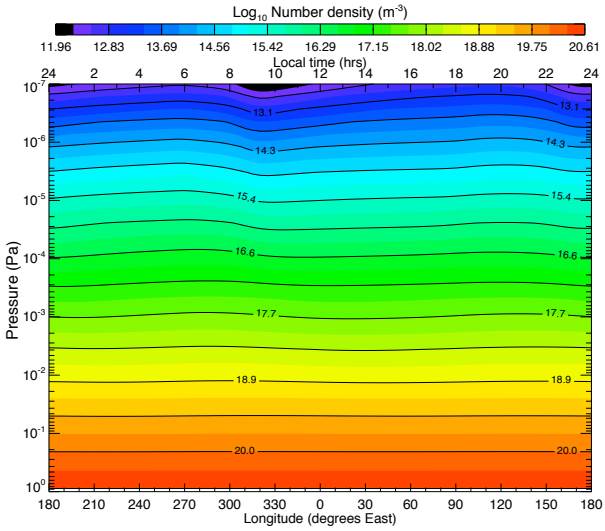

(c) Background atmosphere, CO_2 day 200.

Figure 3.18: Tracer species number density fields ($\log_{10}$) at day 200 versus longitude (along the equator) for experiment 1 (top left), 2 (top right) and CO_2 (bottom).

Again, the upper atmosphere variations in tracer species noted from Figure 3.18 are only very slight. This lack of structure with longitude reflects the much more prominent vertical mixing across pressure levels rather than horizontally along pressure levels. Note also how the tracer species number density

structure in the longitude by pressure level plots of Figure 3.18 is very similar to that of CO_2 in the background atmosphere (bottom plot). Thus, as noted earlier, while lighter mass species are preferentially advected, the heavier species remain in those areas where the lighter species have been removed.

Horizontal Advection of Tracer Species across Pressure Level 10 (9.81×10^{-3} Pa)

Regarding the horizontal advection of tracer species at pressure level 10 from experiments 4, 5 and 6, Figure 3.19 shows their number density distribution at the end of day 200. Then Figure 3.20 shows the background geopotential height and temperature of pressure level 10 and Figure 3.21 shows the background number density for the other four neutral species, also at PL 10. Experiments 5 and 6 (40 and 4 amu) show very similar number density structure (Figure 3.19(b) and 3.19(c)), with a prominent lack of material on the dayside equator versus a buildup at high latitudes on the nightside. From the wind arrows overlaid on these plots and also from the geopotential height structure shown in Figure 3.20(a) it is clear that the flow of tracer species here is created by pressure gradients and by horizontal winds driving material to these locations. For example the prominent lows in geopotential height between $\pm70°$ and $\pm85°$ latitudes deep on the nightside through to mid-morning (0300-hrs to 0900-hrs) are clearly situated in the same regions as the tracer species number density maximums just noted. And the dearth in tracer species on the dayside equator aligns well with the geopotential high between 30°E and 90°E, also over the equator.

For the heaviest tracer species from experiment 4 (60 amu, Figure 3.19(a)) it appears that tracer species material is principally situated over the nighttime in particular joining the two regions of minimum geopotential noted above between $\pm70°$ and $\pm85°$ latitudes and passing through the equatorial minimum at 300°E (0800-hrs, Figure 3.20(a)). Within this nighttime region of 60 amu tracer species there is a clear peak in number density over the equator at 300°E (0800-hrs). Then, also over the equator, there is a secondary, smaller peak in 60 amu number density at the geopotential minimum between 130°E and 150°E (2000-hrs and 2200-hrs). This material seems to have moved as small a distance as possible towards lows in geopotential height. This is to be expected since the wind speeds are very low at PL 10, or are at least generating very little advection at all for this heavy species. But in addition it is important to note that from the colour scale for Figure 3.19(a), we see there is less variation in 60 amu tracer species (less structure) across PL 10 compared with the lighter 40 and 4 amu species. This implies a greater, more uniformed vertical diffusion and advection of this heavy species away from PL 10 at all locations on the pressure level rather than the horizontal advection and structure across the pressure level shown by the lighter species.

Figure 3.21 shows the number densities of the background neutrals (CO_2, N_2, CO and O) at PL 10 and allows us to link the 60, 40 and 4 amu tracer species number density structures to the background atmosphere. This figure clearly shows that the 40 and 4 amu species have very similar structures to N_2 (28 amu), CO (28 amu) and O (16 amu). Thus N_2, CO and O have similar structures to one another. Several important trends can be identified, in particular: as the molecular mass increases, the prominence

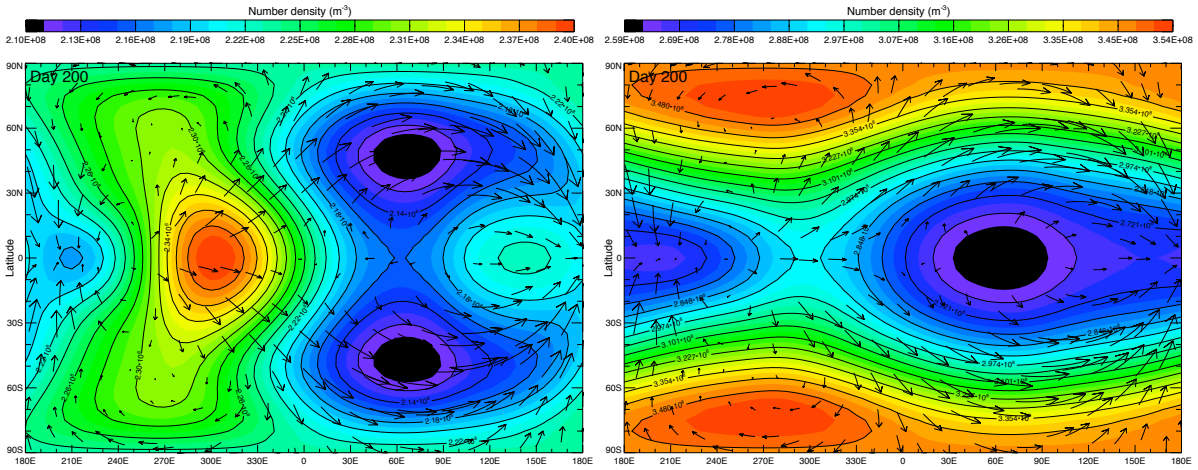

(a) Experiment 4, 60 amu, day 200, PL 10.

(b) Experiment 5, 40 amu, day 200, PL 10.

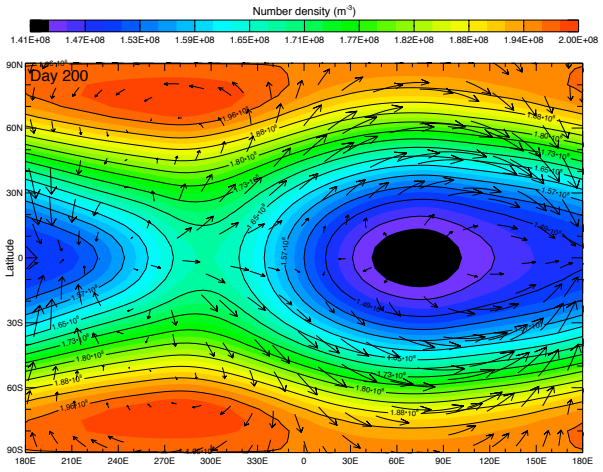

(c) Experiment 6, 4 amu, day 200, PL 10.

Figure 3.19: Tracer species number density fields at day 200 for (a) experiment 4 (60 amu), (b) experiment 5 (40 amu) and (c) experiment 6 (4 amu). PL 10 (9.81×10^{-3} Pa) throughout.

of material in regions of geopotential lows begins to increase. For example note the variation in material as molecular mass increases at (1) deep on the nightside between $\pm70°$ and $\pm85°$ latitudes, also (2) crossing over the equator at 300°E bridging the gap between these high latitude regions and finally (3) at the secondary geopotential minimum, between 130°E and 150°E (2000-hrs and 2200-hrs).

Looking back to Figure 3.19 the various tracer species experiments, especially 40 and 4 amu species, generally agree with this molecular mass trend in the horizontal transport of material. But then, from Figure 3.21(a), we can see how the heavier CO_2 background neutral (44 amu) shows a greater prominence deep on the nightside between $\pm70°$ and $\pm85°$ latitudes than the other (lighter) background neutrals do and in particular has progressed a little closer to the equator. Both structural features noted above. And in turn, the heaviest 60 amu tracer species from experiment 4 seems to be the extension of this trend; it now dominates at the equator at 300°E. But, as noted earlier, with horizontal advection beginning to play a progressively lesser role for the heavier the species there is also less variation between the

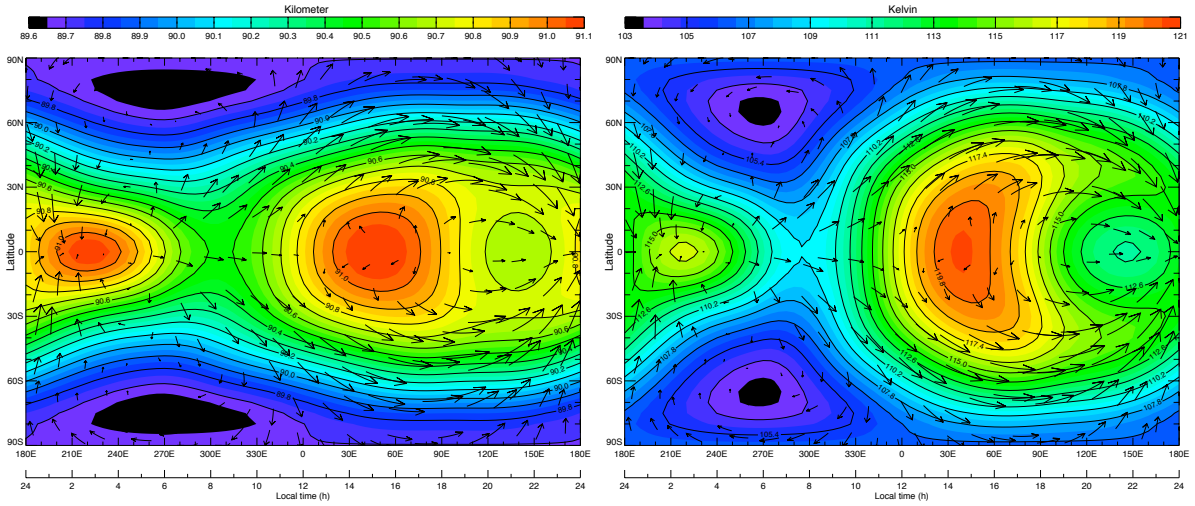

(a) Geopotential heights (km), PL 10.

(b) Temperatures (K), PL 10.

Figure 3.20: Background atmosphere (left plot) geopotential heights (km) and (right plot) temperatures. PL 10 (9.81×10^{-3} Pa) throughout.

maximum and minimum heavier species number density. So the horizontal structure, at PL 10 at least, is becoming less varied for the heavier species. Instead, vertical diffusion and advection at all points across the pressure level moves more and more of these heavy species away resulting in progressively less horizontal structure. Molecular mass determines whether either horizontal advection or vertical diffusion and advection take precedence in species transport.

Vertical Diffusion of Tracer Species

Finally, we consider how the tracer species are diffused and advected in the vertical direction. Referring again to the continuity equation for the mass fraction Y_i of the ith constituent:

$$\frac{\partial Y_i}{\partial t} + u_\theta \frac{1}{a}\frac{\partial Y_i}{\partial \theta} + u_\phi \frac{1}{asin\theta}\frac{\partial Y_i}{\partial \phi} + w\frac{\partial Y_i}{\partial P} = \frac{g}{a^2}\frac{\partial}{\partial P}\left(a^2 \rho Y_i (w_i^D + w_i^{K_\tau})\right) + J_i$$

We solve for both diffusion and advection in the vertical direction. Vertical advection is described by the fourth term on the left hand side while vertical diffusion is described by the first term on the right and side. For the ith constituent, w_i^D is the vertical diffusion velocity and $w_i^{K_\tau}$ is the vertical eddy diffusion velocity and we are solving for $\partial Y_i/\partial t$, the change in mass fraction with time.

Recall we ignored horizontal diffusion because of its relative importance to composition mixing compared to the role (magnitude) of horizontal winds. Horizontally, wind driven mixing was far more dominant than diffusion based mixing. This was because of the large number of molecules, moving chaotically through the atmosphere, meant collisions would dominate the overall rate of transport. Despite their fast molecular speeds ($\sim10^4$ cm/s at standard temperature and pressure) the very short mean free path between collisions meant the actual diffusion velocities were on the order of $\sim$1 cm/s (Marrero and Mason, 1972; Gombosi, 1994) i.e. much less than the typical horizontal wind velocity. In the vertical direction the same concerns apply, however since we assume hydrostatic equilibrium we expect vertical

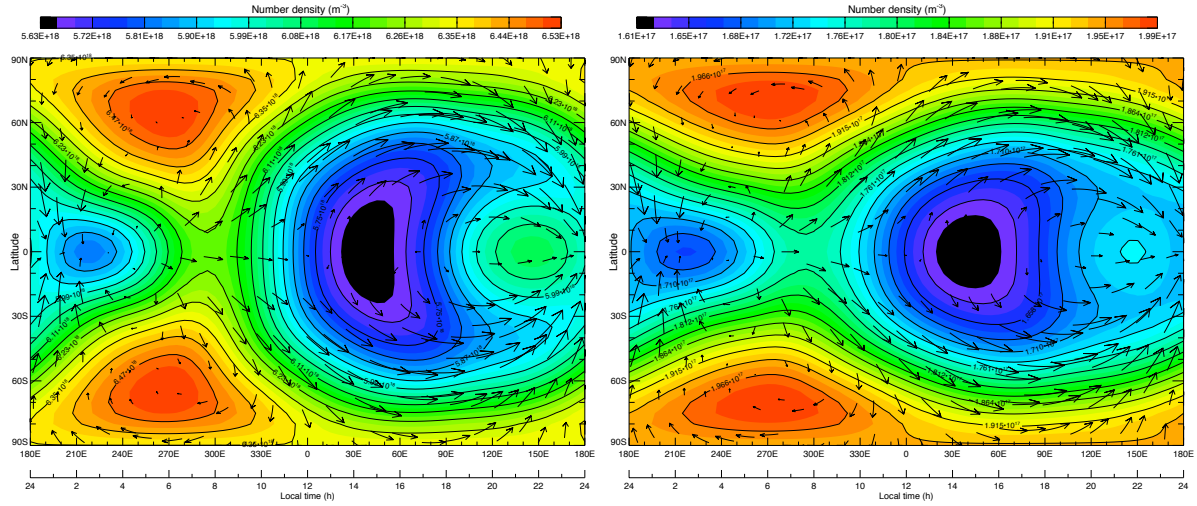

(a) CO_2 number density, PL 10.

(b) N_2 number density, PL 10.

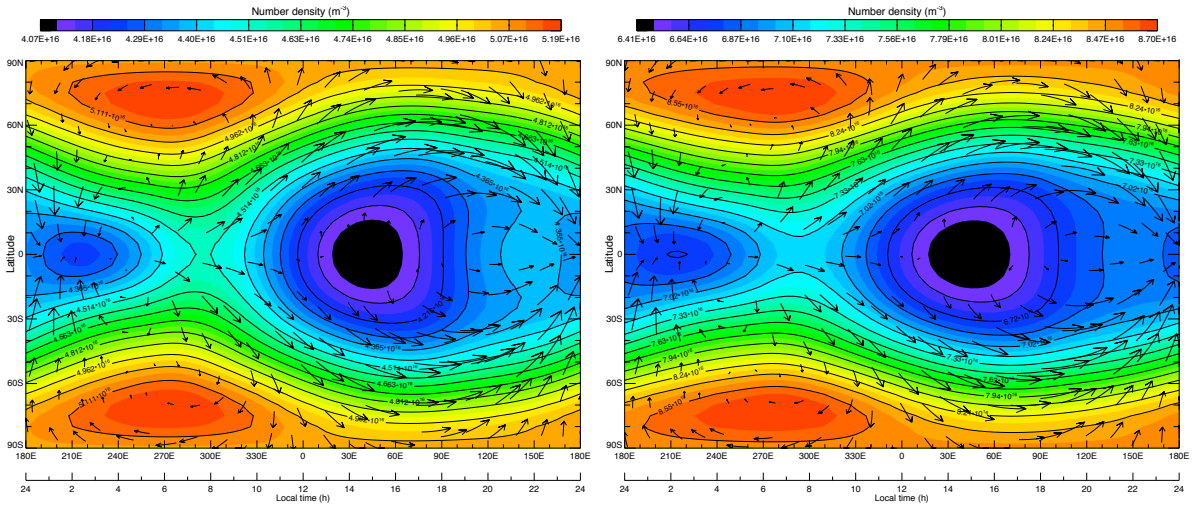

(c) CO number density, PL 10.

(d) O number density, PL 10.

Figure 3.21: Background atmosphere neutral species number densities. PL 10 (9.81×10^{-3} Pa) throughout.

wind speeds (advection) to be no more than a perturbation on this equilibrium. Therefore although vertical diffusion speeds may also be on the order ∼1 cm/s they are of relatively the same magnitude and importance as vertical advection. Thus both need to be considered.

Figure 3.22 shows global average vertical profiles of the number density fields (solid lines), at day 200, alongside a theoretical barometric distribution (dashed lines) using equation 3.6 (see also equation 1.7 from Chapter 1) taking the global average altitude at PL 5 as z_0.

$$n(z) = n(z_0)\frac{T(z_0)}{T(z)} exp\left[-\int_{z_0}^{z} dz'/H(z')\right] \tag{3.6}$$

This equation is simply the variation of number density with altitude discussed earlier in section 1.2.3, Chapter 1 derived by integrating the equation of hydrostatic equilibrium between some arbitrary reference altitude $z'=z_0$ and altitude $z'=z$. Then rearranging and substituting the equation of state (equation

1.3) we arrive at the theoretical vertical distribution of number density, equation 3.6. At and below the turbopause (PL 18), where turbulent mixing dominates, we use the mean molecular weight of the background atmosphere to calculate the scale height $H(z')$ in equation 3.6 whereas above we use the particular molecular mass of the tracers species in question. Pressure level 5 (1.20×10^{-1} Pa) was chosen as the base of this distribution because MarTIM's lower boundary tracer species number density will have been held at zero in all experiments (at all latitude/longitude locations, at all times). Thus it will take a few pressure levels for MarTIM to appropriately represent both the downward diffusing tracer species and the zeroed lower boundary. The curve to the tracer species density profiles (solid lines) between pressure levels 2 to 5 in Figure 3.22 reflects this.

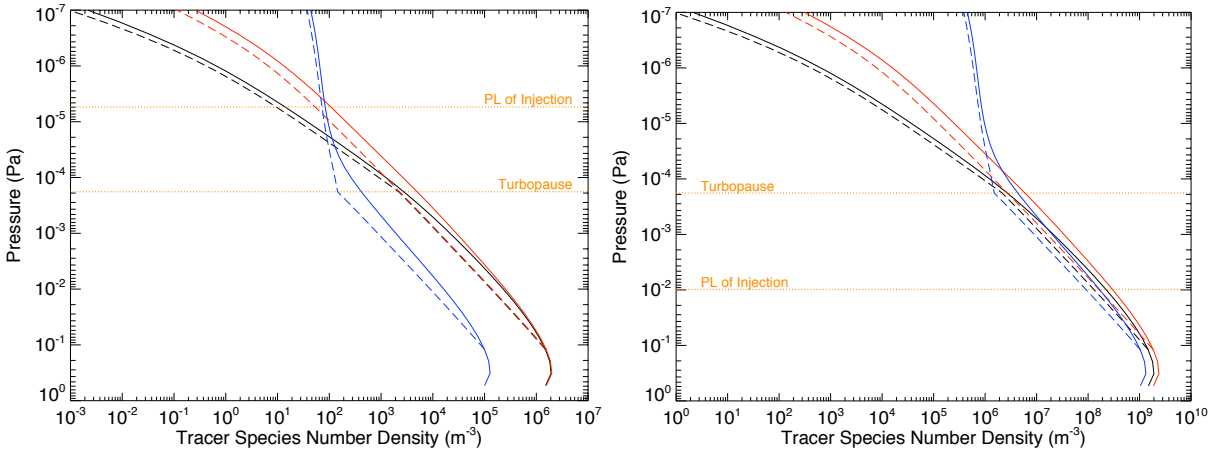

(a) Experiments 1 (black, 60 amu), 2 (red, 40 amu) and 3 (blue, 4 amu).

(b) Experiments 4 (black, 60 amu), 5 (red, 40 amu) and 6 (blue, 4 amu).

Figure 3.22: Number density (m^{-3}) profiles for each injected species at day 200 (solid lines) versus barometric distribution (dashed lines) using PL 5 (1.20×10^{-1} Pa) as a base.

Above PL 5 (1.20×10^{-1} Pa) one would expect MarTIM to be able to simulate tracer species diffusion and advection self-consistently. Bearing in mind we began all simulations with tracer species injected at a single point only the fact that after a 200 day simulation Figure 3.22 shows a good match between the barometric distribution theory (dashed lines) and the MarTIM result (solid lines) is encouraging. Note how the heavier 40 and 60 amu species number densities (red and black lines, respectively) drop continuously with altitude, both below and above the turbopause, while the lighter 4 amu species number density (blue lines) shows a marked decrease in profile gradient above the turbopause. Thus the exponential drop off in density from equation 3.6 reduces for the lighter molecular mass and larger scale height of the 4 amu species. Overall, we conclude that the new diffusion and advection routine can appropriately model the diffusion and advection of neutral species about MarTIM.

3.4.2 The Impact of Multiple Species Diffusion and Advection

Finally we consider whether adding the three extra neutral species (Ar, O_2 and NO) available from the input file actually alters the overall MarTIM simulation either by their individual or combined presence in the model. Additionally we also remove species N_2 and CO from the model and study how different a thermodynamic response this creates. Table 3.3 lists the various experiments to be compared and the neutral species included in the diffusion and advection routine for each. As discussed in section 3.3.1 the total number density of the initial atmosphere remains unchanged regardless of how many neutral species are used. This was because the temperature profile from the initial atmosphere dictates the total number density of the initial atmosphere through the ideal gas equation. Thus the mixing ratios of species already present will remain the same with respect to one another as more species are added. It is simply their individual number densities that will change and thus their proportion with respect to total number density.

Table 3.3: Experiments regarding the impact of multiple species diffusion and advection.

	Number of Species	Species Diffused & Advected
A	2	CO_2, O
B	3	CO_2, N_2, O
C	4	CO_2, N_2, CO, O
D	5	CO_2, N_2, CO, Ar, O
E	6	CO_2, N_2, CO, Ar, O_2, O
F	7	CO_2, N_2, CO, Ar, O_2, NO, O

Figure 3.23 shows the upper atmosphere (pressure level 30, global average altitude ∼188 km) temperature and wind structures for each of the experiments of Table 3.3. Note that part (C) of this figure is identical to the standard base run as already discussed in section 3.3.2. Clearly from Figure 3.23 the most significant difference in the temperature structures comes in the change between when only 2 species (CO_2 and O, experiment (A)) are used versus when 4 or more species are used (CO_2, N_2, CO and O, experiment (C) onwards). Conversely, one can see there is very little difference between the simulations when 4 (C) through 7 (F) species are included.

Differences in temperature structure are mainly associated with the development and prominence of the temperature bifurcation on the dayside (∼60°E) alongside the growing importance of the hot region at ∼330°E. From section 3.3.2 the dayside bifurcation was created by the effect of column integrated IR heating upwards of pressure level 14 that introduced adiabatic expansion and cooling about the equator (equinox conditions) throughout the afternoon. This divided the region of solar EUV/UV heating leaving the localised temperature peaks seen in Figure 3.23. The equatorial hot region at ∼330°E was generated by the convergence of westward and eastward equatorial flows that dump energy near 300°E and introduce

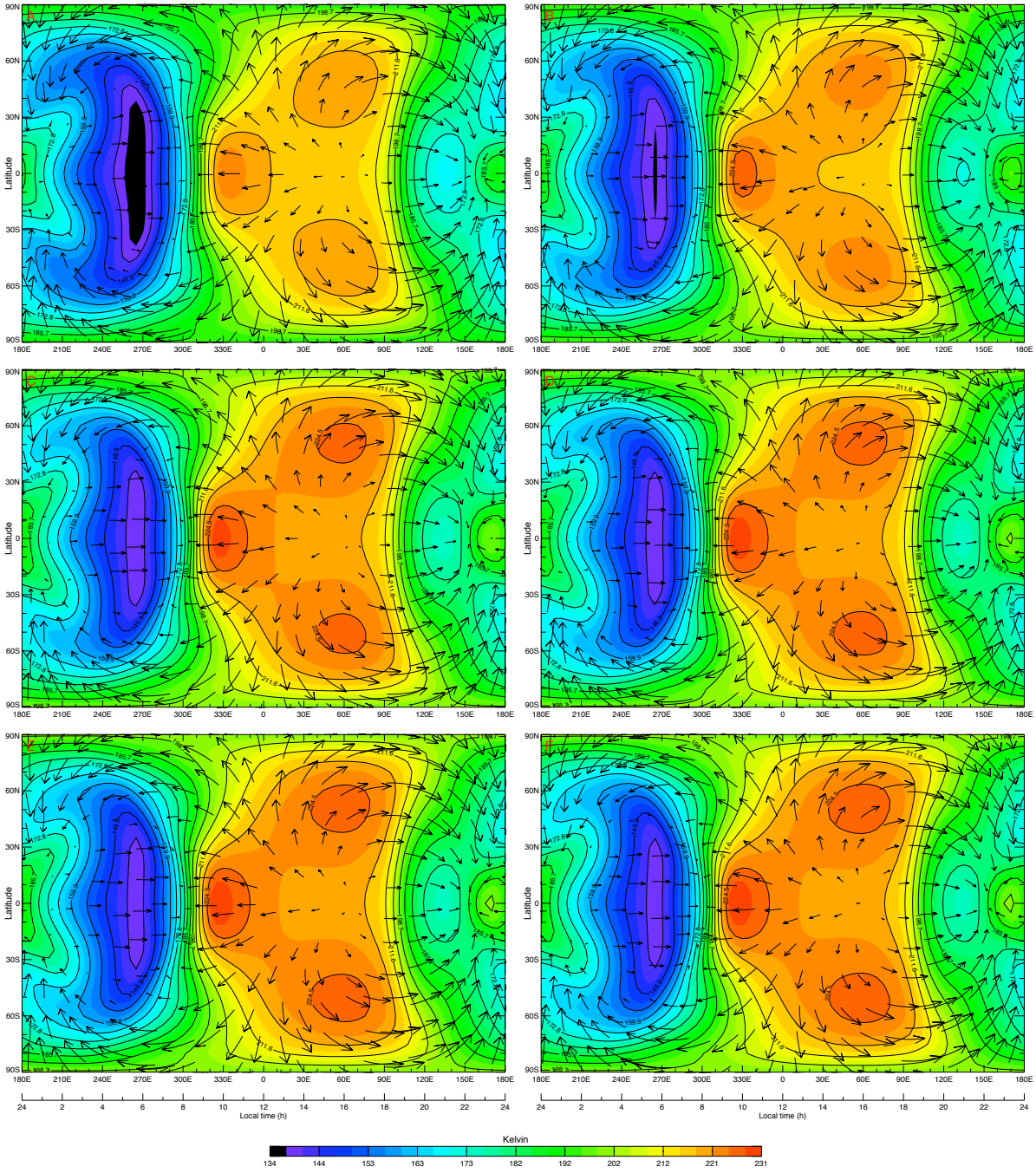

Figure 3.23: MarTIM base run steady state result: day 15, PL 30 (4.45×10^{-7} Pa, ~188 km) temperatures for standard MarTIM base run with (a) 2 species, (b) 3 species, (c) 4 species, (d) 5 species, (e) 6 species and (f) 7 species. Colour scales coordinated against colour bar shown.

a temperature rise a few hours later. The other difference between the 2 and 4 species versions is the minimum temperature region deep on the nightside (0300-hrs to 0700-hrs). This is as low as 134 K with CO_2 and O present (experiment (A)) but is hotter (~139-140 K) with CO_2, N_2, CO and O present (experiment (C)). This reflects a greater amount of energy being transferred from the dayside to heat these nightside regions.

To consider why these results come about Figure 3.24 shows the global average energy balance terms for the 2 and 4 species simulations, i.e. the two results that showed the largest difference in temperature (magnitude and structure) in Figure 3.23. The corresponding global average temperatures are also displayed in Figure 3.24 (solid black line overlaid with symbols). Here we see that the only real difference is in the upper atmosphere where the maximum temperature is ∼192.2 K for the 4 species simulation versus ∼186.7 K for the 2 species result. In the lower half of the atmosphere, up to about 150 km, the energy balance terms all appear to be very similar to one another in the 2 and 4 species results, despite the addition of N_2 and CO. The blue solid line in particular, for CO_2 radiative cooling, is the same for both plots thereby reflecting a similarity in the O to CO_2 ratio. As noted in section 3.2.4, the rate of CO_2 15-μm cooling depends upon the ratio of O to CO_2. In adding N_2 and CO for the 4 species run the volume mixing ratios of both CO_2 and O are reduced by equal amounts. This is because in the initial atmosphere the total number density remains the same (set with the ideal gas law) and so to accommodate N_2 and CO both CO_2 and O number densities are reduced by equal amounts. Since both CO_2 and O volume mixing ratios have changed with respect to the total number density, but their ratio to one another remains the same, CO_2 cooling will largely also be the same, as Figure 3.24 shows. The dominance of CO_2 (in terms of number density) and its relationship to O (in terms of 15-μm radiative cooling) continues to control this region despite the additional species.

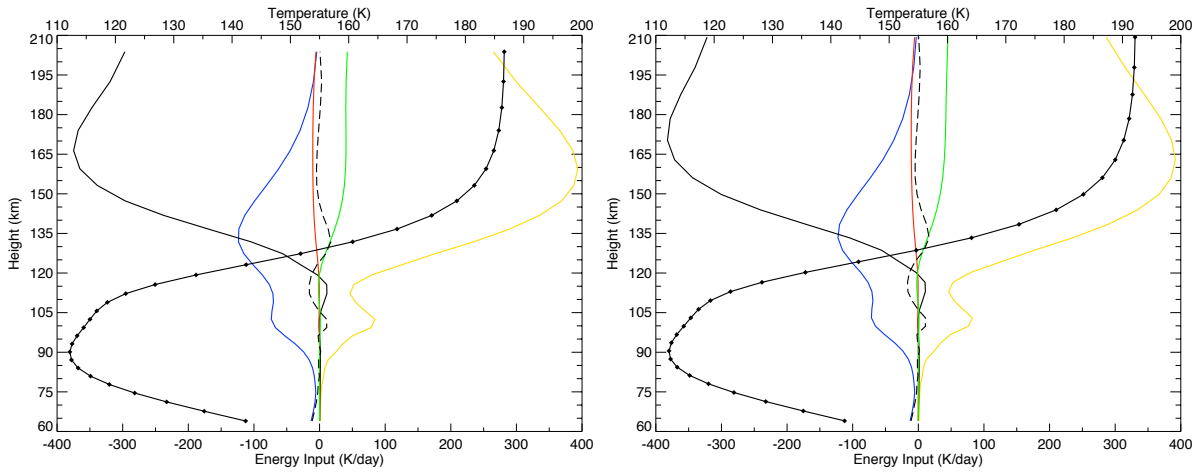

(a) 2 Species (CO_2 and O).

(b) 4 Species (CO_2, N_2, CO and O).

Figure 3.24: Global average temperatures and energy balance terms for MarTIM base run with (left plot) 2 species and (right plot) 4 species. Temperatures (black line with diamond symbols), total solar heating (EUV + IR) (solid yellow line), IR 15-μm cooling (solid blue line), thermal conduction (solid black line), adiabatic term (solid red), horizontal advection of total energy (solid green line) and net energy input (dashed black line).

The difference in upper atmosphere temperatures in Figure 3.24, above ∼150 km, can be seen to come through the total solar EUV+IR heating term (solid yellow line). While both 2 and 4 species results show a maximum of ∼395 K/day, the 4 species run shows a slower decrease in this heating rate with

altitude so that the cumulative solar heating added is greater. The upper atmosphere will be affected the most by both N_2 and CO being added because this is where gravitational fractionation will allow these two species to become relatively more dominant in the composition versus CO_2. Then since both of these species play a heating role within the atmosphere (i.e. they both have photoabsorption cross sections that respond at EUV/UV wavelengths) this will add to the solar heating term, as Figure 3.24 shows.

Beyond these two extra species the addition of Ar, O_2 and NO remains negligible. There are no differences in temperature structure or magnitude in Figure 3.23 and none of these three species has either a great enough number density or sufficient absorption of solar radiation to be able to be usefully included in the simulation. We conclude that using the 4 species CO_2, N_2, CO and O gives the best response and add that this includes a real difference in temperature structure and magnitude shown by the 3 species, CO_2, N_2, O, used in Moffat (2005).

3.5 Conclusions

From the work of this chapter we draw the following conclusions:

- General model improvements and updates to input datasets (versus previous versions) have been introduced. These include (1) an update to the solar XUV/EUV/UV flux model that is used to provide the solar irradiances (see section 3.2.1), (2) an update to the photoabsorption cross sections used in calculating the atmospheric heating rate (see section 3.2.2) and (3) a correction to the initial atmosphere O content that allows a value for the CO_2-O relaxation rate much closer to the values typically cited in the background research to be used (see section 3.2.4).

- In section 3.4 a new neutral diffusion and advection subroutine was introduced. This self-consistently determines the composition of an atmosphere composed of any number of neutral species. First, section 3.4.1 tested the physical consistency of this subroutine by following a tracer neutral species and considering the variation in composition that resulted as it moved through the model. The advection and diffusion of the tracer species produced number density structures, which when compared with the four background neutral species highlighted the role molecular mass plays in determining whether horizontal advection or vertical diffusion dominates.

- Finally in section 3.4.2 we used the new diffusion and advection subroutine to justify why including the mutual diffusion of the four neutral species CO_2, N_2, CO and O is an appropriate selection for capturing the bulk properties of the Martian atmosphere. Adding three extra neutral species (Ar, O_2 and NO) had little effect on the final result (temperatures, wind speeds, etc, see Figure 3.23).

Next, in Chapter 4, we introduce a new IR heating parameterisation into the model and show that this allows MarTIM to simulate temperatures that compare better against Mars Odyssey accelerometer results (Keating et al., 2003; Withers, 2006) than with the old parameterisation.

Chapter 4

The new Near-IR Heating Parameterisation

4.1 Introduction

Following the development of MarTIM reviewed in Chapter 3 leading to the standard base run discussed in section 3.3.2 we now change the basic setup by introducing a new infrared heating parameterisation. We consider the differences introduced by and the advantages of this new parameterisation and the new phenomena that MarTIM can now reproduce. In particular we use MarTIM to simulate thermospheric polar warming features in the winter polar regions during the solstices. These simulations are then compared with Mars Odyssey observations of the same phenomena. Finally we also compare MarTIM to 6 years worth of exospheric temperature measurements from the Mars Global Surveyor spacecraft over a wide range of solar and seasonal conditions.

4.2 The New Infrared Heating Parameteristion

4.2.1 Background

The new infrared heating parameterisation comes from equations 1 and 2 of González-Galindo et al. (2009b), which was itself an updated form of the method described in Forget et al. (1999). This new parameterisation is shown below in equations 4.1 and 4.2. Firstly the heating rate per Martian day at pressure P_0=700 Pa and for a mean Mars-to-Sun distance of r_0=1.52 AU is stated to be:

$$\frac{\partial T}{\partial t}(P_0, r_0, 0) = 1.1956 \text{ K/day} \tag{4.1}$$

for zero solar zenith angle (μ=0). Then the heating rate at some other pressure P, Mars-to-Sun distance r and solar zenith angle μ is calculated with:

$$\frac{\partial T}{\partial t}(P, r, \mu) = \frac{\partial T}{\partial t}(P_0, r_0, 0) \times \frac{r_0^2}{r^2} \sqrt{\frac{P_0}{P}\tilde{\mu}} \left(1 + \frac{P_1}{P}\right)^{-b} \tag{4.2}$$

where P_1=0.0015889 Pa, b=1.9628 and $\tilde{\mu}$ is the cosine of the solar zenith angle corrected for atmospheric refraction (González-Galindo et al. (2009b) use $\tilde{\mu}$=$[(1224\mu^2 + 1)/1225]^{1/2}$).

The comparison of this new parameterisation on the IR heating vertical profile within MarTIM is shown in Figure 4.1 for SMED solstice and equinox conditions. With the new IR heating parameterisation the peak heating (overhead, μ=0) occurs around pressure levels 11 (5.95×10^{-3} Pa) and 12 (3.61×10^{-3} Pa) with magnitudes 216.6, 276.7 and 308.7 K/day for solar longitudes 90° (northern summer solstice), 180° (equinox) and 270° (southern summer solstice) respectively. This is as compared to the old parameterisation which showed negligible variation with season/Mars-to-Sun distance maintaining a peak at pressure level 14 (1.33×10^{-3} Pa) with magnitude 287.5 K/day.

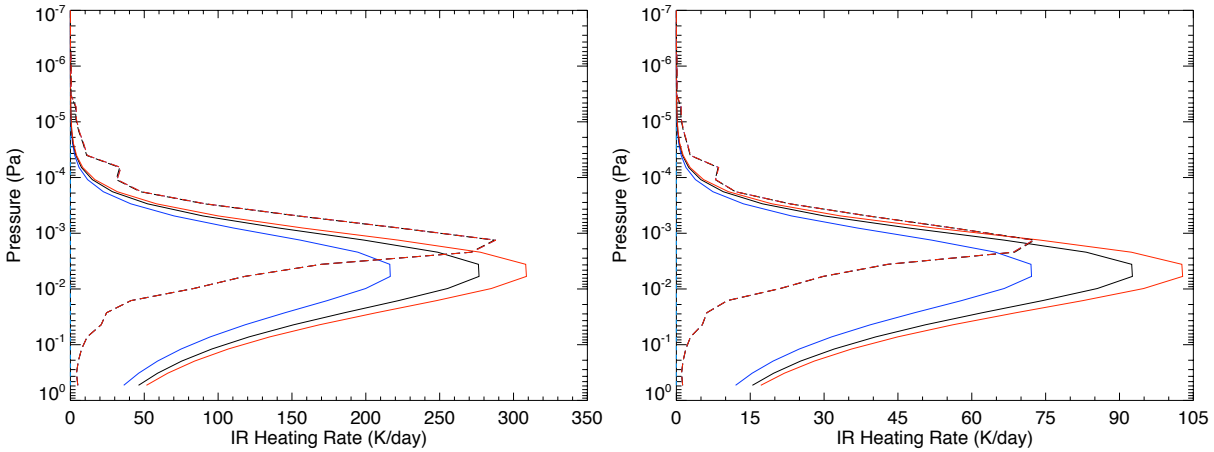

(a) Solar zenith angle 0°

(b) Global average

Figure 4.1: IR heating rate profiles for SMED conditions at Ls 90° (1.657 AU, blue lines), Ls 180° (1.466 AU, black lines) and Ls 270° (1.388 AU, red lines). Solid lines are the new profiles from the González-Galindo et al. (2009b) parameterisation, dashed lines are the old profiles from Moffat (2005) (and used in Chapter 3).

A plot of variation in heating with the advance of the solar cycle is not shown because the pressure level at which the peak IR heating rate occurs and also the magnitude of that peak, with the new parameterisation, does not change with the solar cycle. The magnitude of the peak doesn't change because the IR output from the Sun remains fairly constant from SMIN through to SMAX (as Figure 3.1 showed). Indeed as Bougher et al. (1990) and Bougher et al. (2000) discussed, changes in solar fluxes had little impact on the altitude of the homopause (the 1.26 nbar pressure level, ~125 km, from Mariner and Viking measurements) because the lower atmosphere up to this pressure level is mainly driven by solar near-infrared heating. Also, from the original López-Valverde et al. (1998) near-IR heating study,

detailed calculations of the solar heating rate using a full non-LTE model showed a weak dependence on the temperature and composition of the atmosphere for a range of background atmospheres (and thus solar & season conditions) used in that study (González-Galindo et al., 2009b). So even though the atmosphere is more expanded for SMAX compared to SMIN conditions such changes are more prominent in the EUV and UV regime and thus at higher altitudes such as in the thermosphere. There would be little more than a 1.5 km variation in the altitude of the peak IR heating rate as the solar cycle advances.

The difference between the old and new sets of IR heating profiles is significant both in their form and effect. Regarding their form, the new heating profile does not rely upon any input data sets such as the photoabsorption coefficients used by Moffat (2005) to calculate the rate at which CO_2 molecules are excited (see equation 2.36, Chapter 2). Moffat (2005) could only rely upon the single set of profiles shown by Figure 2.4 and the particular atmospheric conditions they represented. With the new parameterisation, a complete range of solar cycle and seasonal IR heating responses have been parameterised directly from the detailed model of López-Valverde et al. (1998) and the range of neutral atmospheres they considered. These will therefore already include heating rate variation with heliocentric distance, solar zenith angle, pressure etc, and will result in a more physically consistent parameterisation.

The most important difference between the form of the old and new IR heating profiles is that the new parameterisation has quite a broad peak and thus contributes a significantly greater energy input throughout the lower ∼10 pressure levels than the old IR heating profile. The input of the old profile decreases rapidly below its peak (pressure level 14, 1.33×10^{-3} Pa) and provides minimal input below pressure level 10 (9.81×10^{-3} Pa). Consequently the new profile will contribute a much greater column integrated IR heating input, which from Section 3.3.2 of Chapter 3 we already know can have a significant effect on upper pressure level temperature and wind structures. Thus with such a marked change in this heating input we expect significant changes throughout most of the modelled atmosphere.

4.2.2 Effect of new IR heating parameterisation

Latitudinal Temperature and IR Balance Structures

To consider the effect of the new IR heating profile we first consider in Figure 4.2 vertical slices along the equator for SMIN, equinox conditions of the IR radiative balance (again, the sum of IR heating and CO_2 15-μm cooling), the temperature structure and finally the O to CO_2 ratio. The left hand figures use the old IR parameterisation while the right hand figures use the new. For this first comparison all simulations (regardless of the IR parameterisation being used) use the same parameters for the V-T_{CO_2-O} coefficient (1.5×10^{-12} cm^3s^{-1}), the EUV heating efficiency (22%) and the eddy diffusion coefficient (1500 m^2s^{-1}) (as per the setup described in Chapter 3).

Comparing the top row of Figure 4.2 you can see the extent to which the new IR heating profile changes the IR radiative balance throughout the lowest MarTIM pressure levels. While the peak positive IR energy input seems to extend over a slightly larger range of local times when the old IR heating profile is used (0900-hrs to 1200-hrs, top left, Figure 4.2) this is still very much focused on the narrow region

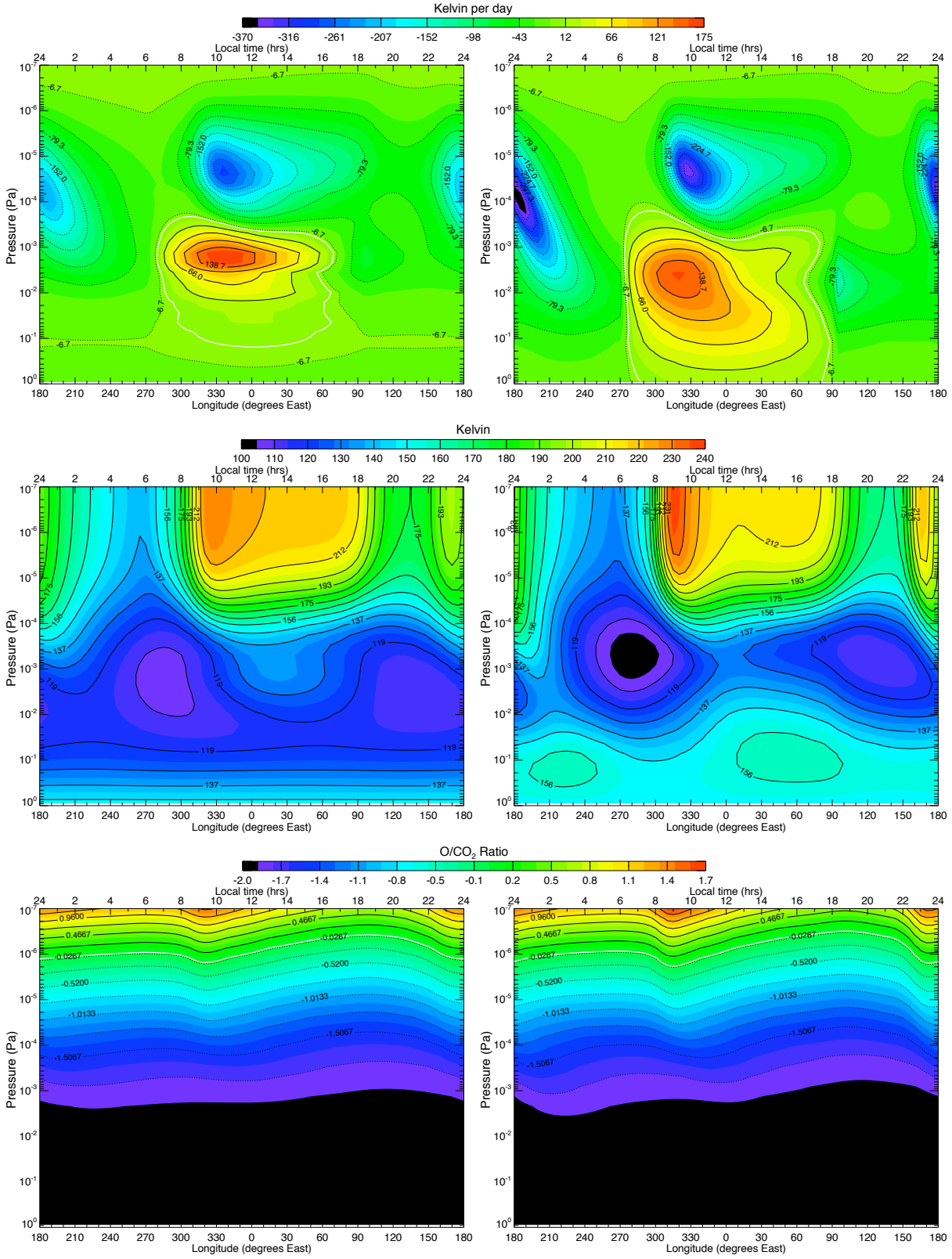

Figure 4.2: Equatorial slice for SMIN, equinox conditions for IR radiative balance (top row) temperatures (middle row) and $\log_{10}$ of the O to CO_2 ratio (bottom row). Left column uses old IR heating profile, right column uses new. Colour scales are coordinated across each row.

between pressure levels 13 through 16 (2.19×10^{-3} to 4.88×10^{-4} Pa). Using the new IR heating profile however (top right, Figure 4.2) the net positive energy input is clearly spread over a much broader region of pressure levels in the lowest parts of the model, as noted earlier. Moreover, in terms of the spread across local times, the positive IR energy input is now significantly enhanced with the new profile versus the old throughout virtually the entire dayside.

This energy input generates a significant heating of the lower atmosphere (middle right, Figure 4.2) that shows a peak of ∼156 K between 1300-hrs and 1900-hrs from PL 3 to 7 (3.25×10^{-1} to 4.40×10^{-2} Pa) with a similar temperature peak also now appearing in the early morning around 0300-hrs over the same pressure levels. On the dayside the temperature peak is created directly by the solar IR input, dominating the afternoon atmosphere. Note how the presence of this temperature structure tends to shift the peak positive IR radiative input to the morning at around 0900-hrs, rather than, say, the 1200-hrs overhead position. Thus with the increase in temperature that the new IR heating introduces in the lower atmosphere the CO_2 15-μm radiative cooling is actually enhanced thereby shifting the emphasis in the IR balance into the mid-morning.

The early morning (0300-hrs) temperature peak is produced by the convergence of circulation flow over the midnight region (given the lack of direct solar heating on the deep nightside). This is analogous to the phenomena discussed in Section 3.3.2 where the solar heating input drives a divergent flow upward and horizontally away from the dayside, which is then deflected eastwards in both hemispheres by the Coriolis force. The convergence of this flow on the nightside equator generates a localised adiabatic heating component there resulting in heating a little to the east of that location, something which is wholly absent at these pressure levels (PL 3 to 7) with the old IR heating parameterisation.

The effect of the new IR heating parameterisation in the lower atmosphere is not limited to these two temperature peaks. In general the lowest 7 pressure levels show a pronounced increase in temperatures throughout the entire ∼24-hour MarTIM Mars day. Temperatures are now typically about 145 to 150 K in this region regardless of the time of day. Such heating and temperature structures were clearly never present with the old IR heating parameterisation (middle left, Figure 4.2). In that plot temperatures would simply steadily drop from their lower boundary setting (149.5 K) to ∼119 K at PL 7 (4.40×10^{-2} Pa), again, regardless of the time of day. This effect reflected the near complete infrared energy balance (i.e. almost zero IR energy inputs and outputs) such that the lapse rate of the atmosphere with altitude (and decrease in pressure) introduced the decrease in temperature shown.

The new IR heating profile also changes the temperature structures and magnitudes in the upper atmosphere. Principally we see a more prominent, more focussed hot region at 0900-hrs upwards from pressure level 24 (8.94×10^{-6} Pa, middle right, Figure 4.2), reaching a peak of ∼238 K. Thus while the overall extent of the hot region in the upper atmosphere seems to be roughly the same, because the EUV/UV component remains unchanged between the two runs (extending from about 0800-hrs to 1900-hrs), the focussed hot region just noted represents a clear difference to the broader, cooler temperature peak (∼228 K) that occurred with the old IR heating parameterisation (middle left, Figure

4.2). Similarly we also see an enhancement to the heating region at 2300-hrs when using the new IR heating parameterisation (∼220 K versus ∼210 K). The specificity of these hot region structures is also shown in the structure of the O to CO_2 ratio in the bottom row of Figure 4.2. The upper atmosphere region of the right hand plot (new IR heating profile) has a larger ratio than the left hand plot (old IR heating profile), with the 0900-hrs and 2300-hrs regions being a particular focus of this change.

Upper and Lower Atmosphere Wind Velocity Changes

Both the enhancements to the 0900-hrs and 2300-hrs upper atmosphere temperatures and the increase in the O to CO_2 ratio at these local times show that the new IR heating profile has enhanced the global circulation in the upper atmosphere. Also, in the lower atmosphere, the fact that a localised temperature peak now appears between pressure levels 3 and 7 (3.25×10^{-1} and 4.40×10^{-2} Pa) deep on the nightside (0300-hrs) indicates that the new IR heating has enhanced the lower atmosphere global circulation as well. The role that Mars global circulation plays in providing a dynamic heating source has already been noted: solar heating input on the dayside drives a divergent flow upward and horizontally around to the nightside where strong subsidence generates a localised adiabatic heating component. Thus hotter temperature structures at 0900-hrs and 2300-hrs in the upper atmosphere and at 0300-hrs in the lower atmosphere imply faster winds and more adiabatic heating. Also, clearly more atomic oxygen is being advected to the 0900-hrs and 2300-hrs regions; its lighter mass making it more susceptible to transport than say CO_2 (as was discussed in Section 3.3.2). Thus again an enhancement to the global circulation will bring more atomic oxygen to these locations.

Sure enough Figure 4.3 shows how both the zonal (top row) and meridional (bottom row) winds at PL 30 (4.45×10^{-7} Pa) with the new IR heating parameterisation (right hand column) have been enhanced versus the old parameterisation (left hand column). Moreover this figure shows that the differences introduced at this upper atmosphere pressure level are of significant magnitude. Maximum eastward (westward) winds now reach ∼220 m/s (∼−212 m/s) with the new parameterisation. This compares to ∼176 m/s (∼−164 m/s) with the old IR heating. In the meridional direction maximum winds now reach ∼±216 m/s against ∼±164 m/s with the old IR heating. However, note how the circulation structures appear to be quite similar regardless of the IR heating used. Thus in the upper atmosphere at least, with the new IR heating parameterisation, we are simply enhancing circulation and temperature structures that were already present with the old parameterisation. So one would expect the location of wind driven adiabatic heating effects to be similar as well, albeit enhanced, just as was shown earlier in Figure 4.2.

Since neither the old nor the new IR heating parameterisations provide much heating above PL 22, 2.43×10^{-5} Pa (and also because the dominant EUV/UV heating in this region is identical to both runs) these faster winds arise because of a greater expansion in the lower and middle atmosphere. The new IR heating causes the entire atmosphere above to expand to higher peak altitudes thereby generating a larger pressure gradient from dayside to nightside that produces faster winds as the greater potential energy is turned into kinetic energy of the wind flow (similar to the discussion earlier in Section 3.3.2).

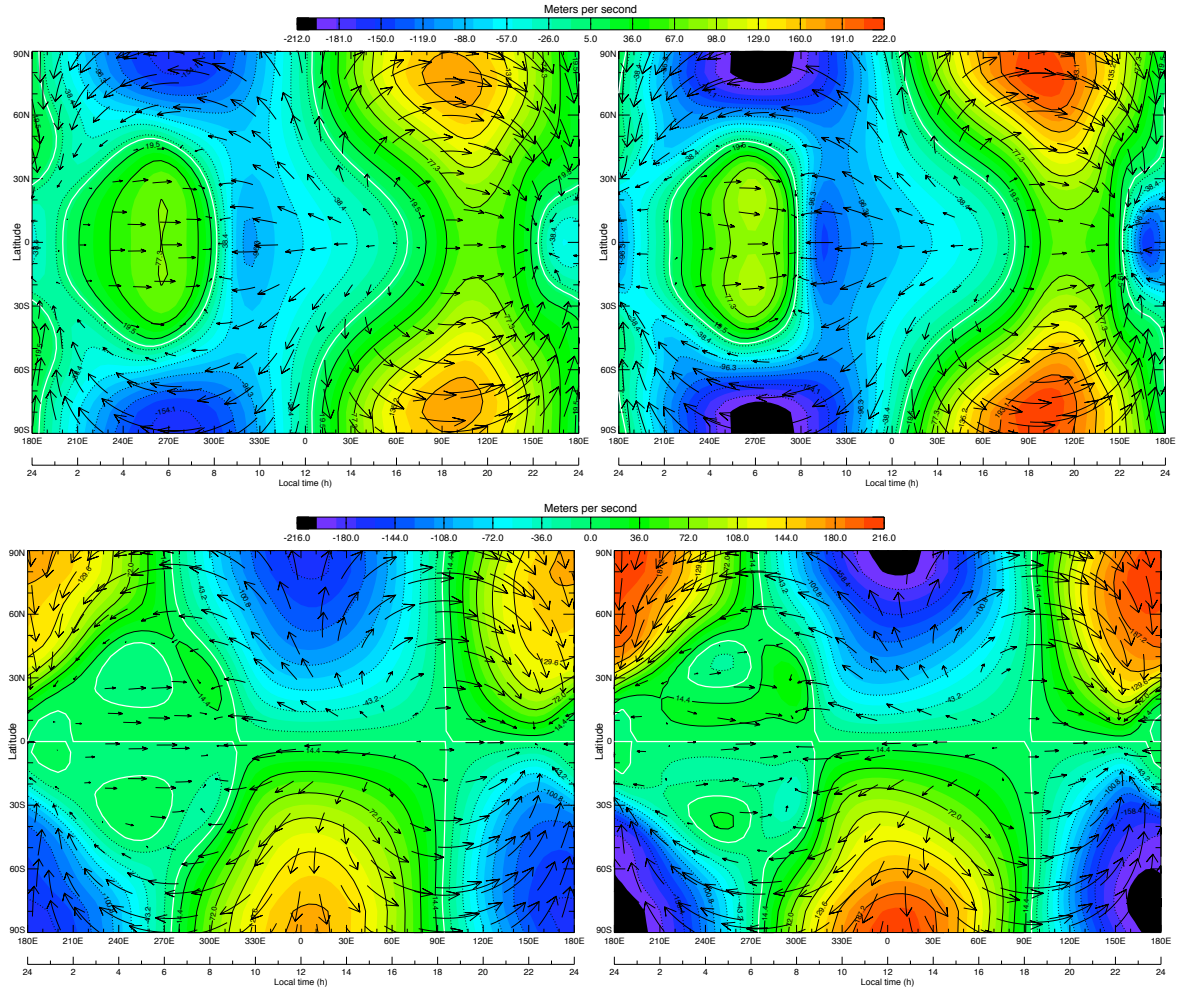

Figure 4.3: Pressure level 30 (4.45×10^{-7} Pa) zonal winds (top row) and meridional winds (bottom row). Positive is eastward and southward respectively. White contours indicate zero magnitudes. Left column uses old IR heating profile, right column uses new. SMIN, equinox conditions throughout. Colour scales are coordinated across each row.

For example with the new IR heating parameterisation the global average height of PL 30 is ∼194 km (equatorial minimum ∼169 km to maximum ∼214 km), which is greater than the ∼188 km average (∼168 to ∼205 km) with the old parameterisation.

A slightly different situation occurs in the lower atmosphere since with the new IR heating parameterisation the temperature peak at 0300-hrs and indeed the enhanced temperatures throughout the lowest 7 pressure levels essentially have no comparison with the old parameterisation. Nonetheless wind structures (not shown) have been enhanced by the presence of the new IR heating parameterisation. Maximum eastward (westward) winds now reach ∼14 m/s (∼−11 m/s) with the new parameterisation. This compares to ∼0.2 m/s (∼−4 m/s) with the old IR heating. In the meridional direction maximum winds now reach ∼±17 m/s against ∼±2 m/s with the old IR heating. Thus once again an enhancement to the magnitudes of circulation features has enhanced adiabatic heating effects and, in the lower atmosphere, created these new temperature structures.

Zonal Mean Circulation

To further consider the changes to the global circulation Figure 4.4 shows a cross-section in latitude comparing the zonal mean zonal and meridional winds that result with the old and new IR heating parameterisations (again, left and right hand columns respectively). General similarities to the latitudinal structures are apparent, for example the peak eastward zonal winds occur at ±60° latitude in the middle atmosphere with weak westward winds in the lowest pressure levels. Also, regarding the mean meridional winds, both sets of results show generally the same distinction between northwards and southwards winds throughout the vertical domain in both hemispheres.

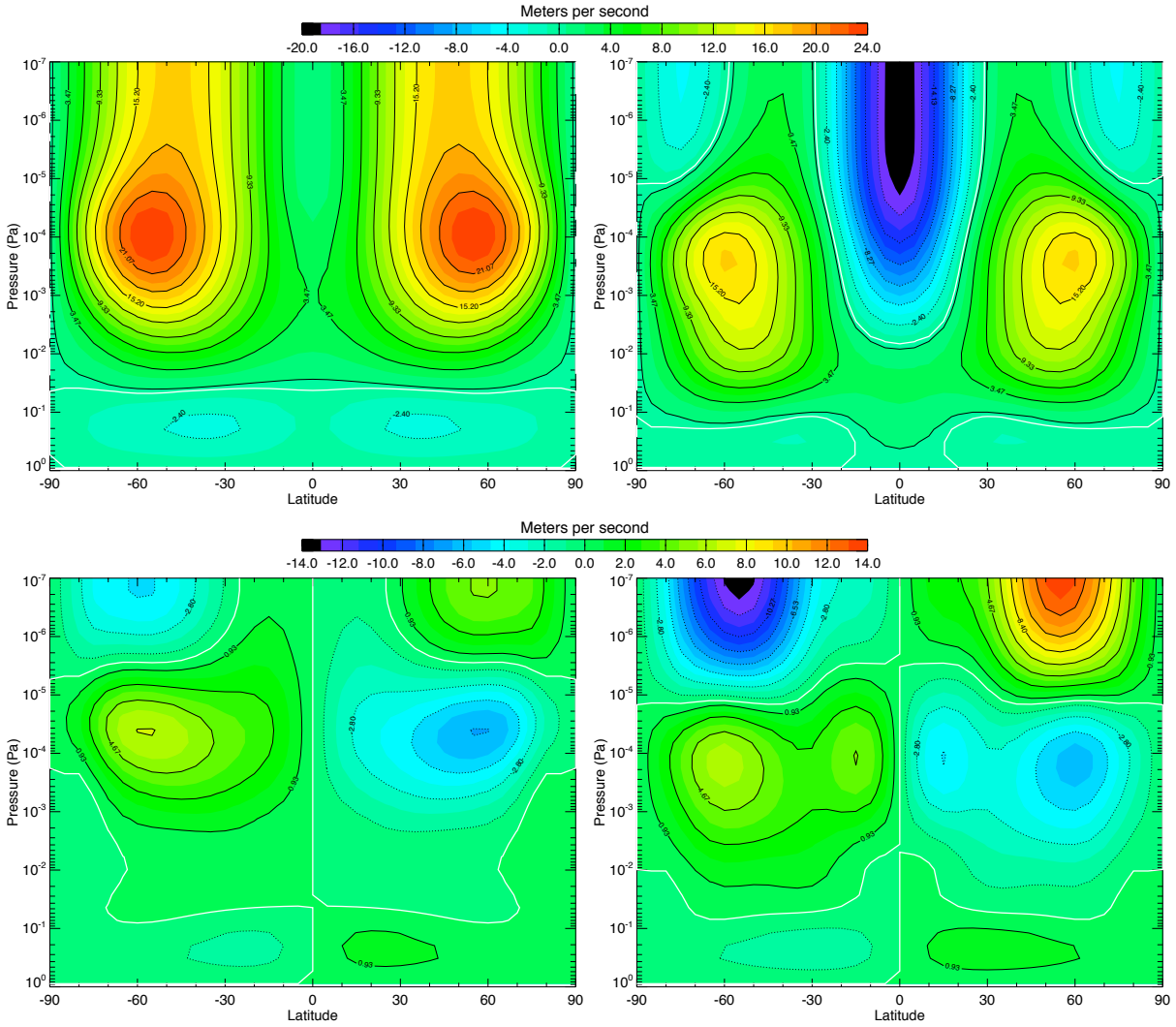

Figure 4.4: Zonal average zonal winds (top row) and zonal average meridional winds (bottom row). Left column uses old IR heating profile, right column uses new. Positive is eastward and southward respectively. White contours indicate zero magnitudes. SMIN, equinox conditions throughout. Colour scales are coordinated across each row.

Those peak eastward winds in the middle atmosphere reflect the dominance of the Coriolis acceleration directing dayside winds to the East, over the dusk terminator round to the nightside. Similarly the

adiabatic heating that occurred on the equator at 2300-hrs in Figure 4.2, which reaches down to at least PL 18 (1.80×10^{-4} Pa) regardless of the IR heating parameterisation used, will have introduced a poleward flow in each hemisphere that will also be directed eastwards by Coriolis forces and thus also contribute to the zonal mean zonal winds plotted. Finally the small zonal mean meridional winds (in the lower and middle atmosphere with the new IR heating parameterisation and throughout the atmosphere with the old) reflects the near equivalence in magnitude of the flow on both the dayside and nightside. The poleward dayside flow generally matching the equatorward nightside flow. Clearly this is not the case in the upper 10 pressure levels (PL 23, 1.47×10^{-5} Pa to PL 33, 9.94×10^{-8} Pa) with the new IR heating parameterisation.

Despite such similarities it is however quite clear that the new IR heating parameterisation has vastly altered the mean circulation structures and magitudes that were present with the old parameterisation. In particular, regarding the zonal mean winds, there is now a strong westward jet located in the equatorial regions throughout the entire upper half of the model, which reaches a maximum of $\sim$20 m/s in the uppermost pressure levels. Next, the two eastward jets, which with the old IR heating parameterisation had a maximum of $\sim$24 m/s, are now slower, with a maximum of $\sim$17 m/s. Moreover, while these zonal average zonal winds with the old parameterisation began in the PL 18 (1.80×10^{-4} Pa) region and extended to the top of the model, with the new parameterisation they are generally restricted to the middle atmosphere (PL 15, 8.05×10^{-4} Pa to PL 19, 1.09×10^{-4} Pa) and are strongly curtailed in the upper atmosphere. Westward jets also now appear at the high polar latitudes reaching an average of approximately 4 m/s.

Regarding the changes in zonal mean meridional winds the principal difference is the enhancement to the equatorward winds in both hemispheres of the upper atmosphere. These have a greater zonal average with the new IR heating parameterisation than with the old ($\sim\pm$14 m/s and $\sim\pm$7 m/s respectively). Considering dayside and nightside averages (rather than the global averages of Figure 4.4) shows that the enhancement to equatorward winds results from faster winds on the nightside shifting the emphasis in the global average as shown. This effect is also seen in the bottom row, right hand plot of Figure 4.3 where the nightside maximum meridional winds (at PL 30, 4.45×10^{-7} Pa) cover a larger horizontal region than do the dayside winds.

To conclude to this point: it appears that the new IR heating parameterisation has greatly altered the lower atmosphere temperature and circulation structures and magnitudes throughout the 24-hr solar day. At least up to PL 7 (4.40×10^{-2} Pa), but in some locations several pressure levels higher. More importantly these changes are not limited to the lower atmosphere but affect the whole vertical domain. In particular MarTIM now simulates significantly enhanced global circulation features in the upper atmosphere as a result of the column integrated heating and subsequent atmospheric expansion from the pressure levels below. This despite the minimal IR heating changes in this region and despite the identical solar EUV/UV heating parameterisations. Finally, since these faster upper atmosphere winds show similar structures regardless of the IR heating parameterisation they do enhance pre-existing

temperature structures.

Tidal Influence of the New IR Heating Parameterisation

How could the new IR heating parameterisation have so effectively altered the temperature and zonal average circulation structures and magnitudes? To consider this we perform a harmonic analysis of MarTIM's temperature structures to establish the differences in tidal amplitudes between simulations with the old and new IR heating parameterisation and/or changes induced by the propagation and breaking of vertically propagating atmospheric tides. We express the tidal oscillations present in the atmosphere following Forbes (2004) (see also Forbes and Hagan (2000) or Forbes (2002)):

$$A_{n,s} \cos\left(n\Omega t + s\lambda - \phi_{n,s}\right) \tag{4.3}$$

where t is the time in solar days, λ is the geographical longitude, n denotes a subharmonic of a solar day (with $n = 1$ for the diurnal tide, $n = 2$ for the semidiurnal tides and so on) and s is the zonal wave number, which assuming n is positive, will itself be positive (negative) if the wave propagates westward (eastward). Its magnitude represents the number of wave crests that occur along a latitude circle around the planet (Hagan et al., 2003). Also, term Ω is the planetary rotation rate ($2\pi/24$ h^{-1}), $A_{n,s}$ is the amplitude of the (n, s) mode and finally $\phi_{n,s}$ is its phase. Then, a particular MarTIM atmospheric field is expressed as a superposition of different modes (n, s) (González-Galindo et al., 2009a; Forbes and Miyahara, 2006):

$$\sum_n \sum_s A_{n,s}(z,\theta) \cos\left(n\Omega t + s\lambda - \phi_{n,s}(z,\theta)\right) \tag{4.4}$$

where both the amplitude and phase are functions of height z and latitude (θ).

From Hagan et al. (2003) the crest of a particular tidal mode occurs where $\phi_{n,s}(z,\theta)$ satisfies:

$$\phi_{n,s}(z,\theta) = n\Omega t + s\lambda \tag{4.5}$$

Then, the horizontal phase speed of the tide, C_{ph} is defined by differentiating this equation while holding the phase constant:

$$\begin{aligned} n\Omega dt + s d\lambda &= 0 \\ c_{ph} \equiv \frac{d\lambda}{dt} &= \frac{-n\Omega}{s} \end{aligned} \tag{4.6}$$

We would expect MarTIM's response in this chapter's work to be dominated by tidal components that move with the apparent motion of the Sun. This is because (1) MarTIM is being irradiated by a longitudinally invariant solar illumination and (2) MarTIM is a zonally symmetric atmosphere in the sense that longitudinal variations in solar heating associated with variations in surface thermal inertia, albedo and with airborne dust and aerosol distributions (Zurek, 1976; Wilson and Hamilton, 1996; González-Galindo et al., 2009a) will not affect our result. Therefore daily variations in MarTIM's atmospheric fields will be independent of longitude, i.e. $n{=}s$ such that $C_{ph}{=}{-}\Omega$ and the tidal components will move with the

apparent motion of the Sun i.e. migrating components. The non-migrating components, for which $n \neq s$, are dealt with in Chapter 5.

Figures 4.5, 4.6 and 4.7 show the maximum amplitudes of MarTIM's temperature fields across pressure levels 10 (9.81×10^{-3} Pa), PL 20 (6.61×10^{-5} Pa) and PL 30 (4.45×10^{-7} Pa) respectively (equinox, SMIN conditions). Firstly, all these figures do indeed only show solar driven westward migrating tides ($n=s$), for the reasons noted above. Thus we generally see that as the solar energy input increases with pressure level, so too does the typical tidal amplitude. The main tidal components at all pressure levels shown, regardless of the IR heating parameterisation used, are the $(1,1)$ mode (diurnal, 24 hour period, wavenumber 1) arising as a direct consequence of the solar heating (EUV/UV heating from PL 20 to PL 30, IR heating at PL 10) on the dayside and the $(2,2)$ mode (semidiurnal, 12 hour period, wavenumber 2) typically produced by both solar heating on the dayside and the adiabatic heating on the nightside (as discussed earlier). Higher frequency waves do make an appearance, especially when the new IR heating parameterisation is used, but these are usually smaller fractions of the main modes just noted. The zonal means are indicated in the figure captions.

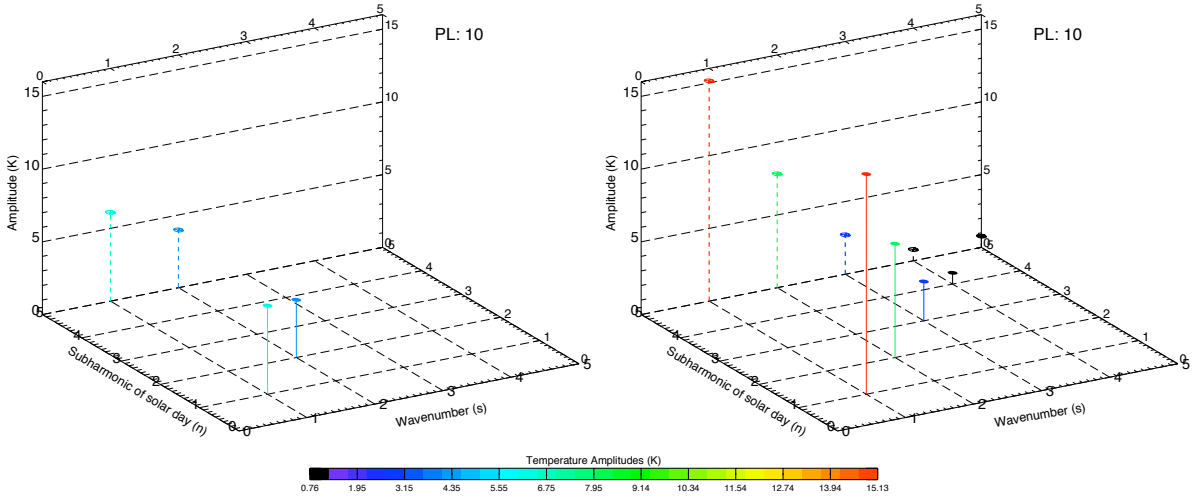

Figure 4.5: Temperature amplitudes at PL 10 (9.81×10^{-3} Pa). Left column uses old IR heating profile, right column uses new. The zonal means were 114.4 and 135.3 K respectively. The colour scales are coordinated.

The major difference that introducing the new IR heating parameterisation produces is an enhancement to the $(2,2)$ tidal mode at all pressure levels. In the case of the $(1,1)$ mode however, the new IR parameterisation only enhances this mode (over what is produced with the old parameterisation) at PL 10. Thus at PL 20 and 30 the old parameterisation still produces a dominant $(1,1)$ mode. Generally, in the lower atmosphere, the far greater IR heating provided by the new parameterisation will enhance the amplitudes of all tidal modes present simply because there was almost a complete net zero energy balance in this region with the old parameterisation. Sure enough the right hand plot of Figure 4.5 shows this difference is more than double for the $(1,1)$ mode ($\sim$15.1 K versus $\sim$6.1 K) and almost double for the $(2,2)$ mode ($\sim$7.8 K versus $\sim$3.9 K).

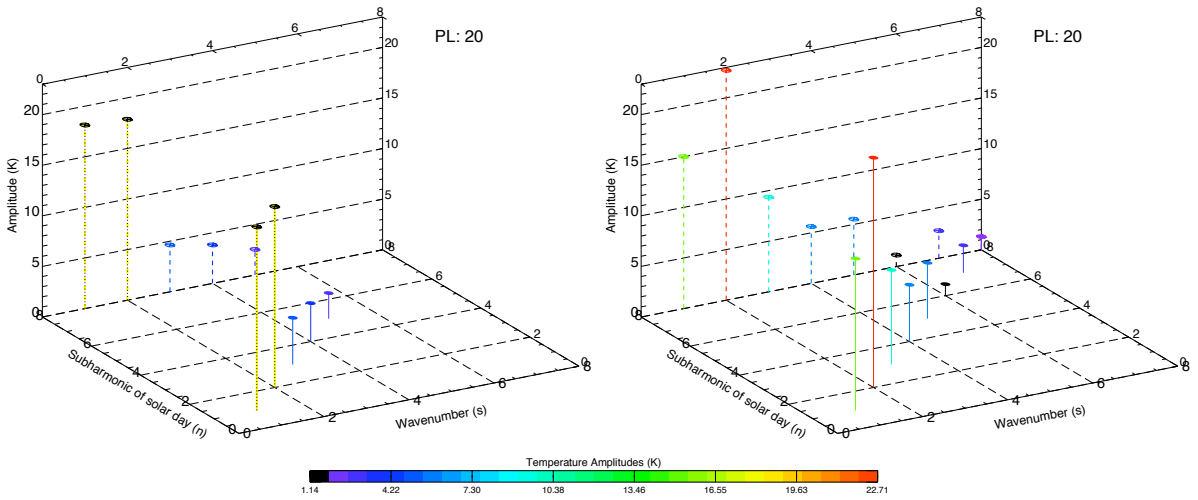

Figure 4.6: Temperature amplitudes at PL 20 (6.61×10^{-5} Pa). Left column uses old IR heating profile, right column uses new. The zonal means were 147.5 and 142.9 K respectively. The colour scales are coordinated.

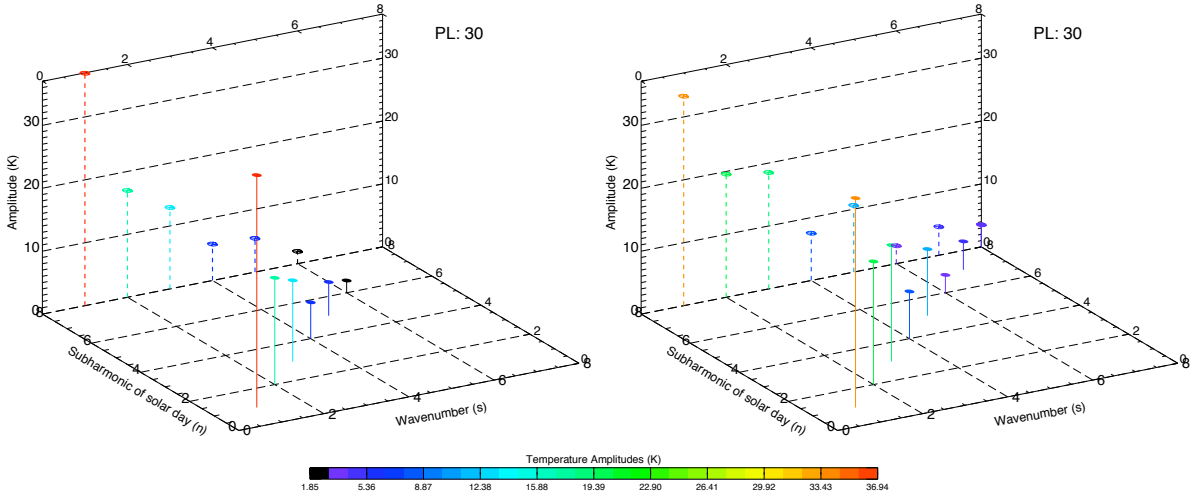

Figure 4.7: Temperature amplitudes at PL 30 (4.45×10^{-7} Pa). Left column uses old IR heating profile, right column uses new. The zonal means were 199.3 and 200.1 K respectively. The colour scales are coordinated.

At pressure levels 20 and 30 the situation is more complex. The enhancement of the $(2, 2)$ mode with the new IR heating parameterisation over the old at these levels could be the result of both enhanced direct solar heating on the dayside and/or enhanced adiabatic heating on the nightside. Sure enough it has already been shown that both the amount of direct IR heating and the global circulation features are of greater magnitude with the new parameterisation. However at PL 20 and 30 the enhancement of $(2, 2)$ mode signatures are more likely to be due to the faster global circulation generating greater adiabatic heating given that (a) the IR heating at these levels is rapidly reducing with altitude, regardless of the parameterisation being used and that (b) the diurnal signal from the solar EUV/UV heating has not yet reached the large values it attains in the upper atmosphere (and is the same for both runs anyway).

In which case the changes shown by Figures 4.6 and 4.7 will come about due to the larger expansion from the atmosphere below (which relates to the greater column integrated IR heating) creating a large pressure gradient and thus faster winds. This can be most easily seen at PL 20 where the new IR heating parameterisation (right hand plot, Figure 4.6) creates a $(2, 2)$ mode amplitude of $\sim$22.7 K versus $\sim$18.0 K for the old parameterisation.

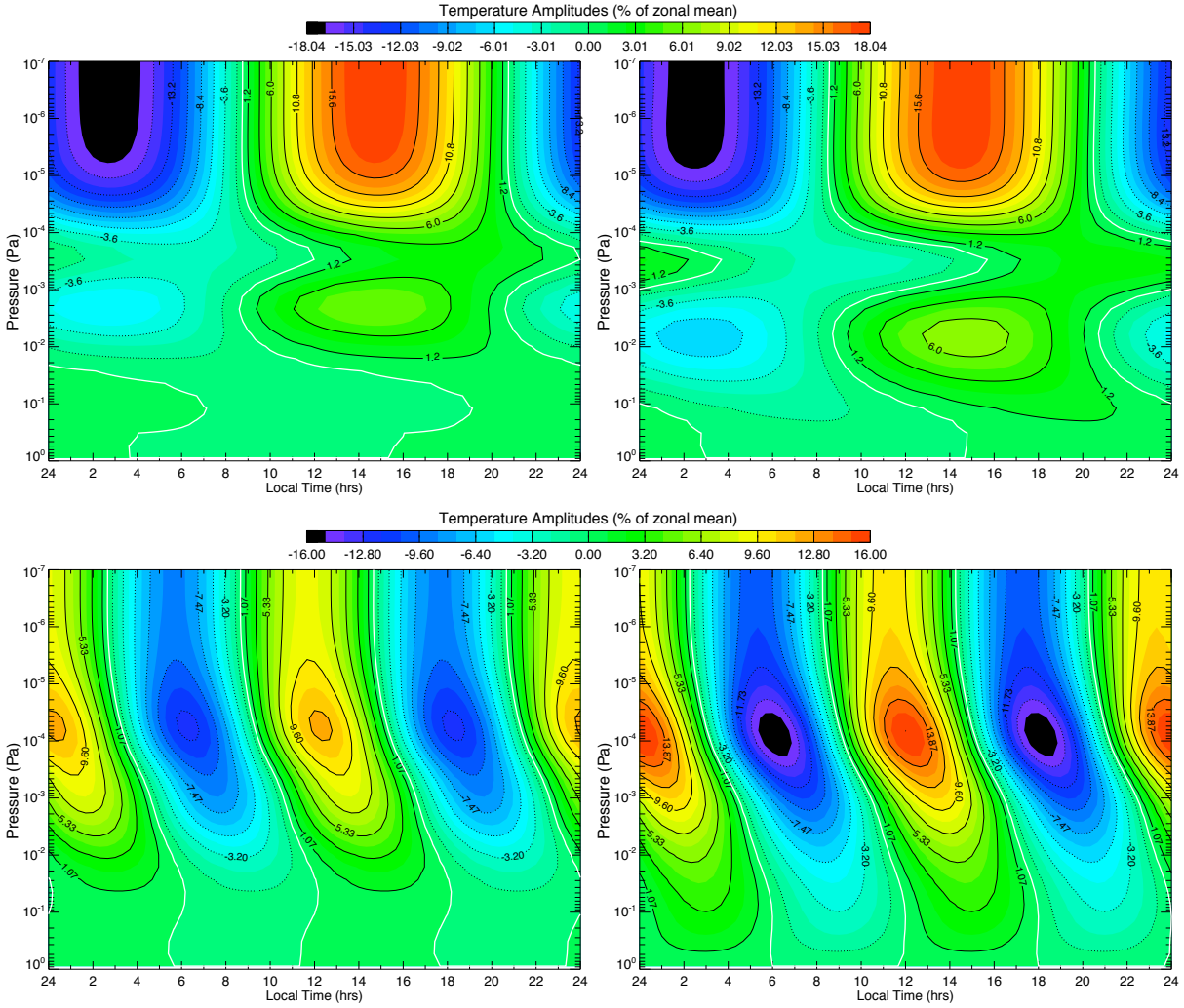

Figure 4.8: Equatorial slice for SMIN conditions of the temperature amplitudes expressed as a percentage of the zonal means. Top row $(1, 1)$ mode, bottom row $(2, 2)$ mode. Left column uses old IR heating profile, right column uses new. White contours indicate zero magnitudes. Colour scales are coordinated across each row.

Figure 4.8 shows the tidal features in a different light. Equatorial slices are shown of temperature amplitudes, expressed as percentages of the background zonal mean, for comparison against the temperature fields themselves, as shown earlier by Figure 4.2 (middle row plots). The structure shown by the $(1, 1)$ mode relates directly to the solar EUV/UV and IR heating with peaks at PL 24 (8.94×10^{-6} Pa) and above for the former (for both old and new IR heating parameterisations) and peaks at PL 13 (2.19×10^{-3}

Pa) and PL 11 (5.95×10^{-3} Pa) for the IR heating (for the old and new parameterisations, respectively). With the $(1,1)$ mode you can clearly see the similarity in the influence of the upper atmosphere solar EUV/UV input, given that this remains unchanged between the two simulations. You can also see the influence of the different IR heating parameterisations that result in the new IR peak occurring at a lower pressure level (as discussed earlier) and with greater magnitude over the background mean. Both heating terms are shifted about 2 hours after midday given the thermal lag of the atmosphere as the planet rotates.

Regarding the $(2,2)$ mode we begin to see significant differences between the old and new IR heating parameterisations. By normalising the amplitudes against the background zonal mean we see how the influence of this mode increases with altitude reaching a maximum of 16% of the zonal mean in the PL 18 to 21 region at midday and midnight for the new IR parameterisation. The maximum influence of the old IR parameterisation is reduced ($\sim$12.1%) and more focussed about the PL 19 to 21 region (1.09×10^{-4} to 4.01×10^{-5} Pa). Both these regions lie about the PL 20 level (6.61×10^{-5} Pa), shown earlier in Figure 4.6 to have a prominant $(2,2)$ component, especially for the new IR heating parameterisation. Now if we recall the striking changes to the zonal mean zonal and meridional winds, shown by Figure 4.4 earlier, these changes included (1) a strong westward jet located in the equatorial regions throughout the entire upper half of the model (reaching $\sim$20 m/s in the uppermost pressure levels), (2) a curtailing in the upper atmosphere of the mid-latitude eastward jets and (3) the appearance of westward jets at high polar latitudes ($\sim$4 m/s). All of these changes, following the introduction of the new IR heating parameterisation, point to significant westward momentum having been deposited throughout the thermosphere. In particular the curtailment of mean eastward zonal winds in the upper atmosphere in Figure 4.4 (top right plot) occurred from PL 20 and above, leaving slower eastward jets about the PL 15 to 19 region (8.05×10^{-4} to 1.09×10^{-4} Pa).

To conclude then, from the above harmonic analysis we can see how the $(2,2)$ mode has been enhanced throughout the atmosphere with the new IR heating parameterisation as too has the $(1,1)$ mode in the lower atmosphere. This enhancement has deposited sufficient westward momentum into the thermosphere that the zonal average global circulation has significantly changed. Consequently adiabatic heating and temperature structures have greatly increased in magnitude while their structure remains similar to that with the old parameterisation. There are both in-situ and vertically propagating aspects to the tidal influence. Regarding the in-situ, the greater lower atmosphere diurnal signal has come directly from the enhanced new IR heating parameterisation. And in the middle and upper atmosphere tidal enhancements have come from column integrated expansion above this greater new IR heating.

However, in addition, the growth of the influence of the $(2,2)$ mode over the background mean, as shown by Figure 4.8 above, suggests a vertically propagating nature to the tidal influence. The angle that the $(2,2)$ mode in this figure makes to the vertical, slanted over to the west as it climbs in altitude is suggestive of phase progression arising from a vertically propagating westward migrating tide. Indeed looking back at the equatorial temperature and IR radiative balance structures introduced by the new

IR heating, shown earlier in Figure 4.2, we can see this same phase progression in the background atmospheric fields. For example the relationship between the temperature peaks at 1300-hrs to 1900-hrs in the lower atmosphere (PL 3, 3.25×10^{-1} Pa to PL 7, 4.40×10^{-2} Pa) to those at 0900-hrs in the upper atmosphere (PL 24, 8.94×10^{-6} Pa and above). Likewise note the peak in the early morning around 0300-hrs (PL 3 to 7) and that at 2300-hrs (PL 24 and above). Finally, the angle that the IR radiative cooling structure that reaches from PL 7, 4.40×10^{-2} Pa (0400-hrs) to PL 29, 7.34×10^{-7} Pa (2300-hrs) in Figure 4.2 makes with the vertical. A vertically propagating aspect is perhaps of no surprise, given the various occasions columnar integrated expansion from the lower atmosphere has been cited as driving the changes observed in the middle and upper atmosphere. Finally then, we would expect that for other heliocentric distances that the difference may be more profound (given that the new IR heating parameterisation actively changes with this variable). And this is what we show next.

4.3 Thermospheric Winter Polar Warming

4.3.1 Background Theory

A very important difference that using the new IR heating parameterisation has introduced can be shown by the simulation of polar warming structures in the lower thermosphere of the winter polar regions. This type of phenomena was first observed in the upper Martian atmosphere during aerobraking of the Mars Odyssey spacecraft (Keating et al., 2003), which was reviewed in the work of Bougher et al. (2006a). Essentially, during northern winter / perihelion conditions as the periapsis of the Mars Odyssey spacecraft orbit passed over the northern winter pole, from the dayside (1700-hrs) to the nightside (0200-0300-hrs), an increase in temperature was observed from 60°N to 90°N from ∼100 K to about 170-200K at periapsis altitudes (100-110 km) and from 110 K to 160-170 K near 120 km (Keating et al., 2003; Bougher et al., 2006a). The study of Withers (2006) using Mars Odyssey accelerometer measurements at 120 km also showed temperatures increasing in the northern polar regions (mean temperatures for 5° latitude bins reached ∼150 K at high latitudes near the northern winter pole). As noted by González-Galindo et al. (2009a) this thermospheric warming was distinct from analogous lower atmosphere features (∼50 km) modelled by e.g. Wilson (1997), Forget et al. (1999) or Medvedev and Hartogh (2007) and observed by e.g. MGS Thermal Emission Spectrometer limb data (Smith et al., 2001). Indeed there was no concurrent lower atmosphere polar warming observed during the Mars Odyssey aerobraking period (Bougher et al., 2006a).

Notably, during the opposite southern winter / aphelion season, as the periapsis (now of the Mars Global Surveyor spacecraft during phase 2 of its aerobraking period) passed over the southern winter pole, measurements did not show any analogous polar warming features (Bougher et al., 2006a). Temperatures near 120 km increased slightly from 130-140 K at the equator up to 160 K at mid-latitudes before dropping to 100 K near the south pole (Bougher et al., 2006a). However recent measurements of temperatures inferred from observations of density by the SPICAM instrument onboard Mars Express (Forget et al.,

2009), which we discuss in Chapter 5, suggest a moderate 20 to 30 K polar warming at this aphelion season between 70 and 115 km (González-Galindo et al., 2009a). This was also indicated by the modelling work of González-Galindo et al. (2009a) (∼125 K at 30°S to ∼160 K at 90°S) while simulations by Bougher et al. (2006a) showed mean temperatures that were up to 20 to 25 K warmer than the day-night averages of MGS observed temperatures. In addition, Mars Reconnaissance Orbiter (MRO) detected a small 10 K polar warming at 110 km (Keating et al., 2008). Finally Lillis et al. (2008) derived mass density measurements from 4 years worth of MGS electron reflectrometry data at 180 km to show southern winter polar warming was generally weak or nonexistent and not a consistently repeating feature (unlike its northern counterpart).

The general circulation modelling of polar warming features has cast much light on some of the driving mechanisms behind these phenomena. Studying the modelled atmospheric thermal balance of the LMD model (González-Galindo et al., 2009a) showed that none of the major heating and cooling terms could explain the high temperatures found in the mesopause / lower thermosphere during the winter polar night. Global meridional transport effects (rather than local radiative effects) and commensurate subsidence / convergence of mass and adiabatic heating above the polar regions was always required to produce the large temperatures modelled. Indeed lower atmosphere models were required to extend the altitudes of their upper boundaries (∼90 km) to properly model the global circulation and allow the polar warming features to develop. These meridional winds are driven in much the same way we have discussed above: direct solar heating causing expansion and mass flow vertically and horizontally around the planet. Thus, as with the similar lower atmosphere warming, the thermospheric features appear to be largely generated by adiabatic heating associated with the downward branch of a diabatically driven interhemispheric Hadley-type circulation (Bougher et al., 2006a; Withers, 2006; González-Galindo et al., 2009a).

In the lower atmosphere Forget et al. (1999) discussed how the mass convergence and adiabatic warming brought about by such a circulation would always produce thermal inversions around the 60 to 70 km region (and above) over the winter polar regions during the solstices and above both poles near equinox. One would expect the effect to be more prominent during southern summer season (perihelion) given the stronger solar insolation and dustier lower atmosphere conditions. Sure enough Bougher et al. (2006a) showed this to be the case in the thermosphere with a simulated adiabatic heating of ∼300 to 400 K/day during aphelion and ∼400 to 1000 K/day during perihelion (polar night conditions at 120 km). Both Bougher et al. (2006a) and Bell et al. (2007) studied the importance of dust loading on the magnitude of the warming. Bell et al. (2007) in particular discussed how the interannual, horizontal and vertical variation of atmospheric dust content could create differences in the polar warming intensity. Finally González-Galindo et al. (2009a) considered the role of atmospheric tides generated in-situ in the upper atmosphere (i.e. by direct solar UV and IR heating) on the thermal and dynamical structure of the atmosphere and thus their role on the transport mechanisms responsible for polar warming features. Importantly, they showed that tides generated by in-situ solar EUV/UV and IR heating were critical for

generating the day-night temperature differences needed to reinforce summer to winter circulation that leads to nightside polar warming.

4.3.2 MarTIM Simulations of Polar Warming Features

First we establish whether MarTIM is capable of simulating polar warming features by comparing MarTIM temperatures to those derived from Mars Odyssey aerobraking measurements of atmospheric density. This data was kindly provided by Dr Paul Withers of the Center for Space Physics, Boston University and we extend our thanks to him for this resource. We also consider how MarTIM's result varies when the old and new IR heating parameterisations are used. In all simulations the influence of the lower atmosphere below MarTIM's lower boundary, e.g. the effect of vertically propagating tides, the effect of dust storms on the geopotential height and the variation in thermal forcing from the Martian topography are not yet considered. This is left until Chapter 5 when the Mars Climate Database v4.3 (MCD) is coupled to MarTIM's lower boundary.

Northern Winter Polar Regions During Perihelion Conditions

First we consider temperatures in the northern winter polar regions for solar minimum perihelion (Ls 270°) conditions. Figure 4.9 shows the comparison between MarTIM temperatures versus latitude at 120 km and Mars Odyssey derived temperatures in the northern winter hemisphere. The spacecraft data chosen were those profiles at 120 km whose local time lay in the early morning when the polar warming features were observed (typically around 0200-hrs with some as early as 0000-hrs and others as late as 0300-hrs). This data had good longitude coverage and was averaged into 5° latitude bins before finally being plotted against latitude (blue line and data points). To highlight the range of structures in MarTIM's results we show latitudinal slices at several local times in Figure 4.9 as well as a night time average (from 1800 to 0600-hrs). Results using the old (black line) and new (red line) IR heating parameterisations are shown. Next, Figure 4.10 shows latitude by longitude contours of temperatures at constant altitude (120 km) simulated by MarTIM. It is from these plots that the results of Figure 4.9 were taken. Again results using the old and new IR heating parameterisation are shown as well as an MCD v4.3 result for a very low dust, solar minimum scenario. This dust setting is probably not the typical condition one would expect during perihelion season, however as noted since in this chapter MarTIM does not yet include the influence of this and other lower atmosphere effects we use this MCD setup for a general comparison to MarTIM's results. Thus, for now we provide a broader picture in the context of changes introduced by the new IR heating parameterisation.

From the plots in Figure 4.9 it is clear that regardless of which local time is chosen that MarTIM generally struggles to match the temperature structure measured by the Mars Odyssey spacecraft. Neither version of MarTIM (with either the old or new IR heating parameterisations) properly reaches the lowest temperatures (∼95 K in the 45°-50°N bin) nor the highest temperatures of the spacecraft data (∼165 K in the 80°-85°N bin). However an interesting result is produced with the new IR parameterisation (red

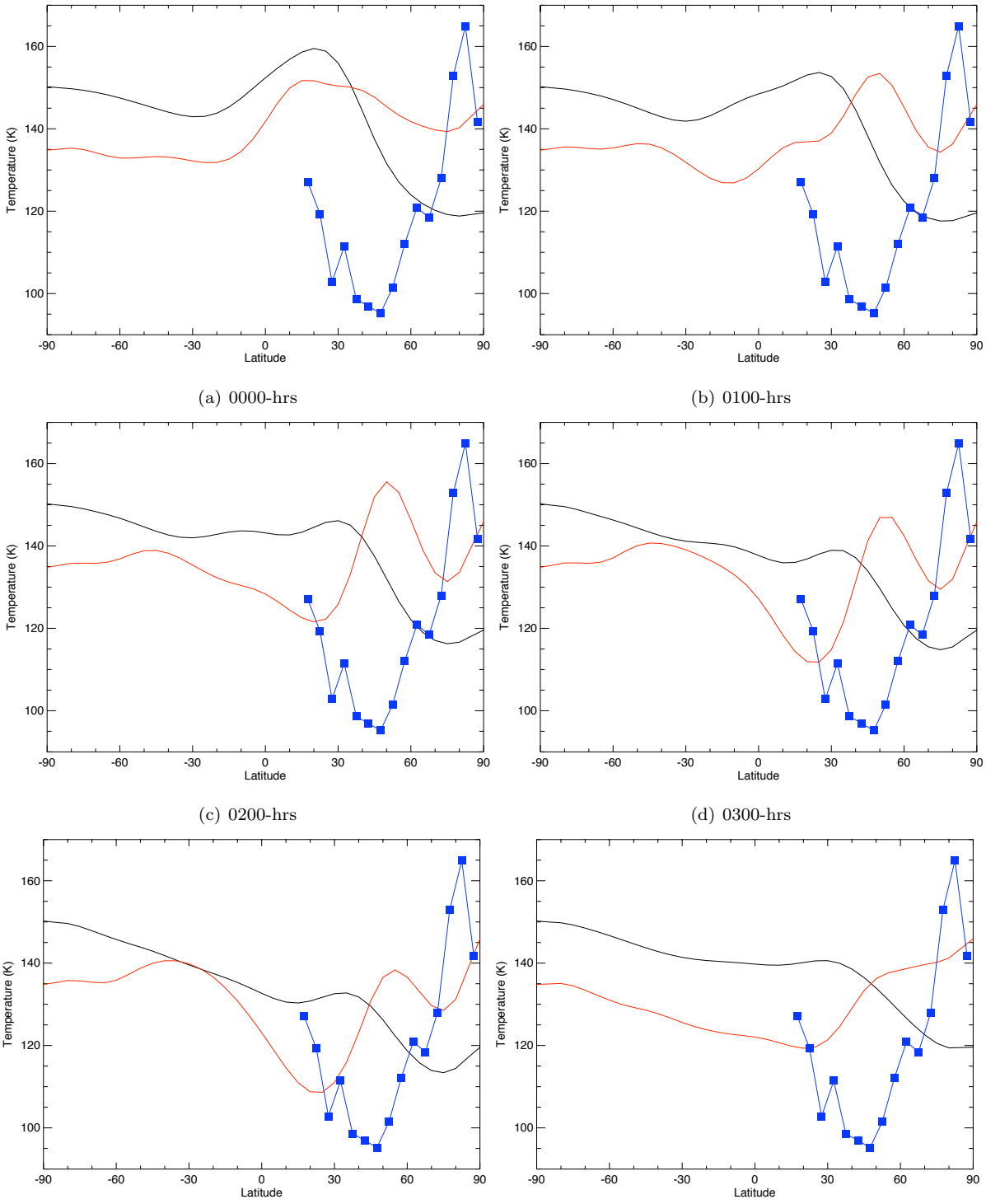

(a) 0000-hrs

(b) 0100-hrs

(c) 0200-hrs

(d) 0300-hrs

(e) 0400-hrs

(f) Night time average (1800 to 0600-hrs)

Figure 4.9: MarTIM perihelion (Ls 270°, SMIN) temperatures (black and red lines) versus Mars Odyssey derived temperatures (blue line and data points) at 120 km over a range of local times. Black lines indicate the old IR heating parameterisation, the red lines indicate the new.

lines of Figure 4.9) that doesn't appear with the old (black lines of Figure 4.9). With the new parameterisation MarTIM persistently shows a good match in temperature with the 85°-90°N bin (∼142 K). Also

you can see that the plots at 0200-hrs, 0300-hrs, 0400-hrs and the night time average (1800 to 0600-hrs) all show an initial drop in temperature just northwards of the equator followed by an increase of about 35 K about the northern hemisphere mid-latitudes. This increase in temperature (alongside the ∼142 K north pole temperature) is shown only by the simulation with the new IR heating parameterisation. The simulation with the old parameterisation shows exactly what you would expect for an Ls 270° southern summer run i.e. a gradual decrease in temperatures as we move toward the northern winter pole. So the fact that the new IR parameterisation produces a clear heating effect in the winter hemisphere the likes of which are expected by the winter polar warming phenomena is significant, even though there is not an exact match to this Mars Odyssey dataset.

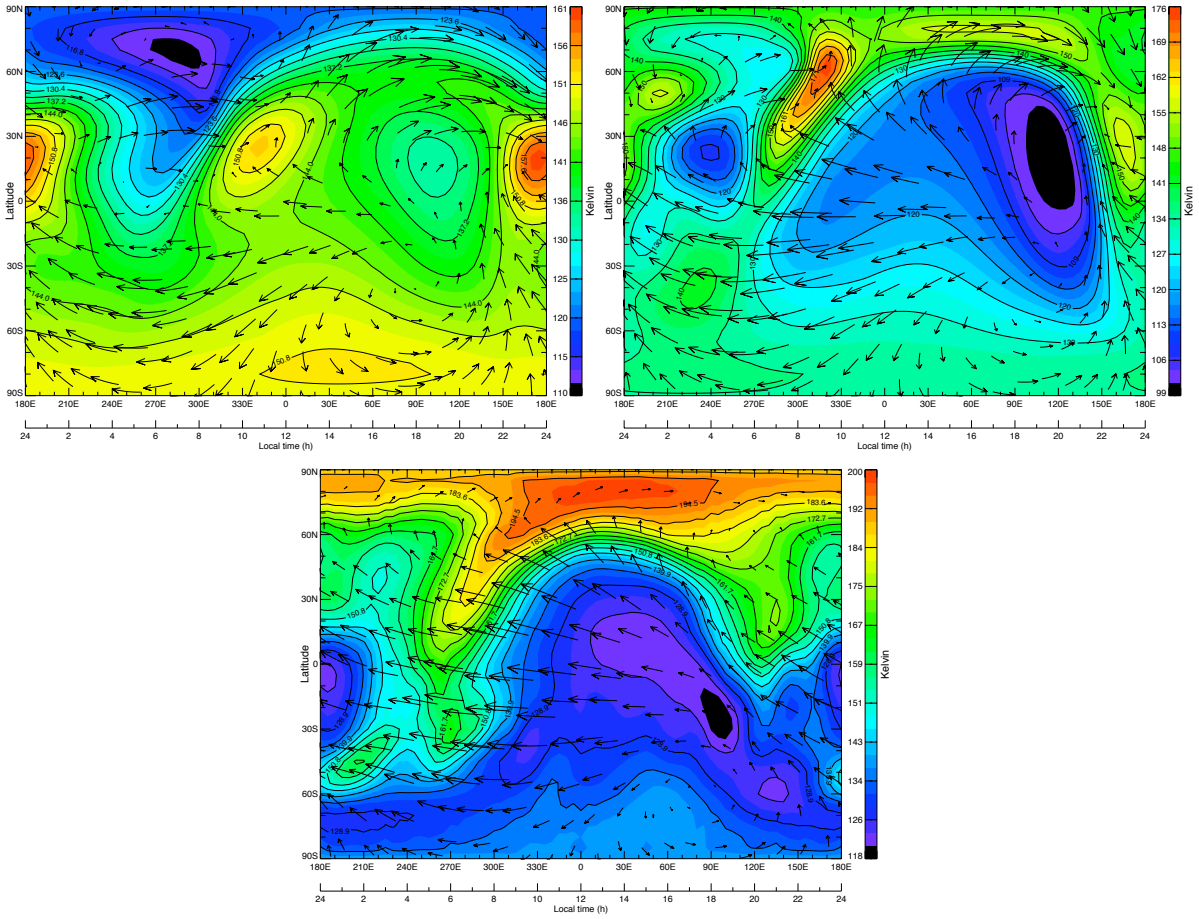

Figure 4.10: MarTIM perihelion (Ls 270°, SMIN) temperatures at constant altitude 120 km with old IR heating parameterisation (top left) and new parameterisation (top right). Also shown (bottom plot) is MCD v4.3 result at 120 km using a low dust scenario. Plots are individually colour coordinated against the scales shown.

Figure 4.10 shows the polar heating introduced by the new IR heating parameterisation (top right plot) in the context of latitude by longitude contour plots (at a constant altitude 120 km). Here then we can clearly see that the new parameterisation has resulted in heating in the northern winter hemisphere at all local times. Again, the old parameterisation (top left plot) maintains a hot summer / cold winter

hemisphere structure. Interestingly, comparing MarTIM's results to the example MCD v4.3 low dust result (bottom plot) shows how some of the structures MarTIM now simulates are also produced by other global circulation models. In particular we see a heating structure from 0600 to 1100-hrs between 20°N and 80°N in both the MCD result and in MarTIM's result with the new IR heating parameterisation. Also, the same can be said to some extent about the hot region near midnight at 30°N. As noted above, most of the high northern latitudes remain significantly hotter then the south in both MarTIM (new parameterisation) and the MCD results.

Regarding global circulation structures, there also seems to be some agreement between the MCD and MarTIM (with the new IR heating parameterisation) results given the similarity in the direction of the overlaid wind arrows in the top right and bottom plots. This dynamical pattern, with a strong divergence of winds from the dayside mid-latitudes and a convergence on the nightside high latitudes, is similar to that obtained in the work of González-Galindo et al. (2009a) and Bougher et al. (2000), being cited as indicative of a net transport of matter from dayside summer hemisphere to nightside winter hemisphere (González-Galindo et al., 2009a). With the old IR heating parameterisation we see the more typical circulation effects that were mentioned earlier. Thus there is a clear semidiurnal signal about the 25°N latitude that is brought about by the convergence of winds flowing away from the hot southern hemisphere dayside. Clearly the new IR heating parameterisation produces a very different balance between heating and global circulation structures for these perihelion conditions (as it was with the equinox results discussed in section 4.2.2).

Figure 4.11 shows another view of the difference introduced by the new IR heating parameterisation versus the old by comparing temperatures in the northern hemisphere to their value at 30°N at the same pressure level. Thus we take the zonal average temperature field and subtract the zonal average temperature at 30°N (at each pressure level). From the background research of other GCM's we are expecting the polar warming heating effects in the northern hemisphere to be generated by meridional transport bringing a convergence of mass and adiabatic heating to the winter polar regions. Sure enough the bottom plot of Figure 4.11 clearly shows how the circulation features with the new IR heating parameterisation creates quite a specific region of heating ($\sim$17 K versus 30°N) about the winter polar region at 120 km. Though the IR heating has little presence in the high latitude of the northern winter hemisphere, regardless of the parameterisation, clearly the new parameterisation has sufficiently altered the circulation (as shown by the overlaid arrows) to create the heating effect shown. Descending vertical winds now reach a maximum of about -120.5 cm/s between 50°N and 60°N in the upper atmosphere for the new parameterisation versus only ~ -35.1 cm/s for the old. It seems to be this penetration of air descending from the thermosphere into the mesosphere that creates a compressional adiabatic heating around 120 km of magnitude $\sim$188 K/day northwards of 50°N for the new parameterisation and only $\sim$30 K/day for the old. With the old parameterisation there is simply no high northern latitude heating at all (dashed contour lines indicate cooling with respect to 30°N). Winds here begin to fall in altitude, just after 30°N, towards the cool north pole before returning to the equator in the lowest 20 km of the

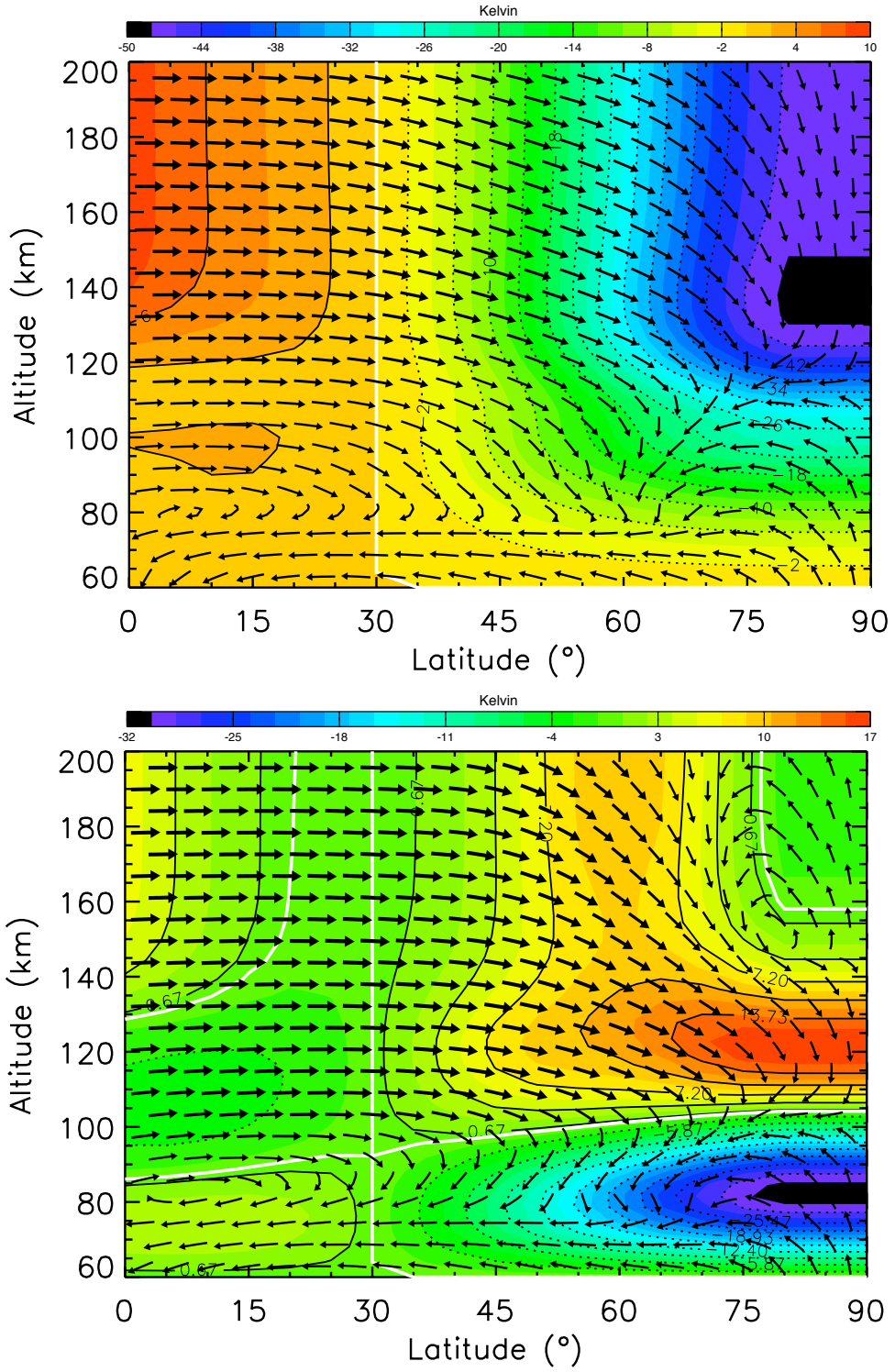

Figure 4.11: Zonal average latitudinal slice of the northern hemisphere temperature difference at each model pressure level (expressed in altitude) against the temperature at 30°N. Top plot uses the old IR heating parameterisation while bottom plot uses the new. Solar minimum, Ls 270° (perihelion). White contours indicate zero magnitudes.

model (as with the new parameterisation).

Finally we show in Figure 4.12 the full latitudinal slice of MarTIM's results for the zonal average total angular momentum. This is no longer the difference in magnitude against some latitude but is the actual atmospheric angular momentum as calculated by equation 4.7:

$$M(z,\theta) = a\cos\theta(\Omega a\cos\theta + v_\phi(z,\theta)) \tag{4.7}$$

Where a is the radius of Mars (3.3962×10^6 m), θ is latitude, Ω is the angular velocity (2π rad/day, 7.0777×10^{-5} s^{-1}) and v_ϕ is the zonal velocity (Wallace and Hobbs, 1977). Now we see the full effect of the interhemispheric circulation. Winds rise in the southern summer hemisphere given the peak solar energy input there and then travel northwards across the equator. With both the old and new IR heating parameterisations the northward flow in the southern hemisphere is 'downhill' as the atmosphere is cooler further away from the solar input, hence atmospheric columns reduce in total height and constant pressure levels drop in altitude hydrostatically. As explained by Forget et al. (1999), regarding the lower atmosphere (∼50 km) polar warming features, assuming this northward meridional flow in the southern hemisphere conserves angular momentum then the Coriolis force will tend to create a westward acceleration as the circulation moves towards the equator and thus away from the axis of rotation. Indeed this will be the case as long as $|\theta|<|\theta_0|$, where θ_0 is the latitude from where the meridional motion began (Forget et al., 1999). This is indicated by the white contour lines overlaid on Figure 4.12 that show only westward zonal winds (that have also been zonally averaged) maximising in the southern mid-latitudes with the old IR heating parameterisation and in the southern tropics with the new.

From equation 2.15 of Chapter 2 the Coriolis force produces an acceleration whose eastward component is equation 4.8:

$$(2\underline{\Omega}\times\underline{v})\hat{\underline{\mathbf{e}}}_\phi = -2\Omega v_\theta\sin\theta\hat{\underline{\mathbf{e}}}_\phi \tag{4.8}$$

Once the meridional flow crosses the equator the difference between the old and new IR heating parameterisations becomes clear. Now, with us approaching the axis of rotation, from equation 4.8 we still have a northward motion ($^-ve\ v_\theta$), but with a positive $\sin\theta$, an eastward flow begins to develop ($^+ve\ v_\phi$). You can see this happening as the westward wind contour line spacing begins to narrow in the northern hemisphere before the westward winds turn to eastward and the contour lines disappear altogether. This change in zonal flow occurs at about 20°N (with respect to the upper atmosphere) with the old parameterisation but as far north as 50°N with the new.

Here is the crux then, that the zonal winds remain westward through a significant part of the (upper atmosphere) northern hemisphere when the new IR heating parameterisation is used. Returning to equation 2.15 of Chapter 2 the Coriolis force also produces an acceleration whose southward component is equation 4.9:

$$(2\underline{\Omega}\times\underline{v})\hat{\underline{\mathbf{e}}}_\theta = 2\Omega v_\phi\sin\theta\hat{\underline{\mathbf{e}}}_\theta \tag{4.9}$$

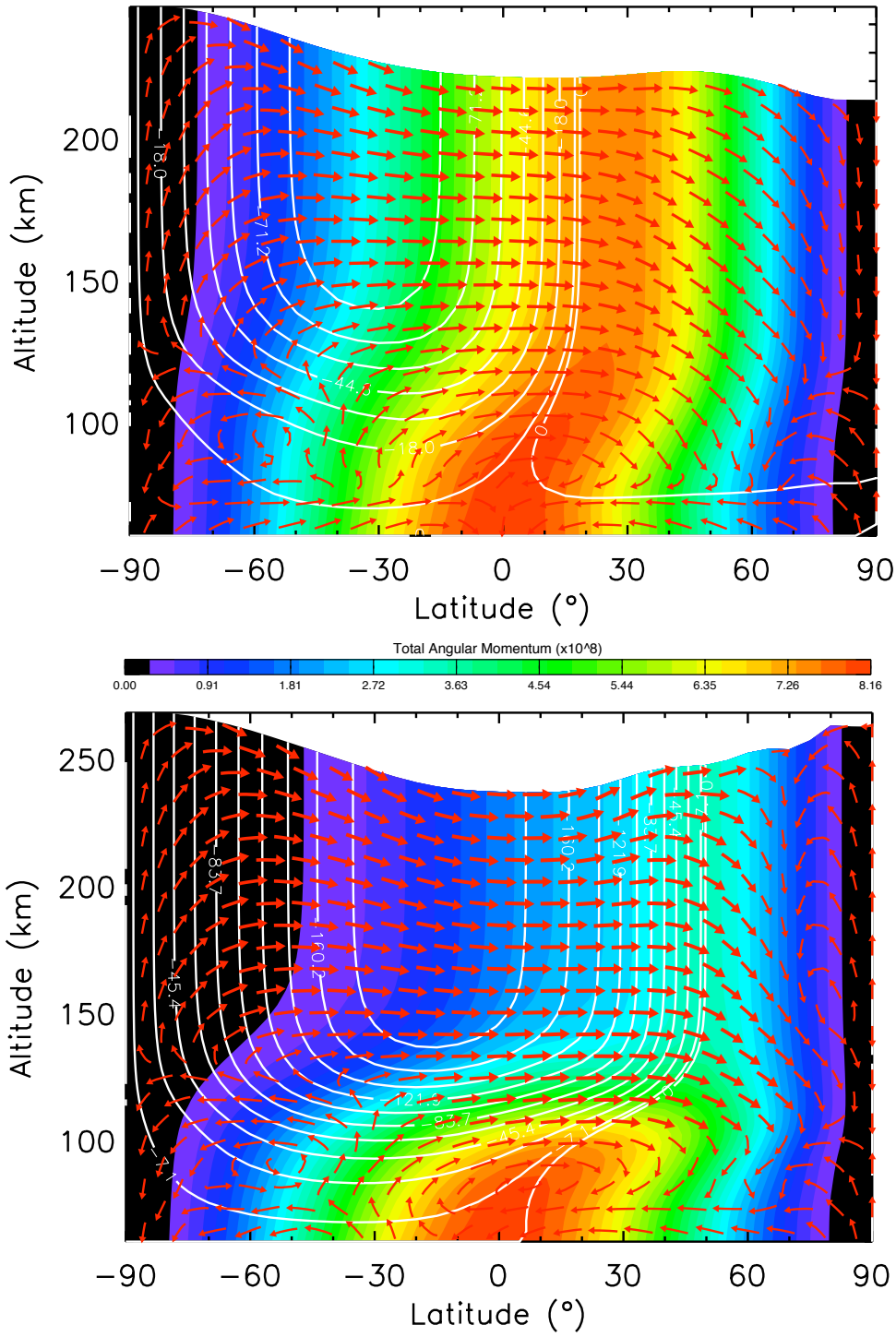

Figure 4.12: Latitudinal slice of MarTIM zonal average total angular momentum (colour contours, 10^8 kg m^2/s), zonal average meridional and vertical winds (red arrows) and zonal average westward winds (white contour lines). Top plot uses old IR heating parameterisation, bottom plot uses new. Solar minimum, Ls 270 (perihelion) for both. Colour scales are coordinated against the scale shown.

Hence in the northern hemisphere (again, $\sin\theta$ is positive) those westward upper atmosphere winds (^-ve v_ϕ) will give a northward acceleration and the meridional flow now actually receives an acceleration

towards the northern winter pole in addition to the acceleration from the gradient of diabatic heating (Forget et al., 1999). Eventually the zonal flow does turn to the east (regardless of the IR heating parameterisation used), so v_ϕ becomes positive and the meridional flow shows a smooth deceleration resulting in a descending motion and adiabatic heating. Since this occurs well into the northern hemisphere itself for the new IR heating parameterisation we can see how the descending branch will lie over the high northern latitudes and produce the polar warming shown. For the old parameterisation the deceleration of northward winds and their descent to the lower atmosphere occurs over a much larger cross-sectional area of the northern hemisphere so that any adiabatic heating is divided over a greater volume of atmosphere and doesn't produce an equivalent polar warming feature.

Southern Winter Polar Regions During Aphelion Conditions

We now take a brief look at the temperatures in the southern winter hemisphere simulated by MarTIM during the opposite aphelion season (Ls 90°). Firstly, Figure 4.13 shows the southern winter equivalent to Figure 4.9 above except that here we consider a constant altitude of 100 km, which is in between where the SPICAM instrument onboard Mars Express measured a moderate 20 to 30 K polar warming (70 and 115 km, Forget et al. (2009)), as noted above. Temperature versus latitude is plotted for the three standard solar cycle conditions (SMIN blue, SMED black and SMAX red). In all three cases the night time average is plotted (1800 to 0600-hrs), the left hand plot using the old IR heating parameterisation, the right hand plot using the new. Next, Figure 4.14 shows latitude by longitude contours of temperatures,

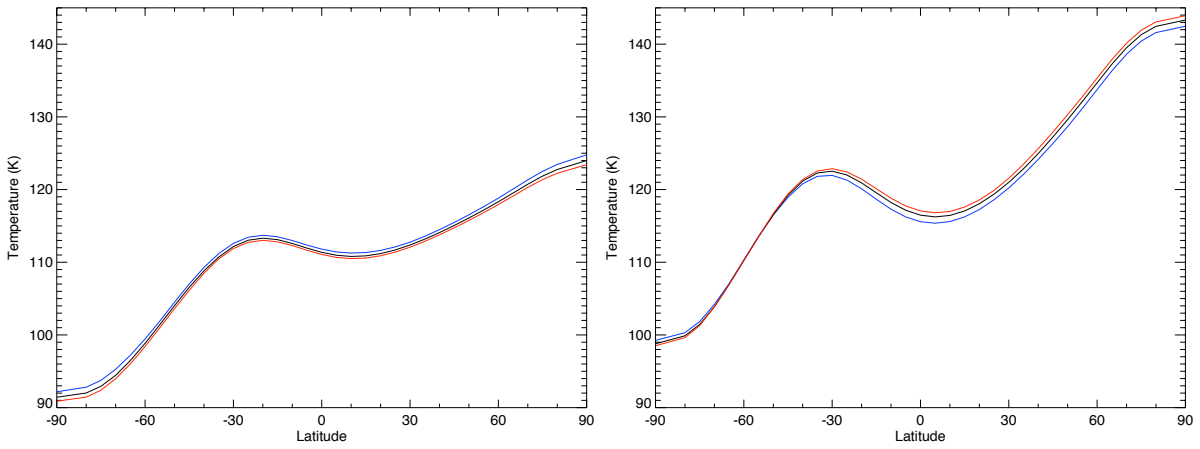

(a) Old IR heating parameterisation

(b) New IR heating parameterisation

Figure 4.13: MarTIM aphelion (Ls 90°) temperatures for SMIN (blue), SMED (black) and SMAX (red) conditions at 100 km for the night time average (1800 to 0600-hrs).

also at constant 100 km altitude simulated by MarTIM for SMIN conditions only. Results using the old (top left) and new (top right) IR heating parameterisation are shown as well as an MCD v4.3 result (bottom) for a very low dust, solar minimum scenario. Now, at aphelion season, this dust setting is a more typical condition that one would expect. Since MarTIM, in this chapter's work, does not yet include lower atmosphere effects (from below MarTIM's lower boundary) this should mean MarTIM and

the MCD are using quite similar background modelling settings, or at least as close as possible without including variations in the thermal signature of Martian surface topography.

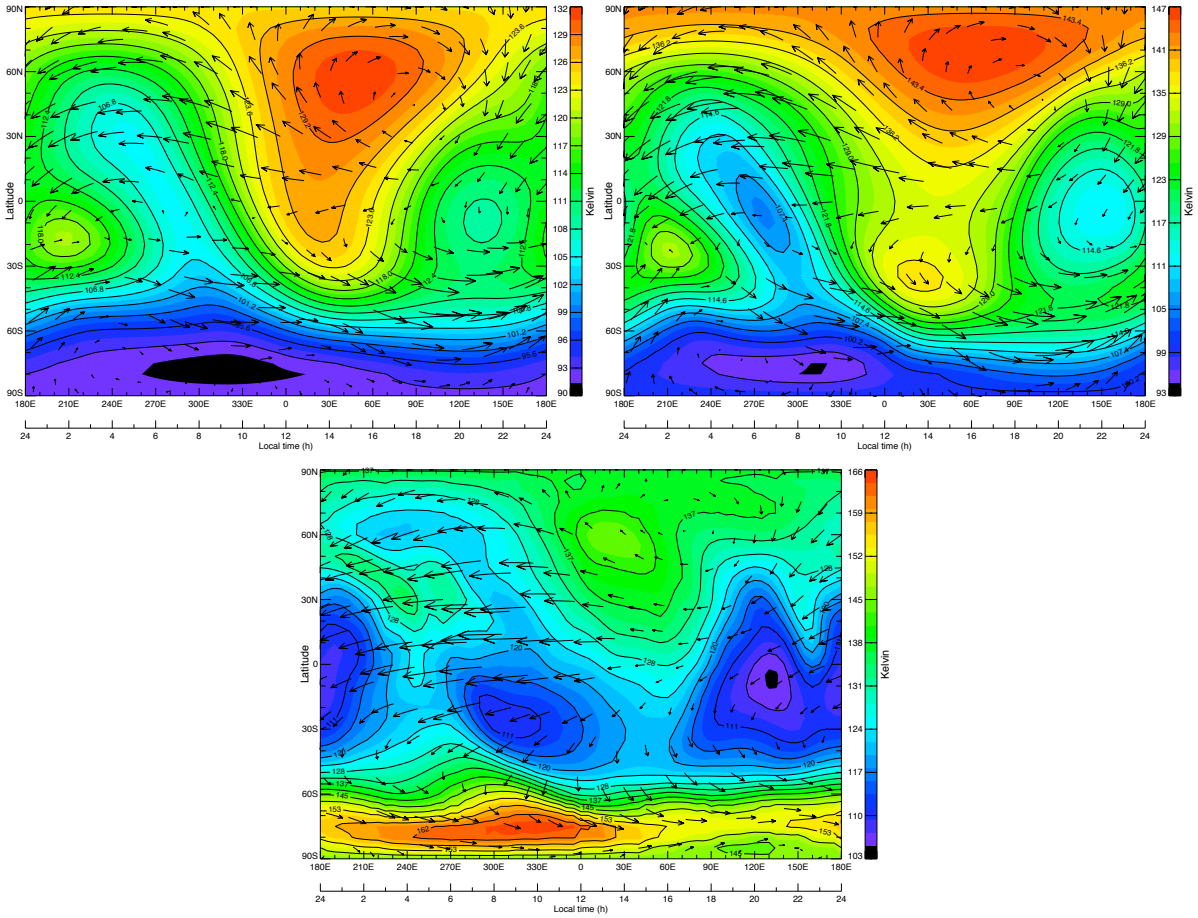

Figure 4.14: MarTIM aphelion (Ls 90°, SMIN) temperatures at constant altitude 100 km with old IR heating parameterisation (top left) and new parameterisation (top right). Also shown (bottom plot) is MCD v4.3 result at 100 km using a low dust scenario. Plots are individually colour coordinated against the scales shown.

The difficulty in simulating possible southern winter hemisphere polar warming effects is that according to spacecraft data (Keating et al., 2008; Forget et al., 2009) and modelling work (González-Galindo et al., 2009a; Lillis et al., 2008) such features are either weak or nonexistent or do not repeat every year. Hence the lack of any winter polar warming could be regarded as a success! Certainly as far as MarTIM and Figure 4.13 are concerned neither the old nor the new IR heating parameterisation produce any discernible polar warming features. There is an increase in temperature in both cases about the 20°S to 50°S region but from Figure 4.14 this actually appears to be a convergence of global wind flow onto the 0000 to 0400-hrs region, having travelled from the dayside northern hemisphere, the likes of which we have seen and discussed several times earlier in Chapter 3 and also earlier here in Chapter 4. It is pointedly different to the southern hemisphere warming that the MCD v4.3 low dust result shows southwards of 50°S (bottom plot, Figure 4.14). This then is perhaps where MarTIM would strongly

benefit from including the influence of lower atmosphere phenomena (below its lower boundary). For example, from Figure 4.13 you can see the strong similarities between the three solar conditions plotted (SMIN blue, SMED black and SMAX red), in addition to the similarity between the old and new IR heating parameterisations. At a constant altitude of 100 km the influence of the IR heating, regardless of the parameterisation used, is probably much reduced from what it would provide in the thermosphere. And certainly a lot less than during the perihelion season (1.657 AU versus 1.388 AU). Hence this is likely to be the season where the lower atmosphere effects that MarTIM currently neglects will have maximum influence on the atmosphere above: because the solar influence is at its weakest. Thus until we can provide MarTIM with a more physically consistent lower boundary (see Chapter 5) we leave this aphelion discussion here.

MarTIM Simulations of Polar Warming Features: Conclusion

We conclude this section on the thermospheric winter polar warming by discussing the results MarTIM simulated during southern summer, perihelion season, when clear differences were modelled between the old and new IR heating parameterisations and when MarTIM showed potential versus the MCD result. Thus, recall section 4.2.2 above regarding the effect of the new IR heating parameterisation on the MarTIM equinox (1.466 AU) solar minimum result. There we highlighted how the new parameterisation had enhanced the lower atmosphere temperatures and general circulation magnitudes. Those lower atmosphere changes influenced right the way to the upper atmosphere because of the greater columnar integrated expansion with a particular emphasis on the $(2, 2)$ tide enhancement in the lower thermosphere. Consequently the structure and magnitude of the zonal average winds were significantly altered, principally because of significant westward momentum deposition.

In this section we are simulating perihelion conditions where the heliocentric distance is near its annual minimum of 1.388 AU. Thus the new IR heating parameterisation now provides a greater global average heating of ∼103 K/day versus 93 K/day at 1.466 AU (still with the new IR heating) and versus ∼72 K/day at 1.388 AU for the old IR heating. We should therefore perhaps expect the difference between the old and new IR heating parameterisations to be similar in form but even greater in magnitude than it was in section 4.2.2. Certainly regarding the form of the difference, Figure 4.12 shows that as in section 4.2.2 significant westward momentum has indeed been deposited throughout the atmosphere with maximum westward (eastward) winds now reaching ∼−198.5 m/s (∼88.6 m/s) for the new parameterisation versus ∼−97.8 m/s (∼101.7 m/s) for the old. Thus faster westward and slower eastward wind speeds. And as noted these westward winds persist well into the northern hemisphere with the new IR heating parameterisation.

What remains to be considered are the differences between MarTIM's temperatures and those derived from Mars Odyssey aerobraking results. As Figure 4.9 showed MarTIM generally struggled to match the temperature structure measured by the Mars Odyssey spacecraft in terms of the magnitude and latitudinal location of the winter polar warming features. Indeed those results (e.g. ∼142 K at 90°N)

were for SMIN conditions. With SMED and SMAX conditions (see section 4.4 below) the differences between MarTIM and Mar Odyssey become greater (e.g. ∼153 K for SMED ∼155 K for SMAX at 90°N). Also Figure 4.11 (bottom plot) showed that although clearly with the new IR heating parameterisation MarTIM was now capable of showing a circulation driven polar warming feature occurring at about 120 km (as was expected from the spacecraft data) in the high northern latitudes its magnitude of ∼17 K (as the difference in temperature at 30°N) was far less than that shown by González-Galindo et al. (2009a), which was more than 40 K (also versus 30°N). Likewise the adiabatic heating of ∼188 K/day northwards of 50°N with the new IR heating parameterisation is towards the lower end of the 100 to 600 K/day adiabatic heating range modelled by González-Galindo et al. (2009a) and even less than the 1200 K/day modelled by Bell et al. (2007).

However in this chapter we have (deliberately) not included lower atmosphere effects (from below MarTIM's lower boundary) such as vertically propagating tides, stationary waves and the effect of dust storms on the geopotential height of MarTIM's lower boundary pressure level. A comparison by González-Galindo et al. (2009a) using a flat globally average topography showed that polar warming features could be up to ∼30 K cooler when these lower atmosphere effects were ignored. It may be, for example, that the basic variation in Martian topography from the southern highlands to the northern plains contributes to the interhemispheric pressure gradient (at constant 120 km altitude), which alongside the gradient of diabatic heating during the southern summer season might enhance the global circulation features still further (than the new IR heating did). On the other hand Moudden and Forbes (2008a) showed how dissipating non-migrating tides deposited significant eastward momentum into the mean flow, which resulted in preventing the intensification of westward winds in favour of eastward jets (for their study of the Ls 60° season). There are therefore important phenomena still to be included in the simulation and their results still to be discussed. We leave this until Chapter 5 when the Mars Climate Database is coupled to MarTIM's lower boundary.

4.4 Global Modelling Parameters: A Discussion

In the above discussion we used the same parameters for the V-T_{CO_2-O} coefficient (1.5×10^{-12} cm^3s^{-1}), the EUV heating efficiency (22%) and the eddy diffusion coefficient (1500 m^2s^{-1}) (as per the setup described in Chapter 3). This was so that we could more closely isolate the effects of the new IR heating profile aside from any changes to model input variables. However choosing such values still remains a somewhat arbitrary exercise i.e. while these values lie within the boundaries implied by spacecraft measurement (Stewart, 1972; Stewart and Hanson, 1982) and by other Mars atmosphere studies (Fox and Dalgarno, 1979; Bougher et al., 1990, 1994; Krasnopolsky, 1993), the boundaries themselves are still quite broadly defined. Thus there remains a fair amount of freedom to choose other combinations of values, also within typically cited boundaries, and still have MarTIM reach an equilibrium. In this subsection then we briefly illustrate by how much the equilibrium result varies when two different sets

of modelling parameters (see Table 4.1) are used. We refer to the set of modelling parameters used up to this point in the thesis as setup A and compare this to the set used throughout the rest of the thesis, which is setup B.

Table 4.1: Comparison of Different Global Modelling Parameters.

Setup	V-T_{CO_2-O} Coefficient	EUV Heating Efficiency	Eddy Diffusion Coefficient
A	1.5×10^{-12} cm^3s^{-1}	22%	1500 m^2s^{-1}
B	2.3×10^{-12} cm^3s^{-1}	23%	1500 m^2s^{-1}

Figure 4.15 considers the influence of the global modelling parameters from Table 4.1 on simulations of the winter northern hemisphere polar warming features discussed in section 4.3.2 earlier. The night time average (1800 to 0600-hrs) of all three of the standard MarTIM solar cycle conditions are shown (blue SMIN, black SMED and red SMAX) as well as the temperatures derived from Mars Odyssey aerobraking measurements of density (blue line with data points). From this figure it seems that using a larger value for the V-T_{CO_2-O} coefficient (setup B), thereby enhancing CO_2 15-μm cooling, has resulted in a uniform cooling of the temperature structures across all latitudes. This is to say that structurally there are few differences between the two plots. For example setup A of Table 4.1, shown in Figure 4.15(a), shows a south pole night time average temperature of ~135 K (SMIN) and a warming of ~25 K (SMIN) northwards of 25°N (from 120 K to 145-146 K at the 90°N). Meanwhile setup B shows a similar magnitude of warming feature, ~25 K but this time it ranges from 115 K to 142-143 K at 90°N i.e. about 5 to 7 K cooler. Likewise the south pole with setup B is now 132 K, so again in the region of 5

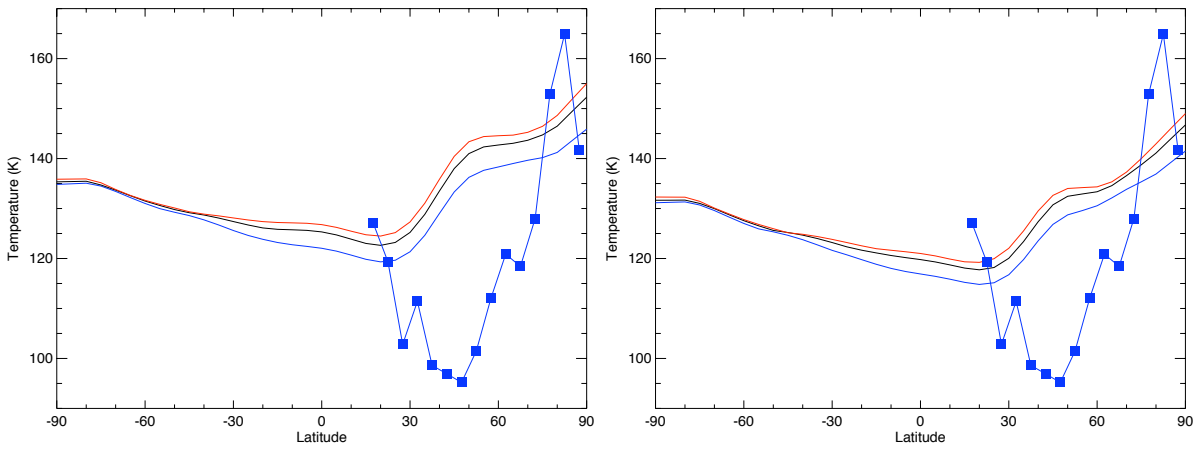

(a) Setup A

(b) Setup B (enhanced CO_2 15-μm cooling)

Figure 4.15: MarTIM perihelion temperatures at 120 km for SMIN (blue), SMED (black) and SMAX (red) simulations versus Mars Odyssey derived temperatures (blue line and data points) at 120 km. Night time average (1800 to 0600-hrs) throughout.

K cooler. Clearly very similar physical processes are being simulated regardless of the global modelling

parameters being used. Or more importantly uniformly increasing the CO_2 cooling has not affected the large-scale feedback mechanisms between the interhemispheric global circulation and adiabatic heating that we are attempting to model.

Next, Figure 4.16 shows MarTIM temperatures at a constant altitude of 120 km for the southern summer conditions we are discussing (results for solar minimum conditions only are shown). Figure 4.16(a) uses setup A from Table 4.1 while Figure 4.16(b) uses setup B (enhanced CO_2 15-μm cooling). As we saw earlier in section 4.3.2, the high northern latitudes at all local times show the effect of the interhemispheric circulation, whereby upon descending from the thermosphere to the mesosphere at high northern latitudes vertical winds generate adiabatic heating that results in the polar warming features plotted (thus Figure 4.16(a) here is the same as Figure 4.10 from section 4.3.2). The effect of the enhanced CO_2 15-μm cooling then (Figure 4.16(b)) is once again to almost uniformly reduce the temperatures across these latitude by longitude plots. So for example the temperature peak at 0900-hrs about 60°N to 70°N has reduced from ∼175.7 K with setup A in Figure 4.16(a) to ∼168.0 K with setup B in Figure 4.16(b). However the structures simulated by MarTIM remain largely untouched, between the two plots of Figure 4.16, regardless of the global modelling parameters used.

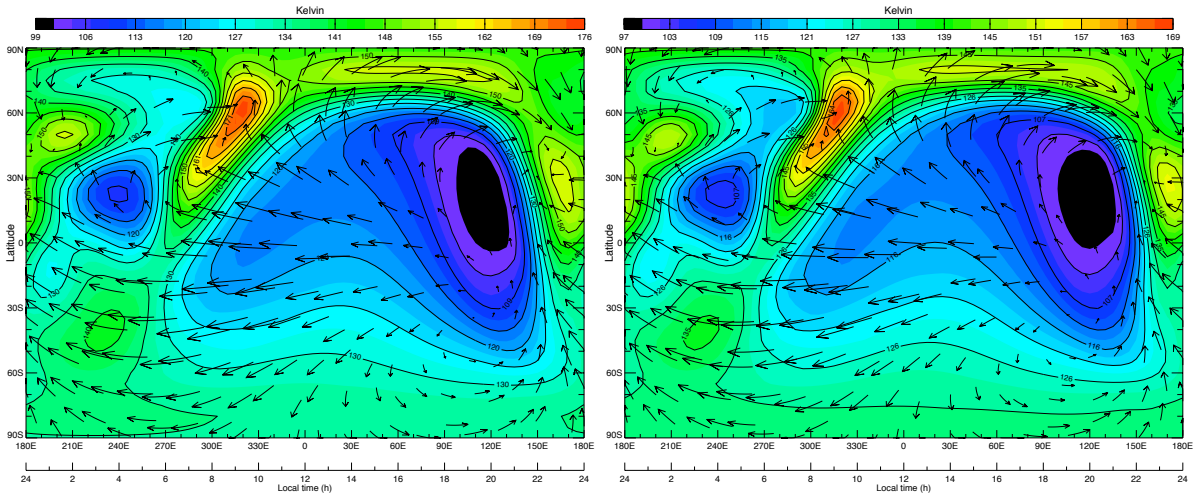

(a) Setup A

(b) Setup B (enhanced CO_2 15-μm cooling)

Figure 4.16: MarTIM perihelion (Ls 270°, SMIN) temperatures at constant altitude 120 km for the two global modelling parameter setups of Table 4.1 (see sub-captions). Colour scales are independent.

Finally in Figure 4.17 we return to the SMIN, equinox (1.466 AU) result discussed earlier in section 4.2.2 regarding the differences brought about by the new IR heating parameterisation. Figure 4.17(c) reminds us what the old IR heating parameterisation result produced alongside setup A. Next, Figure 4.17(a) shows the result using the new parameterisation. It also used setup A from Table 4.1 so we could directly compare the result to the old parameterisation. Finally, Figure 4.17(b) uses setup B as well as the new parameterisation i.e. the combination we use throughout the rest of the thesis.

From Figure 4.17(a) you can see that simply changing from the old to new IR heating parameterisations, while keeping setup A, has enhanced the 0900-hrs adiabatic heating region and made it a dominant

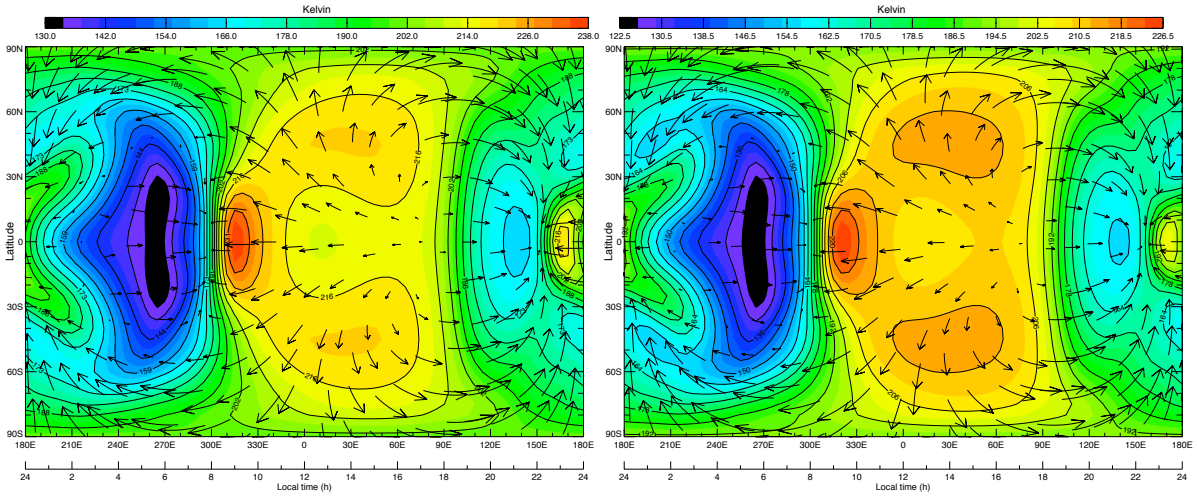

(a) Temperatures (K), PL 30, Setup A, New IR profile.

(b) Temperatures (K), PL 30, Setup B, New IR profile.

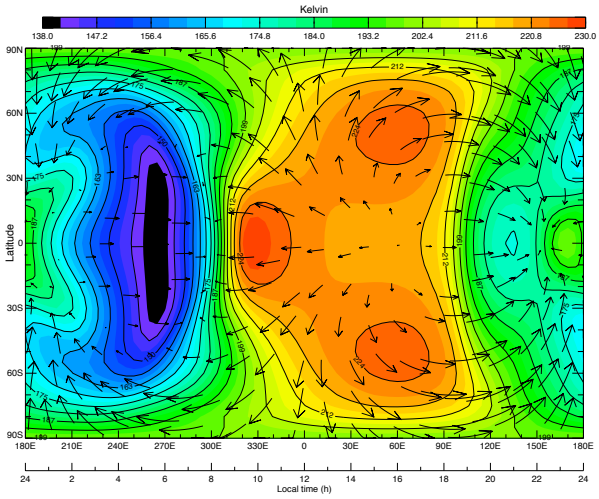

(c) Temperatures (K), PL 30, Setup A, Old IR profile.

Figure 4.17: MarTIM temperatures at PL 30 (4.45×10^{-7} Pa) for the two global modelling parameter setups of Table 4.1 and the old & new IR heating parameterisations (see sub-captions). Colour scales are independent.

feature of the upper atmosphere. The bifurcation of the dayside is no longer as prominent a feature as it was in Chapter 3 (e.g. Figure 4.17(c)). However if we change to setup B (enhanced CO_2 15-μm cooling) with the new IR parameterisation (Figure 4.17(b)) the 0900-hrs temperature peak is efficiently cooled allowing for a better representation of the early afternoon solar EUV/UV driven heating region. Sure enough if you compare Figure 4.17(b) to Figure 4.17(c) you can see both show a more even temperature distribution. The former using the new IR heating and setup B (enhanced CO_2 15-μm cooling), the latter using the old IR heating and setup A. These two figures are much more in-line with what other GCM's suggest is a more physically consistent response of the upper Martian atmosphere e.g. Bougher et al. (1990, 1999b, 2000) as well as what was described in Chapter 3 i.e. that the column integrated IR heating upwards from the middle atmosphere caused upper atmosphere adiabatic expansion and cooling

about the equator throughout the afternoon leaving the localised temperature peaks of Figures 4.17(b) and Figure 4.17(c).

To conclude, it seems that the physical processes modelled by MarTIM, their feedbacks with one another and their overall effect on the result have not changed in structure even though the modelling parameters have. The interhemispheric circulation for example has still generated the polar warming features, which means its structure is also largely untouched between the two parameter setups. And importantly therefore we still see MarTIM approach simulating "real world" phenomena (in the manner we have discussed in section 4.3.2 for example) with the same magnitude, such as this polar warming (in terms of it being the temperature relationship between say 25°N and 90°N as noted above). With this in mind then we have decided to use setup B (enhanced CO_2 15-μm cooling) global modelling parameters in the rest of this thesis. Given that both setup A and B were in steady state we based this opinion on (1) allowing MarTIM's range of solutions for the winter northern hemisphere polar warming features as shown in section 4.3.2 and also Figures 4.15 and 4.16 above to sit more centrally about the northern most point of Mars Odyssey data, which is the case with setup B. Also setup B (enhanced CO_2 15-μm cooling) with the new IR heating parameterisation allowed for a more physically consistent, evenly spread, temperature distribution in the upper atmosphere that we were expecting based upon the background research.

4.5 Solar Cycle Variation of Mars Dayside Exospheric Temperatures

We conclude this chapter by considering MarTIM simulations over a large range of solar conditions ($F_{10.7}$ fluxes) and seasonal conditions. These results are compared against recently obtained Mars exospheric density and temperature data inferred from precise orbit determination (POD) results from the Mars Global Surveyor (MGS) spacecraft (Forbes et al., 2006, 2008).

The precise orbit determination of the MGS spacecraft from early 1999 to mid-2005 allowed exospheric (390 km) density to be measured and temperatures to be inferred based upon the daily analysis of atmospheric drag data. During this period the MGS satellite was in a 93.7° inclination, 1400-0200-hrs sun-synchronous frozen orbit with periapsis confined to 40°S to 60°S latitude (Forbes et al., 2008). The density and temperature results were therefore averages over all longitudes and strongly biased toward the daytime Southern hemisphere. POD data sets were discussed in Forbes et al. (2006) regarding the response of the Martian thermosphere to short term solar flux changes and EUV variability associated with the ∼27-day rotation of the Sun. As noted in Chapter 3, Forbes et al. (2006) highlighted that the exospheric temperature response of Venus and Mars was 10% and 30-50% that of Earth's (respectively). This damping of temperature variability against solar rotation was linked to the relative importance of CO_2 15-μm cooling and O to CO_2 ratios at these two planets over that at Earth.

Then Forbes et al. (2008) used 81-day running means of the POD results to discuss the response of

Mars' exosphere to longer term solar flux changes associated with the 11-year solar cycle. This work showed that the response of Mars' southern hemisphere daytime thermosphere was 36% to 50% that of Earth and about 5 times that of Venus (Forbes et al., 2008). It was suggested that this longer term relationship was connected with adiabatic cooling effects and their progressive importance with solar activity (though differences in CO_2 15-μm cooling rates could also still have a role). Forbes et al. (2008) provided a least squared functional form of the exospheric temperature variation with the solar cycle:

$$T_\infty = 130.7 + 1.53\overline{F}_{10.7} - 13.5 \times \cos\left(L_s - 85^\circ\right) \tag{4.10}$$

Here, the first two terms represent the 81-day mean $F_{10.7}$ flux received at Mars, therefore taking into account the change in heliocentric distance with season (Bougher et al., 2009). The final term is a relatively small seasonal term in solar longitude (L_s) to account for solar declination changes on local insolation (Bougher et al., 2009; Forbes et al., 2008). Note that since Forbes et al. (2008) used averages of data over 4 to 5 days to determine this parameterisation that they were unable to include/comment upon the effects of tides in the lower thermosphere.

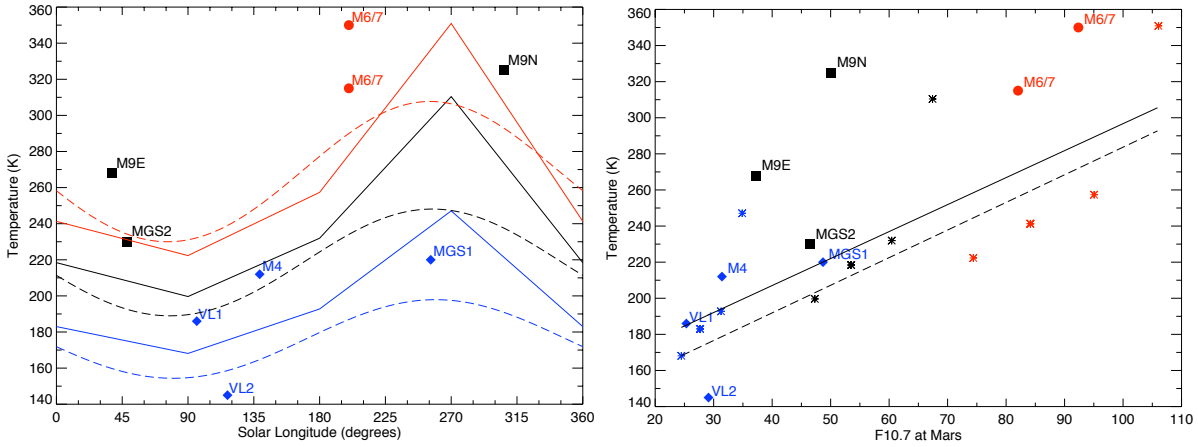

(a) (b)

Figure 4.18: Exospheric temperatures versus (a) solar longitude and (b) $F_{10.7}$ flux at Mars for various MarTIM base runs (solid lines) and MGS Precise Orbit Determination results (dashed lines) (Forbes et al., 2008). Symbols in both figures indicate various spacecraft upper atmosphere data from Bougher et al. (2000), except for asterisks in 4.18(b), which represent MarTIM results. Blue means SMIN $F_{10.7}$=67.2 (at 1 AU), black means SMED $F_{10.7}$=129.9 (at 1 AU), red means SMAX $F_{10.7}$=204.3 (at 1 AU).

The dashed coloured lines of Figure 4.18(a) illustrate the solar cycle variation in temperature of equation 4.10 against solar longitude. We use the same SMIN (blue), SMED (black) and SMAX (red) $F_{10.7}$ fluxes (at 1 AU) as MarTIM, as introduced in section 3.2.1 of Chapter 3, but corrected for heliocentric distance. These dashed lines are to be compared against the similarly coloured solid lines, which come from 12 individual MarTIM simulations using the same set of $F_{10.7}$ flux as well as a full range of seasonal variations in solar declination (L_s= 0°, 90°, 180° and 270°). Next, in Figure 4.18(b) the dashed black

line illustrates the solar cycle variation in temperature against $F_{10.7}$ flux received at Mars using equation 4.10 but with the small seasonal L_s effects removed (i.e. removing the last term in equation 4.10). As in Forbes et al. (2008) and Bougher et al. (2009) this has a gradient of $\Delta T/\Delta\overline{F}_{10.7}\approx1.53$. The coloured asterisks (blue, black and red) in Figure 4.18(b) come from the same 12 MarTIM simulations as Figure 4.18(a) but are now used to produce a least-squares-fit, shown by the solid black line of Figure 4.18(b). This result has a gradient of $\Delta T/\Delta\overline{F}_{10.7}\approx1.49$. Finally, in all plots of Figure 4.18 the coloured symbols that are not asterisks indicate the range of upper atmosphere temperatures measured by various other spacecraft. These are taken from table 1 of Bougher et al. (2000) (see also Table 1.2 in Chapter 1).

As noted, Figure 4.18 includes MarTIM results for similar latitude and local times as the MGS data. Although MGS periapsis altitude was maintained near 390 km (Forbes et al., 2008) we assume isothermal temperatures from MarTIM's simulated exobase (pressure level 35, 3.66×10^{-8} Pa, varies $\sim$185 to 230 km with solar cycle and heliocentric distance) up to this periapsis altitude with the modelled temperatures considered to relate to the thermal (cold) component of the neutral species present, as in the GCM studies of Bougher et al. (2009). Also, from Direct Simulation Monte Carlo modelling of the upper thermosphere/exosphere by Valeille et al. (2010), the temperature is approximately constant with altitude from 200 to 1000 km ($\sim$170 K for SMIN, equinox conditions at 60° solar zenith angle). From Figure 4.18(a) MarTIM simulates well the general variation of exospheric temperatures with solar cycle however it predicts a larger seasonal cycle than observed i.e. the aphelion to perihelion temperature range for each of the blue, black and red $F_{10.7}$ fluxes is larger than that observed. For SMIN (blue) MarTIM temperatures vary by $\sim$79 K (from 168.1 to 247.1 K). For SMED (black) MarTIM temperatures vary by $\sim$110.8 K (from 199.6 to 310.4 K). And finally for SMAX (red) MarTIM temperatures vary by $\sim$128.6 K (from 222.3 to 350.9 K). A larger seasonal cycle variation was also simulated by González-Galindo et al. (2009b).

In Figure 4.18(b) MarTIM simulates well the variation of temperature with $F_{10.7}$. Its $\Delta T/\Delta\overline{F}_{10.7}$ gradient of $\sim$1.49 is close to the $\sim$1.53 for MGS observations. However, MarTIM's result from the least squares fit is typically about 15 K hotter than MGS observations (you can also see an overestimation with the SMIN (blue) and (SMED) solid lines of Figure 4.18(a)). This overestimation of temperatures with season may be due to MarTIM not yet including a parameterisation of neutral photochemistry effects on the atmosphere. The work of González-Galindo et al. (2005) showed that the effect of photochemistry on the upper atmosphere would be to increase the O/CO_2 ratio through the photolysis of CO_2. Since CO_2 heats the atmosphere more effectively than atomic oxygen a higher O/CO_2 ratio would result in less heating. This alongside the enhancement to CO_2 15-μm cooling due to increased O abundance would produce lower temperatures than in simulations without a photochemical scheme. González-Galindo et al. (2005) suggest a maximum temperature difference of about 25 K for zonal mean daytime solar medium conditions at equinox ($\sim$1.594 AU) in the upper atmosphere, where EUV/UV absorption is dominant. Temperatures were up to 25 K hotter when photochemistry was neglected. Future work with MarTIM will have to address this further.

It also seems apparent that MarTIM simulations under SMAX conditions are generally colder than MGS observations for a lot of the Martian year. Indeed by the same token SMED results are not as elevated over MGS observations as the SMIN results are. But as Bauer (1999) explains (see also Bauer and Hantsch (1989) and Rottman (1999)) the $F_{10.7}$ flux is not linearly related to the intensity of EUV radiation outside the absorbing atmosphere. Thus we might not expect SMAX temperatures to increase as greatly against SMED conditions etc. The magnitude of MarTIM's $F_{10.7}$ fluxes were chosen based upon other similar 3D GCM simulations. For example Bougher et al. (1999b) and Bougher et al. (2000) use $F_{10.7}$=200 for SMAX, $F_{10.7}$=130 for SMED and $F_{10.7}$=68 for SMIN conditions. For comparison González-Galindo et al. (2005) use $F_{10.7}$=224.1, 118.3 and 73.8 (for SMAX, SMED and SMIN). Since a single set of $F_{10.7}$ fluxes are not used across these publications there is no reason why our choice for MarTIM is any less valid than these other studies.

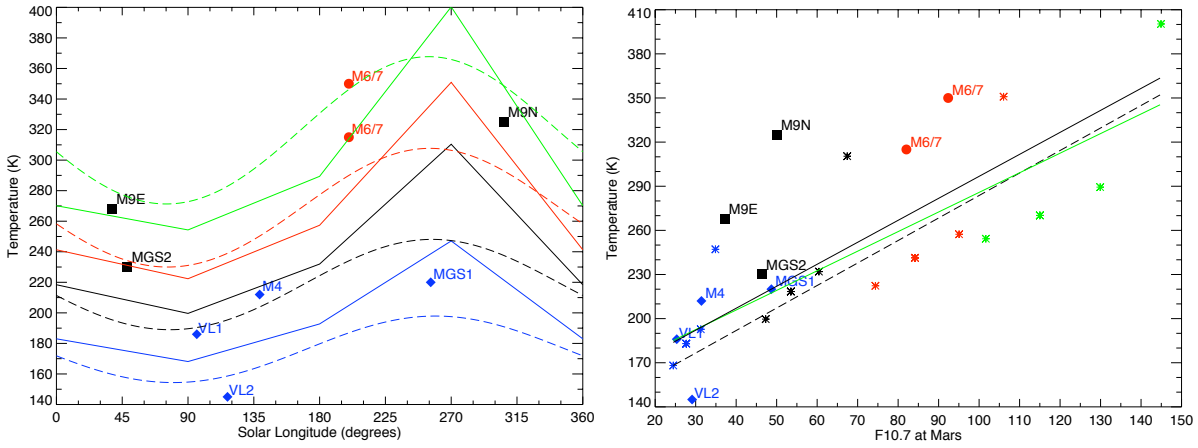

(a) (b)

Figure 4.19: Similar plot to Figure 4.18 but with an additional 4 MarTIM results (green lines & asterisks) that use $F_{10.7}$=279.2 (at 1 AU). (a) Exospheric temperatures versus solar longitude and (b) $F_{10.7}$ flux at Mars. MarTIM results (solid lines) and MGS Precise Orbit Determination results (dashed lines) (Forbes et al., 2008). Blue means SMIN $F_{10.7}$=67.2 (at 1 AU), black means SMED $F_{10.7}$=129.9 (at 1 AU), red means SMAX $F_{10.7}$=204.3 (at 1 AU), green means $F_{10.7}$=279.2 (at 1 AU).

Figure 4.19 considers this further. It shows an additional 4 MarTIM simulations (at L_s= 0°, 90°, 180° and 270°) that used $F_{10.7}$=279.2 at 1 AU (and corrected for the heliocentric distance). With this extra set of results a trend now seems to appear: the gradient $\Delta T/\Delta\overline{F}_{10.7}$ of the green line in Figure 4.19(b) (with the least squares fit now including 16 MarTIM results) is ∼1.33. This versus ∼1.49 from Figure 4.18(b) (with the 12 blue SMIN, black SMED & red SMAX results) and also versus ∼1.53 from the MGS POD data itself. Clearly with a higher $F_{10.7}$ flux MarTIM gets cooler and cooler with respect to what the MGS observations would lead us to expect. This is the effect of a "dynamical thermostat" that Bougher et al. (1999b) and Bougher et al. (2009) mention where the global circulation and molecular thermal conduction combine to regulate upper atmosphere temperature structures and magnitudes. A study by Bougher et al. (1999b) with their Mars upper atmosphere GCM for example showed that when

a steady state SMIN result was switched to SMAX conditions the magnitudes of both the horizontal and vertical winds responded with large increases (both nearly doubled in fact). Thus while at least initially the temperatures did increase under SMAX conditions the nearly doubling of vertical winds at the exobase introduced sufficient adiabatic cooling to actually reduce and eventually reverse this initial temperature increase.

This increasing importance of adiabatic cooling with the solar cycle as a dynamical response of the model to control the dayside upper atmosphere temperatures could also be playing a role in MarTIM. Many examples have already been given throughout this chapter and both Bougher et al. (1999b) and Bougher et al. (2009) (amongst others) discuss how adiabatic heating and cooling associated with global dynamics is especially important on Mars in addition to the role of molecular thermal conduction and CO_2 15-μm cooling. Thus strong vertical winds and expansion on the dayside generate adiabatic cooling while global circulation transports this energy around the planet to the nightside where the descent of air from the thermosphere penetrates the mesosphere and creates a compressional adiabatic heating. These processes were shown in section 4.2.2 to allow the new IR heating parameterisation to influence both the lower and upper atmosphere on the dayside and nightside. Then in section 4.3 these processes were shown to be crucial in producing the winter polar warming effect in the winter hemisphere during southern summer conditions. What has not been addressed however is how lower atmosphere effects from below MarTIM's lower boundary effect our results. In particular how vertically propagating non-migrating tides and dust storm effects on the geopotential height might alter the global circulation and thus affect these adiabatic heating and cooling features.

4.6 Conclusions

From the work of this chapter we draw the following conclusions:

- The new IR heating parameterisation (equations 4.1 and 4.2 and Figure 4.1) was introduced into the model. In section 4.2.2 this was shown to significantly enhance both temperature and circulation magnitudes and structures throughout the atmosphere and at all local times. In particular this was shown to be as a result of significant westward momentum being deposited throughout most of the model (e.g. see Figure 4.4).

- Simulations in section 4.3 showed that with the new IR heating parameterisation MarTIM compared better against Mars Odyssey accelerometer derived temperatures. A distinct region of warming was simulated at high latitude in the northern hemisphere during perihelion conditions (e.g. see Figure 4.11) with the new IR heating.

- Finally, in section 4.5, MarTIM temperatures were compared against 6 years worth of exospheric measurements from MGS Precise Orbit Determination (POD) results over a large range of solar and seasonal conditions. MarTIM's enhanced circulation features (because of the new IR parame-

terisation) alongside molecular thermal conduction were shown to act as a 'dynamical thermostat' to regulate the upper atmosphere temperatures when the solar $F_{10.7}$ flux increases. MarTIM's temperature variation versus $F_{10.7}$ flux showed good comparison with the POD results (e.g. see Figure 4.18).

Next, in Chapter 5, we couple MarTIM (with its new IR heating parameterisation) to a more physically self-consistent description of the 0.883 Pa lower boundary as provided by the the Mars Climate Database. This is then used to study the extent to which the upper atmosphere region is coupled to the lower atmosphere through the middle atmosphere. We also compare model results to recent SPICAM number density and temperature measurements (Forget et al., 2009).

Chapter 5

Coupling MarTIM to the Mars Climate Database

5.1 Introduction

To this point the influence of the lower atmosphere below MarTIM's lower boundary pressure (0.883 Pa) has not been considered. Thus neither the thermal influence of Mars' highly variable topographic relief nor the additional heating generated by the presence of airborne dust have been represented. Also, the interaction between these longitudinally dependent features and the longitudinally invariant solar driven processes have yet to be considered. In this chapter then we discuss how processes such as these have been included by modifying MarTIM's lower boundary using the Mars Climate Database.

5.2 Regarding a Physically Consistent Lower Boundary

The lack of lower atmosphere phenomena has already been cited as a possible reason for some of the limitations in MarTIM's results so far. For example, while in Chapter 4 the upgrade of MarTIM's near-IR heating parameterisation allowed for expected northern winter hemisphere polar warming features to be modelled there were still many aspects of this phenomena that were not simulated accurately. The main conclusion was that perhaps MarTIM was missing an additional component(s) that would enhance the column integrated atmospheric heating and expansion in the same way the new IR heating routine had. It was this enhancement of essentially the entire vertical domain of MarTIM that was responsible for depositing a significant amount of westward momentum into the atmosphere, enhancing the global circulation and, during southern summer season, resulted in heating in the high northern winter latitudes. Thus perhaps including the basic variation in Martian topography from the southern highlands to the northern plains could also contribute to the interhemispheric pressure gradient (at constant altitude). As Withers (2003) points out, one would expect an appreciable hemispheric flux due solely to the extreme

pole-to-pole gradient in topography as well as the changing atmospheric scale height with the seasons that is driven by the condensation and sublimation of CO_2 at the polar caps. Including such pressure variations alongside the gradient of diabatic heating during the southern summer season, which would also be enhanced by including the thermal effect of solar heating of airborne dust (e.g. Forbes (2004), Forbes and Miyahara (2006)), might enhance the global circulation features still further.

The Martian lower atmosphere ($\leq$60-70 km) has long been known to have a significant influence on the upper atmosphere. Regarding the Martian topography, early spacecraft measurements and observations (e.g. Mariner 9 IR spectroscopy (Conrath, 1976)) established that Mars has a large and highly variable relief with topographic heights in some regions exceeding an atmospheric scale height (e.g. see references in Hollingsworth and Barnes (1996), Forbes (2002) and Withers et al. (2003)). Since the surface pressure on Mars is $\sim$100 times smaller than on Earth (Wang and Nielsen, 2004b) there will be a strong solar forcing per unit mass (Lewis and Barker, 2005). Solar thermal forcing will be stronger over high altitude / mountainous areas because essentially the same amount of energy will go into heating a smaller air mass (Zurek and Leovy, 1981). Thus the thermal impression that Mars' topography makes on the atmosphere will remain an influence through a significant vertical domain and the sizeable asymmetry in surface radiation between the southern highlands and the flatter northern plains (recall Figure 1.4 in Chapter 1) will be a significant source of dynamical instability and wave activity, even for low dust conditions (Wilson and Hamilton, 1996; Hollingsworth and Barnes, 1996; Forbes and Miyahara, 2006).

Next, the thermal forcing generated by the presence of airborne dust also plays an important role in influencing the upper atmospheric levels. With a variable lower atmosphere dust opacity there would be an associated variation in solar absorption at that location (Zurek and Leovy, 1981) resulting in an enhanced thermal forcing about the dusty latitude-longitude region. On the other hand, great (planetary-scale) dust storms can introduce significant dust concentrations extending up to $\sim$50 km altitude (Anderson and Leovy, 1978; Smith et al., 2001) that can persist for months after initial injection into the atmosphere (Forbes and Miyahara, 2006). The dust opacity in the lower Martian atmosphere undergoes a strong seasonal variability as well as interannual variations (see references in McDunn et al. (2010)). Total dust loads, dust horizontal extent and the timing and duration of dust storms are relatively consistent from one aphelion season to the next, in contrast to perihelion seasons (McDunn et al., 2010) where dust content is relatively more important given the greater solar insolation (Bougher et al., 2006a).

The enhancement of solar heating in the lower atmosphere due to absorption by dust results in 'inflation' of the entire atmospheric column above (aside from any in-situ energy sources) and increases the heights and densities of constant pressure levels (Bougher et al., 1999b, 2006b). In this sense the lower and upper Martian atmospheres are coupled with the thermosphere sitting atop a highly dynamic lower atmosphere (Bougher et al., 1999b). For example, early spacecraft measurements of atmospheric expansion and contraction observed variation in the height of the ionospheric peak following the onset and abatement (respectively) of global dust storms (e.g. Conrath (1976, 1981); Bougher et al. (1999a)). This also gives rise to significant modifications in the mean atmospheric structure (thermal and zonal

mean winds Forbes and Miyahara (2006)) as well as a whole spectrum of tidal perturbations and wave mechanisms (Angelats i Coll et al., 2004) that are independent of in-situ solar EUV / UV forcing (Bougher et al., 1999a).

This latter point is crucial: the interaction in the lower atmosphere between longitudinally variant and invariant energy inputs is a very important source of tidal activity in the Martian atmosphere. From Lewis and Barker (2005), the interaction between solar EUV / UV forcing and inhomogeneous lower atmosphere thermal properties (e.g. asymmetries in surface thermal inertia, albedo and aerosol distributions) generates tidal components that do not have a constant phase with respect to the Sun. Daily variations in the atmospheric fields will have a dependence on the particular longitude about which the excitation occurred i.e. these are the non-migrating tides we noted in Chapter 4, with $n \neq s$, where n denotes a subharmonic of a solar day and s is the zonal wave number. Their horizontal phase speed ($C_{ph}=\frac{-n\Omega}{s}$) may be different to $-\Omega$, the rotation rate of the planet, and thus they may move faster or slower than the apparent motion of the Sun. Indeed they may even propagate eastward ($C_{ph}>0$) or be standing waves ($C_{ph}=0$) (Hagan et al., 2003).

Accelerometer data (e.g. Withers et al. (2003); Wang et al. (2006)) and radio occultation data (e.g. Hinson et al. (2008)) from more recent spacecraft missions as well as general circulation models (e.g. Wilson and Hamilton (1996); Angelats i Coll et al. (2004); Lewis and Read (2003); Moudden and Forbes (2008b)) have all contributed to our understanding of the non-migrating tides. Mathematically, the surface modulation of solar insolation by topography is given by $\cos(m\lambda - \phi_m)$ and the migrating component by $\cos(n\Omega t + s\lambda - \phi_n)$ (Forbes and Hagan, 2000; Angelats i Coll and Forbes, 2002). Then, from Forbes and Hagan (2000), the interaction between the two is given by the sum and difference terms: $\cos[n\Omega t + (n \pm m)\lambda - (\phi_n \pm \phi_m)]$. Thus Forbes (2004) highlight how if one assumes the topographic component is characterised by zonal wavenumber $m=2$ (the most important topographic zonal wave number component at low to middle latitudes on Mars' surface (Conrath, 1976; Forbes et al., 2002; González-Galindo et al., 2009a)) then the interaction with the 24-h period ($n=1$) westward-migrating solar radiation will excite westward $s=3$ and eastward $s=-1$ propagating diurnal tides.

The eastward $s=-1$ oscillation (the diurnal Kelvin wave (DKW)) is of particular note given that it is in near-resonance in the Martian atmosphere (Forbes, 2004; Lewis and Barker, 2005) because its vertical wavelength is typically comparable to the depth of the effective heating region through which it is excited (Zurek, 1988). Thus constructive interference between the wave structure and the heating region enhances the tides significance. Indeed some of the most important tidal components in the mesosphere / lower thermosphere are the eastward-propagating diurnal tides (Forbes and Miyahara, 2006). For example, comparison between the LMD model and MGS accelerometer data at Ls 65° (Angelats i Coll et al., 2004) showed that the $s=-1$, -2 and -3 components each produced about a 15% variation in density near 115 km. As Moudden and Forbes (2008a) asked, does dissipation of a more complete spectrum of upward propagating tides in the lower thermosphere (100 to 150 km) measurably modify the zonal mean winds temperatures and densities?

The sun-synchronous tides propagating from the lower to upper atmosphere still remain important tidal components. In particular as the dust content of the atmosphere increases the propagating semidiurnal tidal component near the surface and aloft increases by a greater extent than the migrating diurnal response (Wilson and Hamilton, 1996; Forbes and Miyahara, 2006). As Lewis and Barker (2005) and Forbes and Miyahara (2006) explain this is because the relatively shorter vertical wavelength of the diurnal component (∼30-35 km, Forbes and Miyahara (2006)) makes it more susceptible to dissipation than the longer wavelength semidiurnal tide (∼100 km, Lewis and Barker (2005)), especially during dusty conditions when the vertical distribution of solar heating projects well onto the semidiurnal tidal vertical structure. For example Angelats i Coll et al. (2004) showed that for solstice conditions the migrating diurnal tide produced barely a 2% relative density perturbation at 115 km (Forbes and Miyahara, 2006). Also, Lewis and Barker (2005) assimilated thermal and total dust opacity measurements from MGS into the Oxford Mars GCM and showed how closely the migrating semidiurnal tidal amplitude is related to the atmospheric dust content. They found a correlation coefficient of 0.983 between mean dust optical opacity and the amplitude of the surface pressure semidiurnal tide. Finally, the semidiurnal tides relatively long wavelength means it has the potential to propagate into the thermosphere and produce significant density variations at aerobraking altitudes (100 to 170 km) (Forbes and Miyahara, 2006).

None of the above described phenomena can be included with the flat[1], globally averaged, isothermal[2] lower boundary with zero wind velocities used so far. From the above, we have lower atmosphere features that enhance the expansion of the entire vertical atmospheric column above and phenomena that propagate from below and across MarTIM's lower boundary. In this chapter we rely on the Mars Climate Database to provide these to MarTIM's lower boundary and study MarTIM's response.

5.3 The Mars Climate Database Version 4.3

5.3.1 What is the MCD?

To provide MarTIM with a physically self-consistent lower boundary we take values of temperature, geopotential height and horizontal winds (zonal and meridional) from the Mars Climate Database (MCD) version 4.3. The MCD is a database of results derived from multiple runs of circulation models developed by the Atmospheric, Oceanic and Planetary Physics group (AOPP), University of Oxford, the Open University and Laboratoire de Météorologie Dynamique (LMD), Paris (Lewis and Read, 2003; Lewis and Barker, 2005; Lewis et al., 1999; Forget et al., 2008; Millour et al., 2008; Millour and Forget, 2008; Angelats i Coll et al., 2005). Data is supplied both on a DVD or at a live access server[3]. The MCD is queried to provide a description of the 0.883 Pa pressure level that MarTIM can use as a lower boundary rather than using the flat, isothermal and zero wind values of previous chapters.

The MCD atmospheric fields are stored on a 5.625°×3.75° longitude by latitude horizontal grid.

[1] Lower boundary altitude 60 km. See Table 5.1.

[2] Lower boundary temperatures: ∼150 K at SMIN, ∼160 K at SMED and ∼170 K at SMAX. See Table 5.1.

[3] `http://www-mars.lmd.jussieu.fr/`

The vertical grid extends over 50 levels using a hybrid coordinate system such that the lowest 30 levels (l) are essentially terrain-following sigma coordinates ($\sigma(l)=P(l)/P_S$, where P_S is the surface pressure) beginning from near the surface (l=1, ∼5.5 m) and reaching l=19, ∼58 km. The last 20 levels are pressure levels that extend from ∼65 km up to the upper boundary at approximately 275 km (Millour et al., 2008). The data is stored for 12 different universal times in a day with one day stored for each of 12 different Martian months. Martian months cover 30° in solar longitude i.e. 1/12 of a Martian year (Forget et al., 2008), thus given the eccentricity of Mars' orbit the months vary in length from 46 to 66 sols. Software for interpolating to any three-dimensional location, local true solar time and solar longitude are provided on the MCD DVD.

There are four combinations of dust scenarios and three combinations of solar EUV scenarios available from the MCD, designed to reflect the *grosso modo* variability of these forcings in the Martian atmosphere. A dust scenario refers to a prescribed amount and distribution of airborne dust in the simulated atmosphere. The vertical distribution of dust was calculated according to the formula:

$$\frac{Q}{Q_0} = \exp\left(0.007\left(1 - \mathrm{MAX}\left[\left(\frac{P_0}{P}\right)^{(70\mathrm{km}/z_{\max})}, 1\right]\right)\right) \tag{5.1}$$

Where P is pressure (whose dust mixing ratio is Q), P_0 is a standard pressure of 700 Pa (whose dust mixing ratio is Q_0). The MAX function ensures that the dust mixing ratio Q at pressure P is never greater than the ratio Q_0 at the standard pressure P_0=700 Pa. Term $z_{\max}$ is the altitude of the top of the dust layer, which is defined as where $Q=Q_0/1000$ (Millour et al., 2008). Next, the variation in solar EUV output is divided into minimum, medium and maximum scenarios, much like MarTIM uses already. The SMIN scenario has an approximate $F_{10.7}$ value at Earth of 70, that of SMED is 130 while the SMAX scenario refers to a $F_{10.7}$ value of approximately 200. These dust and solar EUV forcings result in eight different combinations of settings, which are:

- (1 to 3) Mars year 24 - representing a typical Martian year in terms of atmospheric dust content as observed by Mars Global Surveyor during Mars year 24-25, but one where no global dust storms occurred. Dust optical depth is taken from the assimilation of MGS TES observations with the dust vertical cut-off altitude as a function of both latitude and solar longitude (see equation 7 in Millour et al. (2008)). This dust scenario is provided for each of the three solar EUV scenarios.

- (4 to 6) Dust storm scenario - representing the Martian atmosphere during a global dust storm (with dust opacity set to τ=4 at 700 Pa and vertical cut-off from equation 7 in Millour et al. (2008)). Solar longitude is restricted to typical dust storm periods i.e. Ls ≥180. This dust scenario is also provided for each of the three solar EUV scenarios.

- (7) Cold scenario - corresponding to an extremely clear atmosphere, with dust optical depth set to τ=0.1 at 700 Pa and the cut-off altitude set to 30 km. This dust scenario is only provided for solar minimum EUV conditions.

- (8) Warm scenario - corresponding to an atmosphere with an upper limit dust opacity during periods that are outside the typical global dust storm periods. Total dust optical depth varies as a function of time to fit Viking Lander observations (but with dust storm measurements removed). This dust scenario is only provided for solar maximum EUV conditions.

Previous work with MarTIM in Moffat (2005) and Moffat-Griffin et al. (2007) has already made use of coupling to the MCD, but with the earlier version 3.1. The main difference between version 3.1 and 4.3 is that the MCD upper boundary has been raised from ∼120 km to ∼275km, meaning we can directly compare MarTIM's results to those of the MCD throughout MarTIM's entire vertical domain. Other changes include better interpolation schemes in solar longitude, local time, vertical and horizontal location (Millour et al., 2008). Lastly, the MCD v4.3 has a more accurate representation of gravity for when integrating the hydrostatic equation during interpolation to a particular pressure level and a new high resolution representation of MOLA topography for accurate computation of the surface pressure.

In Moffat (2005) the coupled MarTIM-MCD model with a low dust setting and solar minimum, equinox conditions was compared directly against the MCD v3.1 result in the region where the two models overlap (PL 1, 0.883 Pa, ∼57 km to PL 9, 1.62×10^{-2} Pa, <120 km) as well as against the MarTIM result without MCD (i.e. with the original flat, isothermal lower boundary). When the MCD was coupled to MarTIM's lower boundary the zonal wind structures began to depart from the MCD only result by pressure level 7 (4.39×10^{-2} Pa) (Moffat, 2005). By this pressure level some of the high latitude zonal wind structures were still present but had begun to spread across the mid-latitudes and equatorial regions in the coupled MarTIM-MCD result. The MCD only result however showed eastward jets still restricted to the high latitudes, with westward winds in the equatorial regions. It became clear in Moffat (2005) that at these higher altitudes (lower pressures) the influence of the MCD at the lower boundary was quickly being replaced with what MarTIM had previously simulated on its own.

Indeed, when the upper atmosphere features were compared (PL 21, 4.01×10^{-5} Pa and PL 29, 7.34×10^{-7} Pa), between the coupled MarTIM-MCD model and MarTIM on its own, the large scale zonal wind structures showed a much better agreement. There were, however, significant increases in the magnitudes of both zonal and meridional winds. From ±60 m/s to +100 and −150 m/s for zonal and ±60 m/s to ±100 m/s for the meridional. Moffat (2005) suggested that the presence of large winds at the lower boundary (as provided by the MCD) were responsible, implying that solar EUV and IR input were not solely responsible for the energetics of the middle and upper atmosphere. Early work in Moffat (2005) had sought to increase MarTIM's middle atmosphere wind field magnitudes with respect to better comparison against other GCM simulations (Bougher et al., 1990; Bougher and Roble, 1991). The presence of the MCD v3.1 at the lower boundary appeared to have gone some way towards that goal.

Moffat (2005) suggested that the differences in IR heating and cooling parameterisations between MarTIM and the MCD could be influencing the middle atmosphere zonal wind patterns and thus cause the differences in lower to middle atmosphere coupled MarTIM-MCD results. Now, in this work, the new

IR heating parameterisation will undoubtedly give us a different result. We have already seen, in Chapter 4, how the new parameterisation markedly altered the zonal wind pattern throughout the atmosphere. Given that this new parameterisation was developed from the LMD model (González-Galindo et al., 2009b) perhaps the comparison between MarTIM-MCD and MCD alone will have improved and made the results comparable over a greater altitude range? Also we can at least continue the comparison between the coupled MarTIM-MCD model to the MCD on its own all the way up to the thermosphere allowing us to see if the dominance of in-situ solar heating affects MCD on its own in the same way it does the coupled model.

5.3.2 Coupling MarTIM to the Mars Climate Database: The New Lower Boundary

It is straightforward to couple the MCD to MarTIM. The pressure level requested from the MCD is fixed at 0.883 Pa and values of temperature, geopotential height and horizontal winds (zonal and meridional) for the particular solar longitude, local true solar time and lower atmosphere dust conditions required are returned on MarTIM's latitude-by-longitude grid. The internal MCD software interpolates the data from its model grid onto MarTIM's, both in terms of 3-D spatial location, but also including interpolating in local true solar time and solar longitude. As with Moffat (2005) the Mars day is divided into 24 hours of universal time[4] (UT) and the MCD is queried for each of these to sample the full range of longitudinal variability with local true solar time ($LTST$). This way the coupling can pass full diurnal variations for each grid point (the local time variation unique to each grid point) at the 0.883 Pa pressure level from the MCD to MarTIM

There are two fundamental differences in this work versus Moffat (2005) regarding how MarTIM is coupled to the MCD. The first regards how Moffat (2005) passed MarTIM's universal time to the MCD, for all latitudes and longitudes. That is, the local true solar time at the prime meridian (0° E) only rather than calculating the specific local true solar time of the particular latitude and longitude east location of the MarTIM grid point being considered. This will have meant that MarTIM's entire latitude-by-longitude grid at 0.883 Pa will have been using MCD input at a single time, that of the universal time (0° E). Although the universal time will have advanced as the planet rotated, the local true solar times of individual grid points away from 0° E were not recalculated, they were instead all set equal to the particular universal time. We now use the universal time and longitude east location within equation 5.2 to correctly calculate the specific local true solar time of the particular grid point being considered.

$$LTST = \text{DMOD}\left[\left(UT + \left[\left(\frac{24.0}{londim}\right) \times (l-1)\right]\right), 24.0\right] \tag{5.2}$$

Where $londim$ is the number of longitude dimensions in MarTIM's horizontal grid and l is the longitude grid counter ($l \in [1 : londim]$). With this change the thermodynamics of each grid point will now uniquely

[4]The local true solar time at the prime meridian - longitude 0° East.

depend not only on its latitude and longitude but also on its particular local time. Consequently the full synoptic variability will be passed from the MCD to MarTIM (within the limitations of whatever averaging has been applied to the MCD data for it to fit onto the supplied DVD).

The second difference in how we couple MarTIM to MCD concerns problems that arose with the horizontal advection of energy and the horizontal geopotential gradients. Simulations with the coupled MarTIM-MCD model (with the above changes made) were typically unstable and thus would often fail to reach an equilibrium or produce non-physical results. Investigation showed that negative temperatures would often be calculated over several thermospheric pressure levels though usually restricted to just a single grid point (or small grouping of points) in latitude and longitude at each of those pressure levels. Moreover, while grid points to the west of the negative temperature point would also be excessively cold those grid points to the east would be far too hot (e.g. 350-400 K for SMIN conditions). Considering each term in the energy equation showed that the zonal advection of total energy (internal plus kinetic) had a huge positive gradient as one moved eastwards across the region of the instability. Thus strongly removing energy and cooling the atmosphere at the point of (and just to the west of) the negative temperature grid point while at the same time strongly heating the point just to the east.

The wind magnitudes had been significantly enhanced at all pressure levels by coupling MarTIM to the MCD. The zonal winds in particular were now depositing much more energy than previously through adiabatic compressional heating in regions where eastward and westward winds converged. The term responsible (equation 5.3) from the energy equation (see equation 2.18), involved horizontal (zonal) gradients of both total energy and geopotential:

$$[-\underline{v}.\nabla_P(\epsilon+\Phi)]\,\hat{\mathbf{e}}_\phi = \frac{-v_\phi}{r\sin\theta}\left(\frac{\partial\epsilon}{\partial\phi}+\frac{\partial\Phi}{\partial\phi}\right) \tag{5.3}$$

$$\text{with energy equation 2.18: } \frac{\partial\epsilon}{\partial t} = -\underline{v}.\nabla_P(\epsilon+\Phi) - \omega\frac{\partial}{\partial P}(\epsilon+\Phi) + \underline{v}.\underline{F} + \dot{Q}$$

$$\text{and del operator 2.2: } \nabla_P = \frac{1}{r}\frac{\partial}{\partial\theta}\hat{\mathbf{e}}_\theta + \frac{1}{r\sin\theta}\frac{\partial}{\partial\phi}\hat{\mathbf{e}}_\phi$$

Where r=$(a + h(n,\theta,\phi))$ is the radius of the planet (a) plus the geopotential height of your location ($h(n,\theta,\phi)$, for pressure level n), ϵ is the total (internal plus kinetic) energy, Φ is the geopotential and $\hat{\mathbf{e}}_\phi$ is the unit vector in the zonal direction. In equation 5.3, $\frac{-v_\phi}{r\sin\theta}\left(\frac{\partial\epsilon}{\partial\phi}\right)$ represents the transport of total energy through the horizontal winds flowing along isobaric levels. Then $\frac{-v_\phi}{r\sin\theta}\left(\frac{\partial\Phi}{\partial\phi}\right)$ represents the work done per unit time by the horizontal winds either against the horizontal pressure gradient or the component of gravity projected along the tilted pressure level (Achilleos et al., 1998).

With further study and private correspondence[5] the large variations in geopotential height with latitude and longitude introduced by coupling to the MCD were identified as a significant contribution to global wind magnitudes. Geopotential heights ($h(n,\theta,\phi)$) appear as Φ=$gh(n,\theta,\phi)$ in the term $\frac{-v_\phi}{r\sin\theta}\left(\frac{\partial\Phi}{\partial\phi}\right)$. From the MCD we take the geopotential heights to be the altitude above the Martian zero datum i.e. the Mars geoid or areoid (Forget et al., 2008). Now, from the MCD DVD the Martian areoid radius ranges from ∼3378.2 km at the poles to ∼3397.4 km at the equator i.e. it is a flattened spheroid.

[5]Professor Alan D. Aylward and Dr Chris Smith of the Atmospheric Physics Laboratory, UCL.

Thus regardless of any local pressure gradients due to localised heating and cooling processes, there is already a variation of ∼19.2 km influencing the geopotential term generating significant winds across MarTIM's pressure levels. This isn't present at all when MarTIM is run with a flat lower boundary and thus will introduce advective heating and cooling processes not dealt with by simulations without the MCD.

Furthermore the very variation in topography across the Martian surface will mean surfaces of constant geopotential in the MCD atmosphere between the surface and MarTIM's lower boundary cannot be easily defined; they will be neither spherical nor aligned with pressure level surfaces as we have approximated for the lower boundary so far. Consequently by coupling MarTIM's lower boundary to the MCD we introduce large variations in geopotential height and the associated pressure gradients will also drive fast winds. Since we cannot be sure MarTIM's lower boundary pressure level is aligned with a surface of constant geopotential we simply decided to assume that the 0.883 Pa surface provided by the MCD was itself a surface of constant geopotential thereby assuming that there are no pressure gradients along MarTIM's lower boundary. Thus regardless of any changes in geopotential height of the 0.883 Pa pressure level there would be no changes in the geopotential across this surface.

The necessary changes were achieved by replacing geopotential height $h(n, \theta, \phi)$ at the location being considered with $(h(n, \theta, \phi) - h(1, \theta, \phi))$ taking the value of $h(1, \theta, \phi)$ from the MCD. This change was made both in equation 5.3 of the energy equation, as well as in the meridional direction (equation 5.4) and finally also in the geopotential gradient terms of the momentum equation (equations 5.5 and 5.6):

$$[-\underline{v}.\nabla_P(\epsilon + \Phi)]\,\hat{\mathbf{e}}_\theta = \frac{-v_\theta}{r}\left(\frac{\partial \epsilon}{\partial \theta} + \frac{\partial \Phi}{\partial \theta}\right) \tag{5.4}$$

$$[-\nabla_P \Phi]\,\hat{\mathbf{e}}_\phi = \frac{-1}{r\sin\theta}\left(\frac{\partial \Phi}{\partial \phi}\right) \tag{5.5}$$

$$[-\nabla_P \Phi]\,\hat{\mathbf{e}}_\theta = \frac{-1}{r}\left(\frac{\partial \Phi}{\partial \theta}\right) \tag{5.6}$$

By relating the geopotential height at some pressure level to its value at the lower boundary we remove any influence from below MarTIM's lower boundary that might create very large gradients in geopotential. Instead the horizontal gradients are now calculated based solely on neighbouring values at the same pressure level. To see how this helps reduce large magnitude pressure gradients and associated winds, consider that if the atmosphere was isothermal, or more realistically if temperature variation between the lower boundary and the first few pressure levels was small, then the altitude difference between these pressure levels and the lower boundary would be constant. Hence there would be no geopotential gradients on those pressure levels. Importantly though the temperature, height and wind structures from the MCD would still be passed over to MarTIM. Thus ultimately since MarTIM will re-calculate all other terms during the simulation run, for example, the geopotential heights upwards from PL 2 (5.36×10^{-1} Pa) being re-calculated using values of temperature and scale height, the entire model still progresses under the MCD's influence.

In section 5.4.1 to 5.4.3 the above changes are used and we discuss its implications and alternatives in section 5.4.4.

5.4 Studies with the Coupled MarTIM-MCD General Circulation Model

5.4.1 General Lower Boundary Influence: Lower Atmosphere

To consider the impact of coupling the MCD to MarTIM on the first few pressure levels of the modelled atmosphere Figures 5.1, 5.2, 5.3 and 5.4 all show latitude by longitude contour plots of temperatures, with wind vectors overlaid, at pressure level 2 (5.36×10^{-1} Pa) for equinox conditions (1.47 AU). Each figure compares the steady state result of (1) top left, a coupled MarTIM-MCD simulation where MarTIM's 3-D volume mixing ratios are used within the CO_2 15-μm cooling routine, (2) top right, a coupled MarTIM-MCD simulation where the MCD's 3-D volume mixing ratios are used within the CO_2 15-μm cooling routine (and are updated from the MCD every hour of the simulation run), (3) bottom left, the MCD result on its own, direct from the DVD and (4) bottom right, the MarTIM result on its own, with the flat, isothermal lower boundary i.e. without the MCD coupled.

A wide range of solar conditions and lower atmosphere dust distributions are shown by the four figures. Figure 5.1 shows the results for solar minimum conditions with very low dust content in the lower atmosphere (scenario 7 from section 5.3.1), Figure 5.2 shows the results for solar minimum conditions with an annually averaged dust content in the lower atmosphere (scenario 1 from section 5.3.1). Figure 5.3 shows the results for solar minimum conditions with dust content typical of a global dust storm present in the lower atmosphere (scenario 4 from section 5.3.1). Finally Figure 5.4 shows the results for solar maximum conditions with very high dust content in the lower atmosphere (scenario 8 from section 5.3.1). Table 5.1 shows the temperatures and geopotential heights introduced at 0.883 Pa (PL 1) by these setups versus MarTIM on its own.

Table 5.1: 0.883 Pa Temperatures and geopotential heights versus MarTIM for various MCD inputs.

Setup	Temperature(K)	Geopotential height (km)
MarTIM alone, SMIN	149.5[a]	60.0
MarTIM alone, SMAX	170.4[a]	60.0
MCD, SMIN, very low dust	153.5[b]	54.0[b]
MCD, SMIN, annually averaged dust	155.4[b]	57.8[b]
MCD, SMIN, global dust storm	172.8[b]	67.9[b]
MCD, SMAX, very high dust	159.8[b]	61.2[b]

[a]Isothermal lower boundary temperature.
[b]Pressure level average value.

From Figures 5.1 through to 5.4 the difference introduced to MarTIM's steady state result at PL 2 (5.36×10^{-1} Pa) by the presence of the MCD at the lower boundary is clearly seen. In all cases PL

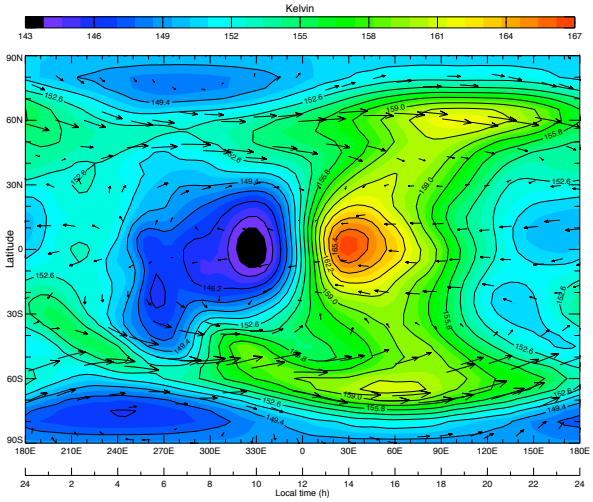

(a) Coupled MarTIM-MCD with MarTIM volume mixing ratios. Average height 58.16 km, temperature 153.5 K.

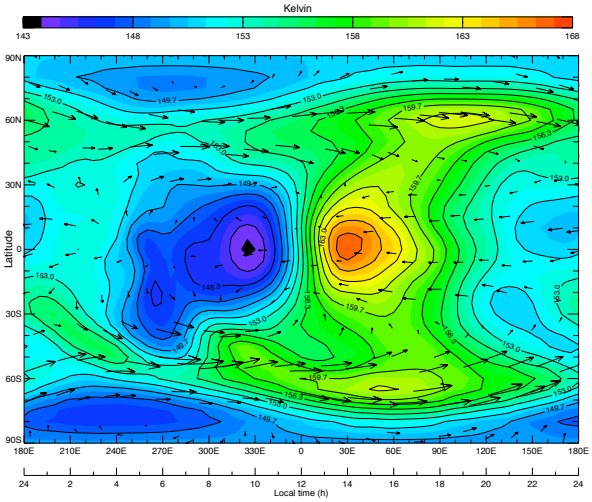

(b) Coupled MarTIM-MCD with MCD volume mixing ratios. Average height 58.16 km, temperature 153.9 K.

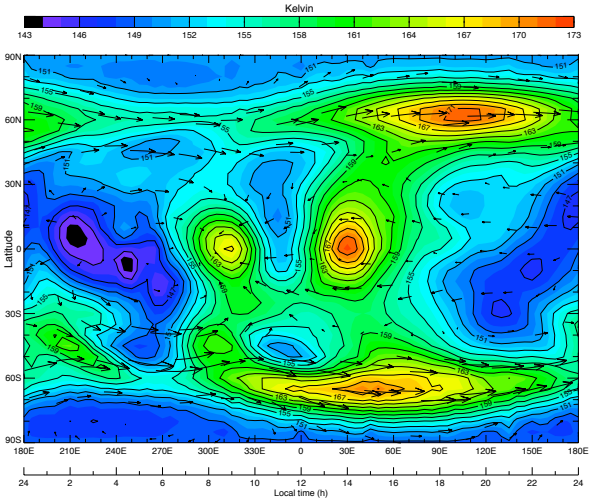

(c) MCD alone (UT 1200-hrs). Average height 58.14 km, temperature 154.9 K.

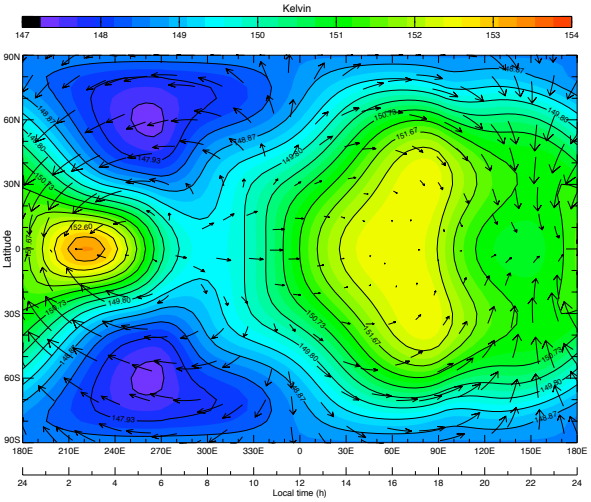

(d) MarTIM alone. 64.02 km, temperature 150.4 K.

Figure 5.1: Temperatures (and wind field vectors) at constant pressure level 2 (5.36×10^{-1} Pa) for coupled MarTIM-MCD simulations (with and without MCD volume mixing ratios for CO_2 15-μm cooling), MarTIM alone (flat lower boundary) and MCD alone (direct from DVD, for UT 1200-hrs). Solar minimum and very low dust (scenario 7) throughout.

2 (5.36×10^{-1} Pa) now shows far more structure in the temperature field when MarTIM is coupled to the MCD (top row plots) than it did with the flat, isothermal lower boundary (bottom right plots). The change in temperature magnitudes between the MarTIM alone and coupled MarTIM-MCD results is also notable. Often the maximum is greater for the coupled result, other times the minimum is lower. From the colour scales shown this trend can be seen to increase as the dust content of the lower atmosphere increases. For example the difference in temperature maximum between the coupled MarTIM-MCD result with very low dust (top left, Figure 5.1) and MarTIM alone (bottom right, Figure

5.1) is ∼13.4 K. With average dust (Figure 5.2) this rises to ∼15.9 K and finally to ∼31.1 K for global dust storm conditions (Figure 5.3). Generally the additional solar heating that the MCD introduces below MarTIM's lower boundary has created these temperature structure and magnitude differences over the lower MarTIM pressure levels (versus MarTIM alone results).

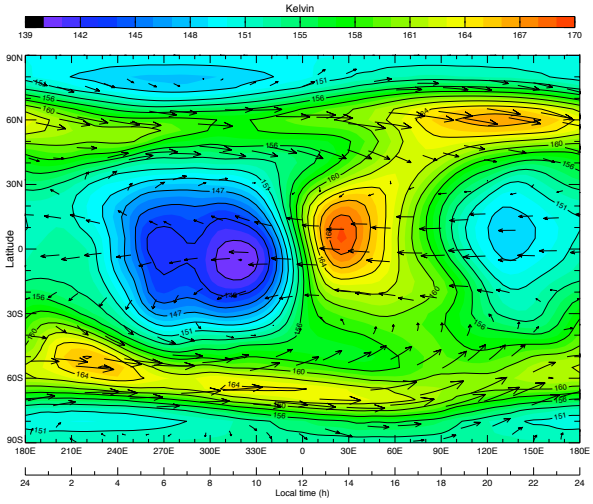

(a) Coupled MarTIM-MCD with MarTIM volume mixing ratios. Average height 61.99 km, temperature 154.9 K.

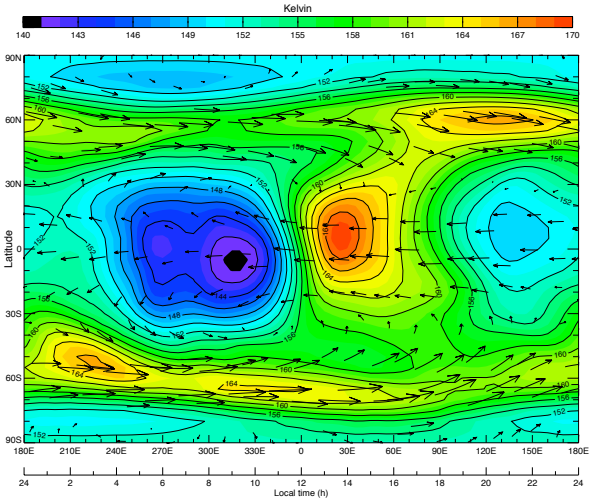

(b) Coupled MarTIM-MCD with MCD volume mixing ratios. Average height 61.99 km, temperature 155.3 K.

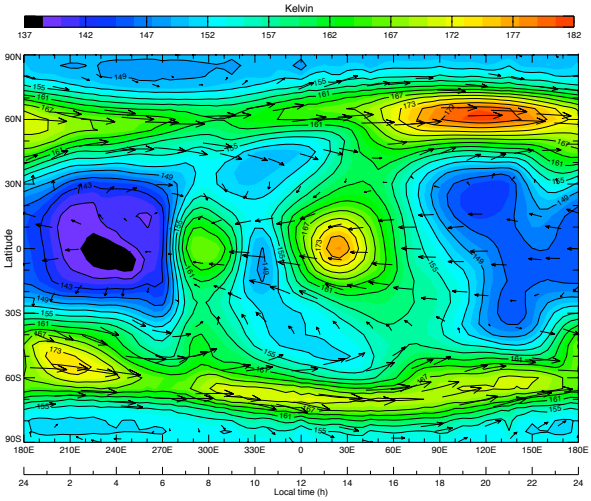

(c) MCD alone (UT 1200-hrs). Average height 61.96 km, temperature 155.5 K.

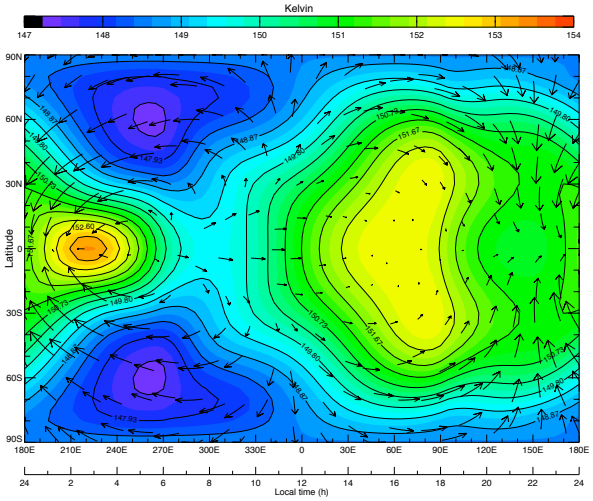

(d) MarTIM alone. Average height 64.02 km, temperature 150.4 K.

Figure 5.2: Temperatures (and wind field vectors) at constant pressure level 2 (5.36×10^{-1} Pa) for coupled MarTIM-MCD simulations (with and without MCD volume mixing ratios for CO_2 15-μm cooling), MarTIM alone (flat lower boundary) and MCD alone (direct from DVD, for UT 1200-hrs). Solar minimum and average Mars year 24 dust (scenario 1) throughout.

Hence, even with very low dust content, the MCD presence creates a greater maximum versus MarTIM alone. At the same time, when dust content is increased, the increased heating this brings to the lower atmosphere will produce the particular trend noted. There is little difference between the coupled results

when MarTIM mixing ratios are used in the CO_2 15-μm cooling routine versus when MCD ratios are used (and updated in 3-D every hour of the simulation). This simply reflects the minimal role the IR cooling has at these high pressures (low altitudes) as well as the very low atomic oxygen content in both mixing ratio sets at PL 2 (5.36×10^{-1} Pa).

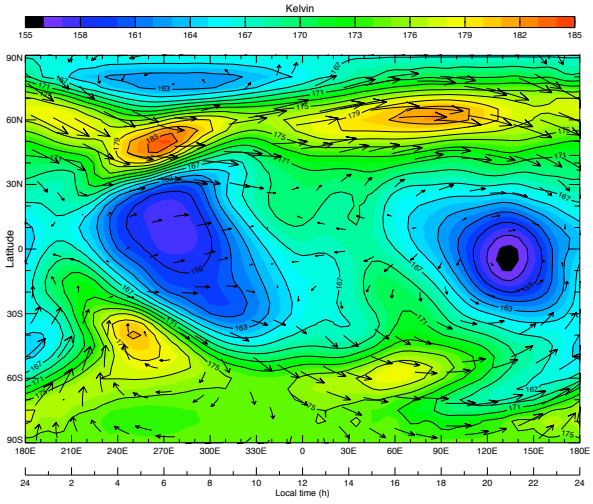

(a) Coupled MarTIM-MCD with MarTIM volume mixing ratios. Average height 72.63 km, temperature 168.3 K.

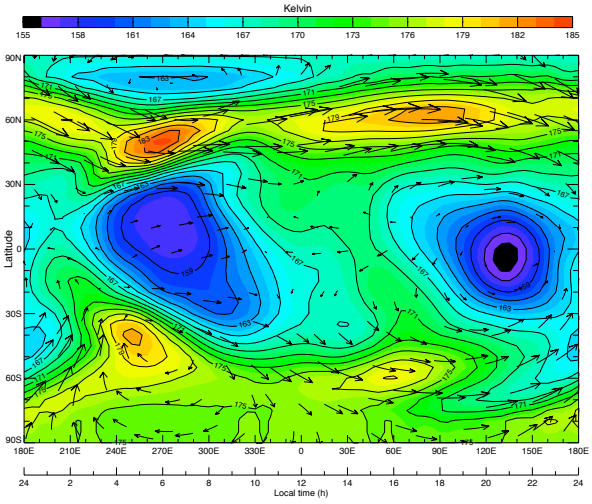

(b) Coupled MarTIM-MCD with MCD volume mixing ratios. Average height 72.63 km, temperature 168.5 K.

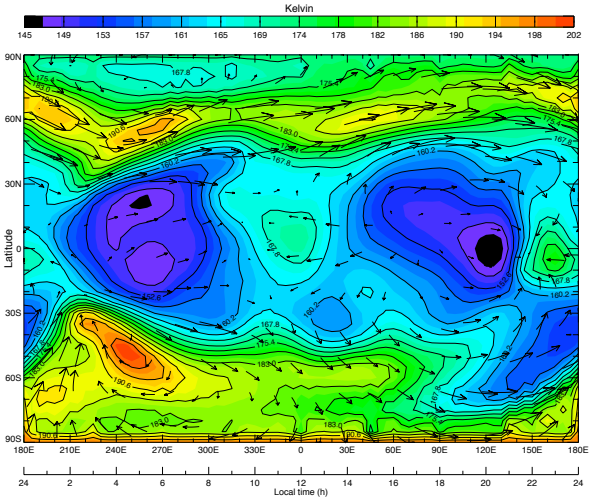

(c) MCD alone (UT 1200-hrs). Average height 72.47 km, temperature 166.1 K.

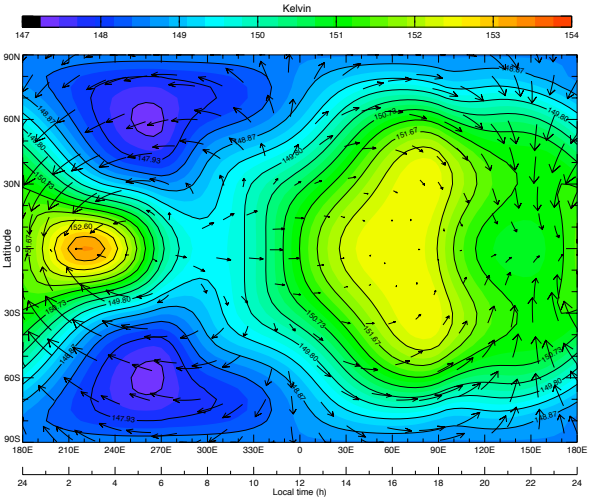

(d) MarTIM alone. Average height 64.02 km, temperature 150.4 K.

Figure 5.3: Temperatures (and wind field vectors) at constant pressure level 2 (5.36×10^{-1} Pa) for coupled MarTIM-MCD simulations (with and without MCD volume mixing ratios for CO_2 15-μm cooling), MarTIM alone (flat lower boundary) and MCD alone (direct from DVD, for UT 1200-hrs). Solar minimum and global dust storm conditions (scenario 4) throughout.

Regarding the temperature structures themselves, a persistent feature regardless of both lower atmosphere dust content and solar conditions seems to be bands of high temperature about the mid-latitudes from $\pm30°$ latitude to approximately $\pm75°$ latitude (typically with maximums at $\pm60°$ latitude). Often

the maximums are situated about the evening terminator (∼1800 to 2200-hrs local time) though with greater dust content in the lower atmosphere usually a much larger range of local times show significant temperature magnitudes (though typically still within the latitude bands noted). These temperature bands are closely aligned with regions of strong eastward wind (see Figure 5.5). Thus mid-latitude (also usually with peaks at ±60°) eastward jets are seen to encircle the planet with westward winds, that are fast but don't usually reach the same peak speeds as the eastward winds, dominating the low latitude tropics.

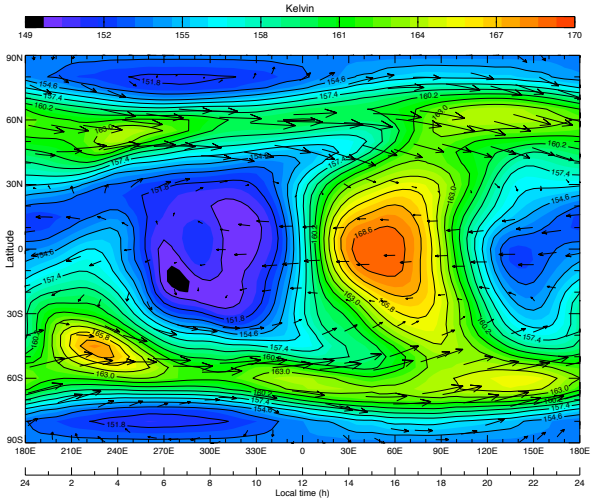

(a) Coupled MarTIM-MCD with MarTIM volume mixing ratios. Average height 65.45 km, temperature 158.2 K.

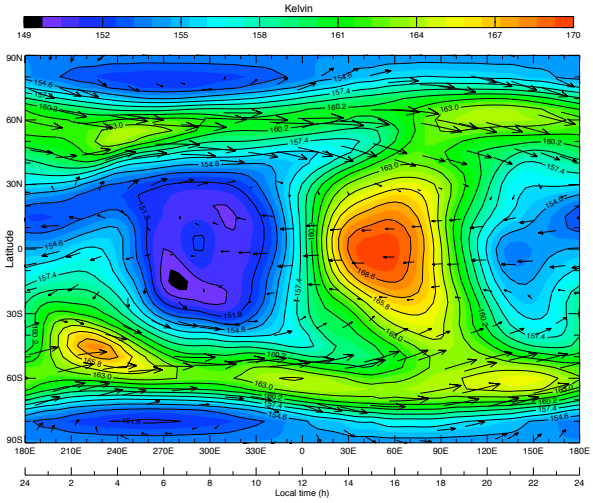

(b) Coupled MarTIM-MCD with MCD volume mixing ratios. Average height 65.45 km, temperature 158.5 K.

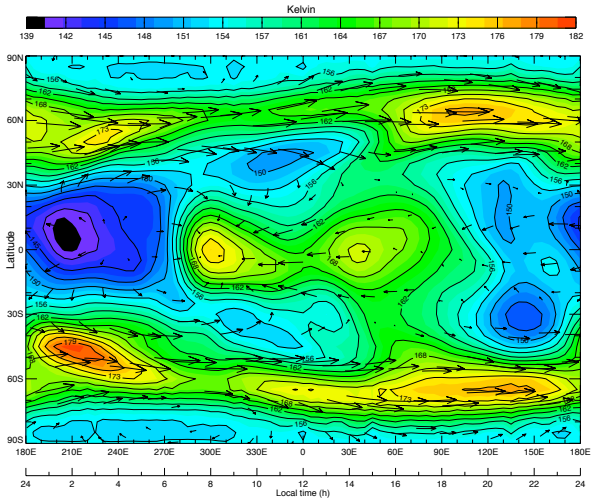

(c) MCD alone (UT 1200-hrs). Average height 65.43 km, temperature 159.1 K.

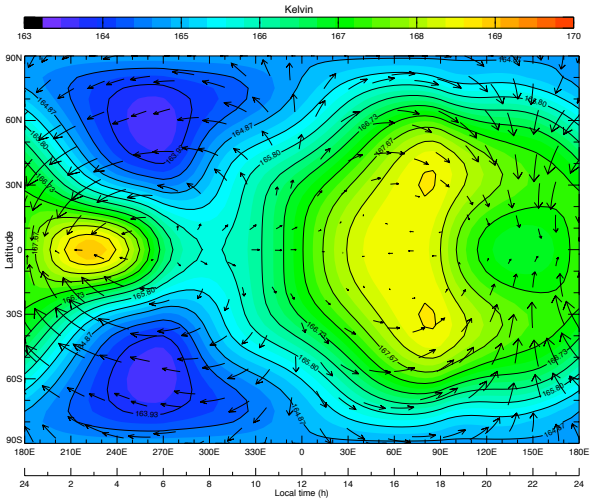

(d) MarTIM alone. Average height 64.58 km, temperature 166.5 K.

Figure 5.4: Temperatures (and wind field vectors) at constant pressure level 2 (5.36×10^{-1} Pa) for coupled MarTIM-MCD simulations (with and without MCD volume mixing ratios for CO_2 15-μm cooling), MarTIM alone (flat lower boundary) and MCD alone (direct from DVD, for UT 1200-hrs). Solar maximum and high dust (scenario 8) throughout.

Mars atmosphere modelling studies (Lewis and Read, 2003; Wilson and Hamilton, 1996) show that lower atmosphere diurnal thermal tides drive super-rotating jets (eastward winds) in the equatorial regions about and below 30 km altitude (Forbes and Miyahara, 2006). Indeed zonal mean winds in this altitude region remain eastward over all latitudes, with peaks about $\pm 60°$ latitude between $\sim$10 to $\sim$1.0 Pa ($\sim$40 to $\sim$60 km). The strength of the equatorial super-rotating jets was shown by Lewis and Read (2003) to be closely related to the dust content of the lower atmosphere and to be strongest for equinox conditions, when latitudinally symmetric tidal modes are forced. The magnitude and range of altitudes covered by super-rotation increased with greater lower atmosphere dust content. Then, at higher altitudes (greater than $\sim$40 km), these eastward winds would become strong westward winds due to the dissipation of the diurnal thermal tides as they propagate upwards (Forbes and Miyahara, 2006) and deposit westward momentum into the background atmosphere (Lewis and Read, 2003). The symmetric latitudinal structure of the diurnal tide, with a single peak over the equator (Lindzen, 1990), determines that this occurs predominantly over equatorial and sub-tropical latitudes.

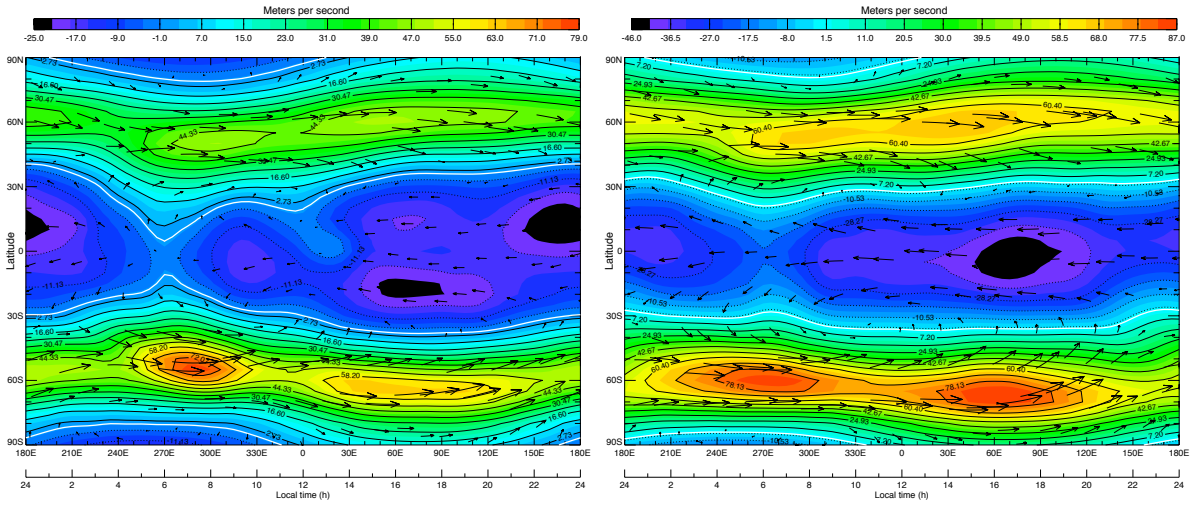

Figure 5.5: Zonal wind (and wind field vectors) at constant pressure level 2 (5.36×10^{-1} Pa) for coupled MarTIM-MCD simulations (with MarTIM volume mixing ratios for CO_2 15-μm cooling). Left plot shows very low dust (scenario 7), right plot shows average Mars year 24 dust (scenario 1). Solar minimum throughout. White contours indicate zero magnitudes.

The westward jets over the equator shown in Figure 5.5 show that this has occurred by MarTIM's lower pressure levels. This figure also shows their greater magnitude when larger dust content (right hand plot, Figure 5.5) is used from the MCD, again as it enhances direct local solar heating of the diurnal tide (Lewis and Read, 2003) thereby depositing greater momentum when it breaks about the region of MarTIM's lower boundary. To summarise: the eastward jets at mid-latitudes in Figure 5.5 arise for two reasons, firstly they are the remaining part of the lower atmosphere zonal mean eastward mid-latitude jets that are yet to be entirely closed off by the deposited westward momentum from the dissipation of vertically propagating diurnal thermal tide. Secondly they correspond to the typical equator to pole

heating gradients present during equinox seasons that produce single Hadley cells in each hemisphere (Forget et al., 1999) as poleward winds are turned eastward at mid-latitudes by the Coriolis force.

An important note about these evening terminator mid-latitude temperature bands and associated eastward wind jets discussed above is that in both cases the magnitudes of these fields are quite different between the MCD alone case (from the DVD) and the coupled MarTIM-MCD result. For the maximum temperatures the difference between the two types of result, for very low dust settings (bottom left and top left, respectively, Figure 5.1), is ∼5.7 K where the maximum from the MCD alone is hotter than from the coupled MarTIM-MCD result. With average dust (Figure 5.2) this trend increases with MCD alone being approximately 11.9 K hotter than the coupled result. Finally the difference is ∼17.3 K for global dust storm conditions (Figure 5.3). Regarding the eastward wind jets, Table 5.2 shows the range of zonal wind magnitudes at PL 2 (5.36×10^{-1} Pa) for the various run types in the very low dust, solar minimum simulation (Figure 5.1). As was the case with temperatures the zonal wind magnitudes are greater for the MCD alone case than the coupled MarTIM-MCD result. All of these differences in magnitudes come despite good comparison between temperature and zonal wind field structures. Briefly, these differences arise simply because MarTIM is beginning to constrain the MCD from above. The nature and implications of this on the coupled MarTIM-MCD result are discussed over the next subsections.

Table 5.2: Maximum zonal wind speeds at PL 2 (5.36×10^{-1} Pa) for equinox, SMIN and very low dust.

Setup	Max eastward wind (m/s)	Max westward wind (m/s)
MarTIM-MCD (MarTIM mixing ratios)	78.06	-24.40
MarTIM-MCD (MCD mixing ratios)	79.46	-23.21
MCD alone	120.74	-41.39
MarTIM alone	2.16	-2.41

With the exception of the simulation with a global dust storm included in the lower atmosphere (Figure 5.3), one other temperature structure that is present at quite a similar location regardless of dust content is the heating region usually situated about the equator at 1400-hrs local time. This is a product of the IR heating present in the MCD below MarTIM's lower boundary, with a peak heating rate at noon producing the hot region a few hours later given the thermal lag of the atmosphere. This structure is larger for the high dust content simulation (Figure 5.4) for which SMAX solar conditions were used versus the low and average dust simulations (Figures 5.1 and 5.2, respectively) for which SMIN conditions were used. Since it has already been noted that the IR output from the Sun remains fairly constant from SMIN through to SMAX (as Figure 3.1 showed, see also Bougher et al. (1990) and Bougher et al. (2000)) we would not expect the different solar conditions to be responsible for the structures larger presence in Figure 5.4. Therefore this indicates the different dust content of the lower atmosphere, absorbing more solar energy, is responsible for the prominence of this feature. Also, Lewis

and Read (2003) noted that the region of maximum solar heating is higher in the atmosphere under high dust conditions thus the temperature maximum will persist with a larger size to higher altitudes when the dust content is greater.

5.4.2 General Lower Boundary Influence: Mesosphere

Temperature Structure and Magnitude Comparison

To show the coupled MarTIM-MCD result further away from the MCD influence at 0.883 Pa Figures 5.6 and 5.7 show exactly the same kind of plots as Figures 5.1 through 5.4 above only now we consider pressure levels 5 (1.20×10^{-1} Pa) and 10 (9.81×10^{-3} Pa) respectively. As before, solar minimum and equinox conditions (1.47 AU) are used throughout but now we focus only on simulations with an annually average dust content in the lower atmosphere (scenario 1 from section 5.3.1).

Figure 5.6 shows that by PL 5 (1.20×10^{-1} Pa) MarTIM's local energy and global dynamic processes have begun to alter both the temperature structures and magnitudes from that of the MCD DVD result (bottom left, Figure 5.6) but are not yet dominating the coupled MarTIM-MCD result (top row of Figure 5.6). For example both the plots on the top row of Figure 5.6 show temperature peaks about the 1600-hrs to 1800-hrs local time period. This is at the same location as similar temperature peaks in the MarTIM alone result, with the flat isothermal lower boundary (bottom right, Figure 5.6). However note that in the coupled model case these temperature peaks are at slightly higher latitudes ($\pm45^\circ$ versus $\pm30^\circ$) and are more like individual structures than the MarTIM alone case where the peaks are clearly part of a larger dayside peak. Therefore this links these temperature structures back to the MCD DVD result where similar temperature peaks exist at even higher latitudes ($\sim60^\circ$ to $\sim70^\circ$) and are clearly separate from one another. In this sense the coupled MarTIM-MCD result at PL 5 (1.20×10^{-1} Pa) represents a transition between the MCD alone and MarTIM alone results.

Other examples of MarTIM's localised influence include the deep minimum temperatures at high latitudes on the nightside and through to mid-morning (0200-hrs to 1000-hrs). Along with the temperature peak on the equator, just after midnight, these features show much closer comparison to the MarTIM alone result than with the MCD DVD result. The temperature minimums suggesting a similar dearth in energy input at nighttime high latitudes in both coupled and MarTIM alone model run types. Likewise the temperature peak just after midnight suggesting similar strong compressional heating on the equator from the convergence of global circulation flows in both model types. The MCD influence at MarTIM's lower boundary seemingly not playing a strong role here. Finally the temperature magnitudes of the coupled result are closer to their MarTIM alone counterparts than to the MCD alone result. Nonetheless there are still other examples that PL 5 (1.20×10^{-1} Pa) of the coupled result is in transition between the MCD alone and MarTIM alone results. For example the coupled MarTIM-MCD results maintain a temperature minimum over the equator about the 1900-hrs to 2200-hrs region where a similar minimum exists in the MCD alone result but is not as prominent in the MarTIM alone case. And those deep nightside to mid-morning (0200-hrs to 1000-hrs) high latitude temperature minimums noted above are

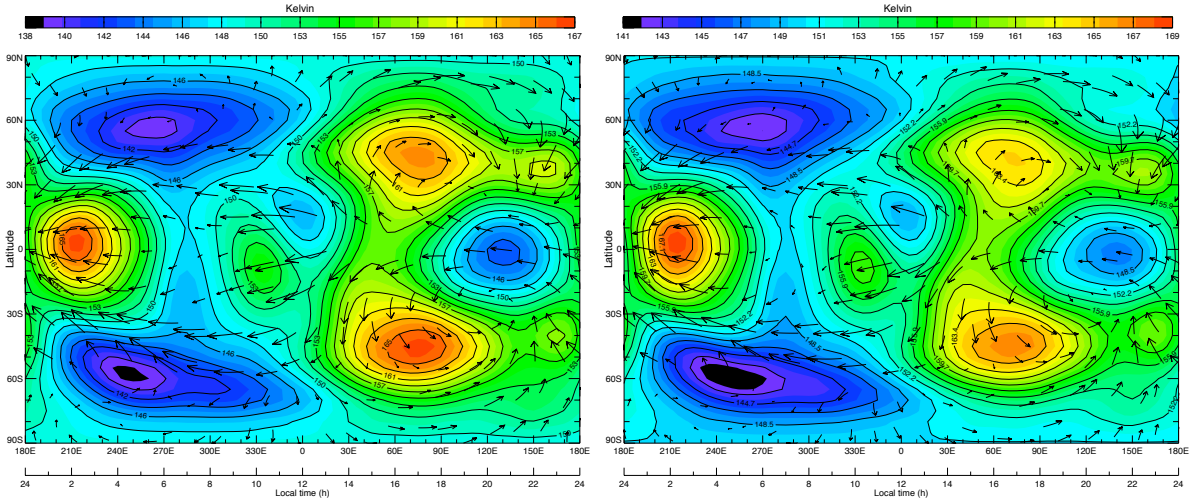

(a) Coupled MarTIM-MCD with MarTIM volume mixing ratios. Average height 74.47 km, temperature 152.1 K.

(b) Coupled MarTIM-MCD with MCD volume mixing ratios. Average height 74.56 km, temperature 154.4 K.

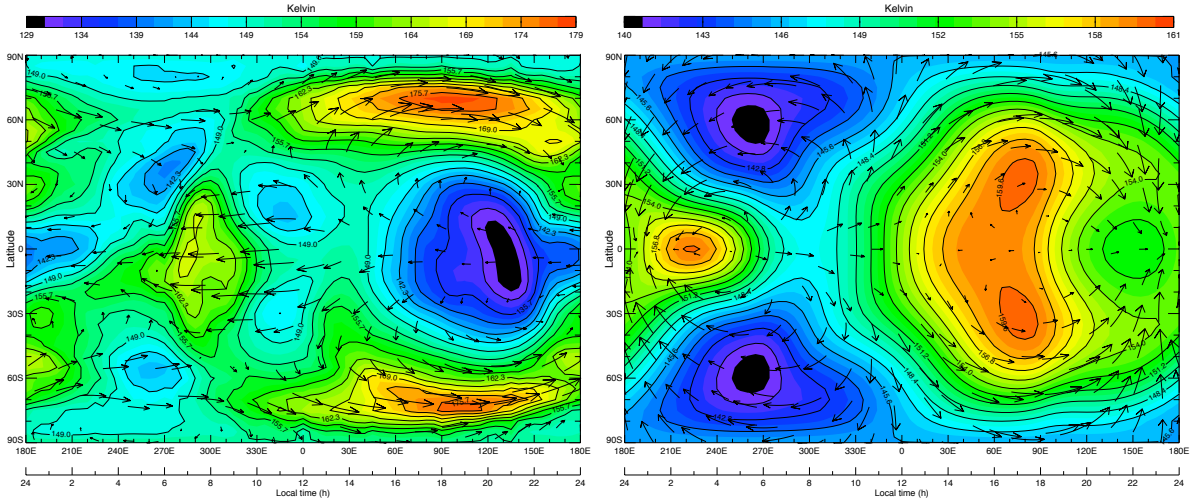

(c) MCD alone (UT 1200-hrs). Average height 74.29 km, temperature 151.4 K.

(d) MarTIM alone. Average height 76.31 km, temperature 151.6 K.

Figure 5.6: Temperatures (and wind field vectors) at constant pressure level 5 (1.20×10^{-1} Pa) for coupled MarTIM-MCD simulations (with and without MCD volume mixing ratios for CO_2 15-μm cooling), MarTIM alone (flat lower boundary) and MCD alone (direct from DVD, for UT 1200-hrs). Solar minimum and average Mars year 24 dust (scenario 1) throughout.

actually present in the MCD DVD result (and at similar latitudes ($\pm60°$)). It is simply that they are not the dominating cold feature as is the case in the MarTIM alone or coupled MarTIM-MCD cases.

From Figure 5.7 at PL 10 (9.81×10^{-3} Pa), now at the pressure level where the new IR heating parameterisation provides its peak input to MarTIM, we see that the transition away from the MCD's influence at 0.883 Pa has continued. Coupled MarTIM-MCD temperatures show clearer comparison with their MarTIM alone counterparts and in turn have moved further away from the structures the MCD DVD simulates. The MCD alone result shows that the peak temperature bands over the evening terminator

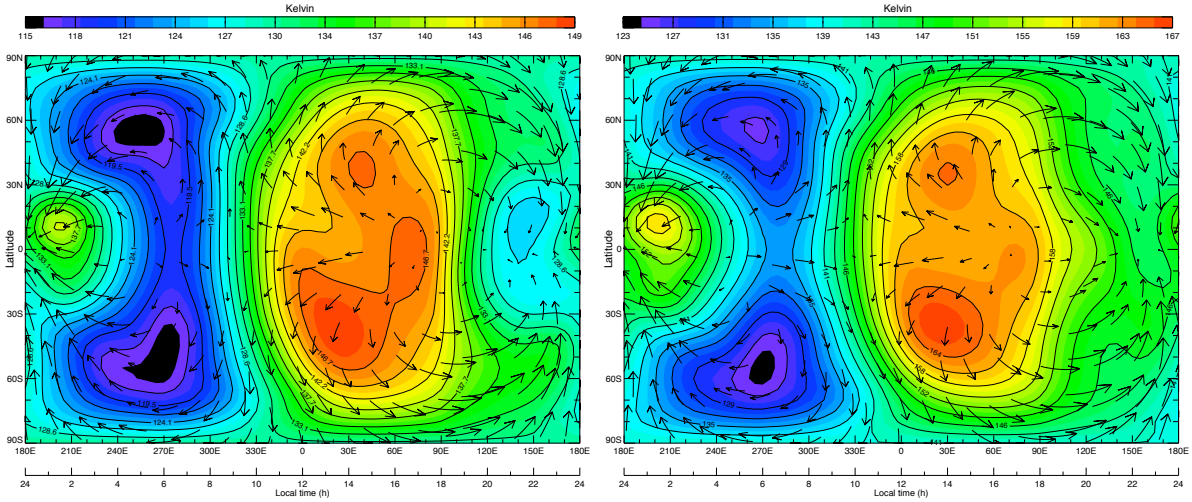

(a) Coupled MarTIM-MCD with MarTIM volume mixing ratios. Average height 94.11 km, temperature 132.2 K.

(b) Coupled MarTIM-MCD with MCD volume mixing ratios. Average height 95.25 km, temperature 147.5 K.

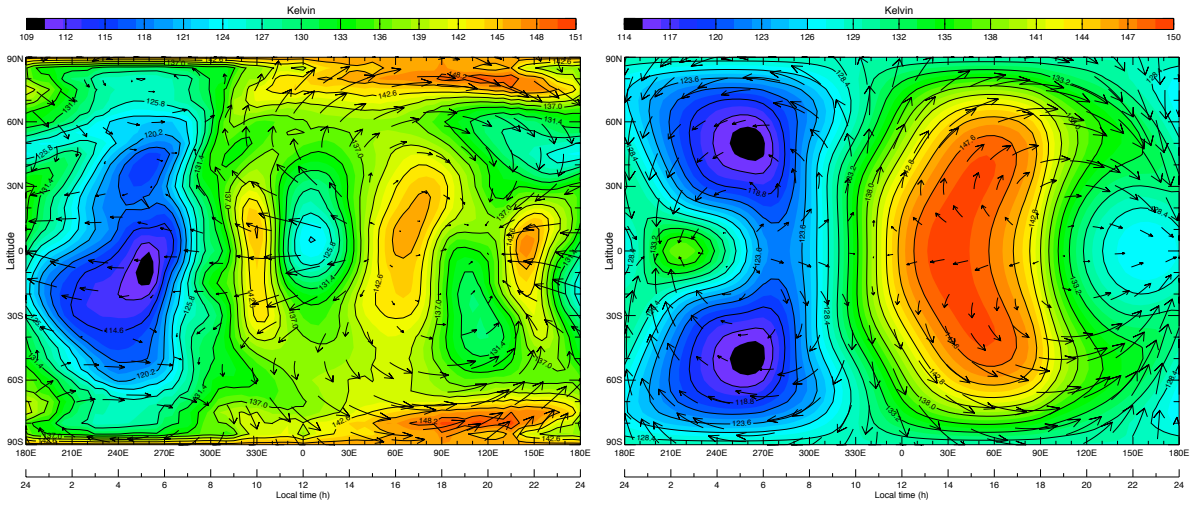

(c) MCD alone (UT 1200-hrs). Average height 93.31 km, temperature 132.0 K.

(d) MarTIM alone. Average height 95.99 km, temperature 133.0 K.

Figure 5.7: Temperatures (and wind field vectors) at constant pressure level 10 (9.81×10^{-3} Pa) for coupled MarTIM-MCD simulations (with and without MCD volume mixing ratios for CO_2 15-μm cooling), MarTIM alone (flat lower boundary) and MCD alone (direct from DVD, for UT 1200-hrs). Solar minimum and average Mars year 24 dust (scenario 1) throughout.

have moved all the way to polar latitudes. This is in comparison to PL 2 (5.36×10^{-1} Pa, bottom left, Figure 5.2) where they were situated at mid-latitudes ($\pm60°$) and to PL 5 (1.20×10^{-1} Pa, bottom left, Figure 5.6) where they had moved to latitudes $\pm70°$. This reinforces the fact that these temperature peaks are separate features to one another in that there are distinct regions of cooler temperatures in the intervening lower latitude regions. In comparison essentially the reverse has happened in the coupled MarTIM-MCD case. In these simulations the separate temperature structures at mid-latitudes at PL 2 ($\pm60°$, top row, Figure 5.2) began to come together at PL 5 ($\pm45°$, top row, Figure 5.6) and now at

PL 10 are generally overhead the equator creating a dominant temperature peak that is largely a single structure. In the MarTIM alone simulation this single structure is a direct consequence of the infrared heating dominating the local dayside energy input. Even though there are subtleties to this peak in the two coupled models (that therefore have a dependence on whether MarTIM or the MCD's mixing ratios were used in the CO_2 15-μm cooling routine) this temperature peak provides a clear link between the coupled MarTIM-MCD result and the MarTIM alone case.

Wind Structure and Magnitude Comparison

Since MarTIM's new IR heating parameterisation is taken from a publication of the Laboratoire de Météorologie Dynamique model (González-Galindo et al., 2009b), which contributed to the MCD, one might expect the IR heating input of MarTIM and the MCD to be quite similar. Therefore the difference between a dominant dayside temperature peak that is situated over the equator in the coupled model case versus the separate polar temperature structures in the MCD alone case is significant. For the MCD alone case we note that Forget et al. (1999) states how prominent gradients in diabatic forcing drive large magnitude circulation features that lead to interhemispheric angular momentum conserving Hadley cells which extend right the way to the poles. It was features such as these during the southern summer (perihelion) case that lead to the northern winter polar warming we discussed in Chapter 4. The Coriolis force accelerated northward flowing winds to get closer to the north pole before finally inducing a mass convergence and adiabatic warming at ∼120 km. With respect to the present discussion therefore Forget et al. (1999) also states that such heating processes are always to be expected above the winter polar regions near solstice and above both poles near equinox. The temperature plots and the associated zonal winds discussed above show that this is indeed the case with the MCD DVD equinox result.

With the above in mind the other main difference between coupled MarTIM-MCD and MCD DVD results at PL 5 and 10 is the variation in global circulation features. As noted earlier with respect to PL 2, the zonal wind (and temperature) structures between the two simulation types were quite similar (e.g. Figure 5.2) but the magnitudes of the MCD alone results were always greater for both temperatures and winds (recall Table 5.2 regarding the zonal winds). Now at PL 10 Figure 5.8 shows that this difference in magnitude (and also structure) of the zonal winds between coupled MarTIM-MCD results (top left plot) and the MCD DVD (top right plot) has increased. The plot of MCD DVD zonal winds shows peak eastward winds over the same 2-D locations (and in particular at high latitudes) as the counterpart temperature maximums discussed just above (bottom left, Figure 5.7). These maximums reach ∼178 m/s eastward (−155 m/s westward) whereas the coupled MarTIM-MCD simulation only reach ∼96 m/s (−72 m/s). In particular MCD DVD high magnitude eastward winds persist through most of the afternoon and early evening local times and indeed are still quite strong throughout the deep nightside. This is in contrast to coupled MarTIM-MCD eastward wind structures, which are more localised about the evening terminators, similar to the MarTIM alone case (bottom plot, Figure 5.8) and in fact are westward through the deep nightside.

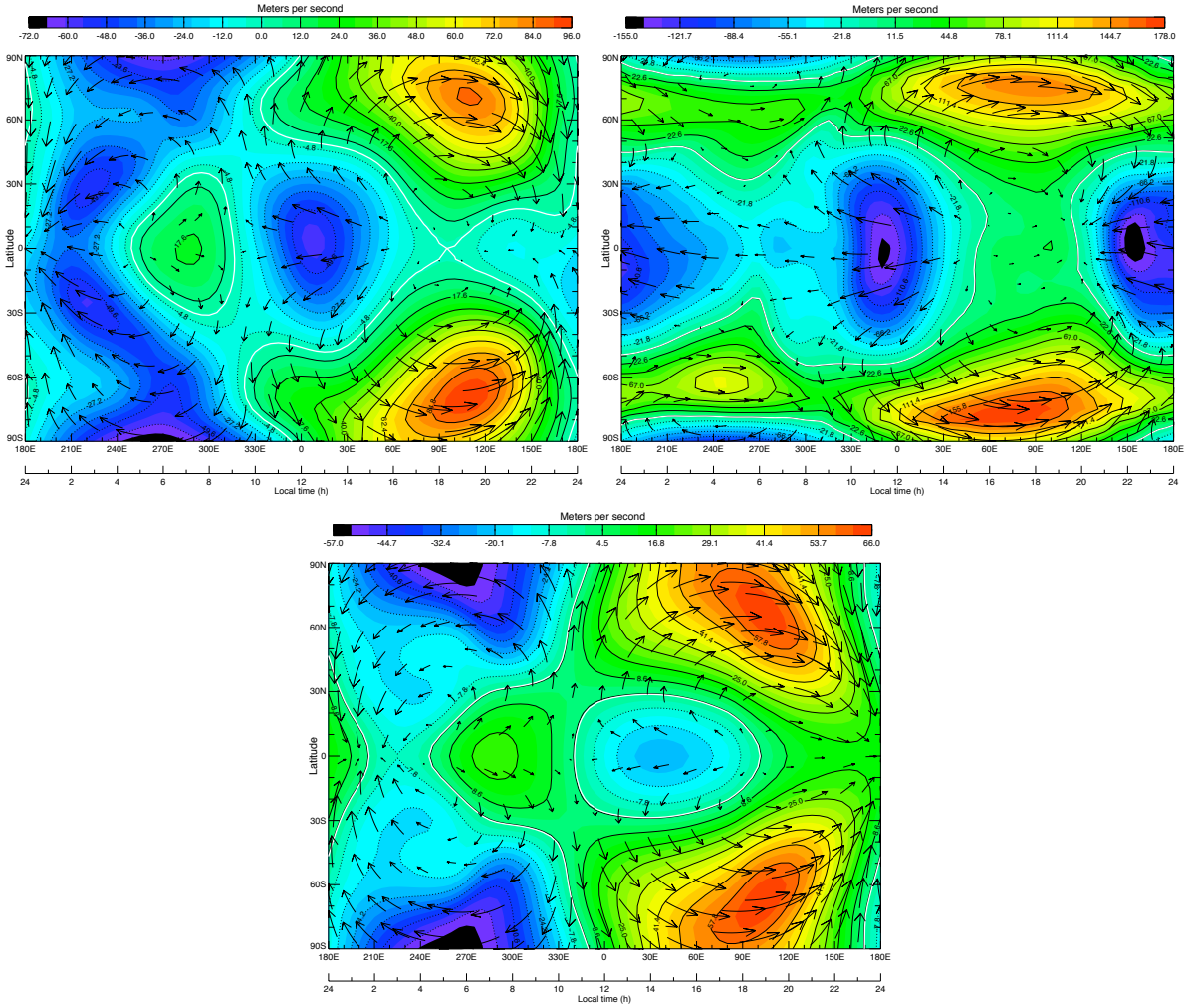

Figure 5.8: Zonal wind (and wind field vectors) at constant pressure level 10 (9.81×10^{-3} Pa) for (top left plot) coupled MarTIM-MCD simulation (with MarTIM volume mixing ratios for CO_2 15-μm cooling), for (top right plot) the MCD alone (direct from DVD, for UT 1200-hrs) and for (bottom) MarTIM alone (flat lower boundary). Solar minimum and average Mars year 24 dust (scenario 1) throughout. White contours indicate zero magnitudes.

One reason that the coupled models wind magnitudes are less than their MCD alone counterparts is due directly to the approximation we had to make in section 5.3.2. There we introduced measuring geopotential height gradients from the 0.883 Pa lower boundary rather than from the planetary surface (Martian areoid). Were it not for this change the coupled MarTIM-MCD simulations would often produce physically inconsistent results due to the zonal advection of total energy term becoming unstable in the energy equation. Wind magnitudes had been significantly increased at all pressure levels by coupling to the MCD and the additional energy deposition through adiabatic compressional heating at thermospheric levels was preventing the model from reaching a steady state. The necessary changes were made to equations 5.3 to 5.6 by replacing the geopotential height $h(n,\theta,\phi)$ with $(h(n,\theta,\phi)-h(1,\theta,\phi))$ in the context of $\Phi{=}gh(n,\theta,\phi)$ within the geopotential gradient terms $\left(\frac{\partial\Phi}{\partial\phi}\right)$. The value of $h(1,\theta,\phi)$ coming

from the MCD at 0.883 Pa.

Now, Figure 5.9 shows the effect these changes have had at PL 10 (9.81×10^{-3} Pa) on the values of geopotential heights that are used in equations 5.3 to 5.6 to calculate those geopotential gradients. The left hand plot shows the $h(10,\theta,\phi)$ term i.e. that which is measured against the planetary surface and which lead to unstable results. The right hand plot shows the replacement $(h(10,\theta,\phi) - h(1,\theta,\phi))$ term that we have used to produce the coupled results currently being discussed. From these two plots we can see that the two-dimensional geopotential height gradients that would be calculated and used within equations 5.3 to 5.6 vary significantly depending on which formulation is used. The meridional geopotential gradients in particular would show the greatest difference (for these equinox conditions). For example in the left hand plot of Figure 5.9 $h(10,\pm90°,\phi)-h(10,0°,\phi)$ has a magnitude on the order of ∼15 km between the peak region over the equator near 1600-hrs and the minimum at the poles. However for the right hand plot the same $h(10,\pm90°,\phi)-h(10,0°,\phi)$ gradient now only has a magnitude of ∼5 km because the individual values of $h(10,\pm90°,\phi)$ and $h(10,0°,\phi)$ have already had $h(1,\pm90°,\phi)$ and $h(1,0°,\phi)$ subtracted, respectively.

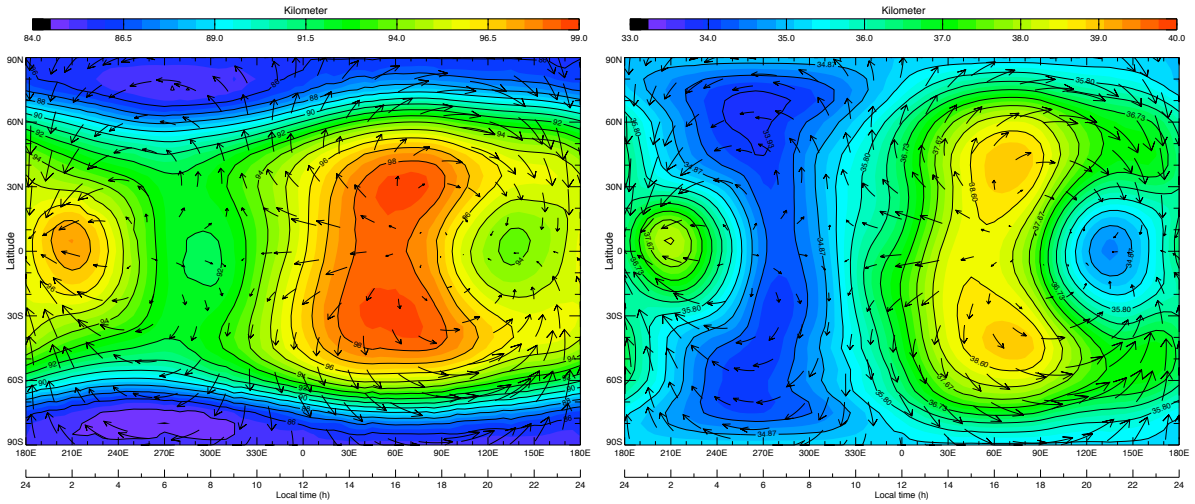

Figure 5.9: Values used to calculate geopotential height gradients in equations 5.3 to 5.6 of the coupled MarTIM-MCD simulation. Left plot shows $h(n,\theta,\phi)$, right plot shows $(h(n,\theta,\phi) - h(1,\theta,\phi))$ with $h(1,\theta,\phi)$ taken from the MCD (at 0.883 Pa). Constant pressure level 10 (9.81×10^{-3} Pa), solar minimum, average Mars year 24 dust (scenario 1) and MarTIM volume mixing ratios for both.

Consequently the Hadley cells mentioned earlier, extending from the equator to the poles, would be of much greater magnitude with the geopotential gradients of the left hand plot setup than with the right hand setup. In turn the subsequent mass convergence and adiabatic warming that would result would also greatly vary. Sure enough this feature is exactly the kind of difference we have already noted in the temperature structures between the coupled MarTIM-MCD results (e.g. top plots of Figures 5.6 and 5.7) that use the right hand plot setup of Figure 5.9 and the MCD alone result (e.g. bottom left plots of Figures 5.6 and 5.7), which essentially use the left hand plot setup of Figure 5.9. Also, the zonal

winds that would be produced over the evening terminators due to the Coriolis force accelerating the meridional flow eastwards would also be much larger for the left hand plot of Figure 5.9. And this is much like what was shown in the comparison of the top left and top right zonal wind plots of Figure 5.8 (again, right hand and left hand plot setup of Figure 5.9, respectively).

Next, Figure 5.10 shows a latitude by altitude view of the (zonally averaged) zonal winds. This plot is restricted to below 120 km to focus on the lower altitude regions we are discussing. For reference coupled MarTIM-MCD simulations result in PL 10 at an average geopotential height of ∼94.1 km against ∼93.3 km for the MCD alone and ∼95.9 km for the MarTIM alone results. From Figure 5.10 you can see how zonally averaged zonal wind structures of coupled MarTIM-MCD simulations move away from those of the MCD alone the further from the lower boundary we consider. In the MCD alone case (bottom plot, Figure 5.10) the latitudinal growth of westward wind structures as we climb in altitude can be clearly seen. This is a continuation of the zonally averaged structure noted earlier i.e. that eastward winds in the lower atmosphere, maximising about ∼40 km at ±60° with superrotation about the equator typically below ∼30 km, are divided almost symmetrically about the equator (given the latitudinally symmetric tidal forcing) by westward winds upwards from ∼40 km as upward propagating diurnal thermal tides deposit westward momentum into the background atmosphere (Lewis and Read, 2003). Now in Figure 5.10 we can see the continued vertical propagation of the diurnal tide, with locations of peak westward winds over the equator at ∼86 and ∼120 km suggesting a ∼34 km vertical wavelength (c.f. ∼30-35 km, Forbes and Miyahara (2006)). Note also how this closes off the eastward mid-latitude jets, thus these jets will indeed seem to migrate to higher latitudes as we noted above.

In the coupled MarTIM-MCD case (top plot, Figure 5.10) there is the same distinction between high latitude eastward jets and equatorial westward winds as there was in the MCD alone result. However clearly the different specific wind structures indicate that different process are acting in the background atmosphere and on the vertically propagating structures introduced by coupling to the MCD. From our discussion regarding the calculation of horizontal geopotential gradients (Figure 5.9) we expect that the poleward and in turn high latitude eastward winds will be reduced from their MCD alone counterparts. The comparison of colour scales in Figure 5.10 showing this is indeed the case. Moreover this has resulted in quite different zonal wind structures developing through the altitude range shown. For example there are specific altitude regions (∼75 to 110 km) where eastward winds peak at high latitude rather than the eastward jets in the MCD result whose presence is continuous over a much larger range of altitudes. In the coupled case these regions arise at the same altitude range where MarTIM's IR energy balance maximises (see Figure 5.11). Thus localised IR heating and its gradient from equator to pole creates the necessary meridional wind flow, which is turned eastward by the Coriolis force at mid-latitudes. Albeit winds that are of lesser magnitude than the MCD alone case.

MarTIM's local IR energy balance is also responsible for depositing significant westward momentum into the background atmosphere (as we saw in Chapter 4). Indeed, the westward wind structures in Figure 5.10 (top plot) from ∼70 km up to ∼100 km show a strong comparison to the structure of

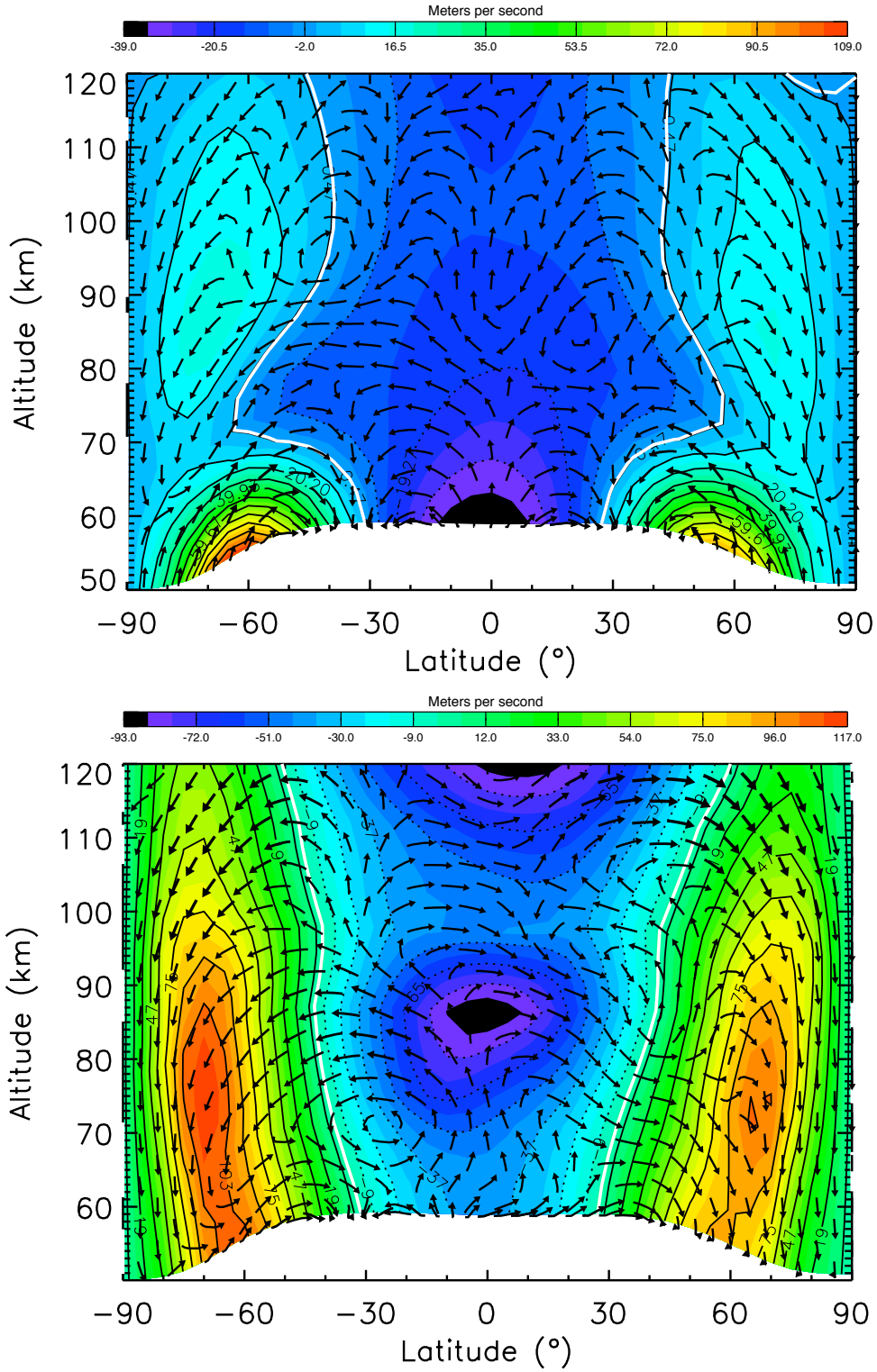

Figure 5.10: Latitudinal slice of zonal average zonal winds (colour contours) and zonal average meridional and vertical winds (black arrows). Top plot is the coupled MarTIM-MCD result, bottom plot is the MCD alone result (direct from DVD, for UT 1200-hrs). Solar minimum and average Mars year 24 dust (scenario 1) for both. White contours indicate zero magnitudes.

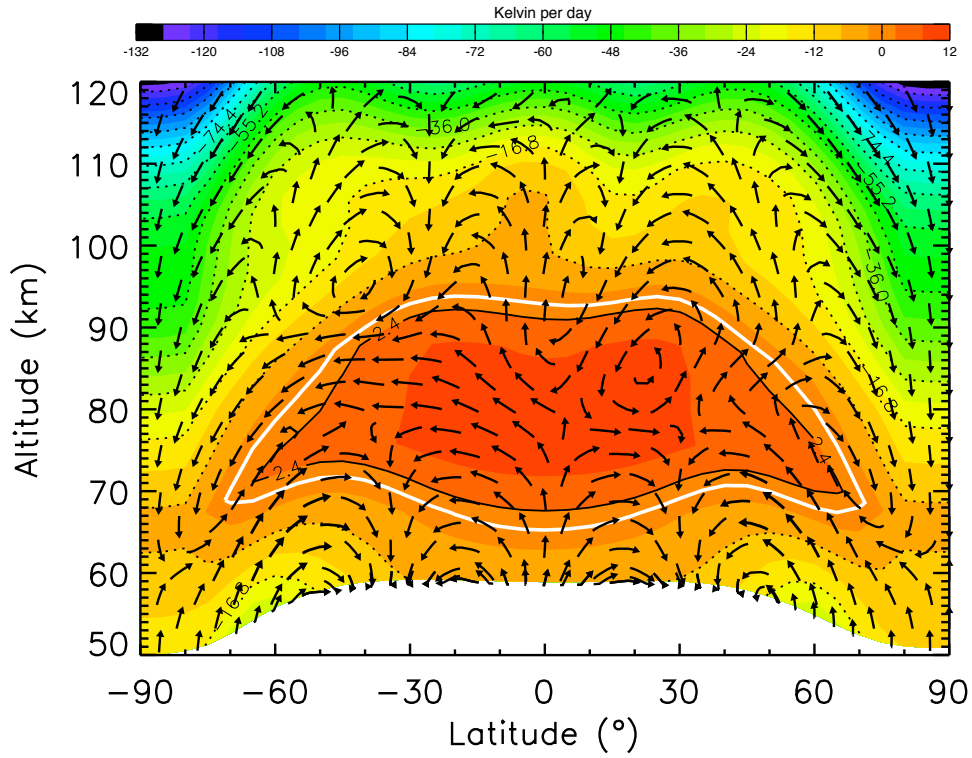

Figure 5.11: Latitudinal slice of coupled MarTIM-MCD zonal average IR energy balance (colour contours) and zonal average meridional and vertical winds (black arrows). Solar minimum and average Mars year 24 dust (scenario 1). White contours indicate zero magnitudes.

positive IR energy input in Figure 5.11 with a 'funnel' shape, narrowing in latitude from ±60° to ±40° as one climbs in altitude. In turn you can see in Figure 5.10 (top plot) that it is this broad region of westward wind extending between ±60° latitude just above 70 km that almost cutoff the high latitude ∼75 to 110 km eastward wind regions from the eastward winds at the lower boundary provided by the MCD. These narrowing regions of eastward wind in the coupled result are where localised IR energy input dominate over any other process, such as any thermal tides that may have vertically propagated from the MCD supplied lower boundary.

But again, since MarTIM's IR heating parameterisation is taken from a publication of the Laboratoire de Météorologie Dynamique model (González-Galindo et al., 2009b), it is unlikely that there is significant variation versus the MCD IR heating. Instead, as we discussed above regarding the calculation of horizontal geopotential gradients (Figure 5.9), the approximation we needed to make to these gradients to allow MarTIM to reach a steady state meant the coupled models horizontal winds were usually underestimated compared with the MCD. Now with the plots in Figure 5.10 it is this that can be seen to have allowed MarTIM's local energy input and output processes to dominate where they would not have in the MCD alone case. The weaker poleward winds actually allow MarTIM's IR energy balance (Figure 5.11) to dominate the local energetics and increasingly so as we gain in altitude. MarTIM is beginning to constrain the MCD from above because the dominance of the horizontal winds (in particular the zonal

winds) and the energy re-distribution they produce to the MCD alone result has been damped in the coupled result.

Tidal Modes Comparison

Figures 5.12, 5.13 and 5.14 show the relative amplitudes (expressed as a percentage of zonal mean) of coupled MarTIM-MCD (left column) and MCD DVD (right column) temperature fields at pressure levels 2, 5 and 10 respectively. Figures 5.13 and 5.14 also show the tides present in the equivalent MarTIM alone result. For all of these plots only tides with amplitudes greater than or equal to 1% of the zonal means were included. Thus because at PL 2 in the MarTIM alone case the only suitable tidal mode present was the diurnal westward wavenumber 1 (1, 1) mode, with an amplitude ∼1.3% of the zonal mean, a plot wasn't produced.

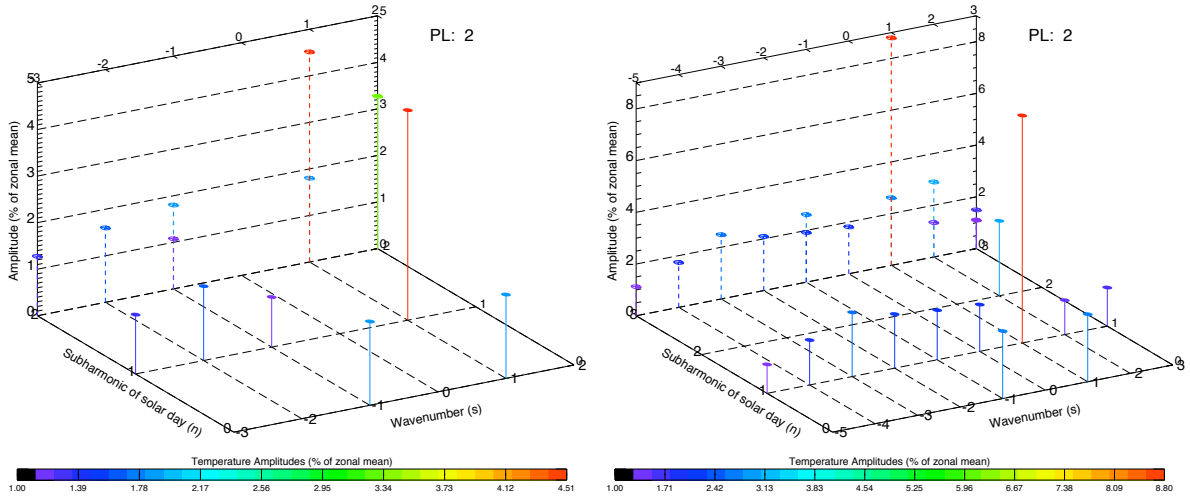

Figure 5.12: Relative temperature amplitudes at PL 2 (5.36×10^{-1} Pa) expressed as percentages of zonal means. Left column is coupled MarTIM-MCD (with MarTIM volume mixing ratios for CO_2 15-μm cooling), right column is MCD alone. Solar minimum and average Mars year 24 dust (scenario 1) throughout.

From these figures it is clear, even as low as PL 2 (5.36×10^{-1} Pa), that quite different ranges of tidal modes play important roles (relative to the zonal mean) in producing the coupled and MCD alone results discussed above. Those tides that are present in both, notably the (1, 1) mode (and the migrating tides in general), typically have an amplitude that is 1/3 to 1/2 as great (relative to their respective zonal means) for the coupled result as for the MCD DVD. However, still with the (1, 1) mode, by the time we get to PL 10 (9.81×10^{-3} Pa) the coupled models' (1, 1) signal is larger than that of MCD alone. This reflects the dominance of MarTIM's IR energy input as we move from MarTIM's MCD lower boundary to PL 10 of MarTIM's IR radiative balance peak, thereby showing its greater influence upon the MarTIM-MCD result than the MCD's parameterisation on the MCD alone result. From our discussion above regarding the differences in the zonal average zonal winds (Figure 5.10) we have already seen how the IR heating had a relatively greater role in the coupled model case in comparison to the MCD alone case where

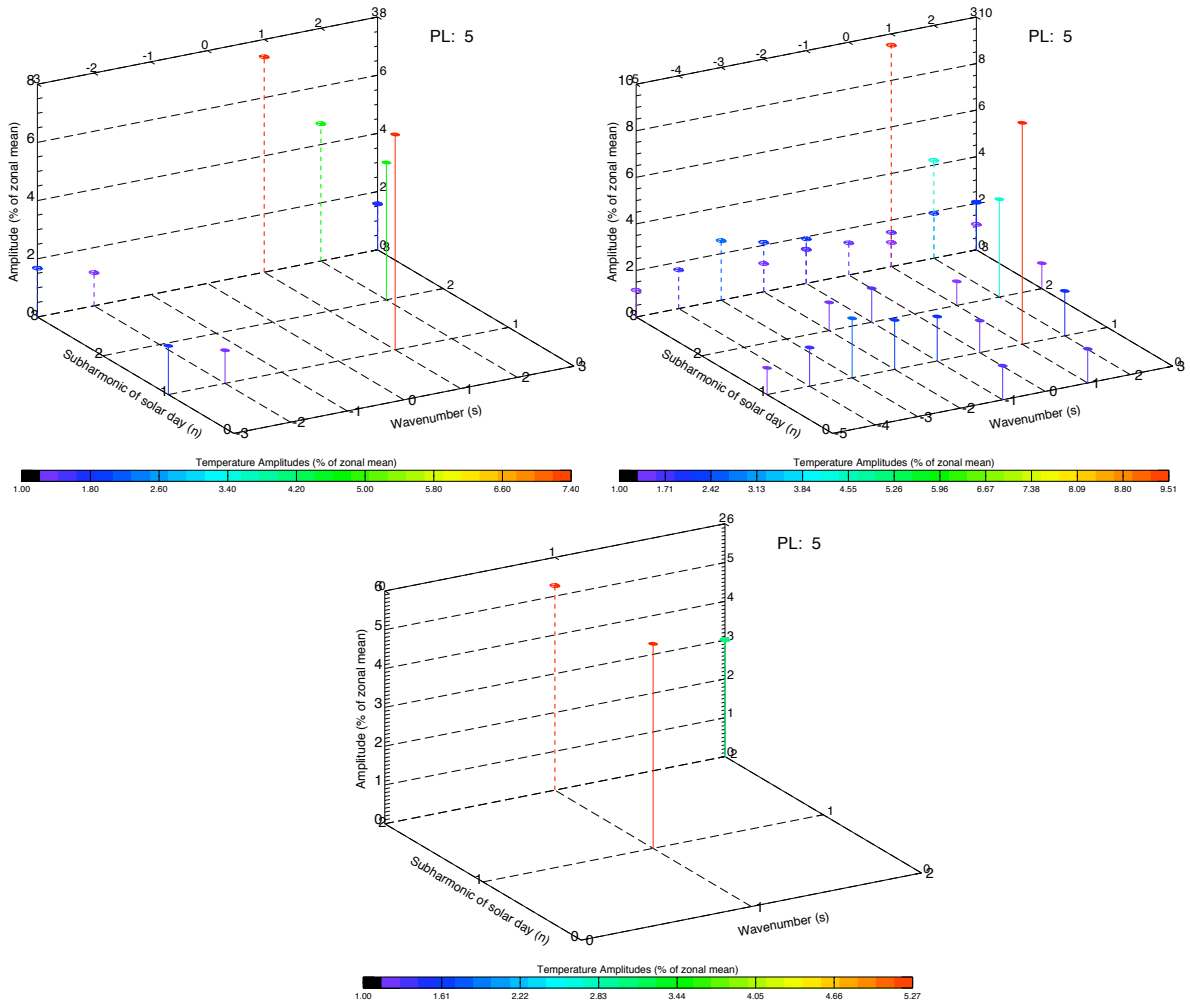

Figure 5.13: Relative temperature amplitudes at PL 5 (1.20×10^{-1} Pa) expressed as percentages of zonal means. Left column is coupled MarTIM-MCD (with MarTIM volume mixing ratios for CO_2 15-μm cooling), right column is MCD alone, bottom row is MarTIM alone. Solar minimum and average Mars year 24 dust (scenario 1) throughout.

horizontal circulation features had the greater energy input role through the energy redistribution they introduced. The reduction in wind magnitudes due to the lesser horizontal geopotential gradients in the coupled model was identified as allowing the IR heating to dominate and this is reflected in the relative importance of the (1, 1) mode shown in Figure 5.14 (for PL 10). In the MCD alone result the IR heating dominance is relatively smaller as those circulation features efficiently redistribute the IR energy thereby creating the different thermal structures discussed earlier and thus changing the relative importance of the tidal modes present.

Next, Figure 5.15 shows the latitude by pressure level structure of the (1, 1) mode for the coupled MarTIM-MCD model (left plot) and the MCD alone (right plot) results. Here we see at PL 2 and 5 the dominance of the (1, 1) signal in the MCD, overhead the equator, versus the complete dearth of amplitude over most latitudes in the coupled model case. From Figures 5.2 and 5.6 earlier this signal is

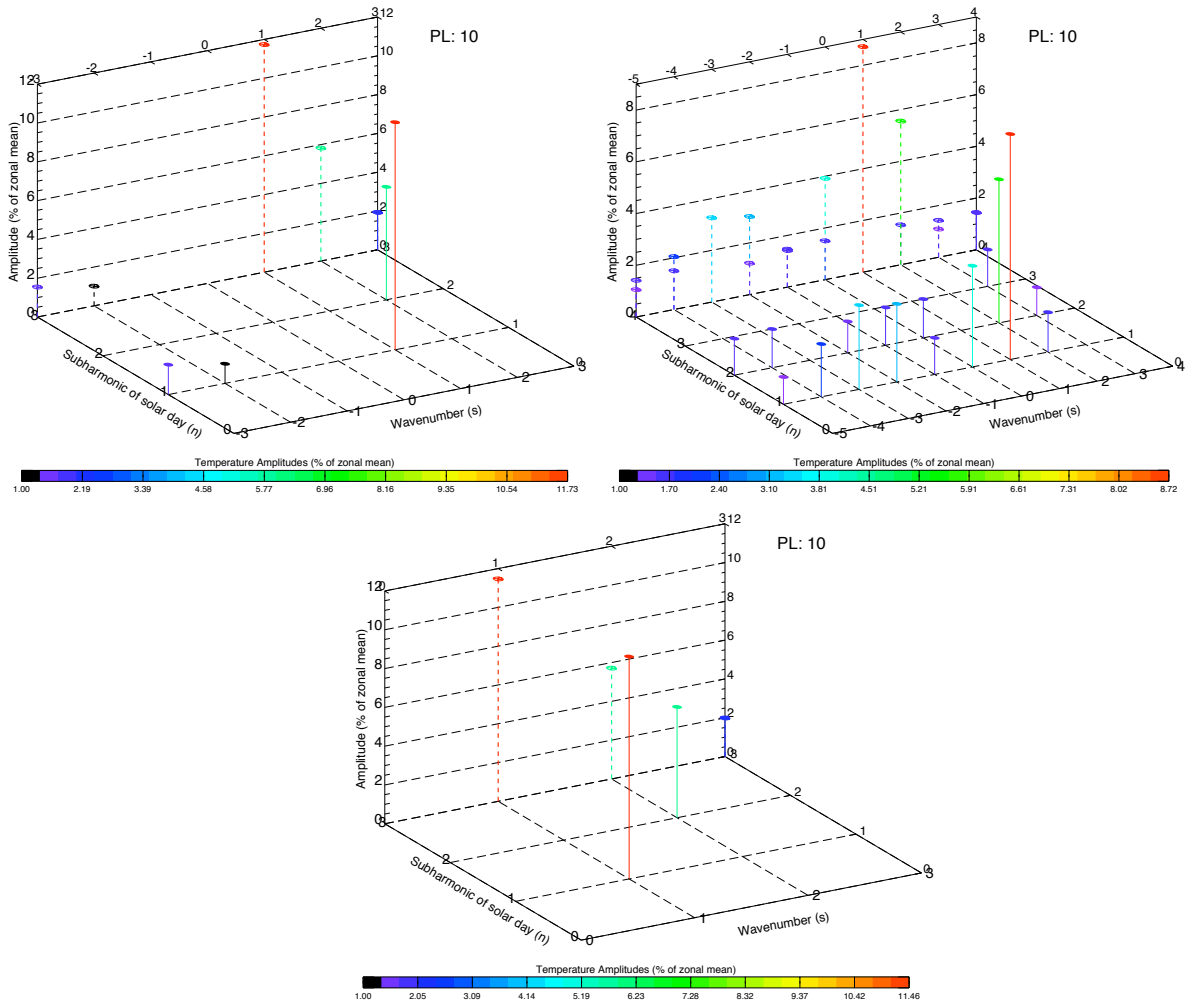

Figure 5.14: Relative temperature amplitudes at PL 10 (9.81×10^{-3} Pa) expressed as percentages of zonal means. Left column is coupled MarTIM-MCD (with MarTIM volume mixing ratios for CO_2 15-μm cooling), right column is MCD alone, bottom row is MarTIM alone. Solar minimum and average Mars year 24 dust (scenario 1) throughout.

provided by regions of prominent temperature maximum and minimum for the MCD alone versus the more complex temperature structures in the coupled model case. Also in the MCD alone case we saw in Figure 5.10 the presence of a vertically propagating diurnal tide breaking above the 0.883 Pa pressure level adding westward momentum to the background atmosphere over progressively greater latitudinal extent.

However, note that there is no reason why the diurnal tide should not be able to propagate over the 0.883 Pa boundary from the MCD into MarTIM. Indeed, at PL 5 for example the (1, 1) signal in the coupled model case is a non-negligible ∼7% of the zonal mean versus ∼9% for the MCD alone case. Instead, as we noted just above, the relative dominance of MarTIM's IR heating is greater at PL 10 in the coupled than the MCD alone result because of the different wind magnitudes. Thus vertical propagation is present but less dominant in the coupled model case than the role of in-situ IR heating. Thus the

IR heating (1, 1) signal is principally all that can be seen in the left hand plot of Figure 5.15, with the dominance of two mid-latitude peaks at PL 10 in the coupled model case. In the MCD alone case the persistence of poleward circulation features, that turn to zonal (eastward) winds at mid-to-high latitude (e.g. Figure 5.8) maintains temperature peaks at similarly high latitudes (e.g. bottom left, Figure 5.7) and in particular prevents as deep a nightside minimum as was noted in the coupled model case (e.g. top left, Figure 5.7). This lessens the (1, 1) signal presence for the MCD alone at PL 10 relative to the (respective) background temperatures (as the colour scales show) and causes the amplitude structure to 'fan-out' to higher latitudes as we climb in pressure levels, as discussed above.

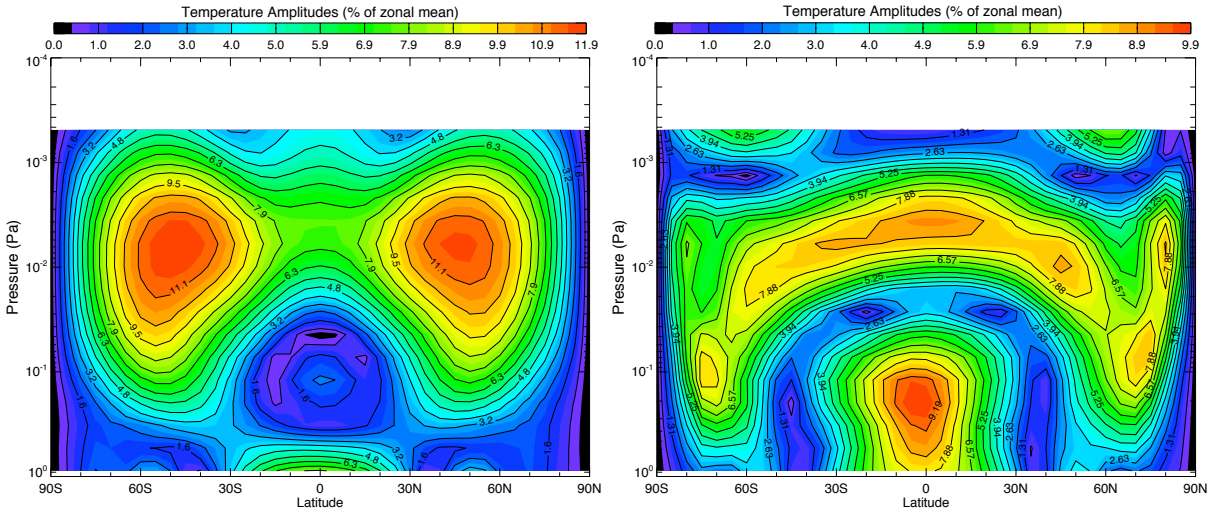

Figure 5.15: Latitude versus pressure level structure of the relative temperature amplitude of the (1, 1) mode expressed as a percentage of the zonal mean (colour contours). Left plot is the coupled MarTIM-MCD result, right plot is the MCD alone result. Solar minimum and average Mars year 24 dust (scenario 1) for both.

From Figures 5.12 to 5.14 note the presence of the migrating semidiurnal westward wavenumber 2 (2, 2) mode that is typically of (slightly) greater presence in the coupled result than with the MCD. At PL 2 the (2, 2) mode has amplitude ∼3.27% in the coupled result versus ∼2.89% in MCD alone. By PL 5 these amplitudes are ∼4.72% and ∼4.20% respectively and at PL 10 are ∼5.82% and are ∼5.55% respectively. In Chapter 4 the role of the (2, 2) mode in the lower MarTIM pressure levels was attributed to the combination of IR heating on the dayside and the global circulation features it generated that converged at about 2400-hrs generating adiabatic heating in the very early morning. This would explain its presence in the coupled model result and also link its greater magnitude in the coupled result (versus the MCD) to the similarly greater (1, 1) magnitude in the coupled model (versus the MCD). The (1, 1) signal coming from direct IR heating, then the (2, 2) arising from the associated global circulation.

For the MCD alone case we note the semidiurnal tides relatively long vertical wavelength means it has greater potential than the diurnal tide to propagate into the thermosphere (Forbes and Miyahara, 2006) as the shorter vertical wavelength of the diurnal components are more susceptible to dissipation

(Wilson and Hamilton, 1996; Forbes and Miyahara, 2006). Thus we see how the dominant tide generation mechanism for the (2, 2) case is different for the coupled model and MCD alone results: localised IR heating and vertical propagation, respectively. The slightly greater role that the (2, 2) mode plays (relative to the zonal mean) in the coupled model suggests that propagation of this tide from the MCD into MarTIM is occurring but alongside MarTIM's local energy processes and in particular the greater (1, 1) magnitude. Thus maintaining the (2, 2) mode with slightly greater relative amplitude in the coupled model than in the MCD alone result. Again, the reduction in wind magnitudes in the coupled result (due to lesser horizontal geopotential gradients) has altered the relative importance of the various (migrating) tides discussed here. There is no reason why the propagation of these tides cannot occur from the MCD into MarTIM over the 0.883 Pa level. But once within MarTIM the different background mean winds completely change their relative importance and principally it is this that Figures 5.12 to 5.15 are indicating.

Tidal modes present in the MCD case but under represented in the coupled MarTIM-MCD model are typically the non-migrating tides ($n \neq s$). And this is immediate right from PL 2. Indeed Figures 5.12 through to 5.14 show the tides that are represented in coupled MarTIM-MCD results begin to resemble those in the MarTIM alone simulations (with the flat, isothermal lower boundary), in both n and s range (thus moving more toward migrating tides only) and amplitude as MarTIM's localised energy inputs begin to dominate. And those non-migrating tides present in coupled results are, again, between 1/3 to 1/2 the amplitude of MCD alone equivalents. Nonetheless it is notable that the coupled result does show the presence at PL 2 of the diurnal eastward wavenumber 1, $(1, -1)$ mode, which is also known as the diurnal Kelvin wave. Other simulations show the presence of this tidal mode at much higher altitudes, e.g. throughout the thermosphere in the work of González-Galindo et al. (2009a) (for the Ls 270 season) and up to 120 km altitude in the work of Angelats i Coll et al. (2004) (for Ls 65 simulations).

Just as with the migrating tides, this reduction in the presence of non-migrating tides is linked to our discussion earlier about the calculation of horizontal geopotential gradients and the resulting reduction in wind magnitudes. Now though this seems to have quite strongly removed the influence (relative to the background mean) of the non-migrating tides. The reduction in magnitude and variation in structure of advective, energetic and dynamic processes has allowed local processes (such as IR heating) to dominate. In turn Figures 5.12 to 5.15 reflect the complexity this creates in the coupled models' tidal response and again it seems particularly to the detriment of non-migrating rather than migrating tides. The coupled model is effectively replacing the influence of vertically propagating tides with localised processes. Although there is no reason why the large range of n and s modes seen in the MCD result cannot be represented by MarTIM the changes made to the coupling method to allow a steady state solution (see section 5.3.2) has produced difficulties in allowing the tidal features to continue propagating within MarTIM because of the different background atmospheric environment they are passing through. And this is clearly affecting the whole range of n and s modes.

5.4.3 General Lower Boundary Influence: Thermosphere

Finally we consider the coupled MarTIM-MCD results in the middle and upper atmosphere. Figures 5.16, 5.17 and 5.18 show pressure levels 15 (8.05×10^{-4} Pa), 20 (6.61×10^{-5} Pa) and 30 (4.45×10^{-7} Pa) respectively. As before, solar minimum and equinox conditions (1.47 AU) are used throughout and we continue to focus only on simulations with an annually averaged dust content in the lower atmosphere (scenario 1 from section 5.3.1). Pressure levels 15 through to 30 represent the middle and upper atmosphere i.e. where the CO_2 15-μm radiative cooling reaches its peak in the non-LTE region

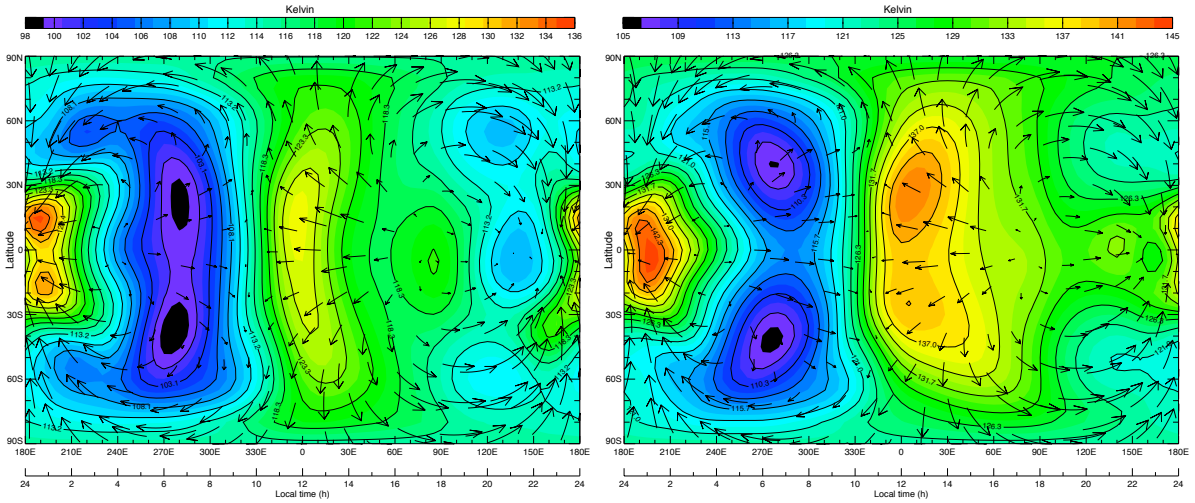

(a) Coupled MarTIM-MCD with MarTIM volume mixing ratios. Average height 111.03 km, temperature 114.5 K.

(b) Coupled MarTIM-MCD with MCD volume mixing ratios. Average height 114.38 km, temperature 126.2 K.

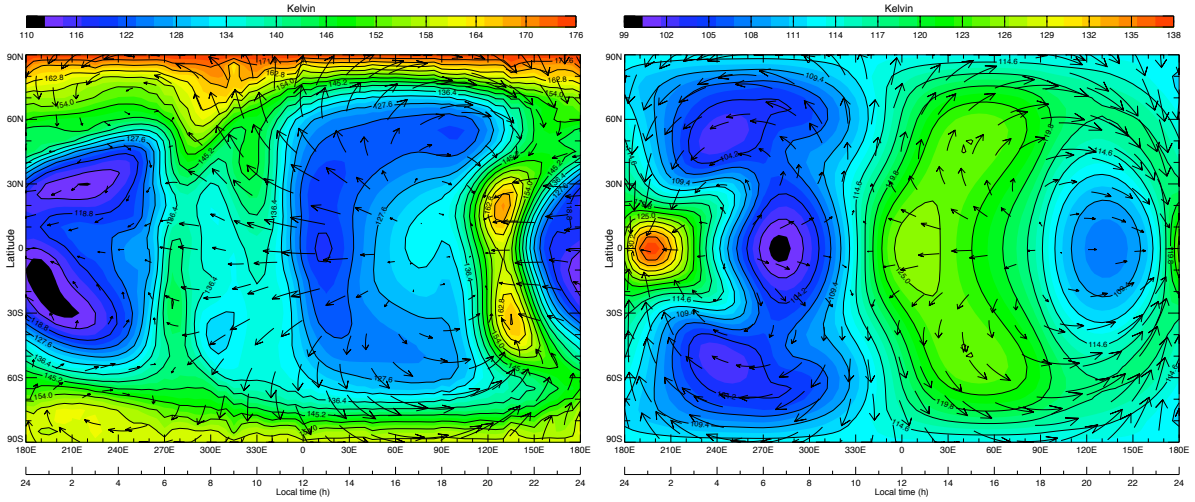

(c) MCD alone (UT 1200-hrs). Average height 111.30 km, temperature 133.3 K.

(d) MarTIM alone. Average height 112.93 km, temperature 114.7 K.

Figure 5.16: Temperatures (and wind field vectors) at constant pressure level 15 (8.05×10^{-4} Pa) for coupled MarTIM-MCD simulations (with and without MCD volume mixing ratios for CO_2 15-μm cooling), MarTIM alone (flat lower boundary) and MCD alone (direct from DVD, for UT 1200-hrs). Solar minimum and average Mars year 24 dust (scenario 1) throughout.

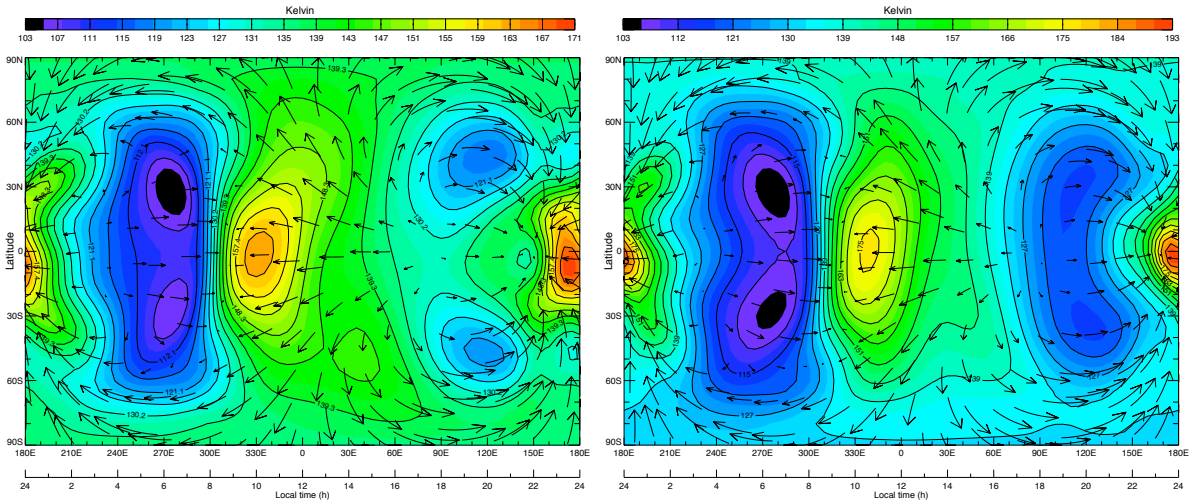

(a) Coupled MarTIM-MCD with MarTIM volume mixing ratios. Average height 128.00 km, temperature 133.9 K.

(b) Coupled MarTIM-MCD with MCD volume mixing ratios. Average height 132.22 km, temperature 135.5 K.

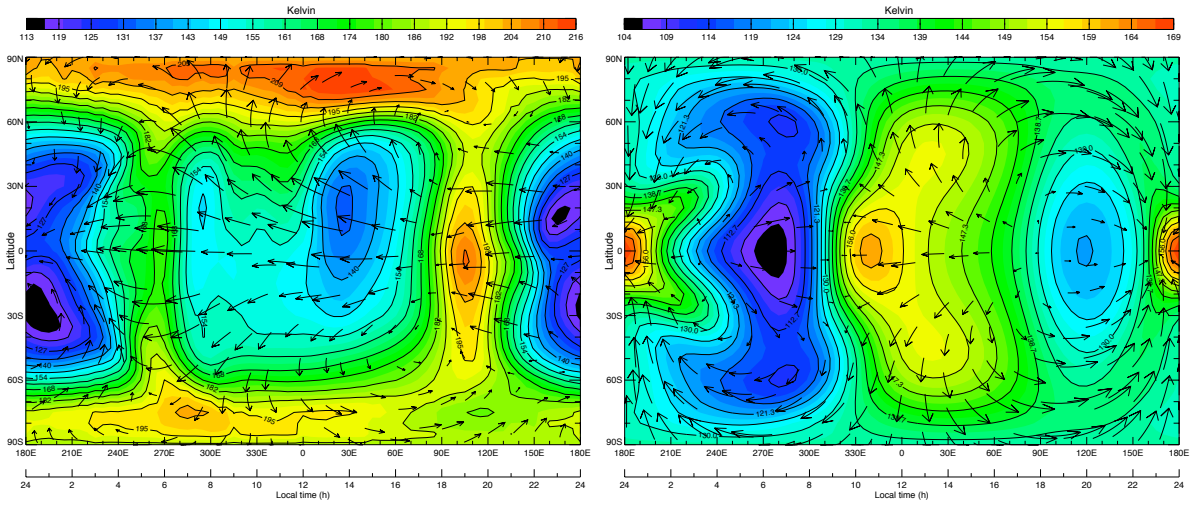

(c) MCD alone (UT 1200-hrs). Average height 131.76 km, temperature 161.4 K.

(d) MarTIM alone. Average height 129.97 km, temperature 134.4 K.

Figure 5.17: Temperatures (and wind field vectors) at constant pressure level 20 (6.61×10^{-5} Pa) for coupled MarTIM-MCD simulations (with and without MCD volume mixing ratios for CO_2 15-μm cooling), MarTIM alone (flat lower boundary) and MCD alone (direct from DVD, for UT 1200-hrs). Solar minimum and average Mars year 24 dust (scenario 1) throughout.

and also where solar EUV / UV heating maximises. Thus we draw attention to the top left and top right plots in Figures 5.16 to 5.18, which show coupled MarTIM-MCD results that used MarTIM's and the MCD's (respectively) CO_2 and O volume mixing ratios in the CO_2 15-μm cooling parameterisation. This is important because MarTIM does not yet include a parameterisation of photochemistry processes, whereas the GCM's upon which the MCD is based do (González-Galindo et al., 2005; Angelats i Coll et al., 2005). Consequently we expect MarTIM's volume mixing ratios to differ from those of the MCD and for this to have knock on effects on CO_2 15-μm radiative cooling rates depending on which are used

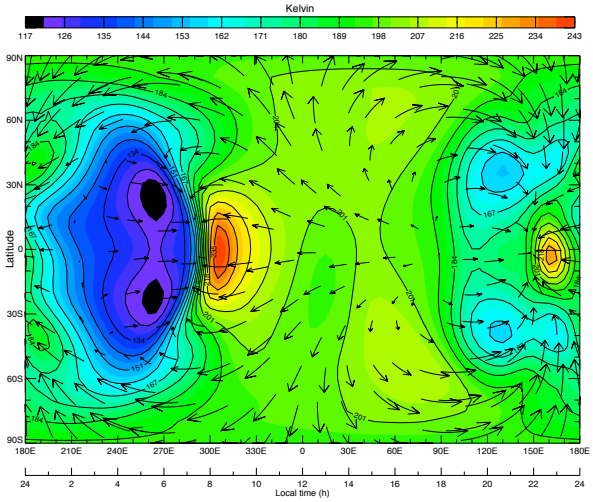

(a) Coupled MarTIM-MCD with MarTIM volume mixing ratios. Average height 186.94 km, temperature 181.1 K.

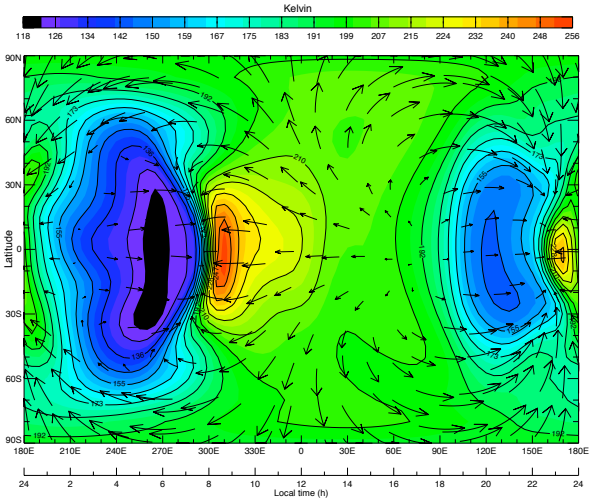

(b) Coupled MarTIM-MCD with MCD volume mixing ratios. Average height 191.93 km, temperature 181.9 K.

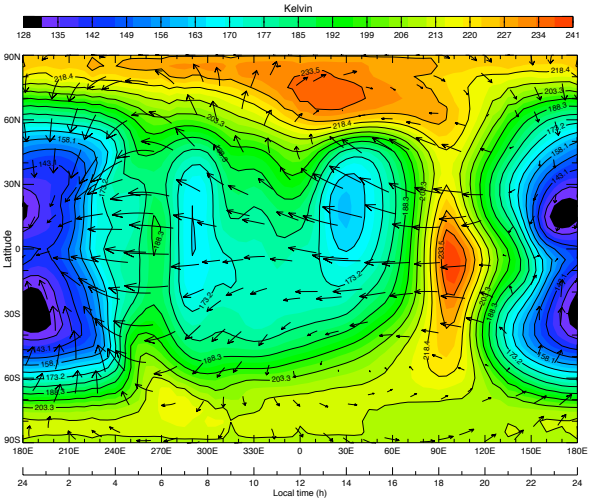

(c) MCD alone (UT 1200-hrs). Average height 201.20 km, temperature 183.2 K.

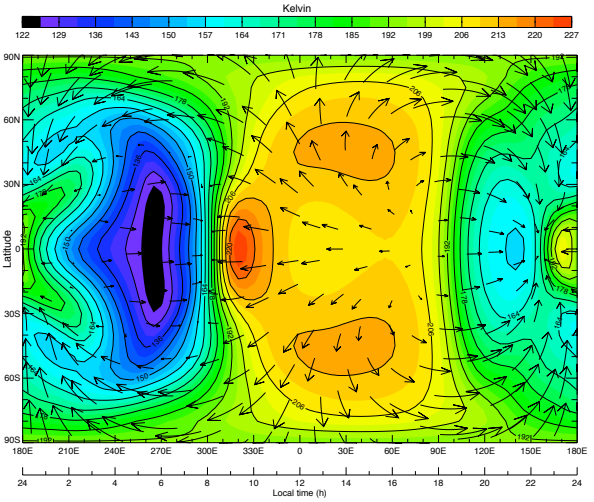

(d) MarTIM alone. Average height 189.32 km, temperature 181.5 K.

Figure 5.18: Temperatures (and wind field vectors) at constant pressure level 30 (4.45×10^{-7} Pa) for coupled MarTIM-MCD simulations (with and without MCD volume mixing ratios for CO_2 15-μm cooling), MarTIM alone (flat lower boundary) and MCD alone (direct from DVD, for UT 1200-hrs). Solar minimum and average Mars year 24 dust (scenario 1) throughout.

in the coupled simulations (aside from any comparison to the MCD alone result).

On the dayside we expect MarTIM mixing ratios to underestimate the amount of atomic oxygen in the thermosphere because photodissociation of CO_2 isn't included. This will result in a reduced rate of CO_2 15-μm cooling when MarTIM's CO_2 and O mixing ratios are used in the CO_2 cooling parameterisation. Thus in the thermosphere we expect coupled MarTIM-MCD results using MarTIM mixing ratios to overestimate dayside temperatures and circulation magnitudes. At the same time since O is transported by advection more efficiently than CO_2, given it's smaller mass, we expect more atomic oxygen on the

nightside in the MCD mixing ratios thereby enhancing nighttime CO_2 cooling when MCD mixing ratios are used in coupled MarTIM-MCD simulations. Note that there will inevitably be subtleties to these suggested relationships. For example, the MCD composition and chemistry calculations will also include CO_2 reformation processes as well as processes which reduce the amount of O. Such chemistry will also involve mixing throughout the entire MCD vertical domain. Therefore our predictions above will likely only be a guide as to how the results may differ.

Finally, a separate complication aside from the particular mixing ratio set used in the CO_2 cooling routine, is that we expect both types of coupled simulation to overestimate the rate of solar EUV heating when they are compared to the MCD alone result. This will be because, again, neither version of the coupled model includes the photodissociation of CO_2. Thus coupled simulations mixing ratio of CO_2 used to calculate solar EUV heating will be too high and since CO_2 heats the atmosphere more effectively than atomic oxygen (as we saw in Chapter 4) the temperatures simulated will be relatively higher as well. Again, this will be a distinct difference between both of the coupled model types and the MCD result, independent of the mixing ratio set used in the coupled model's CO_2 cooling routine.

Following the temperature structures at PL 10 (9.81×10^{-3} Pa, Figure 5.7) we see that at PL 15 (Figure 5.16) coupled MarTIM-MCD results continue to converge toward the standard MarTIM alone results rather than being influenced by the MCD provided lower boundary. For example the broad dayside hot region in the MarTIM alone result at PL 10, generated by peak IR heating, becomes a much smaller, less dominant temperature maximum at PL 15 as the IR heating rate decreases. Moreover its focus shifts by 1 or 2 hours from overhead the equator at 1400-hrs to being between say 1200-hrs to 1300-hrs. This occurs alongside the equatorial 0200-hrs to 0300-hrs hot region also moving to earlier hours. It is now more focussed over 0100-hrs. At both PL 10 and PL 15 the global circulation flow can be seen to be largely comparable i.e. winds flowing poleward from the expansion of the dayside equatorial regions, flowing over the evening terminator to converge on the nightside. However, the shift in local time location of the temperature structures noted reflects almost a doubling of zonal wind speeds. Thus, still referring to MarTIM alone results, zonal wind speeds at PL 15 are now 118.4 m/s eastward (-103.2 m/s westward) versus 65.2 m/s (-56.9 m/s) at PL 10. This results in a stronger convergence of eastward and westward winds at approximately 1000-hrs playing a greater role in heating PL 15 and hence shifting the dayside heating emphasis towards noon away from the afternoon (where, again IR heating would have dominated but now has a reduced influence). Finally this also brings the nightside point of convergence to earlier hours, as noted above. Indeed given the reduction in direct solar heating on the dayside at PL 15 the 0100-hrs hot region is now the dominate temperature structure at this pressure level.

Now, returning to the coupled MarTIM-MCD results, we see similar changes in temperatures structures when moving from PL 10 to 15 as were just noted for the MarTIM alone case. Thus the main dayside temperature peaks have also reduced in size and moved to earlier local times and the dominant temperature maximum is now also in the early morning (from 0000-hrs to 0100-hrs). The differences introduced between the two types of coupled result by the MarTIM and MCD mixing ratios (in the CO_2

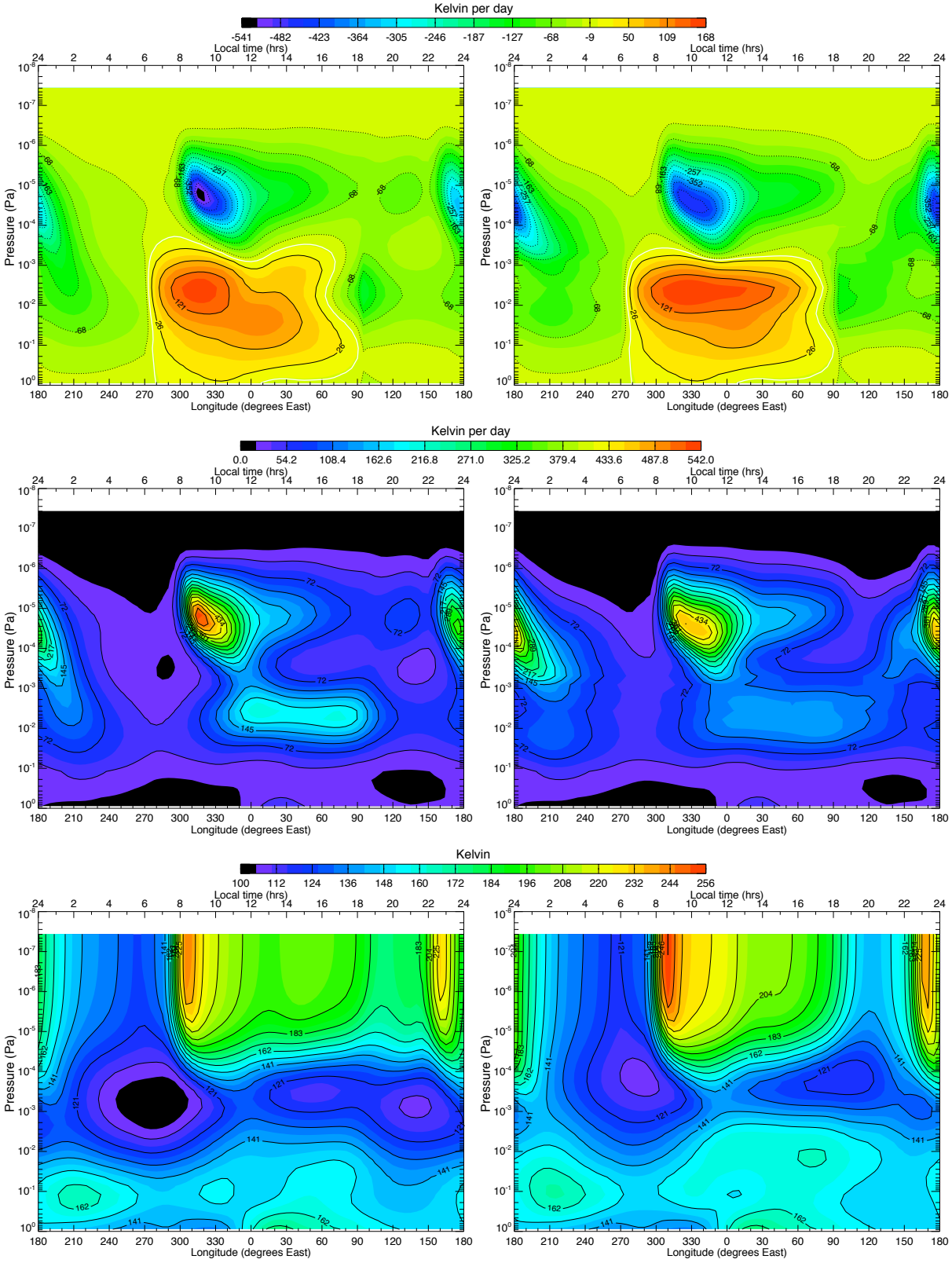

Figure 5.19: Equatorial slice of IR radiative balance (top row), CO_2 15-μm cooling rate (middle row) and temperatures (bottom row) for SMIN, equinox conditions and average Mars year 24 dust. Left column uses MarTIM mixing ratios in the CO_2 cooling routine, right column uses mixing ratios from the MCD.

cooling routine) are now more prominent at PL 15 than at PL 10. Figure 5.19 (top row) shows the IR radiative balance for each of the coupled simulations. Using MarTIM CO_2 and O mixing ratios in the IR cooling routine has resulted in a more focussed and thus smaller IR heating region about the PL 10 to 13 region between 0800-hrs and 1000-hrs (top left plot, Figure 5.19). This is in contrast to the broader peak when the MCD mixing ratios are used (top right plot, Figure 5.19), which covers the same pressure levels but now extends from 0800-hrs / 0900-hrs through to 1300-hrs. This difference is linked to the rate of CO_2 cooling (middle row, Figure 5.19), which is in fact greater around the PL 10 to 13 region when MarTIM's mixing ratios (middle left plot, Figure 5.19) are used in the CO_2 15-μm cooling routine. Consequently when the MCD mixing ratios are used the IR cooling is reduced, so that the IR balance remains more in the positive and thus temperatures are hotter (bottom right plot, Figure 5.19).

In the middle atmosphere the above features contradict our predictions above that MCD O mixing ratios would result in greater CO_2 cooling, although Figure 5.19 does show more CO_2 cooling on the nightside in the thermosphere with the MCD mixing ratios, as we expected. Figure 5.20 shows the $\log_{10}$ O to CO_2 ratio at PL 15 for both MarTIM's mixing ratios (black line) and those from the MCD (red line, UT 1200-hrs). Firstly, clearly this figure shows that the MCD mixing ratios used in the CO_2 cooling routine are very different to those of MarTIM. The MCD has far less O at PL 15 and thus produces less CO_2 cooling. This mainly arises by combination of both (whole atmosphere) diffusion

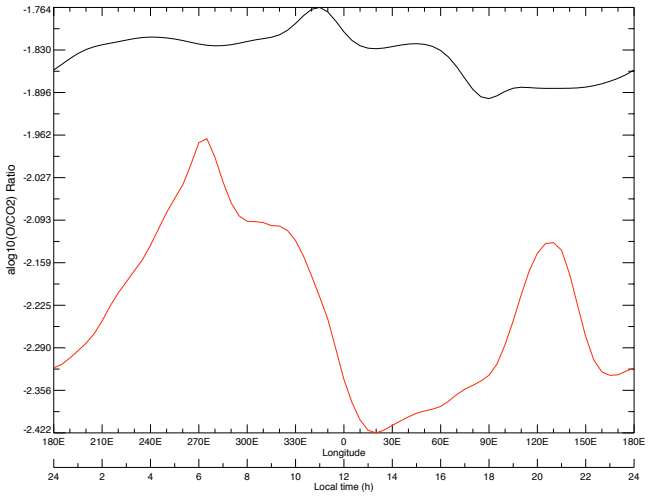

Figure 5.20: Equatorial slice of $\log_{10}$ O to CO_2 ratio at PL 15 for SMIN, equinox conditions and average Mars year 24 dust. Black line is the MarTIM mixing ratios, red line is the mixing ratio from the MCD (for UT 1200-hrs, but which is updated every hour of the simulation).

and advection processes that efficiently transport O to other regions of the model but which also bring other atmospheric constituents into contact with O leading to its removal by swift chemical reaction. For example OH_x radicals that act as catalysts for the reformation of CO_2 (Yung and DeMore, 1999; Wayne, 1985). Equally at these low altitudes the production of O from photodissociation of CO_2 will be negligible because of the optical depth blocking out the required high energy sunlight. Thus what minimal O there is will be swiftly and efficiently removed from the atmosphere. Besides we are referring

to mixing ratios that for both the MCD and MarTIM are very small indeed. Nonetheless the difference in temperatures and IR radiative balance that results (Figure 5.19) does highlight the importance that even small amounts of certain species can play within the atmospheres energy input and output processes.

The greater rate of middle atmosphere (PL 15) IR energy input (given the reduced IR cooling) present on the dayside when MCD mixing ratios are used in the CO_2 15-μm cooling routine results in enhanced wind magnitudes at PL 15 (versus when MarTIM ratios are used). Thus maximum eastward winds reach 180.3 m/s (-160.9 m/s westward) with MCD ratios versus 151.8 m/s (-130.4 m/s) when MarTIM ratios are used. This relationship continues at PL 20 and 30 where peak eastward winds reach 229.4 m/s and 261.0 m/s respectively for the MCD ratios versus 201.8 m/s and 241.7 m/s respectively for the MarTIM ratios. Generally such an increase in winds for both coupled simulations as we move to PL 20 and 30 results in another local time shift of the principal heating region on these pressure levels. Thus the temperature maximums yet again move to earlier times at PL 20 and 30, as we saw them do in the comparison of PL 10 to 15. Now the convergence of eastward and westward winds occurs in the early morning (0600-hrs to 0700-hrs) and leads to a temperature peak over the equator at 0800-hrs local time rather than between 1200-hrs and 1300-hrs as we saw at PL 15. Consequently the peak at midnight has become a lesser feature (and also has moved to 2300-hrs to 2400-hrs) because (at PL 30) solar EUV heating has added significantly to the dayside expansion and westward equatorial winds to allow the morning heating feature in the tropics. In turn, because of the higher wind magnitudes when the MCD mixing ratios are used in the CO_2 cooling routine that this leads to a temperature peak of $\sim$256 K versus $\sim$243 K with the MarTIM ratios.

Finally then the comparison between the two types of coupled MarTIM-MCD result versus the MCD alone result shows that the much faster wind magnitudes in the MCD alone result remains as a major difference. Also, as at the lower pressure levels, the differing in zonal mean wind structures drives differences in the comparison of temperature magnitudes and structures.

5.4.4 Coupled MarTIM-MCD results versus MCD alone: A Discussion

From section 5.4.1 to 5.4.3 we draw the following conclusions regarding coupling the MCD to MarTIM at 0.883 Pa:

- Temperature and wind structures compare well between the MCD alone and the coupled model but only through the lowest few pressure levels, i.e. below about PL 5 (1.20×10^{-1} Pa) for annually averaged lower atmosphere dust content and SMIN conditions.

- The variation in temperature structures and magnitudes with increased lower atmospheric dust content (below 0.883 Pa) also showed the expected trend, with more dust enhancing solar absorption in the MCD and in turn introducing hotter temperatures and faster winds within MarTIM.

- At progressively higher pressure levels (lower pressure, higher altitude) MarTIM's in-situ energy input and output processes (solar EUV and IR heating, CO_2 15-μm radiative cooling) begin to

dominate over the influence from the MCD 0.883 Pa pressure level. Consequently temperature and wind structures in the coupled results begin to look more like their MarTIM alone counterparts (with the flat, isothermal lower boundary) upwards from about PL 10. The magnitudes of circulation structures in particular were greatly reduced in the coupled result against their MCD alone counterparts (e.g. zonal winds ∼96 m/s (−72 m/s) versus ∼178 m/s (−155 m/s), respectively at PL 10). In section 5.4.2, Figure 5.9, this was shown to be a result of the approximation we had to make in section 5.3.2 in order for coupled results to reached a steady state. The approximation of measuring geopotential height gradients from the 0.883 Pa lower boundary was shown to result in horizontal geopotential height gradients that were about 1/3 as great than if they had been measured from the planetary surface (Martian areoid). It was only a matter of vertical distance from the MCD supplied 0.883 Pa level before MarTIM's local energy inputs began to constrain the MCD from above.

- Many of the vertically propagating tidal modes, that within the MCD alone result propagate from the lower to upper atmosphere over the 0.883 Pa pressure level, seem to have a much reduced role in the coupled MarTIM-MCD simulations relative to the background zonal mean. While some non-migrating tides that are important according to background research do make an appearance in the coupled results (e.g. the diurnal eastward wavenumber 1 wave) they usually have at most only 1/2 the amplitude of the MCD alone counterparts. They are present, but their relative importance is reduced; increasingly so the further away from the MCD 0.883 Pa influence. In turn, the range of tidal modes and their amplitudes in the temperature field also begin to show better comparison with the MarTIM alone counterparts from about PL 10 (as was the case in the temperature field itself) thus generally restricted to migrating tides. These effects were also linked to the approximation made in section 5.3.2, the reduced wind magnitudes that this created in the coupled model and thus the interaction between vertical propagating tides and the background zonal winds. For example Ekanayake et al. (1997) and Forbes et al. (2001) state how eastward (westward) propagating nonmigrating tides have larger amplitudes in regions of westward (eastward) mean zonal winds. Thus with an overall reduction in wind magnitudes throughout the coupled model (in particular the reduced eastward zonal jets up to ∼120 km, see Figure 5.10) we would see a reduced presence of any eastward propagating non-migrating tides. This alongside the complex thermal structures in the lower pressure levels that reflected the shift in the dominant energy input and output processes from the MCD 0.883 Pa pressure level to MarTIM's higher altitude in-situ processes contributed to the different tidal responses of each model.

- Differences between the coupled model results that relate directly to the mixing ratios used in the CO_2 15-μm radiative cooling subroutine are apparent. This was most noticeable in the PL 10 to 13 (9.81×10^{-3} to 2.19×10^{-3} Pa) dayside region where the difference in CO_2 cooling was on the order of 70 K/day. MarTIM mixing ratios generating the greater amount of cooling versus MCD ratios. This affected temperature and wind structures to a fair extent throughout the atmosphere (hotter

with the MCD ratios) but in particular resulted in wind magnitudes that were approximately 20% faster about PL 15 when the MCD mixing ratios were used. Such differences were also present at higher pressure levels but to lesser extent given the similarity in solar EUV heating inputs at these levels between the coupled model types.

- Coupled MarTIM-MCD simulations produce wind magnitudes that are significantly faster than their MarTIM alone counterparts (with the flat, isothermal lower boundary) at all pressure levels. However, as above, these magnitudes are in turn not as great as the MCD DVD wind speeds.

The most important difference between coupled MarTIM-MCD and the MCD DVD results occurs at PL 2 (5.36×10^{-1} Pa), since this is the first pressure level away from the MCD input at 0.883 Pa. Table 5.2 and Figure 5.5 showed how the wind magnitudes of the two model types at this pressure level were particularly different. The MCD eastward wind speeds were about 50% faster than the coupled model equivalents. Although the coupled model wind speeds were themselves far greater than the MarTIM alone result (thus clearly positively influenced by the MCD's presence) the associated difference in advective heating between the MCD and the coupled model resulted in e.g. $\sim$11.9 K difference in temperatures for average dust conditions, again, as early as PL 2. Ultimately these differences resulted in temperature structures of the two model types diverging from one another at higher pressure levels.

This immediate disconnect between coupled MarTIM-MCD and MCD alone results suggests an inherent difficulty in coupling two independently developed GCMs. The difference in middle atmosphere (PL 10 to 13) CO_2 15-μm radiative cooling noted above is another example of the great care that must be taken in ensuring equivalence between the various parameterisations used and the important differences that result if this is not the case. Also, it is quite possible that the vertical distribution of dust within the MCD (see equation 5.1, section 5.3.1) extends above MarTIM's 0.883 Pa lower boundary. This is not included at all within MarTIM. The additional heating that this would provide could very well enhance temperatures, atmospheric expansion and wind magnitudes throughout MarTIM's lowest few pressure levels and thus improve the transition from the MCD to MarTIM. And for the tidal modes present in the MCD, it could be that the $5.625^\circ\times3.75^\circ$ longitude by latitude horizontal grid the MCD uses automatically allows a wider range of tides to be represented than with MarTIM's grid. Another point to mention[6] is that the MCD data involve quite a long-term time-averaging at fixed local times and so do not represent full synoptic variability even though tides are fairly comprehensively included on average. The time-averaging will have been necessary to allow the MCD data fit onto the DVD. If MarTIM did not have to rely on the MCD at all but could instead self-consistently describe the lower atmosphere itself then a fuller more comprehensive coupling would be achieved (see section 7.2.2, Chapter 7).

Mostly though it was unfortunate that, regarding the coupling, were it not for the approximation discussed in section 5.3.2 coupled MarTIM-MCD simulations would often produce physically inconsistent results or fail to reach a steady state. This was typically due to the zonal advection of total energy term

[6]Private correspondence with Professor Peter L. Read, Oxford University and Professor Andrew J. Coates, Mullard Space Science Laboratory.

becoming unstable in the energy equation. Significant wind amplitudes were introduced by coupling MarTIM to the MCD due to large variations (and thus horizontal gradients) in geopotential height with latitude and longitude. This generated large compressional heating in regions where eastward and westward winds converged. To reduce the influence of gradients in geopotential height we assumed the 0.883 Pa lower boundary provided by the MCD was a surface of constant geopotential and measured all geopotential heights against this pressure level. This effectively removed any variations in geopotential heights that occurred below 0.883 Pa that would otherwise have contributed to pressure gradients at this level.

However clearly in doing so we have damped the wind magnitudes to such great extent that their influence on temperature structures through advective heating and cooling is greatly diminished. One other alternative solution was simply to use the original relationship of measuring geopotential gradients against the Martian areoid (constant geopotential planetary 'surface') **but** use a reduced resolution in the horizontal grid. This would effectively smooth out the large horizontal gradients in geopotential height and in doing so reduce the possibility of specific latitude-by-longitude regions where advective heating overwhelms the code. At the same time it would not reduce the horizontal geopotential gradients by as much as the assumption of section 5.3.2 had. The cost would be a reduction in detail resolved by the model and therein the possibility of ignoring important heating and cooling phenomena that occur at finer scales.

Reduced Latitude-by-Longitude Resolution

The effect that reducing the latitude-by-longitude resolution (alongside no longer approximating the 0.883 Pa lower boundary as a geopotential surface) has on the coupled MarTIM-MCD result is shown in Figures 5.21, 5.22 and 5.23. These show latitude by longitude contour plots of temperatures, with wind vectors overlaid, at pressure levels 5 (1.20×10^{-1} Pa), 10 (9.81×10^{-3} Pa) and 30 (4.45×10^{-7} Pa). As before, solar minimum and equinox conditions (1.47 AU) are used throughout and we continue to focus only on simulations with an annually average dust content in the lower atmosphere (scenario 1 from section 5.3.1). Each figure compares the steady state result of:

- Top left, a coupled MarTIM-MCD simulation, with MarTIM's 3-D volume mixing ratios used in the CO_2 15-μm cooling routine, all geopotential heights measured from the Martian areoid surface and a 5°×8° latitude-by-longitude grid.
- Top right, a coupled MarTIM-MCD simulation, with MarTIM's 3-D volume mixing ratios used in the CO_2 15-μm cooling routine, all geopotential heights measured from the 0.883 Pa pressure level and a 5°×5° latitude-by-longitude grid (as in sections 5.4.1 to 5.4.3).
- Bottom left, the MCD result on its own, direct from the DVD (5°×5° latitude-by-longitude grid as in sections 5.4.1 to 5.4.3).

- Bottom right, the MarTIM result on its own, with the flat, isothermal lower boundary i.e. without the MCD coupled (5°×5° latitude-by-longitude grid as in sections 5.4.1 to 5.4.3).

From Figures 5.21, 5.22 and 5.23 it is clear that the reduced zonal resolution coupled MarTIM-MCD results (top left plots) do not simulate the kind of detail that the 5°×5° grid MCD alone or coupled MarTIM-MCD results from sections 5.4.1 to 5.4.3 produce (bottom left and top right, respectively). However, on the other hand, the reduced resolution coupled results show significant differences to those

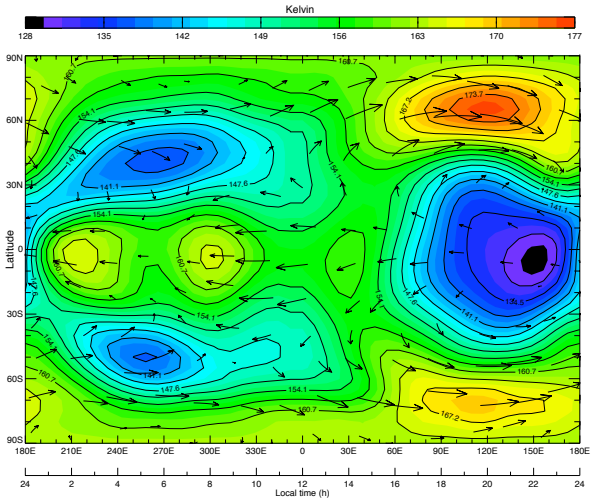

(a) Coupled MarTIM-MCD, MarTIM volume mixing ratios, 5°×8° latitude-by-longitude grid. Average height 74.46 km, temperature 151.6 K.

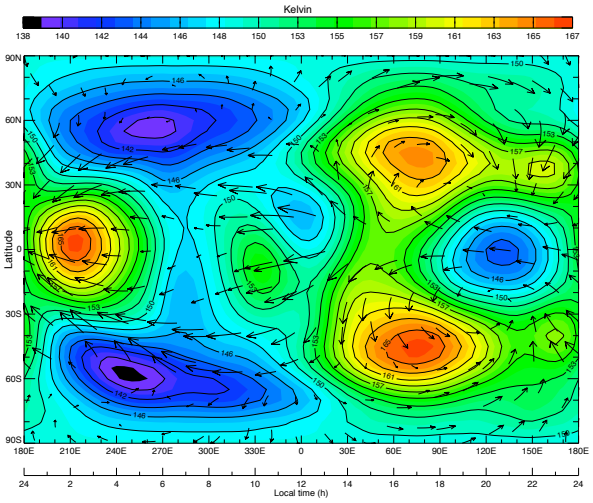

(b) Coupled MarTIM-MCD, MarTIM volume mixing ratios, 5°×5° latitude-by-longitude grid. Average height 74.47 km, temperature 152.1 K.

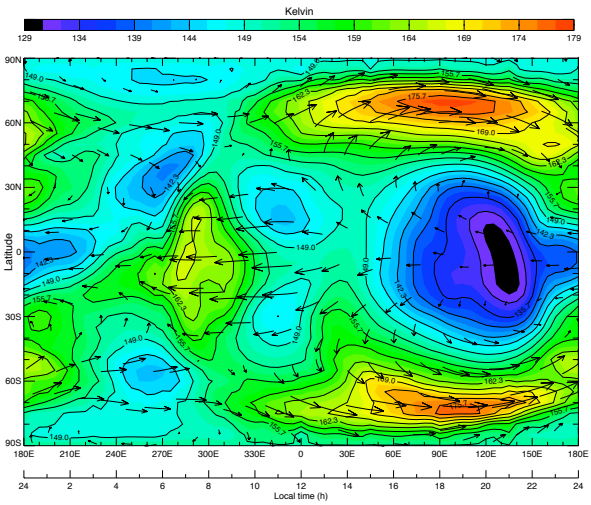

(c) MCD alone (UT 1200-hrs). 5°×5° latitude-by-longitude grid. Average height 74.29 km, temperature 151.4 K.

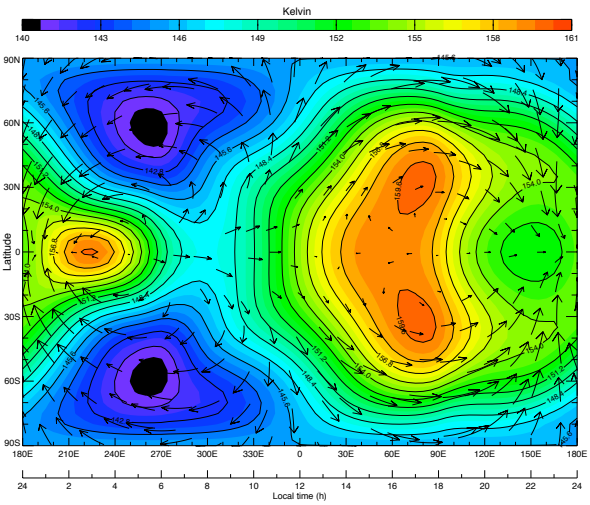

(d) MarTIM alone. 5°×5° latitude-by-longitude grid. Average height 76.31 km, temperature 151.6 K.

Figure 5.21: Temperatures (and wind field vectors) at constant pressure level 5 (1.20×10^{-1} Pa) for coupled MarTIM-MCD simulations (5°×8° and 5°×5° grids) with MarTIM volume mixing ratios for CO_2 15-μm cooling, MarTIM alone (5°×5° grid, flat lower boundary) and MCD alone (5°×5° grid, direct from DVD, for UT 1200-hrs). Solar minimum and average Mars year 24 dust (scenario 1) throughout.

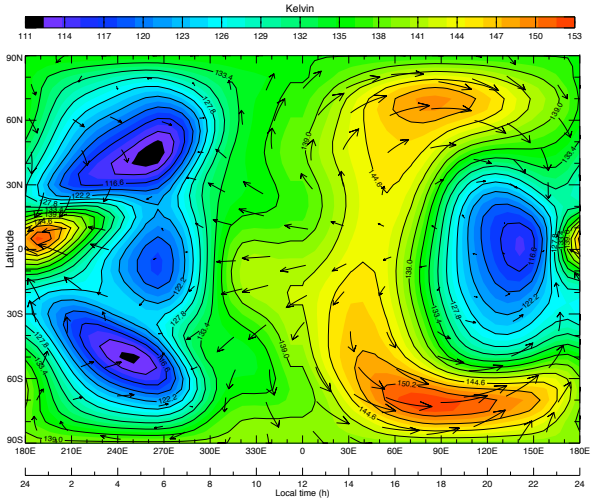

(a) Coupled MarTIM-MCD, MarTIM volume mixing ratios, 5°×8° latitude-by-longitude grid. Average height 94.03 km, temperature 132.6 K.

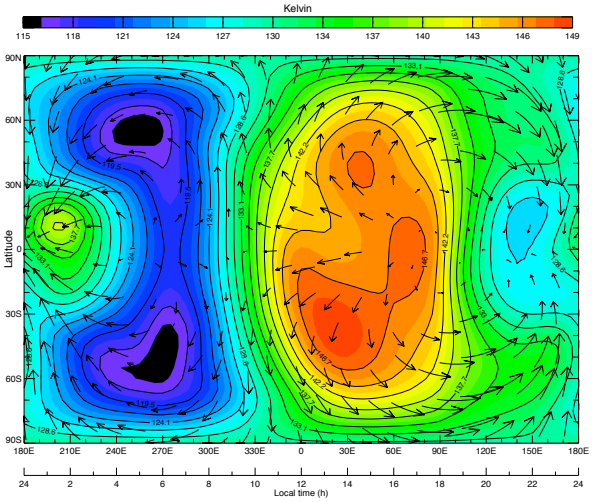

(b) Coupled MarTIM-MCD, MarTIM volume mixing ratios, 5°×5° latitude-by-longitude grid. Average height 94.11 km, temperature 132.2 K.

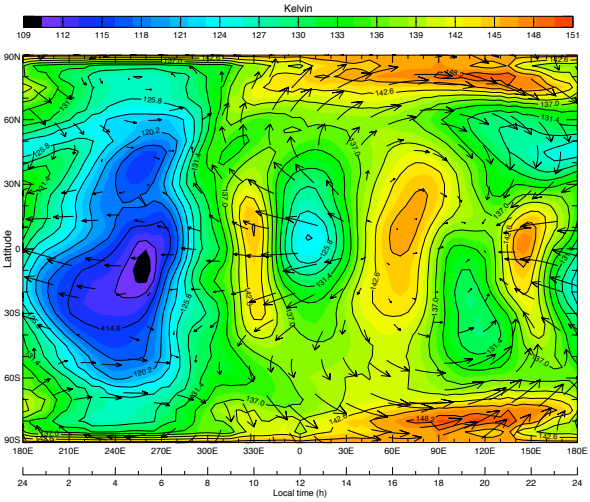

(c) MCD alone (UT 1200-hrs). 5°×5° latitude-by-longitude grid. Average height 93.31 km, temperature 132.0 K.

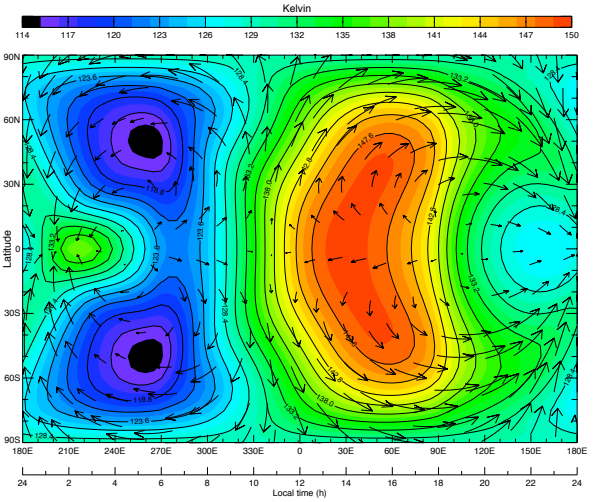

(d) MarTIM alone. 5°×5° latitude-by-longitude grid. Average height 95.99 km, temperature 133.0 K.

Figure 5.22: Temperatures (and wind field vectors) at constant pressure level 10 (9.81×10^{-3} Pa) for coupled MarTIM-MCD simulations (5°×8° and 5°×5° grids) with MarTIM volume mixing ratios for CO_2 15-μm cooling, MarTIM alone (5°×5° grid, flat lower boundary) and MCD alone (5°×5° grid, direct from DVD, for UT 1200-hrs). Solar minimum and average Mars year 24 dust (scenario 1) throughout.

from sections 5.4.1 to 5.4.3 that indicate under these circumstances MarTIM is capable of simulating temperatures that show good comparison to the MCD alone result. For example throughout Figures 5.21 to 5.23 simulations that use the lower 5°×8° resolution (top left plots) maintain temperature peaks at much higher latitudes than those simulations (from sections 5.4.1 to 5.4.3) that measure geopotential gradients to 0.883 Pa (top right plots). In the latter case, recall from previous discussions how MarTIM's localised heating and cooling processes (solar EUV and IR) dominated to generate temperature peaks

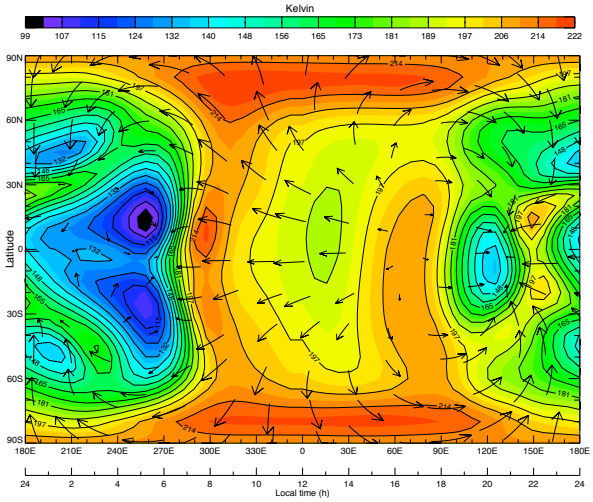

(a) Coupled MarTIM-MCD, MarTIM volume mixing ratios, 5°×8° latitude-by-longitude grid. Average height 182.21 km, temperature 179.6 K.

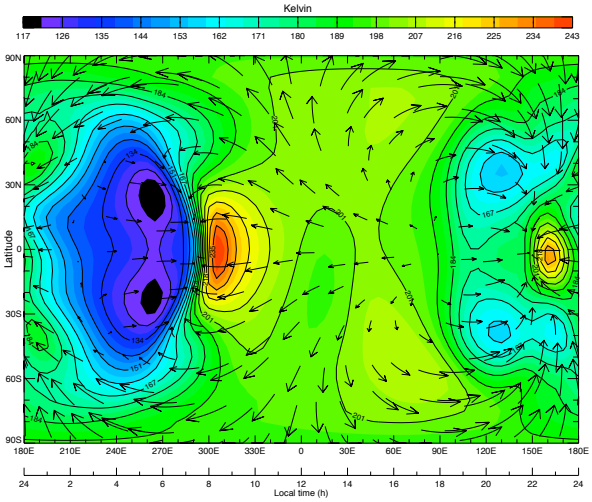

(b) Coupled MarTIM-MCD, MarTIM volume mixing ratios, 5°×5° latitude-by-longitude grid. Average height 186.94 km, temperature 181.1 K.

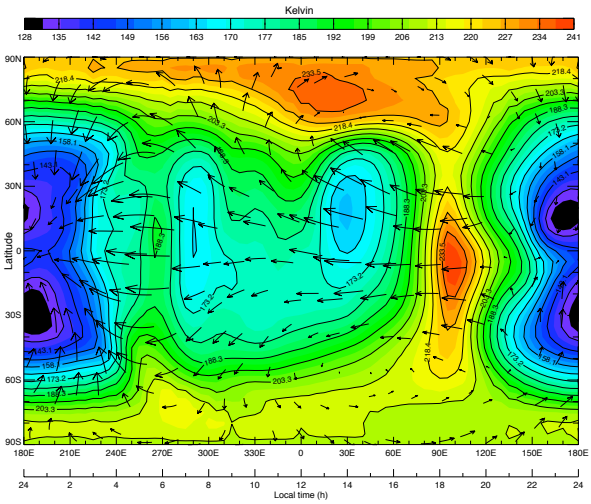

(c) MCD alone (UT 1200-hrs). 5°×5° latitude-by-longitude grid. Average height 201.20 km, temperature 183.2 K.

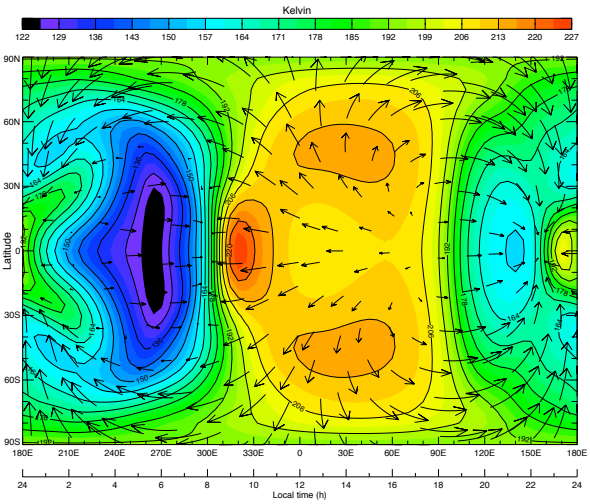

(d) MarTIM alone. 5°×5° latitude-by-longitude grid. Average height 189.32 km, temperature 181.5 K.

Figure 5.23: Temperatures (and wind field vectors) at constant pressure level 30 (4.45×10^{-7} Pa) for coupled MarTIM-MCD simulations (5°×8° and 5°×5° grids) with MarTIM volume mixing ratios for CO_2 15-μm cooling, MarTIM alone (5°×5° grid, flat lower boundary) and MCD alone (5°×5° grid, direct from DVD, for UT 1200-hrs). Solar minimum and average Mars year 24 dust (scenario 1) throughout.

that migrated toward the equator as we climbed in pressure level, eventually becoming single temperature structures overhead the equator (for these equinox conditions). This was in contrast to MCD alone results where the temperature peaks migrated towards the poles, as clear separate entities. Thus it would appear that the lower 5°×8° resolution simulations show a better comparison in this respect with the MCD alone rather than the MarTIM alone result. At PL 5 (1.20×10^{-1} Pa, Figure 5.21), the temperature peaks are overhead the evening terminators at ±70°N, moving right the way to the poles at PL 30 (Figure 5.23).

Again, just as in the MCD alone case. Bear in mind it is still clear that MarTIM's localised heating and cooling processes are strongly affecting the coupled result. For example at PL 10 (Figure 5.22), the IR heating peak, there is a more prominent branch of temperature peak passing over the equator near 1500-hrs, similar to that of the MarTIM alone result. Also there is a adiabatic heating region just after midnight suggesting the global circulation features still maintain a link with their MarTIM alone counterparts. Overall though the lower resolution coupled result still simulates two high latitude temperature peaks that are clearly separate entities, just as in the MCD alone case.

As discussed, the variation in wind structures and magnitudes became a driving source for the differences between the various simulation types. Figures 5.24 and 5.25 show latitude by altitude views of the (zonally averaged) zonal winds. The top plot of Figure 5.24 shows the result for the lower zonal resolution (5°×8° grid) coupled MarTIM-MCD simulation where geopotential heights are measured from the Martian areoid surface. The bottom plot of Figure 5.24 shows the MCD alone result (5°×5° grid). Finally Figure 5.25 shows the result for the coupled MarTIM-MCD simulation discussed in sections 5.4.1 to 5.4.3 with the 5°×5° grid and geopotential heights measured from the 0.883 Pa pressure level. Note how Figure 5.24 (bottom plot) and Figure 5.25 were shown earlier (Figure 5.10) but restricted to below 120 km, whereas here we show the full altitude range simulated.

Now the similarities between the lower 5°×8° resolution coupled simulations and the MCD alone result are clearly seen. The strong comparison in zonally averaged zonal wind structures between the lower resolution coupled simulations and the MCD alone result (top and bottom plots, respectively, Figure 5.24), in particular the continued presence of eastward jets at successively higher latitudes, is striking. Also note in both result types the widening presence of westward winds over the equator and tropics expanding to ±60° latitude at high altitude. Then compare these examples against the coupled results from sections 5.4.1 to 5.4.3 (Figure 5.25) where the eastward high latitude jets were almost completely cut off at ∼70 km by the strong westward momentum introduced by the dominant IR heating peak. At about 90 km, these jets were reinstated to some extent by poleward meridional winds being turned eastward by the Coriolis force but nonetheless were finally replaced entirely across all latitudes by prominent westward winds above ∼120 km.

While the magnitudes of the geopotential gradients will have effectively been reduced (smoothed) in the various terms of the energy and momentum equation that use them (see section 5.3.2) through using a smaller resolution clearly this has not prevented eastward jets from dominating the high latitudes, just as in the MCD alone result. Certainly it hasn't resulted in the kind of differences seen in the comparison with the coupled results from sections 5.4.1 to 5.4.3. However, unfortunately, the lower 5°×8° resolution coupled model does not remain a suitable solution for all the possible lower atmosphere dust and solar conditions that the MCD provides, nor for all solar longitudes that we would wish to study. Indeed for most high dust and global dust storm scenarios from section 5.3.1 the lower 5°×8° resolution coupled model either no longer reaches a steady state or begins to show exactly the same non-physical results we had to deal with originally.

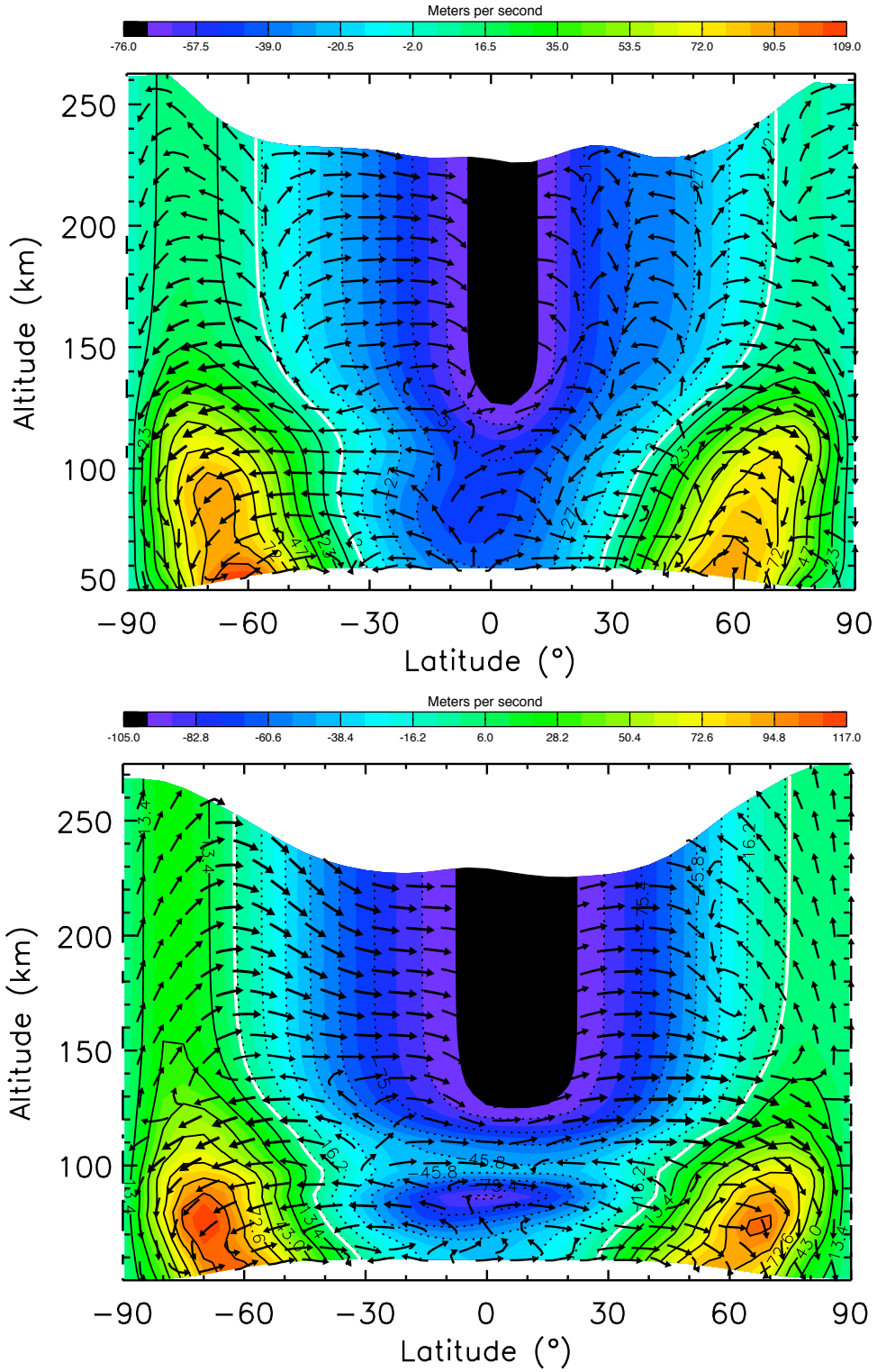

Figure 5.24: Latitudinal slice of zonal average zonal winds (colour contours) and zonal average meridional and vertical winds (black arrows). Top plot is the coupled MarTIM-MCD result with 5°×8° latitude-by-longitude grid, bottom plot is the MCD alone result (5°×5° grid, for UT 1200-hrs). Solar minimum and average Mars year 24 dust (scenario 1) for both. White contours indicate zero magnitudes.

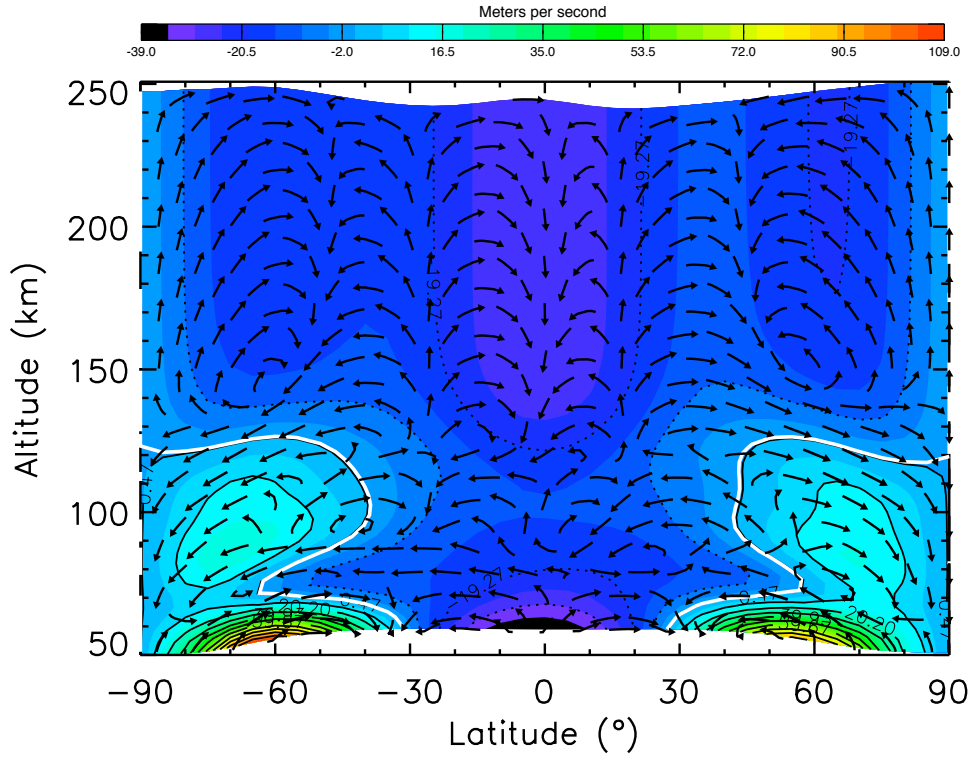

Figure 5.25: Latitudinal slice of zonal average zonal winds (colour contours) and zonal average meridional and vertical winds (black arrows). Coupled MarTIM-MCD result with 5°×5° latitude-by-longitude grid. Solar minimum and average Mars year 24 dust (scenario 1). White contours indicate zero magnitudes.

Only the approximation of measuring geopotential heights from the lower boundary 0.883 Pa level as described in section 5.3.2, whose results were discussed in sections 5.4.1 to 5.4.3, allows for a complete set of coupled MarTIM-MCD results across all possible lower atmosphere inputs. The problem here of course is that this approximation is not fully consistent with the MCD input at 0.883 Pa because with a surface of constant geopotential we have effectively removed any pressure gradients and are thus implying zero horizontal velocities at the lower boundary (which is clearly not the case at 0.883 Pa in the MCD). In some sense we have returned, in part, to the basic lower boundary conditions of earlier chapters i.e. before the MCD was coupled in the first place.

Furthermore, it seems that we will always need to make the assumptions and approximations discussed when we try to couple MarTIM to the MCD. Although these independently developed GCMs are describing the same physical environment, they are both forced to parameterise many processes for the sake of a faster computation or because of the limited availability of suitable coefficients and constants. We have already noted the difference in middle atmosphere (PL 10 to 13) CO_2 15-μm radiative cooling that was predicted when two different sets of mixing ratios were used in the IR cooling routine. This has also been noted in other modelling work, for example Forget et al. (2009) considered the impact of different atomic oxygen profiles on the temperature structure simulated (see figure 17 in that paper). Differences in temperature of up to 50 K were produced near 10^{-4} Pa, and as we saw above such differ-

ences resulted in variations in wind magnitudes and thus advective heating and cooling processes often at entirely different locations to the original discrepancy.

The solar EUV heating parameterisation is another example where differences in parameterisation can inadvertently be introduced. MarTIM's new parameterisation uses a 1 nm solar spectrum grid interval whereas, the LMD model for example, divides the spectrum into 36 subintervals of 20 nm average width (González-Galindo et al., 2005). Thus, again it is possible that discrepancies occur between MarTIM and the LMD that could introduce differences in temperatures. Several steps of computation later and this could contribute to the large magnitude winds that caused the problems originally but specifically because we have combined the influence of the MCD's lower boundary with an independently developed EUV heating parameterisation. The steady state reached by any model requires all processes computed be self-contained and self-consistent within the context of that model. Thus future work with MarTIM should include the extension to lower altitudes to remove all discontinuities between it and the MCD.

Indeed a final point to note is that the MCD will likely calculate a non-negligible dust opacity at altitudes above MarTIM's 0.883 Pa lower boundary. When MarTIM is run without the MCD coupled we set the altitude of the 0.883 Pa level to 60 km. Then, with the MCD coupled this altitude can often be seen to drop to ∼50-55 km. However, term $z_{\max}$, the cut-off altitude of the top of the dust layer in equation 5.1 above, is shown in figures 8 and 9 of Millour et al. (2008) to reach up to maximums of 70 km for the annually averaged and global dust storm dust scenarios during perihelion season (Ls ∼250°, scenarios 1 to 6 from section 5.3.1) and 75 km for the warm scenario (again about Ls ∼250°, scenario 8 from section 5.3.1). Thus the additional heating and expansion that this would introduce to the lowest MarTIM pressure levels could reasonably increase the magnitude of e.g. the poleward circulation features that during equinox conditions had in the above work been too slow. Again this is something that future work will have to address.

5.5 Thermospheric Winter Polar Warming with the Coupled MarTIM-MCD Model

We now return to the discussion from section 4.3 of Chapter 4 regarding polar warming features observed during Mars Odyssey aerobraking in the nighttime northern winter polar regions. We also reconsider the possible presence of similar warming features in the counterpart southern winter polar regions. These phenomena are now simulated with the MCD coupled at MarTIM's lower boundary and compared to the MarTIM alone result (new IR parameterisation) from Chapter 4 as well as the MCD alone result.

5.5.1 Northern Winter Polar Regions During Perihelion Conditions

The plots in Figure 5.26 show temperature versus latitude at constant 120 km for (a) coupled MarTIM-MCD simulations (various colours depending upon solar and dust conditions, see sub-captions), (b) Mars Odyssey derived temperatures in the northern winter hemisphere (blue line and data points) and (c) the

MarTIM alone result with the flat, isothermal lower boundary (black line) from Figure 4.9 of Chapter 4 (new IR heating parameterisation only). There is one important difference to note between the MarTIM-MCD coupled results and the MarTIM alone results plotted in Figure 5.26. Since the result in the coupled model case is now longitudinally variant the specific relationship between the 3-D location plotted and the particular local true solar time at that location must be considered together. Thus to produce the plots of temperature for the coupled MarTIM-MCD model we take full 3-D results every 20 minutes of simulation time (once the model has reached steady state), giving us 3-D temperatures at 72 different universal times. Within each of these 72 different output files we search for the particular local time we wish to plot before zonally averaging the longitudes together. The coupled MarTIM-MCD results are therefore described as the zonal mean temperatures at some constant local time (see sub-captions) and altitude of 120 km for the perihelion Ls 270 season.

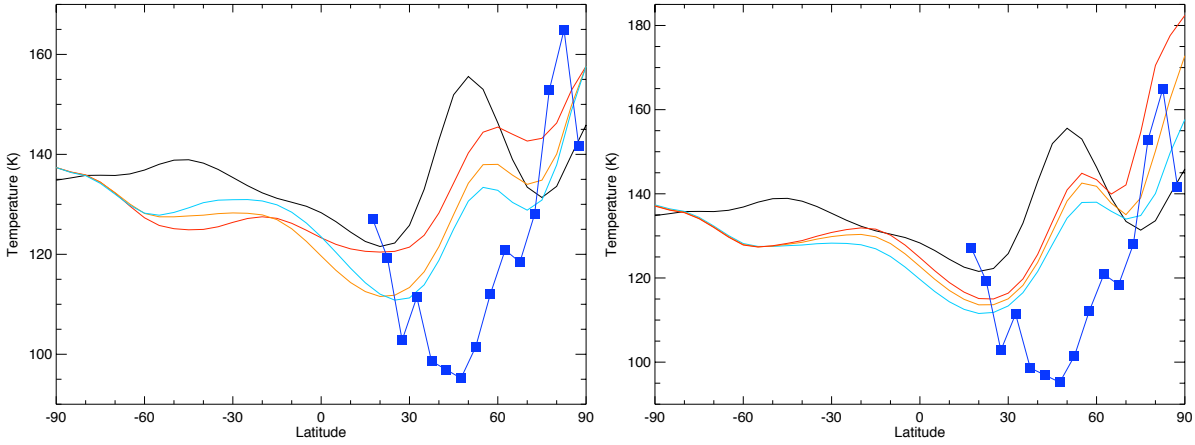

(a) SMIN, average dust, 0100-hrs, 0200-hrs & 0300-hrs

(b) SMIN, SMED, SMAX, average dust, 0200-hrs

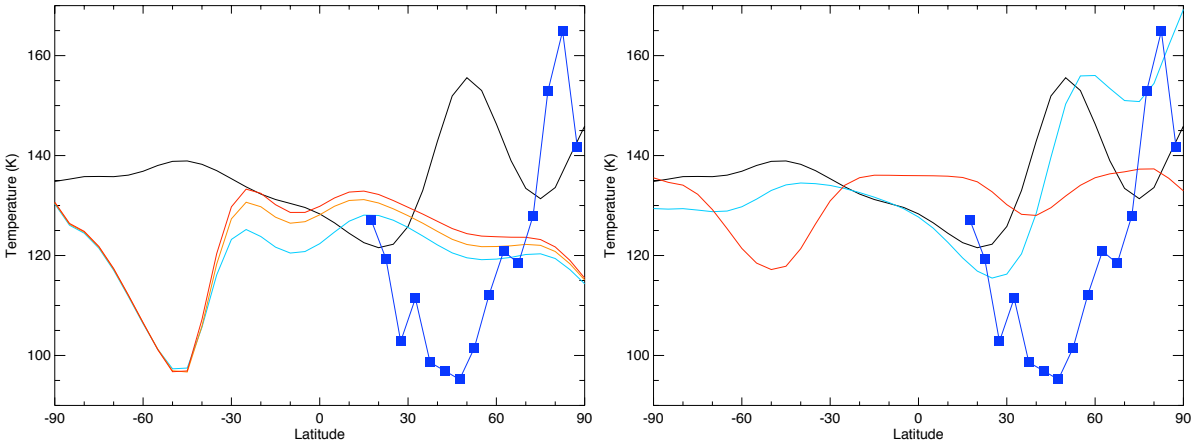

(c) SMIN, SMED, SMAX, dust storm, 0200-hrs

(d) SMIN (low dust), SMAX (high dust), 0200-hrs

Figure 5.26: MarTIM-MCD perihelion (Ls 270) temperatures versus Mars Odyssey derived temperatures (blue line and data points) at 120 km over a range of local times, solar and dust conditions. Black lines indicate MarTIM-only result (from Chapter 4). The cyan, orange and red lines (in that order) indicate coupled MarTIM-MCD results for various solar and dust conditions as indicated in the subcaptions.

Various combinations of solar conditions and lower atmosphere dust opacities are plotted in Figure 5.26. Recall from Chapter 4 that the polar warming features were observed typically around the 0200-hrs local times with some as early as 0000-hrs and others as late as 0300-hrs. Firstly then Figure 5.26(a) shows the variation in temperature for local times 0100-hrs, 0200-hrs and 0300-hrs for solar minimum conditions and average Mars year 24 dust content (cyan, orange and red lines respectively). For comparison to the work of Chapter 4 the 0200-hrs MarTIM-only result is also shown (black line). Next Figure 5.26(b) shows only the 0200-hrs result, again for an average Mars year 24 dust content, but now for a fuller range of solar conditions (cyan (SMIN), orange (SMED) and red (SMAX) lines). In all coupled MarTIM-MCD cases of Figure 5.26 we use MarTIM's mixing ratios in the CO_2 15-μm cooling routine. Results using the MCD mixing ratios are discussed later with respect to Figure 5.30.

From Figure 5.26(a) and 5.26(b) it appears that coupled MarTIM-MCD results still do not precisely match the temperature structure measured by the Mars Odyssey spacecraft. Neither the data temperature minimum of ∼95 K in the 45-50°N bin nor the specific structures shown by e.g. the peak temperature ∼165 K in the 80-85°N bin followed by the drop in temperature to ∼142 K at the north pole are matched exactly by coupled MarTIM-MCD results. However in concluding Chapter 4 we suggested that the presence of lower atmosphere heating, influenced by dust content and southern highland topography, would deposit additional westward momentum into the atmosphere. This would enhance the interhemispheric circulation features responsible for the polar warming in the same way that the new IR heating parameterisation did in section 4.3.2 i.e. the northward flow would persist to more northerly latitudes before descending and introducing adiabatic heating features. Wilson (1997) for example provides evidence that the momentum flux divergence due to dissipating tides enhances the interhemispheric circulation and may enable its extension beyond 70°N to the winter pole (Moudden and Forbes, 2008a).

Sure enough from Figures 5.26(a) and 5.26(b) it does appear that the temperature structures simulated by MarTIM-MCD have indeed moved northwards. For example from Figure 5.26(b) (all for annually averaged dust) the minimum temperatures at ∼20°N and maximum temperatures at ∼50°N from MarTIM alone simulations (black line) have both moved northwards by almost 10° of latitude in the coupled MarTIM-MCD result (cyan line, for SMIN). Next, the minimum is now cooler by ∼15 K (from ∼125 K to ∼110 K) bringing it closer to the ∼95 K minimum of the Mars Odyssey 45-50°N data bin. Finally the coupled result shows a much greater temperature peak right at the north pole (versus all other latitudes) whereas the MarTIM alone case showed an initial temperature peak at ∼50°N where the compressional heating by descending winds first occurs before a lesser secondary peak at the pole.

The reduced minimum temperature of the coupled result, the shifting of temperature structures northwards and the greater north pole peak all show that MarTIM has responded as we would have hoped following the introduction of the MCD. These changes indicate that adiabatic heating features now occur over a smaller range of latitudes much closer to the north pole. This is shown by Figure 5.27; latitude by altitude slices of zonal average zonal winds are plotted. The top plot is MarTIM alone (Ls 270, SMIN) while the bottom plot is the coupled MarTIM-MCD result for annually average dust

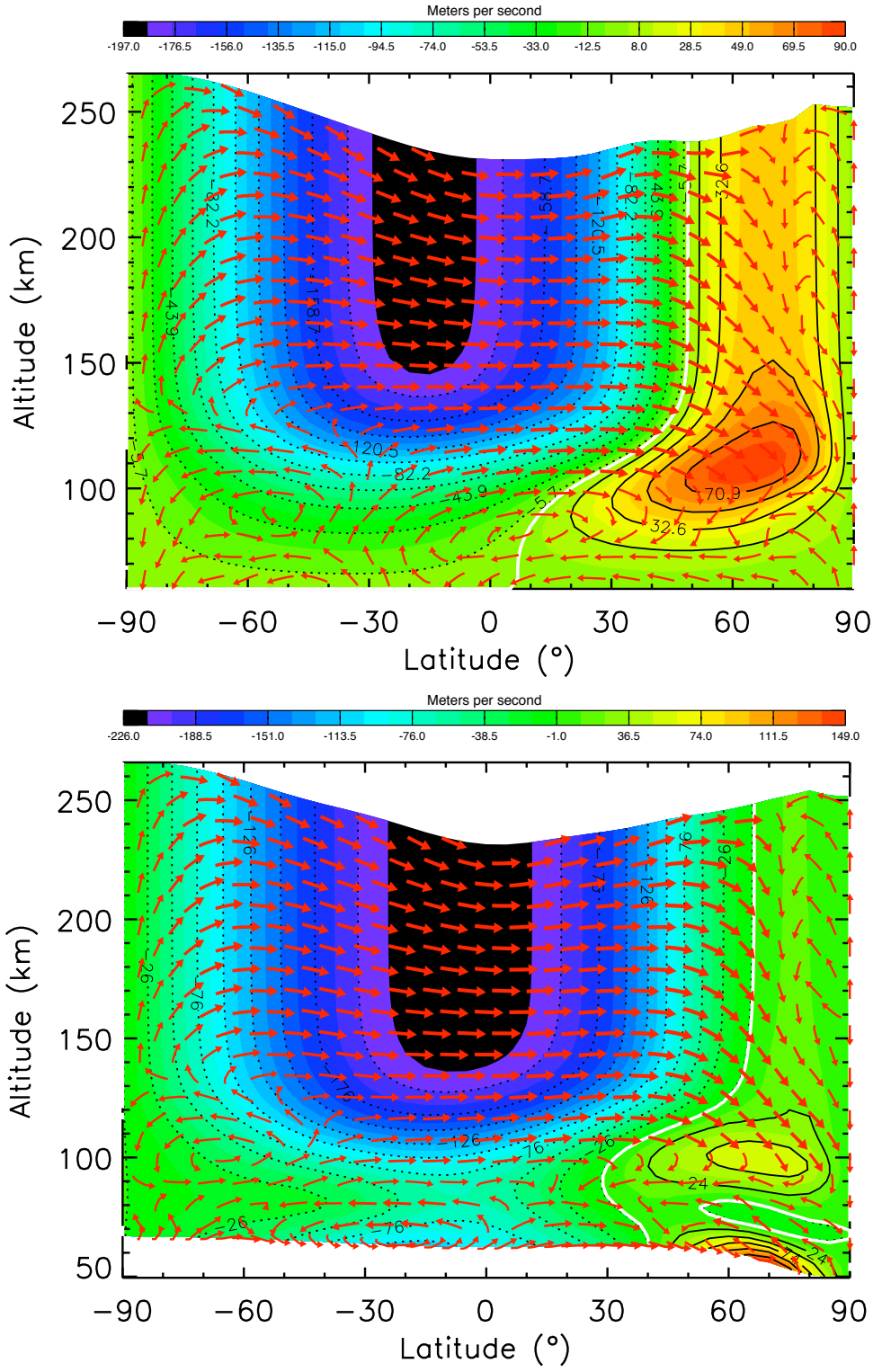

Figure 5.27: Latitudinal slice of zonal mean zonal winds with zonal mean meridional and vertical winds overlaid (red arrows). Top plot is MarTIM alone, bottom plot is coupled MarTIM-MCD result with average Mars year 24 dust (scenario 1). Solar minimum, Ls 270 (perihelion) for both.

and SMIN solar conditions. Clearly from these figures we can see that coupling MarTIM to the MCD has resulted in more prominent westward winds that now extend to higher northern latitudes. Indeed westward winds persist at almost all latitudes in the upper atmosphere (∼65°N coupled case versus ∼50°N MarTIM alone case). Consequently the northward moving meridional circulation is at a much more northerly location (and restricted to a smaller latitudinal range) when these westward winds are decelerated and deposit their energy as adiabatic heating, as a comparison of the wind vector arrows clearly shows. You can also see how the temperature minimum at 120 km and ∼30°N in the coupled MarTIM-MCD result (e.g. cyan line in Figure 5.26(b)) is now colder than in the MarTIM alone result (e.g. black line in Figure 5.26(b)) as this shift in the location of compressional heating occurs right the way down to the lowest MarTIM altitude regions. Thus the region about ∼30°N at 120 km is no longer being heated by the convergence of meridional circulation in the coupled result as much as it was in the MarTIM alone case.

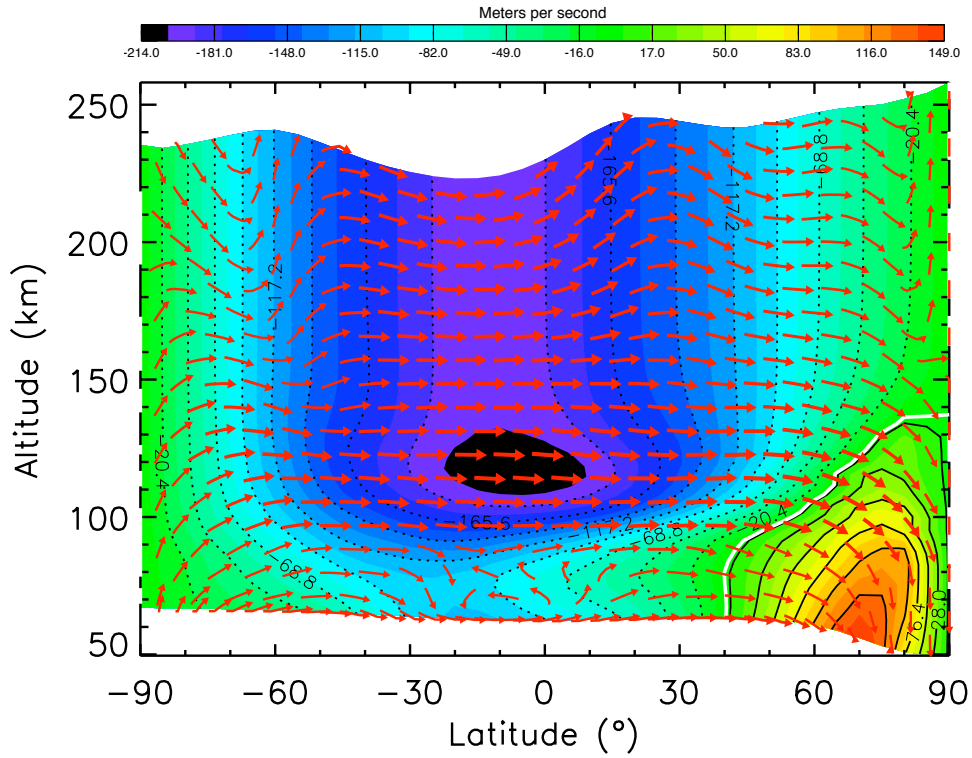

Figure 5.28: Latitudinal slice of MCD solar minimum, Ls 270 (perihelion) zonal mean zonal winds with zonal mean meridional and vertical winds overlaid (red arrows). Average Mars year 24 dust (scenario 1).

Figure 5.28 shows the equivalent MCD alone result (SMIN, annually averaged dust) to be compared against Figure 5.27. Here we can see how westward winds in the upper atmosphere now persist over all northern latitudes. The wind magnitudes for these three plots show that the coupled MarTIM-MCD result of Figure 5.27 (bottom plot) predicts a zonal mean westward (summer) wind maximum of ∼−225 m/s in the thermosphere with an eastward (winter) jet about 100 km altitude of magnitude ∼70 m/s.

In the MarTIM alone case (top plot), the westward maximum is only ~ -199 m/s in the thermosphere while the eastward jet at $\sim$100 km is faster $\sim$90 m/s. So these two plots agree with the statements above that greater westward wind magnitudes result in more prominent polar warming features for perihelion as we suggested earlier. In turn one would expect the MCD alone result to show further increases in wind magnitudes over the coupled result, just as was revealed earlier in sections 5.4.1 to 5.4.3. However Figure 5.28 shows a fair subtlety to the zonal average zonal wind structures and magnitudes with upper atmosphere westward winds reaching no more than ~ -200 m/s.

Linking back to sections 5.4.1 through 5.4.3, the presence but poor transmission of nonmigrating tides through MarTIM's background atmosphere, i.e. because of the differences in wind and temperature magnitudes and structures, can be seen with Figure 5.29. This shows the temperature amplitude of the (1, -1) mode i.e. the eastward propagating diurnal kelvin wave, for both the coupled MarTIM-MCD result (left plot) and the MCD alone result (right plot). Here you can clearly see the prominence of this tidal mode throughout the upper atmosphere of the MCD alone result versus the much weakened presence in the coupled model. The tidal structure shows a dominance in the southern hemisphere where westward winds dominate. From Forbes et al. (2001) the influence of mean winds, specifically

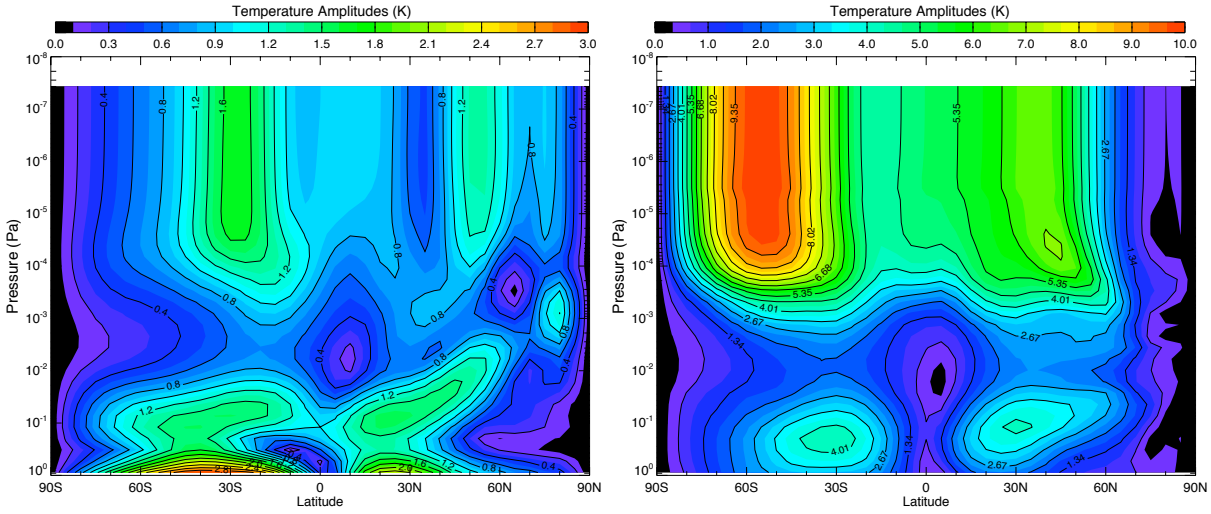

Figure 5.29: Latitude versus pressure level structure of temperature amplitudes for the (1, -1) mode (colour contours). Left plot is the coupled MarTIM-MCD result, right plot is the MCD alone result. Solar minimum and average Mars year 24 dust (scenario 1) for both.

asymmetries in their structure about the equator, impose asymmetries on the atmospheric response to wave forcing. Structural distortions imposed by the mean wind field result in eastward (westward) propagating nonmigrating tides that have larger amplitudes in regions of westward (eastward) mean zonal winds (Ekanayake et al., 1997; Forbes et al., 2001). Consequently the presence of this eastward momentum, alongside the influence of the full spectrum of all the other tides present (though not shown here), results in westward winds in the MCD that are actually less than in the coupled MarTIM-MCD

result (as we saw in Figure 5.27 and 5.28). Indeed, Moudden and Forbes (2008a) states that nonmigrating tides deposit predominantly eastward momentum into the mean flow and therefore appear to counter the mean meridional circulation. Without these subtleties in the tidal modes simulated the coupled result will always struggle to show better comparison to the MCD alone result. Nonetheless, the fact the (1, −1) mode is present at all in the coupled result proves our point from section 5.4.2 (see Figures 5.12 to 5.14) that there is no reason any tidal mode in the MCD cannot be passed over the 0.883 Pa pressure level into MarTIM. It is just unfortunate that the effective damping of background wind magnitudes may complicate the relative importance of those tidal modes.

Next, Figure 5.30 compares polar warming features of the coupled MarTIM-MCD result to those from the MCD alone for a range of dust and solar conditions. Zonal mean temperatures at 120 km are plotted for constant 0200-hrs local time. The left hand plot uses MarTIM mixing ratios in the CO_2 15-μm cooling routine while the right hand plot uses MCD ratios (that are updated every hour of the simulation). From Figure 5.30(a) we see again that the closeness of comparison between the coupled result and the MCD alone is somewhat limited, as it was in sections 5.4.1 to 5.4.3. The MCD alone results are generally hotter, particularly in the northern polar regions where compressional heating is occurring. Since global circulation features are responsible for the polar warming these elevated temperatures suggest faster wind magnitudes for the MCD alone case. This would agree with our discussions earlier in sections 5.4.1 to 5.4.3 regarding equinox conditions that the coupled MarTIM-MCD simulation wind magnitudes were typically greatly reduced from their MCD alone counterparts. Structurally there are differences as well, with the MCD alone showing a much clearer sudden rise in temperature over the northern most 30° of

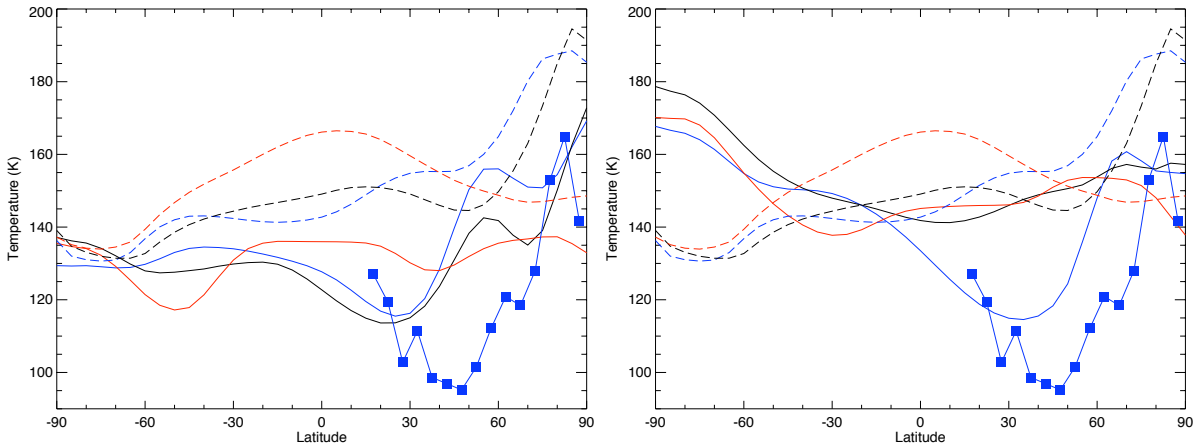

(a) MarTIM mixing ratios in CO_2 cooling routine

(b) MCD mixing ratios in CO_2 cooling routine

Figure 5.30: Perihelion (Ls 270) temperatures versus Mars Odyssey derived temperatures (blue line and data points) at 120 km and 0200-hrs. Blue lines indicate very low dust (scenario 7) and SMIN solar conditions. Black lines indicate annually averaged Mars year 24 dust (scenario 1) and SMED solar conditions. Red lines indicate high dust (scenario 8) and SMAX conditions. Solid lines are coupled MarTIM-MCD result, dashed lines are MCD alone result. Left plot uses MarTIM mixing ratios in CO_2 15-μm cooling routine, right plot uses MCD ratios (updated every hour of the simulation).

latitude against the coupled models initial temperature rise at ∼50 to ∼60°N that is then followed by a greater rise from ∼70 to ∼80°N to the north pole.

Regarding the elevated MCD alone temperatures, González-Galindo et al. (2009a) produce a similar plot to the dashed black lines of Figure 5.30 (see the solid line of Figure 3 in that publication). There are some differences between the two that we attribute to how the results are averaged and the fact they aren't precisely the same model, but nonetheless the polar warming features of both are similar. Thus a temperature increase of about 60 K from ∼140 K at ∼55°N to ∼200 K close to the pole. González-Galindo et al. (2009a) do indeed note that their predicted temperatures are between 30 to 40 K hotter than observed. They also note that MTGCM simulations (Bougher et al., 2006a) also overestimated the temperature by a similar margin. González-Galindo et al. (2009a) state that with respect to the LMD simulations the overestimation can be attributed to an underestimation of the CO_2 15-μm cooling. Then Forget et al. (2009) state how their using a constant atomic oxygen profile within the CO_2 cooling routine rather than the 3-D distribution simulated by the LMD model could be responsible. Since atomic oxygen distributions are known to have an important effect on 15-μm cooling, with variations in cooling up to a factor of 5 when the atomic oxygen profile is modified (López-Valverde and López-Puertas, 1995), then an underestimation of atomic oxygen content could be responsible for the underestimation of cooling and overestimation of temperature. Sure enough they go on to show that with an enhanced O profile temperatures were significantly cooler.

With coupled MarTIM-MCD simulations we can also investigate the effect of variations in O content on the 15-μm cooling rate by using the 3-D CO_2 and O mixing ratios from the MCD within MarTIM's CO_2 cooling parameterisation and compare the results to when MarTIM's ratios are used (as discussed earlier in sections 5.4.1 to 5.4.3). The results with the MCD ratios are shown in Figure 5.30(b) and immediately the differences to using MarTIM's ratios (Figure 5.30(a)) can be seen. In particular the temperature structure for very low dust, SMIN conditions (blue line) shows a striking difference, with a colder minimum of ∼115 K versus ∼118 K that is now between 30°N and 40°N versus 20°N and 30°N for the MCD ratios versus MarTIM ratios respectively. Also, when the MCD mixing ratios are used, there is a clear temperature increase from this minimum to a single maximum of ∼160 K at ∼70°N versus the double peak that is seen in the MarTIM ratios case. There is also the expected high latitude temperature structure, with a drop in temperature from the ∼160 K, ∼70°N peak to ∼155 K at the north pole. Finally, one can see a clearly analogous structure between the blue line coupled model temperatures and those from the Mars Odyssey spacecraft. It seemingly only remains to have the coupled model (with MCD mixing ratios) polar warming located 10° to 20° northwards for a better match.

Clearly the quality of comparison between GCM results and Mars Odyssey data depends highly upon the lower atmosphere dust conditions, the solar conditions and the way heating and cooling processes are parameterised. Indeed coupled MarTIM-MCD results not yet considered include those that show the least comparison with the Mars Odyssey measurements. These are typically the high dust and/or SMAX simulations e.g. Figure 5.26(c) (all coloured lines/solar conditions for lower atmosphere dust storm) and

Figure 5.26(d) (red line, SMAX with high dust conditions). In a similar manner the comparison between coupled results for high dust, SMAX conditions to their MCD alone counterparts in Figure 5.30 (solid and dashed red lines respectively) is also difficult to reconcile. Not least because in turn the MCD alone result for these conditions do not compare well with the Mars Odyssey data either. This last point may simply be that Mars Odyssey data was obtained when the dust content in the nightside winter hemisphere was very low. Sure enough, no global or regional dust storms erupted during the period of Mars Odyssey observations (Bougher et al., 2006a; Smith, 2004). Nonetheless in the coupled MarTIM-MCD cases the greatly reduced wind magnitudes may also be playing a role again in these differences.

5.5.2 Southern Winter Polar Regions During Aphelion Conditions

Now we revisit the southern polar regions during northern summer (aphelion) conditions to see if coupling MarTIM to the MCD has introduced any equivalent winter polar warming features. Figure 5.31 shows zonal mean temperatures at 100 km for constant 0200-hrs local time. A range of dust and solar conditions are shown for coupled MarTIM-MCD simulations (solid coloured lines), the MCD alone result (dashed coloured lines) and also the MarTIM alone result (black solid lines). The left hand plot uses MarTIM mixing ratios in the CO_2 15-μm cooling routine while the right hand plot uses MCD ratios (that are updated every hour of the simulation).

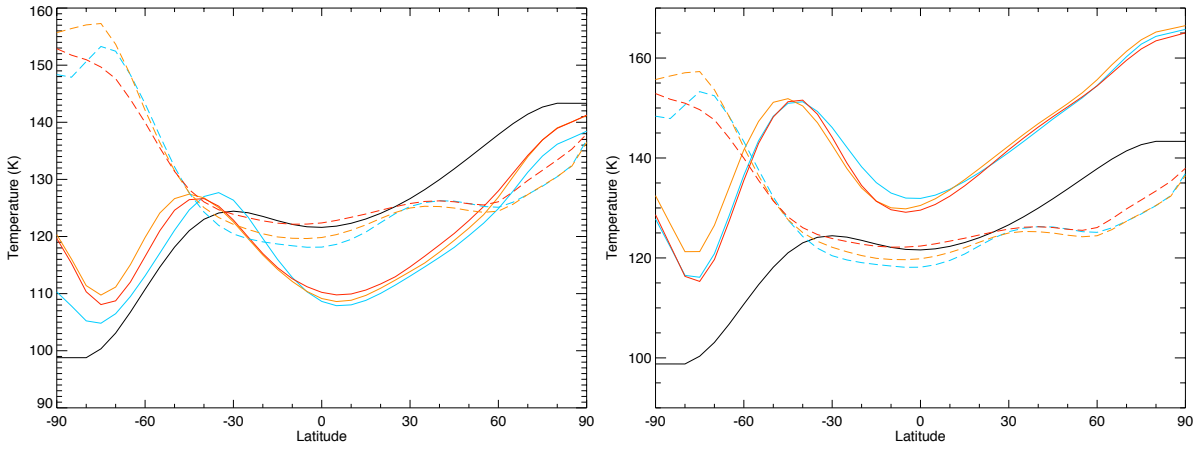

(a) MarTIM mixing ratios in CO_2 cooling routine

(b) MCD mixing ratios in CO_2 cooling routine

Figure 5.31: Aphelion (Ls 90) temperatures at 100 km and 0200-hrs. Cyan lines indicate very low dust (scenario 7) and SMIN solar conditions. Orange lines indicate annually averaged Mars year 24 dust (scenario 1) and SMED solar conditions. Red lines indicate high dust (scenario 8) and SMAX conditions. Black lines indicate MarTIM alone result (SMED). Solid coloured lines are coupled MarTIM-MCD result, dashed coloured lines are MCD alone result. Left plot uses MarTIM mixing ratios in CO_2 15-μm cooling routine, right plot uses MCD ratios (updated every hour of the simulation).

Recall from Chapter 4 that the difficulty in simulating possible southern winter hemisphere polar warming effects was that according to spacecraft data (Keating et al., 2008; Forget et al., 2009) and modelling work (González-Galindo et al., 2009a; Lillis et al., 2008) such features are either weak or

nonexistent or do not repeat every year. Sure enough MarTIM alone simulations (see also the black line in Figure 5.31) did not predict any discernible polar warming features. From Figure 5.31 (black line) we see a general cooling from the northern summer to southern winter hemispheres. There is perhaps some small heating between ∼30°S and ∼40°S but this is nothing like the clear high southern latitude heating in the MCD alone case (coloured dashed lines). The MCD alone results shows an obvious southern winter warming of about 30 K from ∼120 K at ∼30°S to ∼150 K at the south pole.

In the coupled model case the presence of the MCD at 0.883 Pa has produced a clear difference versus the MarTIM alone case. Now there does indeed seem to be a stronger heating feature, which in the case of using MarTIM's CO_2 and O mixing ratios in the CO_2 15-μm cooling routine (coloured solid lines Figure 5.31(a)) results in a temperature rise between 15 K and 20 K from ∼110 K at ∼10°N to ∼125 K at ∼40°S. Moreover this is then followed by a smaller secondary temperature rise between 5 K and 10 K from ∼70°S to the south pole. Next, in the coupled model case where the MCD mixing ratios are used (coloured solid lines Figure 5.31(b)), the two temperature peaks described are of greater magnitude and are contained within a smaller range of latitudes. Thus while the primary temperature peak still occurs about the ∼40°S to ∼50°S region it begins from a temperature minimum at ∼10°S (rather than ∼10°N in the MarTIM ratios case). Also the magnitude of this peak is now at least 20 K (rather than 15-20 K in the MarTIM ratios case) from ∼130K to ∼150 K. The secondary peak when using the MCD mixing ratios also seems to be confined to a narrower latitude region as does the latitudinal spacing between the primary and secondary temperature peaks.

Clearly very similar structures are produced by both types of coupled model result. However, when using the MCD mixing ratios temperatures across all latitudes are elevated by anywhere from 20 to 30 K versus the MarTIM mixing ratio counterparts. In the northern summer hemisphere (e.g. North pole 165 K versus 140 K, respectively) this is because of the reduced CO_2 cooling that the MCD mixing ratios produce versus MarTIM's ratios (that we discussed in section 5.4.3). Consequently the IR radiative balance has a more positive value and thus temperatures will be greater. As was also discussed in section 5.4.3 this means that the wind magnitudes are also elevated when the MCD's mixing ratios are used versus when MarTIM's are used. Thus the adiabatic heating effects in the southern hemisphere will also be greater for the MCD mixing ratios (e.g. primary temperature peak at mid-southern latitudes 150 K versus 125 K).

Nonetheless the difference between the MCD alone result and the coupled MarTIM-MCD results once again reflects the effect of poor transmission of the full spectrum of tides through MarTIM's lower pressure level against the growing dominance of the models in-situ energy inputs and outputs.

5.6 Nightside Results: Comparison to Mars Express SPICAM Temperatures

Finally in this chapter we compare coupled MarTIM-MCD results to remote sensing observations of density and temperature between ∼70 and ∼140 km obtained by the Mars Express UV spectrometer: Spectroscopy for Investigation of Characteristics of the Atmosphere of Mars (SPICAM, Bertaux et al. (2006); Quémerais et al. (2006)). This data was kindly provided by Dr François Forget of Laboratoire de Météorologie Dynamique (LMD), Paris and we extend our thanks to him for this resource. The SPICAM instrument obtained a total of 616 usable (CO_2) density profiles throughout one Mars year. Observations have good longitude coverage although the latitudinal coverage depends on the season with significantly more observations during autumn and winter in each hemisphere (Forget et al., 2009) (see Figure 5.32 below). Most data was obtained on the night side (from 1800-hrs through to 0600-hrs) so that solar light scattered off aerosols and reflected off the surface wouldn't affect the measurement.

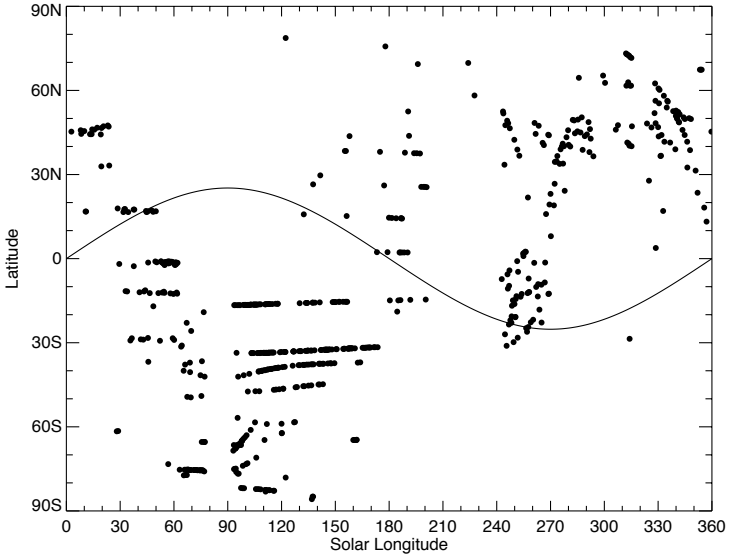

Figure 5.32: Latitudinal distribution of the 616 SPICAM solar occultations as a function of season. The black line indicates the latitude of the subsolar point.

Temperatures are derived from density measurements with a vertical resolution of 1 to 2 km (McDunn et al., 2010) by assuming the atmosphere is in hydrostatic equilibrium and integrating down from the top of the density profile (Forget et al., 2009). However since the temperature at the top of the density profile is not known Forget et al. (2009) used three upper boundary temperatures (100, 175 and 250 K) that fit within the 100 to 250 K range suggested by available in-situ measurements and model results (Seiff and Kirk, 1977; Magalhães et al., 1999; Bougher et al., 1999b; Angelats i Coll et al., 2005). In any event, Forget et al. (2009) found it is reasonable to assume the retrieved temperature profiles below 120 km are insensitive to the assumed upper boundary temperature. Accounting for instrument noise gives typical errors of 3 to 6 K at 115 km and 7 to 15 K at 70 km. Below 0.1 Pa (∼70 km) SPICAM

temperatures are often strongly overestimated and not reliable due to dust affecting the results (Forget et al., 2009).

SPICAM density observations and derived temperatures were studied by Forget et al. (2009) and McDunn et al. (2010) using the LMD and MGCM-MTGCM GCM's respectively. The modelled temperatures seasonal evolution compared well against SPICAM observations. The vertical structure however reproduced the observations only up to the typical simulated mesopause altitude. The precise temperature and altitude of the simulated mesopause was consistently too warm and too low. For example, predictions of 112-120 K at 85-100 km ($\sim 2.5 \times 10^{-3}$ Pa) for nightside profiles in the southern topics during southern winter compared with $\sim$104 K at 100-115 km ($\sim 1.0 \times 10^{-3}$ Pa) for SPICAM observations. This overestimation of temperatures remained the case above the mesopause for most solar longitudes and in both Forget et al. (2009) and McDunn et al. (2010) was linked to a likely underestimation of the CO_2 15-μm cooling rates. This in turn was noted to be due to too low atomic O abundances, which as we have discussed earlier reflects the limited number of measurements available for constraining Mars O abundances and CO_2 cooling rates (Huestis et al., 2008).

Finally both the LMD and MGCM-MTGCM simulated densities also followed the observed seasonal evolution. Both found that the density structure of the middle atmosphere (70-100 km) was closely tied to lower atmosphere dust loads, temperatures and scale heights. McDunn et al. (2010) in particular showed that variations in dust prescription between globally averaged opacities and specific latitude-versus-Ls horizontally structured opacities introduced differences in the simulated results. However both models struggled to reproduce the observed densities at all altitudes regardless of the dust load employed, particularly at the southern summer season (Ls $\sim$ 270). The LMD model (Forget et al., 2009) usually overestimated density (at most altitudes and solar longitudes) while MGCM-MTGCM (McDunn et al., 2010) underestimated density (at lower altitudes and most solar longitudes). The former was linked directly to the overestimation of temperature noted above. This would hydrostatically raise the elevation of constant pressure levels and increase scale heights thereby expanding the atmosphere. In the latter case it was suggested the underestimation related to the simulated lower atmosphere (below the lowest SPICAM observation altitude) being too cold.

5.6.1 Vertical Temperature Structure

First we compare vertical profiles of temperature between SPICAM data and the coupled MarTIM-MCD simulation. Ten different solar longitude by geographic latitude by local solar time groupings are used allowing a large range of the SPICAM data to be compared against MarTIM-MCD simulations. The data and model results are then averaged within each grouping. The groupings are:

1. Top row, Figure 5.33, 17 profiles, Ls 75° to 105°, 30°S-0°S, 4.0-hrs to 4.8-hrs.

2. Middle row, Figure 5.33, 27 profiles, Ls 90° to Ls 120°, 34°S-32°S, 2.4-hrs to 5.2-hrs. See also Forget et al. (2009) (Figure 16, row 2, column 3).

3. Bottom row, Figure 5.33, 39 profiles, Ls 90° to Ls 120°, 17°S-16°S, 2.6-hrs to 4.8-hrs. See also Forget et al. (2009) (Figure 16, row 3, column 1).

4. Top row, Figure 5.34, 48 profiles, Ls 105° to Ls 135°, 60°S-30°S, 0.5-hrs to 2.5-hrs. See also McDunn et al. (2010) (bin 1, Figure 4*a*).

5. Middle row, Figure 5.34, 11 profiles, Ls 165° to Ls 195°, 60°S-30°S, 22.0-hrs to 23.0-hrs.

6. Bottom row, Figure 5.34, 11 profiles, Ls 165° to Ls 195°, 0°N-30°N, 22.0-hrs to 23.0-hrs.

7. Top row, Figure 5.35, 48 profiles, Ls 240° to Ls 270°, 30°S-10°N, 23.5-hrs to 3.6-hrs. See also Forget et al. (2009) (Figure 16, row 3, column 2).

8. Middle row, Figure 5.35, 14 profiles, Ls 240° to Ls 270°, 35°N-50°N, 19.4-hrs to 23.7-hrs. See also Forget et al. (2009) (Figure 16, row 3, column 3).

9. Bottom row, Figure 5.35, 16 profiles, Ls 255° to Ls 285°, 30°S-0°S, 0.0-hrs to 2.0-hrs. See also McDunn et al. (2010) (bin 2, Figure 4*b*).

10. Figure 5.36, 10 profiles, Ls 255° to Ls 285°, 30°N-60°N, 22.0-hrs to 24.0-hrs.

In each case the left hand column uses MarTIM mixing ratios in the CO_2 15-μm cooling routine while the right hand column uses MCD ratios (that are updated every hour of UT).

From Figures 5.33 to 5.36 we see that both types of coupled MarTIM-MCD result are capable of good comparison against the SPICAM data. Generally however simulations that use MarTIM's mixing ratios in the CO_2 15-μm cooling routine (left hand columns) produce colder temperatures and these are typically closer to the SPICAM observed mesopause temperature. As we saw earlier this is because MarTIM has a greater O to CO_2 ratio than the MCD through the lower half of the model to approximately the typical pressure level at the base of the thermosphere (PL ∼15, see also Figure 5.20 for example) and thus will have a greater rate of CO_2 cooling. The best model to data comparisons in terms of matching the SPICAM observed mesopause pressure level and temperature are for groupings 1, 2 and 3 with the MarTIM mixing ratios and groupings 5 and 6 with the MCD ratios. In the MarTIM ratios case the observations were made in the early morning southern tropics about the northern summer solstice. These groupings give mesopause temperature predictions within ∼5 K of the actual SPICAM measurements (∼100-110 K). In the MCD ratios case the observations were made during the northern autumn equinox in the late evening at mid-northern and mid-southern latitudes. These groupings also give mesopause temperature predictions within ∼5 K of the actual SPICAM measurements but are usually at greater pressures (lower altitudes) than the data.

About the region of the mesopause the three simulation types (coloured solid lines in terms of solar activity and lower atmosphere dust content) show the expected trend. Thus typically SMIN low dust predictions (blue solid lines) are the coldest through to SMAX high dust predictions (red solid lines) being the hottest. From the 0.883 Pa lower boundary up to the typical mesopause pressure level simulation

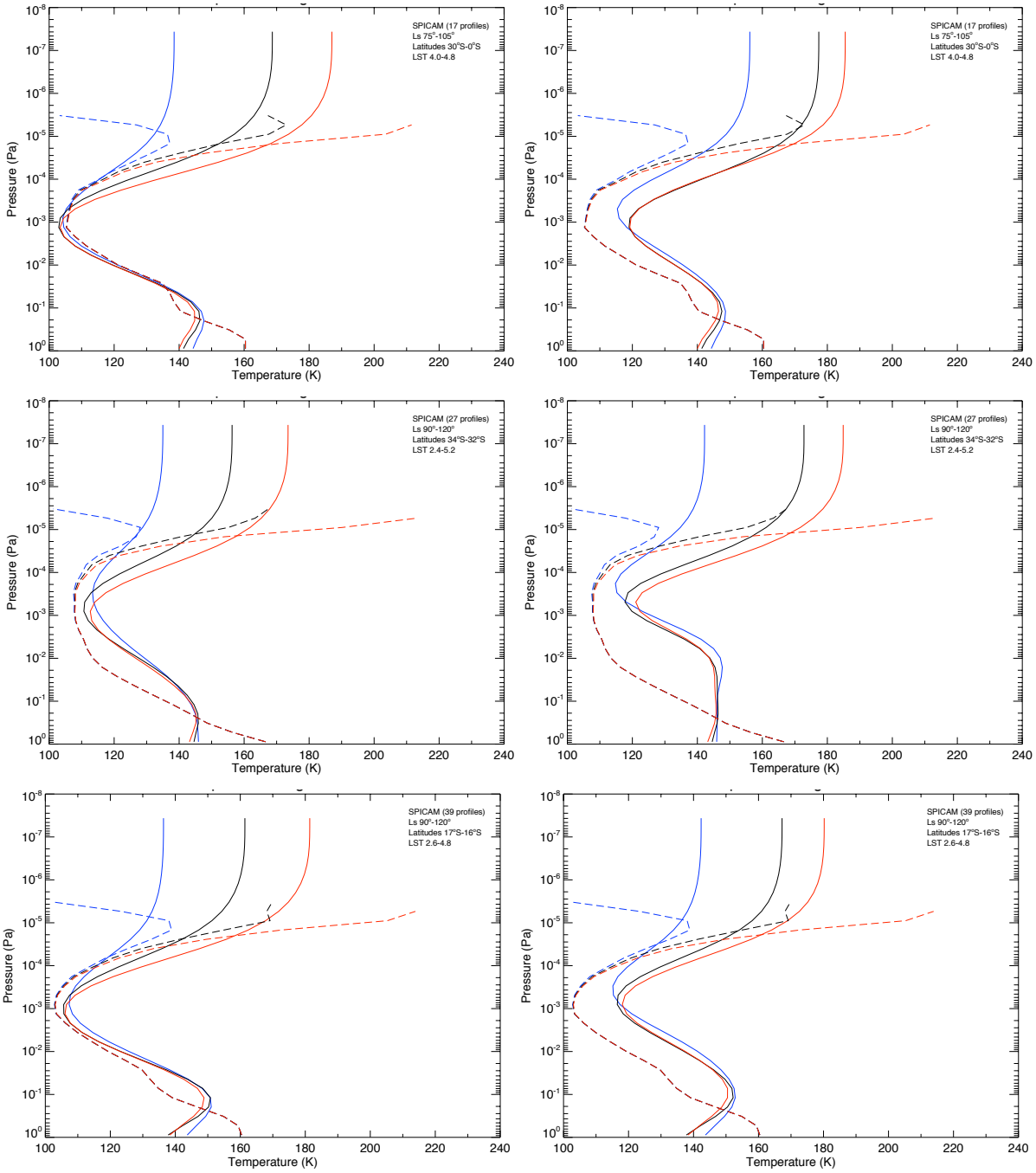

Figure 5.33: Average SPICAM temperature profiles compared to coupled MarTIM-MCD results (groupings 1, 2 and 3). Dashed lines are bin-average SPICAM data assuming upper atmosphere temperatures 100 K (blue), 175 K (black) and 250 K (red). Solid lines are bin-average coupled model results for SMIN very low dust (blue), SMED annual average dust (black) and SMAX high dust (red). Left column uses MarTIM mixing ratios in the CO_2 15-μm cooling routine, right column uses MCD ratios.

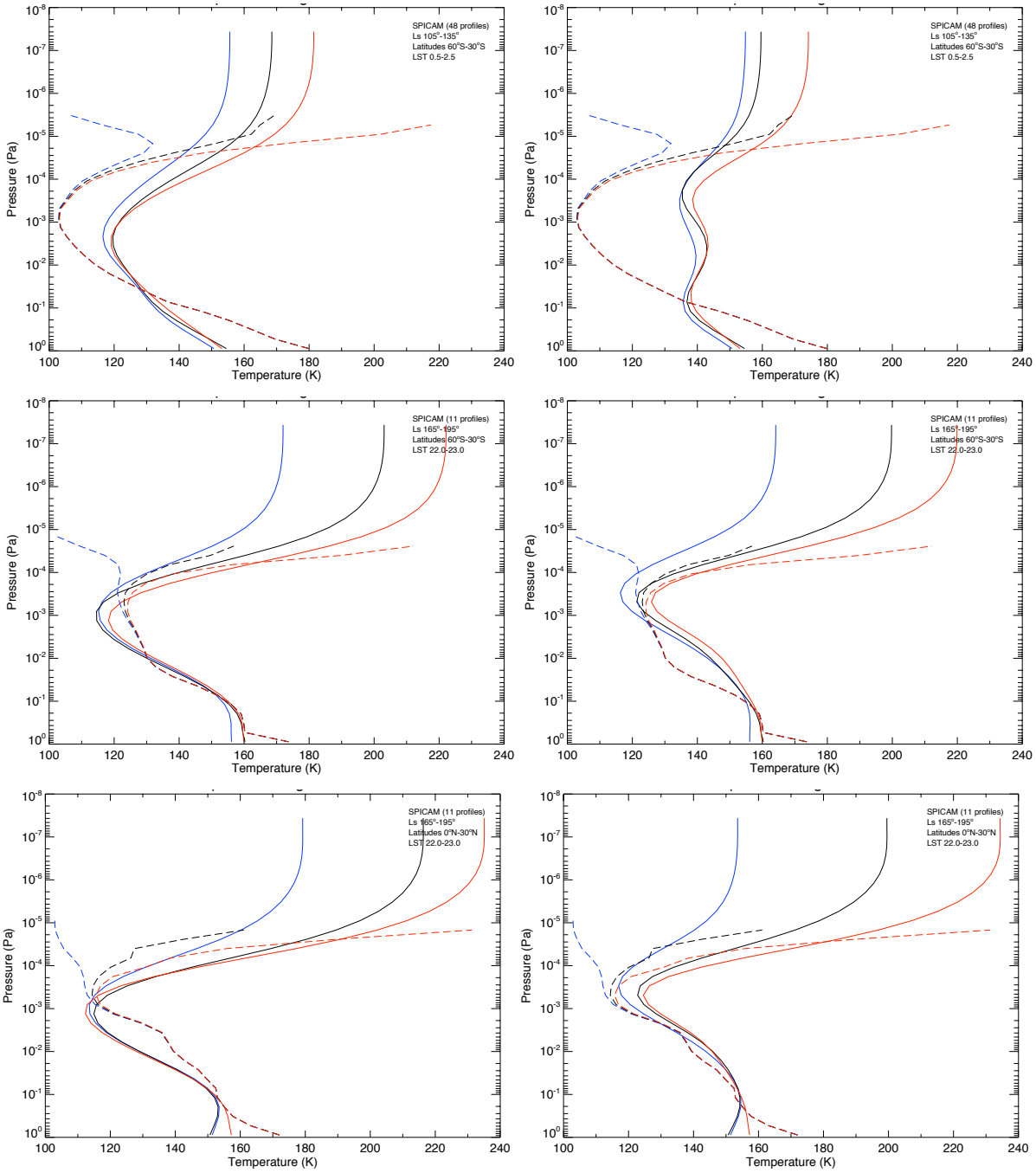

Figure 5.34: Average SPICAM temperature profiles compared to coupled MarTIM-MCD results (groupings 4, 5 and 6). Dashed lines are bin-average SPICAM data assuming upper atmosphere temperatures 100 K (blue), 175 K (black) and 250 K (red). Solid lines are bin-average coupled model results for SMIN very low dust (blue), SMED annual average dust (black) and SMAX high dust (red). Left column uses MarTIM mixing ratios in the CO_2 15-μm cooling routine, right column uses MCD ratios.

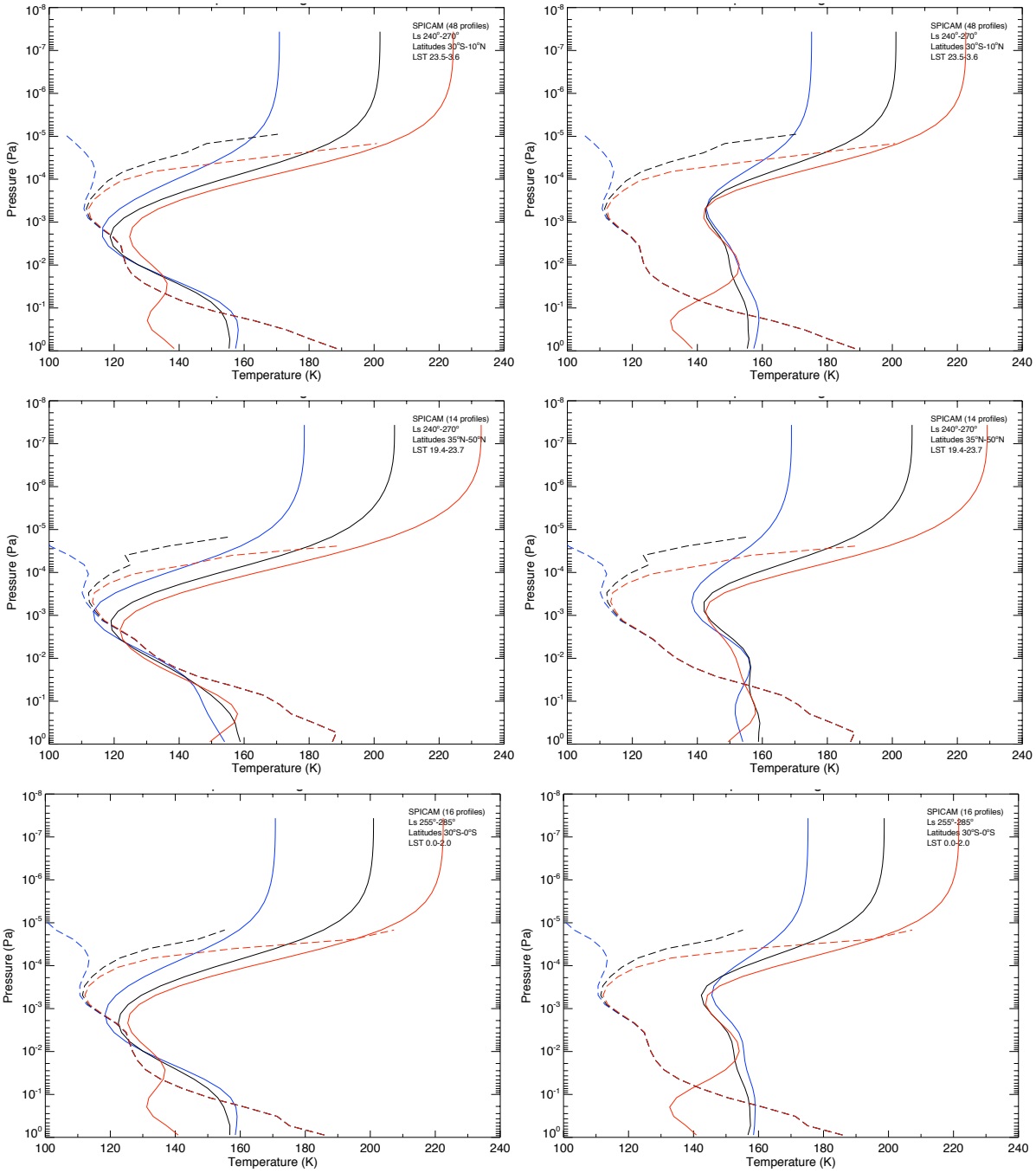

Figure 5.35: Average SPICAM temperature profiles compared to coupled MarTIM-MCD results (groupings 7, 8 and 9). Dashed lines are bin-average SPICAM data assuming upper atmosphere temperatures 100 K (blue), 175 K (black) and 250 K (red). Solid lines are bin-average coupled model results for SMIN very low dust (blue), SMED annual average dust (black) and SMAX high dust (red). Left column uses MarTIM mixing ratios in the CO_2 15-μm cooling routine, right column uses MCD ratios.

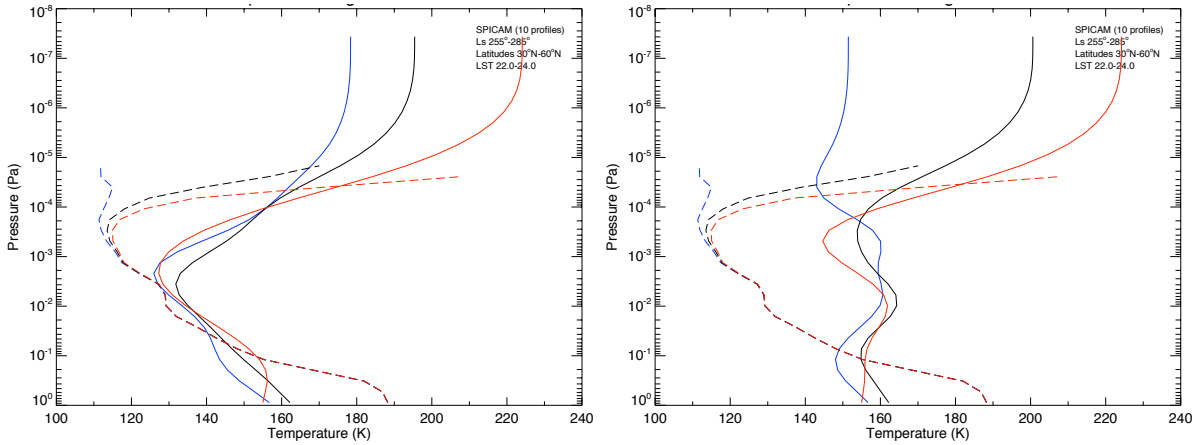

Figure 5.36: Average SPICAM temperature profiles compared to coupled MarTIM-MCD results (grouping 10). Dashed lines are bin-average SPICAM data assuming upper atmosphere temperatures 100 K (blue), 175 K (black) and 250 K (red). Solid lines are bin-average coupled model results for SMIN very low dust (blue), SMED annual average dust (black) and SMAX high dust (red). Left column uses MarTIM mixing ratios in the CO_2 15-μm cooling routine, right column uses MCD ratios.

results usually show good structural comparison with SPICAM in terms of the rate of decrease in temperature (subadiabatic ~1.5 K/km). Exceptions include those instances where the SPICAM data is particularly structured below the mesopause due to vertical wave propagation from below and/or greater instrumentation error (for the lowest altitude data points).

Such good structural comparison below the mesopause is more often seen when the MarTIM mixing ratios are used in the CO_2 15-μm cooling routine. When the MCD mixing ratios are used, coupled results often show more structure in this region. This can be attributed to the greater prominence of tidal features in the MCD DVD results, which will influence the vertical structure of the MCD mixing ratios when used by MarTIM. This wave structure will then affect the structure of CO_2 cooling that the coupled model calculates and hence the temperature profiles predicted. Above the mesopause level model results almost always increase in temperature more rapidly with pressure level than do the SPICAM data. Certainly there is no sign in the data of the isothermal upper atmosphere regions shown by MarTIM. However high altitude SPICAM data is also subject to significant instrumentation error so it's difficult to be sure of any comparison when high above the mesopause.

Next, Figures 5.37 and 5.38 focus on the results from grouping 3 for solar longitude Ls 90° to Ls 120°, latitude 17°S-16°S and 2.6-hrs to 4.8-hrs. This set was also discussed in Forget et al. (2009) (see Figure 16, row 3, column 1 there) and in McDunn et al. (2010) (see Figure 8 and 9 there). Figure 5.37 shows the equivalent density profile to complement the temperature profile in Figure 5.33 (bottom row) while Figure 5.38 shows the equivalent energy balance terms. From Figure 5.37 clearly the coupled results show excellent comparison against the SPICAM density data. Also, as was the case with the temperature profile, the coupled model that uses MarTIM mixing ratios in the CO_2 15-μm cooling routine (left plot) shows a better comparison to the SPICAM data, though the difference in modelled densities is very

small.

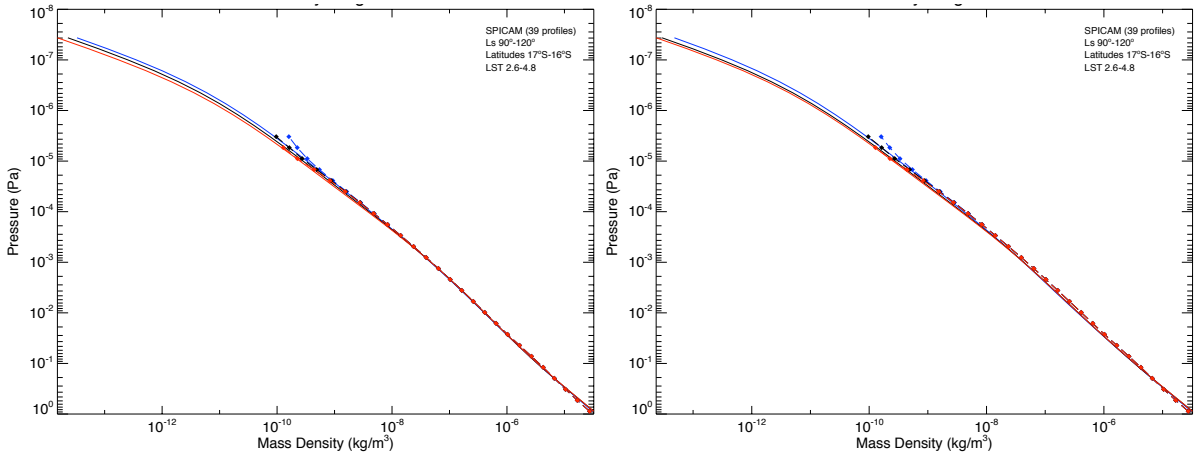

Figure 5.37: Average SPICAM density profiles compared to coupled MarTIM-MCD results (grouping 3 only, Figure 5.33 (bottom row) showed equivalent temperature profile). Dashed lines are bin-average SPICAM data assuming upper atmosphere temperatures 100 K (blue), 175 K (black) and 250 K (red). Solid lines are bin-average coupled model results for SMIN very low dust (blue), SMED annual average dust (black) and SMAX high dust (red). Left column uses MarTIM mixing ratios in the CO_2 15-μm cooling routine, right column uses MCD ratios.

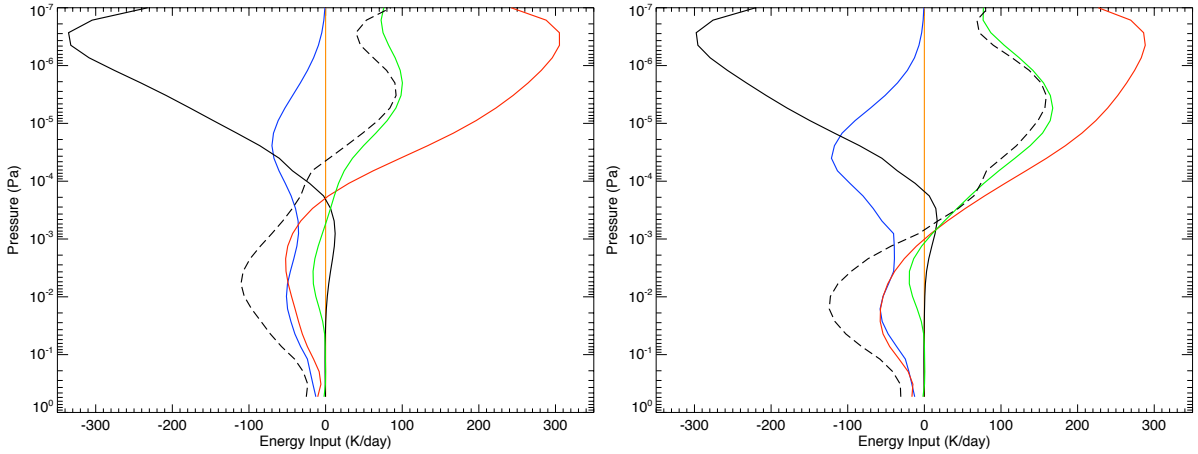

Figure 5.38: Coupled MarTIM-MCD calculated energy balance terms for grouping 3 (Figure 5.33 (bottom row) showed equivalent temperature profile and Figure 5.37 the equivalent density profile). Total solar heating (EUV + IR) (solid orange line), IR 15-μm cooling (solid blue line), thermal conduction (solid black line), adiabatic term (solid red, ω/ρ, equation 2.16), horizontal advection of total energy (solid green line, $-\underline{v}.\nabla_P \epsilon$, equation 2.16) and net energy input (dashed black line). Left plot uses MarTIM mixing ratios in the CO_2 15-μm cooling routine, right plot uses MCD ratios. Both use SMED annual average dust conditions.

The energy balance terms in Figure 5.38 show that around the region of the mesopause ($\sim 10^{-3}$ Pa) the MarTIM mixing ratios (left plot) provide greater net negative energy input (dashed black line), which is consistent with the equivalent temperatures being cooler than with the MCD ratios (Figure 5.33, bottom row, left versus right plot). This greater negative input comes largely from an adiabatic expansion cooling (solid red line, term ω/ρ, equation 2.16) that is also more negative for the MarTIM ratios about the 10^{-3} Pa region. Moreover below the mesopause both types of model run show an important role played by the adiabatic term; a major contributor to the decrease of temperatures with pressure leading up to the mesopause. Also in both model run types this term appears to at least match the magnitude of cooling provided by the CO_2 15-μm cooling routine, which agrees with similar findings of McDunn et al. (2010) (see Figure 9 in that publication). And this comes despite the comparison, in our work, of two independent mixing ratios within the CO_2 cooling routine. The MCD mixing ratios (right plot) produce a negative peak in the adiabatic term at a higher pressure (2.0×10^{-2} Pa) than with the MarTIM ratios (left plot) meaning this does not cool the temperature profile about the mesopause in the same way it did with the MarTIM ratios.

The greater atomic oxygen content in the upper atmosphere with the MCD mixing ratios results in greater CO_2 15-μm cooling about the 5×10^{-5} Pa level. Recall that the elevated O levels came about due to photo-dissociation production on the dayside in the MCD. Subsequent transport to the nightside allows for the enhanced CO_2 cooling rate seen in Figure 5.38 (right plot). However, at the same time the greater wind speeds that result from the MCD ratios (20% greater at PL 15, 8.0×10^{-4} Pa, see the end of section 5.4.3, beginning of section 5.4.4) produce a greater horizontal advection energy input (solid green line, term $-\underline{v}.\nabla_P\epsilon$, equation 2.16) versus the MarTIM ratios. Consequently the lesser net positive energy input in the upper atmosphere above the mesopause when the MarTIM mixing ratios are used results in cooler temperatures in the isothermal region of the thermosphere (161 K versus 167 K). This too agrees with the suggestion by McDunn et al. (2010) that weaker global winds at constant pressure levels would decrease the warm air advection from dayside to nightside thereby raising the vertical level of the mesopause and reducing its temperature magnitude. McDunn et al. (2010) also suggest that including the propagation of gravity waves from lower pressure levels could potentially further slow down global wind speeds by momentum deposition in the middle atmosphere. This point is left as future work for further study with MarTIM but for now it seems varying O to CO_2 mixing ratios can have an important effect on wind magnitudes through the variation of CO_2 cooling and thus energy input.

5.6.2 Subfreezing Mesopause Temperatures

As discussed in Forget et al. (2009) some of the SPICAM temperature profiles exhibit temperatures at the mesopause that are well below the CO_2 frost point, by up to 24 K, despite the often large absolute error bars. Forget et al. (2009) show the six "coldest" SPICAM profiles (relative to the CO_2 condensation temperature) and these are reproduced in Figure 5.39 and 5.40 and compared with coupled MarTIM-MCD simulations. In each case the top row uses MarTIM mixing ratios in the CO_2 15-μm cooling

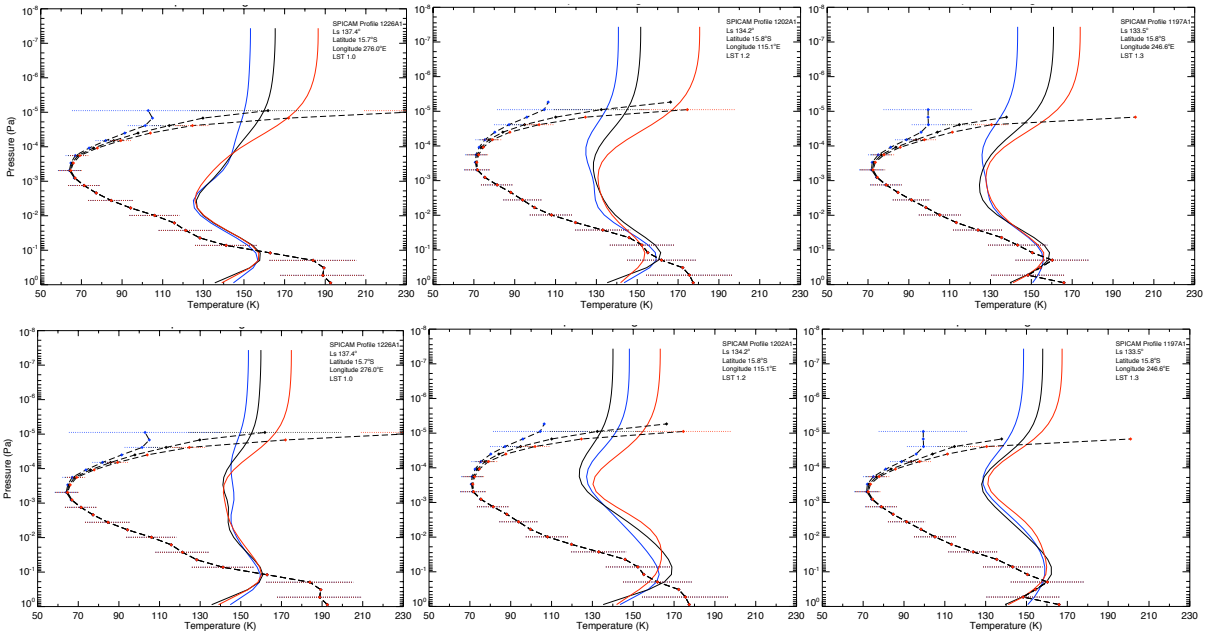

Figure 5.39: First set of three of the six coldest SPICAM temperature profiles (dashed lines with error bars) assuming upper atmosphere temperatures 100 K (blue diamonds), 175 K (black diamonds) and 250 K (red diamonds). Solid lines are equivalent latitude-longitude-local time coupled model results for SMIN very low dust (blue), SMED annual average dust (black) and SMAX high dust (red). Top row uses MarTIM mixing ratios in the CO_2 15-μm cooling routine, bottom row uses MCD ratios.

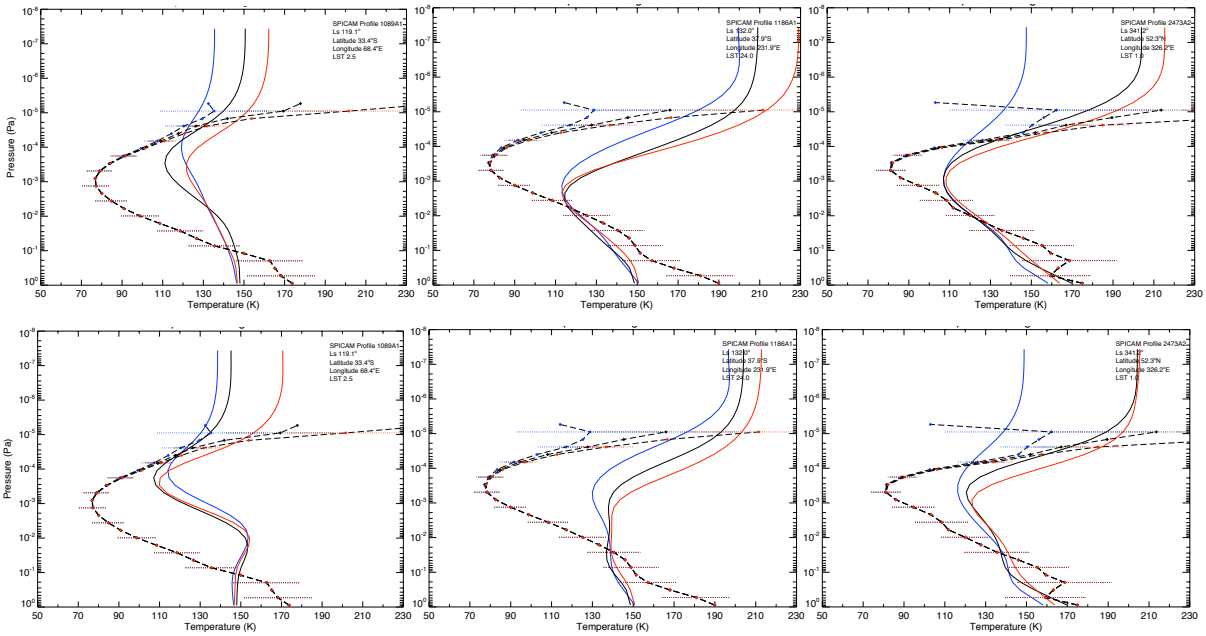

Figure 5.40: Counterpart to Figure 5.39. Second set of three of the six coldest SPICAM temperature profiles (dashed lines with error bars). Solid lines are coupled MarTIM-MCD modelled results. Top row uses MarTIM mixing ratios in the CO_2 15-μm cooling routine, bottom row uses MCD ratios.

routine while the bottom row uses MCD ratios.

Clearly in all six cases shown both types of coupled model struggle to match the mesopause pressure level and temperature. It is still usually the case that using MarTIM mixing ratios produces cooler temperatures than with the MCD ratios (as noted in the section above), though often temperatures near the predicted mesopause are similar between the two model types. The best comparison between SPICAM and the coupled model (for both mixing ratio types) in terms of predicted mesopause pressure and temperature occurs for SPICAM profile 2473A2 (right hand column, Figure 5.40), which is at Ls 341.2° (late southern summer), 52.3°N, 326.2°E and 0100-hrs. Coupled model results using MarTIM mixing ratios in the CO_2 15-μm cooling routine (top plot) predict a mesopause of ∼110 K at ∼10^{-3} Pa while results using the MCD ratios (bottom plot, SMIN, very low dust, blue line) predict ∼115 K at a higher pressure level of ∼5.0×10^{-4} Pa. Nonetheless both these results are hotter and lower than the SPICAM observed mesopause: ∼81K at ∼4.0×10^{-4} Pa.

The Mars Pathfinder entry probe (Schofield et al., 1997; Magalhães et al., 1999) also observed sub-freezing temperatures during its descent. Temperature profiles from the Atmospheric Structure Investigation / Meteorology (ASI / MET) instrument are compared with coupled model results in Figure 5.41 (top row). The left column uses MarTIM mixing ratios in the CO_2 15-μm cooling routine, while the right column uses MCD ratios. The former predicts a mesopause temperature of ∼107 K at ∼1.0×10^{-3} to ∼2.0×10^{-3} Pa while the latter predicts ∼117-122 K at ∼5.0×10^{-4} to ∼7.0×10^{-4} Pa. As was the case in section 5.6.1, the energy balance terms (bottom row) show that the adiabatic term (solid red line, term ω/ρ, equation 2.16) for both coupled model types plays an important role in producing the cold mesopause temperatures, typically matching, sometimes exceeding, the importance of CO_2 15-μm radiative cooling. Note also the slower winds with the MarTIM mixing ratios results (again) in less horizontal advection of warm air from the dayside and thus cooler temperatures for the top left plot. Lastly we see that the overall, column integrated, negative net energy input from 0.883 Pa up to the mesopause (10^{-3} Pa) for the MarTIM mixing ratios plays an important role in the temperature structure and magnitude over the same region. This results in it predicting the cooler mesopause temperature versus that predicted by the MCD ratios.

5.6.3 Seasonal Structure

SPICAM observations cover an entire Martian year (Ls 353.4°, February 2004, MY 26 to Ls 23.3°, March 2006, MY 27). Figure 5.42 shows the seasonal variation in temperature and density for the full range of solar longitudes for SPICAM profiles at low latitudes (45°S-45°N) and at three separate altitudes (80, 100 and 130 km). SPICAM data points are represented as black open circles, coupled MarTIM-MCD results that use MarTIM mixing ratios in the CO_2 15-μm cooling routine are blue filled circles and coupled model results that use MCD mixing ratios are red filled circles. Note that coupled simulations were only run for solar longitudes 0°, 90°, 120°, 135°, 180°, 270° and 340°. All other solar longitudes represented are interpolated from the two adjacent coupled model results at the particular local time, latitude and

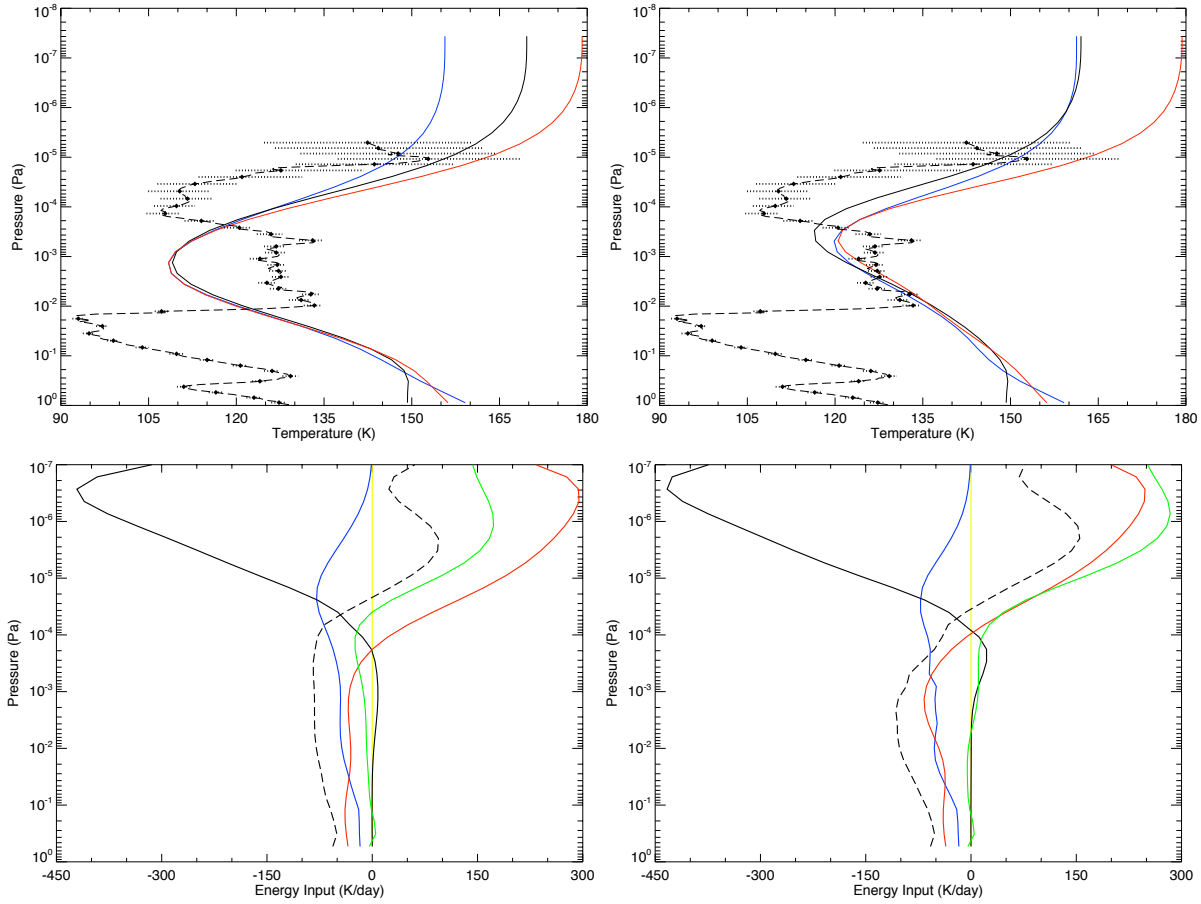

Figure 5.41: **Top row:** Pathfinder temperature profiles (dashed black line with error bars), Ls 142.7°, 19.1°N, 326.5°E, LST 0300-hrs, Magalhães et al. (1999). Solid lines are equivalent latitude-longitude-local time coupled model results for SMIN very low dust (blue), SMED annual average dust (black) and SMAX high dust (red). **Bottom row:** coupled model energy balance terms, total solar heating (EUV + IR) (solid orange line), IR 15-μm cooling (solid blue line), thermal conduction (solid black line), adiabatic term (solid red, ω/ρ, equation 2.16), horizontal advection of total energy (solid green line, $-\underline{v}.\nabla_P \epsilon$, equation 2.16) and net energy input (dashed black line). Left column uses MarTIM mixing ratios in the CO_2 15-μm cooling routine, right column uses MCD ratios.

longitude of the SPICAM data point being considered. Also, Figure 5.43 shows the corresponding net energy balance at 100 km and 130 km.

From Figure 5.42 we see that both types of coupled model result show fair comparison with the magnitudes of SPICAM temperature and density measurements. With respect to the seasonal structure it appears that in many respects the coupled model density measurements (right hand column) show a better variation over the course of the Martian year. Coupled model temperature predictions (left hand column) still show fair seasonal variation though this is more the case at 80 km altitude (bottom left plot), whereas by 130 km (top left plot) some structural differences appear (particularly about Ls 150). For temperature magnitude predictions we see that once again cooler magnitudes are simulated by

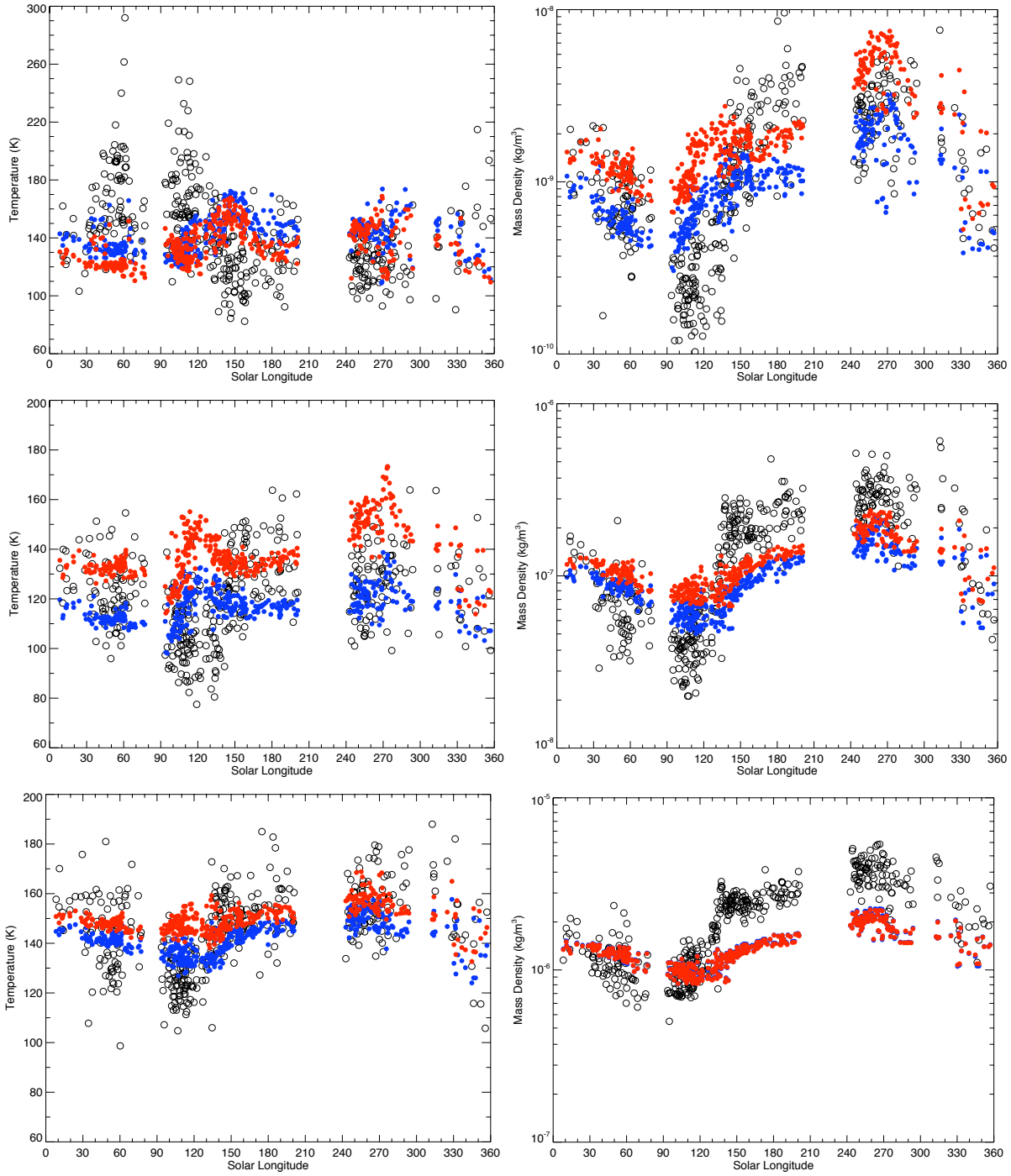

Figure 5.42: SPICAM observed and coupled MarTIM-MCD modelled seasonal temperature (left column) and density (right column) structure. Black open circles represent low latitude data (45°S-45°N) at altitudes (top) 130 km, (middle) 100 km and (bottom) 80 km. Blue filled circles are coupled model results with MarTIM mixing ratios in the CO_2 15-μm cooling routine, red filled circles use MCD mixing ratios. All coupled model results use SMIN and very low dust conditions.

the coupled model using MarTIM mixing ratios in the CO_2 15-μm cooling routine (blue filled circles). However, this distinction is more apparent at 80 and 100 km. Generally, below 100 km, this is the

influence of the greater net negative energy input, as shown earlier in Figure 5.38 or Figure 5.41. See also Figure 5.43 below. This was mostly provided by combination of greater adiabatic expansion cooling and CO_2 radiative cooling for the MarTIM mixing ratios. Then at 130 km we begin to move into the altitude region where the greater thermospheric atomic oxygen content of the MCD mixing ratios, advected to the nightside, begins to dominate the local energy input, thereby producing the cooler temperatures for the MCD ratios (red filled circles).

For the density magnitude predictions Figure 5.42 shows that as we gain altitude the MCD mixing ratio results (red filled circles) are calculated to have a greater magnitude than the equivalent MarTIM ratio results (blue filled circles) and that this relationship increases with altitude. Higher density magnitudes at constant altitude levels would suggest hotter temperatures in the atmosphere below such that the atmospheric column expands and the pressure increases at that altitude. Thus the similar density magnitudes at 80 km from both coupled model types simply reflects the similarity in temperatures at and below the 80 km level. Both coupled model types are using exactly the same MCD input at the 0.883 Pa pressure level (∼50-60 km) and any variation in energy input that may lead to a temperature variation up to 80 km is negligible. In turn, moving up through 100 km and to 130 km the higher temperatures calculated with the MCD mixing ratios (red filled circles) produces greater columnar expansion in the atmosphere up to these altitude levels and hence the greater densities predicted (versus when the MarTIM ratios are used). The greater column integrated expansion as we gain altitude resulting in the trend of increasing density difference between MCD and MarTIM ratio model types.

Solar Longitude Structure: Ls 0° to 90°

Regarding a comparison of density structure variation with solar longitude; through northern spring to summer (Ls 0° to 90°) as the profile locations migrate from northern to southern mid-latitudes (see Figure 5.32) we see a decrease in SPICAM density magnitudes at all altitudes shown. This is to be expected as profiles move into the winter hemisphere and atmospheric columns hydrostatically contract with the cooler temperatures. Thus density at constant altitude levels would also be expected to decrease. However, as McDunn et al. (2010) points out, given that the trend of declining density magnitudes is not so immediately recreated in the seasonal temperature profiles (left hand column) this suggests that the cooler southern winter hemisphere temperatures occur at altitudes below at least 80 km (the lowest altitude plotted in Figure 5.42). Sure enough, as Smith (2004) reports from TES observations, cooling lower atmosphere temperatures are observed during the northern summer, aphelion season. Also occurring alongside the annual minimum in atmospheric dust content (McDunn et al., 2010).

Coupled model density predictions show good comparison to SPICAM data at 130 km in terms of the order of magnitude span from Ls 0° to 80° (where a data gap exists). However it appears that both types of coupled model results have too narrow a density range with the MarTIM mixing ratios (blue filled circles) being biased towards the lowest density magnitude SPICAM values and results using the MCD ratios (red filled circles) being found about the highest density magnitudes. As noted above, the hotter

temperature magnitudes at lower altitudes for the MCD ratios drives a greater expansion producing the density magnitude relationship shown between the coupled model types at 130 km. Also, the disconnect between both SPICAM and coupled model temperatures and their counterpart density magnitudes (at the same altitudes) is much clearer at 130 km than at 100 and 80 km. Specific temperature structures at 130 km seemingly bearing no relationship to density. Bear in mind increased SPICAM instrument error will be playing a greater role at 130 km than at lower altitudes.

Density predictions at 80 and 100 km show a lesser magnitude span from Ls 0° to 80° than the SPICAM data. Both sets of coupled model result also show too narrow a density range (as was the case at 130 km), with density results for MarTIM and MCD mixing ratios at both 80 and 100 km being biased towards the highest density magnitude of the SPICAM data (more so at Ls 80°). As noted earlier, there is a strong connection between MarTIM's response at 80 km (regardless of mixing ratio set used) and what the MCD input simulates at 0.883 Pa, because there is little energy input / output in the intervening region. Thus the fact density magnitudes need reducing at Ls 80° (for both mixing ratio sets) to achieve a better match with SPICAM suggests the need for a cooler less expanded atmosphere below 0.883 Pa than that provided by the MCD.

For temperature seasonal structure; at 80 km, moving from from Ls 0° to 80°, minimum SPICAM temperatures show a decreasing trend of ∼160 K to ∼120 K while the maximum temperatures remain almost constant at ∼160 K. Thus the range of temperatures increases. Coupled MarTIM-MCD results have a much narrower range thereby showing a much clearer single cooling trend as solar longitude progresses. In turn model results sit fairly evenly within SPICAM maximums and minimums, slightly colder (∼145-150 K) than SPICAM at Ls 0° but then quite central (∼140-145 K) within the SPICAM range at Ls 80°. As noted above, MarTIM mixing ratios in the CO_2 15-μm cooling routine (blue filled circles) produce cooler temperatures. By 100 km this becomes more apparent as both adiabatic expansion and CO_2 radiative cooling combine to cool coupled model results with MarTIM ratios more than those with MCD ratios.

At 130 km the temperature trend reverses, with coupled model results using MarTIM mixing ratios (blue filled circles) now hotter than those with the MCD ratios (ref filled circles). This is strange because in the Ls 0° to 80° region of Figure 5.43 (right hand plot for 130 km) the MarTIM mixing ratio model version typically shows greater net negative energy input. This comes about mainly due to greater negative thermal conduction (not shown in Figure 5.43) that reaches a minimum −150 K/day at Ls 80°. It is difficult to explain why this should be. Typically though, at 130 km on the dayside, there is a complex shift from IR heating and cooling controlled region below to the EUV and thermal conduction dominated region above. Furthermore the two different mixing ratios used in the coupled model seems to add to the complexity, creating, on the nightside, a change in the temperature relationship between the two coupled models. Thus in conclusion, it is likely that 130 km covers a range of different pressure levels and conflicting processes that make it difficult to identify particular trends. We also note that throughout the year coupled results show quite similar temperatures at 130 km, reflecting the near

equivalence of processes here, again as we move more into the EUV dominated thermosphere (for which the parameterisation is the same regardless of the coupled model type). Finally, note again that SPICAM data is likely significantly affected by instrumentation errors, which might go some way to explaining the comparison there.

Solar Longitude Structure: Ls 90° to 210°

SPICAM density measurements reach their annual minimum between Ls 90° to 120° where profile locations lie between southern (winter) middle to polar latitudes. Such a deep decrease in magnitude is not recreated by coupled model results at any of the three altitudes plotted in Figure 5.42 and this is more apparent at higher altitudes. This indicates that the atmospheric expansion of the coupled model result is greater than it is for SPICAM, less so at 80 km but increasingly so at 100 and 130 km as the greater coupled model temperatures in this solar longitude region at 80 and 100 km influence the columnar integrated expansion. Thus the difference between 100 and 130 km SPICAM and coupled model densities increases.

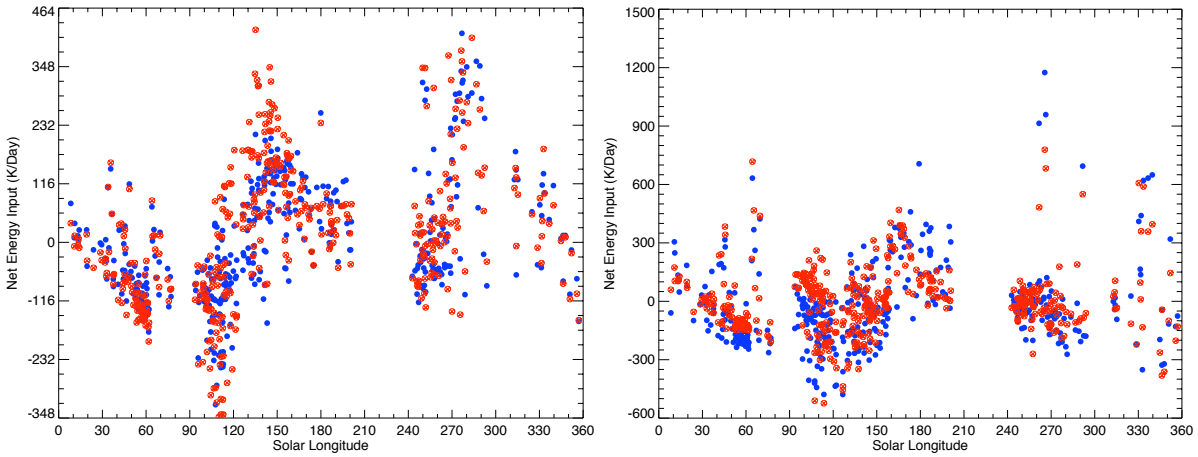

Figure 5.43: Seasonal structure of coupled MarTIM-MCD calculated net energy balance terms at 100 km (left plot) and 130 km (right plot). Blue filled circles are coupled model results with MarTIM mixing ratios in the CO_2 15-μm cooling routine, red filled circles use MCD mixing ratios. SMIN and very low dust conditions for both.

Notably, at 100 km, the simulated temperatures in this Ls 90° to 120° solar longitude range increase dramatically from ∼105 K to ∼130 K (for MarTIM mixing ratios, blue filled circles). Then at altitude 130 km you can see the expansion that results from this 100 km heating by the increase in density over the same range of solar longitudes. Both of these features seem similar to those present in the SPICAM measurements except that there the trend is shifted in solar longitude by approximately 30° to 40°. Thus with SPICAM there is a temperature increase from ∼90 K to ∼145 K (greater than the coupled result) that begins at Ls 120° (rather than Ls 90° in the model) and ends at 160° (rather than 120° in the model). Figure 5.43 at 100 km (left plot) also shows a large positive peak that this is due to a

large positive adiabatic term (not shown) i.e. compressional heating, with profile locations in the winter middle and polar latitudes.

Through the remainder of this solar longitude region (Ls 120° to 210°, passing through southern spring / northern autumn) both types of coupled model result underestimate the density magnitudes at all three altitudes shown despite showing the same increasing trend as the SPICAM data. This coincides with the simulated temperatures also being less than the equivalent SPICAM measurements while also increasing in magnitude through this solar longitude region. Profile locations are typically situated in middle southern latitudes though there are a few profiles at equatorial and northern tropical and middle latitudes but overall representing measurements central to the equinox / spring hemisphere. Again this suggests that the whole modelled atmosphere expansion (i.e. both above and below 0.883 Pa including both MCD on its own and MarTIM on its own) is insufficient versus that measured by SPICAM.

Solar Longitude Structure: Ls 240° to 360°

Passing through the southern summer solstice (Ls 270°) to southern autumnal / northern spring equinox (Ls 360°) SPICAM profile locations move northwards from the southern equatorial region (∼0°S to 15°S) to mid-northern latitudes (∼45°N). The majority of mid-northern profiles occur just after northern winter solstice (Ls 270°) and remain there through to early northern spring at Ls 330° before moving back southwards to ∼15°N to 30°N by Ls 360°.

Initially, from Ls 240° to 290°, neither SPICAM temperatures nor densities show any prominent seasonal trends; both holding fairly constant values at each altitude during this solar longitude period. The range of density magnitudes increases as we climb in altitude but the range of temperature magnitudes generally maintains a broad range at all altitudes (McDunn et al., 2010).

Coupled MarTIM-MCD model temperature predictions compare fairly well with SPICAM data at all three altitudes. Comparison is best at 80 km where both types of coupled model result have values within the range set by SPICAM, though once again the model temperature range is somewhat smaller than that of SPICAM (140-155 K, MarTIM mixing ratios / blue filled circles and 150-170 K, MCD mixing ratios / red filled circles versus 130-180 K, SPICAM at 80 km). Also, as before, the MarTIM mixing ratios give colder temperature magnitudes. At 100 km coupled model results using MarTIM mixing ratios show a better fit within the 100-160 K range of SPICAM temperatures. Their range is more narrow (110-130 K) and biased towards the SPICAM minimum. Coupled results using MCD mixing ratios are biased towards the SPICAM maximum and also show a narrow magnitude range (140-160 K).

At 130 km both types of coupled model result give similar answers and thus are both towards the hotter side of SPICAM measurements. As McDunn et al. (2010) notes temperatures at 130 km are cooler than their counterparts at 80 and 100 km, thereby introducing the largest annual atmospheric lapse rates and suggesting an important role for vertical wave propagation. Coupled results using MCD mixing ratios (red filled circles) appear to also show a larger lapse rate than their MarTIM mixing ratio counterparts (blue filled circles), especially between 100 and 130 km. This agrees with the greater

structure seen in the vertical temperature profiles of Figures 5.33 to 5.36 and 5.39 to 5.41 for the MCD mixing ratio coupled model type and our previous discussion of the additional wave activity seen in this model type coming through the vertical structure of MCD mixing ratios and thus CO_2 cooling rates.

Regarding the Ls 240° to 290° density values, both sets of coupled model results are less than the SPICAM data at 80 and 100 km. Then, at 130 km, coupled results generally sit within the range of magnitudes set by SPICAM, though clearly model results with the MCD mixing ratios are at the high end of this range. This tallies with the temperatures from this model type at 100 km also being situated at the high end of the SPICAM data range and thus the additional expansion provided produces the high density result at 130 km.

Through the remainder of the solar longitude region, Ls 290° to 360°, the comparison between coupled model results (both types) and SPICAM data generally improves. Certainly with respect to model results (temperatures and densities) being situated within the range set by SPICAM. Temperatures at 80 and 100 km show the declining trend with solar longitude, as does SPICAM, and are well placed within SPICAM magnitudes. Modelled densities at all altitudes also show the decline magnitude trend. Values at 100 and 130 km generally agreeing with SPICAM data. However, we remain mindful that coupled model temperatures and densities in the subsequent Ls 0° to 90° typically strayed over the range set by SPICAM such that they had good comparison at Ls 0° but were greater in magnitude than SPICAM at Ls 90°. This therefore reflects how both types of coupled model result show neither the highest of the annual maximums at Ls 270° (near-perihelion) nor the lowest of the annual minimums at Ls 90° (near-aphelion).

5.6.4 SPICAM Measurements versus Coupled Model Results: A Discussion

Overall, coupled MarTIM-MCD simulations showed good comparison versus the SPICAM temperature and density data. Many of the vertical profile comparisons were capable of matching SPICAM profile structures and thus predict the mesopause temperature magnitude and pressure level location with fair accuracy. Quite surprising was how those coupled results that used MarTIM mixing ratios within the CO_2 15-μm cooling routine were usually closer to the SPICAM observed mesopause temperature and consequently also the mesopause pressure level. This is despite MarTIM not yet including parameterisations of neutral chemistry and/or photochemistry. The great dearth in atomic oxygen content through the lower half of the model (up to, say, PL 15) when using the MCD mixing ratios versus the very small, but non-zero content with MarTIM's mixing ratios produced CO_2 radiative cooling (alongside adiabatic expansion cooling) that brought MarTIM's temperatures closer to SPICAM observations.

Comparison of equivalent energy balance terms explained well the modelled temperature profiles reveling that a combination of adiabatic cooling and CO_2 radiative cooling are responsible for the cold mesopause temperatures (and pressure level location). They act together, often with quite similar magnitude, throughout the lower half of the model to create the cooling lapse rate from the lower boundary (0.883 Pa) to the mesopause (typically at $\sim 10^{-3}$ Pa). Comparison of energy balance terms also showed

that horizontal advection of energy, due to warm wind flow from the dayside, could significantly add energy to the nightside region (as other studies have also shown e.g. McDunn et al. (2010)). Consequently, the slower wind magnitudes when the MarTIM mixing ratios were used resulted in horizontal advection being a lesser term (less positive) and thus also aided the comparison between this coupled model type and the SPICAM data. We therefore drew attention to the connection between the mixing ratios used in the CO_2 cooling routine, the different temperature magnitudes this allowed for on the dayside (by IR radiative balance e.g. see Figure 5.19), the different dayside expansion and subsequent wind flow this generated. More atomic oxygen meant cooler dayside temperatures, less expansion, slower winds and thus reduced horizontal advection to the nightside.

Nonetheless model-data comparison was not always accurate. In particular the six "coldest" SPICAM profiles (see section 5.6.2), with mesopause temperatures as low as 80 to 90 K were not matched by either coupled MarTIM-MCD model type. Temperature predictions were always too hot and mesopause locations too high in altitude (low in pressure). As McDunn et al. (2010) suggested for example, the inclusion of gravity wave parameterisation would be an additional mechanism not included yet in MarTIM that could alter the atmospheric circulation features. When gravity waves break and dump momentum into the background atmosphere this could have a braking effect on the wind velocities. In turn this would further reduce the positive energy input from the horizontal advection term. Besides, as discussed in earlier sections, coupled MarTIM-MCD simulations show a different range of tidal modes compared to the MCD DVD because of our need to calculate horizontal geopotential gradients against the 0.883 Pa pressure level rather than against the Martian areoid. We noted earlier the differences this introduced to background wind magnitudes, MarTIM mixing ratios in the coupled model having slower winds than with MCD mixing ratios in the coupled model and both coupled model types in turn being slower than the MCD DVD. With a wider range of tidal modes, particularly the eastward propagating non-migrating tides that would oppose the prominent westward momentum dumped by migrating tides, perhaps the wind magnitudes could be reduced further and temperatures cooled even more?

Then, regarding the seasonal variation in temperature and density, coupled model results again showed fair a comparison to SPICAM data throughout the Martian year. Predicted densities in particular showed the increase in magnitude from northern to southern summer conditions as profile locations migrated northwards from middle southern to middle northern latitudes (respectively). And this was at all altitudes studied. Predicted temperatures in the lower and middle atmosphere (80 and 100 km) also showed fair structural comparison with the SPICAM data. These too increased in value alongside the data as southern summer solstice was approached.

However it was the case that coupled model densities rarely showed the range of magnitudes displayed by the SPICAM data. Also, the increasing and decreasing magnitude trends with solar longitude were usually more limited with the model than in the data - coupled MarTIM-MCD reaching neither the northern summer lows in density (for southern hemisphere profiles) nor the southern summer highs (for northern hemisphere profiles). Interestingly since this was also the case at 80 km one reason for

the discrepancies was due to the lower atmosphere provided by the MCD DVD because of the minimal energy input/output processes between the lower boundary and 80 km constant altitude level. Too warm a lower atmosphere (below MarTIM's 0.883 Pa lower boundary) would mean expansion at the constant altitude levels above (within MarTIM) would be great. Addressing these various problems is left for future work.

5.7 Conclusions

From the work of this chapter we draw the following conclusions:

- In section 5.3.1 and 5.3.2 MarTIM was coupled to the Mars Climate Database (Lewis and Read, 2003; Lewis and Barker, 2005; Lewis et al., 1999; Forget et al., 2008; Millour et al., 2008; Millour and Forget, 2008; Angelats i Coll et al., 2005). The MCD provided a more physically self-consistent description of the lower boundary at 0.883 Pa. Temperatures, horizontal winds and geopotential heights at constant pressure 0.883 Pa were passed from the MCD to MarTIM. Since the MCD includes parameterisation of phenomena such as the topographic relief on Mars and the influence of dust storms MarTIM was able to study the effect that these had on its description of the upper atmosphere. The MCD dust scenarios were described in section 5.3.1 and the coupling was described in section 5.3.2. Importantly, in section 5.3.2, it was noted that to be able to successfully couple MarTIM to the MCD we needed to assume that the 0.883 Pa pressure level was also a surface of constant geopotential. This meant measuring geopotential heights against the lower boundary rather than the surface of the planet. In doing so we effectively damped the geopotential gradients (pressure gradients) throughout the model and thereby influenced the simulated wind magnitudes.

- In section 5.4 the coupled MarTIM-MCD model was used to study the extent to which the upper atmosphere region is coupled to the lower atmosphere through the middle atmosphere. It was shown that while through the first few pressure levels the MCD was clearly influencing the MarTIM result, by virtue of there being fair comparison between the coupled model and the MCD alone results, eventually (at higher pressure levels) it was seen that the basic MarTIM alone result began to reappear. In this way MarTIM was beginning to constrain the MCD from above. At the end of section 5.4.4 it was concluded that this was a direct influence of the approximation made with the lower boundary geopotential surface in section 5.3.2. This conclusion also noted that this approximation was not fully consistent with the MCD input at 0.883 Pa because with a surface of constant geopotential any pressure gradients had been effectively removed thus implying zero horizontal velocities at the lower boundary (which is clearly not the case at 0.883 Pa in the MCD). With a reduced longitudinal resolution we were able to remove the approximation altogether - but this restricted the types of MCD dust scenario that could be input at MarTIM's 0.883 Pa lower boundary. Thus, a full suite of results could no longer be simulated, but those that were showed much closer comparison to the MCD alone results across almost the entire MarTIM model space.

- The coupled MarTIM-MCD simulation was also compared against recent SPICAM nightside number density and temperature measurements (Forget et al., 2009). For several different solar longitudes and solar activities the coupled model simulated vertical temperature profiles faired well against SPICAM data (e.g. see Figure 5.33, top left). For other comparisons, in particular for the coldest SPICAM temperature profiles (see section 5.6.2), coupled model results were typically too warm - unable to reach the subfreezing mesopause temperatures (in the 70 to 90 K region). It was suggested, after McDunn et al. (2010), that weaker global winds at constant pressure levels could decrease the warm air advection from dayside to nightside thereby raising the vertical level of the mesopause and reducing its temperature magnitude.

Finally, in Chapter 6, we introduce a more sophisticated ionosphere model and study the variation in both primary and secondary electron production rate with season and solar cycle.

Chapter 6

MarTIM and TransMars: The New Ionosphere

6.1 Introduction

In this final chapter of experiments performed with MarTIM we present an analytic method for the rapid computation of secondary ion and electron production due to electron impact as suprathermal electrons produced by primary photo-ionisation propagate through the neutral background Martian atmosphere. The work in this chapter was published in the report Nicholson et al. (2009). We use a one-dimensional kinetic model, *Trans*-Mars (Simon et al., 2008), that solves a stationary Boltzmann transport equation to describe the ionosphere of Mars with the neutral background atmosphere (temperatures, number densities and geopotential heights) being provided by MarTIM. Parameters are given to allow the rapid computation of secondary ion production for 11 ion species (CO_2^+, CO_2^{++}, CO^+, C^+, N_2^+, N_2^{++}, N^+, O_2^+, O_2^{++}, O^+, O^{++}) as well as for the secondary electron production. We use MarTIM results to show that while the efficiency (ϵ) of ion and electron production (ratio of secondary to primary production) does vary with solar zenith angle it can be parameterized with a simple function, which is given. Finally we also use MarTIM to show that production efficiency variations with solar cycle and solar longitude are negligible about the region of the primary and secondary production peaks.

6.2 The Martian Ionosphere

Present day observation of the Martian ionosphere continues to reveal new and interesting phenomena. Studies have highlighted features that are similar to those of other planetary ionospheres and features that are specific to the Martian plasma environment. In discussion of the former one can draw upon examples such as the similarities in ionic constituents between the Venusian and Martian ionospheres (Witasse et al., 2008), or the occurrence of auroral phenomena in the upper atmospheres of Mars (e.g.

Bertaux et al. (2005b)), Earth (e.g. Aruliah et al. (2005)) and the giant planets (e.g. Stallard et al. (2008)). In the latter case the unique Martian magnetic topography, typified by the crustal magnetic fields, has a very complex structure and creates so-called 'mini-magnetospheres' that manipulate the solar wind interaction downwards into and horizontal convection across the Martian ionosphere (Breus et al., 2005). Additionally, comparison of ionospheres of different planets provides constraints on our understanding of processes that would not be possible by studying a single (terrestrial) case. For example the enhanced solar high energy X-ray and UV radiation experienced successively at Earth, Mars, Jupiter and Saturn due to a single specific solar flare event (Mendillo et al., 2006). This allowed the rapid effects of solar flux variation on the ionospheric plasma to be studied in isolation away from slower changes in background neutral atmosphere variation with the 11 year solar cycle.

As revealed by the Retarding Potential Analyzer (RPA) instruments onboard the two Viking landers (Hanson et al., 1977) the major ion in the Martian ionosphere is O_2^+, with a peak density of approximately 10^5 cm^{-3} at an altitude of 130 km. Both CO_2^+ and O^+ were also detected. Peak densities for these latter two species are approximately 10^4 cm^{-3} at 140 km and $8{\times}10^2$ cm^{-3} at 230 km, respectively (Witasse et al., 2008). Although the RPA instruments made the first ever *in situ* ionospheric measurements of a planet other than Earth (Nagy et al., 2004) our knowledge of the Martian ionosphere remained incomplete for a good 20-year period before the Mars Global Surveyor (MGS) and more recently the Mars Express (MEX) missions returned with radio science, electron reflectometer and magnetometer instruments to continue observational study. As a consequence an extensive set of electron density profiles have been collated from the aforementioned missions, adding to results from Mariners 4, 6, 7 and 9, Vikings 1 and 2 and Mars 4 and 5 missions (Nagy et al., 2004).

Electron density data from the pre-MGS missions were studied collectively by Zhang et al. (1990) who revealed that, in the region of the peak, the Martian ionosphere is fairly well described by ideal Chapman theory. Thus the peak density shows a close $\cos^{1/2}(\chi)$ dependence (where χ is the solar zenith angle) with a photochemical equilibrium being quickly established between production and loss of electrons (Bougher et al., 2001). Likewise the altitude of the peak, when acting under the local control of photochemical processes, depends upon how deeply into the atmosphere the solar radiation penetrates. The ionosphere also showed a notable degree of consistency in the typical electron density profile structure about the region of the peak (its altitude and magnitude) and the ionospheric scale height exhibited up to approximately 200 km. Further modelling work confirmed that the dayside ionosphere below approximately this altitude is not subject to vertical or horizontal transport of ions (e.g. Bougher et al. (2001)).

Electron density data has been used post-MGS to study the interannual variability of the ionosphere and as a proxy to study neutral atmospheric phenomena such as solar-driven tides by considering the occurrence of those same phenomena in the ionosphere (Hinson et al. (2008), Cahoy et al. (2006), Bougher et al. (2004, 2001)). Both Mars Global Surveyor and Mars Express have also highlighted the complexity of the Martian magnetic field and energetic electron fluxes of the near-Mars space environment (Soobiah

et al. (2006), Withers et al. (2005), Krymskii et al. (2003)). More recently studies using UV and IR spectrometer data from the Mars Express SPICAM instrument (Simon et al. (2008), Shematovich et al. (2008)), including comparison of intensity profiles of the Cameron CO bands and CO_2^+ UV doublet at 289.0 nm, have helped continue to reveal the underlying ionospheric and neutral atmospheric conditions (density and temperature for example).

All-in-all the adherence or otherwise of the Martian ionosphere to Chapman theory and the close dependence on the neutral background atmospheric structure and solar EUV/X-ray radiation has been intensively analyzed, modelled and summarized by many authors in one, two and three dimensions using kinetic, fluid, hybrid and MHD mathematics (see for example Fox (2004a) and references in Wang and Nielsen (2004a) and Nagy et al. (2004)). However, despite these advances much remains to be learnt about the Martian ionosphere (*in-situ* ion measurements for example remain especially limited). The topside Martian ionosphere and its interaction with the solar wind (e.g. Gurnett et al. (2010)), the effect of the crustal magnetic fields on the ion and electron dynamics & energetics (e.g. Lillis et al. (2004)) and finally the description of the nightside ionosphere (e.g. Lillis et al. (2009); Němec et al. (2010)) all remain as perhaps the most challenging areas for further study.

The MARSIS radar onboard Mars Express (Picardi et al., 2004) has begun to address many of these problems (Witasse et al., 2008). It can measure vertical electron density profiles above the main ionospheric peak (Morgan et al., 2008). Here, interesting double echos have been reported (Gurnett et al., 2008) that are correlated with regions of crustal magnetic fields. It has provided data from which the total electron content (TEC) can be retrieved (Safaeinili et al., 2007). This showed interesting nightside behaviour with clearly visible sudden jumps in the TEC that are believed to be linked to the crustal magnetic fields while other TEC variations are clearly correlated with SPICAM ultraviolet observations of the Martian Aurora (Witasse et al., 2008).

In this chapter we look at the relationship between primary photo-production (i.e. through photo-absorption) and secondary electron impact production (i.e. through energetic electron propagation). The computation of ion and electron densities by primary photo-production is straightforward and fast, however the (secondary) ionic production by energetic electron propagation through the background neutral atmosphere and subsequent electron impact is a far more involved and complex computation. Thus we provide a method by which the secondary ion and electron production can be rapidly calculated by using the production efficiency (ϵ, defined as the ratio between the secondary and primary productions) as an intermediary. Our use of the production efficiency is advantageous not only for the swift computation of production rates it affords us but also because it will reflect changes in both the primary and secondary production rates, which in turn will be due to any variation in the background neutral density due to orbital and solar cycle conditions (Forget et al., 2009) and these can be studied with MarTIM.

First in section 6.3 we describe the 1-D kinetic model, *Trans*-Mars, used to model the energetic electron propagation through the background neutral atmosphere. Then in section 6.4 we describe the rapid computation method. Finally we discuss the applicability of our results to various solar and

seasonal conditions in terms of how the variation of MarTIM's neutral background atmosphere affects our results.

6.3 Production Computation

The production calculation of secondary ions and electrons by energetic (primary) electron propagation through the background neutral atmosphere (and subsequent electron impact) was conducted with a one-dimensional kinetic electron transport code developed at Laboratoire de Planétologie, Université Joseph Fourier/CNRS, Grenoble. This model solves a stationary Boltzmann equation for the energetic electron flux. It belongs to the *Trans-** family of models that have been, over recent years, applied to describe the ionospheres and planetary upper atmospheres of Earth, Venus, Titan and Mars (see Lilensten and Blelly (2002), Gronoff et al. (2007, 2008), Galand et al. (1999) and Witasse (2000) respectively). The term *Trans-** is shorthand for 'transport' as in the transport of energetic electrons through an atmosphere. When MarTIM and *Trans*-Mars work together we refer to the coupled model with the name *Trans*-TIM.

6.3.1 The Kinetic Electron Transport Model

The kinetic part of *Trans*-TIM distinguishes between two sub-populations of electrons present in the Martian ionosphere, based on the influence they have on the physics of the ionosphere; the thermal electrons and the suprathermal electrons. In this study we model the propagation in altitude and degradation in energy of the suprathermal electrons as they propagate through the Martian neutral and ionic background atmosphere. The principal source of suprathermal electrons for the kinetic code are the solar produced photo-electrons with a calculated dependence on solar zenith angle, solar activity and solar longitude. Alternative precipitated sources from available plasma observations (e.g. Acuña et al. (1998)) can also be used as an upper boundary condition. Ionospheric plasma acceleration is discussed by e.g. Lundin et al. (2006) and the suprathermal electrons could be used to study e.g. the creation of the Martian nightside aurora from the influx of auroral electrons (see Bertaux et al. (2005b)) or the intricate night side ionospheric structure (Fillingim et al., 2007; Lillis et al., 2009; Němec et al., 2010). In any event we refer to these as 'primary' electrons and model the ionization, excitation and heating caused by their propagation and collision with the ambient atmosphere. Though note again we only study solar produced photo-electrons in this chapter.

The thermal electrons are simply a component of the ambient background and thus the distinction between the two electron populations centers upon a 'cross over' or 'thermal' energy defined (in (eV)) as E_t=$k_B T_e$, with k_B=8.61×10^{-5} (eV K^{-1}) the Boltzmann constant and T_e the temperature of the ambient electrons (Swartz et al., 1971; Lummerzheim and Lilensten, 1994a). We assume the electron distribution is dominated by thermal electrons below E_t and by the streaming suprathermal electrons above E_t. Heating of the ambient thermal electrons occurs either by a continuous friction-like term (the loss function $L(E)$, see equation 6.4) representing energy loss to the thermal electrons at all energies or

when primary electrons degrade in energy into the thermal energy range. Ionization events caused by inelastic collision between primary electrons and neutral components of the ambient atmosphere produce 'secondary' ions and electrons. It is the ratio of these secondary ions and electrons to their primary counterparts that we call the production 'efficiency' (ϵ). However, since the computation of primary electron collision processes and the production of secondary ions and electrons is far more complex than the primary photo-ionization calculation alone our aim is to provide a method that uses the production efficiency to rapidly calculate all ionic components of the Martian ionosphere.

The kinetic model describes the ionosphere using a fixed altitude grid ranging between 80 km and 500 km and an energy grid ranging between 0.1 eV and 280 eV. The energy range is divided into 40 grid points whose spacing is non-uniform and determined by a power law. This type of energy grid means the energy step between successive energy grid points increases with energy and thus the lowest energies are described with a finer resolution. This is advantageous as theory would suggest (Ratcliffe, 1972) that all charged particles ionize neutrals most rapidly near the ends of their paths through the atmosphere before they return to the thermal (ambient) electron background. Thus the ionization is most prominent when the time spent by a primary electron near a background atom is comparable with the period of a thermal electron in a Bohr orbit about that background atom. With a fine energy grid we can better take this into account.

In studies of the terrestrial atmosphere and ionosphere using the *Trans-** suite of kinetic models the z-axis is held as vertical and modelling is restricted to polar regions where primary electrons are guided vertically into the atmosphere by the geomagnetic field. With a vertical magnetic field strong enough to impose a negligible Larmor radius we can assume an axial symmetry around the field line. In turn this removes any dependence on the horizontal coordinate as long as we further assume that the atmosphere is locally horizontally stratified and that photo-production is isotropic, both reasonable assumptions. Such considerations can also be applied to a study of the Martian atmosphere on the assumption that either (1) we are at the edge of one of the Martian anomalies such that a strong magnetic field is aligned vertically, or (2) the induced magnetic field is sufficiently diffused over the region from the upper atmosphere to the altitude of the ionospheric peak (where our study is most concerned) such that it's influence on the electron and ion trajectories can be neglected or (3) that there is no magnetic field at all, such as would likely be experienced away from the localised magnetic anomalies associated with the crustal magnetic fields.

With the above assumptions considered the transport equation can be written (Stamnes and Rees,

1983a):

$$\mu\frac{\partial\Phi(\tau,E,\mu)}{\partial\tau(z,E)} = -\Phi(\tau,E,\mu) + sf(\tau,E,\mu) + \frac{n_e(z)}{\sum_k n_k(z)\sigma_k^T(E)}\frac{\partial\left(L(E)\Phi(\tau,E,\mu)\right)}{\partial E} + \sum_l\left\{\frac{n_l(z)\sigma_l^T(E)}{\sum_k n_k(z)\sigma_k^T(E)}\int_{-1}^{+1}d\mu' \int_E^{E_{max}} dE' R_l\left(E',\mu'\rightarrow E,\mu\right)\Phi(\tau,E',\mu')\right\} \quad (6.1)$$

where $\Phi(\tau,E,\mu)$ is the stationary electron flux ($\mathrm{cm^{-2}s^{-1}eV^{-1}sr^{-1}}$), $\partial\tau(z,E)$ is the electron scattering depth, z is the altitude, μ, μ' are the cosines of scattered and incident electron pitch angles, E, E' are the energies (eV) of scattered and incident electrons, $n_k(z)$, $n_l(z)$ are the number densities of neutral species k and l at altitude (z), $n_e(z)$ is the thermal electron number density at altitude (z), R_l is called the redistribution function and describes the degradation from a state (E',μ') to a state (E,μ) for the neutral l, $\sigma_k^T(E)$, $\sigma_l^T(E)$ are the total collision cross-sections (elastic plus inelastic) for the neutrals k or l for a colliding suprathermal electron of energy (E).

The second term on the right-hand side of equation (6.1) is the primary photo-electron source term ($\mathrm{cm^{-2}s^{-1}eV^{-1}sr^{-1}}$) due either to the solar EUV flux or precipitated into the upper modelled atmosphere. For this study we restricted our primary electron source to be only the solar photo-electron source:

$$sf(\tau,E,\mu) = \frac{1}{4\pi\sum_k n_k(z)\sigma_k^T(E)}\sum_{k,i} q_{k,i}(z,E) \quad (6.2)$$

here $q_{k,i}(z,E)$ is the primary photo-electron production rate ($\mathrm{cm^{-3}s^{-1}eV^{-1}}$) and is equal to:

$$q_{k,i}(z,E) = n_k(z)\sigma_{k,i}^{ion}(E_{h\nu})I_\infty(\lambda_{h\nu}) \times\ exp\left(-\sum_m \sigma_m(E_{h\nu})Ch(z,\chi)\int_z^\infty n_m(z')dz'\right) \quad (6.3)$$

where the relationship between the photon energy $E_{h\nu}$ and the suprathermal electron energy grid is accounted for with the statement $E_W = E_{h\nu} - I_{k,i}$. Thus we take the difference between the energy $E_{h\nu}$ of the incident solar photon and the ionization threshold $I_{k,i}$ of species k and state i to calculate the energy of our created photo-electrons (E_W). Then we simply ensure the energy E_W is associated with the correct suprathermal electron energy grid position E i.e. we use the former to search through the latter to build our source function upon energy grid E. For the other terms we have: $\sigma_{k,i}^{ion}(E_{h\nu})$ photo-ionization cross-section for species k, state i for photon energy $E_{h\nu}$, $I_\infty(\lambda_{h\nu})$ solar EUV flux at the upper boundary of the atmosphere, $\sigma_m(E_{h\nu})$ photo-absorption cross-section of neutral species m for photon energy $E_{h\nu}$.

And finally, regarding the source term (equations 6.2 and 6.3), note how the primary photo-production is calculated by considering a column of atmosphere along the line of sight of the solar photon beam by using the Chapman function provided by Smith III and Smith (1972) to describe high solar zenith angle

(χ) grazing incidence. The Chapman function depends upon both the scale height and the radial distance from the centre of the planet to the point in question ($R_M + z$). For the radius of Mars term (R_M) we require a description of Mars global surface shape. Since the Martian areoid will vary with latitude and longitude due to local topographic features we follow the procedure used by the Mars Climate Database (Lewis et al., 1999) and approximate its shape by an offset spheroid whose characteristics can be found at `http://ssed.gsfc.nasa.gov/tharsis/geodesy.html`. Thus zero elevation (from which our altitude z is measured) is defined as the equipotential surface whose average value at the equator is $3,396,000$ m (after Smith et al. (1999)). Although this means the polar radius is approximately $20,000$ m less than the equatorial radius we would not expect this difference to introduce any significant variation in our calculation of the Chapman function were we instead to approximate Mars' shape by a sphere of radius $3,396,000$ m. For the various values of scale height used we note that this depends upon the particular background neutral atmosphere calculated (see section 6.3.2).

The loss function $L(E)$ was introduced earlier as representing a continuous friction-like term responsible for energy loss from the precipitating energetic suprathermal electrons to the ambient thermal electrons. We assume that the primary electrons are not deflected in this process (Blelly et al., 1996). In equation (6.1) it appears in the third term on the right hand side. The full expression is (Swartz et al., 1971; Lummerzheim and Lilensten, 1994a):

$$L(E) = \frac{3.37 \times 10^{-12}}{E^{0.94} n_e^{0.03}} \left(\frac{E - E_t}{E - 0.53 E_t} \right)^{2.36} \tag{6.4}$$

This term requires self-consistently calculated profiles of electron temperature (T_e, for use in E_t=$k_B T_e$) and of background (thermal) electron density (n_e) to be provided. For the latter recall that about the peak the Martian ionosphere is fairly well described by ideal Chapman theory. With this in mind we use the formulation of Fox and Yeager (2006), equation 5, to describe the electron density input to the kinetic model as a function of solar zenith angle and altitude. In this formulation the Chapman layer is defined as being produced by the photo-ionization of a single molecular species for which the resulting molecular ion (O_2^+, the major ion in the Martian ionosphere) is destroyed locally by dissociative recombination with a rate coefficient α_{dr}. Fox and Yeager (2006) adopt a value for α_{dr} of $1.95{\times}10^{-7}(300/T_e)^{0.7}$ cm^{3}s^{-1} for T_e<1200 K and a value proportional to $(300/T_e)^{0.56}$ for T_e>1200 K. Analysis of the resulting Chapman layer (see the solid line of Figure 6.1) shows that for equinox conditions at heliocentric distance of 1.47 AU for overhead sun conditions, and with our neutral background atmosphere, that the peak electron density reaches a value on the order of 10^5 cm^{-3} at $\sim$125 km.

For the electron temperatures (T_e) we are unfortunately quite limited in our capacity to self-consistently calculate appropriate profiles and instead require the plasma temperatures to be provided as inputs to be read in directly to *Trans*-TIM, either from other models or from available spacecraft data. For this study then we take the profile calculated in the work of Witasse (2000) where a full fluid model component was coupled to the *Trans** kinetic part. This fluid model component solved an 8-moment approximation to Boltzmann's equation for the distribution function (see Blelly et al. (1996)) appropriate to Viking conditions. The resulting electron temperature profile is shown by the dot-dashed line in Figure 6.1. We

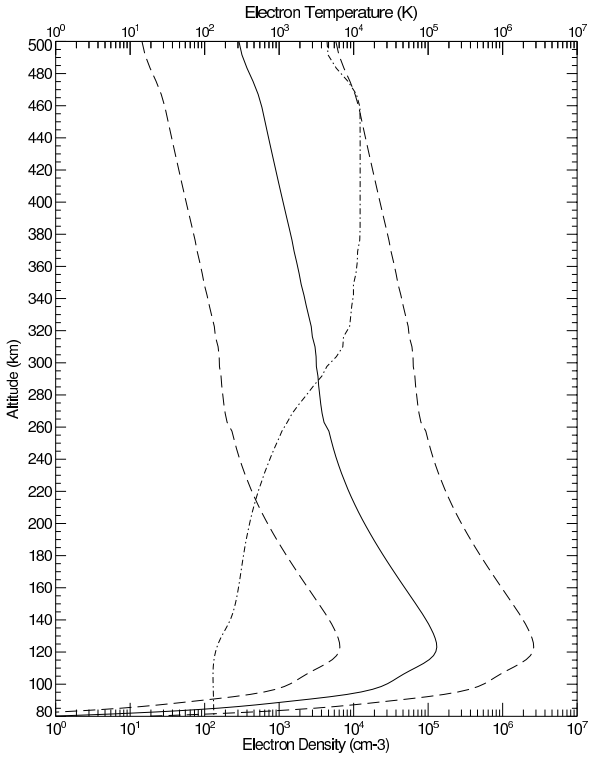

Figure 6.1: Electron density (solid line) profile (n_e) for sun overhead, equinox conditions. Also shown are variations in n_e investigated in preparation for this study (dashed lines, see text). Electron temperature (dot-dashed line) profile (T_e) used throughout this study (see text).

do appreciate the limitations that our choice of both the electron number density and electron temperature bring to the breadth of study we can present while maintaining full self-consistency. However we note that the frictional processes the loss term of equation 6.4 represents (including energy loss through Coulomb collision and Çerenkov wave generation) are more important at low energies (in particular less than the ionization threshold) and so are not expected to influence the secondary electron production (Galand et al., 1999). Consequently since this study is focused on the efficiency of ionization processes i.e. the secondary to primary ionization relationship, we don't consider our choice of n_e nor T_e to limit in any way the range of conditions (solar zenith angle, solar activity, etc) we can consider.

Indeed we studied the effect of using two other electron density profiles as inputs to our coupled model. One with the Chapman layer profile multiplied by a factor of 20 and the other with it divided by a factor of 20 (see the dashed lines of Figure 6.1). This factor was chosen following recent remote sensing observations of neutral CO_2 density using the SPICAM instrument onboard Mars Express (Forget et al., 2009) that revealed density varied annually by a factor of 20 at 120 km. Thus we assume a like-for-like variation is possible in electron densities. In the efficiency profile results, which are not shown here, we found no discernible variation in the production efficiency and therefore feel confident that using the limited plasma inputs discussed throughout the rest of the present study will not affect any of our production efficiency results.

The last term on the right hand side of equation (6.1) represents the electron production due to degradation of higher energy fluxes through collisions between primary electrons and neutral particles (Blelly et al., 1996). In this term R_l is known as the redistribution function and is defined as the ratio of (in the numerator) the sum of differential cross-sections (sum of cross-sections over different elastic and inelastic collisions) between electrons and neutrals to (in the denominator) the total cross-section σ_l^T of neutral species l. The differential cross-sections are deduced from the collision cross-sections as described in Lummerzheim and Lilensten (1994a). Collisions between secondary electrons are neglected.

The solution to the transport equation is formally equivalent to the equation of radiative transfer. The programs originally developed to solve the core of the kinetic model are described in Lummerzheim and Lilensten (1994a) wherein the discrete ordinate method is adopted using the DISORT procedure of Stamnes et al. (1988) where 8 streams (or pitch angles; referring to the angle between the particle velocity and the vertical direction) are used as recommended by Lummerzheim and Lilensten (1994a). In this 'multi-stream' approach we must account for the energy distribution associated with and the angular dependence of secondary electrons generated by inelastic collision between primary electrons and the background atmospheric gases (Opal et al., 1971).

For the angular dependence we assume that during an inelastic collision producing an ionization or excitation the incident primary electron is scattered mostly forward (Blelly et al., 1996) so that the collision phase function (which governs the angular redistribution of energy degraded primary electrons (Lummerzheim et al., 1989)) can be approximated by a Dirac-delta function in the forward direction. We assume that the secondary electrons produced may be scattered in any direction, i.e. they are distributed isotropically. This was justified in the work of Lummerzheim and Lilensten (1994a) whose study of the angular redistribution function for the secondary electrons showed that it had no influence on the altitude profiles of heating rates, energy deposition rates nor emission rates.

For the case of elastic collisions the converse situation is apparent: results are sensitive to the phase function for elastic scattering (Lummerzheim et al., 1989). We use the parameterization developed by Porter and Jump (1978) and Porter et al. (1987) for the angular redistribution and the required equation is:

$$p(\cos\Theta) = \frac{1}{N}\left[\frac{1}{(1+2\epsilon-\cos\Theta)^2} + \frac{\beta}{(1+2\delta+\cos\Theta)^2}\right] \tag{6.5}$$

with the normalisation N given by:

$$N = \frac{1}{4}\left[\frac{1}{\epsilon(1+\epsilon)} + \beta\frac{1}{\delta(1+\delta)}\right] \tag{6.6}$$

Here Θ is the total scattering angle and Porter et al. (1987) provide tabulated values for β, ϵ and δ to fit the phase function to laboratory measurements in the energy range from 2 eV to 1 keV. The first term in the brackets is the usual screened Rutherford term with ϵ the screening parameter. The second term is phenomenologically added to describe backscatter enhancements that appear in the angular elastic cross sections for many gases at lower energies. For energies above 1 keV we set $\beta = 0$ so that this phase function becomes identical to the screened Rutherford phase function. The angular distribution of

the low energy electrons is dominated by elastic scattering and so for energies less than 12 eV isotropic scattering is assumed.

For the energy redistribution and degradation of the primary electrons in the inelastic excitation and ionization collisions we use the scheme proposed by Swartz (1985) where effective cross-sections are defined that accommodate the energy losses in collisions on a given discrete numerical energy grid (see Lummerzheim and Lilensten (1994a) and the last term on the right hand side of equation 6.1 above). For simplicity we assume no energy redistribution in elastic collisions (Lummerzheim and Lilensten, 1994a).

For the purpose of this study it only remains to describe the calculation of primary photo-ions and secondary production of ions and electrons. Here, primary photo-ions refers to those ions produced by the incident solar flux i.e. they are the counterpart to the primary (photo) electrons The primary photo-ion production ($\mathrm{cm}^{-3}\mathrm{s}^{-1}$) for species k is calculated by integrating $q_{k,i}$ over solar photon energy and summing over all states i:

$$P_k^{ion}(z) = \sum_i \int_E q_{k,i}(z,E)dE \tag{6.7}$$

then the primary (photo) electron production is simply the sum of primary photo-ion production over all species k:

$$P^{electron}(z) = \sum_k P_k^{ion}(z) \tag{6.8}$$

For the secondary ion production ($\mathrm{cm}^{-3}\mathrm{s}^{-1}$) for species k we calculate the solution of:

$$P_{s,k}^{ion}(z) = 2\pi n_k(z) \int_{-1}^{+1} d\mu \int_{E_{min}}^{E_{max}} dE \sigma_k^{ion}(E)\Phi(\tau,E,\mu) \tag{6.9}$$

and so finally the secondary electron production is once again the sum of secondary ion production over all species k:

$$P_s^{electron}(z) = \sum_k P_{s,k}^{ion}(z) \tag{6.10}$$

Note finally for the electron production resulting from CO_2^{++}, N_2^{++}, O_2^{++} and O^{++} ionization that a factor of 2 is included as part of equations 6.8 and 6.10 since two electrons are produced per ionization event for each of these species.

6.3.2 The Background Neutral Atmosphere Model

To solve the stationary Boltzmann equation the kinetic model requires a one-dimensional atmospheric profile of the neutral background atmosphere be provided. This is provided by MarTIM and examples of the background neutral atmospheric densities for solar minimum (SMIN $F_{10.7,Mars} = 31.3$), equinox conditions (heliocentric distance 1.466 AU) at solar zenith angle 45° are shown in Figure 6.2(a). This model setup gave us exospheric temperatures of T_{exo}≈224 K and these are shown in Figure 6.2(b) (solid blue line). Also shown in Figure 6.2(b) are the neutral temperatures derived by MarTIM for a similar heliocentric distance at medium solar activity levels (solid black line, SMED, $F_{10.7,Mars} = 60.9$, T_{exo}≈275 K)

and high solar activity levels (solid red line, SMAX, $F_{10.7,Mars} = 95$, T_{exo}≈308 K). These temperatures are also compared against the equivalent results of MTGCM simulations (Bougher et al., 1999b) available from `http://data.engin.umich.edu/tgcm_planets_archive/index.html` (dashed lines). Scale heights calculated by MarTIM about the typical ionospheric peak altitude of 130 km for the profiles of Figure 6.2 were 9.98 km for SMIN, 10.74 km for SMED and 11.14 km for SMAX. Finally note that in Figure 6.2(b) we plot coloured symbols as place-markers representing selected dayside upper atmosphere spacecraft observations, after Bougher et al. (2000) and Table 1.2 in Chapter 1.

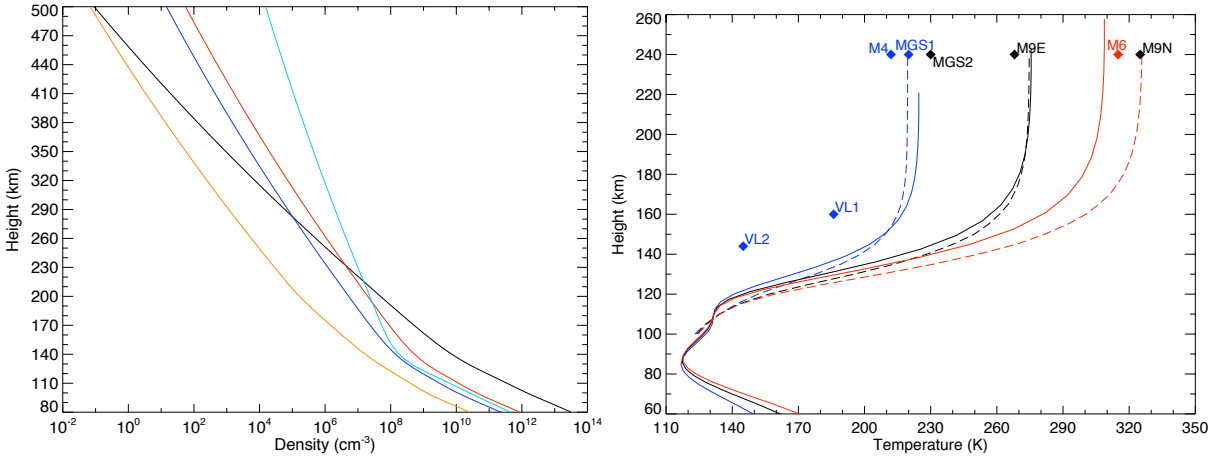

(a) Background atmosphere number density.

(b) Background atmosphere temperature profiles.

Figure 6.2: (a) Background neutral density profiles, CO_2 (black line), CO (blue line), N_2 (red line), O (cyan line) and O_2 (orange line). (b) Background neutral temperature as derived by MarTIM and used in the kinetic code. SMIN (blue), SMED (black) and SMAX (red), for MarTIM (solid lines) and MTGCM (see text) (dashed lines). Symbols represent selected Mars dayside upper atmosphere spacecraft observations, after Bougher et al. (2000) (see Table 1.2).

The model setup shown in Figure 6.2(a) also gave us an O to CO_2 ratio of ≈1.7% at 125 km and ≈2% at 130 km. The O to CO_2 ratio at the altitude of the ionospheric peak (≈130 km) is often quoted as a measure of the dissociation of the Martian atmosphere (Bougher et al., 2000) as the photochemically produced CO_2^+ is quickly converted to O_2^+ by reaction with O (Bougher et al., 1999b). Occasionally this ratio is also quoted at the altitude of the homopause (≈125 km) due to the important implications that O abundance has on the dominance of CO_2 cooling rates in the middle atmosphere. Typical values derived by other investigators range from 0.01 to 0.04 at 130 km over a range of solar activities and heliocentric distances (Bougher et al., 2000; Fox, 2004a). Values derived from MarTIM simulations for solar minimum, medium and maximum conditions (not shown) remain within this cited range.

6.3.3 Coupling the Models

Coupling of the two models into *Trans*-TIM is achieved through interpolation of MarTIM's neutral background atmosphere (in fixed pressure vertical coordinates as noted already) onto the independent

fixed altitude grid of the kinetic model. Number densities for neutral species CO_2, N_2, CO, O and O_2 are required by the kinetic code for the calculation of the column density of the one-dimensional atmospheric column through which the primary electron and solar fluxes are attenuated. These are interpolated from MarTIM's grid onto the *Trans*-TIM grid with a logarithmic interpolation routine. Neutral atmosphere temperatures from MarTIM are also taken and used by the kinetic code for the column density calculation. Finally MarTIM's geopotential heights are required in order to determine the fixed altitude against which the neutral densities and temperatures are defined.

Since the coupled *Trans*-TIM model describes the ionosphere using a fixed altitude grid ranging from 80 km to 500 km the use of MarTIM's background atmosphere demands that we provide a neutral atmosphere from MarTIM's upper boundary (∼200-350 km) to the upper boundary of the kinetic model (500 km). Such an extrapolation was achieved by assuming this upper atmosphere region could be described by a hydrostatic distribution with isothermal structure and starting from the number densities given by MarTIM's upper boundary. Although the altitude region above MarTIM's upper boundary (∼200-350 km) is probably not in hydrostatic equilibrium in the actual Martian atmosphere the assumption should be sufficient in the region of the ionospheric peak, which is where our study is mostly concerned.

The photo-ionization and electron collision cross-sections are the same as those used in a previous Mars atmosphere study using the kinetic model (Simon et al., 2008) namely from Torr and Torr (1985) for N_2, O_2, O, Hitchcock et al. (1980) and Avakyan (1998) for CO_2 and Tian and Vidal (1998) and Lummerzheim and Lilensten (1994a) for the secondary ion productions

Figure 6.3 shows the steady state downward primary electron flux predicted by *Trans*-TIM in comparison with three other Mars ionosphere model simulations. We show this to give an indication of *Trans*-TIM performance against other models that study similar ionospheric phenomena. In Figure 6.3 the *Trans*-TIM result (black solid line) shows the best comparison with that of *Trans*-Mars, from Simon et al. (2008). This is largely to be expected since these two models use the same kinetic electron transport code. The main reason for differences between them is the neutral background atmosphere supplied to that kinetic code. Simon et al. (2008) uses the neutral densities and scale heights of Bougher et al. (1990), Bougher et al. (1999b) and Bougher et al. (2000), which are about 10 years old. In comparison, we use MarTIM, which uses more up to date parameterisations as detailed in earlier chapters. Nonetheless these two curves exhibit similar behaviour with electron flux intensity decreasing from about 4.6×10^8 to 1.9×10^4 $eV^{-1}cm^{-2}s^{-1}sr^{-1}$ as the electron energies increase from 1 to 70 eV.

Next, the Monte Carlo simulations of Shematovich et al. (2008) (blue solid line) show a similar general electron flux versus energy trend to the profile of *Trans*-TIM (black solid line). The main differences between these simulations are (1) the locations of individual peaks and (2) that *Trans*-TIM underestimates the flux intensity predicted of Shematovich et al. (2008) by up to ∼30% across most of the energy range plotted. Similar differences can be seen between *Trans*-Mars (solid red line), from Simon et al. (2008), and Shematovich et al. (2008) (blue solid line). Thus we note that Simon et al. (2008) attributed these differences to the different orbital and global conditions for the various simulations

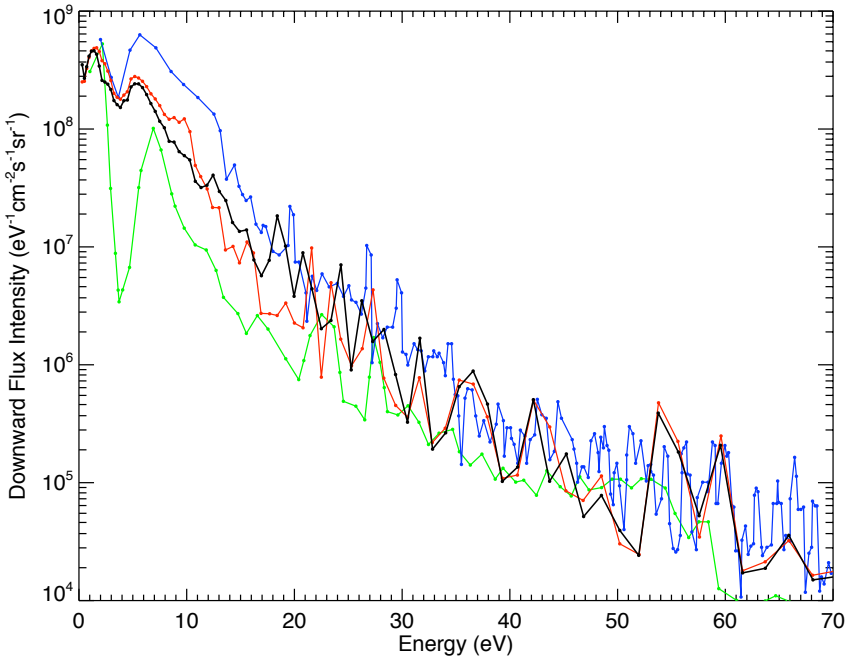

Figure 6.3: Steady state downward primary electron flux versus energy at 135 km altitude, 47.5° latitude and 1200-hrs local time calculated by various simulations. Black solid line is *Trans*-TIM from this study (*Trans*-Mars kinetic code, MarTIM background atmosphere for an energy grid with 125 grid points from 0.1 to 280 eV). Red solid line is *Trans*-Mars result from Simon et al. (2008). Blue solid line is the result from Monte Carlo simulations by Shematovich et al. (2008). Green solid line is the result from Fox and Dalgarno (1979). Based upon Figure 1 in Simon et al. (2008).

(altitude and position of Mars in its orbit). This would have influenced the intensity of the solar fluxes used in the models. And as earlier other differences due to improvements in the models, parameterisations and solar flux models will also play a role, especially in the comparison between *Trans*-TIM (black solid line) and the results of Fox and Dalgarno (1979) (green solid line) where some 30 years of study have past.

6.3.4 The Problem to Solve

As was discussed in section 6.3.1 the computation of ion and electron densities by primary photo-production (equation 6.3) is straightforward. However using the primary electrons calculated to complete the full transport equation calculation for the secondary production by energetic electron propagation through the background neutral atmosphere (as it is described above) is a far more involved and complex computation. Thus in the following section we will describe the results of the full *Trans*-TIM calculation for primary and secondary ion and electron production using the kinetic code with MarTIM providing the neutral background atmosphere.

The main aim is to provide a method by which the secondary ion and electron production can be calculated rapidly using the production efficiency ϵ (defined as the ratio between the secondary and

primary productions) as an intermediary. We will then use different neutral background atmospheres to show that while the production efficiency does vary with solar zenith angle it can be parameterized with a simple function. We also show that variations with solar cycle and solar longitude are negligible about the region of the primary and secondary production peaks.

Our study only considers solar zenith angles up to 90° since beyond this point the illumination rapidly fades as the Sun drops below the horizon. As a consequence we calculate the primary photo-production and secondary electron impact production peaks to rapidly decrease in magnitude to below the minimum value that we considered relevant for consideration (1×10^{-3} $cm^{-3}s^{-1}$). In turn we found that under these swiftly changing conditions the production efficiency did not lend itself to any straight forward parameterization. The approach of this phenomena is discussed further below.

6.4 Results

6.4.1 Polynomial Fit to the Production Efficiency

Following a similar method in Lilensten et al. (2005) where the production efficiency for Titan's ionosphere was studied, we also fit the model efficiency profiles $\epsilon(z, \chi)$ with a simple polynomial law. Initially the production efficiency is defined as a function of altitude z and solar zenith angle χ. Of course given the dependence the ionosphere has on the background neutral atmosphere one would expect efficiency to also be a function of solar cycle and Martian season. To start with then we conducted model runs for a solar zenith angle of $\chi = 0°$ at solar longitude Ls=180° (equinox) for solar minimum conditions ($F_{10.7,Mars} = 31.3$) and then later on studied the effect on the efficiency of varying the three variables solar zenith angle, solar longitude and solar cycle, preferably in an effort to reduce ϵ to a single dependency on altitude z.

Above a given transition altitude we use a logarithmic fit in order to avoid oscillations in the fit due to high-order polynomials:

$$log_{10}\left(\epsilon(z, 0°)\right) = \left(\sum_{i=0}^{N} a_i z^i\right) - 2 \tag{6.11}$$

while below this transition altitude use a direct polynomial fit:

$$\epsilon(z, 0°) = \sum_{i=0}^{M} b_i z^i \tag{6.12}$$

where z is the altitude in kilometers. The transition altitudes as well as the a_i and b_i coefficients for the 11 ion species CO_2^+, CO_2^{++}, CO^+, C^+, N_2^+, N_2^{++}, N^+, O_2^+, O_2^{++}, O^+ and O^{++} studied in this work, and for the electrons, are given in Table B.1 of Appendix B.

Our confidence in the physical consistency of the kinetic model and its calculation of the primary and secondary production rates and thus the efficiency meant we looked for a purely mathematical fit rather than one with some basis in physics (as was the case in Lilensten et al. (2005)). Therefore our

method for determining where the transition altitude should lie and what the most appropriate number (N or M) of coefficients to use in a particular species fit was to consider each species individually and to ensure minimum error between the kinetic model calculated vertical profile of efficiency and the polynomial fitted profile. As noted, the use of a logarithmic fit at high altitude ensured oscillations due to high-order polynomials were minimised and thus aided this process.

6.4.2 Production Efficiency General Trends

The *Trans*-TIM calculated ion production rates ($cm^{-3}s^{-1}$) for the 11 ion species studied in this report (and for the electrons) are shown in Figure 6.4 for N_2^+, N^+, N_2^{++} and the electrons, Figure 6.6 for CO_2^{++}, CO^+, C^+ and O^+ and finally Figure 6.8 for O_2^+, O_2^{++}, O^{++} and CO_2^+. In each case the contribution from photo (primary) ionization, electron impact (secondary) ionization are plotted as well as their total contribution (i.e. the sum of primary and secondary). Then in each case part (b) of the mentioned figures show the production efficiencies (ϵ) i.e. secondary production divided by primary production calculated both by *Trans*-TIM and by the polynomial fit as described above.

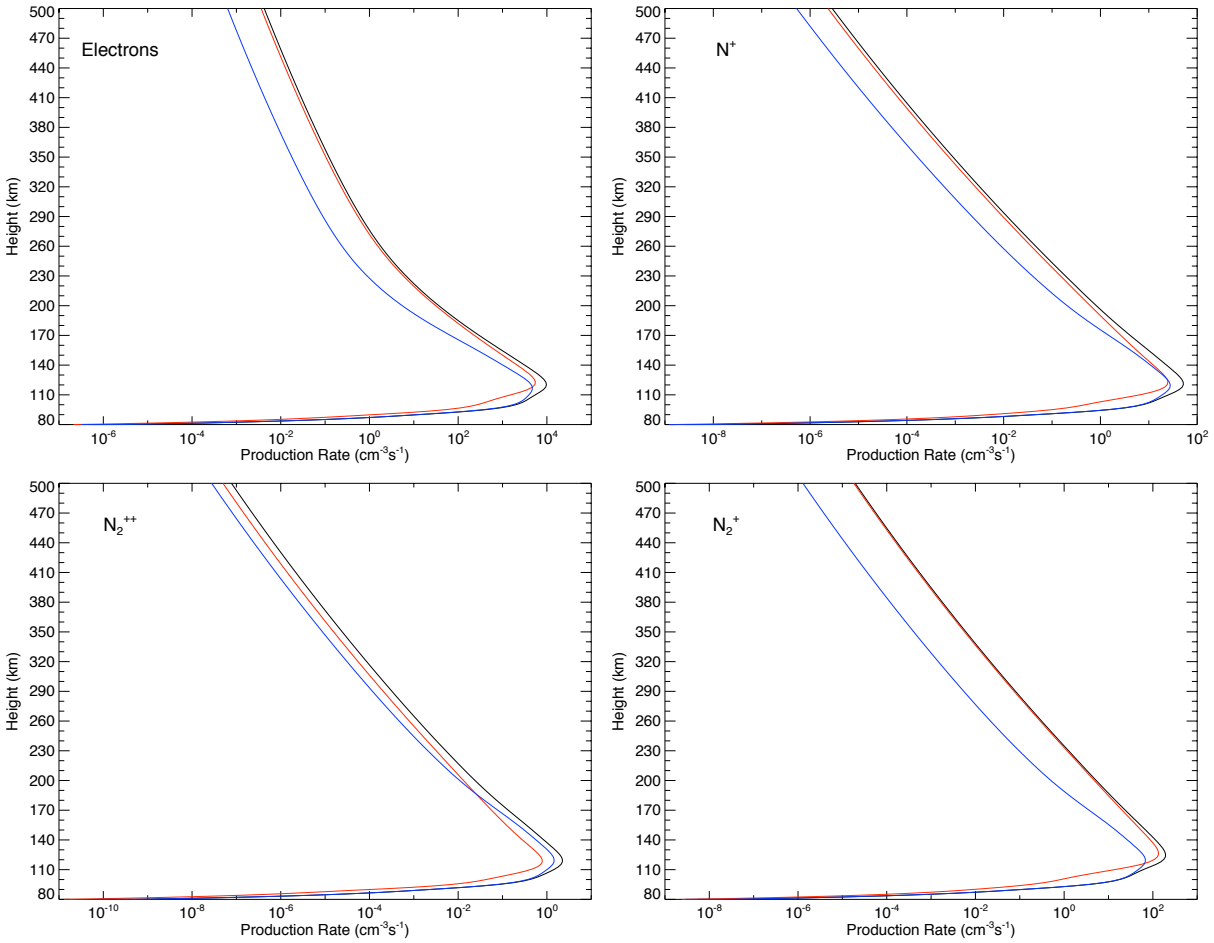

Figure 6.4: Total production (black solid lines), primary (photo) production (red solid lines) and secondary production (blue solid lines) versus altitude (km) for the electrons and for the ion species N^+, N_2^{++} and N_2^+.

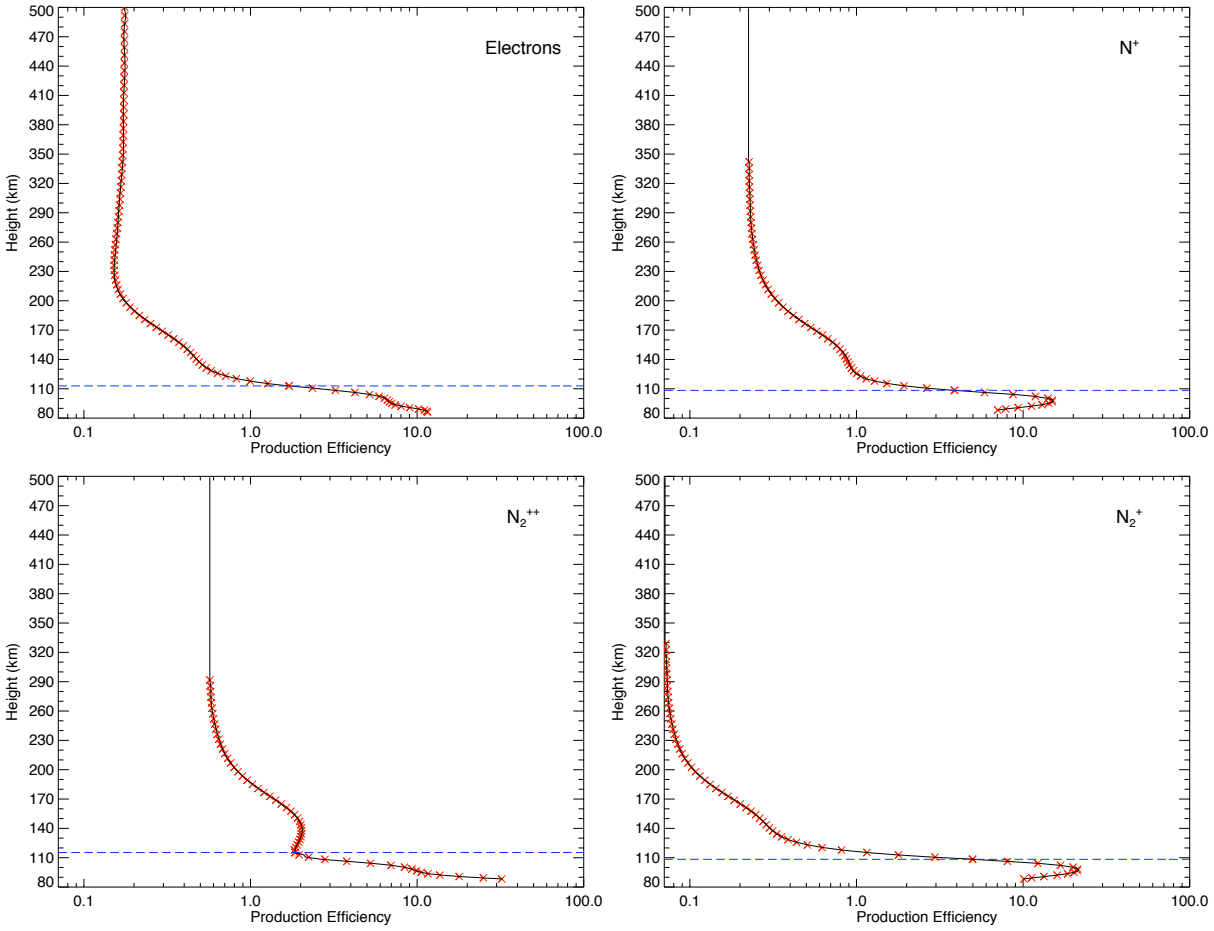

Figure 6.5: Production efficiency (kinetic model result (red crosses), polynomial fit (black solid line) and transition altitude (blue dashed line)) versus altitude (km) for the electrons and for the ion species N^+, N_2^{++} and N_2^+.

The structure observed in the efficiency profiles of figures 6.5, 6.7 and 6.9 deserves further explanation. The shape of the efficiency profiles comes about, in the main, simply due to the numerical effect of dividing the secondary production rate by the primary production rate. So the actual numerical value of the efficiency gives no indication that either primary or secondary production are particularly important at that location. It instead simply refers to their relative importance with respect to one another. Thus an extremely large efficiency can occur when one divides a secondary production rate by a primary production rate that is far smaller in magnitude. But it may well be that both primary and secondary productions are negligibly small because all the efficiency describes is their magnitudes relative to one another. Indeed, as noted briefly already, in all cases we took the decision to set the efficiency to zero when the secondary production dropped below $1{\times}10^{-3}$ $\mathrm{cm}^{-3}\mathrm{s}^{-1}$, showing no regard to whether an immense (or otherwise) primary production rate was in effect because clearly it was not creating a secondary production rate of any notable value.

Physically the only parameters that are specific to each species that could be responsible for the efficiency profile structure plotted are the photo-absorption and electron-impact cross-sections. After all,

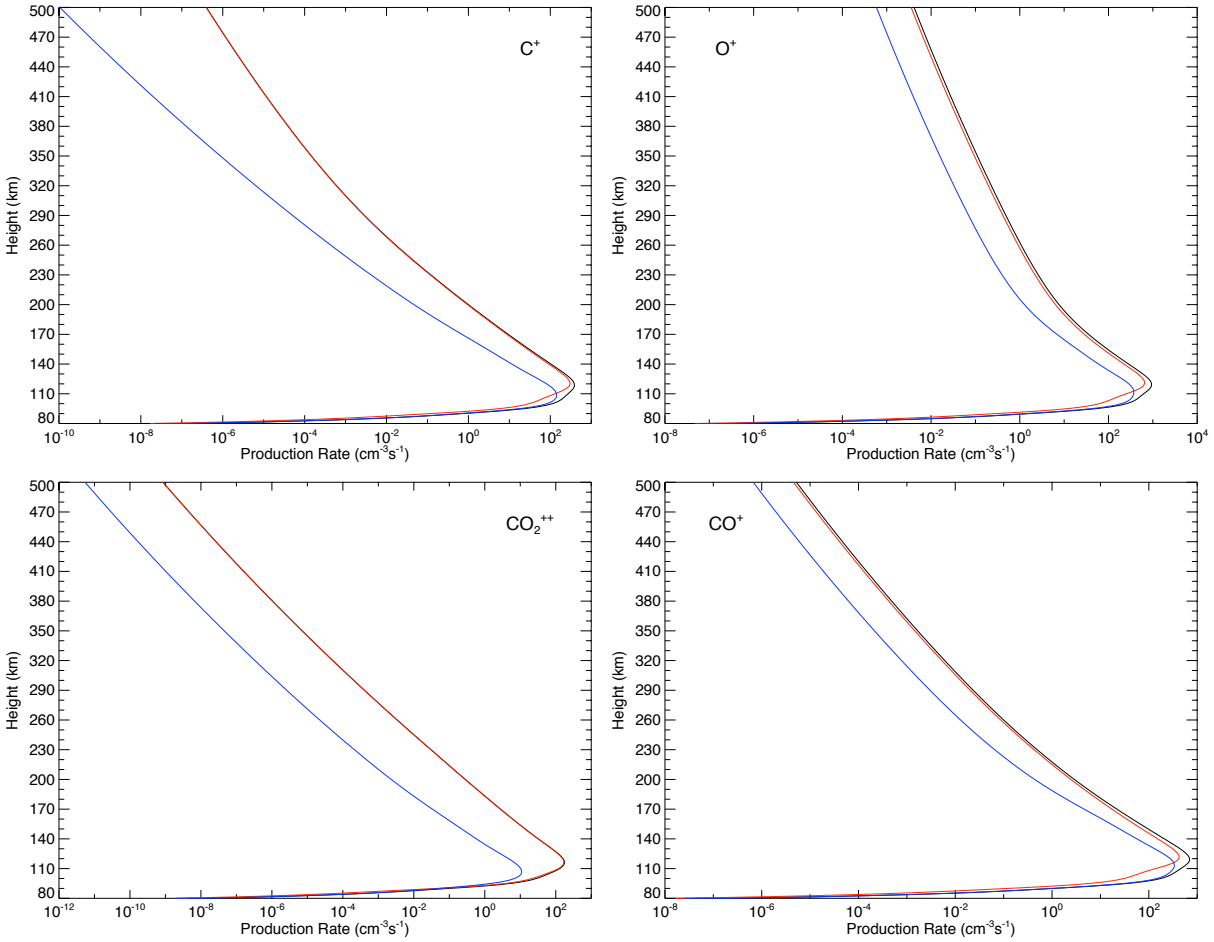

Figure 6.6: Total production (black solid lines), primary (photo) production (red solid lines) and secondary production (blue solid lines) versus altitude (km) for the ion species C^+, O^+, CO_2^{++} and CO^+.

at any particular altitude, each species exists under the same column of atmosphere (i.e. the same column depth) through which the same two sources of energy must pass (the photon and suprathermal electron fluxes). So each species present at a particular altitude will interact with the same intensity of primary energy source (from one species to the next) and with the same intensity of secondary energy source (again from one species to the next). Hence at a particular altitude it is the relationship, expressed in terms of the model energy grid, between the primary and secondary energy sources and the respective cross-sections of the atmospheric species present that will drive different production rate responses for each species. It is the energy spectrum of the photon flux and its match with the photo-absorption cross-sections (in the case of the former) and the suprathermal electron intensity and its match with the electron-impact cross-sections (in the case of the latter) that will dictate which production type (primary or secondary) is dominant.

Bearing these statements in mind we note two general trends in the efficiency profiles of figures 6.5, 6.7 and 6.9 at low altitude. The first is where the efficiency continues to grow larger and larger as we decrease in altitude. So for example the production efficiencies of N_2^{++}, CO_2^{++} and O_2^+ all begin to

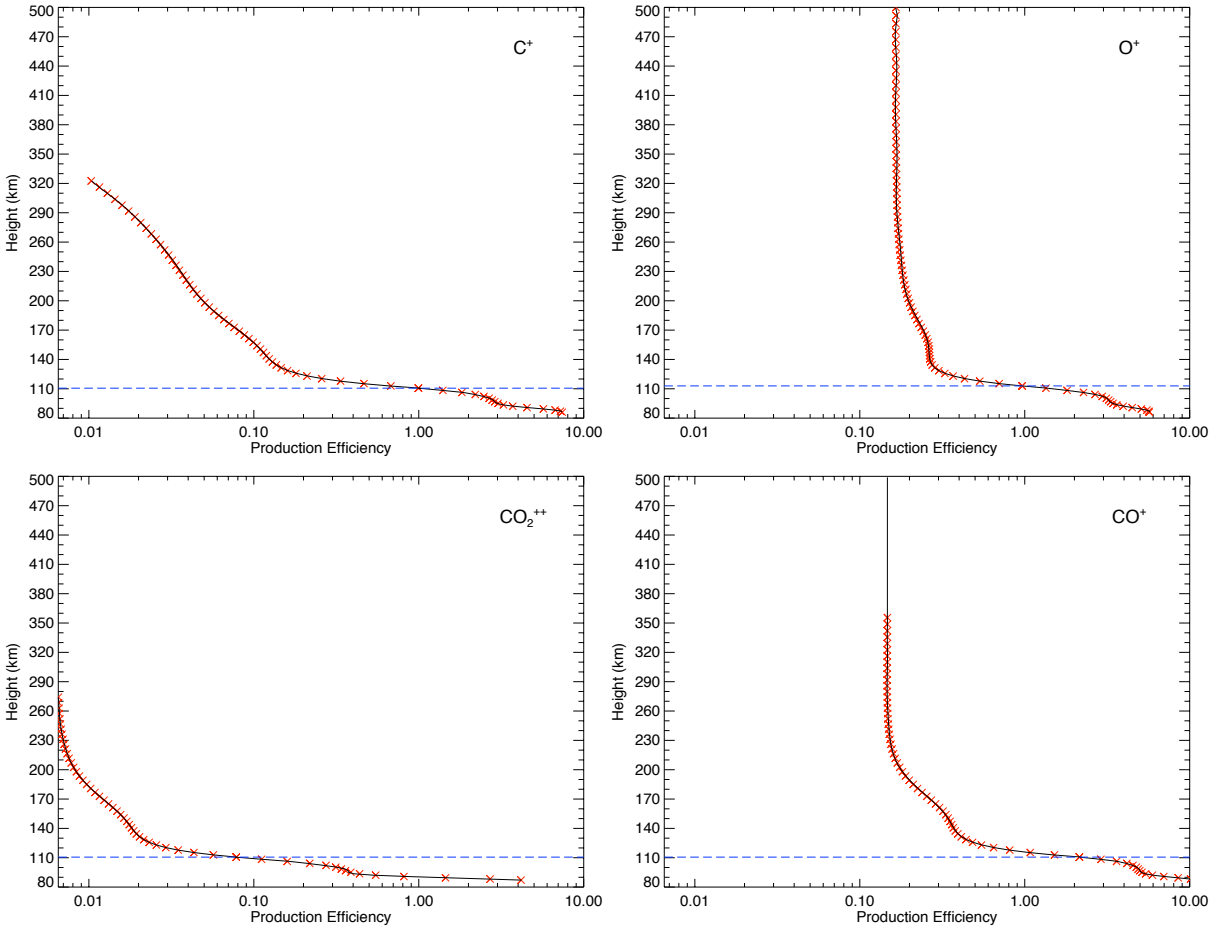

Figure 6.7: Production efficiency (kinetic model result (red crosses), polynomial fit (black solid line) and transition altitude (blue dashed line)) versus altitude (km) for the ion species C^+, O^+, CO_2^{++} and CO^+.

increase very quickly towards positive infinity as we approach the lower altitude boundary. The second trend is where the efficiency reaches a peak as we decrease in altitude before decreasing in the lowest altitude regions of the model. The production of N^+ is an example of this trend, with the efficiency reaching a peak of ∼15 at ∼98.5 km before falling to ∼7 at ∼88 km.

The first trend is principally the numerical effect of dividing the secondary production rate by a primary production rate that is either far smaller or is decreasing more rapidly than the secondary production rate as we descend in altitude. It also indicates that at the lowest altitudes the photo-absorption cross sections for species that exhibit this trend do not respond to the (probably high) photon energies present at these low altitudes and thus primary production remains low. Meanwhile there is a sufficient response by the electron impact cross sections to the suprathermal electron energies present for secondary production to remain greater (relatively speaking) than primary production and thus cause the growth in efficiency observed. Remember here that since every altitude level is potentially a source of suprathermal electrons then transport effects can bring these electrons, with a greater range of energies, down to these low altitudes. That is to say, a greater range of suprathermal energies can be present relative to the range of photon energies present. This first trend is thus exhibited by species

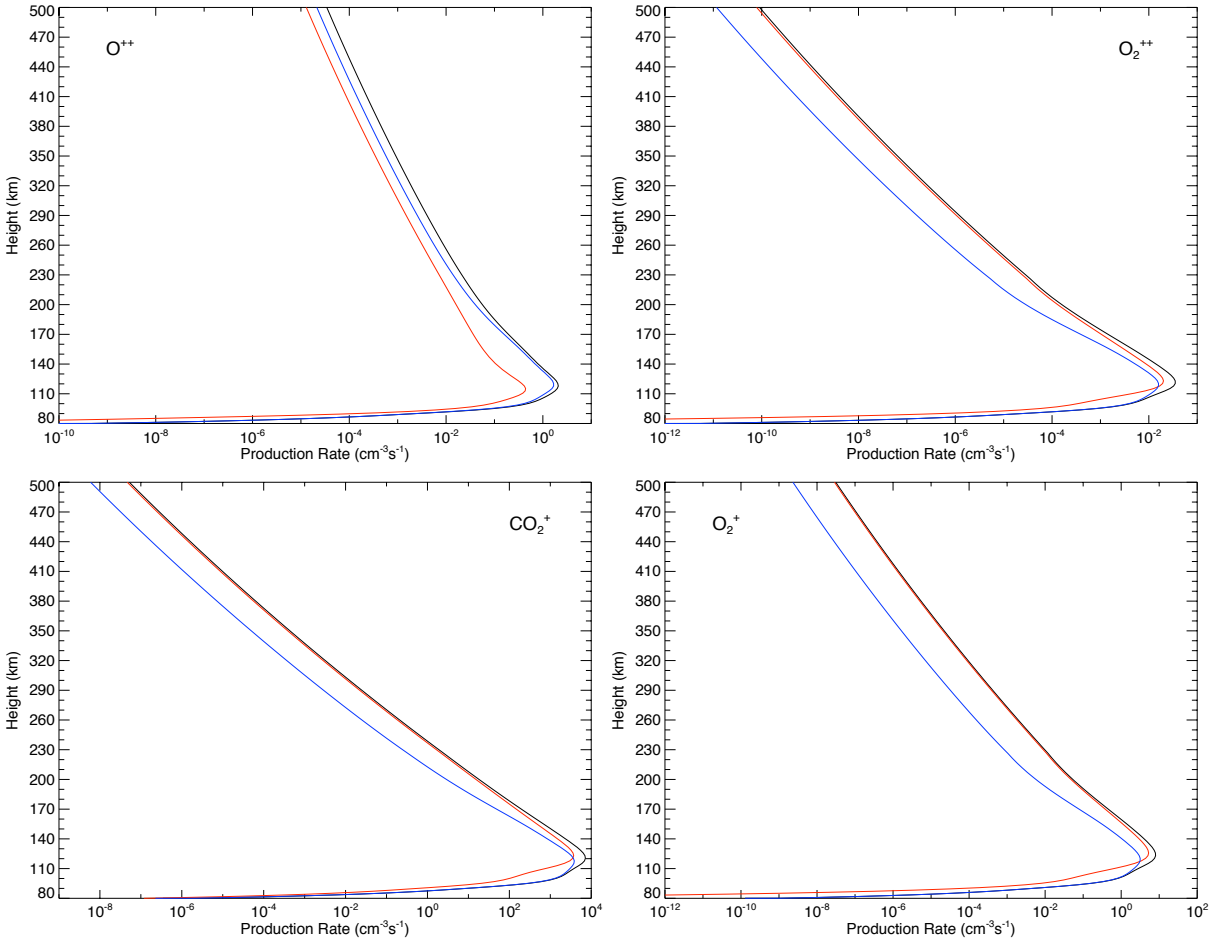

Figure 6.8: Total production (black solid lines), primary (photo) production (red solid lines) and secondary production (blue solid lines) versus altitude (km) for the ion species O^{++}, CO_2^+, O_2^+ and O_2^{++}.

whose primary production is restricted in energy so they don't respond to the typical photon energies present at these altitudes.

For this first trend we take the case of O_2^+ as a good example of the numerical nature of this effect. From 100 to 83 km the primary production rate drops almost 12 orders of magnitude where as the secondary production rate drops by just over 6 orders. Sure enough we see the efficiency climb from $\sim$16 to 1.22×10^7 i.e. almost 6 orders of magnitude. But again this does not imply that some important effect is taking place, such as a production rate with an especially high magnitude or detailed structure. Indeed the primary production rate is shown in Figure 6.9 to be on the order of 5×10^{-2} $cm^{-3}s^{-1}$ at 100 km (while the secondary rate is 8×10^{-1} $cm^{-3}s^{-1}$) before the reductions just described have even begun. Thus despite the efficiency profile growing rapidly below 100 km both production rates are falling rapidly as we descend through the atmosphere. Finally note that for O_2^+ the secondary production rate dropped below 1×10^{-3} $cm^{-3}s^{-1}$ (and so was considered negligible) at and below 88.23 km.

The second trend in the efficiency profiles was noted above as the structure whereby the efficiency reaches a peak as we decrease in altitude before decreasing in the lowest altitude regions of the model.

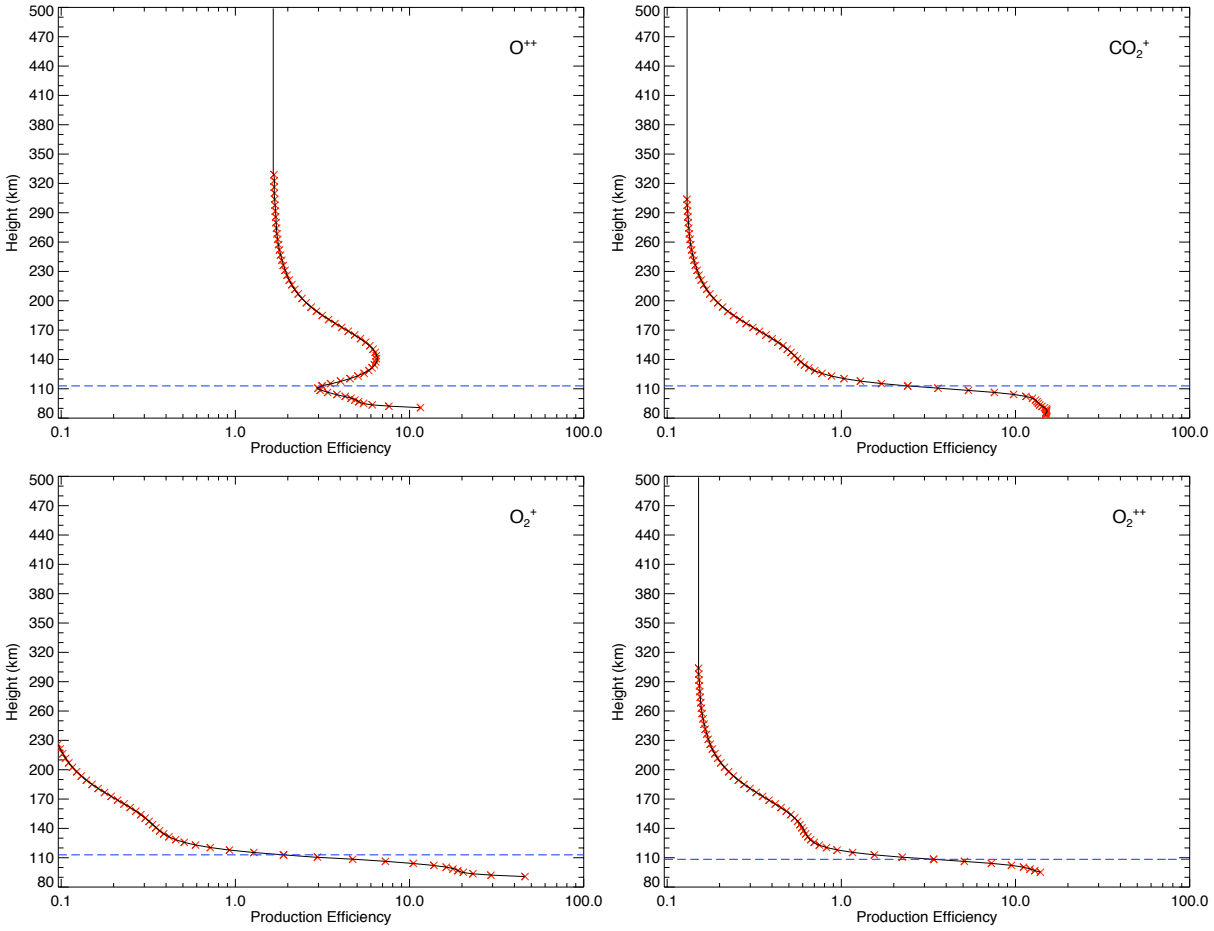

Figure 6.9: Production efficiency (kinetic model result (red crosses), polynomial fit (black solid line) and transition altitude (blue dashed line)) versus altitude (km) for the ion species O^{++}, CO_2^+, O_2^+ and O_2^{++}.

As noted the production efficiency of N^+ is a good example of this trend, with the efficiency reaching a peak of ∼15 at ∼98.5 km before falling to ∼7 at ∼88 km. This can essentially be understood as the converse of the first trend i.e. it is the result of a more rapid drop in the secondary production rate, below the efficiency peak, than there is in the primary production rate. The fact that there is a peak in the production efficiency in the first place is simply due to the growth in secondary production over and above primary production as the transport of suprathermal electrons down towards the peak gives greater opportunity for secondary production. This is to say that the range of suprathermal energies allows electron impact to dominate over photon production.

Typically however we find that in the lowest altitude regions the suprathermal electron flux (e.g. Figure 6.3) has a greater intensity in the lower model energies (say 0.1 to 4 eV) than it does in the upper energy regions, as secondary production can only produce electrons of lower energy and as collisions with the exponentially increasing neutral background atmosphere shifts the energy distribution of the flux toward lower energies. Therefore this second trend is exhibited by species where the particular relationship between their primary and secondary productions favours the high energy photons at the low altitudes rather than the low energy suprathermal electrons. The neutral background swiftly removing

higher energy suprathermals as we lead up to the peak while maintaining and harbouring a lower energy suprathermal presence that begins to dominate below the peak. Species electron impact cross-sections fail to respond to this change and secondary production drops more swiftly than primary production, hence the efficiency drops.

By and large the efficiency profiles at high altitude typically reach some constant value. This is simply because both the primary and secondary production rates remain parallel to one another throughout the upper regions of the model. Thus as primary production falls with increasing altitude and decreasing neutral number density so the secondary production follows suit due to both the reduced localised source function and the reduced likelihood of transport effects from higher altitudes. The only exception to this rule is species C^+ (Figure 6.6) for which secondary production dropped below $1{\times}10^{-3}$ $cm^{-3}s^{-1}$ at and above 325 km before reaching any constant value. Secondary production for this species continues to drop faster than primary production as we gain altitude hence the efficiency does also. We must come down in altitude, building up a sufficient component of transported suprathermals for secondary C^+ production to become important, whereas for other species secondary production due to localised primary production is sufficient up through the highest altitudes to keep secondary and primary profiles almost parallel and thus efficiency constant.

6.4.3 The Effect of Variation in Solar Zenith Angle on Efficiency

To study the effect of the variation in solar zenith angle on the production efficiency we made use of MarTIM's neutral atmosphere. The results are shown in Figure 6.10 for the CO_2^+ production efficiency only. This variable was chosen for our representation of how efficiency responds to χ variation because of the dominance of neutral CO_2 on the composition in both the real and modelled atmospheres. Indeed it was because of the importance of neutral species such as CO_2 that we ensured neutral diffusion processes were carefully modelled within MarTIM so that our description of the underlying physics was appropriate. Thus we expect neutral CO_2 to be a sensitive indicator of any possible χ variation and in turn that CO_2^+ ion production will reflect these changes.

In Figure 6.10(a) we present production efficiency altitude profiles for a spread of four solar zenith angles up to 70° (0°, 25°, 45° and 70°) and then a further four angles from 75° up to 90°. Then in Figure 6.10(b) we present profiles showing the variation in the altitude of the peak primary and secondary production (dot-dashed and dotted lines respectively) as well as a profile of the altitude of the peak efficiency as a function of solar zenith angle (solid line). From part (a) of this figure you can see that the effect of an increasing solar zenith angle, up to ∼80° (the second dotted line), is essentially to move the lower region of the profile (around the primary and secondary production peaks) upwards. Then in part (b) of this figure you can see the extent of this altitude shift with solar zenith angle more clearly as the peak efficiency reaches ∼105 km at χ=90° compared with ∼88 km at χ=0°. Additionally in part (b) we plot a function to describe numerically this increase in efficiency peak altitude (dashed

line):

$$dz(\chi) = z_{peak,\chi=0} + \alpha\cos(\chi) - \beta\left(\cos(\chi)\right)^{1/2} + \gamma \tag{6.13}$$

Where $\alpha = 15$, $\beta = 40$ and $\gamma = 25$.

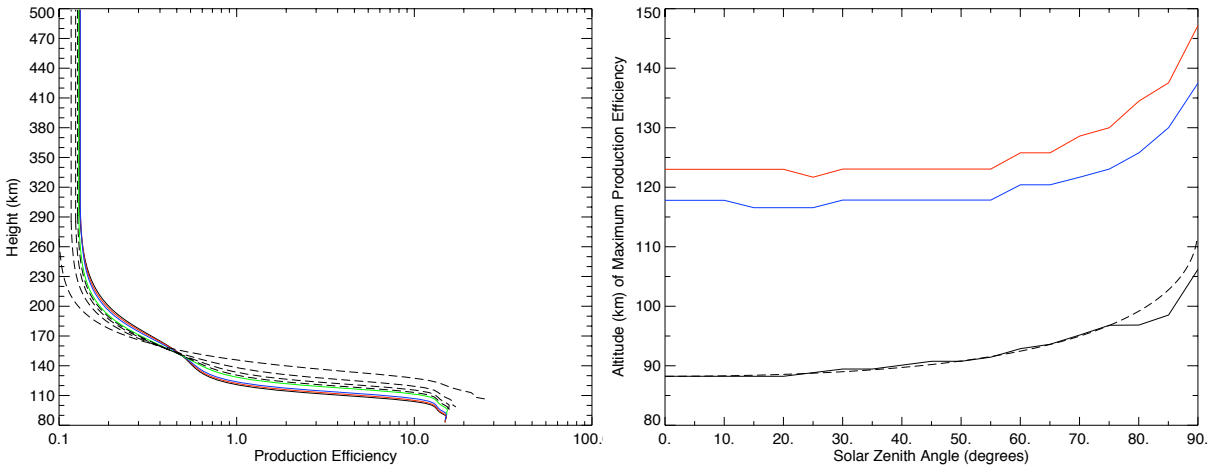

(a) CO_2^+ production efficiency versus altitude.

(b) Altitude of maximum production efficiency.

Figure 6.10: (a) CO_2^+ production efficiency versus altitude (km) for solar zenith angle χ 0° (black solid line), 25° (red solid line), 45° (blue solid line), 70° (green solid line). Then 75°, 80°, 85° and 90° are all shown with black dashed lines. Their profiles can be identified in the lower altitude region up to 160 km by the increasing altitude of their peaks. (b) Altitude of maximum CO_2^+ production efficiency versus χ (black solid line), altitude of the maximum primary and secondary CO_2^+ production (red and blue solid lines respectively) and equation 6.13 (black dashed line). Solar minimum ($F_{10.7,Mars} = 31.3$) and equinox (180°) throughout.

The derivation of this function follows the work of Lilensten et al. (2005) who fitted a similar function to the efficiency profiles from the Titan version of the *Trans** kinetic model (with different coefficients of course). Thus as was the case in Lilensten et al. (2005) there are two components to the χ angle influence on the production efficiency. The first ($\cos(\chi)$) reflects the close approximation the modelled atmosphere makes to an ideal Chapman atmosphere. Since CO_2 is the dominant species throughout a large part of the atmosphere (and certainly in the region of peak primary and secondary production) the altitude of the primary peak when acting under the local control of photochemical processes, depends upon how deeply into the atmosphere the solar radiation penetrates (as was discussed regarding the real Martian atmosphere in section 6.2). Hence the altitude of the primary production peak will follow a $\cos(\chi)$ form. Then from the dotted line of Figure 6.10(b) notice how the secondary peak altitude follows quite closely with the primary peak. This reflects the sufficient uniformity in atmospheric density as a function of solar zenith angle, a product once again of CO_2 dominance, in restricting transport effects (or at least restricting their variation with χ) and thus keeping the primary and secondary peaks almost parallel to one another. As the altitude of the primary peak rises, so does the secondary peak. In turn

the efficiency peak altitude will simply follow suit and maintain a similar dependence on the $\cos(\chi)$ term.

The second component to the variation in efficiency versus χ angle comes from the behaviour of the $(\cos(\chi))^{1/2}$ term, which Lilensten et al. (2005) cite as being due to transport effects. For lower solar zenith angles (we suggest up to 80°) transport effects in the region of the primary and secondary peaks are probably not dominant or are at least restricted, as we've just discussed, so that the $(\cos(\chi))^{1/2}$ term will remain less important. It is only at higher χ angles where transport effects would become important, providing the linkage between a primary peak rising swiftly in altitude while the secondary peak remained at lower altitudes where the neutral density is greater. Since this occurs beyond χ=90° and for secondary production rates that drop significantly below 1×10^{-3} $cm^{-3}s^{-1}$ we don't deal with these situations further.

For the behaviour in the high χ angle range from 75° up to 90° i.e. approaching the limit of our function of equation 6.13, consider the set of dotted lines shown in Figure 6.10(a), which represent this range in χ=5° steps. Notice how the peak of the efficiency profile (and indeed the main body of the profile up to ∼160 km) begins to gain altitude far swifter than it did for the lower solar zenith angles. It is at these high χ angles that the efficiency profiles start to reflect the action of the Sun as it begins to set below the horizon of the tenuous Martian atmosphere. As this occurs the whole primary (photo) production profile shifts upwards in altitude, chasing the remaining illumination. At the same time its magnitude decreases as the background neutral atmosphere rapidly reduces in mass density at high altitude. Meanwhile the secondary production profile does not show nearly the same amount of vertical motion because electron impact still requires a dense neutral background atmosphere for sufficient ionization collisions to occur. The two processes are linked by transport effects bringing down suprathermal electrons from the high primary peak to the lower secondary peak.

Consequently at any particular altitude the magnitude of secondary production will be far greater relative to the primary production since the two profiles now cover completely different altitude ranges for their completely different processes at these high solar zenith angles. The magnitude of production efficiency (secondary production divided by primary production) will therefore also swiftly increase as we move towards higher solar zenith angles and unfortunately it's profile structure will begin to be poorly represented by equation 6.13. We suggest therefore that our polynomial fits in Appendix B and equations 6.11 & 6.12 and the fit with solar zenith angle (equation 6.13) are suitable only up to χ=80°. Beyond this angle we further note however that since the magnitude of the primary production rate is rapidly reducing as the profile climbs in altitude so too will the secondary production magnitude (and to below the rate 1×10^{-3} $cm^{-3}s^{-1}$ that we considered of notable magnitude). Therefore we feel our work describes suitably the main bulk of the dayside ionosphere primary and secondary production.

6.4.4 The Effect of Variation of Solar Longitude on Efficiency

One would expect that with the greater solar insolation at perihelion (∼40% increase) that the atmosphere would expand and conversely as the Sun-Mars distance increased as we approach aphelion that

the atmosphere would contract. Certainly in the region of the thermosphere (120 to 280 km) where solar heating is most dominant we can assume a variation in the distribution height of the neutral background atmosphere as the scale height tracks the changing temperatures: increasing with higher perihelion temperatures, decreasing at aphelion. Consequently the number of atmospheric molecules and atoms in any vertical column ($N_m(\chi)$=$H_m n_m$ above the production peak altitude m) will also mimic this variation with solar insolation. But since the altitude of the peak (in an ideal Chapman atmosphere at least) will remain at wherever $\sigma N_m(\chi) = 1$ occurs then in turn we expect the altitude of the primary production profile will vary with the advancing Martian seasons.

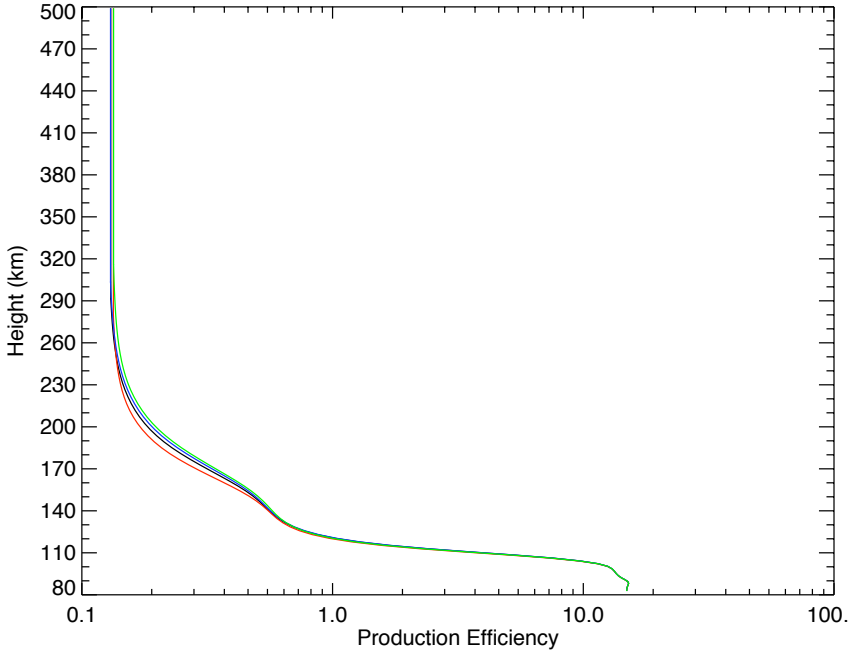

Figure 6.11: CO_2^+ production efficiency versus altitude (km) at solar zenith angle χ=0° for solar longitude 0° (1.56 AU equinox) (black solid line), 90° (1.66 AU northern summer solstice) (red solid line), 180° (1.47 AU equinox) (blue solid line) and 270° (1.39 AU southern summer solstice) (green solid line). Solar minimum ($F_{10.7,Mars} = 31.3$) throughout.

But of course it's a question of variation in the secondary production profile alongside the primary profile that will affect the production efficiency. If the variation in secondary production as solar longitude changes is different to the primary production variation then the efficiency will reflect this. We can see from Figure 6.11 that indeed as solar longitude advances the efficiency does increase in the region of the thermosphere ∼120 to 280 km. Presumably this is as we shift from a localised to a more transport dominated secondary production rate. With a greater primary production at higher altitudes (with the expanded perihelion atmosphere) we have an increased component of transported primary electrons that contribute to secondary ionization. So the secondary production increases proportionately more than primary production due to this additional transported component and hence the efficiency increases. Of course this variation in efficiency is restricted to the thermosphere ∼120 to 280 km where solar heating is dominant and even then to very limited extent.

At lower altitudes there is very little variation in the production efficiency. This is a result of the dominance of CO_2 in the composition of the Martian atmosphere at these altitudes, which results in (a) reduced variation in solar flux intensity at these altitude levels and (b) similar variation in primary and secondary production despite the changing Martian season. This latter point is most likely due to the reduced role transport effects play in the lower atmosphere, regardless of the season, linking secondary production to localised primary production. This situation remains as solar longitude changes since the background lower atmosphere barely varies at all with solar longitude and thus production efficiency remains fairly stable. This situation will only become more apparent throughout the lower atmosphere as the dominance CO_2 continues to increase and the incident solar flux tails off completely. Thus if one is only considering the altitude region of the CO_2^+ production peak then one need not alter the polynomial fit coefficients from those provided as there is little variation to worry about despite the changing Martian season.

6.4.5 The Effect of Variation of the Solar Cycle on Efficiency

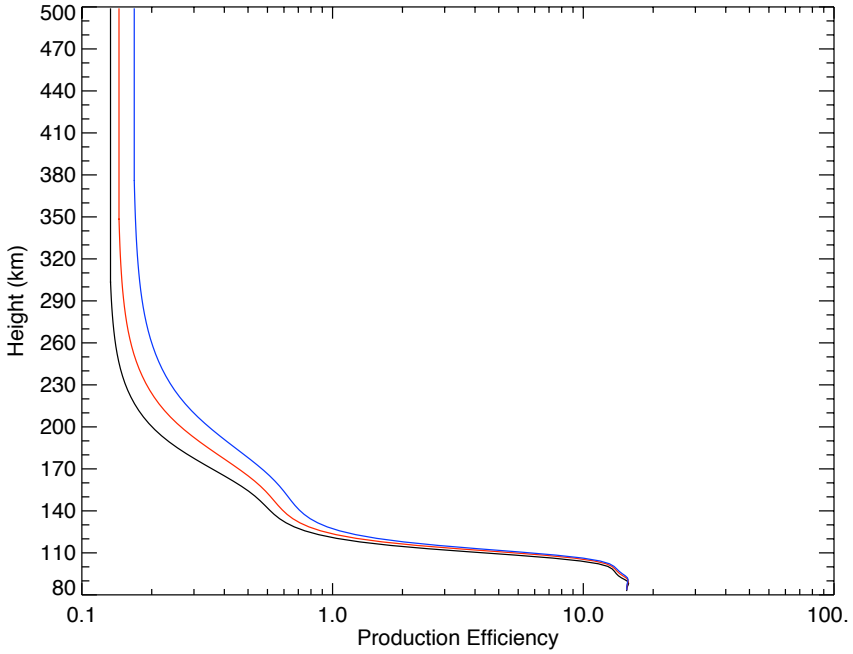

Figure 6.12: CO_2^+ production efficiency versus altitude (km) at solar zenith angle χ=0° and solar longitude 180° for solar minimum ($F_{10.7,Mars} = 31.3$) (black solid line), solar medium ($F_{10.7,Mars} = 60.9$) (red solid line) and solar maximum ($F_{10.7,Mars} = 95$) (blue solid line).

In this final study of variation in production efficiency we note from Figure 6.12 that generally there are only slight changes in the production efficiency as the solar cycle advances. For reasons analogous to the above discussion about the variation in solar longitude we find this to be most apparent in the lower altitude regions given the reduction in incident solar flux as one moves deeper into the atmosphere. Any change in solar flux due to the varying solar cycle will be minimal in these lower altitude regions thus

the primary production will not change much. And since secondary production will remain linked to localised primary production this will not change much either. Hence the production efficiency changes only slightly as the solar cycle advances.

In the upper altitude regions of the thermosphere proper, one wouldn't expect the height of the primary peak to vary with solar cycle in an ideal Chapman atmosphere (Ratcliffe, 1972), it being independent of flux intensity. Although the primary production profile in the thermosphere above the peak will increase as the enhanced solar flux takes effect clearly there must be a relatively larger increase in secondary production since we can see in Figure 6.12 that the efficiency is increasing with the solar flux. We would suggest that, just as in the case of advancing solar longitude, the effect of enhanced primary electron transport from the upper altitude regions will produce this additional secondary production and the increase in production efficiency seen. Of course, again just as with the seasonal variation, the effect is rather limited and we don't consider it necessary to adjust our parameterization to include this effect.

6.5 Conclusions

An analytic method has been discussed for the rapid computation of secondary ion and electron production due to electron impact of suprathermal electrons with the background neutral Martian atmosphere. Parameters were given (see Appendix B) to allow the rapid computation of secondary ion production for 11 ion species (CO_2^+, CO_2^{++}, CO^+, C^+, N_2^+, N_2^{++}, N^+, O_2^+, O_2^{++}, O^+, O^{++}) as well as for the secondary electron production. It was shown that while the efficiency (ϵ) of ion and electron production (ratio of secondary to primary production) does vary with solar zenith angle it could be parameterized with a simple function, given by equation 6.13. It was also shown that variations in the efficiency with solar cycle and solar longitude were negligible about the region of the primary and secondary production peaks and thus that the parameterizations given did not need altering despite these varying conditions. Our future work will concentrate on including ionospheric chemistry in *Trans*-TIM and a better representation of magnetic fields in the code so that features such as the Martian magnetic anomalies can be studied.

Chapter 7

Conclusions and Future Work

7.1 Conclusions

Chapter 3 Conclusions

I have continued to develop MarTIM stage-by-stage for this PhD. Firstly, in Chapter 3, I took the Moffat (2005) model version and updated the solar flux model that provided the solar irradiances from which MarTIM calculates the solar EUV and UV atmospheric heating rate. For this, the 'SOLAR2000 v2.28' model was introduced with the 1 nm binned data rather than the 5 nm wavelength resolution grid used by Moffat (2005). Next the neutral photoabsorption cross-sections were updated so that they too could use a 1 nm wavelength grid. This allowed us to take advantage of the latest high resolution measurements of the spectral structure of neutral species within MarTIM. It also meant I could begin to include the variation in CO_2 cross section with temperature (see Figure 3.2).

Next I performed some extra validation of the simulation and reconsidered some of the approximations that had previously been necessary. We considered the approximation for the CO_2-O relaxation rate coefficient used by MarTIM in the parameterisation of CO_2 15-μm radiative cooling. The value of this coefficient was smaller ($\sim 10^{-13}$ cm^{3}s^{-1}) than the values normally cited (1-3$\times 10^{-12}$ cm^{3}s^{-1}) in other GCM studies (Bougher et al., 2000) and review papers (Bougher et al., 1994; Huestis et al., 2008; López-Valverde and López-Puertas, 1994a,b, 2001). This was linked to a bias in MarTIM's atomic oxygen content that introduced too much O into the initial atmosphere and required Moffat (2005) to reduce the rate of CO_2 cooling (through the CO_2-O relaxation rate coefficient) to bring MarTIM results closer to those of other GCMs. With a suitable correction to the setup of the initial atmosphere we were able to remove the bias in MarTIM's atomic oxygen content and begin using a value of 1.5×10^{-12} cm^{3}s^{-1} for the relaxation rate, much closer to the values typically cited.

Chapter 3 concluded by introducing the new diffusion and advection routine that allowed the transport and mixing of an unlimited number of neutral species within MarTIM. We considered the impact that neutral diffusion and advection has on the atmosphere. Thus rather than including only the three

most prominent neutral species (CO_2, N_2 and O) as in Moffat (2005), we could now add other species that had previously been ignored either because of their low number densities or because of their weak thermodynamic influence on the atmosphere. Alternatively we could remove species from the atmosphere to see if that had an effect. We showed in section 3.4.2 that the most significant difference came in the comparison of simulations with only two species (CO_2 and O) versus those with four (CO_2, N_2, CO and O). There was very little difference to this four species version of MarTIM when the fifth, sixth and seventh species (Ar, O_2 and NO) were added.

The difference between the two and four species version was largely restricted to the thermosphere. With four species (CO_2, N_2, CO and O) the dayside mid-latitude temperature bifurcation and the hot region at ∼330°E both became more dominant (see Figure 3.23, section 3.4.2). Also the nightside minimum temperature region from 0300-hrs to 0700-hrs was warmer in the four species version. Temperatures there were ∼139-140 K versus ∼134 K with the two species version. A comparison of energy balance terms showed that with the addition of N_2 and CO upper atmosphere solar EUV+IR heating had been enhanced. Clearly this was only a very slight change (the decrease in heating rate above the peak was slower resulting in greater columnar integrated heating) but nonetheless resulted in clear changes when four species were used versus two. Finally, since adding the three species Ar, O_2 and NO made no discernible difference to the result we settled upon using the four species CO_2, N_2, CO and O within MarTIM for the rest of the thesis.

Chapter 4 Conclusions

In Chapter 4 we introduced the new solar infrared heating parameterisation (see equations 4.1, 4.2 and Figure 4.1). For solar minimum, equinox conditions this introduced significant changes to the standard MarTIM result altering both temperature and circulation structures throughout the atmosphere and at all local times. The lowest 7 pressure levels showed a pronounced increase in temperature, e.g. 145 K to 150 K equatorial zonal average at PL 7 (4.40×10^{-2} Pa) with the new parameterisation versus ∼119 K with the old. A particular focus was the simulation, with the new parameterisation, of two temperature peaks (∼156 K) between PL 3 to 7 (3.25×10^{-1} to 4.40×10^{-2} Pa) that were wholly absent with the old parameterisation. The first was between 1300-hrs and 1900-hrs and the second between 0100-hrs and 0500-hrs. The 0100-hrs to 0500-hrs temperature peak was notable as its nightside location indicated lower atmosphere circulation had been greatly increased allowing warm air advection from the dayside.

In the upper atmosphere increases in temperature when using the new IR heating parameterisation were focussed about regions of advective and adiabatic compressional heating. The specificity of these hotter regions and in particular the enhancements to nightside temperature peaks suggested (as with the lower atmosphere) that the new routine had enhanced global circulation magnitudes. At PL 30 (4.45×10^{-7} Pa) zonal winds were now up to ∼220 m/s (∼−212 m/s) with the new parameterisation versus ∼176 m/s (∼−164 m/s) with the old while meridional winds now reached ∼±216 m/s with the new against ∼±164 m/s with the old. This meant that localised temperature peaks at 0900-hrs and

2300-hrs were hotter (∼238 K versus ∼228 K and ∼220 K versus ∼210 K, respectively) and reached deeper through almost the entire top half of the model into the lower atmosphere.

The zonal mean wind structures clearly reflected the change in global circulation magnitude with the new IR heating parameterisation. In particular middle latitude eastward jets (equinox conditions) now not only showed a reduced peak magnitude (∼24 m/s with the old, ∼17 m/s with the new) but were also curtailed in the upper atmosphere (restricted to middle atmosphere PL 15 to 19 (8.05×10^{-4} to 1.09×10^{-4} Pa)). Furthermore a strong westward jet was now simulated over equatorial regions throughout the entire upper half of the model reaching a maximum of ∼20 m/s in the uppermost pressure levels. Also, zonal average meridional winds were almost doubled in the upper atmosphere with the new IR heating (∼±14 m/s versus ∼±7 m/s). These changes to zonal mean wind structures showed that using the new IR heating parameterisation had introduced significant westward momentum into the atmosphere. This was confirmed by a harmonic analysis of MarTIM's temperature field, which showed that the (2,2) tidal mode had been enhanced throughout the atmosphere with the new parameterisation. The (1,1) mode had also been enhanced in the lower atmosphere.

This new version of the model was then applied to study winter polar warming structures in the lower thermosphere as had been observed by the Mars Odyssey spacecraft. Such measurements had shown a temperature increase from 110 K to 160-170 K near 120 km (Keating et al., 2003; Bougher et al., 2006a) as the spacecraft passed over the northern winter pole from dayside (1700-hrs) to nightside (0200-0300-hrs). General circulation modelling of these polar warming features (Bougher et al., 2006a; Withers, 2006; González-Galindo et al., 2009a) had shown that global meridional transport effects (rather than local radiative effects) and commensurate subsidence/convergence of mass and adiabatic heating above the polar regions was always required to produce the large temperatures modelled (see section 4.3.1). In this way, thermospheric warming features appeared to result from adiabatic heating associated with the downward branch of a diabatically driven interhemispheric Hadley-type circulation.

Model perihelion temperatures at a constant altitude of 120 km showed that although MarTIM (with either IR heating parameterisation) may have struggled to match the exact temperature structure measured by Mars Odyssey there was a clear winter polar warming effect simulated when the new IR heating was used (see Figures 4.10 and 4.11). For example with the new parameterisation MarTIM showed a good match to Mars Odyssey data in the 85°-90°N bin (∼142 K). Also, deep nightside local times (0200-hrs to 0400-hrs) showed an initial drop in temperature just northwards of the equator followed by an increase of about ∼35 K towards the northern mid-latitudes.

In particular Figure 4.11 (bottom plot) showed that circulation features with the new IR parameterisation created a specific region of heating at the pole at 120 km (∼17 K) in comparison to the temperature at 30°N. Circulation magnitudes had been sufficiently altered such that descending vertical winds now reached a maximum of ∼120.5 cm/s between 50°N and 60°N in the upper atmosphere versus ∼−35.1 cm/s for the old IR heating. Finally, Figure 4.12 showed that these enhancements to circulation magnitudes were apparent throughout the atmosphere. Thus, as was the case for equinox conditions, the

new IR heating parameterisation had introduced significant westward momentum into the atmosphere. So for these perihelion conditions stronger westward winds in the southern summer hemisphere now persisted further into the northern winter hemisphere for the new IR heating versus the old (50°N with the new versus 20°N with the old). The meridional flow was therefore at higher northern latitudes before descent and adiabatic compressional heating occurred focussing the region of heating over the winter pole.

Chapter 4 concluded by comparing MarTIM temperatures to 6 years worth of exospheric measurements from Mars Global Surveyor Precise Orbit Determination (POD) results over a large range of solar and seasonal conditions. From Figure 4.18(a) MarTIM simulated well the general variation of exospheric temperatures with the solar cycle (i.e. temperatures were progressively hotter for SMIN, SMED and SMAX) although it predicted a larger seasonal cycle than that observed (i.e. aphelion to perihelion temperature ranges were too large). Next, Figure 4.18(b) showed that MarTIM simulated well the variation of temperature with $F_{10.7}$ predicting a $\Delta T/\Delta\overline{F}_{10.7}$ gradient of $\sim$1.49, which was close to the $\sim$1.53 from the MGS observations. However this result highlighted how MarTIM's temperatures were typically about 15 K hotter than the the MGS data. This was attributed to MarTIM not yet including a parameterisation of neutral photochemistry. The work of González-Galindo et al. (2005) was cited as showing how temperatures in their GCM were up to $\sim$25 K hotter when photochemistry was neglected because of the variation this introduced to the O/CO_2 ratio and thus CO_2 15-μm cooling. This is discussed further in section 7.2.1 below.

Finally in Chapter 4 we identified the trend that as the $F_{10.7}$ value was increased MarTIM would progressively underestimate the expected seasonal temperature variation (e.g. see Figure 4.19). This was linked to the "dynamical thermostat" effect discussed by Bougher et al. (1999b) and Bougher et al. (2009) where global circulation and molecular thermal conduction act together to regulate upper atmosphere temperatures. The atmosphere would respond to greater $F_{10.7}$ flux and the hotter temperatures produced with increased wind magnitudes. This enhanced global circulation would increase adiabatic cooling to such an extent that temperatures were actually reduced as an overcompensation for the increase in $F_{10.7}$ flux. Therefore throughout Chapter 4 we had shown how global circulation had an important role in the energy balance of the Martian atmosphere. Circulation effects on temperature and atmospheric structure could be wide-reaching in both local time and 3D space, often strongly responding to changes in global model settings. The new IR heating parameterisation playing a driving role in enhancing MarTIM's circulation features.

Chapter 5 Conclusions

Chapter 5 considered the influence on the simulation of the lower atmosphere below MarTIM's 0.883 Pa lower boundary. This was done by using the Mars Climate Database (MCD) version 4.3, a database of results derived from multiple runs of circulation models developed at the Open University (United Kingdom), the University of Oxford (United Kingdom) and at Laboratoire de Météorologie Dynamique

(LMD, France) (Lewis and Read, 2003; Lewis and Barker, 2005; Lewis et al., 1999; Forget et al., 2008; Millour et al., 2008; Millour and Forget, 2008; Angelats i Coll et al., 2005). Rather than using constant values (in space and local time) for lower boundary temperature, horizontal winds and geopotential height fields we instead queried the MCD for these values for the particular solar longitude, local true solar time and lower atmosphere dust conditions required. All other lower boundary values were calculated self-consistently as necessary and the entire lower boundary was updated from the MCD every simulated hour (24-hour day).

Sections 5.4.1 to 5.4.3 looked at the general influence of the MCD and the lower atmosphere on MarTIM's results. This centered on comparing coupled MarTIM-MCD results to those direct from the MCD and discussing the similarities and differences. From section 5.4.4: temperature and wind structures compared well between the two models although this was typically only through the lowest few pressure levels e.g. below PL 5, 1.2×10^{-1} Pa for an annually averaged lower atmosphere dust content and SMIN conditions. Differences between the coupled model and the MCD at progressively lower pressures (higher altitudes) were typified by cooler temperatures and slower winds in the coupled model. In this way the influence of MarTIM's in-situ energy input and output processes (solar EUV and IR heating, CO_2 cooling) began to dominate over the influence from the MCD 0.883 Pa pressure level. This resulted in, for example, a difference in zonal average zonal wind structures. The MCD showing more dominant eastward jets at mid-latitudes that migrated to higher latitudes with altitude as the vertically propagating diurnal tide, centered over the equator, deposited westward momentum over a progressively wider latitudinal extent.

Differences between coupled MarTIM-MCD results and the MCD alone were shown in section 5.4.2, Figure 5.9, to be the result of an approximation we had to make in section 5.3.2 in order for coupled results to reach a steady state. The approximation of measuring geopotential height gradients from the 0.883 Pa lower boundary was shown to result in horizontal geopotential height gradients (when used in momentum and energy equation terms 5.3 to 5.6) that were about 1/3 as great than if they had been measured from the planetary surface (Martian areoid). As a result circulation magnitudes produced by pressure gradients (at constant altitude) were much slower and their influence on energy advection reduced such that it was only a matter of vertical distance from the MCD supplied 0.883 Pa level before MarTIM's local energy inputs began to constrain the MCD from above. Section 5.4.4 discussed an alternative coupled model result, which did not require the approximation just noted. Instead the zonal model grid resolution was reduced. Although this did result in coupled MarTIM-MCD results that showed better comparison to the MCD alone (particularly with the zonal average zonal wind structure) this setup did not allow a complete set of coupled model results for all dust and solar conditions. One implication, that MarTIM should be extended to lower altitudes so that its solution is wholly self-contained and does not require the MCD, is discussed in section 7.2.2 below.

Another aspect of coupling MarTIM to the MCD was discussed in section 5.4.3. Here we compared the upper atmosphere (pressure levels 15, 20 and 30 (8.05×10^{-4}, 6.61×10^{-5} and 4.45×10^{-7} Pa)) tem-

peratures between coupled MarTIM-MCD results that used MarTIM mixing ratios in the CO_2 15-μm cooling routine to those that used ratios from the MCD (which were updated every hour of the simulation). We had expected that dayside MarTIM mixing ratios would underestimate the amount of atomic oxygen in the thermosphere (overestimate temperatures) because photodissociation of CO_2 was not included. Also, we expected nightside O content, advected from the dayside, to be greater with the MCD ratios (temperatures to be generally cooler). However, Figure 5.19 showed that the CO_2 IR cooling rate was actually greater around the PL 10 to 13 region (9.81×10^{-3} to 2.19×10^{-3} Pa) when the MarTIM mixing ratios were used. Then Figure 5.20 showed that at PL 15 (8.05×10^{-4} Pa) although both sets of mixing ratios had little absolute O content the relative difference between MarTIM and MCD mixing ratios (MarTIM maximum O/CO_2 ratio $\sim2\times10^{-2}$ versus MCD minimum 4×10^{-3}) was sufficient to produce significant differences in the IR radiative balance. Consequently middle atmosphere dayside temperatures were hotter and wind magnitudes from about PL 15 upwards were enhanced with the MCD ratios (e.g. zonal winds at PL 15, 180.3 m/s (-160.9 m/s) with MCD ratios versus 151.8 m/s (-130.4 m/s) with MarTIM ratios). In addition, upper atmosphere temperature structures, generated by compressional wind driven heating, were greater when the MCD mixing ratios were used.

These differences, because of the different mixing ratios used in the CO_2 cooling routine, were shown in another light in section 5.6 when I compared coupled MarTIM-MCD simulations to Mars Express, SPICAM measured temperatures. The higher O content and thus greater CO_2 15-μm cooling rate for the MarTIM ratios typically produced cooler temperatures about the mesopause that showed better agreement with SPICAM observations. Also the fact that advection of warm air from the dayside was slower when the MarTIM ratios were used meant horizontal advection of energy was a less important term (providing less heating to the nightside) than with the MCD ratios. More generally, both types of coupled MarTIM-MCD results predicted mesopause temperatures that were $\sim$10-15 K hotter than SPICAM observed temperatures. This was particularly true for the coldest SPICAM measurements in section 5.6.2 that had temperatures below the CO_2 frost point. McDunn et al. (2010) suggested that the inclusion of a gravity wave parameterisation could be an additional mechanism that could alter the atmospheric circulation features. It could have a braking effect on the wind velocities and in turn this would further reduce the positive energy input from the horizontal advection term thereby cooling the simulated temperatures and bring them closer to SPICAM observations.

Chapter 6 Conclusions

Chapter 6 took MarTIM's neutral atmosphere and applied it to a one-dimensional kinetic model of the ionosphere. The kinetic model was then used to model the production of energetic (primary) electrons, their precipitation through the background neutral atmosphere and their degradation in energy. The kinetic model computed the secondary electron and ion production rate due to primary electron impact with the neutral background atmosphere. This was done across MarTIM's horizontal latitude by longitude grid to create a 3-D description of the primary and secondary electron and ion production.

The ratio of secondary to primary electron and ion production, i.e. the efficiency, was studied by using MarTIM's background neutral atmosphere to model its variation with solar cycle and solar longitude. We showed that while the efficiency of ion and electron production did vary with solar zenith angle it could be parameterised with a simple function and this was given. Finally we showed that production efficiency variations with solar cycle and solar longitude were negligible about the region of the primary and secondary production peaks. This work was published in Nicholson et al. (2009).

7.2 Future Work

7.2.1 Introduce photochemistry, neutral-neutral and neutral-ion chemistry

- Only by self-consistently including photochemistry and neutral chemistry within a single model can we properly simulate how neutral species, their response to solar heating and influence on CO_2 cooling by affecting O to CO_2 ratio, influences the result as the composition changes. Though changes to composition due to advective and diffusive processes are already modelled in MarTIM, only by also including neutral chemistry can a more complete simulation be made.

  - In Chapter 4, section 4.5 although MarTIM's upper atmosphere temperatures showed good variation with the solar $F_{10.7}$ flux versus the Mars Global Surveyor Precise Orbit Determination (POD) results they were typically about 15 K hotter than the MGS observations (e.g. see Figure 4.18(b)). Then, González-Galindo et al. (2005) showed that the effect of photochemistry on the upper atmosphere would be to increase the O/CO_2 ratio through the photolysis of CO_2. This resulted in both less solar EUV/UV heating (because CO_2 heats the atmosphere more effectively than O) but also resulted in more CO_2 15-μm cooling due to increased O abundance. González-Galindo et al. (2005) suggested a maximum temperature difference of about 25 K for zonal mean daytime solar medium conditions at equinox ($\sim$1.594 AU) in the upper atmosphere i.e. temperatures were up to 25 K hotter when photochemistry was neglected.

  - Chapter 5, section 5.4.3 compared upper atmosphere temperatures between coupled MarTIM-MCD results that used MarTIM mixing ratios in the CO_2 15-μm cooling routine to those that used ratios from the MCD. Figure 5.19 showed that the CO_2 IR cooling rate was greater around the PL 10 to 13 region (9.81×10^{-3} to 2.19×10^{-3} Pa) when the MarTIM mixing ratios were used. Then as Figure 5.20 at PL 15 (8.05×10^{-4} Pa) showed, although both sets of mixing ratios had little absolute O content the relative difference between MarTIM and MCD mixing ratios (MarTIM maximum O/CO_2 ratio $\sim2\times10^{-2}$ versus MCD minimum 4×10^{-3}) was sufficient to produce significant differences in the IR radiative balance. Consequently middle and upper atmosphere dayside temperatures were hotter and wind magnitudes from about PL 15 upwards were enhanced with the MCD ratios.

- González-Galindo et al. (2005) states how an upper atmosphere neutral chemistry scheme can be simpler than for the lower atmosphere (troposphere) where a more diverse range of processes act such as the Martian water cycle and ozone variability. Nonetheless as Yung and DeMore (1999) state bulk chemistry on Mars hinges upon the self-regulation of atmospheric oxidation, stability of CO_2 and the escape of lighter species (particularly hydrogen and oxygen (Chassefiére and Leblanc, 2010)). MarTIM could be used to study the stability of CO_2 in the atmosphere. This would require fine resolution of HO_X species and careful consideration of their catalytic activity given their very small abundance. A study of other trace neutral species would also be interesting. In particular the chemistry of methane (CH_4) is intriguing because it has a possible biological source (Formisano et al., 2004; Atreya et al., 2007), however this would require MarTIM's lower boundary pressure to be increased (lower altitude), as discussed in the next sub-section. Finally, a consideration of the chemistry of the main neutral species on Mars could be tested against what limited measurements there are e.g. Chaufray et al. (2009) for O content and Billebaud et al. (2009) for CO measurements.

7.2.2 Expand MarTIM to higher pressures (lower altitudes)

- The overarching reason that coupled MarTIM-MCD results in Chapter 5 became progressively different to MCD alone results, above MarTIM's lower boundary, was because wind magnitudes had been damped to such an extent that their influence on temperature structures through advective heating and cooling was greatly diminished. This was an unfortunate consequence of the approximation made in Chapter 5, section 5.3.2 that was necessary to allow coupled simulations to reach steady state rather than producing physically inconsistent results. Without the approximation (of assuming the lower boundary was a surface of constant geopotential and measuring all geopotential height gradients from this level) significant wind amplitudes were simulated in the coupled model due to large horizontal gradients in geopotential height. This generated large compressional heating in regions where eastward and westward winds converged such that the zonal advection of total energy term would become unstable in the energy equation. The problem is however, that the disparity between coupled MarTIM-MCD results and MCD alone results, following the approximation of Chapter 5, reveals the inconsistency at MarTIM's lower boundary between a constant geopotential (implying zero horizontal velocities) versus the non-zero velocities provided by the MCD. This suggests that coupling MarTIM to the MCD (at 5° longitudinal resolution at least) was not successful.

- This is one of several examples how coupling two independently developed models may always cause difficulties.

  - Jarring together all the different parameterisations and model designs with respect to e.g solar EUV/UV heating, IR heating and cooling, neutral species number densities (and their thermodynamic effects), model grid sizes, model design assumptions and approximations, model

design limitations, etc can quite easily lead to the kind of energy input/output imbalance that caused problems for coupled MarTIM-MCD simulations, often far from the level at which the models were coupled in the first place.

  - Although the MCD can influence MarTIM from below (as in Chapter 5), there is no way for MarTIM to feed its results back to influence the MCD from above. For example in both chapters 4 and 5 we discussed winter hemisphere polar warming features. Section 4.3.2 in particular (e.g. Figure 4.11) showed how when interhemispheric flows suddenly descend in altitude they can deposit significant amounts of energy that heat the atmosphere below. If similar phenomena occur near the 0.883 Pa coupling level this energy would not be able to influence the MCD and differences in results could well occur.
  - Such discontinuities in atmospheric fields and/or energy terms will not be a problem when everything is designed within the context of a single model and so all these issues will be much more likely to come to an equilibrium with respect to one another. Thus if MarTIM could remove the need for the MCD to provide a description of the atmosphere below 0.883 Pa then all of the included physics would be self-consistent within the context of a single model.
  - Another point to mention[1] (as noted in Chapter 5, section 5.4.4) is that the MCD data involve quite a long-term time-averaging at fixed local times and so do not represent full synoptic variability even though tides are fairly comprehensively included on average. The time-averaging will have been necessary to allow the MCD data fit onto the DVD. If MarTIM did not have to rely on the MCD at all but could instead self-consistently describe the lower atmosphere itself then a fuller more comprehensive coupling would be achieved.

- Another reason coupled MarTIM-MCD results began to differ from the MCD alone may have been because dust is not included at all within MarTIM. It is possible that the vertical distribution of dust within the MCD (see Chapter 5, section 5.3.1, equation 5.1) extends above MarTIM's 0.883 Pa lower boundary. As noted in Chapter 5, section 5.4.4, the additional heating that this would provide could enhance temperatures, atmospheric expansion and wind magnitudes throughout MarTIM's lowest few pressure levels and thus improve the transition from the MCD to MarTIM. Thus when expanding MarTIM to lower altitudes a proper consideration of dust distribution, transport and heating effects would be important to include. Note also that Bell et al. (2007) discuss how a proper dust content parameterisation must consider both the vertical and horizontal distribution of the dust, reflecting for example how dust storms can begin at certain locations and cause specific heating/cooling processes there.

- Regardless of expanding MarTIM to higher pressures it would be useful to specifically parameterise gravity wave processes such as gravity wave drag (GWD) at MarTIM's 0.883 Pa lower boundary.

[1] Private correspondence with Professor Peter L. Read, Oxford University and Professor Andrew J. Coates, Mullard Space Science Laboratory.

e.g. Parish et al. (2009); Creasey et al. (2006b,a); Collins et al. (1997).

  - For example, Creasey et al. (2006b,a) state how on Earth breaking gravity waves deposit momentum into the mean flow and therein can reverse the direction of zonal mean wind jets (around the 65 to 75 km region). The breaking of a whole spectrum of waves also contributes to turbulent mixing in the Earth's mesosphere (Creasey et al., 2006b). Though the influence of gravity waves on the middle and upper atmosphere of Mars is not as well established as for Earth such turbulent mixing occurring in MarTIM's modelled mesosphere would affect the region where coupled MarTIM-MCD simulations began to depart from MCD alone results i.e. where differences between models already exist. It is therefore important for achieving an accurate simulation to ensure that these wave phenomena are considered to better constrain middle and upper atmospheric regions.
  - Some Mars modeling studies (Joshi et al., 1995; Collins et al., 1997; Forget et al., 1999) have already shown that vertically-propagating gravity waves force the mean flow sufficiently to close off the mid-latitude westerly jet above about 70 km, generating adiabatic warming and heating around the 40 to 60 km, high latitude winter hemisphere region (separate to the thermospheric warming discussed earlier in Chapters 4 and 5). Other modelling work, e.g. Angelats i Coll et al. (2005), suggest a more modest 10 to 20% deviation in the zonal and meridional winds near the equator in the 30 to 60 km altitude range and at high winter latitudes in the thermosphere.
  - Parish et al. (2009) showed that tropospheric gravity waves with parameters consistent with those observed by Mars Global Surveyor (Fritts et al., 2006) were capable of propagating up to thermospheric heights. Gravity waves were able to produce significant heating and cooling at different altitudes and to deposit energy and momentum in the upper atmosphere (Parish et al., 2009). Then, as we suggested in Chapter 5, perhaps the deposition of momentum by breaking gravity waves could further reduce the horizontal advection energy input and bring temperatures closer to (in the case of Chapter 5) SPICAM temperature measurements.
  - Although the MCD already includes a small-scale variability model to simulate perturbations of density, temperature and wind due to the upward propagation of small-scale gravity waves (Millour et al., 2008; Collins et al., 1997), it would be better for MarTIM to include these processes itself. This way the detailed time step by time step changes to the atmospheric fields as the wave energy propagated could be modelled in a more detailed way versus relying on the hourly updates MCD gave us in Chapter 5.

- Finally, if a photochemistry and neutral chemistry scheme was introduced to MarTIM (noted above) it would likely be necessary to expand the model to lower altitudes. Since the real Martian atmosphere behaves as a single entity, over various timescales, then the bulk chemistry (e.g. stability of CO_2, self-regulation of atmospheric oxidation, etc (Yung and DeMore, 1999)) will involve circula-

tion flows across MarTIM's lower boundary. For example, do atmospheric flows across MarTIM's 0.883 Pa lower boundary replenish CO_2 content in the upper atmosphere or is the transport of HO_X to the upper atmosphere required (even at very low concentrations) for CO_2 reformation chemistry to proceed? This study would require chemistry and circulation features below MarTIM's current 0.883 Pa lower boundary to be considered.

7.2.3 Expand MarTIM to lower pressures (higher altitudes)

- Expanding MarTIM to lower pressures (higher altitudes) would allow the study of Mars' near-space environment.
  - As McDunn et al. (2010) notes, simulations of the middle atmosphere provide the lower boundary conditions required for modelling the solar wind interaction with Mars. Thus MarTIM is well placed to parameterise and study e.g. the escape of atmospheric constituents (Lundin et al., 2006, 2009; Pierrard, 2003) also the diffusion of the interplanetary magnetic field (IMF) into the topside atmosphere and the manner in which this controls ion diffusion and advection around the planet (also leading to atmospheric escape) (Witasse, 2000; Blelly et al., 2005).
  - MarTIM extension into the Mars near-space region would require including the physics and mathematics used in MHD and/or hybrid models (e.g. Kallio and Janhunen (2002); Bauske et al. (2000); Liu et al. (2001); Ma et al. (2004); Erkaev et al. (2007)) since these models are often best placed to describe the transition into the increasingly tenuous exosphere.
  - This work could also be linked back to a parameterisation of chemistry and composition that we suggested above. In particular how atmospheric loss may act as a sink of tracer species and/or how the loss of more fundamental species such as oxygen and hydrogen (Chassefiére and Leblanc, 2010) affects overall atmospheric composition. Also, it would be important to include a parameterisation of ion chemistry given that, for example, ion species O^+, CO_2^+, CO^+ and N_2^+ number densities are greatly affected by the abundance of hydrogen (Fox, 2003, 2004b) (given their swift reaction with H_2). Fox (2003) showed how the reactions between and the abundance of these ion and neutral species were important in reproducing the O^+ densities measured by Viking RPA instruments.
- On a different point, Fox (2003) notes how the absorption of solar EUV radiation could be dominated at high altitude by sufficiently large mixing ratios of H and H_2. Thus perhaps adding these species to the model, decreasing the pressure of the upper boundary and adding a neutral chemistry parameterisation MarTIM could identify by how much the solar EUV heating rate varies?
- Further development of the ionosphere would make new comparisons possible. And these would become more fundamental to the simulation of the near-space environment as the upper boundary was raised:

- Development of the model ionosphere, using the kinetic model, should include a parameterisation of the main mechanisms that lead to the emissions observed in the Martian dayglow. This way MarTIM could study the dayglow measured by e.g. SPICAM onboard Mars Express (Leblanc et al., 2006; Cox et al., 2008, 2010). Cox et al. (2008) in particular look at nightside band emission from nitric oxide. This would require we start including NO in the simulations despite its very small abundance.
- It would be very interesting to study the unique Martian magnetic topography. The very complex structure that crustal magnetic fields generate creates 'mini-magnetospheres' that manipulate the solar wind interaction downwards into and horizontal convection across the Martian ionosphere (Breus et al., 2005). The three-dimensional spatial interaction of the IMF with these magnetic fields may be best suited to the MHD models noted above (e.g. Ma et al. (2002)). Then, Coates et al. (2010) discuss using photoelectrons as a diagnostic tool for studying the topology of the solar wind interaction: as a diagnostic tracer of a magnetic connection to the production location i.e. a tracer of the magnetic connection to the dayside ionosphere.
- Modelling work by Bougher et al. (2001) showed that the dayside ionosphere below approximately ∼200 km was not subject to vertical or horizontal transport of ions. Thus extending the vertical range of the model and further work with the ionosphere should include a parameterisation of the vertical and horizontal transport of ions.

7.2.4 Develop the General MarTIM Solution

- As noted in section 2.1.1, Chapter 2 and section 3.3.1, Chapter 3 MarTIM approximates solutions to partial differential equations using a forward Euler time-stepping finite difference method with time steps typically set no higher than 10 seconds. Dividing a 24 hour Martian day into 10 second time steps immediately makes a typical MarTIM simulation quite expensive in computation time. Unfortunately such a short time step is necessary because the forward time-stepping method is less accurate than other schemes (Washington and Parkinson, 1992) and the solution may oscillate or diverge (Riley et al., 2000). Alternative finite difference schemes such as the centered difference (i.e. the leapfrog method), Runge-Kutta or predictor-corrector schemes typically exhibit better stability and accuracy (Kalnay, 2003).
- Another way of understanding the small time step used by MarTIM is to consider the Courant-Friedrichs-Lewy condition or CFL condition e.g. Williamson and Laprise (2000). This is a numerical constraint that ensures a stable solution to the class of finite difference equations used in MarTIM.
  - The physical interpretation of this condition is that the time step should be chosen so that no physical phenomena (e.g. wave structure, neutral species advection, etc) can travel more than one grid size in one time step (Kalnay, 2003).

– The condition is:

$$C = \left| U \frac{\Delta t}{\Delta x} \right| \leq 1 \tag{7.1}$$

where C is the Courant number, U is the propagation speed of physical phenomena in the model (e.g. wave speed or advection speed), Δt is the time step and Δx the horizontal grid resolution. Thus the time step Δt must be chosen to satisfy (Williamson and Laprise, 2000):

$$\Delta t \leq \text{MIN} \left(\frac{\Delta x}{|U|} \right) \tag{7.2}$$

The velocity U is determined by the problem being considered e.g. zonal wind speeds of up to ∼200 m/s were predicted by MarTIM at high latitudes in the upper atmosphere. The grid size Δx was usually set to 5°×5° latitude by longitude, however this means that the actual physical distance in the east-west direction decreases at high latitudes as the meridians converged towards the poles (i.e. Δx=$\Delta\phi \cos\theta$).

– Consequently the maximum allowed time step, while maintaining stability, for a certain phenomena with velocity U decreases at higher latitudes (hence the MIN term in equation 7.2 refers to minimum over all latitudes). Future work should therefore look to deal with this so called "pole problem" (Williamson and Laprise, 2000). Possible solutions include (1) filtering the atmospheric fields in longitude by using Fourier truncation e.g. (Purser, 1988a,b) either to all predicted terms or just to terms in those equations responsible for the instabilities and (2) increasing the longitudinal grid size $\Delta\phi$ as one approaches the poles such that Δx=$\Delta\phi \cos\theta$ is held constant (Williamson and Laprise, 2000). Both of these methods have limitations and introduce their own errors that would need to be dealt with but any increase in time step that they allow would be very important for future studies with MarTIM.

Appendix A

References of Photo-absorption Cross Sections

A.1 Carbon Dioxide

References Stark et al. (2006)[3], Karaiskou et al. (2004)[3], Parkinson et al. (2003)[3], Yoshino et al. (1996)[1], Chan et al. (1993b)[2]

A.2 Nitrogen

References Fennelly and Torr (1992), Chan et al. (1993f)[2]

A.3 Carbon Monoxide

References Chan et al. (1993a)[2]

A.4 Atomic Oxygen

References Fennelly and Torr (1992)

A.5 Molecular Oxygen

References Yoshino et al. (1988), Yoshino et al. (1992)[3], Chan et al. (1993d)[2], Fally et al. (2000)[3], Yoshino et al. (2005)

A.6 Nitric Oxide

References Chan et al. (1993c)[2]

A.7 Argon

References Chan et al. (1992)[2] (and also Chan et al. (1993e)).

[1] See `http://www.cfa.harvard.edu/amp/ampdata/cfamols.html`.
[2] By `ftp` at `chem.ubc.ca` directory `pub/cooper`.
[3] See `http://www.atmosphere.mpg.de/enid/2295`.

Appendix B

Polynomial Coefficients for use in Equations 6.11 and 6.12 of Chapter 6

Table B.1: Polynomial Coefficients in equations 6.11 and 6.12. The transition altitude (km) is shown in bold font.

	Electrons	O_2^{++}	O^{++}	CO_2^{+}	CO_2^{++}	CO^{+}	C^{+}	N^{+}	O_2^{+}	N_2^{+}	N_2^{++}	O^{+}
a_0	6.610274401E+02	1.404887060E+03	−3.549285886E+02	8.640961920E+02	6.608161526E+02	7.332582290E+02	6.135548663E+02	1.139925703E+03	7.265142765E+02	9.843804026E+02	1.648304544E+02	6.453740731E+02
a_1	−2.632588157E+01	−5.905697448E+01	1.606909410E+01	−3.471713960E+01	−2.619816585E+01	−2.919984139E+01	−2.326239304E+01	−4.742398258E+01	−2.714716832E+01	−3.978696855E+01	−6.139890180E+00	−2.547798991E+01
a_2	4.558931794E−01	1.048826790E+00	−3.109944041E−01	6.072614479E−01	4.482054716E−01	5.079651482E−01	3.805048804E−01	8.404232989E−01	4.315022800E−01	7.028448262E−01	9.662075426E−02	4.384613636E−01
a_3	−4.470594485E−03	−9.842519706E−03	3.304128898E−03	−6.050002721E−03	−4.320209506E−03	−5.057170037E−03	−3.499846846E−03	−8.108229906E−03	−3.774025573E−03	−7.111951170E−03	−8.219074079E−04	−4.288387072E−03
a_4	2.702389189E−05	4.567591189E−05	−2.002306056E−05	3.779639483E−05	2.567473439E−05	3.178156709E−05	1.980550808E−05	4.420892285E−05	1.962771814E−05	4.545683986E−05	4.090642995E−06	2.596437447E−05
a_5	−1.007311984E−07	3.619049455E−09	6.006367262E−08	−1.533626303E−07	−9.642024772E−08	−1.309076957E−07	−7.066916922E−08	−1.154901432E−07	−6.076128732E−08	−1.905046447E−07	−1.194806317E−08	−9.750300694E−08
a_6	2.006362068E−10	−1.404369473E−09	7.432810856E−13	4.032987841E−10	2.236603316E−10	3.538587990E−10	1.554140353E−10	−3.514073816E−11	1.037835637E−10	5.240068127E−10	1.901726478E−11	1.986722344E−10
a_7	1.267528772E−16	9.169446666E−12	−5.300515146E−13	−6.602964344E−13	−2.932300780E−13	−6.060315762E−13	−1.927798346E−13	8.790819159E−13	−7.552930040E−14	−9.130399894E−13	−1.275495135E−14	−2.293667699E−14
a_8	−1.177446841E−15	−3.142117772E−14	5.984966577E−16	6.067681784E−16	1.664758148E−16	5.973573923E−16	1.033586325E−16	−1.320788149E−16		9.151792207E−16		−1.080547019E−15
a_9	3.365145885E−18	6.359644968E−17	5.765269390E−18	−2.356829271E−19		−2.584454326E−19		−8.202233732E−18		−4.023230948E−19		3.171787989E−18
a_{10}	−4.785158749E−21	−7.211601141E−20	−2.411793336E−20					−1.256480521E−22				−4.566493384E−21
a_{11}	3.606402984E−24	3.552844620E−23	3.824294509E−23					1.329336168E−22				3.472393897E−24
a_{12}	−1.150162167E−27		−2.286327992E−26					−4.403185142E−25				−1.115699979E−27
a_{13}								6.098474897E−28				
a_{14}								−3.256951018E−31				
	112.93 km	**108.39 km**	**112.93 km**	**112.93 km**	**110.62 km**	**110.62 km**	**110.62 km**	**108.39 km**	**112.93 km**	**108.39 km**	**115.32 km**	**112.93 km**
b_0	−1.314032163E+06	4.889730934E+05	1.660929822E+06	1.159404818E+06	1.808352324E+05	−1.165107657E+06	−4.289489041E+05	6.346190854E+04	3.622091694E+06	5.146111566E+04	2.514721676E+04	−5.934881676E+05
b_1	7.876134162E+04	−2.312661376E+04	−7.852927903E+04	−5.617523193E+04	−7.737651713E+03	4.315606169E+04	1.389059860E+04	−2.623253212E+03	−1.459144190E+05	−1.771736158E+03	−1.773132065E+02	3.546095705E+04
b_2	−1.962256737E+03	4.362321935E+02	1.297733707E+03	8.535640078E+02	1.036546804E+02	−3.480483017E+02	−8.772966691E+01	4.050319629E+01	1.764604914E+03	1.811156914E+01	−6.015888968E+00	−8.806801303E+02
b_3	2.601160514E+01	−4.101108333E+00	−5.198631894E+00	−5.956128524E−01	−1.515144981E−02	−3.831253024E+00	−8.264310891E−01	−2.767987276E−01	1.186141031E+00	3.583722498E−03	−3.706271110E−04	1.163735173E+01
b_4	−1.935040886E−01	1.921153659E−02	−1.005566588E−01	−8.532255532E−02	−1.050898166E−02	4.333167420E−02	4.036116721E−04	7.064439029E−04	−1.331821089E−01	−9.891151731E−04	6.640578877E−04	−8.629924380E−02
b_5	7.659847779E−04	−3.586676640E−05	1.449983068E−03	1.217829692E−04	5.786305533E−05	2.430752910E−04	1.040177360E−04		−3.661686584E−04	3.994474097E−06	5.041910676E−06	3.405473330E−04
b_6	−1.260572216E−06		−7.433710434E−06	9.641535217E−06	3.584971026E−07	−7.835732322E−08	3.657411038E−09		1.934372959E−05		2.048319585E−09	−5.587037506E−07
b_7			1.402843253E−08	−4.502450788E−08	−4.231372991E−09	−3.808598330E−08	6.620891428E−09		−1.307294421E−07		−6.007750320E−10	
b_8				−4.968492046E−10	1.084427196E−11	−1.947628467E−10	−1.019575878E−10		2.846288872E−10		−5.136146431E−12	
b_9				4.830572346E−12		3.440753726E−12	−9.821035600E−13				−2.777076900E−14	
b_{10}				−1.168635127E−14		2.336227916E−14	4.369330883E−15				6.101722255E−16	
b_{11}						−3.575877198E−16	1.100642793E−16				5.927039473E−18	
b_{12}						1.030801684E−18	−3.456752479E−20				−8.418488212E−21	
b_{13}							−8.157880747E−21				−6.708980821E−22	
b_{14}							3.117935951E−23				2.867934563E−24	

Bibliography

N. Achilleos, S. Miller, J. Tennyson, A. D. Aylward, I. Mueller-Wodarg, and D. Rees. JIM: A time-dependent, three-dimensional model of Jupiter's thermosphere and ionosphere. *J.Geophys.Res.*, 103: 20089–20112, September 1998.

M. H. Acuña, J. E. P. Connerney, P. Wasilewski, R. P. Lin, K. A. Anderson, C. W. Carlson, J. McFadden, D. W. Curtis, D. Mitchell, H. Reme, C. Mazelle, J. A. Sauvaud, C. d'Uston, A. Cros, J. L. Medale, S. J. Bauer, P. Cloutier, M. Mayhew, D. Winterhalter, and N. F. Ness. Magnetic field and plasma observations at Mars: Initial results of the Mars Global Surveyor Mission. *Science*, 279:1676–1680, 1998.

A. D. Anbar, M. Allen, and H. A. Nair. Photodissociation in the atmosphere of Mars: Impact of high resolution temperature-dependent CO_2 cross-section measurements. *Journal of Geophysical Research*, 98:10925–10931, 1993. No. E6.

D. E. Jr Anderson and C. W. Hord. Mariner 6 and 7 ultraviolet spectrometer experiment: analysis of hydrogen Lyman alpha data. *Journal of Geophysical Research*, 76:6666–6673, 1971.

E. H. Anderson and C. B. Leovy. Mariner 9 television limb observation of dust and ice hazes on Mars. *Journal of Atmospheric Science*, 35:723–734, 1978.

M. Angelats i Coll and J. M. Forbes. Nonlinear interactions in the upper atmosphere: The s=1 and s=3 nonmigrating semidiurnal tides. *Journal of Geophysical Research*, 107(A8, 1157, doi:10.1029/2001JA900179), 2002.

M. Angelats i Coll, F. Forget, M. A. Lòpez-Valverde, P. L. Read, and S. Lewis. Upper atmosphere of Mars up to 120 km: Mars Global Surveyor data analysis with the LMD general circulation model. *Journal of Geophysical Research*, 109(E01011, doi:10.1029/2003JE002163), 2004.

M. Angelats i Coll, F. Forget, M. A. Lòpez-Valverde, and F. Gonzàlez-Galindo. The first Mars thermospheric general circulation model: The Martian atmosphere from the ground to 240km. *Geophysical Research Letters*, 32(L04201), 2005.

A. L. Aruliah, E. M. Griffin, A. D. Aylward, Ford. E. A. K., M. J. Kosch, C. J. Davis, V. S. C. Howells, S. E. Pryse, H. R. Middleton, and J. Jussila. First direct evidence of meso-scale variability on ion-

neutral dynamics using co-located tristatic FPIs and EISCAT radar in Northern Scandinavia. *Annales Geophysicae*, 23(1):147–162, 2005.

S. K. Atreya, P. R. Mahaffy, and A. Wong. Methane and related trace species on Mars: Origin, loss, implications for life and habitability. *Planetary and Space Science*, 55:358–369, 2007.

S. V. Avakyan, editor. *Collision processes and excitation of UV emission from planetary atmospheric gases: A handbook of cross sections*. Gordon & Breach, 1998.

P. M. Banks and G. Kockarts. *Aeronomy*. Academic Press, New York, USA, 1973.

J. R. Barnes. Possible effects of breaking gravity waves on the circulation of the middle atmosphere of Mars. *J.Geophys.Res.*, 95:1401–1421, 1990.

C. A. Barth, A. I. F. Stewart, S. W. Bougher, D. M. Hunten, S. J. Bauer, and A. F. Nagy. *Mars, Chapter 30: Aeronomy of the current Martian atmosphere*. University of Arizona Press, 1992.

S. J. Bauer. *Physics of Planetary Ionospheres*. Springer-Verlag, Berlin Heidelberg New York, 1973.

S. J. Bauer. Mars upper atmosphere: response to solar activity. *Anzeiger Abt. II*, 136:19–22, 1999.

S. J. Bauer and M. H. Hantsch. Solar cycle variation of the upper atmosphere temperature of Mars. *Geophysical Research Letters*, 16(5):373–376, 1989.

R. Bauske, A. F. Nagy, D. L. DeZeeuw, T. I. Gombosi, and K. G. Powell. 3D Multiscale mass loaded MHD simulations of the solar wind interaction with Mars. *Adv. Space Res.*, 26(10):1571–1575, 2000.

J. M. Bell, S. W. Bougher, and J. R. Murphy. Vertical dust mixing and the interannual variations in the Mars thermosphere. *Journal of Geophysical Research*, 112(E12002), 2007. doi:10.1029/2006JE002856.

J. L. Bertaux, F. Leblanc, S. Perrier, E. Quemerais, O. Korablev, E. Dimarellis, A. Reberac, F. Forget, P. C. Simon, S. A. Stern, and B. Sandel. Nightglow in the upper atmosphere of Mars and implications for atmospheric transport. *Science*, 307:566–569, 2005a.

J. L. Bertaux, F. Leblanc, O. Witasse, E. Quemerais, J. Lilensten, S. A. Stern, B. Sandel, and O. Korablev. Discovery of an aurora on Mars. *Nature*, 435:790–794, 2005b.

J. L. Bertaux, O. Korablev, S. Perrier, E. Quemerais, F. Montmessin, F. Leblanc, S. Lebonnois, P. Rannou, F. Lefévre, F. Forget, A. Fedorova, E. Dimarellis, A. Reberac, D. Fonteyn, and S. Chaufray, J. Y. Guibert. SPICAM on Mars Express: Observing modes and overview of UV spectrometer data and scientific results. *Journal of Geophysical Research*, 111(E10S90), 2006. doi:10.1029/2006JE002690.

F. Billebaud, J. Brillet, E. Lellouch, T. Fouchet, T. Encrenaz, V. Cottini, N. Ignatiev, V. Formisano, M. Giuranna, A. Maturilli, and F. Forget. Observations of CO in the atmosphere of Mars with PFS onboard Mars Express. *Planetary and Space Science*, 57:1446–1457, 2009.

P. L. Blelly, A. Robineau, D. Lummerzheim, and J. Lilensten. 8-moment fluid models of the terrestrial high latitude ionosphere between 100 and 3000 km. In R. W. Schunk, editor, *Solar-terrestrial energy program: Handbook of ionospheric models*, pages 53–72. Scientific Committee on Solar Terrestrial Physics (SCOSTEP), Center for Atmospheric and Space Sciences, Utah State University, Logan, UT, 84322-4406, 1996.

P. L. Blelly, O. Witasse, and J. Lilensten. Self-consistent modeling of the dayside ionosphere of Mars, I: Description of a new coupled kinetic, MHD fluid model. (Paper 1 of an unpublished set of 3), November 2005.

S. Bougher, G. Keating, R. Zurek, J. Murphy, R. Haberle, J. Hollingsworth, and R. T. Clancy. Mars Global Surveyor Aerobraking: Atmospheric trends and model interpretation. *Adv. Space Res.*, 23(11): 1887–1897, 1999a.

S. W. Bougher and R. E. Dickinson. Mars mesosphere and thermosphere 1: Global mean heat budget and thermal structure. *J.Geophys.Res.*, 93(A7):7325–7337, 1988.

S. W. Bougher and R. G. Roble. Comparative terrestrial planet thermospheres 1, Solar cycle variation of global mean temperatures. *Journal of Geophysical Research*, 96(A7):11045–11055, 1991.

S. W. Bougher, R. G. Roble, E. C. Ridley, and R. E. Dickinson. Mars thermosphere 2: General circulation with coupled dynamics and composition. *J.Geophys.Res.*, 30:14811–14827, August 1990.

S. W. Bougher, D. M. Hunten, and R. G. Roble. CO_2 cooling in terrestrial planet thermospheres. *Journal of Geophysical Research*, 99(E7):14609–14622, 1994.

S. W. Bougher, J. Murphy, and R. M. Haberle. Dust storm impacts on the Mars upper atmosphere. *Adv. Space Res.*, 19(8):1255–1260, 1997.

S. W. Bougher, S. Engel, R. G. Roble, and B. Foster. Comparative terrestrial planet thermospheres 2. Solar cycle variation of global structure and winds at equinox. *J.Geophys.Res.*, 104:16591–16611, 1999b.

S. W. Bougher, S. Engel, R. G. Roble, and B. Foster. Comparative terrestrial planet thermospheres 3. Solar cycle variation of global structure and winds at solstices. *J.Geophys.Res.*, 105:17669–17692, July 2000.

S. W. Bougher, S. Engel, D. P. Hinson, and J. M. Forbes. Mars Global Surveyor Radio Science electron density profiles: Neutral atmosphere implications. *Geophysical Research Letters*, 28(16):3091–3094, August 2001.

S. W. Bougher, S. Engel, D. P. Hinson, and J. R. Murphy. MGS Radio Science electron density profiles: Interannual variability and implications for the neutral atmosphere. *Journal of Geophysical Research*, 109, 2004. doi: 10.1029/2003JE002154, E03010.

S. W. Bougher, J. M. Bell, J. R. Murphy, M. A. López-Valverde, and P. G. Withers. Polar warming in the Mars thermosphere: seasonal variations owing to changing insolation and dust distributions. *Geophysical Research Letters*, 33(L02203), 2006a. doi:10.1029/2005GL024059.

S. W. Bougher, J. R. Murphy, J. M. Bell, and R. W. Zurek. Prediction of the structure of the martian upper atmosphere for the Mars Reconnaissance Orbiter (MRO) mission. *The International Journal of Mars Science and Exploration*, 2:10–20, 2006b.

S. W. Bougher, T. M. McDunn, K. A. Zoldak, and J. M. Forbes. Solar cycle variability of Mars dayside exospheric temperatures: Model evaluation of underlying thermal balances. *Geophysical Research Letters*, 36(L05201), 2009. doi:10.1029/2008GL036376.

G. Brasseur and S. Solomon. *Aeronomy of the middle atmosphere*. D. Reidel Publishing Company, 2nd edition, 1986.

G. Brasseur and S. Solomon. *Aeronomy of the Middle Atmosphere*. Springer, 2005.

T. K. Breus, N. F. Ness, A. M. Krymskii, D. H. Crider, M. H. Acuna, J. E. P. Connerney, D. Hinson, and K. K. Barashyan. The effects of crustal magnetic fields and the pressure balance in the high latitude ionosphere/atmosphere at Mars. *Advances in Space Research*, 36:2043–2048, 2005.

K. L. Cahoy, D. P. Hinson, and G. L. Tyler. Radio science measurements of atmospheric refractivity with Mars Global Surveyor. *Journal of Geophysical Research*, 111, 2006. E05003, doi:10.1029/2005JE002634.

W. F. Chan, G. Cooper, X. Guo, G. R. Burton, and C. E. Brion. Absolute optical oscillator strengths for the electronic excitation of atoms at high resolution. III. The photoabsorption of argon, krypton, and xenon. *Physical Review A*, 46(1):149–171, 1992.

W. F. Chan, G. Cooper, and C. E. Brion. Absolute optical oscillator strengths for discrete and continuum photoabsorption of carbon monoxide (7-200 eV) and transition moments for the $X^1\Sigma^+ \rightarrow A^1\Pi$ system. *Chemical Physics*, 170:123–138, 1993a.

W. F. Chan, G. Cooper, and C. E. Brion. The electronic spectrum of carbon dioxide. Discrete and continuum photoabsorption oscillator strengths (6-203 eV). *Chemical Physics*, 178:401–413, 1993b.

W. F. Chan, G. Cooper, and C. E. Brion. Absolute optical oscillator strengths for the photoabsorption of nitric oxide (5-30 eV) at high resolution. *Chemical Physics*, 170:111–121, 1993c.

W. F. Chan, G. Cooper, and C. E. Brion. Absolute optical oscillator strengths for the photoabsorption of molecular oxygen (5-30 eV) at high resolution. *Chemical Physics*, 170:99–109, 1993d.

W. F. Chan, G. Cooper, X. Guo, G. R. Burton, and C. E. Brion. Erratum: Absolute optical oscillator strengths for the electronic excitation of atoms at high resolution. III. The photoabsorption of argon, krypton, and xenon. *Physical Review A*, 48(1):858–860, 1993e.

W. F. Chan, G. Cooper, R. N. S. Sodhi, and C. E. Brion. Absolute optical oscillator strengths for discrete and continuum photoabsorption of molecular nitrogen (11-200 eV). *Chemical Physics*, 170: 81–97, 1993f.

S. Chapman and T. G. Cowling. *The mathematical theory of non-uniform gases*. Cambridge University Press, 3rd edition, 1970.

E. Chassefiére and F. Leblanc. Explaining the redox imbalance between the H and O escape fluxes at Mars by the oxidation of methane. *Planetary and Space Science*, 2010. doi:10.1016/j.pss.2010.09.013.

J. Y. Chaufray, F. Leblanc, E. Quémerais, and J. L. Bertaux. Martian oxygen density at the exobase deduced from O I 130.4-nm observations by Spectroscopy for the Investigation of the Characteristics of the Atmosphere of Mars on Mars Express. *Journal of Geophysical Research*, 114, 2009. E02006, doi:10.1029/2008JE003130.

P. R. Christensen, D. L. Anderson, S. C. Chase, R. T. Clancy, R. N. Clark, B. J. Conrath, H. H. Kieffer, R. O. Kuzmin, M. C. Malin, J. C. Pearl, T. L. Roush, and M. D. Smith. Results from the Mars Global Surveyor Thermal Emission Spectrometer. *Science*, 279:1692–1698, March 1998.

A. J. Coates, S. M. E. Tsang, A. Wellbrock, R. A. Frahm, J. D. Winningham, S. Barabash, R. Lundin, D. T. Young, and F. J. Crary. Ionospheric photoelectrons: Comparing Venus, Earth, Mars and TItan. *Planetary and Space Science*, 2010. doi:10.1016/j.pss.2010.07.016.

M. Collins, S. R. Lewis, and P. L. Read. Gravity wave drag in a global circulation model of the Martian atmosphere: Parameterisation and validation. *Advances in Space Research*, 19(8):1245–1254, 1997.

B. J. Conrath. Influence of Planetary-Scale Topography on the Diurnal Thermal Tide During the 1971 Martian Dust Storm. *Journal of Atmospheric Sciences*, 33:2430–2439, 1976.

B. J. Conrath. Planetary-scale wave structure in the Martian atmosphere. *Icarus*, 48:246–255, 1981.

A. N. Cox, editor. *Allen's Astrophysical Quantities*. Academic Press, 4th edition, 2000.

C. Cox, A. Saglam, J. C. Gérard, J. L. Bertaux, and F. González-Galindo. Distributions of the ultraviolet nitric oxide Martian night airglow: Observations from Mars Express and comparisons with a one-dimensional model. *Journal of Geophysical Research*, 113, 2008. E08012, doi:10.1029/2007JE003037.

C. Cox, J. C. Gérard, B. Hubert, J. L. Bertaux, and S. W. Bougher. Mars ultraviolet dayglow variability: SPICAM observations and comparison with airglow model. *Journal of Geophysical Research*, 115, 2010. E04010, doi:10.1029/2009JE003504.

J. E. Creasey, J. M. Forbes, and D. P. Hinson. Global and seasonal distribution of gravity wave activity in Mars' lower atmosphere derived from MGS radio occultation data. *Geophysical Research Letters*, 33, 2006a. L01803, doi:10.1029/2005GL024037.

J. E. Creasey, J. M. Forbes, and G. M. Keating. Density variability at scales typical of gravity waves observed in Mars' thermosphere by the MGS accelerometer. *Geophysical Research Letters*, 33, 2006b. L22814, doi:10.1029/2006GL027583.

W. B. DeMore and M. Patapoff. Temperature and pressure dependence of CO_2 extinction coefficients. *Journal of Geophysical Research*, 77:6291–6293, 1972.

E. M. P. Ekanayake, T. Aso, and S. Miyahara. Background wind effect on propagation of nonmigrating diurnal tides in the middle atmosphere. *Journal of Atmospheric and Solar-Terrestrial Physics*, 59(4): 401–429, 1997.

N. V. Erkaev, A. B$\acute{}$oßwetter, U. Motschmann, and H. K. Biernat. Aspects of solar wind interaction with Mars: comparison of fluid and hybrid simulations. *Ann Geophys*, 25:145–159, 2007.

S. Fally, A. C. Vandaele, M. Carleer, C. Hermans, A. Jenouvrier, M. F. Mérienne, B. Coquart, and R. Colin. Fourier transform spectroscopy of the O_2 Herzberg bands. III. Absorption cross sections of the collision-induced bands and of the Herzberg continuum. *Journal of Molecular Spectroscopy*, 204: 10–20, 2000.

J. A. Fennelly and D. G. Torr. Photoionization and Photoabsorption cross sections of O, N_2, O_2 and N for aeronomic calculations. *Atomic data and nuclear data tables*, 51:321–363, 1992.

M. O. Fillingim, L. M. Peticolas, R. J. Lillis, D. A. Brain, J. S. Halekas, D. L. Mitchell, R. P. Lin, D. Lummerzheim, S. W. Bougher, and D. L. Kirchner. Model calculations of electron precipitation induced ionization patches on the nightside of Mars. *Geophys. Res. Lett.*, 34, 2007. L12101, doi: 10.1029/2007GL029986.

J. M. Forbes. Tides in the middle and upper atmospheres of Mars and Venus. *Advances in Space Research*, 33:125–131, 2004.

J. M. Forbes. Wave coupling in terrestrial planetary atmospheres. In M. Mendillo, A. Nagy, and J. H. Waite, editors, *Atmospheres in the solar system: Comparative aeronomy*, pages 171–190. Geophysical Monograph Series 130, 2002.

J. M. Forbes and M. E. Hagan. Diurnal Kelvin wave in the atmosphere of Mars: towards an understanding of 'stationary' density detructures observed by the MGS accelerometer. *Geophys. Res. Lett.*, 27:3563–3566, November 2000.

J. M. Forbes and S. Miyahara. Solar semidiurnal tide in the dusty atmosphere of Mars. *Journal of Atmospheric Science*, 63:1798–1817, 2006.

J. M. Forbes, M. E. Hagan, S. W. Bougher, and J. L. Hollingsworth. Kelvin wave propagation in the upper atmospheres of Mars and Earth. *Adv. Space Res.*, 27(11):1791–1800, 2001.

J. M. Forbes, A. F. C. Bridger, S. W. Bougher, M. E. Hagan, J. L. Hollingsworth, G. M. Keating, and J. Murphy. Nonmigrating tides in the thermosphere of Mars. *Journal of Geophysical Research*, 107, 2002. No. E11, doi: 10.1029/2001JE001582.

J. M. Forbes, S. L. Bruinsma, and F. G. Lemoine. Solar rotation effects on the thermospheres of Mars and Earth. *Science*, 312:1366–1368, 2006. doi:10.1126/science.1126389.

J. M. Forbes, F. G. Lemoine, S. L. Bruinsma, M. D. Smith, and X. Zhang. Solar flux variability of Mars' exosphere densities and temperatures. *Geophysical Research Letters*, 35(L01201), 2008. doi:10.1029/2007GL031904.

F. Forget, Y. Wanherdrick, C. Hourtolle, H. Fraysse, and S. R. Lewis. Mars Climate Database 3.1. "ATMEMCD" subroutine programmer's guide. Technical report, ESTEC, 1995.

F. Forget, F. Hourdin, R. Fournier, C. Hourdin, O. Talagrand, M. Collins, S. R. Lewis, P. L. Read, and J. P. Huot. Improved general circulation models of the martian atmosphere from the surface to above 80 km. *Journal of Geophysical Research*, 104:24155–24176, 1999.

F. Forget, E. Millour, and S. R. Lewis. Mars Climate Database v4.3 User Manual. Technical report, ESTEC, 2008. Contract 11369/95/NL/JG.

F. Forget, F. Montmessin, J. L. Bertauz, F. Gonzáez-Galindo, S. Lebonnois, E. Quémerais, A. Reberac, E. Dimarellis, and M. A. López-Valverde. Density and temperatures of the upper Martian atmosphere measured by stellar occultations with Mars Express SPICAM. *Journal of Geophysical Research*, 114, 2009. E01004, doi: 10.1029/2008JE003086.

V. Formisano, S. Atreya, T. Encrenaz, N. Ignatiev, and M. Giuranna. Detection of Methane in the Atmosphere of Mars. *Science*, 306:1758–1761, 2004.

J. L. Fox. Effect of H_2 on the Martian ionosphere: Implications for atmospheric evolution. *Journal of Geophysical Research*, 108, 2003. No. A6, 1223, doi:10.1029/2001JA000203.

J. L. Fox. Response of the Martian thermosphere/ionosphere to enhanced fluxes of solar soft X rays. *Journal of Geophysical Research*, 109, 2004a. A11310, doi: 10.1029/2004JA010380.

J. L. Fox. Advances in the aeronomy of Venus and Mars. *Advances in Space Research*, 33:132–139, 2004b.

J. L. Fox and A. Dalgarno. Ionisation, luminosity and heating of the upper atmosphere of Mars. *J.Geophys.Res.*, 84(A12):7315–7333, 1979.

J. L. Fox and K. E. Yeager. Morphology of the near-terminator Martian ionosphere: A comparison of models and data. *Journal of Geophysical Research*, 111, 2006. A10309, doi:10.1029/2006JA011697.

J. L. Fox, P. Zhou, and S. W. Bougher. The Martian thermosphere/ionosphere at high and low solar activities. *Advances in Space Research*, 17(11):203–218, 1996.

J. L. Fox, M. I. Galand, and R. E. Johnson. Energy deposition in planetary atmospheres by charged particles and solar photons. *Space Science Reviews*, 139:3–62, 2008.

D. C. Fritts, L. Wang, and R. H. Tolson. Mean and gravity wave structures and variability in the Mars upper atmosphere inferred from Mars Global Surveyor and Mars Odyssey aerobraking densities. *Journal of Geophysical Research (Space Physics)*, 111(A10), December 2006. doi: 10.1029/2006JA011897.

M. Galand, J. Lilensten, D. Toublanc, and S. Maurice. The ionosphere of Titan: Ideal diurnal and nocturnal cases. *Icarus*, 140:92–105, 1999.

M. Giuranna, D. Grassi, V. Formisano, L. Montabone, F. Forget, and L. Zasova. PFS/MEX observations of the condensing CO_2 south polar cap of Mars. *Icarus*, 197:386–402, 2008.

T. I. Gombosi. *Gaskinetic Theory*. Cambridge University Press, 1994.

F. González-Galindo, M. A. López-Valverde, M. Angelats i Coll, and F. Forget. Extension of a Martian general circulation model to thermospheric altitudes: UV heating and photochemical models. *Journal of Geophysical Research*, 110, 2005. E09008, doi: 10.1029/2004JE002312.

F. González-Galindo, F. Forget, M. A. López-Valverde, and M. Angelats i Coll. A ground-to-exosphere Martian general circulation model: 2. Atmosphere during solstice conditions - thermospheric polar warming. *Journal of Geophysical Research*, 114, 2009a. E08004, doi: 10.1029/2008JE003277.

F. González-Galindo, F. Forget, M. A. López-Valverde, M. Angelats i Coll, and E. Millour. A ground-to-exosphere Martian general circulation model: 1. Seasonal, diurnal, and solar cycle variation of thermospheric temperatures. *Journal of Geophysical Research*, 114, 2009b. E04001, doi: 10.1029/2008JE003246.

G. Gronoff, J. Lilensten, C. Simon, O. Witasse, R. Thissen, O. Dutuit, and C. Alcaraz. Modelling dications in the diurnal ionosphere of Venus. *Astronomy and Astrophysics*, 465:641–645, 2007. doi:10.1051/0004-6361:20065991.

G. Gronoff, J. Lilensten, C. Simon, M. Barthelemy, F. Leblanc, and O. Dutuit. Modelling the Venusian airglow. *Astronomy and Astrophysics*, 482:1015–1029, 2008. doi:10.1051/0004-6361:20077503.

D. A. Gurnett, R. L. Huff, D. D. Morgan, A. M. Persoon, T. F. Averkamp, D. L. Kirchner, F. Duru, F. Akalin, A. J. Kopf, E. Nielsen, A. Safaeinili, J. J. Plaut, and G. Picardi. An overview of radar soundings of the martian ionosphere from the Mars Express spacecraft. *Advances in Space Research*, 93(1):1335–1346, 2008.

D. A. Gurnett, D. D. Morgan, F. Duru, F. Akalin, J. D. Winningham, R. A. Frahm, E. Dubinin, and S. Barabash. Large density fluctuations in the martian ionosphere as observed by the Mars Express radar sounder. *Icarus*, 206(1):83–94, 2010.

R. M. Haberle. Mars. In J. R. Holton, J. A. Curry, and J. A. Pyle, editors, *Encyclopedia of atmospheric sciences*, pages 1745–1755. Elsevier Science Ltd, 2002.

M. Hagan, J. M. Forbes, and A. Richmond. Atmospheric tides. In J. R. Holton, J. A. Curry, and J. A. Pyle, editors, *Encyclopedia of atmospheric sciences*, pages 159–165. Elsevier Science Ltd, 2003.

W. B. Hanson, S. Sanatani, and D. R. Zuccaro. The Martian ionosphere as observed by the Viking Retarding Potential Analyzers. *Journal of Geophysical Research*, 82(28):4351–4363, 1977.

M. J. Harris. *A new coupled middle atmosphere and thermosphere general circulation model: studies of dynamic, energetic and photochemical coupling in the middle and upper atmosphere.* PhD thesis, University College London, UK, 2001.

D. P. Hinson, M. Pätzold, R. J. Wilson, B. Häusler, S. Tellmann, and G. L. Tyler. Radio occultation measurements and MGCM simulations of Kelvin waves on Mars. *Icarus*, 193:125–138, 2008.

A. P. Hitchcock, C. E. Brion, M. J. van der Wiel, and A. Seiff. Absolute oscillator strengths for valence-shell ionic photofragmentations of N_2O and CO_2 (8-75 eV). *Chemical Physics*, 45:461–478, 1980.

J. L. Hollingsworth and J. R. Barnes. Forced stationary planetary waves in Mars' Winter Atmosphere. *Journal of the Atmospheric Sciences*, 53(3):428–448, 1996.

J. R. Holton. *An introduction to dynamic meteorology.* Elsevier Academic Press, 4th edition, 2004.

D. L. Huestis, S. W. Bougher, J. L. Fox, M. Galand, R. E. Johnson, J. I. Moses, and J. C. Pickering. Cross sections and reactions rates for comparative planetary aeronomy. *Space Science Reviews*, 139: 63–105, 2008.

M. N. Izakov. Comparison of structure and dynamics of the Earth's, Mars' and Venus' thermospheres. *Journal of Atmospheric and Terrestrial Physics*, 38:847–862, 1976.

M. Z. Jacobson. *Fundamentals of Atmospheric Modeling.* Cambridge University Press, 1999.

P. B. James, H. H. Kieffer, and D. A. Paige. *Mars, Chapter* 27*: The seasonal cycle of carbon dioxide on Mars.* University of Arizona Press, 1992.

M. M. Joshi, B. N. Lawrence, and S. R. Lewis. Gravity wave drag in three-dimensional atmospheric models of Mars. *Journal of Geophysical Research*, 100:21235–21245, 1995.

R. A. Kahn, T. Z. Martin, R. W. Zurek, and S. W. Lee. *Mars, Chapter* 29*: The Martian dust cycle.* University of Arizona Press, 1992.

E. Kallio and P. Janhunen. Ion escape from Mars in a quasi-neutral hybrid model. *Journal of Geophysical Research*, 107(A3, 1035, doi:10.1029/2001JA000090), 2002.

E. Kalnay. *Atmospheric modeling, data assimilation and predictability.* Cambridge University Press, 2003.

A. Karaiskou, C. Vallance, V. Papadakis, I. M. Varsavas, and T. P. Rakitzis. Absolute absorption cross section measurements of CO_2 in the ultraviolet from 200 to 206 nm at 295 and 373 K. *Chemical Physics Letters*, 400:30–34, 2004.

G. M. Keating, S. W. Bougher, R. W. Zurek, R. H. Tolson, G. J. Cancro, S. N. Noll, J. S. Parker, T. J. Schellenberg, R. W. Shane, B. L. Wilkerson, J. R. Murphy, J. L. Hollingsworth, R. M. Haberle, M. Joshi, J. C. Pearl, B. J. Conrath, M. D. Smith, R. T. Clancy, R. C. Blanchard, R. G. Wilmoth, D. F. Rault, T. Z. Martin, D. T. Lyons, P. B. Esposito, M. D. Johnston, C. W. Whetzel, C. G. Justus, and J. M. Babicke. The structure of the upper atmosphere of Mars: In situ accelerometer measurements from Mars Global Surveyor. *Science*, 279:1672–1676, 1998.

G. M. Keating, M. E. Theriot, R. H. Tolson, S. W. Bougher, F. Forget, and J. Forbes. Brief review of the results obtained with the MGS and Mars Odyssey 2001 accelerometer expriments. In *Mars Atmosphere: Modelling and Observations Workshop, Eur. Space Agency, Granada, Spain,* 13-15 *January*, 2003.

G. M. Keating, S. W. Bougher, M. E. Theriot, R. H. Tolson, R. W. Zurek, R. C. Blanchard, J. R. Murphy, and J. L. Bertaux. Mars neutral upper atmosphere temporal and spatial variations discovered from the accelerometer science experiment aboard Mars Reconnaissance Orbiter. In *Lunar and Planetary Science XXXVIII*, 2007.

G. M. Keating, S. W. Bougher, M. E. Theriot, R. H. Tolson, and J. M. Forbes. Response of the Mars thermosphere to dynamical effects. In *AGU Fall Meeting Abstracts*, 2008.

T. T Koskinen. *Stability of Short Period Exoplanets.* PhD thesis, University College London, UK, 2008.

V. A. Krasnopolsky. Mars' upper atmosphere and ionosphere at low, medium, and high solar activities: Implications for evolution of water. *Journal of Geophysical Research*, 107, 2002. No. E12, doi: 10.1029/2001JE001809.

V. A. Krasnopolsky. Solar cycle variations of the hydrogen escape rate and the CO mixing ratio on Mars. *Icarus*, 101:33–41, 1993.

V. A. Krasnopolsky and P. D. Feldman. Detection of molecular hydrogen in the atmosphere of Mars. *Science*, 294:1914–1917, 2001.

A. M. Krymskii, T. K. Breus, N. F. Ness, D. P. Hinson, and D. I. Bojkov. Effect of crustal magnetic fields on the near terminator ionosphere at Mars: Comparison of in situ magnetic field measurements with the data of radio science experiments on board Mars Global Surveyor. *Journal of Geophysical Research*, 108, 2003. No. A12, doi: 10.1029/2002JA009662.

K. R. Lang and C. A. Whitney. *Wanderers in space. Exploration and discovery in the solar system.* Cambridge University Press, 1991.

F. Leblanc, J. Y. Chaufray, J. Lilensten, O. Witasse, and J. L. Bertaux. Martian dayglow as seen by the SPICAM UV spectrograph on Mars Express. *Journal of Geophysical Research*, 111, 2006. E09S11, doi:10.1029/2005JE002664.

B. R. Lewis and J. H. Carver. Temperature dependence of the carbon dioxide photoabsorption cross section between 1200 and 1970Å. *Journal of Quantitative Spectroscopic Radiative Transfer*, 30(4): 297–309, 1983.

S. R. Lewis and P. R. Barker. Atmospheric tides in a Mars general circulation model with data assimilation. *Advances in Space Research*, 36:2162–2168, 2005.

S. R. Lewis and P. L. Read. Equatorial jets in the dusty Martian atmosphere. *Journal of Geophysical Research*, 108, 2003. (E4), 5034, doi: 10.1029/2002JE001933.

S. R. Lewis, M. Collins, P. L. Read, F. Forget, F. Hourdin, R. Fournier, C. Hourdin, O. Talagrand, and J. P. Huot. A climate database for Mars. *Journal of Geophysical Research*, 104:24177–24194, 1999.

J. Lilensten and P. L. Blelly. The TEC and F2 parameters as tracers of the ionosphere and thermosphere. *Journal of Atmospheric and Solar-Terrestrial Physics*, 64:775–793, 2002.

J. Lilensten, C. Simon, O. Witasse, O. Dutuit, R. Thissen, and C. Alcaraz. A fast computation of the diurnal secondary ion production in the ionosphere of Titan. *Icarus*, 174:285–288, 2005.

R. J. Lillis, D. L. Mitchell, R. P. Lin, J. E. P. Connerney, and M. H. Acuña. Mapping crustal magnetic fields at Mars using electron reflectometry. *Geophysical Research Letters*, 31, 2004. L15702, doi:10.1029/2004GL020189.

R. J. Lillis, S. W. Bougher, D. L. Mitchell, D. A. Brain, R. P. Lin, and M. H. Acuña. Continuous monitoring of nightside upper thermospheric mass densities in the Martian southern hemisphere over 4 Martian years using electron reflectometry. *Icarus*, 194:562–574, 2008. doi:10.1016/j.icarus.2007.09.031.

R. J. Lillis, M. O. Fillingim, L. M. Peticolas, D. A. Brain, R. P. Lin, and S. W. Bougher. Nightside ionosphere of Mars: Modeling the effects of crustal magnetic fields and electron pitch angle distributions on electron impact ionization. *Journal of Geophysical Research*, 114, 2009. E11009, doi:10.1029/2009JE003379.

R. S. Lindzen. *Dynamics in Atmospheric Physics.* Cambridge University Press, 1990.

Y. Liu, A. F. Nagy, T. I. Gombosi, D. L. DeZeeuw, and K. G. Powell. The solar wind interaction with Mars: results of three-dimensional three-species MHD studies. *Adv. Space Res.*, 27(11):1837–1846, 2001.

M. López-Puertas and F. W. Taylor. *Non-LTE radiative transfer in the atmosphere*. World Scientific, 2001.

M. A. López-Valverde and M. López-Puertas. Radiative energy balance of CO_2 non-LTE infrared emissions in the Martian atmosphere. *Icarus*, 114:113–129, 1995.

M. A. López-Valverde and M. López-Puertas. A non-local thermodynamic equilibrium radiative transfer model for infrared emissions in the atmosphere of Mars 1. Theoretical basis and nighttime populations of vibrational levels. *J.Geophys.Res.*, 99:13093–13115, 1994a.

M. A. López-Valverde and M. López-Puertas. A non-local thermodynamic equilibrium radiative transfer model for infrared emissions in the atmosphere of Mars 2. Daytime populations of vibrational levels. *J.Geophys.Res.*, 99:13117–13132, 1994b.

M. A. López-Valverde and M. López-Puertas. CO_2 non-LTE cooling rate at 15-μm and its parameterization for the Mars atmosphere. Technical report, ESA, March 2001. March 31st.

M. A. López-Valverde, D. P. Edwards, M. López-Puertas, and C. Roldán. Non-local thermodynamic equilibrium in general circulation models of the Martian atmosphere 1. Effects of the local thermodynamic equilibrium approximation on thermal cooling and solar heating. *J.Geophys.Res.*, 103:16799–16811, 1998.

M. A. López-Valverde, M. López-Puertas, and C. Roldán. Non-LTE effects in the atmosphere of Mars. Technical report, ESA, November 1999. November 18th.

J. G. Luhmann, C. T. Russell, L. H. Brace, and O. L. Vaisberg. *Mars, Chapter* 31*: The Intrinsic Magnetic Filed and Solar-Wind Interaction of Mars*. University of Arizona Press, 1992.

D. Lummerzheim and J. Lilensten. Electron transport and energy degradation in the ionosphere: evaluation of the numerical solution, comparison with laboratory experiments and auroral observations. *Ann.Geophysicae*, 12:1039–1051, 1994a.

D. Lummerzheim and J. Lilensten. Electron transport and energy degradation in the ionosphere: evaluation of the numerical solution, comparison with laboratory experiments and auroral observations. *Ann. Geophysicae*, 12:1039–1051, 1994b.

D. Lummerzheim, M. H. Rees, and H. R. Anderson. Angular dependent transport of auroral electrons in the upper atmosphere. *Planetary Space Science*, 37(1):109–129, 1989.

R. Lundin, D. Winningham, S. Barabash, R. A. Frahm, H. Andersson, M. Holmstrom, A. Grigoriev, M. Yamauchi, H. Borg, J. R. Sharber, J. A. Sauvaud, A. Fedorov, E. Budnik, J. J. Thocaven, K. Asamura, H. Hayakawa, A. J. Coates, D. R. Linder, D. O. Kataria, C. Curtis, K. C. Hsieh, B. R. Sandel, M. Grande, M. Carter, D. H. Reading, H. Koskinen, E. Kallio, P. Riihela, W. Schmidt, T. Sales, J. Kozyra, N. Krupp, J. Woch, M. Franz, J. Luhmann, S. McKenna-Lawler, R. Cerulli-Irelli,

S. Orsini, M. Maggi, E. Roelof, D. Williams, S. Livi, P. Cson Brandt, P. Wurz, and P. Bochsler. Ionospheric plasma acceleration at Mars: ASPERA-3 results. *Icarus*, 182:308–319, 2006.

R. Lundin, S. Barabash, M. Holmstrom, H. Nilsson, M. Yamauchi, E. M. Dubinin, and M. Fraenz. Atmospheric origin of cold ion escape from Mars. *Geophysical Research Letters*, 36, 2009. L17202, doi:10.1029/2009GL039341.

Y. Ma, A. F. Nagy, K. C. Hansen, D. L. DeZeeuw, T. I. Gombosi, and K. G. Powell. Three dimensional multispecies MHD studies of the solar wind interaction with Mars in the presence of crustal fields. *Journal of Geophysical Research*, 107, 2002. A10, doi:10.1029/2002JA009293.

Y. Ma, A. F. Nagy, I. V. Sokolov, and K. C. Hansen. Three-dimensional, multispecies, high spatial resolution MHD studies of the solar wind interaction with Mars. *Journal of Geophysical Research*, 109, 2004. A07211, doi:10.1029/2003JA010367.

J. A. Magalhães, J. T. Schofield, and A. Seiff. Results of the Mars Pathfinder atmospheric structure investigation. *Journal of Geophysical Research*, 104(E4):8943–8955, 1999.

T. R. Marrero and E. A. Mason. Gaseous Diffusion Coefficients. *Journal of Physical Chemistry Reference Data*, 1(1):3–118, 1972.

T. L. McDunn, S. W. Bougher, J. Murphy, M. D. Smith, F. Forget, J. L. Bertaux, and F. Montmessin. Simulating the density and thermal strructure of the middle atmosphere ($\sim$80$-$130 km) of Mars using the MGCM-MTGCM: a comparison with MEX-SPICAM observations. *Icarus*, 206:5–17, 2010. doi:10.1016/j.icarus.2009.06.034.

A. S. Medvedev and P. Hartogh. Winter polar warmings and the meridional transport on Mars simulated with a general circulation model. *Icarus*, 186(1):97–110, 2007.

M. Mendillo, P. Withers, H. Rishbeth, and B. Reinisch. Effects of solar flares on the ionosphere of Mars. *Science*, 311:1135–1138, 2006.

E. Millour and F. Forget. Mars Climate Database v4.3 Validation Document. Technical report, LMD, Paris, 2008.

E. Millour, F. Forget, and S. R. Lewis. Mars Climate Database v4.3 Detailed Design Document. Technical report, ESTEC, 2008. Contract 11369/95/NL/JG.

T. Moffat. *The UCL Martian Thermosphere and Ionosphere Global Circulation Model: Development and Validation*. PhD thesis, University College London, UK, 2005.

T. Moffat-Griffin, A. D. Aylward, and W. Nicholson. Thermal structure and dynamics of the Martian upper atmosphere at solar minimum from global circulation model simulations. *Annales Geophysicae*, 28:2147–2158, 2007.

D. D. Morgan, D. A. Gurnett, D. L. Kirchner, J. L. Fox, E. Nielsen, and J. J. Plaut. Variation of the Martian ionospheric electron density from Mars Express radar soundings. *Journal of Geophysical Research*, 113, 2008. A09303, doi:10.1029/2008JA013313.

Y. Moudden and J. M. Forbes. Effects of vertically propagating thermal tides on the mean structure and dynamics of Mars' lower thermosphere. *Geophysical Research Letters*, 35, 2008a. L23805, doi:10.1029/2008GL036086.

Y. Moudden and J. M. Forbes. Topographic connections with density waves in Mars' aerobraking regime. *Journal of Geophysical Research*, 113, 2008b. E11009, doi:10.1029/2008JE003107.

I. C. F. Müller-Wodarg. *Modeling Perturbations Propagating Through the Mesopause into the Earth's Upper Atmosphere*. PhD thesis, University College London, UK, 1997.

I. C. F. Müller-Wodarg, M. Mendillo, R. V. Yelle, A. D. Aylward, and L. A. Young. The thermosphere of Titan simulated by a global three-dimensional time-dependent model. *J.Geophys.Res.*, 105:20833–20856, September 2000.

I. C. F. Müller-Wodarg, M. Mendillo, R. V. Yelle, and A. D. Aylward. A global circulation model of Saturn's thermosphere. *Icarus*, 180:147–160, January 2006.

I. C. F. Müller-Wodarg, D. F. Strobel, J. I. Moses, J. H. Waite, J. Crosvisier, R. V. Yelle, S. W. Bougher, and R. G. Roble. Neutral Atmospheres. *Space Science Reviews*, 139:191–234, 2008.

A. F. Nagy, D. Winterhalter, K. Sauer, T. E. Cravens, S. Brecht, C. Mazelle, D. Crider, E. Kallio, A. Zakharov, E. Dubinin, M. Verigin, G. Kotova, W. I. Axford, C. Bertucci, and J. G. Trotignon. The plasma environment of Mars. *Space Science Reviews*, 111:33–114, 2004.

W. P. Nicholson, G. Gronoff, J. Lilensten, A. D. Aylward, and C. Simon. A fast computation of the secondary ion production in the ionosphere of Mars. *Monthly Notices of the Royal Astronomical Society*, 400(1):369–382, 2009.

A. O. Nier and M. B. McElroy. Structure of the neutral upper atmosphere of Mars. *Science*, 194, 1976.

A. O. Nier and M. B. McElroy. Composition and structure of Mars' upper atmosphere: results from the neutral mass spectrometers on Viking 1 and 2. *Journal of Geophysical Research*, 82(28):4341–4349, 1977.

F. Němec, D. D. Morgan, D. A. Gurnett, and F. Duru. Nightside ionosphere of Mars: Radar soundings by the Mars Express spacecraft. *Journal of Geophysical Research*, 115, 2010. E12009, doi:10.1029/2010JE003663.

M. E. O'Neill and F. Chorlton. *Viscous and Compressible Fluid Dynamics*. Ellis Horwood Limited, Chichester, England, 1989.

C. B. Opal, W. K. Peterson, and E. C. Beaty. Measurements of secondary-electron spectra produced by electron impact ionization of a number of simple gases. *Journal of Chemical Physics*, 55:4100–4106, 1971. No. 8.

H. F. Parish, G. Schubert, M. P. Hickey, and R. L. Walterscheid. Propagating of tropospheric gravity waves into the upper atmosphere of Mars. *Icarus*, 203:28–37, 2009.

W. H. Parkinson, J. Rufus, and K. Yoshino. Absolute absorption cross section measurements of CO_2 in the wavelength region 163-200 nm and the temperature dependence. *Journal of Quantitative Spectroscopy & Radiative Transfer*, 290:251–256, 2003.

M. Pätzold, S. Tellmann, B. Häusler, D. Hinson, R. Schaa, and G. L. Tyler. A sporadic third layer in the ionosphere of Mars. *Science*, 310:837–839, 2005. doi:10.1126/science.1117755.

B. Peters. A Martian Thermosphere / Ionosphere General Circulation Model. Master's thesis, University College London, 2001.

G. Picardi, D. Biccari, R. Seu, J. Plaut, W. T. K. Johnson, R. L. Jordan, A. Safaeinili, D. A. Gurnett, R. Huff, R. Orosei, O. Bombaci, D. Calabrese, and E. Zampolini. MARSIS: Mars advanced radar for subsurface and ionosphere sounding. In A. Wilson, editor, *SP*-1240 *'Mars Express: A European Mission to the Red Planet'*, pages 51–70. ESA Publications Division, ESTEC, Noordwijk, The Netherlands, 2004. ISBN 92-9092-556-6 ISSN 0379-6566.

V. Pierrard. Evaporation of hydrogen and helium atoms from the atmospheres of Earth and Mars. *Planetary and Space Science*, 51:319–327, 2003.

H. S. Porter and F. W. Jump. Analytic total and angular elastic electron cross sections for planetary atmospheres. *Ann.Geophysicae*, 12:1039–1051, 1978.

H. S. Porter, F. Varosi, and H. G. Mayr. Iterative solution of the multistream transport equation 1. Comparison with laboratory beam injection experiments. *Journal of Geophysical Research*, 92:5933–5959, 1987. No. A6.

W. H. Press, S. A. Teukolsky, W. T. Vetterling, and B. P. Flannery. *Numerical recipes in Fortran. The art of scientific computing*. Cambridge University Press, 2nd edition, 1992.

R. J. Purser. Degradation of numerical differencing caused by Fourier filtering at high latitudes. *Monthly Weather Review*, 116:1057–1066, 1988a.

R. J. Purser. Accurate numerical differencing near a polar singularity of a skipped grid. *Monthly Weather Review*, 116:1067–1076, 1988b.

E. Quémerais, J. L. Bertaux, O. Korablev, E. Dimarellis, B. R. Cot, C. Sandel, and D. Fussen. Stellar occultations observed by SPICAM on Mars Express. *Journal of Geophysical Research*, 111(E09S04), 2006. doi:10.1029/2005JE002604.

J. A. Ratcliffe. *An introduction to the ionosphere and magnetosphere*. Cambridge University Press, 1972.

M. H. Rees, A. I. Stewart, and J. C. G. Walker. Secondary electrons in aurora. *Planet.Space.Sci*, 17: 1997–2008, 1969.

K. F. Riley, M. P. Hobson, and S. J. Bence. *Mathematical Methods for Physics and Engineering*. Cambridge University Press, 2000.

H. Rishbeth and O. K. Garriott. *Introduction to ionospheric physics*. Academic Press, New York and London, 1969.

G. Rottman. Solar ultraviolet irradiance and its temporal variation. *Journal of Atmospheric and Solar-Terrestrial Physics*, 61(1-2):37–44, 1999.

O. Rouzaud, J. Hylkema, J. Tessé, and F. Longueteau. Numerical simulation of radiative heating for atmospheric reentry in Martian atmosphere. *Computational Fluid Dynamics*, 6:257–262, 2004.

A. Safaeinili, W. Kofman, J. Mouginot, Y. Gim, A. Herique, A. B. Ivanov, J. J. Plaut, and G. Picardi. Estimation of the total electron content of the Martian ionosphere using radar sounder surface echoes. *Geophysical Research Letters*, 34, 2007. L23204, doi:10.1029/2007GL032154.

M. L. Salby. *Fundamentals of atmospheric physics*. Academic Press, 1996.

S. P. Sander, R. R. Friedl, D. M. Golden, M. J. Kurylo, G. K. Moortgat, H. Keller-Rudek, P. H. Wine, A. R. Ravishankara, C. E. Kolb, M. J. Molina, B. J. Finlayson-Pitts, R. E. Huie, and V. L. Orkin. Chemical kinetics and photochemical data for use in atmospheric studies evaluation number 15. In *JPL Publication* $06-2$. JPL, July 2006.

J. T. Schofield, D. Crisp, J. R. Barnes, R. M. Haberle, J. A. Magalhães, J. R. Murphy, A. Seiff, S. Larsen, and G. Wilson. The Mars Pathfinder Atmospheric Structure Investigation/Meteorology (ASI/MET) experiment. *Science*, 278:1752–1757, 1997.

R. W. Schunk and A. F. Nagy. *Ionospheres. Physics, Plasma Physics, and Chemistry*. Cambridge University Press, 2000.

A. Seiff and D. B. Kirk. Structure of the atmosphere of Mars in summer at mid-latitudes. *Journal of Geophysical Research*, 82(28):4364–4378, 1977.

R. Shapiro. Smoothing, filtering, and boundary effects. *Reviews of Geophysics and Space Physics*, 8: 359–387, May 1970.

V. I. Shematovich, D. V. Bisikalo, J. C. Gérard, C. Cox, S. W. Bougher, and F. Leblanc. Monte Carlo model of electron transport for the calculation of Mars dayglow emissions. *Journal of Geophysical Research*, 113(E02011), 2008.

C. Simon, O. Witasse, F. Leblanc, G. Gronoff, and J. L. Bertaux. Dayglow on Mars: Kinetic modelling with SPICAM UV limb data. *Planet. Space Sci.*, 2008. doi:10.1016/j.pss.2008.08.012.

C. G. A. Smith. *Modeling the thermospheres of giant planets*. PhD thesis, University College London, UK, 2006.

D. E. Smith, M. T. Zuber, S. C. Solomon, R. J. Phillips, J. W. Head, J. B. Garvin, W. Bruce Banerdt, D. O. Muhleman, G. H. Pettengill, G. A. Neumann, F. G. Lemoine, J. B. Abshire, O. Aharonson, C. David Brown, S. A. Hauck, A. B. Ivanov, P. J. McGovern, H. Jay Zwally, and T. C. Duxbury. The global topography of Mars and implications for surface evolution. *Science*, 284:1495–1503, 1999.

M. D. Smith. Interannual variability in TES atmospheric observations of Mars during 1999-2003. *Icarus*, 167:148–165, 2004.

M. D. Smith, J. C. Pearl, B. J. Conrath, and P. R. Christensen. Thermal Emission Spectrometer results: Mars atmospheric thermal structure and aerosol distribution. *Journal of Geophysical Research*, 106: 23929–23945, 2001.

F. L. Smith III and C. Smith. Numerical evaluation of Chapman's grazing incidence integral $ch(X, \chi)$. *J.Geophys.Res*, 77:3592–3597, July 1972.

Y. Soobiah, A. J. Coates, D. R. Linder, D. O. Kataria, J. D. Winningham, R. A. Frahm, J. R. Sharber, J. R. Scherrer, S. Barabash, R. Lundin, M. Holmström, H. Andersson, M. Yamauchi, A. Grigoriev, E. Kallio, H. Koskinen, T. Säles, P. Riihela, W. Schmidt, J. Kozyra, J. Luhmann, E. Roelof, D. Williams, S. Livi, C. C. Curtis, K. C. Hsieh, B. R. Sandel, M. Grande, M. Carter, J. A. Sauvaud, A. Fedorov, J. J. Thocaven, S. McKenna-Lawler, S. Orsini, R. Cerulli-Irelli, M. Maggi, P. Wurz, P. Bochsler, N. Krupp, J. Woch, M. Fränz, K. Asamura, and C. Dierker. Observations of magnetic anomaly signatures in Mars Express ASPERA-3 ELS data. *Icarus*, 182:396–405, 2006.

T. Stallard, S. Miller, M. Lystrup, Achilleos. N., E. J. Bunce, C. S. Arridge, M. K. Dougherty, S. W. H. Cowley, S. V. Badman, D. L. Talboys, R. H. Brown, K. H. Baines, B. J. Buratti, R. N. Clark, C. Sotin, P. D. Nicholson, and P. Drossart. Complex structure within Saturn's infrared aurora. *Nature*, 456 (7219):214–217, 2008.

K. Stamnes and M. H. Rees. Inelastic scattering effects on photoelectron spectra and ionospheric electron temperature. *Journal of Geophysical Research*, 88:6301–6309, 1983a. No. A8.

K. Stamnes and M. H. Rees. Inelastic scattering effects on photoelectron spectra and ionospheric electron temperature. *Journal of Geophysical Research*, 88:6301–6309, 1983b. No. A8.

K. Stamnes, S. Chee Tsay, W. Wiscombe, and K. Jayaweera. Numerically stable algorithm for discrete-ordinate-method radiative transfer in multiple scattering and emitting layered media. *Applied Optics*, 27:2502–2509, 1988. No. 12.

G. Stark, K. Yoshino, P. L. Smith, and K. Ito. Photoabsorption cross section measurements of CO_2 between 106.1 and 118.7 nm at 295 and 195 K. *Journal of Quantitative Spectroscopy & Radiative Transfer*, 103:67–73, 2006.

A. I. Stewart. Mariner 6 and 7 ultraviolet spectrometer experiment: Implications for the CO_2^+, CO and O airglow. *Journal of Geophysical Research*, 77:54–68, 1972.

A. I. F. Stewart, M. J. Alexander, R. R. Meier, L. J. Paxton, S. W. Bougher, and C. G. Fesen. Atomic oxygen in the Martian thermosphere. *J.Geophys.Res.*, 97(A1):91–102, 1992.

A. J Stewart and W. B. Hanson. Mars' upper atmosphere: mean and variations. *Adv. Space Res.*, 2: 87–101, 1982.

D. F. Strobel. Aeronomic systems on planets, moons and comets. In M. Mendillo, A. Nagy, and J. H. Waite, editors, *Atmospheres in the solar system: Comparative aeronomy*, pages 171–190. Geophysical Monograph Series 130, 2002.

W. E. Swartz. Optimization of energetic electron energy degradation calculations. *Journal of Geophysical Research*, 90:6587–6593, 1985. No. A7.

W. E. Swartz, J. S. Nisbet, and A. E. S. Green. Analytic expression for the energy-transfer rate from photoelectrons to thermal-electrons. *Journal of Geophysical Research*, 76:8425–8426, 1971. No. 34.

G. E. Thomas and K. Stamnes. *Radiative Transfer in the Atmosphere and Ocean*. Cambridge University Press, 1999.

C. Tian and C. R. Vidal. Electron impact dissociative ionization of CO_2: measurements with a focusing time-of-flight mass spectrometer. *Journal of Chemical Physics*, 108:927–936, 1998.

W. K. Tobiska. SOLAR2000 Research Grade Installation Manual and User Guide. Technical report, Space Environment Technologies, 2004a.

W. K. Tobiska. SOLAR2000 irradiances for climate change, aeronomy and space system engineering. *Adv. Space. Res.*, 34:1736–1746, 2004b.

W. K. Tobiska, T. Woods, F. Eparvier, R. Viereck, L. Floyd, D. Bouwer, G. Rottman, and O. R. White. The SOLAR2000 empirical solar irradiance model and forecast tool. *Journal of Atmospheric and Solar-Terrestrial Physics*, 62:1233–1250, 2000.

M. R. Torr and D. G. Torr. Ionization frequencies for solar cycle 21: Revised. *J.Geophys.Res.*, 90(A7): 6675–6678, 1985.

A. Valeille, M. R. Combi, V. Tenishev, S. W. Bougher, and A. F. Nagy. A study of suprathermal oxygen atoms in Mars upper thermosphere and exosphere over the range of limiting conditions. *Icarus*, 206: 18–27, 2010. doi:10.1016/j.icarus.2008.08.018.

J. M. Wallace and P. V. Hobbs. *Atmospheric science. An introductory survey.* Academic Press, New York, USA, 1977.

J. S. Wang and E. Nielsen. Evidence for topographic effects on the Martian ionosphere. *Planetary and Space Science*, 52:881–886, 2004a.

J. S. Wang and E. Nielsen. Possible hydrodynamic waves in the topside ionospheres of Mars and Venus. *Journal of Geophysical Research*, 107(A4), 2002.

J. S. Wang and E. Nielsen. Evidence for topographic effects on the Martian ionosphere. *Planetary and Space Science*, 52:881–886, 2004b.

L. Wang, D. C. Fritts, and R. H. Tolson. Nonmigrating tides inferred from the Mars Odyssey and Mars Global Surveyor aerobraking data. *Geophysical Research Letters*, 33, 2006. L23201, doi:10.1029/2006GL027753.

W. M. Washington and C. L. Parkinson. *An introduction to three-dimensional climate modeling.* University Science Books, 20 Edgehill Road, Mill Valley, CA, 94941, 1992.

R. P. Wayne. *Chemistry of atmospheres. An introduction to the chemistry of the atmospheres of Earth, the planets, and their satellites.* Oxford Science Publications, 1985.

D. L. Williamson and R. Laprise. Numerical approximations for global atmospheric general circulation models. In P. Mote and A. O'Neill, editors, *Numerical modeling of the global atmosphere in the climate system*, pages 127–219. Kluwer Academic Publishers, 2000.

J. Wilson, Y. Takahashi, F. Forget, M. Mischna, T. Kuroda, Y. Moudden, and A. Medvedev. Mars general circulation model intercomparison. In *Second Mars Atmosphere Modeling and Observations Workshop.* Instituto de Astrofisica de Andalucia, Laboratoire de Meteorologie Dynamique, AOPP, University of Oxford, Centre National D'Etudes Spatiales, European Space Agency, 27^{th} Feb 2006. Palacio de Congresos y Exposiciones, Granada, Spain.

R. J. Wilson. A general circulation model simulation of the Martian polar warming. *Geophysical Research Letters*, 24:123–127, 1997.

R. J. Wilson and K. Hamilton. Comprehensive model simulation of thermal tides in the Martian atmosphere. *Journal of the Atmospheric Sciences*, 53(9):1290–1326, 1996.

O. Witasse. *Modélisation des ionosphéres planétaires et de leur rayonnement: La Terre et Mars.* PhD thesis, Université Joseph Fourier, Grenoble, France, 2000.

O. Witasse, T. Cravens, M. Mendillo, J. Moses, A. Kliore, A. F. Nagy, and T. Breus. Solar system ionospheres. *Space Science Reviews*, 139:235–265, 2008.

P. Withers. Mars Global Surveyor and Mars Odyssey accelerometer observations of the martian upper atmosphere during aerobraking. *Geophysical Research Letters*, 33, 2006. L02201, doi: 10.1029/2005GL024447.

P. Withers, S. W. Bougher, and G. M. Keating. The effects of topographically-controlled thermal tides in the martian upper atmosphere as seen by the MGS accelerometer. *Icarus*, 164:14–32, 2003.

P. Withers, M. Mendillo, H. Rishbeth, D. P. Hinson, and J. Arkani-Hamed. Ionospheric characteristics above Martian crustal magnetic anomalies. *Geophysical Research Letters*, 32, 2005. L16204, doi: 10.1029/2005GL023483.

P. G. Withers. *Tides in the Martian atmosphere and other topics*. PhD thesis, The University of Arizona, USA, 2003.

T. N. Woods, W. K. Tobiska, G. J. Rottman, and J. R. Worden. Improved solar Lyman α irradiance modeling from 1947 through 1999 based on UARS observations. *Journal of Geophysical Research*, 105 (A12):27195–27215, 2000.

K. Yoshino, A. S. C. Cheung, J. R. Esmond, W. H. Parkinson, and D. E. Freeman. Improved Absorption cross sections of oxygen in the wavelength region 205-240 nm of the Herzberg continuum. *Planetary Space Science*, 36(12):1469–1475, 1988.

K. Yoshino, J. R. Esmond, A. S. C. Cheung, D. E. Freeman, and W. H. Parkinson. High resolution absorption cross-sections in the transmission window region of the Schumann-Runge bands and Herberg continuum of O_2. *Planetary Space Science*, 40:185–192, 1992.

K. Yoshino, J. R. Esmond, Y. Sun, W. H. Parkinson, K. Ito, and T. Matsui. Absorption cross-section measurements of carbon dioxide in the wavelength region 118.7-175.5 nm and the temperature dependence. *Journal of Quantitative Spectroscopy & Radiative Transfer*, 55(1):53–60, 1996.

K. Yoshino, W. H. Parkinson, K. Ito, and T. Matsui. Absolute absorption cross-section measurements of Schumann-Runge continuum of O_2 at 90 and 295 K. *Journal of Molecular Spectroscopy*, 229:238–243, 2005.

Y. L. Yung and W. B. DeMore, editors. *Photochemistry of Planetary Atmospheres*. Oxford University Press, 1999.

M. H. G. Zhang, J. G. Luhmann, A. J. Kliore, and J. Kim. A post-Pioneer Venus reassessment of the Martian dayside ionosphere as observed by radio occultation methods. *Journal of Geophysical Research*, 95:14829–14839, 1990. No. B9.

R. W. Zurek. Diurnal tide in the martian atmosphere. *Journal of Atmospheric Science*, 33:321–327, 1976.

R. W. Zurek. Free and Forced Modes in the Martian Atmosphere. *Journal of Geophysical Research*, 93: 9452–9462, 1988. No. D8.

R. W. Zurek. *Mars, Chapter* 24*: Comparative aspects of the climate of Mars: An introduction to the current atmosphere*. University of Arizona Press, 1992.

R. W. Zurek and C. B. Leovy. Thermal Tides in the Dusty Martian Atmosphere: A Verification of Theory. *Science*, 213:437–439, 1981.